

# ISI

## bilimi ve tekniđi dergisi

### Journal of Thermal Science and Technology

2021 Cilt/Volume 41 Sayı/Number 1  
ISSN 1300-3615

Türk Isı Bilimi ve Tekniđi Derneđi tarafından yılda iki kez  
Nisan ve Ekim aylarında yayınlanır.

*A publication of the Turkish Society for Thermal Sciences and  
Technology, published twice a year, in April and October.*

**TIBTD Adına Yayın Sahibi Sorumlu Yayımcı/Publisher:**  
Prof. Dr. Nuri Yücel, Gazi Üniversitesi

**Sorumlu Yazı İşleri Müdürü-Editör/Editor-in-Chief:**  
Prof. Dr. Zafer DURSUNKAYA  
Orta Dođu Teknik Üniversitesi Makina Mühendisliđi Bölümü  
06800 ANKARA Tel: 312 210 5232  
editor@tibtd.org.tr

**Yayın Türü:** Yaygın, süreli

#### Editörler Kurulu/Editorial Board:

Prof. Dr. Tuba OKUTUCU ÖZYURT, İstanbul Teknik  
Üniversitesi  
Prof. Dr. Almıla GÜVENÇ YAZICIOĐLU, Orta Dođu  
Teknik Üniversitesi  
Doç. Dr. Barbaros ÇETİN, İhsan Doğramacı Bilkent  
Üniversitesi

#### Teknik Danışman/Technical Advisor

Dr. Öğr. Üyesi Nureddin DİNLER, Gazi Üniversitesi

**Baskı/Printed at:** KALKAN Matbaacılık San. Tic. Ltd.  
Büyük Sanayi 1. Cadde, Alibey İş Ham No: 99/32 İskitler,  
ANKARA 312 342 16 56

#### TIBTD

**Türk Isı Bilimi ve Tekniđi Derneđi:** Dernek ve bu dergi,  
Türkiye'de ısı bilimi ve tekniđini geliřtirmek amacıyla 1976  
yılında Prof. Dr. Yalçın A. GÖĐÜŐ tarafından kurulmuřtur.

**Turkish Society of Thermal Sciences and Technology:** The  
association and the journal was founded by Prof. Dr. Yalçın  
A. GÖĐÜŐ in 1976 to improve thermal sciences and  
technology in Turkey.

**Adresi/Address:** TIBTD, Mühendislik Fakóltesi, Zemin Kat  
No.22 Gazi Üniversitesi, 06570 ANKARA  
**http://www.tibtd.org.tr**  
tibtd@tibtd.org.tr

**Üyelik aidatları için:** İş Bankası Maltepe Şubesi Hesap No:  
42120867567 IBAN: TR08 0006 4000 0014 2120 8675 67

#### Yönetim Kurulu/Executive Board:

Prof. Dr. Nuri YÜCEL (Bşk.), Prof. Dr. Zafer  
DURSUNKAYA (Bşk. Yard.), Prof. Dr. Ođuz TURGUT  
(Genel Sek.), Prof. Dr. İlhami HORUZ (Muhasisp Üye), Prof.  
Dr. L. Berrin ERBAY, Prof. Dr. Tuba OKUTUCU ÖZYURT,  
Prof. Dr. Selin ARADAĐ ÇELEBİOĐLU

## İÇİNDEKİLER / CONTENTS

Sayfa / Page

Releasing Hydrogen from NABH <sub>4</sub> via Hydrogel Based CoF <sub>2</sub> Catalyst <i>Hidrojel Esaslı CoF<sub>2</sub> Katalizör İle NABH<sub>4</sub>'den Hidrojen Salınımı</i> Tuđba AKKAŐ BOYNUEĐRİ and Metin GÜRÜ	1
Performance and Emission Characteristics of Pyridine and Isobutanol Added Gasoline- Ethanol-Water Blends in A Single Cylinder SI Gasoline Engine <i>Piridin ve İzobütanol Katkılı Benzin-Etanol-Su Karıřımlarının Tek Silindirli Benzin</i> <i>Motorundaki Performans ve Emisyonlarının İncelenmesi</i> Amir Khan GARAYEV, Silver GÜNEŐ and Çiđdem GÜLDÜR	11
Design and Optimization of PCM-Air Cold Energy Storage Device to Be Used for Peak Electricity Shaving <i>Elektrikte Pik Talebi Törpüleme İçin Kullanılacak FDM-Hava Sođuk Enerji Depolama Cihazı</i> <i>Tasarımı ve Optimizasyonu</i> Göker TÜRKAKAR	23
Computational Analysis of Pulverized Coal Co-Firing with Biomass in 150MWe Unit of Tuncbilek Thermal Power Plant <i>Tunçbilek Termik Santralinin 150MWe Ünitesinde Pülvürize Kömürün Biyokütle İle</i> <i>Eő Yanmasının Hesaplamalı Analizi</i> Cansu DENİZ CANAL, Yakup Erhan BOKE, Ozer AYDIN and Ali Cemal BENİM	37
Analytical and Numerical Analyses of the Heat Conduction of Carbon Nanotubes Under Applied Voltages <i>Karbon Nanotüplerin Isı İletiminin Uygulanan Voltajlar Altında Analitik ve Sayısal Analizi</i> Yahya ÖZ	51
Numerical Investigation of Non-Premixed Combustion Inside a Three Layered Porous Burner with Flamelet Model <i>Uç Katmanlı Gözenekli Yakıtıda Ön Karıřımsız Yanmanın Flamelet Modeli İle Sayısal</i> <i>İncelenmesi</i> Tanju ERGEN, Tamer ŐENER, Onur TUNCER and A. Cihat BAYTAŐ	63
SU <sup>2</sup> Real Gas Models' Performance Predictions on a Cold Gas Thruster <i>SU<sup>2</sup> Gerçek Gaz Modellerinin Sođuk Gaz İlicisi Performans Tahminleri</i> Aysu ÖZDEN, Özgür UđraŐ BARAN, Mehmet Halük AKSEL ve Mehmet Ali AK	77
A Numerical Investigation of Nanofluid Flow in Rectangular Finned Microchannel <i>Kanatçıklı Dikdörtgen Kesitli Mikrokanalda Nanoakıřkan Akıřının Sayısal İncelenmesi</i> Halime ÇELİK* and Nezaket PARLAK	89
A Comparative Study of Diffusion, Thermal Wave and Dual-Phase-Lag Heat Conduction in Thin Layer <i>İnce Tabakada Difüzyon, Termal Dalga ve Çift Fazlı-Lag Isı İletiminin Karıřılařtırılmalı</i> <i>Bir Çalıřması</i> R. YUVARAJ and D. SENTHILKUMAR	101
Çift Kabuk Cephe Sisteminin Bina Isıl Performansına Etkisinin Deneysel ve Sayısal Olarak İncelenmesi <i>Experimental and Analytical Examination of the Effect of Double Skin Facade System</i> <i>on Building Thermal Performance</i> Selin HÜLAGÜ, Türkan GÖKSAL ÖZBALTA ve Tahsin BAŐARAN	119
Effective Flow Control Around a Circular Cylinder by Using Both a Splitter Plate and Plasma Actuators as Passive and Active Control Methods <i>Pasif ve Aktif Kontrol Yöntemleri Olarak Hem Bir Ayırıcı Plaka Hem de plazma Aktüatörler</i> <i>Kullanılmasıyla Dairesel Bir Silindir Etrafında Etkili Akıř Kontrolünün Sađlanması</i> Hürrem AKBIYIK and Yahya Erkan AKANSU	133
Nodal Thermodynamic and Dynamic Analysis of a Free Displacer Stirling Engine <i>Serbest Displeysirli Bir Stirling Motorunun Nodal Termodinamik ve Dinamik Analizi</i> Can CINAR, A. Onur ÖZDEMİR, Halit KARABULUT and Mesut DUZGUN	141
Buhar Sıkıřtırılma Sođutma Test Ünitesine İleri Ekserji Metodunun Uygulanması <i>Application of Advanced Exergy Method to the Vapor Compression Cooling Test Unit</i> Betül SARAÇ	157

#### Amaç/Objective

Isı bilimi ve tekniđinin geliřtirilmesini teřvik etmek, ısı bilimi ve tekniđi alanında  
özgün, teorik, sayısal ve deneysel çalıřmaların yayınlanmasına olanak sađlamaktır.  
*To contribute to the improvement of thermal sciences and technology and publication*  
*of original, theoretical, numerical and experimental studies in thermal sciences and*  
*technology.*

#### İçerik/Content

Isı bilimi ve tekniđi alanındaki özgün ve derleme makaleler.  
*Original and review articles in thermal sciences and technology.*

#### Deđerlendirme/Evaluation

Dergi hakemli bir dergi olup, her bir makale konusunda uzman en az iki hakem  
tarafından deđerlendirilir.

*Each article published in this journal is evaluated by at least two referees.*

Dergimiz Science Citation Index Expanded (SCIE), Engineering Index (EI), EBSCO ve Mühendislik ve Temel  
Bilimler Veri Tabanı (TÜBİTAK-ULAKBİM) tarafından taranmaktadır.  
*Indexed by Science Citation Index Expanded (SCIE), Engineering Index (EI), EBSCO and Engineering and Natural*  
*Sciences Data Base (TÜBİTAK-ULAKBİM).*

# ACI KAYBIMIZ



**PROF. DR. NURİ SARYAL**  
**02.09.1929–22.12.2020**

Derneğimizin önceki Yönetim Kurulu Başkanlarından (1981-1993), ODTÜ Emekli Öğretim Üyesi ve önceki Rektörlerinden (1977-1979) Prof. Dr. Nuri Saryal yaşlılığa bağlı nedenlerle aramızdan ayrılmıştır, nur içinde yatmasını dileriz.

1929 da Azerbaycan'da doğan Prof. Dr. Nuri Saryal 1931 de ailesiyle beraber Ankara'ya göç etmiştir. İlkokulu TED Ankara Kolejinde, Ortaokul ve Liseyi Ankara Atatürk Lisesinde okumuş, bu yıllarda babasının Müdürü olduğu Elektrik ve Havagazı Fabrikası atmosferinde teknolojiye olan ilgisi ve altyapısı güçlenmiştir. Robert Kolejde (şimdi Boğaziçi Üniversitesi) Makine Mühendisliği lisans ve Purdue Üniversitesi/ABD'de yüksek lisans öğrenimlerinden sonra doktorasını 1953–1956 yıllarında Berlin Teknik Üniversitesinde buhar türbinlerinin değişim şartlarında sıcaklık dağılımını elektrik analogisiyle inceleyerek tamamlamış ve buluşunun patenti araştırmayı destekleyen şirket tarafından değerlendirilmiştir.

Askerlikten ve sanayide dört yıl başmühendis olarak çalıştıktan sonra, kuruluş yıllarındaki ODTÜ Makina Mühendisliği Bölümünden aldığı davet üzerine 1962 yılında Yard. Prof. olarak bu bölüme katılmış, 1966 yılında Doçentliğe, 1975 yılında Profesörlüğe yükseltilmiş, 1996 yılında emekli oluncaya kadar burada eğitim ve araştırmalarına devam etmiş, sonrasında da vefatına kadar araştırmadan kopmamıştır.

Prof. Saryal'ın ülkemize hizmetlerinin belki de en önemlisi ODTÜ'de 1977 yılında 9 ay yapılamayan eğitimi, hayati tehlikeye rağmen Rektörlüğü kabul edip başlatması ve öğretim üyelerinin desteğiyle ek dönemlerde telafi etmesidir. Hatta bu iki yıllık görev süresinde, artan bütçenin de yardımıyla üniversitenin akademik başarımında önemli artış sağlanmıştır. Öncesinde de Kemal Kurdaş'ın rektörlüğü sırasında beş buçuk yıl rektör yardımcısı olarak üniversitenin hızla gelişmesinde ve olumsuz saldırılara karşı direnmesinde katkıları önemlidir. TIBTD'nin on iki yıl başkanlığı yanı sıra Azerbaycan Kültür Derneği Danışma Kurulunun ve Türk-Alman İstişare Kurulunun Başkanlığı gibi sosyal etkinliklerle de ülkesine hizmet etmiştir.

Prof. Saryal'ın bilimsel ve uygulamaya yönelik araştırmaları birçok buluş ve patentler almasını sağlamış, bunları ticari amaçla değerlendirmemiştir. Kısa süreyle ordumuz tarafından desteklenen ORDOT projesinde yönettiği küçük fakat seçkin bir grup ile güdümlü tanksavar füzesi geliştirmekte başarıya ulaştı, fakat maalesef yurt dışı silah sanayii, yurt içindeki taşeronları aracılığıyla, projenin ve devlet desteğinin devamını engelledi, ülkemiz önemli bir gelişme fırsatını kaçırdı.

TIBTD adına Prof. Dr. Yalçın Göğüş

Değerli Okurlar,

Dört yıldır sürdürmekte olduğum dergimizin editörlüğünden ayrılıyorum. Bu süreçte birlikte çalıştığımız Editörler Kurulu üyeleri Prof. Dr. Tuba Okutucu Özyurt, Prof. Dr. Almıla Güvenç Yazıcıoğlu, Doç. Dr. Barbaros Çetin ve Doç. Dr. Cüneyt Sert'e teşekkür ediyor; görevi devralan Prof. Dr. Selin Aradağ Çelebioğlu'na ve yeni Editörler Kuruluna başarılar diliyorum.

Prof. Dr. Zafer Dursunkaya

Editör

Dear Readers,

I am completing my term as the editor of our journal. I'd like to thank the members of the Editorial Board, with whom I had the pleasure of working with, Dr. Tuba Okutucu Özyurt, Dr. Almıla Güvenç Yazıcıoğlu, Dr. Barbaros Çetin and Dr. Cüneyt Sert and welcome the new editor Dr. Selin Aradağ Çelebioğlu and members of the new Editorial Board.

Zafer Dursunkaya Ph.D.

Editor



## RELEASING HYDROGEN FROM $\text{NaBH}_4$ VIA HYDROGEL BASED $\text{CoF}_2$ CATALYST

Tuğba AKKAŞ BOYNUEĞRİ\* and Metin GÜRÜ\*\*

\*Etimaden, Development of Technology Department, Bahçekapı Mh., FSM Blv., No:179,  
Etimesgut, Ankara, tugbaakkas@etimaden.gov.tr, ORCID: 0000-0003-1047-6267

\*\* Gazi Üniversitesi Mühendislik Fakültesi Kimya Mühendisliği Bölümü  
Maltepe, 06570, Ankara, mguru@gazi.edu.tr, ORCID: 0000-0002-7335-7583

(Geliş Tarihi: 11.11.2019, Kabul Tarihi: 02.11.2020)

**Abstract:** In this paper, the dehydrogenation reaction of  $\text{NaBH}_4$  was performed in the presence of Co-ion loaded hydrogel catalyst. The reactions took place within 27, 18 and 9 hours at 25, 35 and 45 °C, respectively. In addition, the relation between the initial concentration of  $\text{NaBH}_4$  and released hydrogen was investigated at 45°C. A linear relationship between initial borohydride concentration and produced  $\text{H}_2$  was determined. Also, differential method was used to determine reaction rate constants and rate order. Hence, first-order-kinetics was proved by using experimental data. After that, the activation energy was found as 58.26 kJ/mol by means of the slope of the graph of  $\ln k$  versus  $1/T$  for the dehydrogenation reaction. This value is nearly equal to 50kJ/mol, which was expected in literature for the studies of the catalytic dehydrogenation. As the hydrophilic and macroporous structure of the prepared poly(acrylamide-co-acrylic acid) (p(AAm-co-AAc)-Co) hydrogel catalyst allowed inlet of  $\text{NaBH}_4$  solution up to its interior and release of produced  $\text{H}_2$ , effect of pore diffusion limitation was neglected. Dehydrogenation index of  $\text{NaBH}_4$  was calculated as 2526.31 mL  $\text{H}_2$ /g  $\text{NaBH}_4$  according to the amount of  $\text{NaBH}_4$  in the aqueous solution.

**Keywords:** Sodium borohydride, dehydrogenation, hydrogel catalyst, activation energy.

## HİDROJEL ESASLI $\text{CoF}_2$ KATALİZÖR İLE $\text{NaBH}_4$ 'DEN HİDROJEN SALINIMI

**Özet:** Bu makalede,  $\text{NaBH}_4$ 'ün dehidrojenasyon reaksiyonu, Co iyon yüklü hidrojel katalizör varlığında gerçekleştirilmiştir. Reaksiyonlar sırasıyla 25, 35 ve 45 °C'de 27, 18 ve 9 saat içinde gerçekleşmiştir. Bununla beraber,  $\text{NaBH}_4$ 'ün başlangıç konsantrasyonu ile salınan hidrojen arasındaki ilişki 45 °C' de araştırılmıştır. Başlangıç borohidür konsantrasyonu ile üretilen  $\text{H}_2$  arasında doğrusal bir ilişki olduğu belirlenmiştir. Ayrıca, reaksiyon hız sabitleri ve reaksiyon mertebesini belirlemek için diferansiyel yöntem kullanılmıştır. Böylece, deneysel veriler kullanılarak birinci derece kinetik kanıtlanmıştır. Daha sonra, dehidrojenasyon reaksiyonu için  $\ln k$ 'ya karşılık  $1/T$  grafiğinin eğiminden aktivasyon enerjisi 58.26 kJ/mol olarak bulunmuştur. Bu değer, katalitik dehidrojenasyon çalışmaları için literatürde beklenen 50 kJ/mol'e neredeyse eşittir. Hazırlanan poli (akrilamid-ko-akrilik asit) (p (AAm-co-AAc)-Co) hidrojel katalizörün hidrofilik ve makro-gözenekli yapısı  $\text{NaBH}_4$  çözeltisinin katalizörün iç kısımlarına kadar girebilmesine ve üretilen  $\text{H}_2$ 'nin salınmasına olanak verdiği için gözenek difüzyon sınırlaması etkisi ihmal edilmiştir.  $\text{NaBH}_4$ 'ün dehidrojenasyon indeksi, sulu çözeltideki  $\text{NaBH}_4$  miktarına göre 2526,31 mL  $\text{H}_2$ /g  $\text{NaBH}_4$  olarak hesaplanmıştır.

**Anahtar Kelimeler:** Sodyum borhidür, dehidrojenasyon, hidrojel katalizör, aktivasyon enerjisi.

### INTRODUCTION

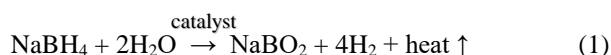
Renewable and alternative energy resources have attracted great attention owing to the fact that fossil fuels will not exist forever. In addition, the more population and energy demand have increased, the more energy resources will be needed. A variety of alternatives can be offered instead of gasoline such as natural gas etc. However, hydrogen is a strong candidate among them to overcome the energy problem all over the world (Nayar, 1981). Moreover, fossil fuels are the largest source of carbon dioxide, a greenhouse gas which contributes to climate change, and their production causes both environmental and human health impacts. Hydrogen is a promising candidate as an environment-friendly energy

carrier and within this scope lots of studies have been carried out by national labs, industry, and academia separately and in collaborations. Differently from electricity, hydrogen can be stored and easily transported in many forms to keep up with demand by time and place. For that reason, there is considerable interest in its use as a possible fuel to operate industry, heat homes, generate electricity etc. Essentially, two methods identified as physical and chemical are used for hydrogen storage. Hydrogen molecules can be stored in solid compounds using chemical reactions. The chemical bonds (covalent or ionic interactions) between hydrogen and a host compound form relatively safe storage option (Eberle et al., 2009). Among hydride compounds, especially metal borohydrides are the best hydrogen

carrier materials due to their properties including hydrogen-storage capacity, kinetics, cyclic behavior, toxicity, pressure and thermal response (Çakanyıldırım and Gürü, 2009). Recently, most of the studies have been carried out to find out a perfect hydrogen release method from sodium borohydrides (NaBH<sub>4</sub>). In other words, studies are aimed to come out desired uninterrupted energy particularly for the fuel cells (Çakanyıldırım and Gürü, 2010). Portable electricity generation based on hydrogen and proton exchange membrane fuel cell (PEMFC) has become essential for humans especially in the fields of medical appliances, electronic equipment and toys etc. (Fernandez-Moreno et al. 2013). In this scope, a portable batch mini-reactor for hydrogen generation from catalytic hydrolysis of NaBH<sub>4</sub> was developed in order to supply possible energy for less developed areas in the worldwide (Nunes et al., 2016). Especially, among of all chemical hydrides, sodium borohydride (NaBH<sub>4</sub>) is the most prevalently used hydrogen carrier because of its high hydrogen storage capacity of 10.8 wt%.

Principally two techniques are performed to release the hydrogen of NaBH<sub>4</sub>, thermal and catalytic dehydrogenation. Catalytic technique comes into the forefront because hydrogen and water can be recovered. On the other hand, thermal dehydrogenation process causes additional operation cost which depends on high-temperature requirement so the kind of dehydrogenation is not preferred (Kaya et al., 2011; Çakanyıldırım and Gürü, 2008).

It is seen that investigations have been performed predominantly by using NaBH<sub>4</sub> among metal borohydrides to release hydrogen. Hydrogen can be produced by the reaction between the water and NaBH<sub>4</sub> in the presence of a catalyst. In order to obtain hydrogen, an alkaline borohydride solution in water is prepared with its metal hydroxide to prevent sudden hydrogen release. High storage capacities could be achieved on a material basis via metal hydrides because the hydrogen from the hydride besides the hydrogen from the water is liberated (Schüth et al., 2004). According to the reaction given Eq.(1), theoretically four mole hydrogen was generated from the two of them coming from water and the other from NaBH<sub>4</sub>. The effect of catalyst is very substantial for dehydrogenation reactions of borohydrides.



1 g of fully hydrolyzed NaBH<sub>4</sub> produces 2.37 L of hydrogen gas at standard temperature and pressure according to the ideal hydrolysis reaction in the literature (Schlesinger et al., 1953). Experimentally, it is expected hydrated crystalline sodium metaborate as a by-product at the end of the reaction, the coefficient x given in Eq.(2) can change depending on the used catalyst type. The hydrogen in the structure of water can be recovered

in the presence of the catalyst during the reaction (Çakanyıldırım and Gürü, 2010).



The reaction, dehydrogenation of NaBH<sub>4</sub>, is exothermic and no heat supply is required. In recent years, researchers prepared a catalyst using a polymeric material as support of metal active sites. These polymers are considerable to make progress the efficiency of the catalyst (Sahiner and Yaşar, 2014). Functional groups in the hydrogel networks, such as –COOH, –OH, –SO<sub>3</sub>H, –SH and –NH<sub>2</sub>, differ according to used monomers and among them, carboxylic acid groups have been shown to be highly effective. Pt, Pd, Rh, Ru, Co, Ni and their compounds can be used as a metal source to prepare catalyst but Co and Ni have been widely chosen because of their low cost (Boynuegri et al., 2016; Sahiner et al., 2011). Also, it was reported that Co metal containing hydrogel produced hydrogen faster than Ni metal containing hydrogel composites for the given reaction (Seven and Sahiner, 2013). Obviously, the hydrogen release should be consistent for the fuel cell to operate in desired time so used catalyst has become vital from this perspective. On the other hand, comparable low activation energy values were gained for hydrogen release from NaBH<sub>4</sub> in the literature, when NaOH-p(AAM)-Co composite system and super-porous p(AAC)-Co metal composites were used as catalysts (Seven and Sahiner, 2013; Seven and Sahiner, 2014).

Previously, we reported the synthesis of Co-ion loaded poly(acrylamide-co-acrylic acid) (p(AAm-co-AAc)) hydrogel catalyst. According to amounts of cobalt ion, the catalyst was selected and used in the dehydrogenation of NaBH<sub>4</sub> reaction. The experimental and theoretical ratio of released hydrogen from 0.0965 g NaBH<sub>4</sub> at 25 °C was found by 90%. Released hydrogen amount was satisfactory in comparison to the given value in literature 240mL and 250 mL, respectively, in the presence of ppm level Co metal active sites (Boynuegri et al, 2016, Seven and Sahiner, 2013).

Still, catalyst is mostly investigated topic in the field of continuous hydrogen production from metal borohydrides. In the current study, synthesized and selected p(AAm-co-AAc)-Co ion loaded hydrogel catalyst was employed in the NaBH<sub>4</sub> dehydrogenation reactions at three different temperatures to investigate reaction kinetic. Our aims are identifying the behaviors of the catalyst and carrying out a study to obtain kinetic parameters in detail. Additionally, the effect of dried and swollen hydrogel catalysts usage on catalytic dehydrogenation was observed in this way it was reflected that slow or fast hydrogen release can be supplied by using these catalysts.

## MATERIALS AND METHOD

### Preparation of Hydrogel Based Catalyst

In this study, Co-ion loaded hydrogel catalyst was used to carry out dehydrogenation experiments. For this purpose, the catalyst's support material had synthesized by using the monomer, acrylamide (AAM) (Merck, purity  $\geq 99\%$ ) and acrylic acid (AAc) (Merck, purity  $\geq 99\%$ ), the crosslinker, N,N'-methylenebis acrylamide (MBAAm) (Sigma, purity  $\geq 99.5\%$ ), the initiator, ammonium persulfate (APS) (Sigma-Aldrich, purity 98%), and the accelerator, N,N,N',N'-tetramethylethylenediamine (TEMED) (Merck, purity  $\geq 99\%$ ) by means of free-radical crosslinking polymerization and then metal ion was loaded to polymeric matrices. Specific amount of  $\text{CoF}_2$ , metal ion source, was dissolved in 100 mL deionized water (DI-water), and 0.1 g hydrogel was placed in this solution for the duration of 24 h with the aim of metal ion uptake. Metal ion-loaded hydrogel was washed with deionized water 2 h or so to remove free metal ions from hydrogel support material. After all these steps, Atomic Absorption Spectroscopy (AAS, Varian, AA240FS) analysis was performed to determine amounts of metal ions. Thus, metal-ions was transferred from hydrogel material to solution, the metal-ion loaded hydrogel was placed in a 50 mL 5 M HCl solution for 12 h repetitively two times.

### Catalytic Dehydrogenation of $\text{NaBH}_4$

Dehydrogenation reactions were performed by using 50 ml 50 mM (0.0965 g)  $\text{NaBH}_4$  (Merck, purity  $\geq 98\%$ ) aqueous solution with 0.5 g NaOH (Merck, purity  $\geq 98\%$ ). As metal hydrides are sensitive to moisture in the air, the enclosed chambers, GLOVE-BOX (LABstar, MBRAUN), was used to weight  $\text{NaBH}_4$ . It is known that self-hydrolysis of borohydrides must be prevented by using its metal hydroxide. Here, the amount of NaOH is important as mentioned in the literature. It was represented that released hydrogen from  $\text{NaBH}_4$  solution diminished via increasing NaOH concentration because of suppression of hydrogen formation by hydroxide ions (Jeong et al., 2005). In other words, the hydrogen generation rate increases for lower NaOH concentrations in the alkaline  $\text{NaBH}_4$  solution and decreases after reaching a maximum value. During the process, pH value remains between 12 and 14 because of the presence of NaOH (Ingersoll et al., 2007). It can be inferred that amount of NaOH is arranged according to pH. In addition, this pH value can eliminate probable toxic fluorine (F) exposure according to graph of the equilibrium concentrations of various fluorine species versus solution pH given in literature (Zhao et al., 2016). F ions exist in the state of the soluble form in the aqueous solution having pH 7 and above.

The aqueous solution was poured into the reactor and then 0.1 g of p(AAm-co-AAc)-Co hydrogel catalyst was added to it. p(AAm-co-AAc)-Co hydrogel catalyst

involve 135.82 mg Co for per gram of hydrogel as given in the literature (Boynuegri et al., 2016). The reactor lid was closed tightly whenever catalyst was placed in the dehydrogenation reactor containing the solution. Released hydrogen was measured with the inverse burette system, as seen in Fig. 1.

Dehydrogenation reaction of  $\text{NaBH}_4$  occurs according to the Eq.(1) given above. P(AAm-co-AAc)-Co hydrogel catalyst should be washed with water at the end of the reaction. It can help removing borate compounds probably remained on the pores of the catalyst (Xu et al., 2007).

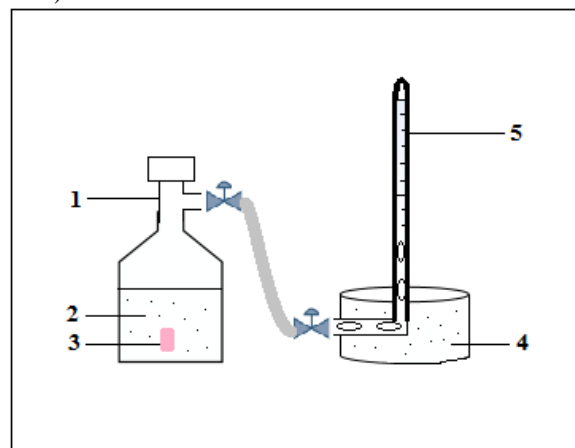


**Figure 1.** Inverse burette system: (1) Reactor, (2)  $\text{NaBH}_4$  and NaOH solution, (3) catalyst, (4) water reservoir, and (5) burette.

Theoretically, the amount of released hydrogen is twice as many as expected due to hydrolysis of the water. Dehydrogenation reactions were carried out both dried and swollen p(AAm-co-AAc)-Co catalysts to clarify its effect at 45°C. In addition, the effect of the catalyst's surface area was investigated according to measured hydrogen volume. For this purpose, two catalysts which have the same weight and the different surface area were prepared and the amounts of their released hydrogen were compared. We, also, investigated effect of hydrogel catalyst's surface area on the reaction of  $\text{NaBH}_4$  dehydrogenation

### Kinetic studies

Dehydrogenation reactions of  $\text{NaBH}_4$  were performed to clarify catalyst's kinetic properties at 25, 35, 45 °C. All of these experiments were performed to find out the reaction rate order and the activation energy ( $E_a$ ) of the related hydrolysis reaction. P(AAm-co-AAc)-Co hydrogel catalyst was used in each experiment and the amount of hydrogen released was continuously recorded. Furthermore, the pre-exponential factor (A) presented in Arrhenius equation was calculated according to the related equation given below (Eq.(3)).

$$k = A \cdot e^{-E_a/RT} \quad (3)$$

While the reactions were occurring at selected temperature, a water bath was used to maintain the constant temperature. Thus, the reaction temperature did not change by the exothermic nature of the hydrolysis reaction. The amounts of released hydrogen of the dehydrogenation reactions catalysed by p(AAm-co-AAc)-Co hydrogel catalyst were calculated for different NaBH<sub>4</sub> initial concentrations. Hence, the relation between the initial concentration of the reactant and the amount of released hydrogen was clarified.

## RESULTS AND DISCUSSION

Recently, studies demonstrate that metal ion loaded hydrogel catalysts have had a pleasant performance in dehydrogenation reactions of metal borohydrides because of their high capabilities to load metal active sites and high catalytic activities (Sahiner and Yaşar, 2014; Sahiner et al., 2011; Sahiner et al., 2012).

In this study, it is estimated that hydrogel support material's egg-shaped porous structure having pore size from 11 μm to 231 μm proven by SEM (Scanning electron microscope) analysis display a significant role as for activity of the catalyst.

In the end of catalyst preparation procedure given previously, amount of the Co-ion was found as 135.82 mg Co/g hydrogel according to Atomic Absorption Spectroscopy (AAS) (Varian, AA240FS) as given previous research study in detail (Boynuegri et al., 2016). Dehydrogenation reactions were carried out by using this characterized p(AAm-co-AAc)-Co hydrogel catalyst.

Released hydrogen amounts and reaction times were measured as 225, 230, 240 mL and 27, 18, 9 hours at 25, 35, 45 °C, respectively. When the dehydrogenation reaction of NaBH<sub>4</sub> temperature was increased, the reaction time decreased as seen in Fig. 2.

When the released hydrogen amount compared with the results given in the literature, the produced H<sub>2</sub> amount (No:3) via dehydrogenation of 0.095 g NaBH<sub>4</sub> (prepared as 50 mM NaBH<sub>4</sub> solution) was almost same with the amounts of released H<sub>2</sub> (No:1, 2, 4) given in the literature as seen in the Table 1.

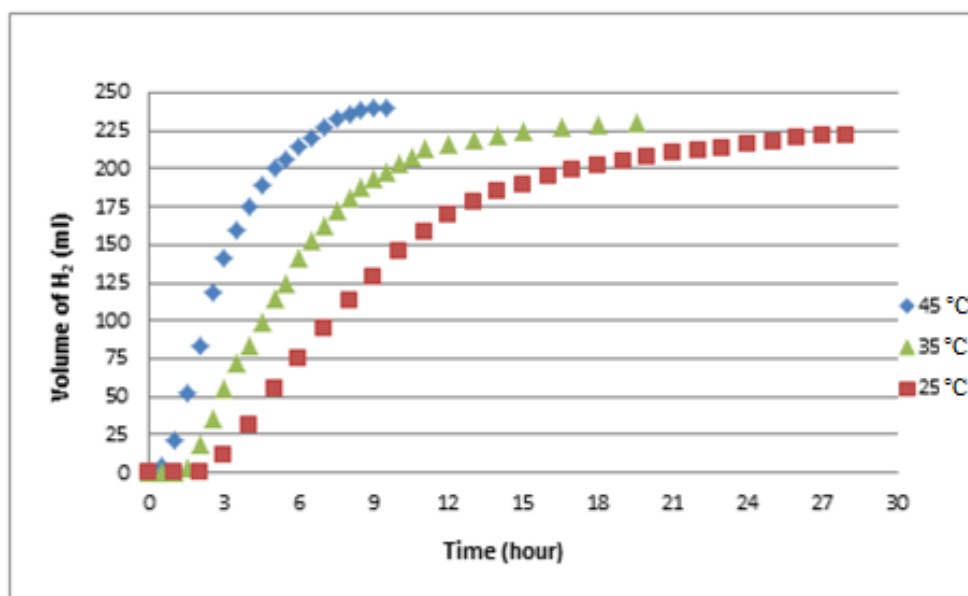


**Figure 2.** The effect of temperature on dehydrogenation reaction of NaBH<sub>4</sub> (T= 25, 35, 45 °C, 0.0965 g NaBH<sub>4</sub>, 0.5 g NaOH)

**Table 1.** Comparison of released H<sub>2</sub> amount and activation energy from 0.095 g NaBH<sub>4</sub>

No	Amount of mg Co/g hydrogel	Released H <sub>2</sub> (mL)	Released H <sub>2</sub> (x10 <sup>-2</sup> mol)	Activation Energy (kJ/mol)	Dehydrogenation Parameters
1	92.0	≈250	1.11	26.62	%5 NaOH, 30°C (Sahiner, Butun and Turhan, 2012)
2	128.0	247	1.10	38.14	%5 NaOH, 30°C (Sahiner, Ozay, Inger and Aktas, 2011)
3	135.8	230	1.03	58.26	%1 NaOH, 35°C
4	218.5	248	1.11	20.36	%5 NaOH, 30°C (Seven and Sahiner 2014)



According to the ideal hydrolysis, it is expected that 0.1 g of fully hydrolyzed  $\text{NaBH}_4$  produces mL of hydrogen gas at standard temperature and pressure. If we take into account temperature effect, produced  $\text{H}_2$  gas should be 241 mL and 245 mL at 30 °C and 35 °C be regarding ideal gas law. As a result, in this study (No: 3), amount of released  $\text{H}_2$  was nearly equal anticipated theoretical value. In addition, it is remarkable that the amount of released hydrogen is in coherent with expected theoretical value for released  $\text{H}_2$  was  $1.02 \times 10^{-2}$  mol according to Eq.(1).

This reaction can be accelerated by the increase of temperature or by addition of any acidic compound as stated in the literature (Balbay and Şahin , 2014). It is possible to arrange hydrogen release time which depends on amount of loaded active metal source, different features of polymer like the percentage of swelling degree and reaction temperature and etc. It was reported that hydrogen release time changed from nearly 60 min to 3000 min in literature.

When amounts of theoretically and experimentally released hydrogen were compared, the ratio was found by 90 %.  $\text{NaBH}_4$  was weighted at the inert atmosphere in GLOVE-BOX, so there was an experimental error nearly 5% because of the change in pressure. As a result of this, the yield could be taken by 95 %. After the hydrogen released via catalytic dehydrogenation process used Co-ion loaded hydrogel catalyst's color turned over from pink to black as seen in Fig. 3.

This figure represents in situ metal particle preparation in the p(AAm-co-AAc) hydrogel matrix, and their camera images. Metal ion absorption from their solution occurred via the functional groups such as  $-\text{COOH}$  and  $-\text{OH}$  which exist on the p(AAm-co-AAc) hydrogel matrix. As soon as metal ion loaded hydrogels contact with a reducing agent like  $\text{NaBH}_4$ , these metal particles can be formed in situ within the hydrogel. This kind of change in color corresponds to literature (Seven and Sahiner, 2013) .

Amount of loading metal particles was determined by using Atomic Absorption Spectroscopy (AAS) as given in the literature in detail (Boynuegri et al., 2016).

In addition, dehydrogenation reaction of  $\text{NaBH}_4$  was carried out at 45 °C to show the effect of area of p(AAm-co-AAc)-Co hydrogel catalyst on the production of hydrogen. The areas of these two catalysts were calculated by using mathematical equations according to their geometric shapes without any other measurement technique like BET (Brunauer, Emmett and Teller) or etc. The reason is that noticeably high the percentage of swelling degree in aqueous phase of the prepared hydrogel material (p(AAm-co-AAc)), 6500 %, could not allow proper analysis of BET.

In this study, probable impact of size or area of hydrogels investigated by using two catalysts having same weight but different size as given Table 2, 125 and 150  $\text{mm}^2$  , hydrogen was released by 91.0 % and 91.2 % yield, respectively.

**Table 2.** Effect of catalyst area on released hydrogen

Used $\text{NaBH}_4$ ( $\times 10^{-4}$ mol)	Area of catalyst ( $\text{mm}^2$ )	Volume of released $\text{H}_2$ (mL)	Yield (%)
8.46	125	80	91.0
8.19	150	78	91.2

It was inferred that released hydrogen does not change remarkably with catalyst surface area according to given results in Table 2. Besides, hydrogel catalyst was used as dried and swollen, and reaction time was determined as 9 and 25 hours, respectively as given Fig. 4. Thus, the option of using dried or swollen state of the catalyst can be done by the expectation of its place of use.

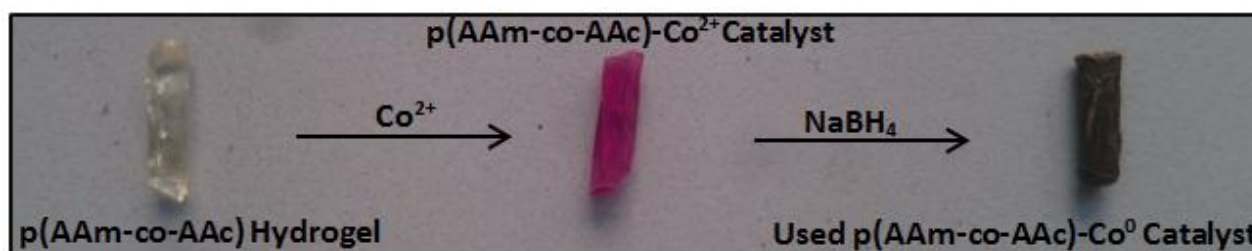


**Figure 3.** Color changing of hydrogel catalyst. Images of dried p(AAm-co-AAc) hydrogel, Co(II) ions absorbed p(AAm-co-AAc) hydrogel and the reduction of these ions within hydrogel matrices, respectively.

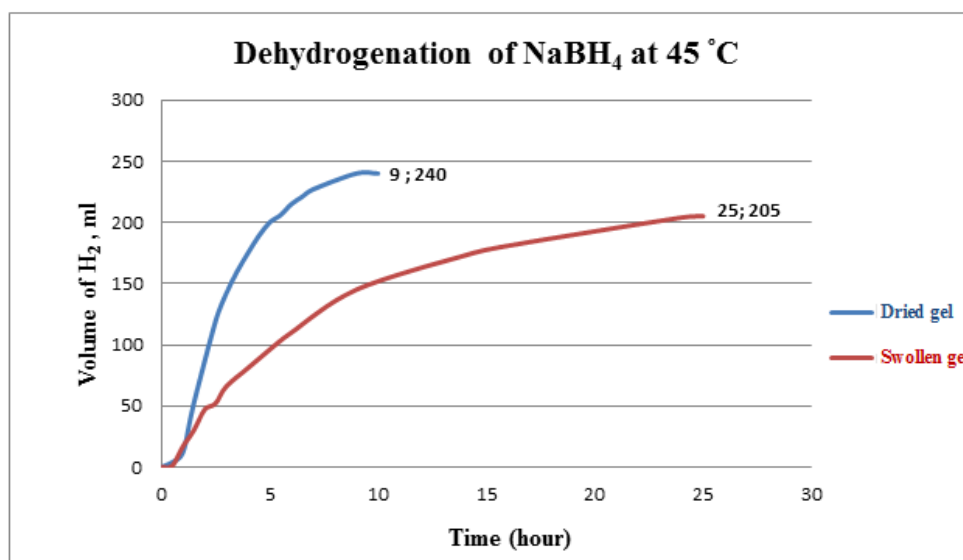


**Figure 4.** Dehydrogenation of NaBH<sub>4</sub> by using dried and swollen Co-ion loaded hydrogel catalyst (T=45 °C, 0.0965 g NaBH<sub>4</sub>, 0.5 g NaOH)

Previously, catalytic dehydrogenation reactions were performed by using dried hydrogel based catalyst, as given in Fig. 1. We used the same data to plot the blue line that represents produced H<sub>2</sub> versus time for the dehydrogenation reaction, carried out at 45 °C by using dried hydrogel in Fig. 4. In this experiment, hydrogel based catalyst was immersed in deionized water and then kept in it to swell.

It was predicted that swollen hydrogel caused smaller pore sizes in compared to pores in the structure of dried hydrogel so the released amount of hydrogen was less than that of dried hydrogel catalyst. In this scope, it is obvious that pore sizes important as for diffusion. It means that when the specific pore sizes in the structure of catalyst support materials decrease, the pore diffusion limitation will emerge because of their sizes. Previously, we determined pores sizes of freeze-dried hydrogel and selected using dried p(AAm-co-AAc) hydrogel catalyst.

Hence, we carried out the dehydrogenation reaction by neglecting the pore diffusion limitation.

The dehydrogenation reactions were carried out by taking different initial amount of NaBH<sub>4</sub> to produce H<sub>2</sub>. It was found that initial amount of NaBH<sub>4</sub> and amounts of released hydrogen increased linearly as seen in Fig. 5.

It is obvious that there is a linear relationship between used initial amount of NaBH<sub>4</sub> and the released hydrogen. In other words, H<sub>2</sub> production rate does not change with the increase in the amount of NaBH<sub>4</sub>. As a result of this, it can be approved that specific dehydrogenation rate does not change according to initial amount of NaBH<sub>4</sub>. In addition, it is clear that amount of the used metal catalyst source is already enough to proceed the reaction so its amount is not confining parameter for the dehydrogenation reaction of NaBH<sub>4</sub>.

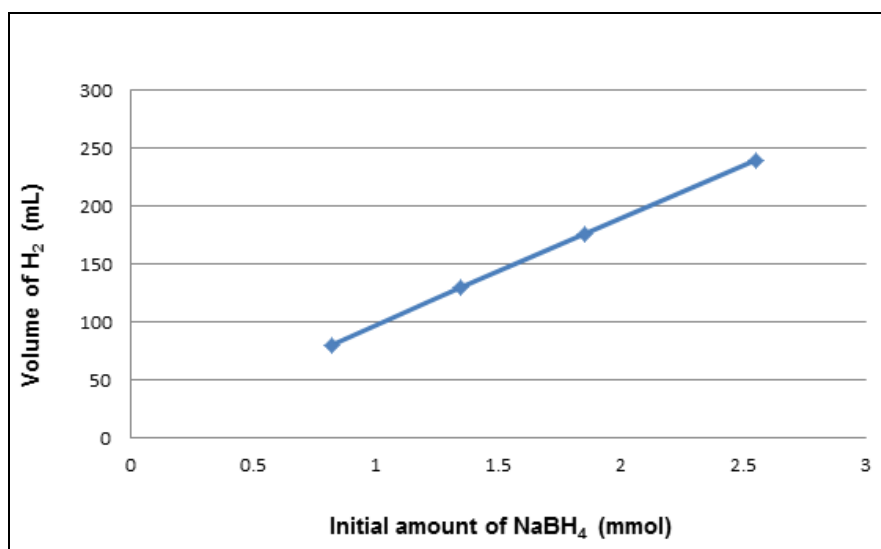


**Figure 5.** Released H<sub>2</sub> by changing initial amount of NaBH<sub>4</sub> (T= 45 °C, 0.5 g NaOH)

We assumed that the amount of H<sub>2</sub>O was very high in compared to the amount of NaBH<sub>4</sub> in aqueous solution so we neglected it in the reaction equation as given in the Eq.(4). As a result of this, the reaction equation turned into Eq.(5).

$$-\frac{dC_A}{dt} = kC_A^n C_B^m \quad (4)$$

$$-\frac{dC_A}{dt} = kC_A^n \quad (5)$$

According to the differential method, kinetic calculations were made to determine the rate constants and the reaction rate order. Graphs were plotted by using these data and reaction rate order (n) was found as 1 from the slope of these graphs.

Here, the graph which was plotted for the dehydrogenation reaction performed at 25 °C are demonstrated in Fig.6.

As a result of this, the differential equation was arranged as given Eq. (6) and (7). Rate constants were calculated depending on time and concentration differences by using experimental results for both three dehydrogenation reactions carried at 25 °C 35 °C and 45 °C.

$$-\frac{dC_A}{dt} = kC_A^n, n=1 \quad (6)$$

$$k = \left(-\frac{dC_A}{dt}\right)/C_A \quad (7)$$

These rate constants and other essential data for getting lnk versus 1/T graph are given in Table 3.

**Table 3.** Data for lnk versus 1/T graphs

T(K)	1/T(x10 <sup>-4</sup> )	k (x10 <sup>-1</sup> )	lnk
298	33.56	1.37	-1.98
308	32.47	3.27	-1.12
318	31.45	5.99	-0.51

It is known that the slope of the graph of lnk versus 1/T as given Fig. 7 is used to obtain the activation energy. However, if Arrhenius Equation is rearranged as seen Eq.(8), why we used the slope of this graph should be more apprehensible.

$$\ln k = \ln A - \frac{E_a}{R.T} \quad (8)$$

The activation energy was calculated as 58.26 kJ/mol by using the slope of lnk versus 1/T graph.

The activation energy is almost equal 50 kJ/mol as it is demanded and compatible with the literature (Seven and Sahiner, 2013). As mentioned before carboxylic acid groups have been shown to be highly effective in the networks of hydrogels and also NaOH-p(AAm)-Co composite system and super-porous p(AAc)-Co metal composites, as catalysts, enable to get low E<sub>a</sub> values respectively 20.07 ± 0.05 kJ/mol and 29.35 kJ/mol. However, prepared and used p(AAm-co-AAc)-Co hydrogel catalyst was not show E<sub>a</sub> value as low as reported in literature (Seven and Sahiner, 2014; Ingersoll et al., 2007).

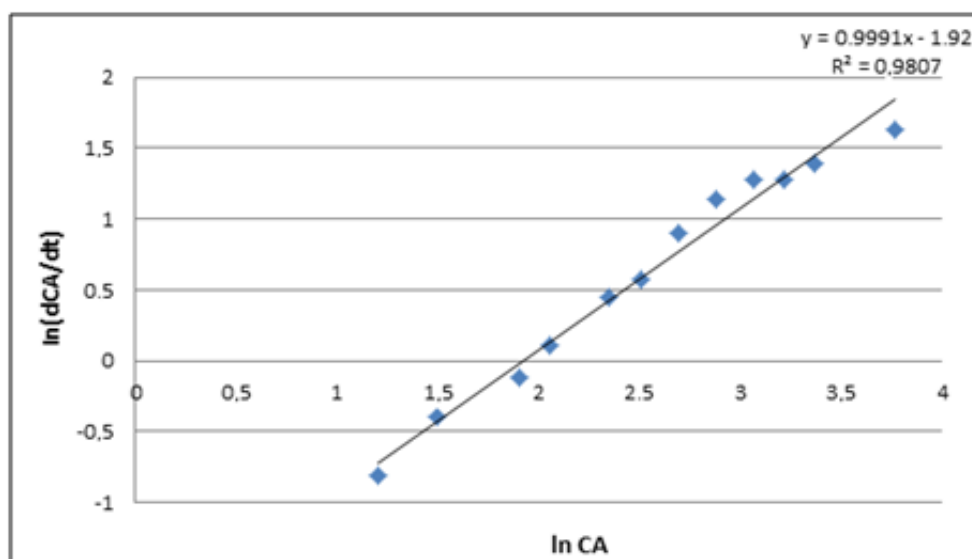


**Figure 6.** Graph of ln (dC<sub>A</sub>/dT) versus ln C<sub>A</sub> for the reaction at 25 °C

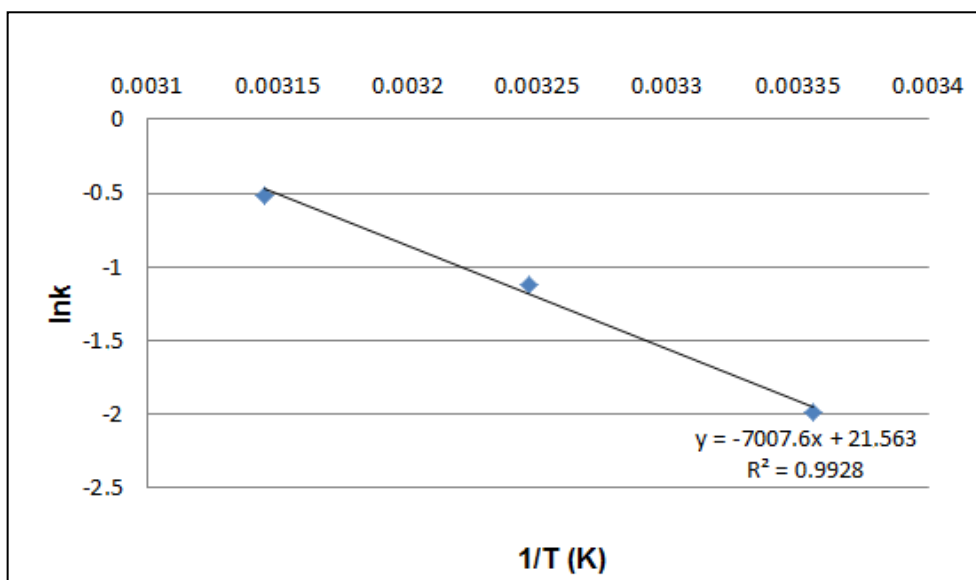


Figure 7. Graph of lnk versus 1/T

On the other hand, calculated  $E_a$  is lower than gained in the literature, 132 kJ/mol and 79 kJ/mol, when diatomite and  $\gamma\text{-Al}_2\text{O}_3$  supported heterogeneous Co based catalyst was used for the dehydrogenation of  $\text{NaBH}_4$  (Çakanyıldırım and Gürü, 2010). It is obvious that low-level  $E_a$  in a chemical reaction is ideal therefore this novel p(AAm-co-AAc)-Co catalyst should be preferred in comparison to heterogeneous Co based catalyst. This study mentioned that hydrogel based catalysts are the most preeminent among other types of catalysts as for this given feature.

In this study, the effect of pore diffusion limitation was not taken into consideration. Because, the hydrophilic and macroporous structure of the prepared p(AAm-co-AAc)-Co hydrogel catalyst allowed inlet of  $\text{NaBH}_4$  solution up to its interior and release of produced  $\text{H}_2$ .

## CONCLUSION

In this study, dehydrogenation reactions of  $\text{NaBH}_4$  were carried out at three different temperatures for investigation of kinetic parameters. P(AAm-co-AAc)-Co hydrogel catalyst was synthesized and prepared by using  $\text{CoF}_2$  metal source as given our previous study and was used to figure out hydrogen release characteristic of  $\text{NaBH}_4$  in this study. Dehydrogenation index of  $\text{NaBH}_4$  was calculated as 2526.31 mL  $\text{H}_2$ /g  $\text{NaBH}_4$  according to the amount of  $\text{NaBH}_4$  in the aqueous solution. It was seen that this value is relatively higher than given value in literature, 2387 mL  $\text{H}_2$ /g  $\text{NaBH}_4$ , when the comparison was made. On the other hand, used Co amount, 135.82mg, was less than that of literature, 167.93mg (Çakanyıldırım and Gürü, 2009). Despite the less amount of Co, p(AAm-co-AAc)-Co hydrogel catalyst provided higher dehydrogenation index for same amount of metal borohydride hydrolysis. In addition, the reaction rate was found as first order and activation energy of the reaction calculated as 58.26 kJ/mol.

Cobalt metal active sites can be taken away from hydrogel support material in an acidic solution so reusability of these sites is possible. Previously, p(AAm-co-AAc)-Co hydrogel catalyst was used in 10 consecutive runs to perform reusability test for the catalyst in the dehydrogenation reaction of  $\text{Ca}(\text{BH}_4)_2$ . It was reported that the produced hydrogen amount diminished gradually when the run number has risen. However, the activity of the catalyst was compatible with relatively similar catalyst given in the literature (Boynuegri and Guru, 2017).

To sum up, this novel catalyst has great potential especially for the generation of hydrogen from metal borohydrides.  $\text{NaBH}_4$  is mostly used source for  $\text{H}_2$  production among metal borohydrides. Thus, this study provides opportunity to compare experimental results and make evaluation for getting additional improvements in related scopes.

## ACKNOWLEDGEMENTS

This study was supported by ETİMADEN in Turkey Project No.400.02 [TGD.2013/4].

## REFERENCES

- Balbay A. and Şahin Ö., 2014, Hydrogen production from sodium borohydride in boric acid- water mixtures, *Energy Sources, Part A*, 36 (11), 1166-74.
- Boynuegri T.A., Karabulut A.F. and Gürü M., 2016, Synthesis of borohydride and catalytic dehydrogenation by hydrogel based catalyst, *J Electronic Materials*, 45 (8), 3949-56.
- Boynuegri T.A. and Guru M., 2017, Catalytic dehydrogenation of calcium borohydride by using hydrogel catalyst, *Int. J Hydrogen Energy*, 42, 17869-73.

- Çakanyıldırım Ç. and Gürü M., 2009, Production of  $\text{NaBH}_4$  and hydrogen release with catalyst, *Renew Energy*, 34, 2362-65.
- Çakanyıldırım Ç. and Gürü M., 2010, Supported  $\text{CoCl}_2$  catalyst for  $\text{NaBH}_4$  dehydrogenation, *Renew Energy*, 35, 839-844.
- Çakanyıldırım Ç. and Gürü M., 2008, Processing of  $\text{LiBH}_4$  from its elements by ball milling method, *Renew Energy*, 33, 2388-92.
- Eberle U., Felderhoff M. and Schüth F., 2009, Chemical and physical solutions for hydrogen storage, *Angewandte Chemie Int. Ed.*, 48(36), 6608-30.
- Fernandez-Moreno J., Guelbenzu G., Marti'n A.J., Folgado M.A., Ferreira-Aparicio P., Chaparro A.M., 2013, A portable system powered with hydrogen and one single air-breathing PEM fuel cell, *Appl Energy*, 109, 60-6.
- Ingersoll J.C., Mani N., Thenmozhiyal J.C. and Muthaiah A., 2007, Catalytic hydrolysis of sodium borohydride by a novel nickel-cobalt-boride catalyst, *J Power Sources*, 173(1), 450-57.
- Jeong S.U., Kim R.K., Cho E.A., Kim H.J., Nam S.W., OH I.H., Hong S.A. and Kim S.H., 2005, A study on hydrogen generation from  $\text{NaBH}_4$  solution using the high performance Co-B catalyst, *J Power Sources*, 144 (1), 129-134.
- Kaufman C.M., 1981, *Catalytic Generation of Hydrogen from the Hydrolysis of Sodium-Borohydride: Application in a Hydrogen/Oxygen Fuel Cell*, Ph.D. Thesis, The Louisiana State University and Agricultural and Mechanical College, Baton Rouge, LA.
- Kaya S., Gürü M. and Ar I., 2011, Synthesis of magnesium borohydride from its elements and its usage in hydrogen recycle, *Energy Sources, Part A*, 33 (23), 2157-70.
- Nayar M.G., 1981, Hydrogen Energy: An inexhaustible abundant clean energy system, *Proc. Indian Acad. Sci. Section C: Engineering Sciences*, 4, 57-73.
- Nunes H.X., Ferreira M.J.F., Rangel C.M. and Pinto A.M.F.R., 2016, Hydrogen generation and storage by aqueous sodium borohydride ( $\text{NaBH}_4$ ) hydrolysis for small portable fuel cells ( $\text{H}_2$  - PEMFC), *Int. J Hydrogen Energy*, 41, 15426-32.
- Sahiner N. and Yaşar A.O., 2014,  $\text{H}_2$  generation from  $\text{NaBH}_4$  and  $\text{NH}_3\text{BH}_3$  using metal catalysts prepared within p(VI) capsule particles, *Fuel Processing Tech.*, 125, 148-154.
- Sahiner N., Ozay O., Inger E. and Aktas N., 2011, Superabsorbent hydrogels for cobalt nanoparticle synthesis and hydrogen production from hydrolysis of sodium boron hydride, *Applied Catalysis B: Environmental*, 102, 201-6.
- Sahiner N., Butun S. and Turhan T., 2012, p(AAGA) hydrogel reactor for in situ Co and Ni nanoparticle preparation and use in hydrogen generation from the hydrolysis of sodium borohydride, *Chem. Engineering Sci.*, 82, 114-20.
- Schlesinger H.I., Brown H.C., Finholt A.E., Gilbreath J.R., Hoekstra H.R. and Hyde E.K., 1953, Sodium borohydride, its hydrolysis and use as a reducing agent and in the generation of hydrogen, *J. Am. Chem. Soc.*, 75, 215-19.
- Schüth F., Bogdanovic' B. and Felderhoff M., 2004, Light metal hydrides and complex hydrides for hydrogen storage, *The Royal Society of Chemistry*, 2249-58.
- Seven F. and Sahiner N., 2013, Poly(acrylamide-co-vinyl sulfonic acid) p(AAm-co-VSA) hydrogel templates for Co and Ni metal nanoparticle preparation and their use in hydrogen production, *Int. J Hydrogen Energy*, 38, 777-784.
- Seven F. and Sahiner N., 2014, NaOH modified P(acrylamide) hydrogel matrices for in situ metal nanoparticles preparation and their use in  $\text{H}_2$  generation from hydrolysis of  $\text{NaBH}_4$ , *J Applied Polymer Sci.*, 131 (22).
- Xu D., Zhang H., and Ye W., 2007, Hydrogen generation from hydrolysis of alkaline sodium borohydride solution using Pt/C catalyst, *Catal Commun.*, 8(11), 1767-71.
- Zhao M., McCormack A. and Keswani M., 2016, The formation mechanism of gradient porous Si in a contactless electrochemical process, *J. Mater. Chem. C*, 4, 4204.



## PERFORMANCE AND EMISSION CHARACTERISTICS OF PYRIDINE AND ISOBUTANOL ADDED GASOLINE-ETHANOL-WATER BLENDS IN A SINGLE CYLINDER SI GASOLINE ENGINE

Amirkhan GARAYEV\*, Silver GÜNEŞ\*\* and Çiğdem GÜLDÜR\*\*\*

\*\*\*Gazi University, Engineering Faculty, Chemical Engineering Department  
Maltepe, 06570, Ankara, Turkey

amirxan.karaev@gmail.com, ORCID: 0000-0001-8442-2638

cguldur@gazi.edu.tr, ORCID: 0000-0002-4404-6882

\*\*Gazi University, Graduate School of Natural and Applied Sciences  
Beşevler, 06500, Ankara, Turkey, silver@gazi.edu.tr, ORCID: 0000-0001-7608-3779

(Geliş Tarihi: 26.02.2020, Kabul Tarihi: 20.11.2020)

**Abstract:** The phase equilibria, engine performance and gas emissions of gasoline-ethanol-water blends with pyridine and isobutanol added for increased water tolerance, were investigated. It was observed that pyridine addition produced slightly higher ratios of ethanol and water in the stable fuel blend when compared to isobutanol, and the water ratio increased with the additive amount. Engine performances and combustion characteristics of the fuel blends were measured in a single cylinder, four-stroke, spark-ignition (SI) gasoline engine using different engine speeds and compared with the commercial gasoline. The best engine performance results were obtained from the HEP2 blend, consisting of 8.94% ethanol, 4.26% water and 4.21% pyridine. Using this fuel blend, engine torque increased by 8.3% at low speeds, engine effective power increased by %5 at high speeds while specific fuel consumption decreased by 14% at optimum engine speeds. Compared to the commercial gasoline blend, NO<sub>x</sub>, CO and HC emissions were found to be reduced by as much as %32, %17.9 and %45.9, respectively. Results showed that the fuel properties of pyridine and isobutanol added gasoline-ethanol-water blends were enhanced due to increased ethanol and water content and the HEP2 blend can be used in SI engines as an alternative to commercially available gasoline, with advantages of increased engine performance and reduced emission rates.

**Keywords:** Ethanol fuel, Hydrous ethanol, Gasoline additive, Pyridine, Isobutanol

## PİRİDİN VE İZOBÜTANOL KATKILI BENZİN-ETANOL-SU KARIŞIMLARININ TEK SİLİNDİRLİ BENZİN MOTORUNDAKİ PERFORMANS VE EMİSYONLARININ İNCELENMESİ

**Özet:** Su toleransını artırmak amacıyla piridin ve izobütanol ile katkılanmış benzin-etanol-su yakıt karışımlarının faz dengesi, motor performansı ve gaz emisyonları incelenmiştir. İzobütanol ile kıyaslandığında, piridin katkısının daha yüksek oranda etanol ve su içeren kararlı yakıt karışımları oluşturduğu, katkı miktarının artırılması ile su oranının da arttığı görülmüştür. Yakıt karışımlarının motor performansı ve yanma karakteristikleri tek silindri, dört zamanlı, buji ateşlemeli (SI) benzin motorunda, değişen motor hızlarında ölçülmüş ve ticari benzin ile karşılaştırılmıştır. En iyi motor performans sonuçları %8,94 etanol, %4,26 su ve %4,21 piridin içeren HEP2 karışımından elde edilmiştir. Söz konusu yakıt karışımı kullanılarak, düşük devirlerde motor torkunda %8,3 artış, yüksek devirlerde ise motor efektif gücünde %5 artış görülmüş, ayrıca optimum devirde özgül yakıt sarfiyatının %14 oranında azaldığı tespit edilmiştir. Ticari benzin karışımı ile kıyaslandığında, NO<sub>x</sub>, CO ve HC emisyonlarında sırasıyla %32, %17,9 ve %45,9'a varan oranlarda düşüş kaydedilmiştir. Elde edilen bulgular, piridin ve izobütanol katkılanmış benzin-etanol-su karışımlarında yakıt özelliklerinin artan etanol ve su oranına bağlı olarak iyileştiğini ve HEP2 karışımının buji ateşlemeli motorlarda daha yüksek motor performansı ve daha düşük emisyon oranı avantajı ile ticari benzin karışımlarına alternatif olarak kullanılabilceğini göstermektedir.

**Anahtar Kelimeler:** Etanolü yakıt, Sulu etanol, Benzin katkı maddesi, Piridin, İzobütanol

## NOMENCLATURE

### Symbols

$\lambda$	Air-fuel equivalence ratio
$b_e$	Specific fuel consumption [g/kWh]
$C_f$	Correction factor
$M_c$	Torque, corrected [Nm]
$m_f$	Fuel consumption rate [g/h]
$n$	Engine rotation speed [rpm]
$P_d$	Inlet dry air pressure [kPa]
$P_e$	Engine effective power [kW]
$T_0$	Ambient temperature [°C]

### Abbreviations

BSFC	Brake-specific fuel consumption [g/kWh]
CO	Carbon monoxides
G1	Commercial gasoline reference fuel
HC	Hydrocarbons
HE	Hydrous ethanol
HE <sub>n</sub>	Hydrous ethanol gasoline blend, n is the blend number
HE <sub>In</sub>	Isobutanol added hydrous ethanol gasoline blend, n is the blend number
HEP <sub>n</sub>	Pyridine added hydrous ethanol gasoline blend, n is the blend number
LHV	Lower heating value
NO <sub>x</sub>	Nitrogen oxides
PM	Particulate matter emissions
SFC	Specific fuel consumption [g/kWh]
SI	Spark-ignition
UHC	Unburned hydrocarbons

## INTRODUCTION

There is growing demand for petroleum based fuels such as gasoline and fuel-oil, although obtained from irreversibly depleting sources. Moreover, combustion of these fuels produces carbon monoxide (CO), unburned hydrocarbons (UHCs), nitrogen oxides (NO<sub>x</sub>s) and particulate matter (PMs) emissions which pose a serious threat to the environment and human health (Bergthorson, 2015; Martins, 2019). Therefore, ways to reduce the use of gasoline must be seriously taken into consideration for a sustainable energy policy. Several alternatives to the gasoline-powered engines have been proposed, including fuel cells, solar-photovoltaic cells, air-zinc batteries, plug-in hybrids and gas-electric hybrids. Despite the recent surge of interest in zero-emission, electrical power based technologies, the traditional internal combustion engine is still the dominant technology in transportation and seems to remain so for the next few decades, especially in developing countries. In this context, it is of crucial importance to develop alternative fuels for internal combustion engines, which would provide the demanded power in a more cost effective and environmental-friendly way.

Ethanol is a decent option as an alternative fuel for the internal combustion systems, which has already been in commercial use for a long time in different parts of the world (Awad, 2018). Ethanol can be produced from biomass in large quantities (Gnansounou, 2005). It can be mixed with gasoline in different ratios, creating fuel blends with similar properties to pure gasoline. Either in pure form or as a gasoline-ethanol blend, ethanol can be used in spark-ignition (SI) engines without requirement of any significant modification (Çelikten, 2015). One of the most important advantages of ethanol is that it has a higher octane number than gasoline, which can increase the performance of an internal engine.

For optimum operational parameters, namely the compression ratio, air/fuel ratio and ignition time, it is possible to obtain higher engine performance by ethanol based fuels than with gasoline (Bechtold, 1997; Thakur, 2017; Rao, 2020). It has been reported that ethanol-gasoline blends increase the brake-specific fuel consumption (BSFC), which is an important measure of the fuel efficiency (Eyidoğan, 2010). The ethanol-gasoline blends cause less soot formation compared to gasoline, according to Lemaire et al. (Lemaire, 2010). The ratio of the ethanol in the blend is also known to effect the engine performance. Higher ethanol ratios were reported to increase the heat value of the fuel and decrease the burning time in the combustion chamber (Bayraktar, 2005). Besides its beneficial effects on the engine performance, ethanol can also reduce the harmful emissions, depending on the blending ratio and engine operational parameters. Indeed, many studies in the literature reported that ethanol-gasoline blends have significantly lower CO, NO<sub>x</sub> and UHC emissions compared to gasoline (Wicker, 1999; Zhuang, 2013; Elfasakhany, 2015; Costagliola, 2016; Costa, 2020). It has been suggested that higher ethanol content in the fuel blends lead to lower emissions (Durbin, 2007; Clairotte, 2013). Due to these facts, many countries including United States, China, India and Brazil have set targets for the near future, to increase the ethanol or biofuel usage, typically by ratios varying between 10% and 20% (Suarez-Bertoa, 2015). Considering the growing emphasis on the renewable fuels, it is likely that the ethanol concentrations in the gasoline will increase in the future.

One of the drawbacks of using ethanol is the high cost associated with the production of anhydrous ethanol. Ethanol is primarily produced by distillation from biomass, and the end product typically comes with a water content of 5%. Further separation of ethanol and water causes an exponential rise in the cost because of the azeotropic properties of the solution. Even after the separation is achieved, anhydrous ethanol has a great tendency to absorb moisture, which can lead to difficulties with its storage and transport, adding further cost for use of anhydrous ethanol (Belincanta, 2016). To avoid these difficulties, hydrous ethanol (HE) containing gasoline blends were proposed as an alternative to anhydrous ethanol blends. Hydrous ethanol is much cheaper than anhydrous ethanol, due to skipping of the

costly drying process after the distillation (Melo, 2012). Hydrous ethanol is used in Brazil, with up to 4.9% (vol/vol) water content.

Although ethanol can be homogeneously mixed with either gasoline or water, the ternary gasoline-ethanol-water system does not mix well in every ratios. These blends have a low stability even in the presence of small concentrations of water, and high water content often leads to hazy and separated phases. This fact makes the direct use of stable gasoline-ethanol-water blends as fuel in gasoline engines an interesting research topic. According to Shirazi et al., most of the physiochemical properties of low to midlevel hydrous ethanol blends, apart from viscosity and phase separation temperature, are not significantly different from those corresponding to the anhydrous blends (Shirazi, 2018).

In the literature, hydrous ethanol blends have been generally associated with increased engine performance and reduced emissions, thanks to improvements in compression ratio, flame speed and combustion efficiency (Rajan, 1983; Chen, 2010, Schifter, 2013, Venugopal, 2013). Deng et al. reported better thermal efficiency and significantly decreased CO and HC emissions by hydrous ethanol gasoline, while the torque and power values were comparable with those obtained by pure gasoline (Deng, 2018). It is possible to increase the water tolerance of gasoline-ethanol-water blends by using additives. Muzikova et al. studied the phase stability of petrol blends with ethanol and found that ethyl tert-butyl ether reduced the phase separation temperature for the gasoline-ethanol-water blends (Muzikova, 2009). Nour et al. reported that pentanol and octanol addition to hydrous ethanol/diesel blend provides a better mixing stability with enhanced engine performance (Nour, 2019). Kyriakides et al. showed that oxygen rich molecules, such as ethyl tert-butyl ether, tertiary amyl methyl ether and palmitic promote water tolerance in the ethanol-gasoline blends, leading to reduced NO<sub>x</sub> emissions (Kyriakides, 2013). In the same study, it was reported that use of gasoline containing 40% ethanol and 40% ethanol-water did not require a modification in the engine for an efficient combustion.

There is still a need for further research on the stability, performance and emission characteristics of gasoline-ethanol-water blends with different compositions. This study concerns the SI engine performances and emission

characteristics of gasoline-ethanol-water blends with increased ethanol and water content through the use of isobutanol and pyridine as additives. Pyridine is highly hydrophylic and readily soluble in gasoline, ethanol and water. Isobutanol has a poor solubility in water, but a good solvent for organic molecules and may increase the inter-solubility of ethanol containing systems (Liu, 2016). Blends were subjected to performance tests in a single cylinder engine test bed. Engine performances, specific fuel consumptions and the emissions were measured and compared to those obtained with commercial gasoline.

## EXPERIMENTAL

### Preparation of Fuel Blends and the Effect of Additives on Phase Equilibria

Since the triple phase properties of gasoline-ethanol-water blend may vary with different labels of gasoline, seven blends with different gasoline/ethanol/water ratios were prepared to see the stability of ethanol and water in the gasoline without use of any additives. The gasoline ratios in the blends varied between 35% and 95% (Table 1). Blends were denominated as HEn, where HE stood for hydrous ethanol and n for the blend sample number. A certified commercial gasoline blend (95 octane) was used as the reference fuel. The reference fuel itself contains up to 5% ethanol. Anhydrous ethanol was obtained from Sigma-Aldrich in 99.9% purity. The blends were mechanically stirred and taken to a separating funnel after allowing enough time for any phase separation to occur. Then, the separated phases were distilled in a three-neck round bottom flask to determine the ratios of ethanol and water in the gasoline-rich phase.

To see the effect of pyridine and isobutanol, four different fuel blends were prepared in different additive ratios (Table 2). In all four blends, ethanol and water ratios were set to 10% and 5%, respectively. Blends were denominated as HEP and HEI, with P and I standing for pyridine and isobutanol, respectively. Pyridine (99.8%, anhydrous) and isobutanol (99%) were obtained from Sigma Aldrich. Physical properties of gasoline, ethanol, isobutanol and pyridine are summarized in Table 3. The ethanol, water and additive ratios in equilibrium with gasoline were measured using the same method as in the gasoline-ethanol-water blends, with the only exception that the distillation was conducted at 80 °C and 100 °C.

**Table 1.** Gasoline-ethanol-water blending ratios

Blend	Gasoline, %	Anhydrous ethanol, %	Water, %
HE1	95	5	0
HE2	85	10	5
HE3	75	15	10
HE4	65	20	15
HE5	55	25	20
HE6	45	30	25
HE7	35	35	30



**Table 2.** Gasoline-ethanol-water-additive blending ratios

Blend	Gasoline (%)	Ethanol %99.9 (%)	Water (%)	Pyridine (%)
HEP1	82.5	10	5	2.5
HEP2	80	10	5	5

Blend	Gasoline (%)	Ethanol %99.9 (%)	Water (%)	Isobutanol (%)
HEI1	82.5	10	5	2.5
HEI2	80	10	5	5

**Table 3.** Physical properties of ethanol, isobutanol and pyridine (Arning, 2009; Elfakhany, 2018; İnternet-1; İnternet-2; İnternet-3).

Physical property	Gasoline	Ethanol	Isobutanol	Pyridine
Formula	C <sub>8</sub> H <sub>15</sub>	C <sub>2</sub> H <sub>5</sub> OH	C <sub>4</sub> H <sub>10</sub> O	C <sub>5</sub> H <sub>5</sub> N
Boiling point, °C	25-210	78.24	107.8	115.2
Density, kg/m <sup>3</sup>	720-775	789.3	801.8	982.7
Vapor Pressure, mmHg	337-675	59.3	10.4	20.8
Solubility in water, ml/100 ml H <sub>2</sub> O	<0.1	Miscible	10.6	Miscible
LHV, MJ/kg	43.5	27.0	33.3	34.1

### Engine Performance and Emission Tests

Fuel blends were subjected to engine performance tests to measure the engine torques, engine effective powers and specific fuel consumptions. Measurements were conducted in engine speeds varying between 1600-3200 rpm, representing a typical operating range for a common automobile. All tests were performed in a Cussons P8160 single cylinder, four stroke, water cooling spark ignition (SI) gasoline engine equipped with a dynamometer (Fig.1). All tests were conducted in 6.4:1 compression ratio with full stoichiometric air-fuel equivalence ratio and engine load. For each test, the engine spark advance was adjusted to give the maximum torque. Other technical parameters of the engine are given in Table 4. The engine speeds and air/fuel ratios were controlled by a control panel. Engine torque and fuel consumption data were recorded after the engine reached steady state for the corresponding engine speed. Engine torque data were

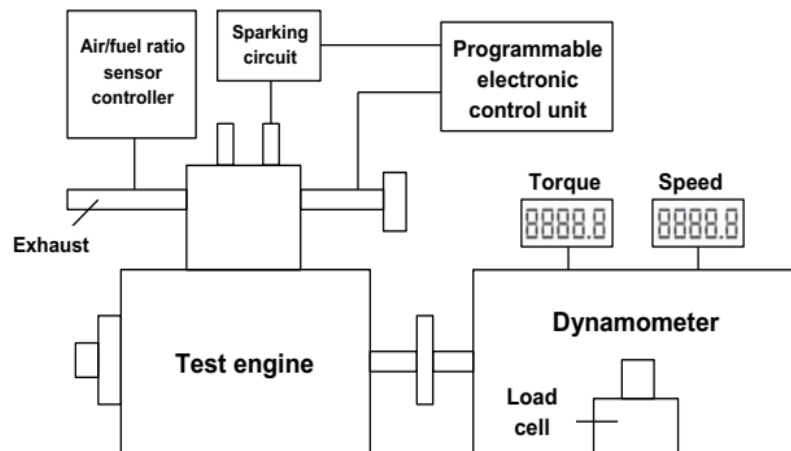
temperature and pressure corrected according to Eq. (1) (SAE, 2004). Engine effective power and specific fuel consumption were calculated from corrected torque values using Eq. (2). Specific fuel consumption values were calculated using Eq. (3).

$$C_f = \left(\frac{99}{P_d}\right) \left(\frac{T_0 + 273}{298}\right)^{0.5} \quad (1)$$

$$P_e = \frac{M_c n}{9549} \quad (2)$$

$$b_e = \frac{m_f}{P_e} \quad (3)$$

NO<sub>x</sub>, CO and HC emissions in the exhaust gas were analyzed using a Sun MGA 1500S model infrared-type exhaust analyzer. Technical specifications of the exhaust analyzer are also given in Table 5.

**Figure 1.** Schematic illustration of the experimental setup

**Table 4.** Technical parameters of the Cussons P8160 engine

Model	Cussons P8160
Number of cylinders	1
Maximum rotation torque	30 Nm
Maximum power	7.35 kW
Diameter x Stroke (mm)	77.79 x 82.55
Compression ratio	6.4:1
Fuel system	Injection

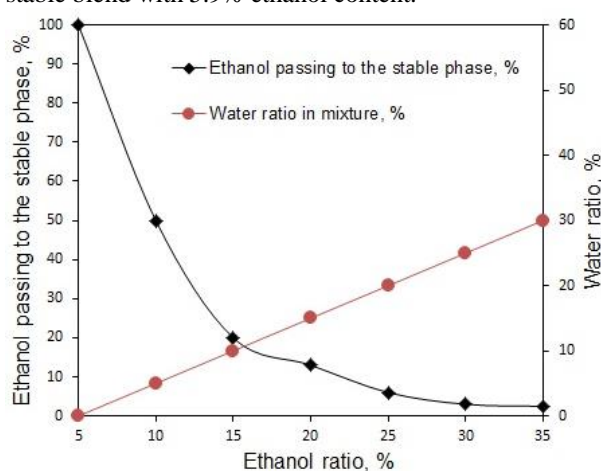
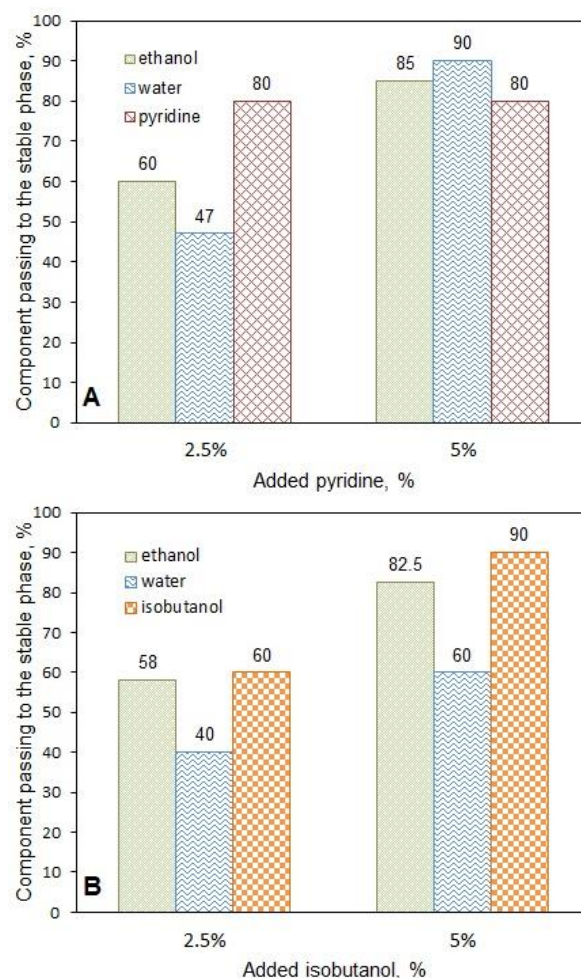
**Table 5.** Technical specifications of Sun MGA 1500S exhaust analyzer

Parameter	Measurement Range	Sensitivity
$\lambda$	0-15	0.001%
CO	0-14%	0.001%
NO <sub>x</sub>	0-50000 ppm	1
HC (ppm)	0-9999 ppm	1
CO <sub>2</sub> (% vol.)	0-19%	0.01%
O <sub>2</sub> (% vol.)	0-25%	0.01%

## RESULTS AND DISCUSSION

### Phase Equilibria in Fuel Blends

The stability of gasoline-ethanol-water blends depends on the amount of water added and the properties of gasoline. For all mixing ratios containing water, phase separation occurred. The exception was HE1 blend containing 5% ethanol and 95% gasoline, in which all of ethanol was mixed in the blend. For other blends, the volumetric ratios of ethanol in the stable (gasoline-rich) phases to the total ethanol volumes were measured after phase separation (Fig. 2). It was clearly seen that the amount of ethanol passing to the stable phase decreased with the increasing water addition, because of the formation of strong hydrogen bonds between water and ethanol. These hydrogen bonds create the separate ethanol-water rich bottom phase which increases in volume with the water addition. The optimum mixing ratio was determined to be 85% gasoline, 10% ethanol and 5% water (HE2) which was to be taken as basis to study the effect of pyridine and isobutanol addition. For this mixing ratio, 50% of initial ethanol passed to the gasoline rich phase, producing a stable blend with 5.9% ethanol content.

**Figure 2.** Percentage of ethanol passing to the stable gasoline-rich phase**Figure 3.** A) Percentages of ethanol, water and pyridine passing to the gasoline-rich phase B) Percentages of ethanol, water and isobutanol passing to the gasoline-rich phase

**Table 6.** Ratios of ethanol, water and pyridine/isobutanol in top (gasoline-rich) and bottom phases

Fuel Blend	Volume (ml)	Gasoline rich top phase (ml)	Bottom phase (ml)	Ethanol in top phase		Water in top phase		Pyridine / Isobutanol in top phase	
				ml	%	ml	%	ml	%
HEP1	194	180	14	12	6.67	4.7	2.61	4	2.22
HEP2	196	190	6	17	8.94	9	4.26	8	4.21
HEI1	196	179	17	11.5	6.42	4	2.23	3	1.68
HEI2	196	187	9	16.5	8.82	6	3.21	9	4.81

After addition of 2.5% pyridine to the HE2 blend, 60% of ethanol and 47% of water passed to the gasoline-rich stable phase (Fig. 3A). When the ratio of pyridine was increased to 5% (HEP2), the ratios of ethanol and water passing to the gasoline rich phase increased to 85% and 90%, respectively. HEP2 blend produced a stable fuel consisting of 82.6% gasoline, 8.94% ethanol, 4.26% water and 4.21% pyridine (Table 6). After addition of 2.5% isobutanol, 58% of ethanol and 40% of water passed to the gasoline-rich phase (Fig. 3B).

After the isobutanol ratio was increased to 5% (HEI2), these ratios increased to 82.5% and 60% for ethanol and water, respectively, producing a stable fuel solution of 79.2% gasoline, 8.82% ethanol, 3.21% water and 4.81% isobutanol. Overall, results show that pyridine addition is leading to slightly higher ratios of ethanol and water in the stable blend. The stronger hydrogen bonds forming between pyridine and water molecules may account for the increased ratio of water in the gasoline. On the other side, isobutanol molecules consist of a polar hydroxyl group which is hydrophilic, and a nonpolar alkyl group which is hydrophobic in nature. Isobutanol also increases the stable water content by acting as a cosolvent between the nonpolar hydrocarbon molecules and the polar water molecules.

### Engine Performance

The gasoline-ethanol-water blends prepared by addition of different amounts of pyridine and isobutanol were subjected to engine performance tests and results were compared to those obtained from the commercial gasoline blend, which was denoted as G1.

Variation of the engine torques for different fuel blends at different engine speeds is given in Fig. 4A. At full engine load, the highest engine torques were obtained at 2400 rpm for each blend. The blends containing ethanol and water generally performed better than commercial gasoline, while the best results were obtained from the blends with higher additive ratios (5% pyridine or isobutanol). Results show that the performance was significantly improved by ethanol, while the presence of stable water did not cause any deterioration even at high ratios. At the optimum engine speed, the maximum engine torque was obtained as 21.3 Nm from the HEP2 blend, which is 3% higher than that obtained from G1 (20.7 Nm). The gap between HEP2 and G1 is even higher at low engine speeds (8.3% for 1400 rpm) and high engine

speeds (4.4% for 3200 rpm). Low engine torques at low speeds are often associated with high rates of heat loss, where the compressed air/fuel loses a greater portion of its heat energy to the environment before ignition can occur. Considering that other possible factors such as valve leakages and ignition timing are equally affecting the blends, it can be deduced that the higher ethanol and water content in the blends increases the performance via reducing the heat losses at lower engine speeds. Another cause for low torque may be poor homogeneity due to low turbulence, which is often the case for low speeds. The fact that HEP2 gives higher performance than G1 at low engine speed shows that the blend is well mixed even at low turbulence.

On the other side, the engine effective power values are very close for all blends, except for those obtained at 3200 rpm (Fig. 4B). The HEP2 blend gave the highest effective power, which is 5% higher than G1 blend at the highest engine speed. The difference in effective power diminishes at lower engine speeds. The increased effective power in HEP2 and HEI2 blends can be explained by the improved combustion efficiency due to presence of hydrous ethanol. Yüksel et al. similarly reported that the ethanol-gasoline blends have higher effective power values compared to gasoline, especially at higher engine speeds (Yüksel, 2004).

The improved performance can be explained by increased octane number of the fuel due to increased hydrous ethanol content thanks to the additives. This results in a more advanced spark timing and increased knock resistance (Lanzanova, 2013; El-Faroug, 2016). Isobutanol also has a considerably high octane number, which is an additional contribution to the overall octane number of the blend (Allerman, 2020). Pyridine however, possibly has a greater effect on octane number by providing a higher hydrous ethanol ratio in the stable blend. Olberding et al., attributed the improvement of brake thermal efficiency in ethanol-water blend to reduced heat transfer losses due to lower burned gas temperature (Olberding, 2005). It is also reported that the increased amount of H, O and OH radicals resulting from dissociation of water can enhance the combustion (Zhang, 2012).

In terms of specific fuel consumption (SFC), the effect of increased ethanol and water ratio was more pronounced, as all gasoline-ethanol-water blends had

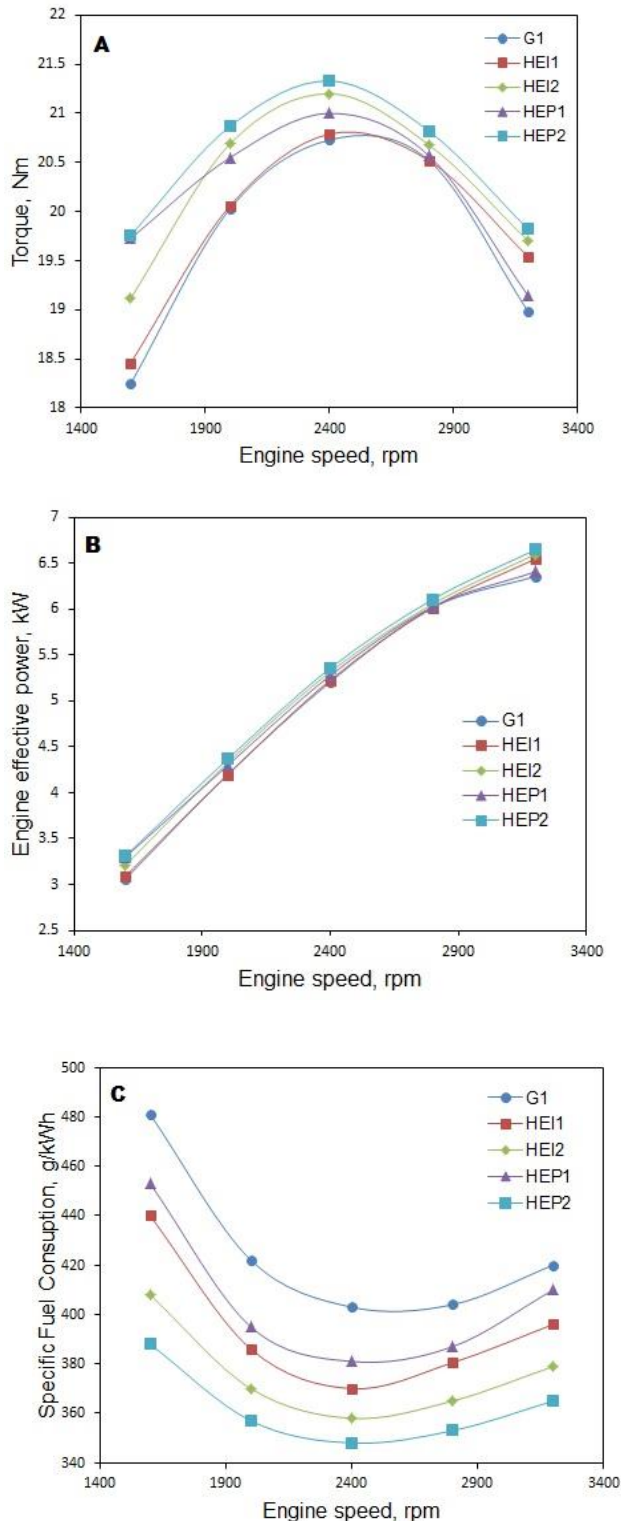


**Figure 4.** Variations of the torque (A), engine effective power (B) and specific fuel consumption (C) by the engine speed.

significantly lower fuel consumptions than the commercial gasoline blend (Fig. 4C). HEP2 and HEI2 blends containing the highest ethanol contents, gave the lowest fuel consumption values at the optimum engine speed of 2400 rpm with 347 g/kWh and 358 g/kWh, respectively. Those values are 14% and 11% lower than that of G1 blend, respectively. The increased ethanol

content is thought to be the main contributing factor to the lower specific fuel consumption. Melo et al., reported an increase in SFC with hydrous ethanol, which they attributed to the lower heating value of hydrous ethanol (Melo, 2012). Ambros et al., however, found that increasing the water ratio in the ethanol led to an increase in the in-cylinder pressure and a decrease in the SFC (Ambros, 2015). Lanzasova also reported a decreased brake specific fuel consumption, which was attributed to the improved spark advance due to increased water content (Lanzasova, 2013).

### NO<sub>x</sub>, CO and HC Emissions

The variation of the NO<sub>x</sub> emissions by the engine speed for different fuel blends is shown in Fig. 5A. The commercial gasoline blend has the highest NO<sub>x</sub> emission concentration among all blends. The 5% pyridine added blend (HEP2) has the lowest amount of emission, in spite of the presence of N containing pyridine. It has been reported that, higher temperatures promote the formation of NO and N<sub>2</sub>, in oxy-fuel combustion of pyridine, with the conversion ratios depending on the oxygen concentration (Wang, 2012). Therefore, the contribution of pyridine in the fuel seem to be less pronounced in total NO<sub>x</sub> formation, compared to the reaction between air nitrogen and oxygen containing hydrocarbons. In general, higher cylinder temperature is known to facilitate NO<sub>x</sub> formation, and the cylinder temperature increases with the engine speed, due to reduced heat transfer rate (Koç, 2009). The lower NO<sub>x</sub> emissions on the side of ethanol-water blends may be due to lower in-cylinder temperature, as hydrous ethanol – gasoline (specifically, 10% ethanol) reportedly gives higher peak in-cylinder pressures and peak heat release rates compared to ethanol-gasoline (Wang, 2015). According to Lin et al., the high molar heat capacity and high heat absorption during vaporization may be effective in minimizing the peak flame temperature and reducing the NO<sub>x</sub> formation rate (Lin, 2004). According to Fig. 5A, the difference in NO<sub>x</sub> emissions is more pronounced at low engine speeds, where the NO<sub>x</sub> emissions in HEP2 blend are 32% lower than that of commercial gasoline. Due to its limited heat absorbing capacity, water has a diminished effect at higher cylinder temperatures as evidenced by decreasing of NO<sub>x</sub> emission differences at high speeds.

Variation of CO emissions with the engine speed can be seen in Fig. 5B. It is well known that the CO emissions are mainly due to insufficient oxygen concentration needed for a complete combustion. CO emissions seem to be slightly lower at optimal engine speeds (around 2400-2600 rpm) thanks to an increased amount of air intake and increased oxygen concentration in the cylinder. The lowest CO emission is obtained from HEP2 blend at 2400 rpm with 1.25%, which is 17.9% lower than that produced by commercial G1 fuel. At high engine speeds (3200 rpm), the CO emissions are increased due to reduced air intake. At this speed, CO emissions from HEP2 blend are still lower by 9.54% compared to G1 blend. Similarly in literature, the

ethanol-gasoline blends are reported to reduce CO emissions (Li, 2015). Hydrous ethanol (10% ethanol) is also reported to produce slightly less CO emissions at low to medium load conditions (Wang, 2015). Water presence in the blend may decrease the CO emissions by way of altering the water-gas shift mechanism.

HC emissions are primarily resulting from incomplete burning of fuel, as in CO emissions. However, HC emissions are associated with low cylinder temperatures rather than low oxygen levels. To some degree, escaping fuel is another factor. In Fig. 5C, it can be seen that HC emissions decrease with engine speed due to increased temperature, even at low oxygen concentrations at high speeds. The increased CO emissions and reduced HC emissions at high speeds mainly result from the partial oxidation of HCs to CO at high temperature and low oxygen concentrations. The best results for HC emissions were again obtained from the HEP2 blend, whose HC emission is 21.9% lower than that of G1 fuel at 1600 rpm. The HC emissions are further reduced by 45.9% at 3200 rpm. This significant difference is due to several factors including higher heating value of ethanol, higher oxygen content and reduced heat transfer losses. Luo et al. similarly showed that hydrous ethanol blends decrease the HC emissions (Luo, 2017). Apart from the role of ethanol, water may also contribute to enhanced hydrocarbon combustion, because of the thermal dissociation of water molecules to produce free radicals.

## CONCLUSIONS

Pyridine and isobutanol were used as additives to prepare gasoline-ethanol-water blends with increased ethanol and water ratios. Pyridine addition gave slightly higher ratios of stable ethanol and water compared to those obtained by isobutanol. In all blends, ethanol ratios varied between 6.42% and 8.94%, while water ratios varied between 2.23% and 4.26%. The best engine performance were obtained by the HEP2 blend, consisting of 8.94% ethanol, 4.26% water and 4.21% pyridine. Use of this blend significantly increased the engine torque and reduced the specific fuel consumption, while the engine effective power was not considerably affected, compared to commercial gasoline blend. The HEP2 blend also produced significantly lower NO<sub>x</sub>, CO and HC emissions, with reductions up to 32%, 17.9% and 45.9% respectively, at optimal operating conditions. The isobutanol added HEI2 blend also performed better than commercial gasoline, in terms of engine performance and emissions. Considering the favorable results obtained by higher ethanol and water ratios, the effect of pyridine and isobutanol seem to be due to increasing the aforementioned components ratios rather than being directly involved in the combustion process. It can be concluded that HEP2 and HEI2 blends can be used as alternative fuels in place of commercially available gasoline.

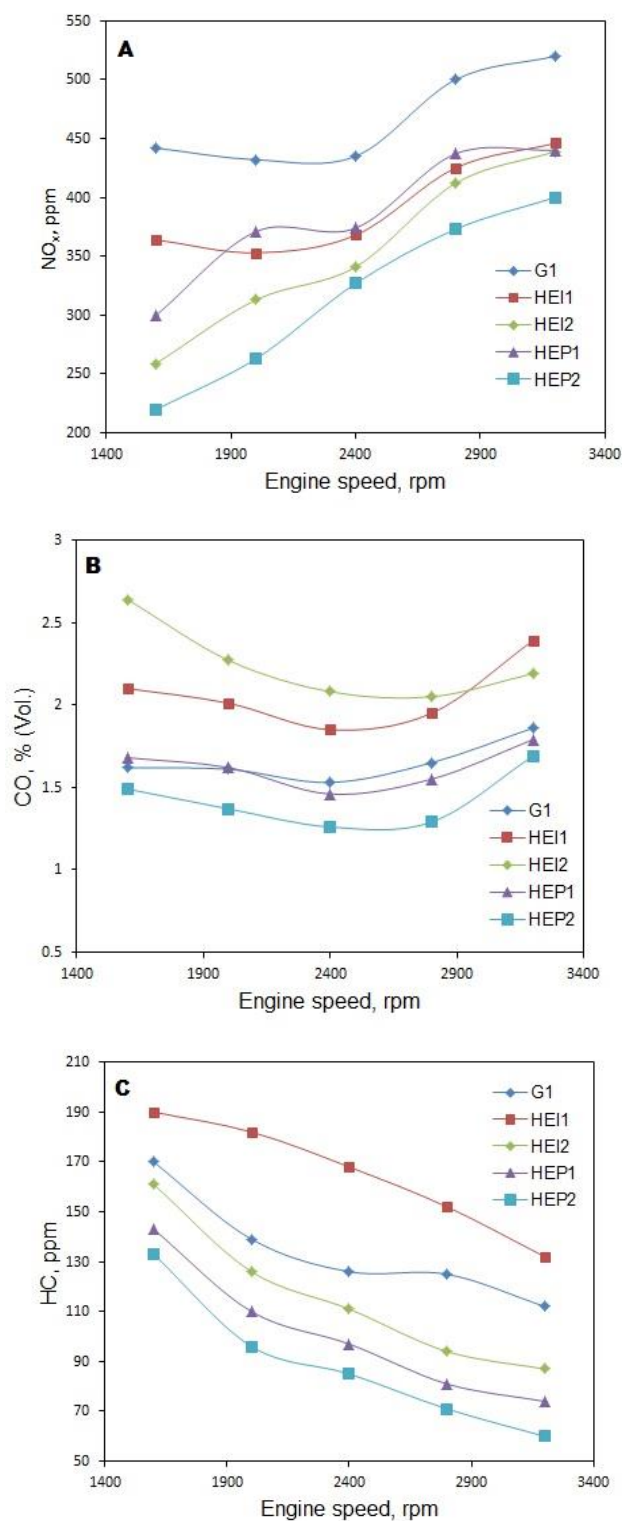


**Figure 5.** Variations of the NO<sub>x</sub> emissions (A), CO emissions (B) and HC emissions (C) by the engine speed.

## ACKNOWLEDGMENT

This study was conducted by the financial support of Gazi University Scientific Projects Unit (Project no. 06/2017-12). Assistance of Gazi University Automotive Engineering Department in conducting the engine tests is also greatly acknowledged.

## REFERENCES

- Alleman T. L., Singh A., Christensen E. D., Simmons E. and Johnston G., 2020, Octane Modeling of Isobutanol Blending into Gasoline, *Energy Fuels*, 34(7), 8424–8431.
- Ambros W., Lanzanova T., Fagundez J., Sari R., Pinheiro D. Martins M. and Salau N., 2015, Experimental Analysis and Modeling of Internal Combustion Engine Operating with Wet Ethanol, *Fuel*, 158, 270-278.
- Arning J.,P., Peters W., Rieger B., Schmidt T., Schopf N. and Sternberg J., 2009, *Saacke Combustion and Energy Systems Pocket Formula Guide*, Saacke GmbH, Bremen.
- Awad O.I., Mamat R., M. Ali O., Sidik N.A.C., Yusaf T., Kadirgama K. and Kettner M., 2018, Alcohol and Ether as Alternative Fuels in Spark Ignition Engine: A Review, *Renew. Sust. Energ. Rev.*, 82, 2586-2605.
- Bayraktar H., 2005, Experimental and Theoretical Investigation of Using Gasoline Ethanol Blends in Spark Ignition Engines. *Renew. Energy*, 30(11), 1733-1747.
- Bechtold R.L., 1997, *Alternative Fuels Guidebook*, Society of Automotive Engineers Inc., pp. 47-56.
- Belincanta J., Alchorne J.A. and da Silva M.T., 2016, The Brazilian Experience with Ethanol Fuel: Aspects of Production, Use, Quality and Distribution Logistics, *Braz. J. of Chem. Eng.*, 33(4), 1091-1102.
- Bergthorson J.M. and Thomson, M.J., 2015, A Review of the Combustion and Emissions Properties of Advanced Transportation Biofuels and Their Impact on Existing and Future Engines. *Renew. Sust. Energ. Rev.*, 42, 1393-1417.
- Chen R.H., Chiang L.B., Wu M.H. and Lin T.H., 2010, Gasoline Displacement and NO<sub>x</sub> Reduction in an SI Engine by Aqueous Alcohol Injection. *Fuel*, 89 (3), 604-610.
- Clairotte M., Adam T.W., Zardini A.A., Manfredi U., Martini G., Krasenbrink A., et al., 2013, Effects of Low Temperature on the Cold Start Gaseous Emissions from Light Duty Vehicles Fuelled by Ethanol-Blended Gasoline. *Appl. Energy*, 102:44–54.
- Costa R.C. and Sodré J.R., 2010, Hydrous Ethanol vs. Gasoline-Ethanol Blend: Engine Performance and Emissions. *Fuel*, 89(2), 287–293.
- Costagliola M.A., Prati M.V., Florio S., Scorletti P. and Terna D., 2016, Iodice P., Buono D. and Senatore, A. Performances and Emissions of a 4-Stroke Motorcycle Fuelled with Ethanol/Gasoline Blends. *Fuel*, 183, 470–477.
- Çelikten İ., Karaaslan E., Solmaz H., Okur M. and Polat S., 2015, Experimental Investigation of the Effects of Gasoline Additives on Engine Performance and Exhaust Emissions. *J. Therm. Sci. Tech.*, 35(1), 87-95.
- Deng X., Chen Z., Wang X., Zhen H. and Xie R., 2018, Exhaust Noise, Performance and Emission Characteristics of Spark Ignition Engine Fuelled with Pure Gasoline and Hydrous Ethanol Gasoline Blends, *Case Stud. Therm. Eng.*, 12, 55-63.
- Durbin T.D, Miller J.W., Younglove T., Huai T. and Cocker K., 2007, Effects of Fuel Ethanol Content and Volatility on Regulated and Unregulated Exhaust Emissions for the Latest Technology Gasoline Vehicles. *Environ. Sci. Technol.*, 41:4059–64.
- El-Faroug M.O, Yan F., Luo M. and Turkson R.F., 2016, Spark Ignition Engine Combustion, Performance and Emission Products from Hydrous Ethanol and Its Blends with Gasoline, *Energies*, 9, 984.
- Elfasakhany A., 2015, Investigations on the Effects of Ethanol-Methanol-Gasoline Blends in a Spark-Ignition Engine: Performance and Emissions Analysis. *Eng. Sci. Technol. Int. J.*, 18(4), 713-719.
- Elfasakhany A., 2018, Exhaust Emissions and Performance of Ternary Isobutanol-Biomethanol-Gasoline and n-butanol-Bioethanol-Gasoline Fuel Blends in Spark-Ignition Engines: Assessment and Comparison, *Energy*, 830-844.
- Eyidogan M., Ozsezen, A.N., Canakci, M. and Turkcan, A., 2010, Impact of Alcohol–Gasoline Fuel Blends on the Performance and Combustion Characteristics of an SI Engine. *Fuel*, 89(10), 2713–2720.
- Gnansounou E. and Dauriat A., 2005, Ethanol Fuel from Biomass: A Review. *J. Sci. Ind. Res.*, 64(11), 809-821.
- İnternet-1, 2020, <https://pubchem.ncbi.nlm.nih.gov/compound/702>.
- İnternet-2, 2020, <https://pubchem.ncbi.nlm.nih.gov/compound/Isobutanol> 1.
- İnternet-3, 2020, <https://pubchem.ncbi.nlm.nih.gov/compound/1049>.
- Koç M., Sekmen Y., Topgül T. and Yücesu H.S., 2009, The Effects of Ethanol–Unleaded Gasoline Blends on Engine Performance and Exhaust Emissions in a Spark-Ignition Engine. *Renew. Energy*, 34(10), 2101–2106.
- Kyriakides A., Dimas V., Lymperopoulou E., Karonis D. and Lois E., 2013, Evaluation of Gasoline–Ethanol–Water Ternary Mixtures Used as a Fuel for an Otto Engine. *Fuel*, 108, 208–215.

- Lanzanova T., Vielmo H., Sari R., Dornelles H., Tatsch G., Martins M. and Michels L., 2013, *Performance Analysis of a Spark Ignited Engine Running on Different Water-in ethanol Mixtures*, Society of Automotive Engineers Papers, Warrendale, USA.
- Lemaire R., Therssen E. and Desgroux P., 2010, Effect of Ethanol Addition in Gasoline and Gasoline–Surrogate on Soot Formation in Turbulent Spray Flames. *Fuel*, 89(12), 3952–3959.
- Li L., Wang M., Peng Z., Song Y., Zhang L. and Yuan W., 2015, Exhaust and Evaporative Emissions from Motorcycles Fueled with Ethanol Gasoline Blends. *Sci. Total Environ*, 502, 627–631.
- Lin C.Y. and Wang K.H., 2004, Effects of Diesel Engine Speed and Water Content on Emission Characteristics of Three-Phase Emulsions. *J. Environ. Sci. Health Part A*, 39(5):1345-1359.
- Liu H., Hu B. and Jin C., 2016, Effects of Different Alcohols Additives on Solubility of Hydrous Ethanol/Diesel Fuel Blends, *Fuel*, 184, 440-448.
- Luo M., El-Faroug M. O., Yan F. and Wang Y., 2017, Particulate Matter and Gaseous Emission of Hydrous Ethanol Gasoline Blends Fuel in a Port Injection Gasoline Engine. *Energies*, 10, 1263.
- Martins F., Felgueiras C., Smitkova M. and Caetano N., 2019, Analysis of Fossil Fuel Energy Consumption and Environmental Impacts in European Countries, *Energies*, 12, 964.
- de Melo T.C., Machado G.B., Belchior C.R.P., Colaço M.J., Barros J.E.M., de Oliveira E.J., et al., 2012, Hydrous Ethanol–Gasoline Blends – Combustion and Emission Investigations on a Flex-Fuel Engine. *Fuel*, 97:796–804.
- Muzikova Z., Pospisil M. and Sebor G., 2009, Volatility and Phase Stability of Petrol Blends with Ethanol, *Fuel*, 88(8), 1351-1356.
- Nour M., Attia A.M.A. and Nada S., 2019, Pentanol and Octanol Addition to Hydrous Ethanol/Diesel Blend Achieves Better Blending Stability with Improved Engine Performance and Reduced Emissions. *Fuel*, 251, 10-22.
- Olberding, J., Beyerlein, D., Steciak, J. and Cherry, M., 2005, Dynamometer Testing of an Ethanol-Water Fueled Transit Van, *SAE Tech.*, 2005-01-3706.
- Rajan S. and Saniee F.F., 1983, Water–Ethanol–Gasoline Blends as Spark Ignition Engine Fuels. *Fuel*, 62 (1), 117–121.
- Rao, R.N., Silitonga, A.S., Shamsuddin, A.H., Milano J., Riayatsyah M.I., Sebayang A.H., Bin Nur T., Sabri M.,
- Yulita M.R. and Sembiring R.W., 2020, Effect of Ethanol and Gasoline Blending on the Performance of a Stationary Small Single Cylinder Engine. *Arab. J. Sci Eng.*, 45, 5793–5802.
- SAE, 2004, *Engine Power Test Code – Spark Ignition and Compression Ignition – Net Power Rating*, SAE J 1349.
- Schifter I., Diaz L., Gomez J.P. and Gonzalez U., 2013, Combustion Characterization in a Single Cylinder Engine with Mid-Level Hydrated Ethanol–Gasoline Blended Fuels. *Fuel*, 103, 292-298.
- Shirazi S.A., Abdollahipoor B., Martinson J., Reardon K.F. and Windom B., 2018, Physiochemical Property Characterization of Hydrous and Anhydrous Ethanol Blended Gasoline, *Ind. Eng. Chem. Res.* 57(32), 11239–11245.
- Suarez-Bertoa R., Zardini A.A., Keuken H. and Astorga C., 2015, Impact of Ethanol Containing Gasoline Blends on Emissions from a Flex-Fuel Vehicle Tested over the Worldwide Harmonized Light Duty Test Cycle (WLTC). *Fuel*, 143, 173-182.
- Thakur A. K., Kaviti A. K., Mehra R. and Mer K. K. S., 2017, Progress in Performance Analysis of Ethanol Gasoline Blends on SI Engine, *Renew. Sustain. Energy Rev.*, 69, 324-340.
- Venugopal, T., Sharma A., Satapathy S., Ramesh A. and Gajendra Babu M., 2013, Experimental Study of Hydrous Ethanol-Gasoline Blend (E10) in a Four-Stroke Port Fuel Injected Spark Ignition Engine, *Int. J. Energy Res.*, 37(6): 638-644.
- Wang B., Sun L. S., Su S., Xiang J., Hu S. and Fei H., 2012, A Kinetic Study of NO Formation During Oxy-Fuel Combustion of Pyridine. *Appl. Energy*, 92, 361-368.
- Wang X., Chen Z., Ni J., Liu S. and Zhou H., 2015, The Effects of Hydrous Ethanol Gasoline on Combustion and Emission Characteristics of a Port Injection Gasoline Engine. *Case Stud. Therm. Eng.*, 6, 147-154.
- Wicker R.B., Hutchison, P.A., Acosta, O.A. and Matthews, R.D., 1999, Practical Considerations for an E85-Fueled Vehicle Conversion. *SAE Tech. Pap.*, 1999-01-3517.
- Yüksel F. and Yüksel B., 2004, The Use of Ethanol–Gasoline Blend as a Fuel in an SI Engine. *Renew. Energy*, 29(7), 1181–1191.

Zhang, W., Shu, G., Chen, Z., Shen, Y. and Weng, J., 2012, Chemical Kinetics of Ignition Timing of Diesel Engine Fueled with Water Emulsion Diesel. *Nongye Gongcheng Xuebao/Transactions of the Chinese Society of Agricultural Engineering*, 28, 59-66.

Zhuang Y. and Hong G., 2013, Primary Investigation to Leveraging Effect of Using Ethanol Fuel on Reducing Gasoline Fuel Consumption. *Fuel*, 105, 425–431.





## DESIGN AND OPTIMIZATION OF PCM-AIR COLD ENERGY STORAGE DEVICE TO BE USED FOR PEAK ELECTRICITY SHAVING

Göker TÜRKAKAR

Zonguldak Bülent Ecevit University, Mechanical Engineering Department Zonguldak, Turkey  
turkakar@beun.edu.tr, ORCID: 0000-0002-5468-604X

(Geliş Tarihi: 24.03.2020, Kabul Tarihi: 25.11.2020)

**Abstract:** Parametric analysis and dimensional optimization study for the melting process of the phase changing material placed in cold energy storage devices have been conducted. Phase changing material, PCM, is used to store the cold energy. A cross-flow tubular PCM-air heat exchanger is used. An electricity peak shaving for a summer day in Antalya for 5 hours (10:00-15:00) is aimed. The cooling load of a room (33 m<sup>2</sup>) in Antalya is taken as a reference value. A minimum cooling load of 2850 W is supplied throughout 5 hours to maintain the building's comfort temperature. Contrary to the studies handling air velocity constant, it is varied during melting in the present study to satisfy the minimum cooling load. The melting process is analyzed using a numerical model. A computational algorithm is implemented in MATLAB environment. The numerical model is validated for the same conditions and the dimensions with an analytical model presented in the literature. A transient analysis has been employed, and the problem is discretized for the time and space domain. A dimensional optimization algorithm is employed. A parameter “performance ratio/ cooling index”, the ratio of total cooling to fan energy consumption, is defined. Spacing between the tubes giving the maximum performance ratio is sought for aligned and staggered tube bank arrangements using this algorithm. The best performance ratio is obtained at 0.2 m/s initial velocities for both arrangements. In addition, the effect of sizing/arrangement of the tubes, PCM mass, and thermal conductivity of the PCM on the melting characteristics is investigated. As a result of increasing the thermal conductivity from 0.2 W/(m·K) to 0.6 W/(m·K), the performance ratios are raised 4.58 and 3.52 times for aligned and staggered orders, respectively. It is calculated that 10 kg PCM can be saved thanks to enhancing the thermal conductivity of the PCM.

**Keywords:** Cold energy storage, Phase change materials, PCM-air heat exchanger.

## ELEKTRİKTE PİK TALEBİ TÖRPÜLEME İÇİN KULLANILACAK FDM-HAVA SOĞUK ENERJİ DEPOLAMA CİHAZI TASARIMI VE OPTİMİZASYONU

**Özet:** Soğuk enerji depolama cihazındaki faz değişim malzemesinin ergime sürecinin parametrik analiz ve boyutsal optimizasyon çalışması yürütülmüştür. Faz değişim malzemesi FDM, soğuk enerjiyi depolamak için kullanılır. Çapraz akışlı borulu FDM-hava ısı değiştiricisi kullanılmıştır. Antalya’da bir yaz günü için 5 saat boyunca elektrikte pik talebi törpüleme amaçlanmıştır. Antalya’da 33m<sup>2</sup>’lik bir odanın soğutma yükü referans değer olarak alınmıştır. Binanın 5 saat boyunca sıcaklığını sabit tutmak için gerekli soğutma yükü olan minimum 2850 W’lık soğutma sağlanmıştır Hava hızını sabit olarak ele alan çalışmaların aksine; bu çalışmada minimum soğutma yükünü karşılayabilmek amacıyla ergime süreci boyunca hava hızı değiştirilmiştir. Ergime süreci sayısal bir model ile analiz edilmiştir. Hesaplama algoritması MATLAB ortamında uygulanmıştır. Sayısal model aynı boyutlar ve koşullar için literatürdeki bir çalışma ile kıyaslanarak doğrulanmıştır. Zamana bağlı analiz yürütülmüş olup, problem zaman ve konum için ayrıklaştırılmıştır. Boyutsal optimizasyon algoritması ele alınmıştır. Toplam ısı geçişinin toplam fan enerji tüketimine oranı olarak bilinen “performans oranı/ soğutma indeksi” parametresi tanımlanmıştır. Bu algoritma ile sıralı ve kademeli demeti dizilimleri için performans oranını maksimize eden borular arası optimum mesafeler araştırılmıştır. En iyi performans oranı her iki düzen için de 0.2 m/s başlangıç hızı için elde edilmiştir. Ayrıca boruların boyut/dizilim, FDM kütlesi ve ısı iletim katsayısının FDM ergime karakteristiğine etkisi incelenmiştir. FDM ısı iletim katsayısının 0.2 W/(m·K)’den 0.6 W/(m·K)’ye çıkarılması sonucu performans katsayısının sıralı ve kademeli dizilim için sırasıyla 4.58 ve 3.52 kat arttığı bulundu. Isı iletim katsayısının iyileştirilmesi sonucu FDM’den 10 kg tasarruf edilebileceği hesaplandı.

**Anahtar kelimeler:** Soğuk enerji depolama, Faz değişim malzemeleri, FDM-hava ısı değiştiricileri

### NOMENCLATURE

		$f'$	friction factor
		$f_m$	melt fraction
$A_o$	heat tr. area based on outer surface [m <sup>2</sup> ]	$h$	heat transfer coefficient [W/(m <sup>2</sup> K)]
$C_{air}$	heat capacity of the air [W/K]	$h_{sl}$	latent heat of fusion [J/kg]
$D$	diameter	$H$	HEX height [m]

$k$	thermal conductivity [W/(mK)]
$L$	total HEX length [m]
$m_{\text{pcm}}$	total mass of the PCM
$\dot{m}$	mass flow rate [kg/s]
$N_T$	number of tubes per row
$N_L$	number of tube row
$q$	heat transfer [J]
$\dot{q}$	heat transfer [W]
$P$	pressure [Pa]
Re	Reynolds number
$S_L$	Tube spacing in the flow direction [m]
$S_T$	Tube spacing in the transverse flow dr. [m]
$t$	time, thickness
$T_R$	room comfort temperature [K]
$U$	Overall heat tr. coef. [W/(m <sup>2</sup> K)]
$u_{\infty}$	mean air velocity [m/s]
$V$	volume [m <sup>3</sup> ]
$v$	specific volume [m <sup>3</sup> /kg]
$W$	total HEX width [m]

#### Greek Letters

$\eta$	fan efficiency
$\dot{V}$	volumetric flow rate [m <sup>3</sup> /s]
$\rho$	density [kg/m <sup>3</sup> ]
$\mu_b$	average free stream viscosity, [(N·s)/ m <sup>2</sup> ]

#### Subscripts

air	air
i	inner
in	inlet
init	initial
l	liquid
lm	logarithmic mean
m	melting
out	outer
pcm	phase change material
s	surface, solid
t	total, tube

#### Superscripts

p	time interval
---	---------------

## INTRODUCTION

Phase change materials, PCM, are widely used in energy storage and thermal management applications thanks to their high latent heat of fusion values. In addition to sensible heat storage capacity, PCMs can store high amounts of energy while maintaining its temperature stable around the melting temperature. They are mainly used in the area of electronics cooling, solar energy storage systems, building heating/cooling energy storage applications, battery thermal management systems, cold chain logistics, and photovoltaic panel's cooling applications. There are many studies related to heating/cooling applications of the buildings with PCM in the literature (Chaiyat et al., 2014). In cold energy

storage systems for building applications, PCM's are generally located in the ceiling of the building. PCM is solidified with nighttime cool air with the help of a fan. Stored cold energy is released during the daytime by a fan or natural convection effect (Souayfane et al., 2016). Therefore, PCM use for building cooling applications is reasonable for the regions where the temperature difference of night and the daytime is high. Some studies stored the cold energy using vapor compression refrigeration systems. Taking advantage of cold air and low electricity cost in the nighttime, PCM use in building cooling applications has become feasible. PCM placed in the specifically designed evaporator section of the refrigeration cycle should effectively store and supply the thermal energy. A similar case is valid for PCM-air heat exchangers, which are used in building cooling applications. PCM-air heat exchangers are used to storing cold energy supplied by nighttime outdoor cold air or by refrigerated cold air. The melting period of fully solidified PCM by the refrigerated air flow in the nighttime is analyzed in the current work. Stored cold energy is provided by forced airflow in the daytime, so the building's temperature is kept at comfort temperature. In the present study, the melting characteristics of the tubular cross flow PCM-air cold energy storage HEX unit is examined. Parameters affecting this type of HEX's performance are the air mean velocity, the diameter of the tubes, tube arrangement, the distance between the tubes, thermal conductivity of the PCM, and mass of the PCM. Considering these parameters, PCM-air heat exchangers should be designed to require minimum electricity caused by the fan while satisfying the necessary cold energy requirement. Besides, the use of PCM mass should be kept minimum because of their high cost. The design should comply with the other components of the system and reduce the energy cost. Hence, it is essential to conduct a parametric analysis and optimize the dimension of the heat exchanger. For such a system, PCM mass and the fan power should be minimized. Detailed information about the present study's scope is provided in the last paragraph of the Introduction section.

Due to the melting process's natural characteristics, total heat transfer absorbed by the PCM reduces with time for the constant airflow velocity. Therefore, mean air velocity should be increased as the melt fraction increases so that the constant heat transfer is provided. Studies in the literature related to PCM-Fluid HEX have examined the HEX melting performance for the constant fluid velocity (Koz and Khalifa, 2018; Dubovsky et al., 2011; Asker and Günerhan, 2016). In this case, HEX performance gets poorer as the melt fraction rises, and it is not possible to keep the room at comfort temperature. It is more reasonable to use an adjustable speed fan and dynamically modify the fan speed according to the cooling demand that changes with time.

Thermal energy storage with PCMs has attracted the attention of researchers in recent years. Researchers have designed, simulated, and tested various types of PCM-air

heat exchangers. Some researchers have focused on packed bed systems (Chaiyat et al., 2014; Fang et al., 2010). In these studies, PCM is filled in capsuled, and air/water is used for the charge or discharge process. Packed bed energy storage systems are used for building cooling or heating processes. Besides, PCM encased parallel slabs are used in several studies (Koz and Khalifa, 2018; Hed and Bellander, 2006, Kuznik et al., 2015). Air is flowing through the parallel slabs and melt/freeze the PCM. They both theoretically and experimentally analyzed the system. Koz and Khalifa (2018) have explored the effects of the slab thickness, distance between the slabs, and PCM thermal conductivity on the cold energy storage device's melting performance. They aimed to create a microenvironmental control system (local cooling for a person) and provide more than 50W cooling at the end of the 8.5h cooling period under a constant air flow rate. Hed and Bellander (2006) developed an algorithm of PCM-air heat exchanger to be used in the building. A numerical model is developed using the finite-difference model, and results are compared with the prototype heat exchanger. Air is flowing (air gap is 8 mm) through 8 mm thick PCM slabs. The heat transfer coefficient is calculated using the Reynolds Colburn analogy using the rough surface. Simulations and tests have been performed for constant airflow and inlet temperature. The results of the simulations and the experiments have matched well. Kuznik et al. (2015) have designed a PCM to air rectangular heat exchanger using dimensionless parameters. The air was flowing through PCM slabs. The aim was electricity peak shaving (for 2 hours) for a winter day in France. They have developed a methodology for a specific geometry of the storage unit. This methodology determines the suitable PCM and the PCM's thermal conductivity satisfying the required specifications of the application. Erdemir and Altuntop (2018) have performed experimental work to reduce a hypermarket's cooling cost using encapsulated ice thermal storage system. The storage system is integrated with the air conditioning system of the hypermarket. They noted that the stored energy needs to be used in electricity peak hour as much as possible. The shortest payback period is 1.5 years in both load leveling and 10% partial storage strategies.

There are some studies using shell and tube heat exchangers as TES units. Zhao and Tan (2015) used shell and tube type HEX unit with fins to increase the coefficient of performance, COP, of the air-conditioning system. They have developed a numerical model for the analyses. While the PCM in the HEX serves as a heat sink for the air conditioner (condenser heat rejection) in the daytime, PCM freezes thanks to the cold nighttime air. Air is used to freeze the PCM, and water melts the PCM in the daytime. They reported that COP is increased by about 25.6% with the help of PCM-air-water shell and tube HEX. Dhumane et al. (2019) used PCM to store condenser heat to improve the vapor compression cycle performance's performance. Dhumane et al. (2019) have designed and tested shell and tube type PCM-HEX with helical coils. They employed a dynamic model to analyze

the system using Modelica software. They have investigated the melting temperature of the PCM, maximizing the COP of the system. As a result of the experiments, an increase of 11% in the COP is observed.

Dubovsky et al. (2011) have analyzed the melting of a PCM-air heat exchanger storage unit both analytically and numerically. Crossflow tubular HEX is investigated. Tubes are filled with the PCM. Air is a fan-driven across aligned order tube banks. They have investigated time-dependent parameters like PCM melt fraction, heat transfer rate, air temperature analytically. The numerical solution has supported the prediction ability of the developed analytical model. Asker and Günerhan (2016) have conducted a parametric study for similar geometry with Dubovsky et al. (2011). They numerically investigated the effects of the tube interval, fan speed, PCM material on total melting time.

Generally, studies related to the PCM-air storage units have conducted their simulations at a constant airspeed. Due to the melting process's natural characteristics, total heat transfer absorbed by the PCM reduces with time at the constant airflow velocity. This situation makes it difficult to maintain the building's temperature at the comfort level for a certain period. The use of a variable speed fan during the melting process tolerates the drawback of the low heat transfer performance towards the end of melting. However, fan speed increase brings about the increase in the pressure drop and the pumping power. That is why a new parameter, which is the ratio of total heat transfer to the fan's energy requirement, is defined. The heat exchanger is designed and analyzed such that it would provide minimum cooling of 2850 W cooling for 5 hours. An electricity peak shaving is aimed, using a cold energy storage unit at this period. A time-dependent melting analysis is conducted numerically for a cross-flow tubular PCM-air heat exchanger. Distinctive to the studies in the literature, airspeed is adjusted without exceeding a critical pumping power value so that the constant heat transfer can be provided for a certain period. Contrary to most of the studies focusing on parametric analysis in the literature, a dimensional optimization study for a PCM-air cold energy storage HEX has been conducted for variable air velocity. Both aligned and staggered tube bank order is analyzed, dimensionally optimized, and their performance is compared. The study aims to find an optimum configuration and dimensions of the cross-flow tubular PCM-air heat exchanger for the specified conditions and constrictions while minimizing the fan energy consumption and PCM mass.

## PROBLEM DEFINITION

In this section, the geometry and the dimensions of the cross-flow tubular PCM-air heat exchanger are given. Besides, governing equations of the melting process are provided.

### Geometry and Assumptions

PCM-air HEX is intended to provide comfort temperature (25°C) of a room (33 m<sup>2</sup>) of a building

located in Antalya/TURKEY on the date of 21<sup>th</sup> of July (10:00-15:00) during which electricity demand peaks. The cooling load of the mentioned room is provided in Table 1.

**Table 1.** Cooling Load of the room (Erkmen and Gedik, 2007)

Time Interval	Cooling Load, W
10:00-11:00	2870
11:00-12:00	2768
12:00-13:00	2803
13:00-14:00	2887
14:00-15:00	2927

If 2850 W (mean value) of cooling power is handled, the room comfort temperature can be kept at around comfort temperature with slight changes. The minimum cooling load of 2850 W during the 5 hr period is considered a reference value in the present study. The air inlet temperature to the HEX is fixed at the room comfort temperature, 25°C. Fully solidified PCM by the refrigerated air in the nighttime is discharged during the daytime. The schematic of the system is depicted in Fig. 1.

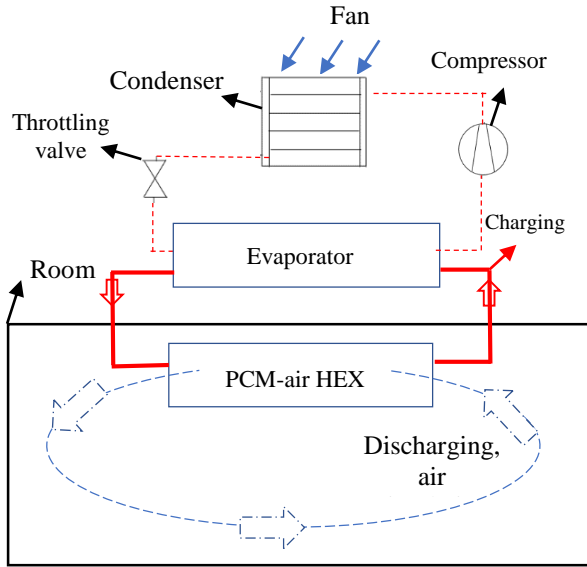


**Figure 1.** Schematic of the system

Heat exchangers are generally evaluated for steady-state conditions. As the hot/cold energy is stored in PCM-air HEX, a transient solution is necessary. HEX consists of a tube bundle, and the PCM is placed inside the tubes. Aligned and staggered tube arrangements in the HEX are examined separately. The thermal and hydrodynamic behavior of these arrangements is distinctive as the velocity profile inside the HEX differs. Therefore, the best performing configuration is sought. The air temperature varies by time and by location as well. The melt ratio is different for all tube rows at a specific instant. Thus, for a specific period, the geometries shown in Fig 2 and Fig 3 are divided into segments in the streamwise direction for the aligned and staggered arrangements, separately. Thermal and hydrodynamic calculations are evaluated for each tube row. After

completing the calculations for a specific time period, calculations are performed for the following time step using the current time step results. General geometries and the computational domains for aligned and staggered geometry are provided in Fig. 2 and Fig. 3, respectively.

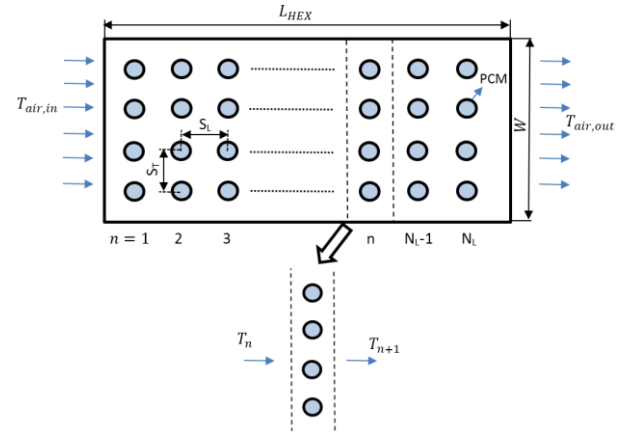


**Figure 2.** General view of the PCM-air heat exchanger (Aligned order) and computational domain

The general geometry of staggered order tube bank PCM-air HEX is given in Fig 3.

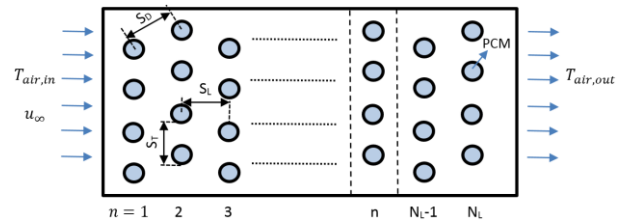


**Figure 3.** General view of staggered order PCM-air heat exchanger

As many cases are evaluated to find the optimum dimensions and operating conditions, it is necessary to simplify the complexity of the problem and reduce the computational effort. The problem is discretized in the time domain. In each time step, the First Law of Thermodynamics is handled by neglecting kinetic and potential energy changes in the air. Axial conduction (flow direction) in the air is also neglected. Heat transfer between the PCM and the air is found using the overall heat transfer coefficient. The air-side heat transfer coefficient is obtained using experimental tube bank correlations. It is assumed that the PCM is in the melting temperature (completely solid at the beginning of the melting process), so the sensible heat transfer effect is neglected. For the temperature range (18-25°C) at which the problem is handled, the PCM's sensible heat capacity is less than 6% of the latent heat of fusion of it. The sensible heat effect of the tube material is also negligible because its mass is less than the PCM material. Mass of the tube material changes case by case, but its sensible heat effect corresponds to approximately 4% of the PCM's latent heat of fusion capacity. The convection effect in the liquid layer formed during PCM melting is neglected, so only the heat conduction effect in the liquid layer is put into account as it is done in many studies in

the literature (Dubovsky et al., 2011; Asker and Günerhan, 2016).

### Governing Equations

Thermal and hydrodynamic calculations are provided as two subsections in this part.

#### Thermal calculations

The energy balance for the control volume shown in Fig. 2 (or Fig. 3) is given in Eq. (1). It is essential to remind that the PCM's heat is discharged only through latent heat of fusion. The PCM is at the melting temperature initially. Kinetic and potential energy changes are neglected in Eq. (1),

$$q_n^p = \dot{m}_{air} C_{p,air} (T_{air,n}^p - T_{air,n+1}^p) = U_n^p A \Delta T_{lm,n}^p \quad (1)$$

$$= U_{i,n}^p A_i \Delta T_{lm,n}^p$$

As the time and space domain is discretized, it is necessary to represent them in the formulas. Superscript, p, represents the time step of the analysis. Similarly, subscript n refers to the control volume (tube row) number. If the parameters are to be explained in Eq. (1); the air mass flow rate can be expressed as  $\dot{m}_{air} = u_\infty \rho_{air} (W \cdot H)$ ,  $A_i$  is the total heat transfer surface area of a tube row (depicted in Fig. 2) and given as  $A_i = \pi D_i H N_T$ . Logarithmic mean temperature difference (LMTD) is defined as

$$\Delta T_{lm} = \frac{(T_{air,n}^p - T_{melt}) - (T_{air,n+1}^p - T_{melt})}{\ln\left(\frac{T_{air,n}^p - T_{melt}}{T_{air,n+1}^p - T_{melt}}\right)} \quad (2)$$

To find the air outlet temperature of a segment from the Eq. (1), the thermal resistances and the overall heat transfer coefficient needs to be calculated. Neglecting the convection effect of the PCM liquid layer, the overall heat transfer coefficient, U, is given in Eq. (3) as

$$\frac{1}{U A} = \frac{1}{U_{i,n}^p A_i} = \frac{\ln(D_i/D_{sl,n}^p)}{2 \pi k_{pcm,l} H} + \frac{\ln(D_o/D_i)}{2 \pi k_{tube} H} + \frac{1}{h_{air} (\pi D_o H)} \quad (3)$$

$D_{sl,n}^p$  is the diameter of the solid-liquid interface. The diameter of the solid-liquid interface varies for each tube row. The first term in Eq. (3) is the time and space-dependent liquid layer conduction thermal resistance. It depends on the thickness of the liquid layer formed during melting. Time and space-dependent overall heat transfer coefficient is given in Eq. (4),

$$\frac{1}{U_{i,n}^p} = \frac{D_i \ln(D_i/D_{sl,n}^p)}{2 k_{pcm,l}} + \frac{D_i \ln(D_o/D_i)}{2 k_{tube}} + \frac{D_i}{h_{air} D_o} \quad (4)$$

Melt fraction,  $f_n^p$  is the ratio of the liquid mass of the PCM to the total mass of the PCM for a computational domain. At the beginning of the analysis ( $t=0$  s), the melt fraction is zero. It means that all PCM is in the solid phase initially. Melt fraction for the following time step can be calculated using the Eq. (5),

$$f_n^{p+1} = f_n^p + \frac{q_n^p \Delta t}{m_{pcm,row} h_{sl}} \quad (5)$$

$m_{pcm,row}$  is the total mass in the tubes per row (number of tubes in the transverse direction), and it can be calculated as  $m_{pcm,row} = \rho_{PCM,l} V_{tube} N_T$ . For the same density of the liquid and solid phases of the PCM, melt fraction can be expressed as

$$f_n^p = 1 - \left(\frac{D_{sl,n}^p}{D_i}\right)^2 \quad (6)$$

If the time-dependent conduction thermal resistance of the liquid layer in Eq. (4) is expressed in terms of  $f_n^p$ ,

$$\frac{1}{U_{i,n}^p} = \frac{-D_i \ln(1 - f_n^p)}{4 k_{pcm,l}} + \frac{D_i \ln(D_o/D_i)}{2 k_{tube}} + \frac{D_i}{h_{air} D_o} \quad (7)$$

The average heat transfer coefficient for aligned/staggered order tube bank is calculated using a correlation proposed by Zukauskas (1972), Incropera and DeWitt (2002).

$$\overline{Nu}_D = C_1 Re_{D,max}^m Pr^{0.36} \left(\frac{Pr}{Pr_s}\right)^{1/4} \quad (8)$$

$$\left\{ \begin{array}{l} N_L \geq 20 \\ 0.7 \leq Pr \leq 500 \\ 10 \leq Re_{D,max} \leq 2 \times 10^6 \end{array} \right\}$$

All properties except  $Pr_s$  are evaluated at an arithmetic average of HEX inlet and outlet temperatures.  $C_1$  is a constant, and its value depends on the  $Re_{D,max}$  (Incropera and DeWitt, 2002). Reynolds number is based on the maximum velocity occurring in the tube bank is defined as

$$Re_{D,max} = \frac{\rho u_{max} D}{\mu} \quad (9)$$

Maximum velocity occurring in the tube bank for the aligned order is given in Eq. (10) as

$$u_{max} = \frac{S_T}{S_T - D} u_\infty \quad (10)$$

Maximum velocity occurring in the tube bank for the staggered order is derived using conservation of mass for the incompressible flow and given in Eq. (11),

$$u_{max} = \frac{S_T}{2(S_D - D)} u_{\infty} \quad (11)$$

A dimensionless time-dependent heat transfer is defined. It is a ratio of heat transfer in the HEX to the maximum possible heat transfer in the HEX.

$$q_0^p = \frac{\sum_{n=1}^{N_L} q_n^p}{\dot{m}_{air} C_{p,air} (T_{air,in} - T_{melt})} \quad (12)$$

A criterion for the performance of the HEX is defined. It is named as performance ratio or cooling index (Yang et al., 2015). It is the ratio of the total energy absorbed by the HEX during melting to the fan's energy consumption. This ratio is expressed in Eq. (13).

$$PR = \frac{\sum_{p=1}^{t_{total}/\Delta t} \sum_{n=1}^{N_L} q_n^p \Delta t}{\sum_{p=1}^{t_{total}/\Delta t} W_{fan}^p \Delta t} \quad (13)$$

### Hydrodynamic calculations

The pressure drop in the HEX can be calculated using Eq. (14). As a variable speed fan is used in the analysis, pressure drop and the fan power are time-dependent parameters.

$$\Delta P^p = \frac{2 f'^p (G_{max}^p)^2 N_L}{\rho_{air}} \left( \frac{\mu_w}{\mu_b} \right)^{0.14} \quad (14)$$

The density of air is evaluated for free stream conditions.  $f'$  is the friction factor that is given for aligned and staggered order tube banks in Eq. (15) and Eq. (16), respectively.

$$f'^p = \left\{ 0.044 + \frac{0.08 \left( \frac{S_L}{D_{out}} \right)}{\left[ \frac{S_T - D_{out}}{D_{out}} \right]^{0.43 + 1.13 \left( \frac{D_{out}}{S_L} \right)}} \right\} (Re_{max}^p)^{-0.15} \quad (15)$$

$$f'^p = \left\{ 0.25 + \frac{0.118}{\left[ \frac{S_T - D_{out}}{D_{out}} \right]^{1.08}} \right\} (Re_{max}^p)^{-0.16} \quad (16)$$

Superscript p in  $f'$  represents the time at which the friction factor is evaluated. As the air velocity varies during melting,  $(Re_{max}^p)$  changes with time,  $Re_{max}$  and  $G_{max}$  are calculated based on the  $u_{max}$ .  $u_{max}$  is the maximum velocity occurring in the tube bank. Detailed information is given in (Holman and White, 1992). Pumping/fan power is given in Eq. (17).

$$W_{fan}^p = (\dot{V})_{air}^p \frac{\Delta P^p}{\eta_{fan}} \quad (17)$$

$\eta_{fan}$  is the fan efficiency. The fan is assumed to be ideal, so fan efficiency is taken as 1.

### COMPUTATIONAL ALGORITHM

The computational algorithm developed for the present study is compared with a study from the literature. While the present study employs the Logarithmic Mean Temperature Difference Method, "LMTD" for the segmented computational domain, Dubovsky et al. 2011 used an alternative approach for their numerical model. They defined a factor,  $0 \leq \epsilon \leq 1$  to determine the average air temperature for a specific tube row (computational domain). If this factor is equal to 0, the average air temperature is attained as the row's inlet temperature. On the other hand,  $T_{av}$  is taken as the air outlet temperature if the value of  $\epsilon$  is 1. For example, the arithmetic average of the inlet and outlet air temperature of the computational domain corresponds to  $\epsilon = 0.5$ . Dubovsky et al. (2011) concluded that the value of the  $\epsilon$  is not so crucial for the investigation of the whole time of phase change. It is noted that there is only a 5% difference between two extreme cases,  $\epsilon = 0$  and  $\epsilon = 1$ . They have used both numerical and numerical ones and got a perfect match. In the present study, the LMTD method use is preferred to get a more realistic temperature difference between the air and the PCM, instead of using the arithmetic average temperature of the air as the air temperature of the segment. After defining the main dimensions and the tubes' order (aligned or staggered) of the heat exchanger, the computational domain is divided into the number of tube rows. For a specific time step, thermal calculations are conducted in each tube row one by one. Fundamental energy balance is applied using the LMTD method. Some parameters like melt ratio, air temperature, heat transfer is recorded for any tube row and instant. In general, calculations are conducted for a constant total mass of the PCM. After defining the total mass of the PCM, the diameter of the tubes is determined. As the main dimensions of the HEX, the distance between the tubes and the PCM density are known, diameter and the number of the tubes are calculated using this information. Depending on the arrangement of the tubes, aligned or staggered order heat transfer and pressure drop correlations are employed. The distinctive part of the present study is that evaluating the air velocity variable with respect to time. Suppose the total heat absorbed by the PCM for a specific time step is lower than the specified minimum heat transfer requirement. In that case, the mean air velocity is increased by 0.5% so that the minimum heat transfer requirement is satisfied. Performance of the HEX is evaluated using "Performance Ratio". A schematic representation of the computational algorithm is given in Fig. 4.

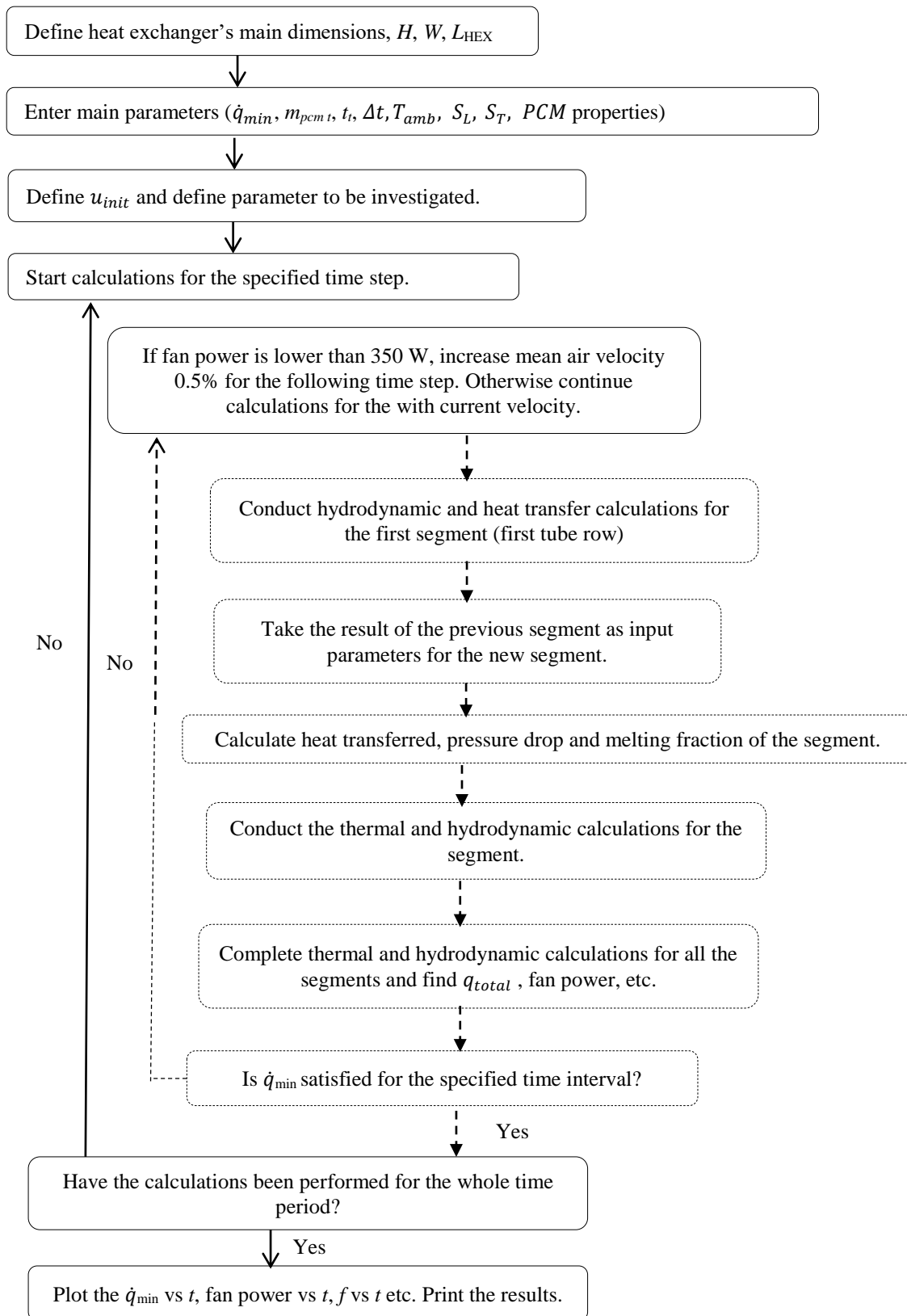


**Figure 4.** Computational algorithm (Dashed lines represent calculation for a time step)

### Computer Code Validation

The developed thermal model is validated using a typical study from the literature (Letan and Ziskind, 2006; Dubovsky et al., 2011). The computational algorithm is

implemented in MATLAB environment. For the same geometry and the operating conditions, the present study results are compared with Dubovsky et al. (2011)'s. Operating conditions and the dimensions of the HEX given by Dubovsky et al. (2011) are presented in Table 2.

**Table 2.** Dimensions and the operating conditions of Dubovsky et al. (2011)

$A_{o,t}$	32 m <sup>2</sup>
$m_{pcm}$	60 kg
$h_{sl}$	206 kJ/kg
$N_T$	14
$N_L$	90
$k_{pcm}$	0.2 W/(m·K)
$\dot{m}_{air}$	0.277 kg/s
$h_{air}$	86 W/(m <sup>2</sup> ·K)
$D_i$	0.01 m
$D_{out}$	0.012 m
$T_m$	23°C
$T_{in}$	35°C

The melting analysis of the PCM-air heat exchanger has been conducted using the computational algorithm presented in Fig. 4 for the same dimensions and the conditions used in Dubovsky et al. (2011). This comparison is presented in Fig.5 and Fig. 6.

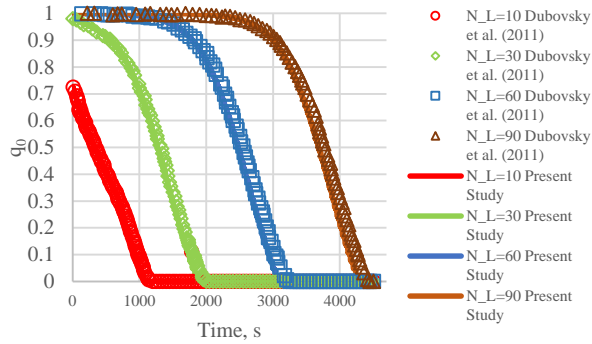


**Figure 5.** Comparison of present study (solid lines) with Dubovsky et al. (2011) (markers)

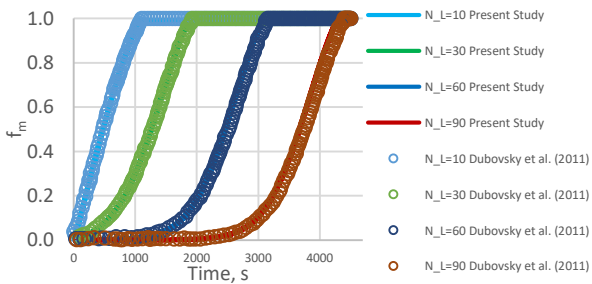


**Fig. 6** Comparison of melt fraction of present study (solid lines) with Dubovsky et al. (2011) (markers)

Dubovsky et al. (2011) have investigated the PCM-air heat exchanger's melting characteristics with a numerical and an analytical method. The results of the analyses using these methods have not led to significant discrepancies. Numerical results of the present study are compared with Dubovsky et al. (2011)'s analytical results in Fig. 5 and Fig. 6. A very good match is obtained. It is obvious that for the higher number of tube rows, it takes longer for the last tube row to reach a fully liquid phase. The reason is that the last tube rows contact with heated air, so the melting process takes longer. Because of the melting process's natural characteristics, total heat stored by the PCM reduces with time for the constant airflow

velocity. Because the liquid film layer is formed, and this layer creates an additional thermal resistance. This resistance increases while the melting process takes place. In Fig. 5, a sharp decrease in heat transfer is observed after a specific time for all the cases. The mean air velocity should be increased during melting to keep the heat transfer constant. It is possible to keep the heat transfer value over a particular value using a variable speed fan. Thus, the present study has focused on how the pumping power requirement could be kept low while the minimum cooling requirement is satisfied for a certain time period. Parameters affecting the pumping energy requirement are tube placement, size, PCM amount, PCM melting temperature. The effect of these parameters on the design of the PCM-air heat exchanger is investigated.

## MAIN DIMENSIONS AND OPERATING CONDITIONS

Cold energy storage unit performance is evaluated as parametric analysis and dimensional optimization (performance ratio comparison).

### Geometry and Operating Conditions for Parametric Analysis

Firstly, it is aimed to understand the effect of the air mean velocity, PCM mass, and thermal conductivity on fan power and the heat transfer for a fixed HEX geometry. After determining the melting characteristics of the PCM-air Hex, a dimensional optimization study is conducted for a constant PCM mass. The main geometry and operating conditions are presented in Table 3.

**Table 3.** System geometry and inspected parameters

Size of the system	$L_{HEX}= 1.35$ m, $W=0.8$ m, $H=0.8$ m
$m_{pcm}$	230kg
$S_T$	30 mm
$S_L$	30 mm
$t_{tube}$	0.2 mm
$\dot{q}_{min}$	2850 W
$q_{total}$	14.25 kWh
$T_R$	25°C
$T_m$	18°C
$\Delta t$	0.5 s
$u_{\infty,init}$	0.3 m/s

The commercial Rubitherm RT18HC's thermophysical properties are employed, and its thermophysical properties are given in Table 4.

**Table 4.** Properties of the PCM, RT18HC (Khan et al., 2016)

Melting Temperature, $T_m$	18°C
Latent heat of fusion, $h$	250 kJ/kg
Specific heat capacity	2 kJ/(kg K)
Density of solid, at 15°C, $\rho_s$	880 kg/m <sup>3</sup>
Density of liquid, at 25°C, $\rho_l$	770 kg/m <sup>3</sup>
Thermal conductivity (both phases), $k_{pcm}$	0.2 W/ (m K)



PCM filled tubes are made of aluminum ( $k_{AL} = 205 \text{ W / (m K)}$ ).

### Dimensional Optimization and Performance Ratio Evaluation

Optimization parameters for the melting analysis of the present study is summarized in Table 5.

**Table 5.** Synthesis of the technical specification requirements

<b>Function:</b>	Cooling load (2850 W) for 5h
<b>Objective:</b>	Maximization of the perf. ratio (minimization of fan energy consumption)
<b>Constraint:</b>	HEX main dimensions ( $H, L, W$ ), $PP_{air} \lesssim 350 \text{ W}$
<b>Design variables:</b>	<b>Parametric analyses:</b> thermal conductivity, air velocity, PCM mass <b>Optimization:</b> $S_L, S_T$ .
<b>Examined Cases:</b>	Tube arrangement (Aligned/Staggered), $u_{\infty,init}$
<b>Fixed parameters:</b>	PCM mass, room comfort temperature, melting temperature, cooling load

As stated in the Introduction section, airspeed varies during melting. If the required cooling is not satisfied, the mass flow rate of the channel is increased. Maximum allowed air velocity is limited such that fan/pumping power would not exceed 350 W. If this fan power value is reached during the melting process, fan velocity is not increased further. This value is chosen considering the fan specifications on the market.

The performance ratio of cold energy storage HEX is compared for different  $S_L$  and  $S_T$  combinations for aligned and staggered orders. Total HEX volume and PCM mass are kept constant for the sake of comparison. A grid search optimization algorithm is employed in the present study (Türkakar and Okutucu-Özyurt, 2012). The design variable interval is divided into grids, and for each  $S_L$  and  $S_T$  combination, the performance ratio is determined. Among these values, the minimum one is recorded as optimum geometry. The grid interval is determined to be 0.5 mm. This means the performance ratio is calculated for  $21 \times 21$  combination of  $S_L$  and  $S_T$  for the design variables interval of  $25 \leq S_L \leq 35$  and  $25 \leq S_T \leq 35$ . It has been decreased to 0.1 mm to understand the effect of grid interval on the optimum geometry and the performance ratio. In this case, the performance ratio is calculated for  $101 \times 101$  combination of  $S_L$  and  $S_T$ . This procedure is applied for the conditions presented for the first row of Table 7 (Aligned,  $u_{\infty,init} = 0.3 \text{ m/s}$  initial velocity, of  $25 \leq S_L \leq 35$  and  $25 \leq S_T \leq 35$  case). The augmented resolution caused 3.4% and 4.8% deviations for the optimum dimensions of  $S_L$  (29 mm) and  $S_T$  (31.3 mm). The performance ratio for these optimum dimensions is found as 263.8, which corresponds to a 2.5% difference. The increased resolution has not yielded significant discrepancies, but it tremendously increased the computational effort. A similar check has been performed

for the time interval. A time interval of 0.5s is utilized for the optimization procedure. As a check, the optimization code is run for a smaller time step ( $\Delta t = 0.1 \text{ s}$ ) for the conditions presented in the first row of Table 7. Optimum dimensions have been found the same with the  $\Delta t = 0.5 \text{ s}$  case. Only 0.1% deviation has been observed for the performance ratio. Therefore, it can be concluded that a time interval of 0.5 s is quite enough to get accurate results.

**Table 6.** Optimization parameters

Objective Function	Performance ratio
Design Variables	$25 \leq S_L \leq 35$
	$25 \leq S_T \leq 35$
	$35 \leq S_L \leq 45$ $35 \leq S_T \leq 45$
Grid Interval	0.5 mm
Fan Power	$PP_{air} \lesssim 350 \text{ W}$
$u_{\infty,init}$	0.2, 0.25, 0.3 m/s

Operating conditions and sizes, which are not presented in Table 6 for the optimization study, are taken from Table 3 and Table 4. It is guaranteed that the optimum geometries shown in Table 7 satisfy  $\dot{q}_{min}$  value of 2850 W. However, this criterion might not be satisfied for some combinations of  $S_L$  and  $S_T$ .

## RESULTS

A parametric analysis has been conducted to understand the melting phenomena in cold energy storage HEX. After determining critical values satisfying the system's cooling load like mean air velocity, PCM mass, and fan power, optimum arrangement, and the dimensions have been determined.

### Parametric Analysis

Unlike the other analyses in this section, a transient heat transfer analysis has been conducted for constant velocity. By doing so, the melting characteristics of the PCM at constant velocity is discovered in Fig. 7. For the rest of the analyses, heat transfer is desired to be slightly higher or equal to the minimum cooling load using a variable speed fan. Contrary to the computational algorithm explained in Fig. 4, air velocity is kept constant in the analysis depicted in Fig 7.

Heat transfer during melting at constant velocity is examined for five different air velocities in Fig. 7. Corresponding  $Re_{max}$  values for the air velocities from lowest to highest are 1843, 2304, 2764, 3225, and 3686. As can be understood from Fig. 7, heat transfer performance gets poorer towards the end of the 5 hours of the cooling period due to the increment in the liquid form and the decreasing melting energy ( $m_s h_{sl}$ ). As the liquid form in the tubes develops, total thermal resistance (PCM to air) increases. Variation in the heat transfer during the cooling period causes deviations in the temperature for the place to be cooled. Hence, using an adjustable speed fan in the HEX, a stable heat transfer during the melting process is achieved.

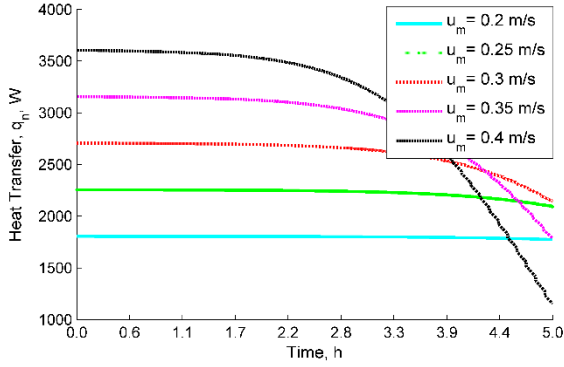


**Figure 7.** Heat transfer during cooling period for constant velocity,  $m_{pcm, total} = 230$  kg (Aligned,  $S_T = 30$  mm,  $S_L = 30$  mm,  $D_o = 24.7$  mm)

To design an economically feasible cold storage HEX, the total mass of the PCM used in the system should be minimized. The total amount mass satisfying the constant cooling load of 2850 W for 5 hours (14.25 kWh) is sought in the analysis shown in Fig. 8.

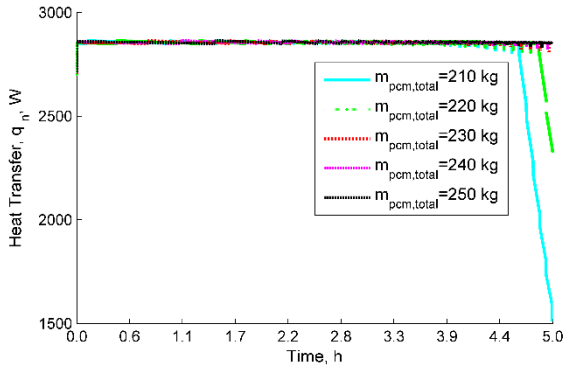


**Figure 8.** Heat transfer during cooling period for variable speed fan, (Aligned,  $S_T = 30$  mm,  $S_L = 30$  mm)

The minimum mass required to keep the building at room comfort temperature is found as 230 kg. Although the system's air mass flow rate is increased, especially after 14000<sup>th</sup> (3.88h) second, the minimum heat transfer requirement could not be satisfied for 210 and 220 kg PCM. Small fluctuations observed in heat transfer value stems from the air velocity variation during melting. The heat transfer performance of the system sharply reduces for these two cases. Fan power requirements with respect to the time of these cases are presented in Fig 9.

For all the cases, fan velocity increases towards the end of the 5 hours of the cooling period. Fan velocity is increased during the melting process because the liquid film's thermal resistance formed during melting brings about an increase in the system's total thermal resistance. As can be seen from Fig. 5 and Fig. 7, this situation reduces the system's heat transfer performance, especially at higher melt fraction values. The air-side heat transfer coefficient is increased to overcome increasing thermal resistance caused by the liquid film formation. In this way, the system's total thermal resistance is kept constant during melting. PCM mass equal to or higher than 230 kg successfully completed the cooling period. A lower mass

than 230 kg could not satisfy the cooling load requirement despite reaching the critical pumping power (350 W) at the end of the cooling period. It could be inferred from Fig. 8 and Fig. 9 that the minimum mass requirement should be 230 kg.

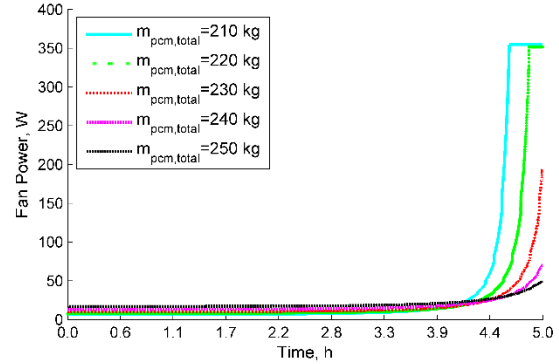


**Figure 9.** Fan power requirement of the system (Aligned,  $S_T = 30$  mm,  $S_L = 30$  mm)

Total thermal resistance between PCM-air can be diminished using highly conductive PCM or using thermal enhancement methods. Khan et al. (2016) summarized thermal enhancement methods for paraffin-based PCM's. They noted that the most common methods are the use of fins in the storage unit and the use of highly conductive additives. They also emphasized the importance of the PCM container's shape and orientation. Aydin et al. 2018 have improved the horizontally placed shell and tube PCM container's thermal performance using a fin attached to the bottom of the inner tube. Cheng et al. (2010) have improved paraffin-based PCM's thermal conductivity 4 times with the addition of expanded graphite. They have reached the 1.36 W/(m·K) thermal conductivity value of the PCM composite with the 4.6% mass fraction of expanded graphite. The effect of thermal conductivity on fan power is presented in Fig. 10.

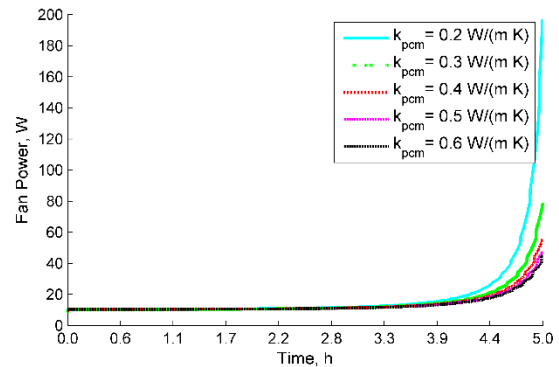


**Figure 10.** The effect of thermal conductivity of the PCM on fan power at constant heat transfer (Aligned,  $S_T = 30$  mm,  $S_L = 30$  mm,  $q_n \cong 2850$  W,  $m_{pcm, total} = 230$  kg)

Thanks to the reduction in the liquid PCM layer's conductive thermal resistance in the tubes, PCM with 0.6 W/(m·K) thermal conductivity requires the lowest fan energy consumption with (0.065213 kWh). This value corresponds to the average fan power of 13.04 W for 5

hours melting period. While the total fan energy consumption at the end of 5 hours cooling period for  $k_{pcm}=0.2 \text{ W/(m}\cdot\text{K)}$  case 0.089607 kWh (average fan power of 17.92 W), it is 0.065213 kWh for the thermal conductivity value of  $0.6 \text{ W/(m}\cdot\text{K)}$ . By increasing the thermal conductivity three times, fan energy consumption has been decreased 27.2%. It is important to note that all cases satisfied the minimum heat transfer requirement. The algorithm has kept the heat transfer value at 2850 W by increasing the air velocity if necessary. There is still solid phase in some tubes near the air outlet at the end of the melting period. The last tube row gives an idea about the solid portion in the HEX. The melting ratio of the last tube row of the inspected cases are presented in Fig. 11.

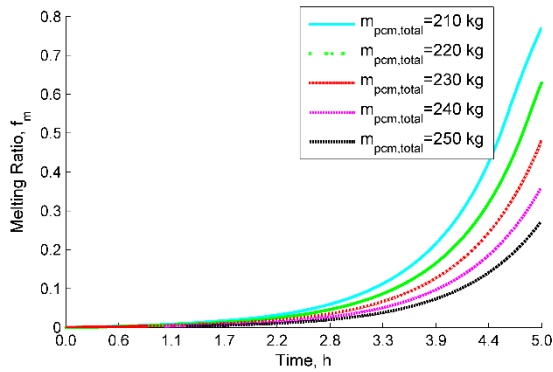


**Figure 11.** Melting ratio of the last row tubes for different  $m_{pcm,t}$ , (Aligned,  $S_T=30 \text{ mm}$ ,  $S_L=30 \text{ mm}$ )

There is still the solid phase at the end of 5 hours of the melting process for all cases. Although 230kg PCM use is enough to fulfill the present study's cooling requirement, more than half of the total PCM is still solid at the end of 5 hours for the last row of the tubes. This means there is still cold energy stored in the PCM. It is important to note that tube rows close to the air inlet region melt faster, and they are completely melted at the end. Fig 11 shows the melt fraction of the last tube row through which heated airflows.

### Performance Analysis and Dimensional Optimization

Optimum configuration of the PCM-air HEX has been sought in this section. According to the algorithm provided in the ‘‘Dimensional Optimization and Performance Ratio Evaluation’’ section. The performance ratio is the ratio of the energy used for cooling to the energy consumed as fan work for the total time. This ratio is significant in terms of system performance. A higher value of the performance ratio means high cooling capacity and low fan energy consumption. An optimum configuration of the tubes can be found using this ratio. Optimum distance between the tubes in the airflow direction and transverse air flow direction can be found. Fig. 12 and Fig. 13 show the performance ratio for aligned and staggered order arrangement, respectively.

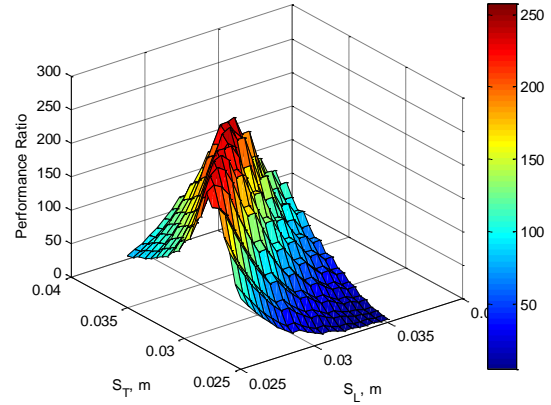


**Figure 12.** Effect of heat exchanger configuration to performance ratio for aligned order ( $m_{pcm,t}=230 \text{ kg}$ ,  $u_{\infty,init} = 0.3 \text{ m/s}$ )

The maximum performance of the heat exchanger is obtained as 257.2 for optimum configuration of  $S_L=30 \text{ mm}$  and  $S_T=32.5 \text{ mm}$ . For larger values of  $S_L$  and  $S_T$  heat exchanger performance reduces. Keeping the tubes distant from each other necessitates the use of larger diameter tubes. As a result, the heat transfer area for one tube increases but it reduces in total. While distant tubes are advantageous in terms of pressure drop and heat transfer, it reduces the total heat transfer area, thus it causes poor heat transfer performance. Therefore, it is better to use closely packed narrow tubes to some extent but after a critical point, it negatively affects the pressure drop.

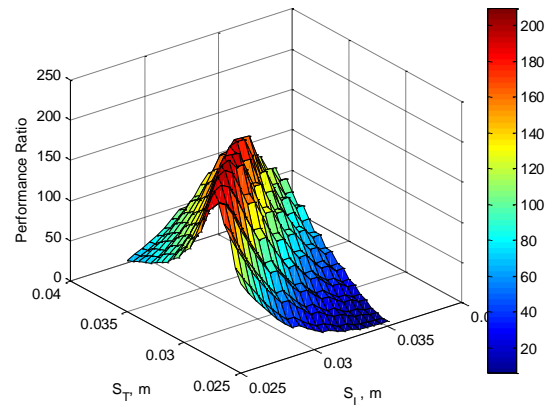


**Figure 13.** Effect of heat exchanger configuration to performance ratio for staggered order ( $m_{pcm,t}=230 \text{ kg}$ ,  $u_{\infty,init} = 0.3 \text{ m/s}$ )

The heat exchanger's maximum performance is obtained as 209.8 for optimum configuration of  $S_L=27 \text{ mm}$  and  $S_T=29 \text{ mm}$ . When compared to aligned order, staggered order performs 18.4% worse. If the  $S_L$  and  $S_T$  are kept shorter than the optimum values, the pressure drop remarkably increases.

When Fig. 7 is examined, heat transfer at the beginning of the melting process varies depending on the air velocity. As the optimum dimensions strongly depend on the air's initial velocity, the optimization procedure is applied for different

initial air velocities. Optimum configurations for different initial velocities are provided in Table 7.

According to the results presented in Table 7, the maximum performance ratio among the examined conditions is obtained for 0.2 m/s initial velocity case. At this value, although the minimum heat transfer requirement is barely satisfied, fan energy consumption is very low. For the 0.3 m/s initial velocity value case, slightly higher heat than the minimum requirement is transferred, but the fan energy demand is high. When the fan power is not an issue ( $u_{\infty,init} = 0.2$  m/s), the optimum  $S_L$  gets the lowest value (25 mm) of the design interval, the optimum  $S_T$  gets the maximum value (35 mm) of the design interval. On the other hand, the  $S_L$  and  $S_T$ 's optimum values are somewhere in the middle of the design intervals for higher initial velocity values. Results show that optimum distances between the tubes in transverse and the longitudinal directions get closer so that the performance ratio is maximized, and the fan energy consumption is reduced at higher velocities. To understand the effect of the design variables interval ( $35 \leq S_L \leq 45, 35 \leq S_T \leq 45$ ), an alternative analysis has been conducted for 0.3 m/s initial velocity case. The use of distant and larger diameter tubes in the HEX has resulted in poor performance ratio. For the lower values of the initial velocity (0.2 and 0.25 m/s), the minimum cooling limit could not be satisfied for the larger design variable intervals for  $S_L$  and  $S_T$  ( $35 \leq S_L \leq 45$  and  $35 \leq S_T \leq 45$ ), even for the optimized cases. Therefore, they are not

presented in Table 7. The difference between the lower and the upper limit of the design variables interval could not be increased further than the presented values because the distance between the tubes should be higher than the outer tube diameter. For the constant initial velocity value, aligned order arrangement has performed better for all cases. Although the staggered order's thermal performance is enough or even better for most of the cases, it causes high fan energy consumption.

It was previously explained that there are many studies conducting research on the thermal enhancement of the PCMs. It has been succeeded that the thermal conductivity of paraffin wax is increased to 1.36 W/(m·K) using expanded graphene. Staying on the safe side ( $k_{pcm} = 0.6$  W/(m·K)), the optimization procedure is applied for the same conditions used for Table 7 except the PCM's thermal conductivity. The results are shown in Table 8.

If the results of Table 8 are interpreted, higher performance ratios are obtained compared to the low thermal conductivity scenario for all cases. The most dramatic increase is observed for larger design variable interval cases ( $35 \leq S_L \leq 45, 35 \leq S_T \leq 45, u_{\infty,init} = 0.3$  m/s). Performance ratios increase 4.58 and 3.52 times for aligned and staggered orders, respectively. The use of larger diameter tubes has become reasonable for higher thermal conductivity cases. Higher thermal conductivity has improved the thermal and hydrodynamic

**Table 7.** Optimum Configurations ( $m_{pcm,t}=230$  kg,  $k_{pcm}=0.2$  W/(m·K))

$u_{\infty,init}$	Order*	Opt. $S_L$ , mm	Opt. $S_T$ , mm	Design Var. Interval of $S_L$	Design Var. Interval of $S_T$	Opt. $D_i$ , mm	Heat Tr., kWh	Fan Energy Cons, kWh	Perf. Ratio
0.3 m/s	A	30	32.5	$25 \leq S_L \leq 35$	$25 \leq S_T \leq 35$	20.6	14.3426	0.055764	257.2
	S	27	29			18.4	14.4334	0.068787	209.8
	A	35	39	$35 \leq S_L \leq 45$	$35 \leq S_T \leq 45$	24.1	14.34	0.0807	177.8
	S	35	37			23.5	14.28	0.09883	144.5
0.25 m/s	A	26	34	$25 \leq S_L \leq 35$	$25 \leq S_T \leq 35$	19.5	14.32	0.016628	861
	S	25	32.5			18.8	14.40	0.02482	580.3
0.2 m/s	A	25	35	$25 \leq S_L \leq 35$	$25 \leq S_T \leq 35$	19.6	14.2768	0.011763	1213.7
	S	25	35			19.6	14.2786	0.017131	833.5

\*A: Aligned, S: Staggered.

**Table 8.** Optimum Configurations ( $m_{pcm,t}=230$  kg,  $k_{pcm}=0.6$  W/(m·K))

$u_{\infty,init}$	Order*	Opt. $S_L$ , mm	Opt. $S_T$ , mm	Design Var. Interval of $S_L$	Design Var. Interval of $S_T$	Opt. $D_i$ , mm	Heat Tr., kWh	Fan Energy Cons, kWh	Perf. Ratio
0.3 m/s	A	30	35	$25 \leq S_L \leq 35$	$25 \leq S_T \leq 35$	21.4	14.8507	0.027503	539.9
	S	30.5	35			21.7	14.8091	0.037427	395.7
	A	36.5	45	$35 \leq S_L \leq 45$	$35 \leq S_T \leq 45$	26.7	14.6550	0.017799	814.2
	S	38.5	45			27.5	14.4926	0.028436	509.6
0.25 m/s	A	25	35	$25 \leq S_L \leq 35$	$25 \leq S_T \leq 35$	19.6	14.7755	0.009902	1492.1
	S	26	35			19.9	14.6424	0.015666	934.6
0.2 m/s	A	25	35	$25 \leq S_L \leq 35$	$25 \leq S_T \leq 35$	19.6	14.2795	0.007641	1868.6
	S	25	35			19.6	14.2813	0.011310	1262.7

\*A: Aligned, S: Staggered.

performance of the system. The question is ‘could the minimum cooling be satisfied with 220 kg PCM with increased thermal conductivity?’ Although the performance ratio decrement, the answer is yes for all the cases in Table 8. The optimization code is executed for 220 kg PCM for the aligned cases presented in Table 8. The performance ratio reduction in the order from higher velocity to the lower velocity case are found as (539.9 → 392.5, 1492.1 → 1087.8, 1868.6 → 1547.1). The maximum deviation in the optimum dimensions is found negligible (1mm).

## CONCLUSION

Melting analysis of a cold energy storage device has been investigated. It is desired to design such a system that satisfies the minimum cooling requirement (2850 W) for 5 hours and requires minimum fan energy consumption. An optimum arrangement and the cross-flow tubular PCM-air cold energy storage HEX configuration has been determined using a variable speed fan. By increasing the fan speed during the melting process, heat transfer between the air and the PCM is kept stable.

- It is observed that the heat transfer ratio in the HEX sharply decays, especially at high air velocities (at constant velocity) due to rapid melting rate at earlier stages of the melting, and thus decreasing melting energy.
- Although it is stable at low velocities, the minimum heat transfer requirement could not be satisfied for the constant velocity case. Therefore, it is necessary to use variable-speed fan to keep the room's comfort temperature.
- The minimum PCM mass required to overcome the specified cooling load (2850 W for 5 hours, 14.25 kWh) is determined to be 230 kg.
- As a result of the optimization study ( $k_{\text{pcm}}=0.2$  W/(m·K)), maximizing the performance ratio, the aligned order performed better than the staggered order for the same design variable interval and the initial velocity of the air.
- The best performance ratio is obtained for the initial velocity of 0.2 m/s for both staggered and aligned arrangements. According to the optimization results of this case, while the tubes are closely placed in the longitudinal direction, they are kept distant in the transverse direction.
- For the highest initial velocity value of 0.3 m/s, space between the tubes in transverse and longitudinal directions becomes closer. At this initial velocity, heat transfer is slightly higher than the minimum limit (2850 W) initially, but the fan speed is increased afterward because of the worsening thermal performance of the system.
- Although the heat transferred is the maximum for 0.3 m/s initial velocity case, the performance ratio is the lowest because of the high fan energy consumption. All the cases tabulated in Table 7 have successfully provided the minimum required cooling. Keeping the

tubes distant and using larger diameter tubes has resulted in low-performance ratios.

- If 0.3 m/s initial velocity, aligned order,  $k_{\text{pcm}}=0.2$  W/(m·K) case is inspected, keeping the design variables interval at larger values required 44.7% higher fan energy consumption for the same heat transfer rate.
- The use of larger diameter tubes has become reasonable for the optimization study performed for  $k_{\text{pcm}}=0.6$  W/(m·K). When compared to low thermal conductivity case, performance ratios increase 4.58 and 3.52 times for aligned and staggered orders, respectively.
- It is possible to save 10 kg PCM thanks to the enhanced thermal conductivity of the PCM.

## REFERENCES

- Asker, M., & Günerhan, H. (2016). Faz değişim malzemeli isi değiştirici üzerine parametrik bir çalışma. *Journal of the Faculty of Engineering and Architecture of Gazi University*, 31(3), 555–565. <https://doi.org/10.17341/gummfd.76037>
- Aydin, O., Avci, M., Yazici, M. Y., & Akgun, M. (2018). Enhancing storage performance in a tube-in shell storage unit by attaching a conducting fin to the bottom of the tube. *Isi Bilimi Ve Teknigi Dergisi/ Journal of Thermal Science and Technology*, 38(2), 1–13.
- Chaiyat, N., & Kiatsiriroat, T. (2014). Energy reduction of building air-conditioner with phase change material in Thailand. *Case Studies in Thermal Engineering*, 4, 175–186. <https://doi.org/10.1016/j.csite.2014.09.006>
- Cheng, W. L., Zhang, R. M., Xie, K., Liu, N., & Wang, J. (2010). Heat conduction enhanced shape-stabilized paraffin/HDPE composite PCMs by graphite addition: Preparation and thermal properties. *Solar Energy Materials and Solar Cells*, 94(10), 1636–1642. <https://doi.org/10.1016/j.solmat.2010.05.020>
- Dhumane, R., Qiao, Y., Ling, J., Muehlbauer, J., Aute, V., Hwang, Y., & Radermacher, R. (2019). Improving system performance of a personal conditioning system integrated with thermal storage. *Applied Thermal Engineering*, 147(June 2018), 40–51. <https://doi.org/10.1016/j.applthermaleng.2018.10.004>
- Dubovsky, V., Ziskind, G., & Letan, R. (2011). Analytical model of a PCM-air heat exchanger. *Applied Thermal Engineering*, 31(16), 3453–3462. <https://doi.org/10.1016/j.applthermaleng.2011.06.031>
- Erdemir, Dogan, and Necdet Altuntop. 2018. “Effect of Encapsulated Ice Thermal Storage System on Cooling Cost for a Hypermarket.” *International Journal of Energy Research* 42 (9): 3091–3101. <https://doi.org/10.1002/er.3971>.

- Erkmen, F. İ., Gedik, G.Z., (2007) Örnek Bir Konutun Farklı Yöntemlerle Hesaplanan Soğutma Yüklerinin Karşılaştırılması : Antalya Ve Diyarbakır Örneği. İstanbul Ticaret Üniversitesi Fen Bilimleri Dergisi, Yıl 6 Sayı 11, 143–163.
- Fang, G., Wu, S., & Liu, X. (2010). Experimental study on cool storage air-conditioning system with spherical capsules packed bed. *Energy and Buildings*, 42(7), 1056–1062. <https://doi.org/10.1016/j.enbuild.2010.01.018>
- Hed, G., & Bellander, R. (2006). Mathematical modelling of PCM air heat exchanger. *Energy and Buildings*, 38(2), 82–89. <https://doi.org/10.1016/j.enbuild.2005.04.002>
- Holman, J P, and P R. S. White. Heat Transfer. London: McGraw-Hill, 1992. Print.
- Incropera, Frank P, and David P. DeWitt. Fundamentals of Heat and Mass Transfer. New York: J. Wiley, 2002. Print.
- Khan, Z., Khan, Z., & Ghafoor, A. (2016). A review of performance enhancement of PCM based latent heat storage system within the context of materials, thermal stability and compatibility. *Energy Conversion and Management*, 115, 132–158. <https://doi.org/10.1016/j.enconman.2016.02.045>
- Koz, M., & Khalifa, H. E. (2018). Phase change material melting in an energy storage module for a micro environmental control system. *Journal of Thermal Science and Engineering Applications*, 10(6). <https://doi.org/10.1115/1.4040896>
- Kuznik, F., Arzamendia Lopez, J. P., Baillis, D., & Johannes, K. (2015). Design of a PCM to air heat exchanger using dimensionless analysis: Application to electricity peak shaving in buildings. *Energy and Buildings*, 106, 65–73. <https://doi.org/10.1016/j.enbuild.2015.03.046>
- Letan, R., Ziskind, G., Thermal design and operation of a portable PCM cooler. in: M. Kutz (Ed.), Heat Transfer Calculations. McGraw-Hill, New York, 2006 (Chapter 39)
- Souayfane, F., Fardoun, F., & Biwole, P. H. (2016). Phase change materials (PCM) for cooling applications in buildings: A review. *Energy and Buildings*, 129, 396–431. <https://doi.org/10.1016/j.enbuild.2016.04.006>
- Türkakar, G., & Okutucu-Özyurt, T. (2012). Dimensional optimization of microchannel heat sinks with multiple heat sources. *International Journal of Thermal Sciences*, 62, 85–92. <https://doi.org/10.1016/j.ijthermalsci.2011.12.015>
- Yang, N., Zhang, X., Li, G., & Hua, D. (2015). Assessment of the forced air-cooling performance for cylindrical lithium-ion battery packs: A comparative analysis between aligned and staggered cell arrangements. *Applied Thermal Engineering*, 80, 55–65. <https://doi.org/10.1016/j.applthermaleng.2015.01.049>
- Zhao, D., & Tan, G. (2015). Numerical analysis of a shell-and-tube latent heat storage unit with fins for air-conditioning application. *Applied Energy*, 138, 381–392. <https://doi.org/10.1016/j.apenergy.2014.10.051>
- Zukauskas, A. “Heat Transfer from Tubes in Cross Flow,” Adv. Heat Transfer, vol. 8, pp. 93–160, 1972.



**Gökter TÜRKAKAR** received BS degree from Mechanical Eng. Dept, Osmangazi University, 2006 Eskisehir Turkey. He obtained his MS on 2010 from Mechanical Eng, Middle East Technical University (METU), Ankara, Turkey. He got his PhD degree from Mech Eng, METU in 2016. He joined Thermal Analysis, Microfluidics and Fuel Cell Lab in Rochester Institute of Technology on March 2015 (9 months) as a visiting scholar. He focused on designing a microscale refrigeration cycle for electronics cooling in his Ph.D. study. He works as a faculty member in Mechanical Department of Zonguldak Bülent Ecevit University since 2017.



## COMPUTATIONAL ANALYSIS OF PULVERIZED COAL CO-FIRING WITH BIOMASS IN 150MWe UNIT OF TUNÇBILEK THERMAL POWER PLANT

Cansu DENİZ CANAL\*, Yakup Erhan BOKE\*\*, Ozer AYDIN\*\*\* and Ali Cemal BENİM\*\*\*\*

\*\*\*Department of Mechanical Engineering, Istanbul Technical University, Istanbul, Turkey

\*cansudeniz@itu.edu.tr, ORCID: 0000-0001-5564-0919, \*\*boke@itu.edu.tr, ORCID: 0000-0003-0449-0329

\*\*\*Department of Mechanical Engineering, Kutahya Dumlupınar University, Kutahya, Turkey

ozel.aydin@dpu.edu.tr, ORCID: 0000-0002-6397-5601

\*\*\*\*Center of Flow Simulation, Faculty of Mechanical and Process Engineering,

Duesseldorf University of Applied Sciences, Germany,

alicemal@prof-benim.com, ORCID: 0000-0002-8642-2225

(Geliş Tarihi: 15.06.2020, Kabul Tarihi: 28.12.2020)

**Abstract:** Pulverized coal and biomass co-firing in the 150MWe unit of Tuncbilek power plant is computationally investigated, within the scope of a preliminary feasibility study. The considered furnace, burning Turkish lignite, has totally eighteen burners, positioned at three different levels. First, the pulverized coal combustion in the furnace is calculated and the predicted temperatures in the boiler first pass are compared with the previous measurements. Subsequently, a co-firing scenario is computationally analyzed, where the burners of the lowest level that supply 43% of the total fuel mass are fed by biomass, instead of coal. Turkish red pine is assumed to be the source of the biomass. In replacing the coal by biomass, the mass flow rates of the biomass and the corresponding air are adjusted in such a way that the thermal load and the equivalence ratio remain unaltered. Due to the lack of more accurate data for the biomass, the rate constants for the pyrolysis and chemical conversion of biomass are assumed to be the same as those of coal, along with the assumption of the same particle size distribution for both fuels. It is observed that the resulting flame structure for the case of co-firing is very similar to that of coal combustion. This result is encouraging for the application of biomass co-firing in the considered furnace.

**Keywords:** Computational Fluid Dynamics, Pulverized Fuel Combustion, Coal and Biomass Co-firing

## TUNÇBILEK TERMİK SANTRALİNİN 150MWe ÜNİTESİNDE PÜLVERİZE KÖMÜRÜN BİYOKÜTLE İLE EŞ YANMASININ HESAPLAMALI ANALİZİ

**Özet:** Pülverize kömür ve biyokütlenin birlikte yanması Tunçbilek termik santralinin 150MWe kapasitesindeki ünitesi için, bir ön fizibilite çalışması kapsamında, sayısal olarak incelenmiştir. Türk linyit kömürü yakmakta olan söz konusu fırın, üç seviyeye yerleştirilmiş toplam on sekiz brülörden beslenmektedir. İlk olarak, fırında pülverize kömür yanması hesaplanmış ve kazan birinci geçiş kanalı içinde bulunan sıcaklıklar daha önceki ölçümlerle karşılaştırılmıştır. Akabinde, toplam yakıt kütlelerinin %43'ünü sağlayan en alt seviyedeki brülörlerden, kömür yerine biyokütle gönderilmesini öngören bir eş yanma senaryosu hesaplamalı olarak analiz edilmiştir. Türk kızıl çamı biyokütle kaynağı olarak kabul edilmiştir. Kömürü, biyokütle yakıtı ile değiştirirken, biyokütle ve hava debileri termik güç ve hava fazlalık katsayısının sabit kalacağı şekilde ayarlanmıştır. Her iki yakıt için de aynı partikül büyüklük dağılımı kabul edilirken, elde daha hassas bilgi olmamasından dolayı, biyokütlenin piroliz ve kimyasal dönüşümü ile ilgili hız sabitlerinin, kömür için kullanılanlar ile aynı olduğu kabul edilmiştir. Birlikte yanma durumunda elde edilen alev yapısının kömür yanmasıninkine çok benzer olduğu gözlemlenmiştir. Bu netice, incelenen kazanda biyokütlenin kömür ile birlikte yanmasını teşvik edici niteliktedir.

**Anahtar Kelimeler:** Hesaplamalı Akışkanlar Dinamiği, Pülverize Yakıt Yanması, Kömür ile Biyokütle Birlikte Yanması

### NOMENCLATURE

A	Fuel ash mass fraction [-]
A, A <sub>i</sub>	Pre-exponential factor [case dependent units]
E, E <sub>i</sub>	Activation energy [J/kmol]
FC	Fuel fixed carbon mass fraction [-]
k	Turbulence kinetic energy [m <sup>2</sup> /s <sup>2</sup> ]
k, k <sub>i</sub> , K <sub>i</sub>	Reaction rate coefficient [units case dependent]

LHV	Lower heating value [J/kg]
m	Mass flow rate [kg/s]
M	Fuel moisture mass fraction [-]
n <sub>j</sub>	Rate exponent belonging to species j [-]
T	Gas temperature [K]
HHV	Higher heating value [J/kg]
V	Velocity magnitude [m/s]
VM	Fuel volatile matter mass fraction [-]

$X_i$  Mole fraction of species  $j$  [-]  
 $y^+$  Non-dimensional wall distance [-]

### Greek Symbols

$\varepsilon$  Dissipation rate of turb. kin. energy [ $m^2/s^3$ ]  
 $\omega$  Turbulence frequency ( $=\varepsilon/k$ ) [1/s]

### Abbreviations

DAF Dry and Ash Free substance  
EDM Eddy Dissipation Model  
L Lower burner level  
M Middle burner level  
MF Mixture fraction  
MFR Mass fraction in percent  
PDF Probability Density Function  
RANS Reynolds Averaged Navier Stokes  
U Upper burner level

### Subscripts

aver Area averaged value  
C Char, Coal  
B Biomass  
D Diffusion  
K Kinetic  
p Pyrolysis

## INTRODUCTION

For the generation of power and heat, combustion is being used as the major process since many decades (Benim et al., 2005, Kim et al., 2007, Benim, 1990, Benim et al. 2017). For solid fuels, gasification techniques are additionally used (Yilmazoglu and Durmaz, 2012, Benim and Kuppaa, 2016). In parallel to the efforts of utilizing renewable energies (Ehrlich, 2013), as well as recovery techniques (DuBois and Mercier, 2009, Ebling et al., 2016), combustion continues to play an important role in renewable energies. This is due to the fact that the biomass, which is a renewable fuel, is also converted by combustion (Açikkalp et al., 2018, Kaltschmitt, 2019, Shi et al., 2019, Smith et al., 2019). Thus, the energetic utilization of biomass via combustion process is the main focus of the present contribution.

In large and medium scale utility boilers that are designed to fire pulverized coal, the common way of burning biomass is co-combustion (Kaltschmitt et al., 2016). In utility boilers, usually only a rather small portion of the energy feed (<50%) is provided by the biomass. This limited use of biomass is caused, on the one hand, by the different fuel properties of biomass, especially with respect to its ash that can lead to increased corrosion problems (which are not addressed in the present study). On the other hand, the logistic reasons play here a role, as the available biomass in the

catchment area of the power plant with affordable transport costs limits the extent of biomass usage.

Co-combustion of biomass in pulverized coal firing utility boilers was investigated by many researchers. One of the early, detailed studies is due to Hein and Spliethoff (1995), who experimentally investigated the co-combustion of biomass in pulverized fuel and fluidized bed systems, which was extended to the investigation of the slagging (Heinzel et al., 1998) and corrosion behaviour (Stephan et al., 2017) in further studies. Nitrogen oxide (NO<sub>x</sub>) emissions were in the focus of the experimental investigations of Nimmo et al. (2010) and Munir et al. (2011). Co-firing of pulverised coal and biomass in a small-scale furnace with a single burner was computationally investigated by Bhuiyan and Naser (2015a), who also analysed large scale power plants for oxy-fuel combustion (Bhuiyan and Naser, 2015b). Experimental and computational studies of pulverised coal and biomass co-combustion in a large scale furnace was provided by Tamura et al. (2014), which was focussing on the effect of grinding. In a rather recent investigation, Pérez-Jeldres et al. (2017) presented a computational modelling of a large scale pulverized fuel furnace for co-firing of coal and biomass, with emphasis on pollutant emissions.

In Turkey, the lignite is the dominating fossil fuel source. The Turkish lignite is characterised by rather high ash content, and consequently, with rather low calorific values (Atımtay et al., 2017). Pulverized combustion of Turkish lignite was computationally investigated in different applications by various researchers (Aydin and Durak, 2012).

Pulverized combustion of Turkish lignite in the presently considered furnace, i.e. the 150MWe unit of the Tuncbilek thermal power plant was computationally investigated, previously, by Ozdemir and Boke (2015). In that work, a mixture fraction based presumed PDF (MF-PPDF) approach (Libby and Williams, 1994) was used as the turbulent combustion model for the gas phase reactions, which assumes a purely mixing controlled combustion. In the presently applied Eddy Dissipation Model (EDM) based methodology, the kinetics effects are additionally considered. An additional difference to the work of Ozdemir and Boke (2015) is the analysis of biomass co-firing.

As a future perspective for biomass utilization in the Tuncbilek thermal power plant, it is envisaged to co-fire Turkish forest red pine. The present study can be considered as a preliminary exploration of biomass (Turkish forest red pine tree wood) co-firing capability in the 150MWe furnace of Tuncbilek thermal power plant, by means of computational modelling.

Compared to the previous work (Ozdemir and Boke, 2015), the novelty of the present work resides mainly in two points. Firstly, the EDM is used as turbulent



combustion model that explicitly addresses kinetics effects. In the previous work, MF-PPDF model was used, which assumes infinitely fast chemistry in the gas phase. It shall also be noted that the use of the MF-PPDF in cases with multiple fuels (like in the present case of biomass co-firing) becomes cumbersome and more prone to inaccuracies, since multiple mixture fractions and their interaction need to be modelled. Secondly, the biomass co-firing is investigated in the present study, while only coal combustion was studied in the previous work.

The above-mentioned preliminary nature of the present study is due to the missing empirical data to characterize the pyrolysis and solid phase oxidation of Turkish forest red pine, which are currently substituted by well-established coal data. In case of the availability of such data for Turkish forest red pine, it would be possible to obtain more accurate predictions in the future.

## MODELING

The general-purpose Computational Fluid Dynamics (CFD) code ANSYS Fluent 19.0 R3 (ANSYS Fluent Theory Guide, 2019) is used, which utilizes a finite volume method of discretization. The density of the gas mixture is calculated assuming an ideal gas. The specific heat capacity of the gas mixture is calculated via fourth order polynomials of temperature. Temperature dependence of the molecular transport properties are neglected (Turns, 2012). The SIMPLE algorithm is used to treat the velocity-pressure coupling. The second-order upwind scheme is utilized to discretize the convection terms. The gradient computation technique was least squares cell based. Stabilization was achieved by a standard cell to face slope limiter. For convergence, it was required that the scaled residuals of all balance equations except the energy and radiation transport equation are smaller than  $10^{-3}$ . For the energy and the radiation transport equations, the required threshold value was  $10^{-6}$ .

### Two-Phase Flow and Convective Transport

For the modelling of the two-phase flow, it has previously been shown that an Eulerian-Eulerian formulation offers computational advantages over the Eulerian-Lagrangian formulation, in the modelling of utility boilers (Benim et al., 2005). Still, in the present work, an Eulerian-Lagrangian approach is adopted, as it is the built-in standard formulation of the employed software, for pulverized coal combustion. The gas phase and particle phase equations are solved alternately, where, the particle iterations are performed after each 30<sup>th</sup> gaseous phase iteration.

The volume occupied by particles, and particle-particle interactions are neglected. Only the gravity and drag force on particle are considered, assuming a spherical shape for the latter (Morsi and Alexander, 2006). The

size distribution is assumed to follow the Rosin-Rammler distribution (Lefebvre and McDonnell, 2017).

A uniform particle temperature is assumed calculating the convective heat transfer coefficient using the correlation of Ranz and Marshall (1952).

### Turbulence

The Reynolds Averaged Navier Stokes (RANS) approach is used to model the turbulent gas flow, where using a turbulent viscosity based turbulence model. Although  $\omega$ -based turbulence models ( $k-\omega$ , SST) became popular in recent years (Menter, 1994), which are especially suitable for wall-driven turbulent flows (Bhattacharyya et al., 2017), in the present case that is governed by free shear layers, turbulence is described by the Standard  $k-\epsilon$  model, amended by the standard wall-functions for the near-wall turbulence (Launder and Spalding, 1974). For the turbulent diffusion of the scalar quantities, the gradient-diffusion approximation is used assuming constant Prandtl-Schmidt numbers for the prevailing fully developed turbulent flow (0.9 for the energy, 0.7 for the species transport equations). The effect of gas turbulence on the particle motion is modelled by the so-called “discrete random walk” model (Gosman and Ioannides, 1983), whereas the influence of the particle phase on the gas turbulence is neglected.

### Radiative Heat Transfer

The radiative heat transfer is modelled by the P1 model (Benim, 1988). The absorption coefficient of the gas mixture is calculated using the Weighted Sum of Gray Gases Model (WSGGM) (Smith et al. 1982), assuming an equivalent path length for the domain. The particle phase radiation is taken into account assuming the value of 0.9 for particle emissivity and scattering factor. The walls are assumed to reflect diffusely. The wall emissivity is assumed to be 0.9.

### Combustion Modelling

The solid fuel particle experiences an evaporation and pyrolysis with increasing particle temperature. The residual char burns via heterogeneous reactions, as the combustible volatile matter reacts homogeneously in the gas phase.

Please note that small amounts of Sulphur and Nitrogen contained in the fuel are also allowed to react to  $SO_2$  and  $NO_2$ , respectively, assuming single-step global reactions. However, this is done for the sake of consistency, without paying special attention to an accurate modelling of the reaction rates (as these reactions do not remarkably affect the velocity, temperature and main species concentrations). Therefore, these reactions will not additionally be referred to in the following. The assumed reactions and combustion models are outlined in more detail below:

## Pyrolysis

During the pyrolysis, the swelling of the particles is accounted for, with an assumed swelling coefficient of 1.4. The combustible volatile matter is represented by a molecule  $C_xH_yO_z$ , assuming a molar mass of 30 kg/kmol, where  $x$ ,  $y$ ,  $z$  depend on the elementary analysis of the fuel.

Following Badzioch and Hawksley (1970), a first-order, single-rate pyrolysis is assumed, where the rate coefficient is expressed by an Arrhenius rate expression. For the rate constants, the commonly used values for lignite are employed (Epple, et al. 2012) that are listed in Table 1.

**Table 1.** Pyrolysis model rate constants.

$A_p$	$E_p$
$3.82 \cdot 10^5$	$74 \cdot 10^6$

Pyrolysis kinetics of biomass (Neves et al., 2011) is, however, not well established. Due to the lack of data for the currently envisaged biomass, i.e. the Turkish red pine, the same pyrolysis rate coefficients as the coal (Table 1) are used for the biomass, too. This potential source of uncertainty is to be reduced in future studies trying to incorporate more specific data.

## Char oxidation

Char is assumed to oxidize to carbon monoxide in a single-step irreversible heterogeneous surface reaction. The rate coefficient is calculated considering a combined rate limiting effects of kinetic and diffusion processes (Field et al., 1967, Baum and Street, 1971). The kinetic rate is described by an Arrhenius rate expression. The diffusion rate is calculated as function of particle size, boundary layer temperature and diffusion coefficient. The used model rate constants are presented in Table 2 (Field et al., 1967, Baum and Street, 1971).

**Table 2.** Char oxidation model rate constants.

$A_K$	$E_K$	$K_D$
$2 \cdot 10^{-5}$	$79.4 \cdot 10^6$	$5.0 \cdot 10^{-12}$

It is considered that the released heat by combustion is partially absorbed by the particle itself. In the current study, heat of reaction absorbed by the particle is assumed to be 30% in ratio.

## Gas phase reactions

The combustion in the gas phase is assumed to occur via a global reaction scheme comprising two irreversible reactions (Turns, 2012). In the first reaction, the volatile matter is assumed to react to CO and  $H_2O$ . The second reaction is the oxidation of CO to  $CO_2$ .

As the rate constants for the chemical kinetics, the default values suggested by the used software have been

used, which are displayed in Table 3. They represent a modified set of the empirical constants suggested by Dryer and Glassmann (1973) and Westbrook and Dryer (1981) for two-step oxidation of hydrocarbons.

It should be admitted that the rate constants for the first reaction (Table 3) are rather arbitrary, since the assumed, hypothetical volatile molecule structure as  $C_xH_yO_z$  is not necessarily corresponding to the hydrocarbons underlying the empirical constants.

**Table 3.** Kinetic rate constants for gas phase reactions.

1 <sup>st</sup> reaction	A	E	$n_{C_xH_yO_z}$	$n_{O_2}$
	$2.119 \cdot 10^{11}$	$2.027 \cdot 10^8$	0.2	1.3
2 <sup>nd</sup> reaction	A	E	$n_{CO}$	$n_{O_2}$
	$2.239 \cdot 10^{12}$	$1.7 \cdot 10^8$	1	0.25

Nevertheless, it is currently assumed to be a reasonable assumption to take the chemical kinetics effects on the reaction at least approximately into account, in the absence of more accurate information. The same rate constants are used for the oxidation of the volatile matter from coal and biomass.

The effect of turbulence is considered by a rather simple approach. The resultant time-averaged volumetric species conversion rate is assumed to be limited by the smaller one of the kinetic and mixing rates.

The mixing rate, i.e. the rate of mass transfer to smallest scales via dissipation of turbulence eddies, is modelled by the Eddy Dissipation Model (EDM) of Magnussen and Hjertager (1976). The original model constants (Magnussen and Hjertager, 1976) are used.

A brief summary of the applied mathematical and numerical modelling is provided in Table 4.

**Table 4.** A brief overview of the modelling.

Two-Phase flow	Eulerian-Lagrangian formulation
Turbulence	RANS, Standard k-ε model
Radiation	P1 model
Pyrolysis	Single-step scheme
Char oxidation	Kinetics and diffusion controlled
Gas combustion	2 step mechanism, EDM
Pressure correction	SIMPLE
Upwinding	Second order upwind

## THE FURNACE UNDER CONSIDERATION

Figure 1 provides a sketch of the longitudinal section of the considered furnace (Aydin, 2013), with a nominal power of 150 MWe, of the Tuncbilek thermal power plant.

The boiler top wall is at an elevation of approx. 80m from the ground. The burners, which are 18 in total, are placed at three elevations. They are indicated by arrows and the given labels L (lower), M (middle), and U (upper) in the figure.

In a previous study (Ozdemir and Boke, 2015), flue gas temperature measurements were performed at six stations along the boiler first pass. The positions of these stations are also indicated by arrows and the labels S1-S6 in Figure 1. Measured from the position of the upper burner level (U), the elevations of the stations S1- S6 are 13.515m, 19.015m, 22.465m, 28.025m, 30.115m and 32.965m, respectively.

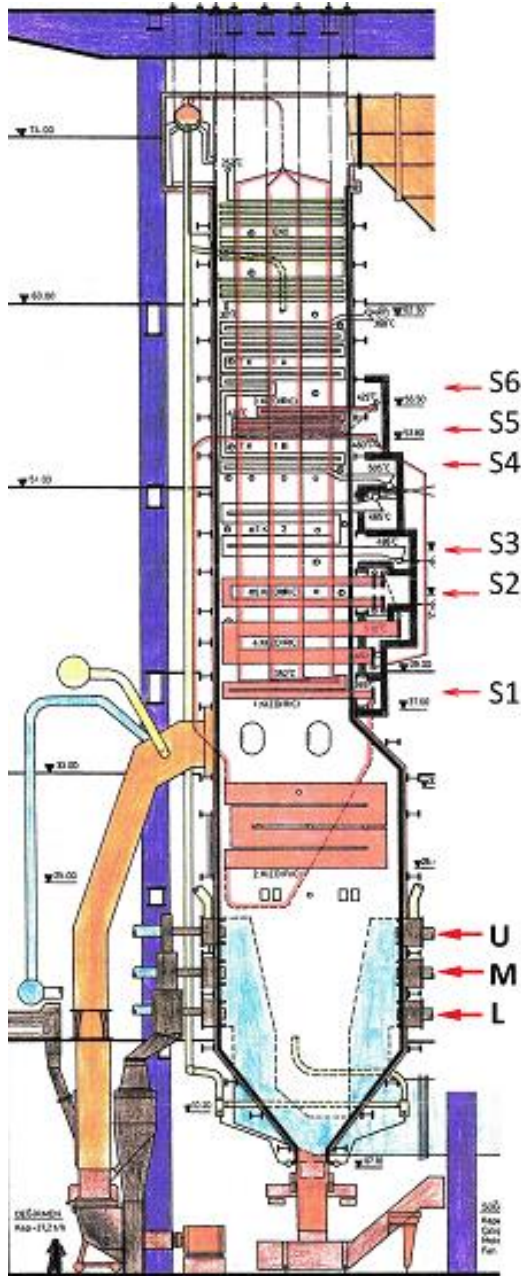


**Figure 1.** Sketch of longitudinal section of furnace (Aydin, 2013), with indication of burners and measuring stations.

The burner arrangement at a level is basically that of a tangential firing, with four corner and two additional frontal burner groups. The burner configuration at a level is depicted in Figure 2 (Ozdemir and Boke, 2015). As can be seen in Figure 2, the frontal burner pair (on the upper and lower walls, referring to Figure 2) is positioned in a slightly inclined and staggered manner to

support the swirling motion generated by the corner burners.

The mass flow rates ( $m$ ) and temperatures ( $T$ ) of the coal as well as primary and secondary air feeds to the furnace are presented in Table 5. The prescribed mass flow rates (Table 5) of coal and total air imply an overall excess air ratio of about 1.25.

**Table 5.** Coal and air feed conditions.

Coal		Primary Air		Secondary Air	
$m$	$T$	$m$	$T$	$m$	$T$
38.6	573	130.7	573	69.1	613

The total coal and total air streams are unevenly distributed among the three burner levels. The percentage distribution of the total coal and air streams among the three burner elevations are presented in Table 6.

**Table 6.** Distribution of coal and air mass flow rates among burner levels.

Burner Level	Coal	Air
U	22 %	14 %
M	35 %	43 %
L	43 %	43 %

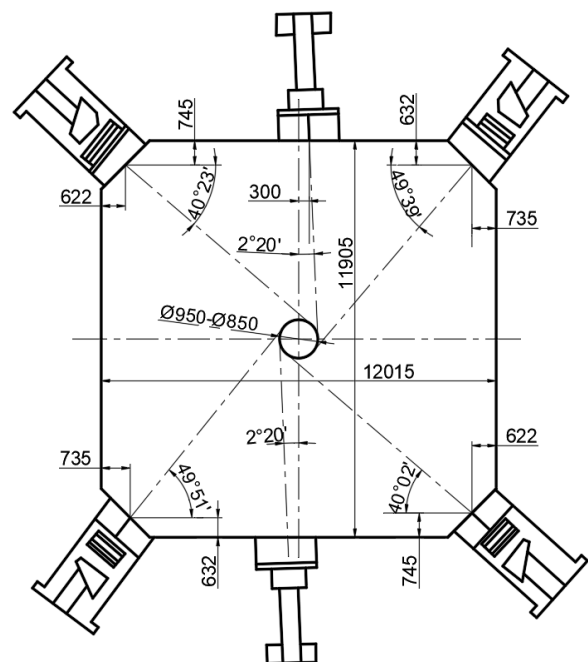


**Figure 2.** Burner arrangement (Ozdemir and Boke, 2015).

At a given burner level, the corresponding, primary and secondary air mass flow rates are equally distributed among the six burners of the level. The coal mass flow rate is equally distributed among five burners, excluding one corner burner, since one of the corner burners were not firing for the considered furnace operation.

The properties of the Turkish lignite used in the regular operation of the boiler are summarized in Table 7.

**Table 7.** Properties of the used coal (Ozdemir and Boke, 2015).

Proximate Analysis		Ultimate Analysis (DAF)	
Substance	MFR (%)	Element	MFR (%)
VM	28.4	C	72
FC	20.4	H	5
A	40.2	O	16.2
M	15.6	N	2.7
		S	4.1
HHV / LHV		1.2852·10 <sup>7</sup> / 1·1960·10 <sup>7</sup>	

### ASSUMED BIOMASS CO-FIRING CONDITIONS

For biomass co-firing, it is envisaged to utilize Turkish red pine chips. The properties of the Turkish red pine chips have been borrowed from the study of Atimtay et al. (2017). The presently adopted set of properties is displayed in Table 8.

In Tables 7 and 8, the heating values are obtained from the corresponding chemical composition according to the ultimate analysis of the solid fuel (coal or biomass) applying the relationships provided by Eppler et al. (2012).

Comparing both fuels, major differences can be observed in their contents of ash and volatile matter. The present lignite coal has a strikingly high ash content (Table 7), which leads to a comparably low heating value. One can also observe that the red pine chips has a much higher content on the volatile matter (Table 8), compared to coal, which is rather typical for biomass fuels.

**Table 8.** The assumed properties of the Turkish red pine chips (Atimtay et al. 2017).

Proximate Analysis		Ultimate Analysis (DAF)	
Substance	MFR (%)	Element	MFR (%)
VM	65.27	C	57.34
FC	16.16	H	9.07
A	1.56	O	33.35
M	17.01	N	0.24
		S	0
HHV / LHV		2.1512·10 <sup>7</sup> / 1·9415·10 <sup>7</sup>	

In biomass co-firing, in general, a full replacement of coal by biomass is hardly found for large scale utility boilers. A reason is simply the limited availability of the necessary biomass in the catchment area of the power plant.

A further important reason is the increasing potential of hazardous effects (such as high temperature corrosion), depending of the properties of biomass in hand. A replacement by 10-20% is rather frequently encountered in large scale utility boilers (Kaltschmitt, 2019).

In the present, preliminary feasibility study, it is assumed that the lower level burners (L, Figure 1), which, in total, provide 43% (Table 6) of the total fuel supply are completely fired by biomass. This choice of

the lower burner level for the biomass co-firing is also in line with the suggestion of Tamura et al. (2014).

Thus, the case of biomass co-firing differs from the coal combustion in the mass flow rates of fuel and air at the lower level of burners. The mass flow rate of the biomass is adjusted in such a way that the thermal load compared to coal remains unchanged, i.e.

$$m_B = m_C \text{ LHV}_C / \text{LHV}_B$$

The ratio of the LHV is about 0.62, leading to a biomass flow rate, which is 62% of the coal mass flow rate of the burner (L). The air supply is adjusted to keep the burner (L) equivalence ratio unchanged between the coal and biomass co-firing cases. The stoichiometric air requirement of biomass is larger compared to coal, due to its larger content on combustibles. The current stoichiometric air requirement ratio of biomass to coal is about 1.61. This means that the burner (L) air mass flow rate for the biomass remains practically unchanged ( $0.61 \times 1.61 = \text{approx. } 1$ ).

### GEOMETRY, BOUNDARY CONDITIONS, GRID

The modelled geometry of the furnace is illustrated in Figure 3. As it can be seen in Figure 1, the upper parts of the furnace are frequently obstructed by heat exchanger tube bundles. These tubes were not resolved in generating the geometry. The increased flow resistance in these regions are approximately modelled by defining this region as a porous media, with a porosity of 0.8.

The solution domain is enclosed by three types of boundaries: inlet, outlet and walls. The inlet boundaries are attached to the burners (Figure 3c). The outlet boundary is placed at the entry to the second pass of the furnace, which is represented by the gray rectangular zone at the top of the furnace geometry (Figure 3a).

The remaining boundaries are walls. At walls, the no-slip boundary condition applies for the momentum equations, which are amended with the wall-functions approach (Launder and Spalding, 1974) for treating the near-wall turbulence. The wall temperature is prescribed to be 659 K, which is 50 K above the saturation temperature of the water in the pipes. Wall emissivities are assumed to be 0.9.

At the outlet a constant gauge pressure is prescribed. The outlet is assumed to be black for thermal radiation.

There are two types of inlet boundaries, one for the supply of pulverized fuel and the primary air, and one for the secondary air. The configuration of these boundaries for a burner is illustrated in Figure 3c. On the rectangular inlet surface of a burner, there are four sub-rectangles representing the inlet boundaries for the pulverized fuel and primary air. The remaining area is the inlet boundary for the secondary air.

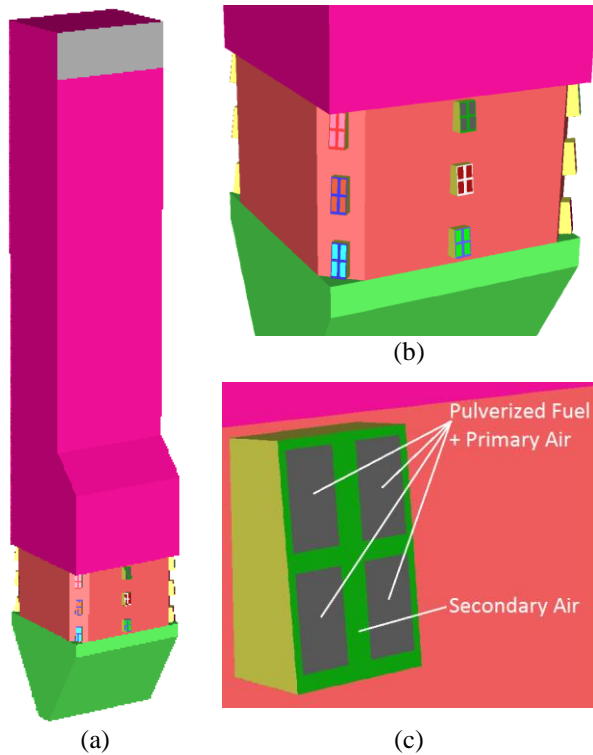


**Figure 3.** Geometry, (a) a full view, (b) detail view of the burner belt, (c) detail of a single burner.

At inlets mass flow rates and temperatures for air and coal are prescribed in accordance with the furnace operating conditions as summarized in the previous section, in Tables 5 and 6. The inlet boundary conditions for the turbulence quantities are estimated based on the prevailing hydraulic diameter and an assumed turbulence intensity of 10%. Inlet boundaries are assumed to behave as black surfaces for thermal radiation.

Depending on the particle size analysis, particle diameters of  $90\mu\text{m}$ ,  $500\mu\text{m}$ ,  $100\mu\text{m}$  are prescribed as the minimum, maximum and mean diameters for the assumed Rosin-Rammler distribution, along with a spread parameter of 4.2 (Lefebvre and McDonnell, 2017). At inlets, the particle velocities are assumed to be equal to the local gas velocity. In experimental trials, it was observed that the pulverization of the used biomass seem to lead to similar results to coal. Thus, for the case of biomass, the same size distribution is applied.

The grid is generated by an unstructured gridding strategy, applying a fine resolution especially in the vicinity of the burners. A detail view of the surface grid in the region of the burner belt is displayed in Figure 4.

The grid has 4.2 million cells in total (base grid). The maximum and average skewness in the grid were 0.85 and 0.29, respectively. The resulting  $y^+$  value of the next-to-wall cells was about 550 on the average, which can be considered to be quite adequate for the present free shear-layer dominated turbulent flow, as already pointed out above. A formal grid independence study

was not performed. However, the inspection of the recent literature shows that the total number of cells used in discretizing similar furnaces is not necessarily larger than the present one. For example, Madjeski (2018) simulated a 500Wth pulverized furnace with eighteen frontal burners and used a grid with 3 million cells. This may be seen to support the adequacy of the presently used grid. For a further confirmation of the present grid, results are also obtained on a finer grid with 7.3 million cells, for the case of coal combustion.

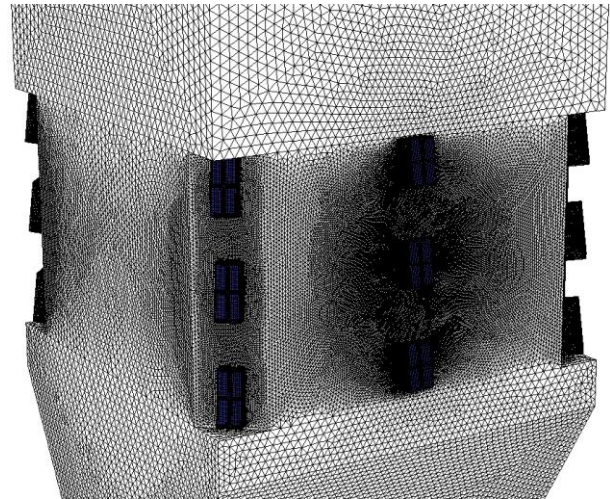


**Figure 4.** Detail view of surface grid.

## RESULTS

Please note that all results presented in this section are obtained on the grid with 4.2 million cells (base grid), unless otherwise stated explicitly. The above mentioned finer grid with 7.3 million cells is used for comparison, only for the predicted temperatures along the boiler first pass, discussed at the end of the Coal Combustion sub-section.

### Coal Combustion

For the pulverized coal combustion, the predicted distributions of velocity vectors at the three burner levels (L, M, U, Figure 1) are displayed in Figures 5a-c (coloring with the velocity vector magnitude). The rotational motion, which is typical for tangentially fired furnaces can be recognized. Due to the difference in the mass flow rates (Table 6) the jets in the levels L and M have higher velocities and penetration compared to those at the level U.

The predicted temperature fields at three burner levels are presented in Figures 5d-f. At the low and middle burner levels (L, M) with rather high burner speeds, one can observe that the high-temperature zone is concentrated rather in the middle parts of the furnace. At the upper burner level (U) with comparably low burner velocities, one can see that the temperature distribution is more homogeneous.

Velocity magnitude and static temperature distributions in the furnace, in a middle, longitudinal plane through the frontal burners are presented in Figure 6.

Comparably higher velocities and penetration of the jets of the L and M burner levels compared to the U level can again be observed (Figure 6a). High temperatures are predicted in the furnace region, which gradually diminish along the boiler first pass due to heat loss to furnace walls (Figure 6b).

The predicted temperatures (PRED) at the stations S1-S6 (Figure 1) are compared with the measurements in Figure 7.

In the figure, the predicted temperature values by the finer grid with 7.3 million cells (PRED Finer Grid) are also displayed. The previous predictions of Ozdemir and Boke (2015) using a different combustion model (MF-PPDF) are also shown in the figure.

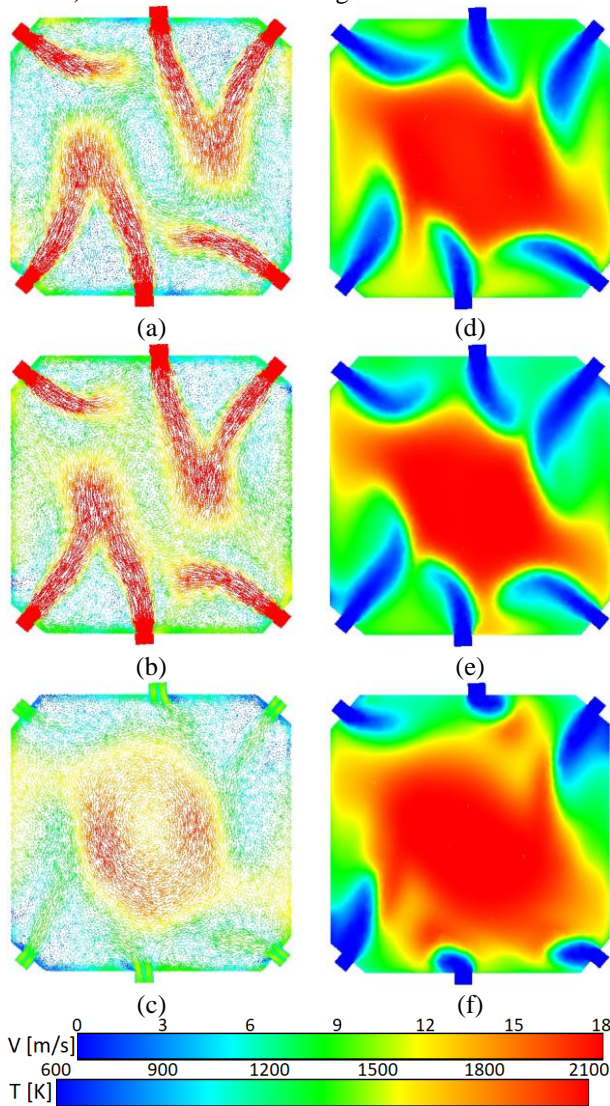


**Figure 5.** Coal combustion – Predicted fields at three burner levels, velocity vectors: (a) L, (b) M, (c) U, static temperature: (d) L, (e) M, (f) U.

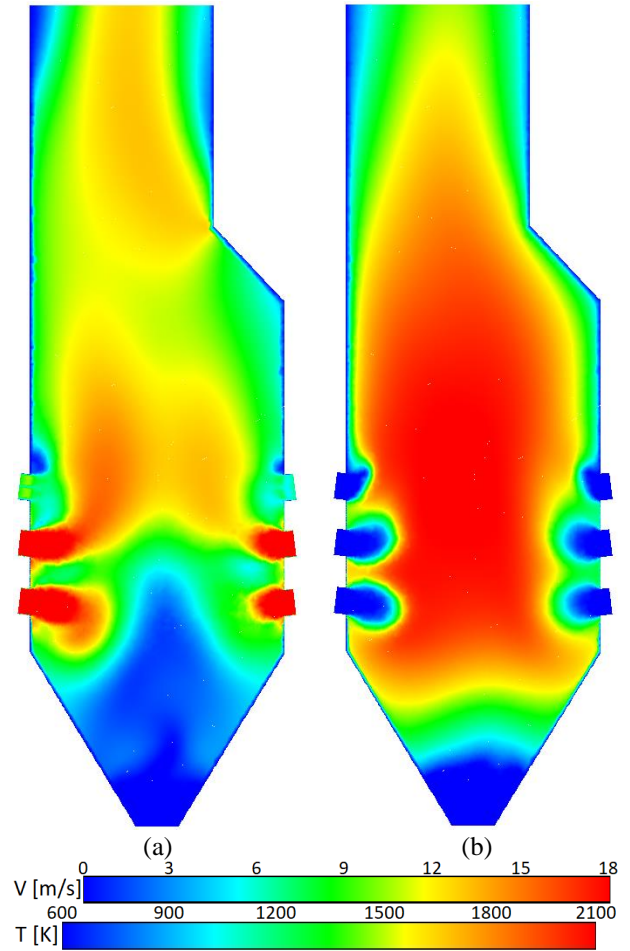


**Figure 6.** Coal combustion - Predicted fields in the furnace in the longitudinal middle plane through the frontal burners, (a) velocity magnitude, (b) static temperature.

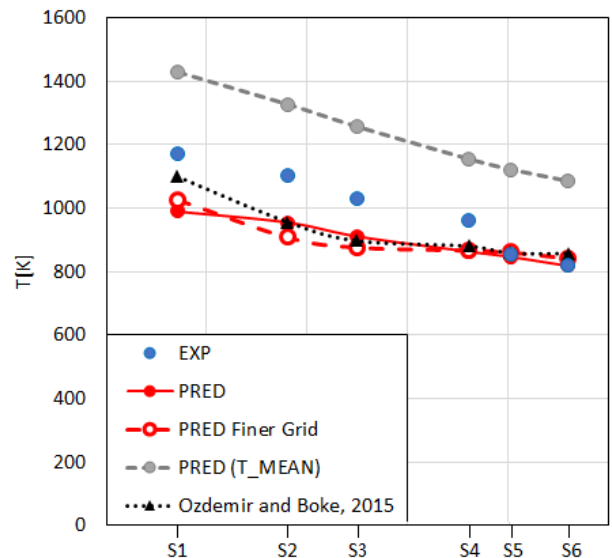


**Figure 7.** Coal combustion - Measured and predicted temperatures at stations S1-S6 (Figure 1) along the boiler first pass.

At this stage, the performed measurements need to be explained in more detail. The temperature measurements were performed along horizontal lines that are running parallel to furnace walls with a 45 cm distance to the wall.

Such measurements were performed only for the two walls without frontal burner (the left and right walls, referring to Figure 2).

Thus, at a given station, there are two lines, where temperature was measured as described above. Along each line, the temperature is averaged. For each station, the average temperatures of the both corresponding lines are again averaged. The displayed experimental and predicted temperatures (EXP, PRED, PRED Finer Grid, Ozdemir and Boke, 2015, Figure 7) are obtained in this manner.

One should note that the significance of these temperatures may be seen to be disputable to an extent, since, being obtained on lines quite near the wall, they may not necessarily be seen to be very representative.

Thus, as complementary information, the predicted average temperatures (mass weighted averaging) at the corresponding cross sections along the boiler first pass are also displayed in the figure (T\_MEAN, Fig. 7).

In Figure 7, one can see that for the lines where temperature was measured, the results generally underpredict the measurements, but agree well with the latter for the last two station. One can also see that the cross-sectional mean temperatures are much higher, compared to the line-averaged temperatures. Since the latter are rather close to the relatively cold walls, this is an expected behavior.

At this stage, it should also be noted that the heat transfer (heat extraction) through the heat exchanger tube bundles, which are positioned along the boiler first pass (Figure 1) has not been modelled (although their aerodynamic influence was modelled by assuming a porous media, as indicated above), which can be seen as an argument to explain observed the over-prediction by the mean temperatures.

Although the comparison is not very conclusive, one can still note that the predicted temperatures show a similar general trend to the measurements (Figure 7).

In Figure 7, one can also observe that the results of the finer grid (7.3 million cells) are rather close to those of the base grid supporting the assumption of an adequate grid resolution by the base grid (4.2 million cells), which is also used in the simulation of biomass co-firing, discussed in the following sub-section.

It can also be observed in Figure 7 that the temperatures predicted previously by Ozdemir and Boke (2015) using a different combustion model (MF-PPDF) are very close to the present predictions. This can be seen as a further verification of the present results. At the first station, S1, the predicted value of Ozdemir and Boke (2015) is closer to the experimental value. However, since the measurements are very local along lines close to wall and, therefore, have a disputable representativeness, this

shall not necessarily be taken as an indication of a possible superiority of the MF-PPDF model. As already mentioned above, the EDM principally provides a more convenient and flexible framework for modelling the co-firing of different types of fuels and considering chemical kinetics effects.

### Biomass Co-firing

For the co-firing case, the predicted distributions of the velocity vector fields at the three burner levels (L, M, U, Figure 1) are displayed in Figures 8a-c, while the predicted static temperature fields at the three burner levels are shown in Figures 8d-f. One can see that both the velocity vector field and temperature patterns obtained for the biomass co-firing (Figure 8) are very similar to those obtained for the coal combustion (Figure 5).

Distributions of the velocity magnitude as well as the static temperature in the furnace region, in a middle, longitudinal plane through the frontal burners are presented in Figure 9.

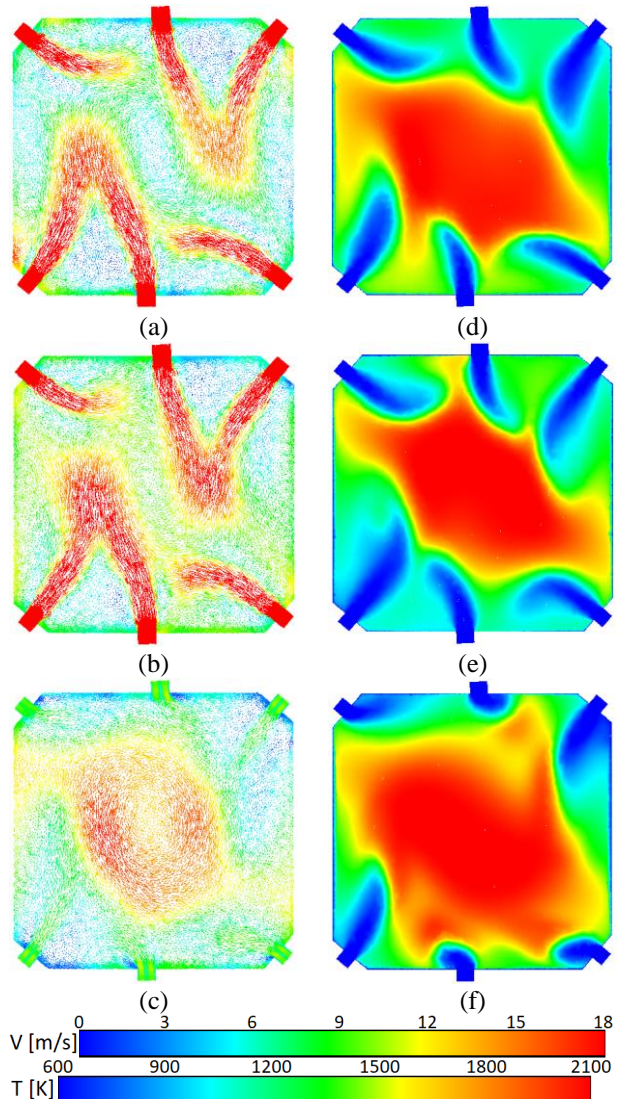


**Figure 8.** Biomass co-firing – Predicted fields at three burner levels, velocity vectors: (a) L, (b) M, (c) U, static temperature: (d) L, (e) M, (f) U.

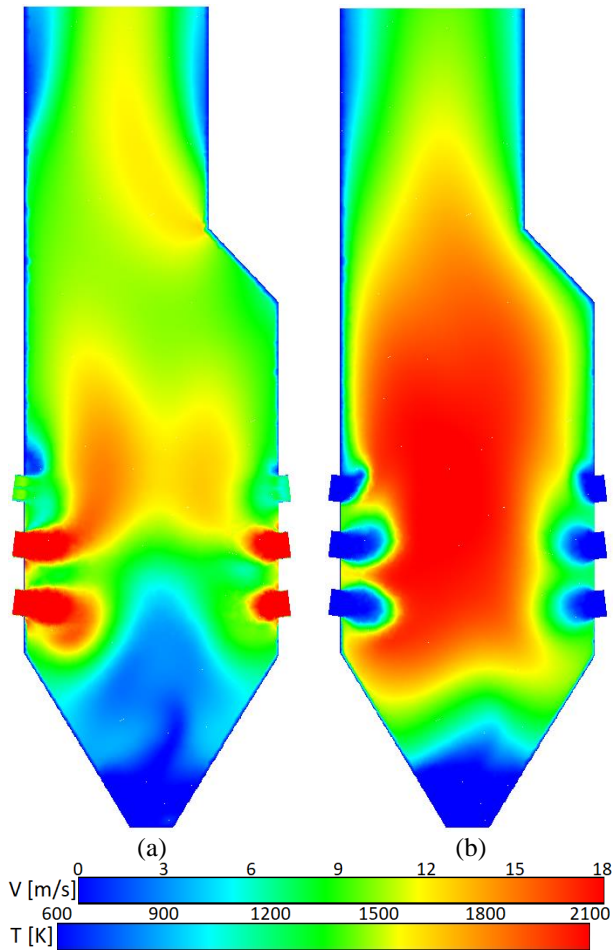


**Figure 9.** Biomass co-firing - Predicted fields in the furnace in the longitudinal middle plane through the frontal burners, (a) velocity magnitude, (b) static temperature.

It can be observed, again, that the resulting velocity and temperature distributions for the biomass co-firing are (Figure 9) very similar to those of the coal combustion (Figure 6).

One can also see the flame (the high temperature zone) is slightly shorter for the biomass co-firing (Figure 9b) compared to coal combustion (Figure 6b). This may be attributed to the high volatile content of the biomass that can burn, in the gas phase, more rapidly compared to solid char.

In addition to the comparison based on the contour plots (Figures 5, 6, 8, 9), a quantitative comparison is provided in Table 9, which presents the area averaged values of the predicted velocity magnitude, temperature and H<sub>2</sub>O, CO and CO<sub>2</sub> mole fractions at three burner levels for coal and biomass co-firings. The percentage deviation of the biomass co-firing values from those of coal are also provided in the table (the difference is normalized by the value for coal).

One can see that the velocity and temperature values predicted for both types of firing are, in general, quite close to each other, which was also implied by the comparison of the contour plots.

**Table 9.** Area averaged velocity magnitude, temperature and species mole fractions predicted for coal and biomass co-firing and their percentage deviation (the latter is calculated on the basis of coal firing and given in absolute value).

	Coal firing	Biomass co-firing	% deviation
Lower Burner Level (L)			
V <sub>aver</sub> [m/s]	10.50	10.46	0.4
T <sub>aver</sub> [K]	1525	1472	3.5
X <sub>H2O,aver</sub> [-]	0.057	0.068	19.3
X <sub>CO,aver</sub> [-]	0.0046	0.0042	8.7
X <sub>CO2,aver</sub> [-]	0.114	0.1	12.3
Middle Burner Level (M)			
V <sub>aver</sub> [m/s]	11.70	11.72	0.2
T <sub>aver</sub> [K]	1464	1432	2.2
X <sub>H2O,aver</sub> [-]	0.049	0.056	14.3
X <sub>CO,aver</sub> [-]	0.0038	0.0038	0
X <sub>CO2,aver</sub> [-]	0.102	0.0918	10.0
Upper Burner Level (U)			
V <sub>aver</sub> [m/s]	9.70	9.69	0.1
T <sub>aver</sub> [K]	1627	1600	1.7
X <sub>H2O,aver</sub> [-]	0.057	0.063	10.5
X <sub>CO,aver</sub> [-]	0.0043	0.0041	4.7
X <sub>CO2,aver</sub> [-]	0.1226	0.112	8.7

The deviations are comparably larger for the species mole fractions (Table 9), due to the differences in the fuel compositions. Biomass has a lower carbon and a higher hydrogen content compared to coal (Tables 7, 8). Consequently, water vapor and carbon monoxide/dioxide mole fractions for biomass co-firing result in higher and lower values compared to coal firing, respectively.

Additionally, one can also observe that the deviations between the two firings, in general, are at largest for the low burner level, and gradually decrease at the middle and the upper burner levels (Table 9). This is an expected trend, since biomass is fired at the low burner level.

Obviously, from the viewpoint of conserving the primary energy resources, biomass has the advantage of being a renewable energy resource. From the environmental point of view, as already mentioned above, an additional advantage of biomass is, that its combustion causes smaller amounts of carbon dioxide emissions, compared to coal, simply due to its comparably lower content on carbon (Tables 7, 8).

For the present situation, this is demonstrated in Figure 10, where the predicted carbon dioxide mole fractions at the exit of the furnace (mass averaged values) are compared for coal combustion and biomass co-firing.

A reduction of the carbon dioxide emissions with approximately 10% by the biomass co-firing can be observed (Figure 10).



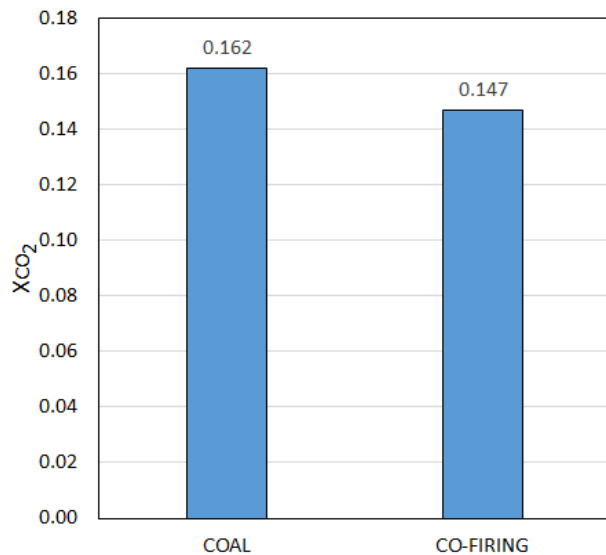


**Figure 10.** Predicted mean carbon dioxide mole fractions at furnace exit.

## CONCLUSIONS

Within a preliminary feasibility study, pulverized coal and biomass co-firing in the 150MWe unit of Tuncbilek power plant is computationally investigated.

Turkish red pine is assumed to be the biomass source. The eighteen burners of the furnace were arranged at three levels, having six burners at each level. In the assumed co-firing scenario, the burners of the lowest level that supply 43% of the total fuel mass are fed by biomass, instead of coal. In replacing the coal by biomass, the mass flow rates of the biomass and the corresponding air are adjusted in such a way that the thermal load and the equivalence ratio remain unaltered. The results show that the biomass co-firing results in a very similar flame structure compared to the coal firing. This is encouraging for the application of biomass co-firing in the considered furnace.

For more accurate results and more precise conclusions, further studies are necessary. In the present modelling, there are several sources uncertainty including e.g. the rate constants for the pyrolysis and chemical conversion of biomass being identical to those of coal. Model improvements along these lines will be considered in the future work.

## ACKNOWLEDGEMENT

Computing resources used in this work were provided by the National Center for High Performance Computing of Turkey (UHeM) under grant number 1007492020.

## REFERENCES

- Acikkalp, E., Zeng, T., Ortwein, A., Burkhardt, H. and Klenk W., 2018, Exergy, Exergoeconomic and Enviroeconomic Evaluation in a Biomass-Steam Engine Micro-CHP System, *Chemical Engineering and Technology*, 41(11), 2141-2149.
- ANSYS Fluent Theory Guide, 2019, Release 2019 R3, ANSYS Inc., Canonsburg.
- Atimtay, A. T., Kayahan, U., Unlu, A., Engin, B., Varol, M., Olgun, H. and Atakul, H., 2017, Co-firing of Pine Chips with Turkish Lignites in 750 kWth Circulating Fluidized Bed Combustion System, *Bioresource Technology*, 224, 601-610.
- Aydin, Ö., 2013, Tunçbilek Termik Santralinde Kömür Kazan Uyumunun Araştırılması, *TÜBİTAK Araştırma Projesi Gelişme Raporu*, Proje No. 112M871.
- Aydin, Ö. and Durak, M. M., 2012, The Effect of Temperature Distribution on Tube Rupture, *Journal of Thermal Science and Technology*, 7(4), 753-766.
- Badzioch, S. and Hawskey, 1970, *Kinetics of Thermal Decomposition of Pulverized Coal Particles*, Industrial & Engineering Chemistry Process Design and Development, 9, 521-530.
- Baum, M. M. and Street, P.J., 1971, Predicting the Combustion Behaviour of Coal Particles, *Combustion Science and Technology*, 3, 231-243.
- Benim, A. C., 1988, A Finite Element Solution of Radiative Heat Transfer in Participating Media Utilizing the Moment Method, *Computer Methods in Applied Mechanics and Engineering*, 67(1), 1-14.
- Benim, A. C., 1990, Finite Element Analysis of Confined Turbulent Swirling Flows, *International Journal for Numerical Methods in Fluids*, 11, 697-717.
- Benim, A. C., Epple, B. and Krohmer, B., 2005, Modelling of Pulverised Coal Combustion by a Eulerian-Eulerian Two-Phase Flow Formulation, *Progress in Computational Fluid Dynamics – An International Journal*, 5(6), 345-361.
- Benim, A. C., Iqbal, S., Meier, W., Joos, F. and Wiedermann, A., 2017, Numerical Investigation of Turbulent Swirling Flames with Validation in a Gas Turbine Model Combustor, *Applied Thermal Engineering*, 110, 202-212.
- Benim, A. C. and Kuppa, K., 2016, Modeling of Entrained-Flow Coal Gasification by an Eulerian-Eulerian Two-Phase Flow Formulation, *Isi Bilimi ve Teknigi Dergisi / Journal of Thermal Science and Technology*, 36(2), 93-102.

- Benim, A. C., Stegelitz, P. and Epple, B., 2005, Simulation of the Two-Phase Flow in a Laboratory Coal Pulveriser, *Forschung im Ingenieurwesen – Engineering Research*, 69, 197-204.
- Bhattacharyya, S., Chattopadhyay, H. and Benim, A. C., 2017, Computational Investigation of Heat Transfer Enhancement by Alternating Inclined Ribs in Tubular Heat Exchanger, *Progress in Computational Fluid Dynamics – An International Journal*, 17(6), 390-396.
- Bhuiyan, A. A. and Naser, J., 2015a, Numerical Modeling of Biomass Co-Combustion with Pulverized Coal in a Small Scale Furnace, *Procedia Engineering*, 105, 504-511.
- Bhuiyan, A. A. and Naser, J., 2015b, CFD Modelling of Co-Firing of Biomass with Coal under Oxy-Fuel Combustion in a Large Scale Power Plant, *Fuel*, 159, 150-168.
- Dryer, F. L. and Glassmann, L., 1973, High Temperature Oxidation of CO and CH<sub>4</sub>, *Proceedings of the 14<sup>th</sup> Symposium (Int.) on Combustion*, The Combustion Institute, Pittsburgh.
- DuBois, E. and Mercier A. (Eds.), 2009, *Energy Recovery*, Nova Science Publishers, New York.
- Ebling, D. G., Krumm, A., Pfeiffelmann, B., Gottschald, J., Bruchmann, J., Benim, A. C., M. Adam, M., Labs, R., Herbertz, R. R. and Stunz, A., 2016, Development of a System for Thermoelectric Heat Recovery from Stationary Industrial Processes, *Journal of Electronic Materials*, 45(7), 3433-3439.
- Ehrlich, R., 2013, *Renewable Energy*, CRC Press, Boca Raton.
- Epple, B., Leithner, R., Linzer, W. and Walter H. (Eds.), 2012, *Simulation von Kraftwerken und Feuerungen*, Springer, Vienna.
- Field, M. A., Gill, D. W., Morgan, B. B. and Hawskley, 1967, *Combustion of Pulverized Coal*, The British Coal Utilization Research Association, Letherhead.
- Gosman A. D. and Ioannides, E., 1983, Aspects of Computer Simulation of Liquid-Fuelled Combustors, *Journal of Energy*, 7(6), 482–490.
- Hein, K. R. G. and Spliethoff, 1995, Co-combustion of Coal and Biomass in Pulverized Fuel and Fluidized Bed Systems, *The Institute of Energy's Second International Conference on Combustion & Emissions Control*, 127-136.
- Heinzel, T., Siegle, V., Spliethoff H. and Hein, K. R. G., 1998, Investigation of Slagging in Pulverized Fuel Co-Combustion of Biomass and Coal at a Pilot-Scale Test Facility, *Fuel Processing Technology*, 54 (1-3),109-125.
- Kaltschmitt, M. (Ed.), 2019, *Energy from Organic Materials*, Springer, New York.
- Kaltschmitt, M., Hartmann, H. and Hofbauer, H. (Eds), 2016, *Energie aus Biomasse*, 3<sup>rd</sup> ed., Springer, Berlin.
- Kim, J. P., Schnell, U., Scheffknecht, G., and Benim, A. C., 2007, Numerical Modelling of MILD Combustion for Coal, *Progress in Computational Fluid Dynamics – An International Journal*, 7(6), 337-346.
- Launder, B. E. and Spalding, D. B., 1974, The Numerical Computation of Turbulent Flows, *Computer Methods in Applied Mechanics and Engineering*, 3(2), 269-289.
- Lefebvre, A. H. and McDonnel, V. G., 2017, *Atomization and Sprays*, 2<sup>nd</sup> ed., CRC Press, Boca Raton.
- Libby, P. A. and Williams. F. A., 1994, *Turbulent Reacting Flows*, Academic Press, Cambridge.
- Madjeski, P., 2018, Coal Combustion Modelling in a Frontal Pulverized Coal-Fired Boiler, *E3S Web of Conferences*, 46, 00010.
- Magnussen, B. F. and B. H. Hjertager, 1976, On Mathematical Modelling of Turbulent Combustion with Special Emphasis on Soot Formation and Combustion, *Proceedings of the 16<sup>th</sup> Symposium (Int.) on Combustion*, The Combustion Institute, Pittsburgh, 719-729.
- Menter, F. R., 1994, Two-Equation Eddy-Viscosity Turbulence Models for Engineering Applications, *AIAA Journal*, 32(8), 1598-1605.
- Morsi, S. A. and Alexander, A. J., 2006, An Investigation of Particle Trajectories in Two-Phase Flow Systems, *Journal of Fluid Mechanics*, 55(2), 193-208.
- Munir, S., Nimmo, W. and Gibbs, B. M., 2011. The Effect of Air-Staged, Co-Combustion of Pulverised Coal and Biomass Blends on NO<sub>x</sub> Emissions and Combustion Efficiency, *Fuel*, 90, 126-135.
- Neves, D., Thunman, H., Matos, A., Tarelho, L. and Gomez-Barea, A., 2011, *Progress in Energy and Combustion Science*, 27, 611-630.
- Nimmo, W., Daood, S. S. and Gibbs, B. M., 2010, The Effect of O<sub>2</sub> Enrichment on NO<sub>x</sub> Formation in Biomass Co-Fired Pulverised Coal Combustion, *Fuel*, 89, 2945-2952.
- Ozdemir, F. and Boke. E., 2015, Tunçbilek Termik Santrali 5 Ünite Kazanının Sayısal Modellemesi, *13. Uluslararası Yanma Sempozyumu*, Bursa, 9 Eylül 2015.

Pérez-Jeldres, R., Cornejo, P., Flores, M., Gordon, A. and Garcia.X., 2017, A Modeling Approach to Co-Firing Biomass/Coal Blends in Pulverized Coal Utility Boilers: Synergetic Effects and Emissions Profiles, *Energy*, 120, 663-674.

Ranz W. E. and Marshall, Jr. W. R., 1952, Evaporation from Drops, Part I and Part II, *Chemical Engineering Progress*, 48(4), 173–180.

Shi, X., Gao, J. and Lan, X., 2019, Modelling the Pyrolysis of a Centimeter-Sized Biomass Particle, *Chemical Engineering Technology*, 2019, 42(12), 2574-2579.

Smith, J. D., Alembath, A., Al-Rubaye, H., Yu, J., Gao, X. and Golpour, H., 2019, Validation and Application of a Kinetic Model for Downdraft Biomass Gasification Simulation, *Chemical Engineering and Technology*, 42(12), 2505-2519.

Smith, T. F., Shen, Z. F. and Friedman, J. N., 1982, Evaluation of Coefficients for the Weighted Sum of Gray Gases Model, *Journal of Heat Transfer*, 104, 602–608.

Stephan, A., Wolf, C., Fendt, S. and Spliethoff, H., 2017, Online Corrosion Measurements in Small- and Mid-Scale During Pulverized Biomass/Coal Co-Combustion, *Energy Procedia*, 120, 309-316.

Tamura, M., Watanabe, S., Kotake, N. and Hasegawa, M., 2014, Grinding and Combustion Characteristics of Woody Biomass for Co-Firing with Pulverised Coal Boilers, *Fuel*, 134, 544-553.

Turns, S. R., 2012, *An Introduction to Combustion*, 3<sup>rd</sup> ed., McGraw-Hill, New York.

Yilmazoglu, M. Z. and Durmaz, A., 2012, Thermodynamic Analysis of an Integrated Gasification Combined Cycle Power Plant, *Isi Bilimi ve Teknigi Dergisi / Journal of Thermal Science and Technology*, 32, 43-53.

Westbrook, C. K. and Dryer, F. L., 1981, Simplified Reaction Mechanisms for the Oxidation of Hydrocarbon Fuels in Flames, *Combustion Science and Technology*, 27, 31-43.



**Cansu Deniz Canal, M.Sc.**, graduated from Marmara University, Environmental Engineering and Mechanical Engineering Department of Engineering Faculty in 2011. She earned her MSc. degree at İstanbul Technical University, Energy Science and Technology Department in 2014. She is working as a research assistant at Istanbul Technical University, Mechanical Engineering Faculty since 2014. She worked as a guest researcher at Heat and Mass Transfer Institute of RWTH Aachen University and Center of Flow Simulation of Düsseldorf University of Applied Sciences. She is currently working on her PhD. Thesis, which is related to pulverized coal and biomass co-firing. Her research topics are combustion, hydrogen production technologies and renewable energy systems.



**Prof. Dr. Yakup Erhan Boke** graduated from Yıldız Technical University, Faculty of Mechanical Engineering in 1983. His MSc. study was completed at İstanbul Technical University, Mechanical Engineering Department in 1985, and PhD was finished at the same university in 1993. He worked as a guest researcher at Clausthal Technical University between 1990 and 1992, as a research assistant between 1984 and 1994 at İstanbul Technical University and as Assist. Prof. Dr. between 1994-2013. Between 2013-2018, he was Assoc. Prof. Dr. at the same university. Now, he is working as Prof. Dr. at İstanbul Technical University, Mechanical Engineering Faculty. His research topics are combustion, steam boilers, CFD and heat technology.



**Prof. Dr. Ozer Aydin** completed his BSc. degree at Kutahya Dumlupınar University, Mechanical Engineering Department. He received his MSc. and PhD degrees in 1999 and 2005, respectively, from Eskisehir Osmangazi University, Mechanical Engineering Department. He worked as a research assistant between 1997 and 2003 at Kutahya Dumlupınar University and as Assist. Prof. Dr. between 2006-2014. Between 2014-2019, he was Assoc. Prof. Dr. at the same university. He is working at Kütahya Dumlupınar University, Mechanical Engineering Department as a Prof. Dr. since 2006. His research topics are combustion, emission control technologies and internal combustion engines.



**Prof. Dr.-Ing. Ali Cemal Benim** received his B.Sc. and M.Sc. degrees in Mechanical Engineering at the Boğaziçi University, Istanbul, Turkey. He received his Ph.D. degree at the University of Stuttgart, Germany, in 1988, on the topic “Finite Element Modeling of Turbulent Diffusion Flames” with “Degree of Distinction”. Following a post-doctoral period at the University of Stuttgart, in 1990 he joined ABB Turbo Systems Ltd. in Baden, Switzerland, where he was the manager of the “Computational Flow and Combustion Modeling” group. Since January 1996, he is Professor for Energy Technology and Head of Center of Flow Simulation at the Duesseldorf University of Applied Sciences, Duesseldorf, Germany.



## ANALYTICAL AND NUMERICAL ANALYSES OF THE HEAT CONDUCTION OF CARBON NANOTUBES UNDER APPLIED VOLTAGES

Yahya ÖZ

Turkish Aerospace, R&D Directorate, Advanced Composite Materials Technology Center  
06980 Kahramankazan, Ankara, yahya@unam.bilkent.edu.tr, ORCID: 0000-0003-3784-0495

(Geliş Tarihi: 14.02.2020, Kabul Tarihi: 14.01.2021)

**Abstract:** Electron field emission experiments of carbon nanotubes (CNT) show that due to heat CNTs breakdown faster under applied voltage than expected. Therefore, different systems with varying temperature distributions are considered analytically and numerically by use of the heat conduction equation. This methodology yields a phenomenological understanding and description of the thermoelectric behavior of CNTs under applied voltages.

**Keywords:** Carbon Nanotubes, Electron Field Emission, Heat Conduction.

### KARBON NANOTÜPLERİN ISI İLETİMİNİN UYGULANAN VOLTAJLAR ALTINDA ANALİTİK VE SAYISAL ANALİZİ

**Özet:** Karbon nanotüplerin (KNT) elektron alanı emisyonu deneyleri, ısı nedeniyle KNT'lerin uygulanan voltaj altında beklenenden daha hızlı bozulduğunu göstermektedir. Bu nedenle, değişen sıcaklık dağılımlarına sahip farklı sistemler, ısı akışı denklemini kullanarak analitik ve sayısal olarak değerlendirilmektedir. Bu metodoloji, KNT'lerin termoelektrik davranışının uygulanan voltaj altında fenomenolojik davranışını ve tanımını sağlamaktadır.

**Anahtar Kelimeler:** Karbon Nanotüp, Elektron Alan Emisyonu, Isı İletimi.

#### NOMENCLATURE

$U$	Applied Voltage [V]
$k_B$	Boltzmann Constant [J/K]
$A$	Contact Area [m <sup>2</sup> ]
$I$	Current [A]
$j$	Current Density [A/m <sup>2</sup> ]
$\sigma_{el}$	Electrical Conductivity [S/m]
$E$	Electric Field [V/m]
$\rho_{el}$	Electrical Resistivity [ $\Omega$ m]
$q_e$	Elementary Charge [C]
$\rho$	Mass Density [kg/m <sup>3</sup> ]
$\vec{x}$	Position Vector [m]
$R_c$	Quality of Thermal Contact [K/W]
$r$	Radius of a CNT [m]
$c$	Specific Heat [J/(kg K)]
$\sigma$	Stefan-Boltzmann Constant [W/(m <sup>2</sup> K <sup>4</sup> )]
$T_0$	Surrounding Temperature [K]
$T$	Temperature [K]
$k$	Thermal Conductivity [W/(m K)]
$t$	Time [s]
$g$	Volumetric Heat Source [W/m <sup>3</sup> ]

#### INTRODUCTION

Electron beams are involved in various applications and basic research tools like cathode ray tubes, x-ray tubes, scanning electron microscopes and transmission electron

microscopes. Typically a high density of narrow electron beams is desired in such applications. Therefore, in contrast to electron guns that use thermionic emission of electrons from hot cathodes, which cause thermal broadening, cold cathodes are gaining interest. However, these cathodes need large electric fields, which yield migration of atoms at the tip surface. Hence, stable operation over long periods of time is quite difficult. However, CNTs offer a solution to this problem and are accordingly focused on (Bonard *et.al*, 2001; Cheng and Zhou, 2003; Ha *et.al*, 2013). Compared to metal or diamond tips, nanotube tips are inert and stable to long periods of operation. Moreover, other advantages like low threshold voltages for cold field emission, low temperature of operation, fast response times, low power and small sizes are available (de Jonge *et.al*, 2005; Charlier *et.al*, 2007). Many examples of these kinds of applications are known in the literature (de Heer *et.al*, 1995; Choi *et.al*, 1999; Sugie *et.al*, 2001; Croci *et.al*, 2004; Zhang *et.al*, 2005).

Due to the high electric fields, materials for field emission tips must be resistant to high temperatures caused by Joule heating and high stress. This framework may lead to the breakdown of the device. The breakdown occurs most likely at the point of the CNT where the temperature is at its maximum.

The breakdown is usually completed in three consecutive phases. First, the device performance decreases. Afterwards, a structural failure arises in the form of a crack. Finally, the CNT is burned off (Wei *et.al*, 2007). Different models (Vincent *et.al*, 2002; Bocharov and Eletsii, 2013; Giubileo *et.al*, 2018) and experiments (Wang *et.al*, 2002; Bonard *et.al*, 2003; Fairchild *et.al*, 2019) were analyzed to understand the breakdown behavior of CNTs. The proposed theoretical models are based on Joule heating. The existence of two sources for the generation and dissipation of heat are assumed; electrical resistance (Joule heating) and heat radiation. The full solution of the heat conduction equation for this case is still an open question, because besides the advanced mathematical structure involved in the related equation, the temperature dependance of the resistivity and boundary conditions are needed (Collins *et.al*, 2001).

The goal of this article is the solution and investigation of the heat conduction equation with focus on applications of CNTs for electron field emission. The motivation for this research is two-fold. First, the systematic procedure for the analytic solution of the heat conduction equation with arbitrary boundary conditions and temperature dependance of the resistivity is introduced. The procedure is carried out using CNTs with constant boundary conditions as an example. Second, an efficient numerical algorithm (controlled by the analytical calculations) is used for the modeling of thermal dissipation in CNTs. In fact, possible solutions for the breakdown due to a self-heating process are analyzed.

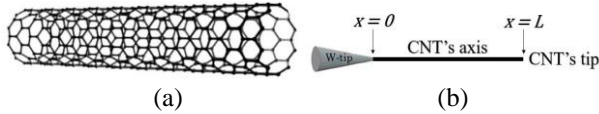


**Figure 1.** Schematic depiction of (a) single-walled CNT and (b) its associated field emission tip of length  $L$  connected to a tungsten (W) tip. The configuration shows that the heat conduction is essentially one-dimensional.

## HEAT TRANSFER THROUGH CNT WITH BOUNDARY CONDITIONS

The heat conduction equation in a non-uniform anisotropic medium is given by Eq. (1)

$$\rho(\vec{x})c(\vec{x},t)\partial_t T(\vec{x},t) = \nabla(k(\vec{x},t)\nabla T(\vec{x},t)) + g(\vec{x},t), \quad (1)$$

where  $\rho(\vec{x})$  is the mass density,  $c(\vec{x},t)$  the specific heat,  $T(\vec{x},t)$  the temperature distribution measured in K,  $k(\vec{x},t)$  the thermal conductivity,  $g(\vec{x},t)$  the volumetric rate of internal energy generation,  $t$  the time and  $\vec{x}$  the position vector. Note that specific heat, thermal conductivity and volumetric heat source generally depend on the temperature and thus implicitly on position vector and time.

The configuration of the heat transfer problem considered is shown in Fig. 1.

As a result of the geometry of CNTs they are modeled as one-dimensional rods and Eq. (1) simplifies to its one-dimensional form.  $\vec{x}$  and  $\nabla$  are replaced with  $x$  and  $\partial_x$ , respectively. However, the mathematical analysis in this article can in principle be used for arbitrary dimension  $d$  if the need arises due to a use of another emitter in contrast to Fig. 1.

For the purpose of determining the volumetric heat source Ohm's law is used due to Joule heating which leads to

$$j(x,t)E(x,t) = \frac{I^2}{A^2\sigma_{el}(x,t)} = \frac{U^2\rho_{el}(x,t)}{\left(\int_0^L dx\rho_{el}(x,t)\right)^2}, \quad (2)$$

where  $j(x,t)$  is the current density,  $E(x,t)$  the electrical field,  $\sigma_{el}(x,t)$  the electrical conductivity and  $\rho_{el}(x,t)$  the electrical resistivity while the contact area is denoted with  $A$ . The Stefan-Boltzmann law which describes heat radiation as well as consideration of CNTs with lengths  $L$  along the  $x$ -axis attached to a tungsten tip in combination with Eq. (2) yields Eq. (3)

$$g(x,t) = \frac{U^2\rho_{el}(x,t)}{\left(\int_0^L dx\rho_{el}(x,t)\right)^2} - \frac{\sigma}{L}(T^4(x,t) - T_0^4) \quad (3)$$

as expression for the volumetric heat source, where  $U$  is the applied voltage and  $\sigma$  the Stefan-Boltzmann constant. Furthermore,  $T(0 < x < L, 0) = T_0$  is assumed. For the purpose of defining the boundary conditions, the tips of the CNTs are considered. At the interface with the tungsten microtip a temperature drop due to the thermal contact resistance occurs. The microtip and surroundings temperatures are expressed as  $T_0$  while  $R_c$  represents the contact quality, i.e. the thermal contact resistance. These assumptions yield the boundary condition in Eq. (4)

$$T(0,t) = T_0 + R_c Ak(x,t)\partial_x T(x,t)\Big|_{x=0}. \quad (4)$$

Nevertheless, the interesting boundary is the free end of the nanotube. Electron emission on this end cools the tip since each electron carries energy  $\frac{3}{2}k_B T(L,t)$  due to classical statistical mechanics and the equipartition theorem (Tolman, 1918), where  $k_B$  is the Boltzmann constant. Hence, the heat flux can be written down by

$\frac{3k_B I T(L,t)}{2q_e A}$  with the elementary charge  $q_e$ . Note that in

metals this effect is much smaller than radiative cooling. Contrarily, in CNTs it is a dominant factor due to high field emission current density and low surface area for radiative cooling (Chernozatonskii *et.al*, 1995; Rinzler *et.al*, 1995). Hence, the Stefan-Boltzmann law for radiation and Fourier's heat conduction relation yield Eq. (5)

$$\partial_x T(x,t)|_{x=L} = -\frac{\sigma}{k} (T^4(L,t) - T_0^4) - \frac{3k_B I T(L,t)}{2q_e A k(L,t)}, \quad (5)$$

where  $I$  is the current.

### Analytical Solution

In the following mass density, specific heat and thermal conductivity are taken as constants for the analytic treatment of Eq. (1).

### Separation of variables

Separation of variables is widely applied for the analytical solution of heat conduction problems. This section introduces the most general solution of the presented physical problem achievable by use of this method. Correspondingly, the Stefan-Boltzmann term in Eq. (3) and (5) is set to zero and Eq. (3) is assumed to be time-independent, since separation of variables is not applicable otherwise because the homogeneous boundary conditions for the Sturm–Liouville problem are not fulfilled. This corresponds to the assumptions that heat radiation is negligible and that Joule heating occurs instantaneously. In fact, Fig. 7 shows that the influence of time-dependent Joule heating is negligible in accordance with the literature (Wei *et.al*, 2007). Moreover, regarding the neglect of heat radiation it should be noted that this analytical approach is mainly used to control the numerical analysis. The numerical experiments are compared with the analytical results in Figs. 2-5. In Fig. 9, however, the heat radiation is also included numerically.

First, Eq. (1) is split into two simpler problems in Eq. (6) for the purpose of separation of variables; one steady state that is described by a nonhomogeneous ordinary differential equation with nonhomogeneous boundary conditions and one transient described by a homogeneous partial differential equation with homogeneous boundary conditions as well as a modified initial condition, i.e.

$$T(x,t) = T_H(x,t) + T_{SS}(x). \quad (6)$$

Accordingly, one finds two separate problems formulated in Eqs. (7) and (8), i.e.

$$\begin{aligned} \partial_x^2 T_H(x,t) &= \frac{\rho c}{k} \partial_t T_H(x,t), \\ R_c A k \partial_x T_H(x,t)|_{x=0} &= T_H(0,t), \\ \partial_x T_H(x,t)|_{x=L} &= -\frac{3k_B I}{2q_e A k} T_H(L,t), \\ T_H(x,0) &= T_0 - T_{SS}(x) \end{aligned} \quad (7)$$

and

$$\begin{aligned} \partial_x^2 T_{SS}(x) &= -\frac{g(x)}{k}, \\ R_c A k \partial_x T_{SS}(x)|_{x=0} &= T_{SS}(0) - T_0, \\ \partial_x T_{SS}(x)|_{x=L} &= -\frac{3k_B I}{2q_e A k} T_{SS}(L) \end{aligned} \quad (8)$$

for  $0 \leq x \leq L$  and  $t \geq 0$ .

Second, the steady state part in Eq. (8) can be solved trivially using traditional ordinary differential equation solution techniques, i.e. sum of the homogeneous and particular solutions. For this purpose  $T_{SS}(x) = T_A(x) + T_B(x)$  is used as an approach which leads to Eqs. (9) and (10)

$$\begin{aligned} \partial_x^2 T_A(x) &= 0, \\ R_c A k \partial_x T_A(x)|_{x=0} &= T_A(0) - T_0, \\ \partial_x T_A(x)|_{x=L} &= -\frac{3k_B I}{2q_e A k} T_A(L) \end{aligned} \quad (9)$$

and

$$\begin{aligned} \partial_x^2 T_B(x) &= -\frac{g(x)}{k}, \\ R_c A k \partial_x T_B(x)|_{x=0} &= T_B(0), \\ \partial_x T_B(x)|_{x=L} &= -\frac{3k_B I}{2q_e A k} T_B(L). \end{aligned} \quad (10)$$

Obviously, Eq. (9) yields Eq. (11)

$$T_A(x) = T_0 \frac{L + \frac{2q_e A k}{3k_B I} - x}{L + R_c A k + \frac{2q_e A k}{3k_B I}} \quad (11)$$

while Eq. (10) leads to an apparent particular solution in Eq. (12)

$$T_B(x) = -\int_a^x dx' \int_b^{x'} \frac{dx''}{k} g(x''), \quad (12)$$

where  $a$  and  $b$  follow from the homogeneous boundary conditions in Eq. (10) and are chosen such that Eqs. (13) hold

$$\begin{aligned} R_c A(G(b) - G(0)) &= T_B(0), \\ G(L) - G(b) &= \frac{3k_B I}{2q_e A} T_B(L), \end{aligned} \quad (13)$$

where  $G(x)$  is the antiderivative of  $g(x)$ . In total, one finds Eq. (14)

$$\begin{aligned} T_{SS}(x) &= \frac{T_0}{1 + \frac{3k_B \lambda I A k}{2q_e A k + 3k_B L I}} - \frac{T_0 x}{L + \lambda A k + \frac{2q_e A k}{3k_B I}} \\ &\quad - \int_a^x dx' \int_b^{x'} \frac{dx''}{k} g(x''). \end{aligned} \quad (14)$$

Note that this approach holds for any integrable volumetric heat source  $g(x)$  and its antiderivative  $G(x)$ .

Third, the transient problem in Eq. (7) is handled by a separation into space-dependent and time-dependent functions of a single variable each, i.e.  $T_H(x, t) = \Psi(x)\Gamma(t)$ . This produces two different ordinary differential equations given in Eqs. (15) and (16);

$$\begin{aligned} X''(x) + \lambda_n^2 X(x) &= 0, \\ R_c A k X'(0) - X(0) &= 0, \\ X'(L) + \frac{3k_B I}{2q_e A k} X(L) &= 0 \end{aligned} \quad (15)$$

and

$$\Gamma'(t) + \frac{k\lambda_n^2}{\rho c} \Gamma(t) = 0. \quad (16)$$

Solving both equations separately, using the boundary conditions and recombining both solutions yields Eq. (17)

$$T_H(x, t) = \sum_{n=0}^{\infty} C_n \underbrace{\left( \lambda_n \cos(\lambda_n x) + \frac{\sin(\lambda_n x)}{R_c A k} \right)}_{=X_n(x)} e^{-\frac{k\lambda_n^2 t}{\rho c}} \quad (17)$$

with the roots  $\lambda_n$  given by the transcendental Eq. (18)

$$\tan(\lambda_n L) = \frac{\lambda_n + \frac{3k_B \lambda I \lambda_n}{2q_e}}{R_c A k \lambda_n^2 - \frac{3k_B I}{2q_e A k}}, \quad (18)$$

and the constants  $C_n$  determined in Eq. (19) by the nonhomogeneous initial condition of Eq. (7)

$$C_n = \frac{2R_c A k \int_0^L dx (T_0 - T_{SS}(x)) X_n(x)}{1 + \left(1 + (R_c A k \lambda_n)^2\right) \left[ \frac{L}{R_c A k} + \frac{\frac{3k_B I}{2q_e q_e (A k)^2}}{\lambda_n^2 + \left(\frac{3k_B I}{2q_e A k}\right)^2} \right]}. \quad (19)$$

In total Eqs. (6), (14), (17)-(19) solve the formulated problem. The explicitness of the analytic solution should be noted. Obviously Eq. (19) can be simplified even further by inserting Eq. (14) and calculating the integral. Even though the expressions are lengthy, the calculations are straightforward and lead to Eq. (20)

$$\begin{aligned} C_n &= \frac{12k_B R_c I T_0 A^2 k^2}{\lambda_n^2 (2q_e A k + 3k_B I (L + R_c A k))} \\ &\quad \cdot \left( (1 + R_c A k \lambda_n^2 (L + R_c A k)) \sin(L \lambda_n) - L \lambda_n \cos(L \lambda_n) \right) \\ &\quad \cdot \left( 1 + (R_c A k \lambda_n)^2 \right) \left[ 2L A k + \frac{3k_B I}{q_e \left( \lambda_n^2 + \left( \frac{3k_B I}{2q_e A k} \right)^2 \right)} \right] \\ &\quad + 2R_c A^2 k^2)^{-1}. \end{aligned} \quad (20)$$

### Solution by Green's function

Use of Green's function provides an efficient and straightforward method for constructing exact analytic solutions of various heat conduction problems. However, appropriate Green's functions must be available. The approach is used in mathematical physics for the solution of partial differential equations (Aizen *et.al*, 1974). Contrarily to the separation of variables, it is the most general method to solve nonhomogeneous, time-dependent conduction problems. Thus, a plane surface heat source of unit strength located at  $x'$  and an instantaneous heat source releasing its energy spontaneously at time  $t'$  into a zero temperature medium, both represented by Dirac delta functions, are considered for the auxiliary problem in Eq. (21) for  $0 < x < L$

$$\frac{\rho c}{k} \partial_t G(x, t | x', t') = \partial_x^2 G(x, t | x', t') + \frac{\delta(x - x') \delta(t - t')}{k} \quad (21)$$

with boundary conditions in Eqs. (22)

$$\begin{aligned} R_c A k \partial_x G(x, t | x', t') \Big|_{x=0} - G(0, t | x', t') &= 0, \\ \partial_x G(x, t | x', t') \Big|_{x=L} + \frac{3k_B I}{2q_e A k} G(L, t | x', t') &= 0 \end{aligned} \quad (22)$$

and initial condition  $G(x, t | x', t') = 0$  for  $t < t'$ . The formulated auxiliary problem is quite useful since the



solution of the original problem can be expressed just in terms of Green's function in Eq. (23)

$$T(x,t) = T_0 \int_0^L dx' G(x,t|x',0) + \frac{1}{\rho c} \int_0^t dt' \int_0^L dx' G(x,t|x',t') g(x',t') - \frac{T_0}{R_c A \rho c} \int_0^t dt' G(x,t|0,t'). \quad (23)$$

Note the time-dependency in  $g(x,t)$  in contrast to the method of separation of variables.

Typically Laplace transformations or the method of images are used for the determination of Green's function (Bilodeau, 1962). Instead, a general approach that uses separation of variables is applied here. Therefore, the homogeneous version of the original problem with nonhomogeneous initial condition is considered. A separation in space- and time-dependent functions of a single variable each is assumed. The solution of this problem can be constructed in a simple manner in Eqs. (24) and (25) with the previously shown methodology. It is given by

$$T(x,t) = \sum_{n=0}^{\infty} \tilde{C}_n X_n(x) e^{-\frac{k\lambda_n^2 t}{c\rho}} \quad (24)$$

and

$$\tilde{C}_n = \frac{\frac{2T_0}{\lambda_n} (1 - \cos(\lambda_n L) + R_c A k \lambda_n \sin(\lambda_n L))}{1 + \left(1 + (R_c A k \lambda_n)^2\right) \left( \frac{L}{R_c A k} + \frac{\frac{3k_B I}{2R_c q_e (A k)^2}}{\lambda_n^2 + \left(\frac{3k_B I}{2q_e A k}\right)^2} \right)}. \quad (25)$$

Considering Eqs. (24) and (25) carefully, defining the norm in Eq. (26)

$$N_n^{-1} = \int_0^L dx X_n^2(x) = \frac{2R_c A k}{1 + \left(1 + (R_c A k \lambda_n)^2\right) \left( \frac{L}{R_c A k} + \frac{\frac{3k_B I}{2R_c q_e (A k)^2}}{\lambda_n^2 + \left(\frac{3k_B I}{2q_e A k}\right)^2} \right)}, \quad (26)$$

that already appeared explicitly in Eq. (19) as well as (25), and using the property  $G(x,t|x',t') = G(x,t-t'|x',0)$

as well as the Heaviside step function  $H(x)$  yields Green's function

$$G(x,t|x',t') = H(t-t') \sum_{n=0}^{\infty} \frac{X_n(x) X_n(x')}{N_n} e^{-\frac{k\lambda_n^2 (t-t')}{\rho c}}. \quad (27)$$

Putting Eqs. (23) and (27) together produces the full analytic solution

$$T(x,t) = \sum_{n=1}^{\infty} \frac{X_n(x)}{N_n} e^{-\frac{k\lambda_n^2 t}{\rho c}} \left( T_0 \left( \sin(\lambda_n L) + \frac{2 - \cos(\lambda_n L)}{R_c A k \lambda_n} \right) + \int_0^t dt' \int_0^L \frac{dx'}{\rho c} X_n(x') e^{-\frac{k\lambda_n^2 (t-t')}{\rho c}} g(x',t') - \frac{T_0}{R_c A k \lambda_n} \right). \quad (28)$$

Note that the analytically derived Eq. (27) is applicable for all cases of volumetric heat source. Comparison with the originally formulated problem shows that just the Stefan-Boltzmann term in Eq. (5) is neglected. Hence, just the heat radiation at the free end is neglected in the analytical approach. Furthermore, the thermal conductivity is taken as constant. Investigations for a linear temperature dependence were performed in the literature (Zhang *et al.*, 2018).

## Numerical Analysis

The numerical treatment of Eq. (1) is done by utilizing the temperature dependence of the electrical resistivity. Hence, for the volumetric heat source in Eq. (3)  $g(x,t) = g(T(x,t)) = g(T)$  is used, which corresponds to the expected physics, since the heat generation at location  $x$  and time  $t$  depends on the temperature at this location and time. The explicit dependance varies in different publications due to varying conduction mechanisms. Purcell (Purcell *et al.*, 2002) uses  $\rho_{el}(T) = \rho_0(1 - \alpha T)$ . This assumption takes hopping along thermally activated defect sites into account. This effect is well-known for large defect densities (Jang *et al.*, 2004; Dehghani *et al.*, 2012). The wave functions of electrons are highly localized in disordered systems which leads to a vanishing electrical conductance at temperature zero. Nonetheless, electrons are hopping between localized states at finite temperatures resulting in electrical conduction. Hence, increasing temperature leads to a decreasing electrical resistivity. However, electron-phonon scatterings (scattering of electrons by the thermal motion of the lattice) should also be considered since the electrical resistivity  $\rho_{el}(T)$  decreases indefinitely otherwise. Therefore,  $\rho_{el}(T) = \rho_0(1 - \alpha_1 T + (\alpha_2 T)^{3/2})$  is used in this manuscript (Suzuura and Ando, 2002) while  $\alpha_1$  and  $\alpha_2$

are chosen such that they are fitting the experimental data.

The partial differential Eq. (1) is solved numerically by approximating it with difference equations while the derivatives are replaced with finite differences. Accordingly, this method leads to the recursive relation in Eq. (29)

$$T(x_j, t_{k+1}) = T(x_j, t_k) + \frac{\Delta t}{\Delta x^2 \rho(T(x_j, t_k)) k(T(x_j, t_k))} \cdot \left( \partial_T \frac{k(T(x_j, t_k))}{4} (T(x_{j+1}, t_k) - T(x_{j-1}, t_k))^2 + k(T(x_j, t_k)) (T(x_{j-1}, t_k) - 2T(x_j, t_k) + T(x_{j+1}, t_k)) + \Delta x^2 g(T(x_j, t_k)) \right) \quad (29)$$

where the temperature dependency of mass density, specific heat and thermal conductivity is used. Moreover, the evaluation is performed by utilization of the discretization  $x_1, \dots, x_N$  and  $t_1, \dots, t_M$  with  $x_j = (j+1)\Delta x$  and  $t_k = (k+1)\Delta t$ , where  $\Delta x$  and  $\Delta t$  are step sizes. Due to the recursive relation the temperature at location  $x_j$  and time  $t_{k+1}$  depends on the temperatures at the locations  $x_{j-1}, x_j, x_{j+1}$  and time  $t_k$ .

The boundary conditions given in Eqs. (4) and (5) are valid for  $x = x_1$  and  $x = x_N$ . C++ was used as programming language for the recursive solution of Eq. (29). This approach yields an efficient algorithm that is easy to implement (Fraser, 1909; Fornberg, 1988; Flajolet and Sedgewick, 1995; Zachos, 2008; Curtright and Zachos, 2013). However, instabilities for large time steps that disturb the data quality have to be treated carefully (Jaluria and Atluri, 1994). A von Neumann stability analysis for  $g(T)=0$  yields  $\frac{k\Delta t}{\rho c(\Delta x)^2} \leq \frac{1}{2}$  as a

criterion for the stability (Charney et.al, 1950; Crank and Nicolson, 1996). In the numerical analysis  $\frac{\Delta t}{(\Delta x)^2} \leq 1$  is used unless stated otherwise.

## RESULTS AND DISCUSSIONS

For the sake of checking the obtained results and proving the usefulness of Eq. (28) numerical and analytic solutions are being compared. To test the numerical results with regard to their stability, rather obscure initial temperatures  $T(0 < x < L, 0)$  such as rectangular  $\tilde{T}H\left(x - \frac{L}{4}\right)H\left(\frac{3L}{4} - x\right)$ , linear  $\tilde{T}\frac{x}{L}$  or quadratic  $\tilde{T}\left(\frac{x}{L}\right)^2$  expressions for  $L = 40 \cdot 10^{-6}$  m and  $\tilde{T} = 10$  K are used. For simplicity the volumetric heat source  $g(T)$  and the boundary condition  $T(0, t)$  are set to zero in this numerical experiments. Furthermore, the method of images, i.e.  $T(x_{N-1}, t) = T(x_{N+1}, t)$  is used for

the boundary condition at  $x=L$  in the numerical analysis. Hence, for these experiments the physically motivated Eqs. (3)-(5) are not considered.

All other constants are summarized in Table 1, in which physical parameters describing the behavior of multiwalled CNTs and field emission devices are taken from (Dai et.al, 1996; Ebbesen et.al, 1996; Hone et.al, 1999; Bachtold et.al, 1999; Yi et.al, 1999; Yang et.al, 2002; Milne et.al, 2003; Sveningsson et.al, 2004; Fujii et.al, 2005; Karim et.al, 2006; Karim et.al, 2007; Park et.al, 2010).

**Table 1.** Physical parameters of multiwalled nanotubes

$T_0$	300 K
$\lambda$	$1.774 \cdot 10^7$ K/W
$U$	500-2000 V
$r$	$10^{-8}$ m
$L$	$0.5-40 \cdot 10^{-6}$ m
$\rho$	$1300$ kg/m <sup>3</sup>
$k$	100 W/(m K)
$c$	740 J/(kg K)
$\rho_0$	$3.26 \cdot 10^{-5}$ $\Omega$ m
$\alpha_1$	$8.5 \cdot 10^{-4}$ K <sup>-1</sup>
$\alpha_2$	$9.8 \cdot 10^{-6}$ K <sup>-1</sup>

The results of the numerical experiments are shown in Figs. 2-5. Fig. 2 depicts the rectangular initial temperature  $\tilde{T}H\left(x - \frac{L}{4}\right)H\left(\frac{3L}{4} - x\right)$  as well as the analytical and numerical result after 10 ns. The dots show the analytical solutions obtained by separation of variables in Eq. (6) as well as Green's function in Eq. (28). Moreover, Eq. (17) is considered two-fold. The sum is evaluated for the first ten and 100 summands, respectively. The dots therefore consist of a total of three different analytical solutions. Hence, every dot is actually a superposition of three different dots. It can be seen that both solution methods are equivalent as expected. In addition, the sums in Eqs. (17) and (28)

converge fast due to the factor  $e^{-\frac{k\lambda_n^2 t}{\rho c}}$ . For large times zero temperature is found everywhere along the CNT

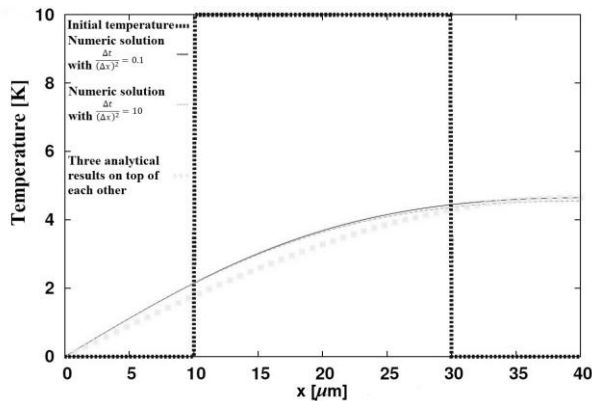
due to the factor  $e^{-\frac{k\lambda_n^2 t}{\rho c}}$  in Eq. (28). By virtue of the fixed boundary conditions, the curves obtained by the means of numerics agree with the analytical results at both ends. These curves were obtained for two different ratios, i.e.  $\frac{\Delta t}{(\Delta x)^2} = 0.1$  and  $\frac{\Delta t}{(\Delta x)^2} = 10$  and almost lie

on top of each other. However, a discrepancy between exact and numerical solutions can be observed in the middle of the CNT due to the discontinuous initial distribution. Accordingly, the numerical and analytical results agree in the other polynomial initial temperature cases for all times in Figs. 3-5. In analogy to Fig. 1, Fig.

3 and Fig. 5 illustrate the linear initial conditions  $\tilde{T} \sim \frac{x}{L}$  and  $\tilde{T} \left(\frac{x}{L}\right)^2$ , respectively. The analytical result depicted with plus signs in Fig. 3 is obtained by separation of variables with 100 summands for 10 ns. It is compared to two different numerical solutions due to varying ratios  $\frac{\Delta t}{(\Delta x)^2} = 0.1$  and  $\frac{\Delta t}{(\Delta x)^2} = 10$ . The exact and numerical curves agree with each other. Fig. 5 emphasizes this result. The analytical solution obtained by Green's function with 100 summands completely fits the numerical result evaluated for  $\frac{\Delta t}{(\Delta x)^2} = 0.1$ .

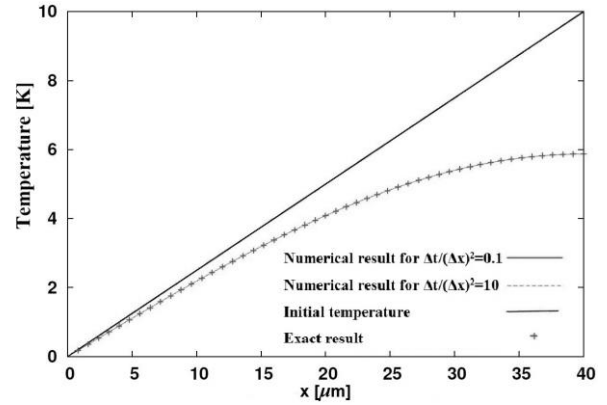
Additionally, Fig. 4 shows the influence of time on the temperature distribution. The temperature distribution for the linear initial condition is obtained by Green's function and by numerics with  $\frac{\Delta t}{(\Delta x)^2} = 0.1$  for varying times, i.e., 5, 10, ..., 50 ns, and are in good agreement. As expected, the temperature along the CNT is decreasing for increasing times.

Fig. 6 shows the numerical result for the initial condition  $T(0 < x < L, 0) = T_0 = 300$  K and  $\frac{\Delta t}{(\Delta x)^2} = 0.1$ , but the inhomogeneities in the boundary conditions and in the heat conduction equation are neglected, i.e. the Stefan-Boltzmann term in Eq. (5) that describes heat radiation at the free end, the electron emission term of Eq. (5) and the volumetric heat source  $g(T)$  are set to zero. As expected, the maximum temperature is reached at the free end since tip cooling effects are neglected. The time dependence of the temperature distribution is examined in the inset of Fig. 6. It can be seen that the steady-state is reached very fast, which was used as an assumption in previous publications (Huang *et.al*, 2004). However, the scale varies between ns and  $\mu$ s with varying lengths which can be seen in Fig. 7.



**Figure 2.** Temperature distribution at 10 ns along the  $x$ -axis for a rectangular initial condition denoted with the blue dashed line. Three different exact results obtained by separation of variables with ten and 100 summands and

Green's function with 100 summands are depicted as dots and lie on top of each. Furthermore, numerical results for  $\frac{\Delta t}{(\Delta x)^2} = 0.1$  and  $\frac{\Delta t}{(\Delta x)^2} = 10$  are illustrated with red and green lines and show good agreement with each other.



**Figure 3.** Temperature distribution at 10 ns along the  $x$ -axis for a linear initial condition illustrated with a blue line. As expected, numerical and analytic result are in good agreement even for large step sizes  $\Delta t$ . The error is of order 0.01 %.

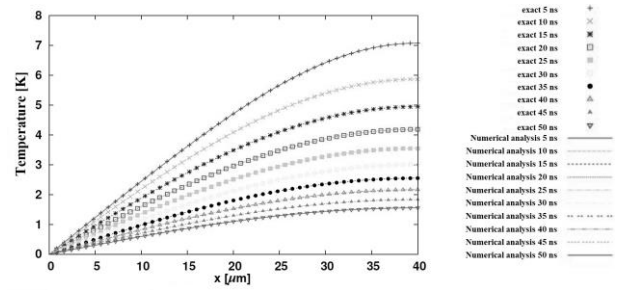


**Figure 4.** Temperature distribution along the  $x$ -axis for a linear initial condition and the corresponding time evolution. Exact and numerical solutions are observable. The temperature is decreasing for increasing time. Numerically, the steady-state temperature zero of this numerical experiment is found everywhere for 100 ns. Hence, the time scale shows that the steady-state is reached rather fast.

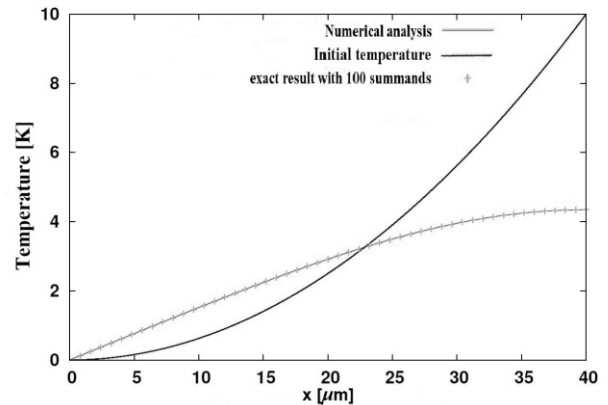


**Figure 5.** Temperature distribution at 10 ns along the  $x$ -axis for a quadratic initial condition illustrated with a blue line. As expected, numerical and analytic result, i.e. red line and green plus signs, are in good agreement.

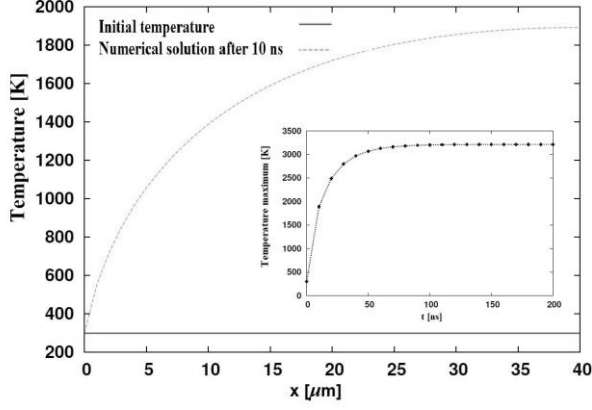


**Figure 6.** Temperature distribution after 10 ns along the  $x$ -axis for initial condition  $T_0 = 300$  K. The numerical solution was obtained for  $\frac{\Delta t}{(\Delta x)^2} = 0.1$ . The inset shows the maximum temperature reached at the free end of the CNT in this configuration after several time intervals. The temperature at the free end increases up to 3213 K. This steady-state behavior is observable after approximately 100 ns.

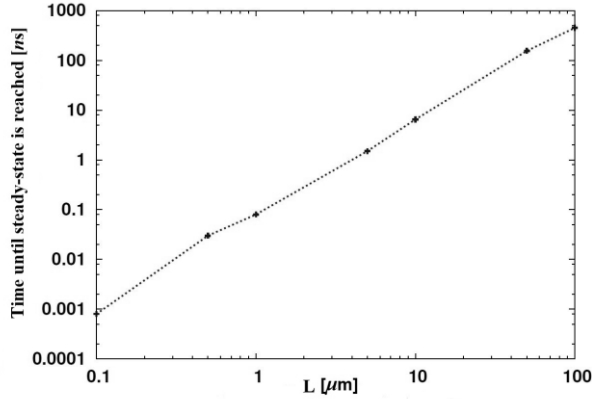


**Figure 7.** Time until the steady-state is reached for different CNT lengths. Growing lengths yield higher times.

Steady-state results of analytical evaluations with 100 summands and numerical calculations with  $\frac{\Delta t}{(\Delta x)^2} = 0.1$  are shown in Fig. 8 and 9, respectively. In addition to the temperature distribution, the influence of varying CNT lengths is also studied in these Figures.

The analytical solution takes all terms in Eqs. (3)-(5) with the exception of the Stefan-Boltzmann term in Eq. (5) into account and uses the CNT length  $L = 5 \cdot 10^{-7}$  m as well as  $U = 2000$  V as voltage. Note that the Stefan-Boltzmann term occurring in the volumetric heat source in Eq. (3) is considered. However, for the evaluation of Eq. (28) in combination with Eq. (3) and temperature-dependent electrical resistivity  $\rho_{el}(T)$  discretization as well as iteration is used. For fixed parameters given in Table 1 the maximum temperature is not reached at the free end of the CNT due to the electrons carrying energy. Hence, a tip cooling effect is observed in Fig. 8.

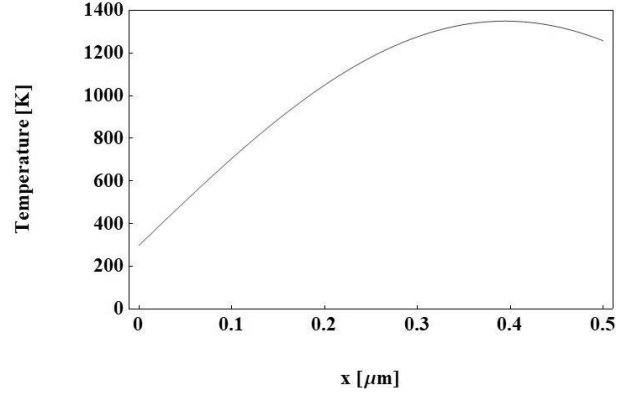


**Figure 8.** Illustration of the steady-state analytical result of the original problem for a CNT of  $5 \cdot 10^{-7}$  m while just the Stefan-Boltzmann term in Eq. (5) is neglected.

In contrast to the analytical treatment, the numerical analysis takes all terms in Eqs. (3)-(5) into account. Moreover, the CNT length  $L = 4 \cdot 10^{-5}$  m and 500 V for the voltage is used.

A similar but increased tip cooling effect is observed in the numerical calculations since in this case the in the analytic calculations neglected term of the boundary condition in Eq. (5) is taken into account. This additional heat radiation at the free end of the CNT leads to a greater decrease in temperature at this end if Fig. 8 and 9 are compared.

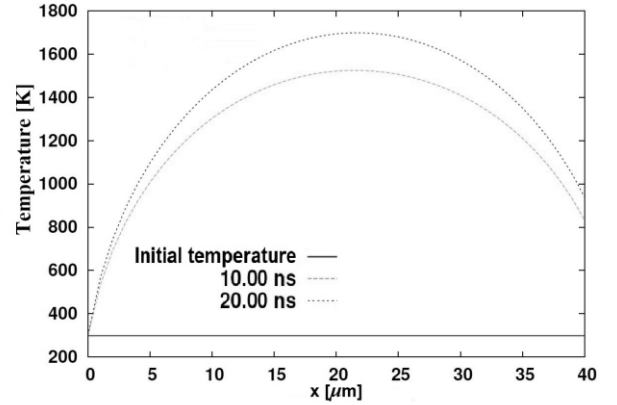


**Figure 9.** Numerically calculated temperature distribution for the original problem along the CNT with length  $4 \cdot 10^{-5}$  m, where  $\frac{\Delta t}{(\Delta x)^2} = 0.1$  was used.

Notwithstanding this subtle difference, both analytical and numerical calculations predict breakdown of the CNT during electron field emission some space away of the free tip since it occurs most likely at the point of the CNT where the temperature is at its maximum. In fact, this is in good agreement with experiments (Liu *et.al.*, 2019; Lin *et.al.*, 2019).

Note that comparison of both results shows different maximum temperatures for different CNT lengths. Shortening the length decreases the maximum temperature, which is an important mechanism for the

stability of the CNT field emission tip. This observation is strengthened by different numerical experiments. However, in comparison with Fig. 9 a higher voltage according to Table 1 was applied in Fig. 8 for the purpose of demonstrating the breakdown behavior with just analytical results and proving the existence of the experimentally observed threshold voltage at which breakdown occurs (Bonard *et.al*, 2002; Doytcheva *et.al*, 2006).

Another strategy for preventing the breakdown behavior are alternating voltages that are set to zero in certain time intervals. For this purpose Eq. (30)

$$U(t) = U_0 \sum_{n \in \mathbb{N}_0} H(t - nt_1) H(nt_1 + t_2 - t) \quad (30)$$

is used as voltage, where  $U_0 = 2000 \text{ V}$ ,  $t_1 = 100 \text{ ns}$  and  $t_2 = 20 \text{ ns}$ . Note that for this analysis time steps  $\Delta t$  have to be smaller by at least an order than the period  $\Delta t$  of the alternating voltage due to the Nyquist–Shannon sampling theorem (Shannon, 1949). Furthermore, the period  $t_1$  should be large enough since the physical system needs time to adjust. Hence,  $\Delta t = \frac{t_1}{10}$  is used besides  $\frac{\Delta t}{(\Delta x)^2} = 0.1$  and Table 1 for this purpose. Moreover, for simplicity, heat radiation is neglected in Eq. (3) and (5) for this numerical evaluation. These assumptions lead to a periodic cooling and heating of the CNT in Fig. 10. This method might be a possible solution for the avoidance of breakdown. In fact, this strategy is in the focus of experiments (Zhang *et.al*, 2020).

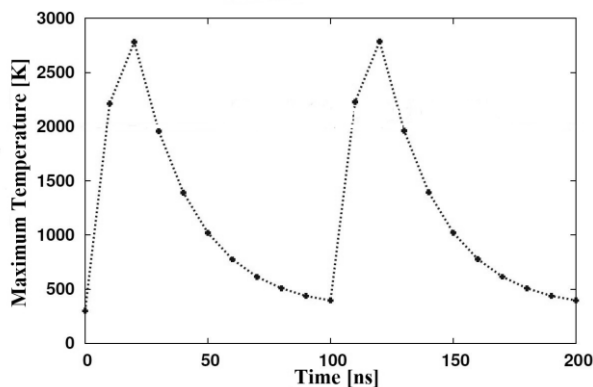


**Figure 10.** Maximum temperature of CNTs under applied alternating voltages

## CONCLUSIONS

In summary, the thermal behavior of CNTs during electron field emission was analyzed by construction of analytical solutions of the heat conduction equation as well as numerical experiments. The influence of different inhomogeneities encoded in the volumetric heat source  $g(x,t)$  in Eq. (1) as well as initial and

boundary conditions in Eqs. (4)-(5) was analyzed. In contrast to prior publications the time-dependence and the Stefan-Boltzmann term in the boundary condition of the free end as well as the contact quality were taken into account. Nevertheless, temperature dependent thermal conductivity, quantum size effects (Sandomirskii, 1967) and stresses in axial as well as radial direction that occur due to the electrostatic force were neglected. However, this simplification still yields good agreement with experiments. The breakdown mechanism of CNTs under applied voltages is explained completely by use of Joule heating, heat radiation and electron emission at the tip. In particular, this study was able to confirm the experimental knowledge that the breakdown does not occur at the end of the CNT but rather a short distance beforehand due to tip cooling caused by electron emission.

## ACKNOWLEDGEMENTS

The author acknowledges financial support by the Scientific and Technological Research Council of Turkey within the support program 1515 and 1004 for research and laboratory developments within the projects 5189901 and 20AG001, respectively. Moreover, the author is grateful to the Institute of Materials Science and Nanotechnology at Bilkent University and Department of Engineering Sciences at Middle East Technical University for providing the needed infrastructure.

## REFERENCES

- Aizen A. M., Redchits I. S. and Fedotkin I. M., 1974, On improving the convergence of series used in solving the heat-conduction equation, *Journal of Engineering Physics*, 26, 453-458.
- Bachtold A., Strunk C., Salvétat J., Forró L., Nussbaumer T. and Schönenberger, 1999, Aharonov–Bohm oscillations in carbon nanotubes, *Nature*, 397, 673-675.
- Bilodeau G. G., 1962, The Weierstrass transform and Hermite polynomials, *Duke Mathematical Journal*, 29, 293-308.
- Bocharov G. S. and Eletsckii A. V., 2013, Theory of Carbon Nanotube (CNT)-Based Electron Field Emitters, *Nanomaterials*, 3, 393-442.
- Bonard J., Dean K. A., Coll B. F. and Klinker C., 2002, Field Emission of Individual Carbon Nanotubes in the Scanning Electron Microscope, *Physical Review Letters*, 89, 197602.
- Bonard J., Kind H., Stöckli T. and Nissson L., 2001, Field emission from carbon nanotubes: the first five years, *Solid-State Electronics*, 45, 893-914.

- Bonard J., Klinke C., Dean K. A. and Coll B. F., 2003, Degradation and failure of carbon nanotube field emitters, *Physical Review B*, 67, 115406.
- Charlier J., Blasé X. and Roche S., 2007, Electronic and transport properties of nanotubes, *Reviews of Modern Physics*, 79, 677-732.
- Charney J. G., Fjörtoft R. and J. Von Neumann, 1950, Numerical Integration of the Barotropic Vorticity Equation, *Tellus*, 2, 237-254.
- Cheng Y. and Zhou O., 2003, Electron field emission from carbon nanotubes, *Comptes Rendus Physique*, 4, 1021-1033.
- Chernozatonskii L. A., Gulyaev Y. V., Kosakovskaja Z. J., Sinitsyn N. I., Torgashov G. V., Zakharchenko Y. F., Fedorov E. A. and Val'chuk V. P., 1995, Electron field emission from nanofilament carbon films, *Chemical Physics Letters*, 233, 63-68.
- Choi W. B., Chung D. S., Kang J. H., Kim H. Y., Jin Y. W., Han I. T., Lee Y. H., Jung J. E., Lee N. S., Park G. S. and Kim J. M., 1999, Fully sealed, high-brightness carbon-nanotube field-emission display, *Applied Physics Letters*, 75, 3129-3131.
- Collins P. G., Hersam M., Arnold M., Martel R. and Avouris P., 2001, Current Saturation and Electrical Breakdown in Multiwalled Carbon Nanotubes, *Physical Review Letters*, 86, 3128-3131.
- Crank J. and Nicolson P., 1996, A practical method for numerical evaluation of solutions of partial differential equations of the heat-conduction type, *Advances in Computational Mathematics*, 6, 207-226.
- Croci M., Arfaoui I., Stöckli T., Chatelain A. and Bonard J., 2004, A fully sealed luminescent tube based on carbon nanotube field emission, *Microelectronics Journal*, 35, 329-336.
- Curtright T. L. and Zachos C. K., 2013, Umbral Vade Mecum, *Frontiers in Physics*, 1, 15.
- Dai H., Wong E. W. and Lieber C. M., 1996, Probing Electrical Transport in Nanomaterials: Conductivity of Individual Carbon Nanotubes, *Science*, 272, 523-526.
- de Heer W. A., Châtelain A. and Ugarte D., 1995, A Carbon Nanotube Field-Emission Electron Source, *Science*, 270, 1179-1180.
- de Jonge N., Allieux M., Oostveen J. T., Teo K. B. K. and Milne W. I., 2005, Optical Performance of Carbon-Nanotube Electron Sources, *Physical Review Letters*, 94, 186807.
- Dehghani S., Moravvej-Farshi M. K. and Sheikhi M. H., 2012, Temperature dependence of electrical resistance of individual carbon nanotubes and carbon nanotubes network, *Modern Physics Letters B*, 26, 1250136.
- Doytcheva M., Kaiser M. and de Jonge N., 2006, In situ transmission electron microscopy investigation of the structural changes in carbon nanotubes during electron emission at high currents, *Nanotechnology*, 17, 3226-3233.
- Ebbesen T. W., Lezec H. J., Hiura H., Bennett J. W., Ghaemi H. F. and Thio T., 1996, Electrical conductivity of individual carbon nanotubes, *Nature*, 382, 54-56.
- Fairchild S. B., Zhang P., Park J., Back T. C., Marincel D., Huang Z. and Pasquali M., 2019, Carbon Nanotube Fiber Field Emission Array Cathodes, *IEEE Transactions on Plasma Science*, 47, 2032-2038.
- Flajolet P. and Sedgewick R., 1995, Mellin transforms and asymptotics: Finite differences and Rice's integrals, *Theoretical Computer Science*, 144, 101-124.
- Fornberg B., 1988, Generation of finite difference formulas on arbitrarily spaced grids, *Mathematics of Computation*, 51, 699-706.
- Fraser, D. C., 1909, On the Graphic Delineation of Interpolation Formulæ, *Journal of the Institute of Actuaries*, 43, 235-241.
- Fujii M., Zhang X., Xie H., Ago H., Takahashi K., Ikuta T., Abe H. and Shimizu T., 2005, Measuring the Thermal Conductivity of a Single Carbon Nanotube, *Physical Review Letters*, 95, 065502.
- Giubileo F., Di Bartolomeo A., Iemmo L., Luongo G. and Urban F., 2018, Field Emission from Carbon Nanostructures, *Applied Sciences*, 8, 526.
- Ha J. M., Kim H. J., Raza H. S. and Cho S. O., 2013, Highly stable carbon nanotube field emitters on small metal tips against electrical arcing, *Nanoscale Research Letters*, 8, 355.
- Hone J., Whitney M., Piskoti C. and Zettl A., 1999, Thermal conductivity of single-walled carbon nanotubes, *Physical Review B*, 59, R2514-R2516.
- Huang N. Y., She J. C., Deng S. Z., Xu N. S., Bishop H., Huq S. E., Wang L., Zhong D. Y., Wang E. G. and Chen D. M., 2004, Mechanism Responsible for Initiating Carbon Nanotube Vacuum Breakdown, *Physical Review Letters*, 93, 075501.
- Jaluria Y. and Atluri S. N., 1994, Computational heat transfer, *Computational Mechanics*, 14, 385-386.
- Jang W. Y., Kulkarni N. N., Shih C. K. and Yao Z., 2004, Electrical characterization of individual carbon

- nanotubes grown in nanoporous anodic alumina templates, *Applied Physics Letters*, 84, 1177-1179.
- Karim S., Toimil-Molares M. E., Balogh A. G., Ensinger W., Cornelius T. W., Khan E. U. and Neumann R., 2006, Morphological evolution of Au nanowires controlled by Rayleigh instability, *Nanotechnology*, 17, 5954-5959.
- Karim S., Toimil-Molares M. E., Ensinger W., Balogh A. G., Cornelius T. W., Khan E. U. and Neumann R., 2007, Influence of crystallinity on the Rayleigh instability of gold nanowires, *Journal of Physics D: Applied Physics*, 40, 3767-3770.
- Lin C., Xiang Y. and Zhang J., 2019, Post-breakdown field emission behavior of a planar-structured single SWNT bundle in air, *Journal of Micromechanics and Microengineering*, 29, 065005.
- Liu Z., Zhang Y., Zhao P., Ye Y., Chen J., Xu N. and Deng S., 2019, In situ study of field emission vacuum breakdown of individual multi-wall carbon nanotube, *Micro & Nano Letters*, 14, 206-210.
- Milne W. I., Teo K. B. K., Chhowalla M., Amaratunga G. A. J., Lee S. B., Hasko D. G., Ahmed H., Groening O., Legagneux P., Gangloff L., Schnell J. P., Pirio G., Pribat D., Castignolles M., Loiseau, Semet V., Binh V. T., 2003, Electrical and field emission investigation of individual carbon nanotubes from plasma enhanced chemical vapour deposition, *Diamond and Related Materials*, 12, 422-428.
- Park S., Chae S., Rhee J. and Kang S., 2010, A Study on Electrical and Thermal Properties of Polyimide/MWNT Nanocomposites, *Bulletin of the Korean Chemical Society*, 31, 2279-2282.
- Purcell S. T., Vincent P., Journet C. and Binh V. T., 2002, Hot Nanotubes: Stable Heating of Individual Multiwall Carbon Nanotubes to 2000 K Induced by the Field-Emission Current, *Physical Review Letters*, 88, 105502.
- Rinzler A. G., Hafner J. H., Nikolaev P., Nordlander P., Colbert D. T., Smalley, R. E., Lou L., Kim S. G. and Tománek D., 1995, Unraveling Nanotubes: Field Emission from an Atomic Wire, *Science*, 269, 1550-1553.
- Sandomirskii V. B., 1967, Quantum Size Effect in a Semimetal Film, *Soviet Physics Journal of Experimental and Theoretical Physics*, 25, 101-106.
- Shannon C. E., 1949, Communication in the Presence of Noise, *Proceedings of the IRE*, 37, 10-21.
- Sugie H., Tanemura M., Filip V., Iwata K., Takahashi K. and Okuyama, F., 2001, Carbon nanotubes as electron source in an x-ray tube, *Applied Physics Letters*, 78, 2578-2580.
- Suzuura H. and Ando T., 2002, Phonons and electron-phonon scattering in carbon nanotubes, *Physical Review B*, 65, 235412.
- Sveningsson M., Morjan R. E., Nerushev O. and Campbell E. E. B., 2004, Electron field emission from multi-walled carbon nanotubes, *Carbon*, 42, 1165-1168.
- Tolman R. C., 1918, A General Theory of Energy Partition with Applications to Quantum Theory, *Physical Review*, 11, 261-275.
- Vincent P., Purcell S. T., Journet C. and Binh V. T., 2002, Modelization of resistive heating of carbon nanotubes during field emission, *Physical Review B*, 66, 075406.
- Wang Z. L., Gao R. P., de Heer W. A. and Poncharal P., 2002, *In situ* imaging of field emission from individual carbon nanotubes and their structural damage, *Applied Physics Letters*, 80, 856-858.
- Wei W., Liu Y., Wei Y., Jiang K., Peng L. and Fan S., 2007, Tip Cooling Effect and Failure Mechanism of Field-Emitting Carbon Nanotubes, *Nano Letters*, 7, 64-68.
- Yang D. J., Zhang Q., Chen G., Yoon S. F., Ahn J., Wang S. G., Zhou Q., Wang Q. and Li J. Q., 2002, Thermal conductivity of multiwalled carbon nanotubes, *Physical Review B*, 66, 165440.
- Yi W., Lu L., Dian-lin Z., Pan Z. W. and Xie S. S., 1999, Linear specific heat of carbon nanotubes, *Physical Review B*, 59, R9015-R9018.
- Zachos C. K., 2008, Umbral deformations on discrete space-time, *International Journal of Modern Physics A*, 23, 2005-2014.
- Zhang P., Park J., Fairchild S. B., Lockwood N. P., Lau Y. Y., Ferguson J. and Back T., 2018, Temperature Comparison of Looped and Vertical Carbon Nanotube Fibers during Field Emission, *Applied Sciences*, 8, 1175.
- Zhang Y., Tan Y., Wang L., Li B., Ke Y., Liao M., Xu N., Chen J. and Deng S., 2020, Electron emission and structure stability of carbon nanotube cold cathode driven by millisecond pulsed voltage, *Vacuum*, 172, 109071.
- Zhang J., Yang G., Cheng Y., Gao B., Qiu Q., Lee Y. Z., Lu J. P. and Zhou O., 2005, Stationary scanning x-ray source based on carbon nanotube field emitters, *Applied Physics Letters*, 86, 184104.



**Yahya Öz** is the Chief Engineer of the Advanced Composite Materials Technology Center of the R&D Directorate at Turkish Aerospace, a researcher in the Institute of Materials Science and Nanotechnology at Bilkent University and a Visiting Assistant Professor in the Department of Engineering Sciences at the Middle East Technical University, Ankara, Turkey. He received his B.Sc. (2011) in Applied Physics and Chemistry, his M.Sc. (2013) and his Ph.D. (2017) in Physics in the Faculty of Mathematics and Natural Sciences at the University of Wuppertal, Germany, where he constructed and solved the Hubbard model with impurity at arbitrary temperature as well as manipulated the host's density of states by keeping integrability. Following his PhD, he became a postdoctoral researcher and worked on transport properties of integrable systems as well as the hydrodynamic approach for integrable systems out of equilibrium. In 2019, he joined Turkish Aerospace. His current research interests include integrable models, modeling of nanomaterials as well as nanocomposites properties and modeling, fabrication and experimentation of composite materials for aerospace applications. Dr. Yahya Öz is the recipient of the full scholarship (2010-2017) by Germany's largest, oldest and most prestigious scholarship foundation, the German Academic Scholarship Foundation, and the 2014 Outstanding Young Scientist Award by the German Association for the Promotion of Mathematics and Natural sciences.





## NUMERICAL INVESTIGATION OF NON-PREMIXED COMBUSTION INSIDE A THREE LAYERED POROUS BURNER WITH FLAMELET MODEL

Tanju ERGEN\*, Tamer ŞENER\*\*, Onur TUNCER\*\*\* and A. Cihat BAYTAŞ\*\*\*\*  
Faculty of Aeronautics and Astronautics, Istanbul Technical University, 34467 Sarıyer, Istanbul,  
\*ergent@itu.edu.tr, ORCID: 0000-0001-5049-0448  
\*\*senerta@itu.edu.tr, ORCID: 0000-0002-1964-3263  
\*\*\*tuncero@itu.edu.tr, ORCID: 0000-0002-2803-1146  
\*\*\*\*baytas@itu.edu.tr, ORCID: 0000-0002-9660-5578

(Geliş Tarihi: 15.05.2020, Kabul Tarihi: 25.01.2021)

**Abstract:** Purpose of this study is to numerically investigate combustion within a porous channel, which has three layers with different pore densities. Non-premixed combustion inside the porous channel is modelled with thermal non-equilibrium energy equations. Flow and chemistry are decoupled with tabulated chemistry using flamelets, thereby reducing the computational cost. GRI 3.0 mechanism is used to account for methane/air combustion. Simulations are performed for different pore densities at the third layer in 8-30 PPI range. Also, the effects of thermal power and excess-air-ratio (EAR) are investigated for the porous burner. Temperatures and species mass fraction distributions are obtained. Maximum temperature in the burner found to be similar for all cases since combustion occurs in stoichiometric conditions at the flame front as a result of the non-premixed combustion model. NO<sub>x</sub> and CO emissions values of all simulations are compared against international gas emission standards. This comparison showed that while CO emissions are always below all international standards, NO<sub>x</sub> emissions are below these limits only for high values of excess air ratio and thermal power. Besides, as the pore density of the third layer is decreased, the values of emissions decrease strongly.

**Keywords:** Porous media, Combustion, Flamelet model, Thermal Non-equilibrium

## ÜÇ KATMANLI GÖZENEKLİ YAKICIDA ÖN KARIŞIMSIZ YANMANIN FLAMELET MODELİ İLE SAYISAL İNCELENMESİ

**Özet:** Bu çalışmanın amacı üç farklı gözeneklilik yoğunluğuna sahip bir yakıcıyı sayısal olarak incelemektir. Bu kanalda ön karışimsız yanma, gözenekli katı ortam ile akışkan arasında ısı dengesi olmadığı kabulü ile ısı dengesiz enerji denklemleri kullanılarak modellenmiştir. Yanma modelinde akış ve yanma mekanizmaları flamelet tablolama modeli ile ayrılmıştır ve böylece hesaplama maliyeti düşürülmüştür. Metanın hava ile yanması GRI 3.0 mekanizması ile modellenmiştir. Üçüncü gözenekli katmanın zararlı gaz salımına etkisini gözlemlemek için, son katmanın 8-30 PPI aralığında değişen farklı gözeneklilik değerleri ile hesaplamalar yapılmıştır. Ek olarak, yakıcı gücünün ve fazla hava oranının yakıcıya etkisi de incelenmiştir. Hesaplamalar sonucunda sıcaklık dağılımı ve türlerin kütle kesirleri elde edilmiştir. Ön karışimsız yanmada tepkime tam oranlı şartlarda gerçekleşeceğinden yakıcı içerisindeki en yüksek sıcaklık her durum için benzer bulunmuştur. Yakıcının NO<sub>x</sub> ve CO salım değerleri uluslararası standartlar ile kıyaslanmıştır ve CO salımlarının her durumda standartların altında olduğu fakat NO<sub>x</sub> salımlarının sadece yüksek hava oranları ve ısı güçleri ile düşük çıktığı görülmüştür. Ek olarak üçüncü katmanın gözenek yoğunluğu (PPI değeri) düşürüldükçe zararlı gaz salım değerlerinin de çokça düştüğü görülmüştür.

**Anahtar Kelimeler:** Gözenekli ortam, Yanma, Flamelet modeli, Isıl dengesiz model

### NOMENCLATURE

$a_{gs}$	Surface per unit volume [ $m^{-1}$ ]	$MW_i$	Molecular weight of $i^{th}$ species [ $kg\ mol^{-1}$ ]
$c_p$	Heat capacity at constant pressure [ $Jkg^{-1}K^{-1}$ ]	$Nu_v$	Volumetric Nusselt number [-]
$d_p$	Pore diameter [m]	$n$	Normal direction [-]
$D_z$	Mixture fraction diffusivity [-]	$q_r$	Radiation flux in solid region [ $Wm^{-2}$ ]
$h$	Interfacial heat transfer coefficient [ $Wm^{-2}K$ ]	$Re$	Reynolds number [-]
$h_{gs}$	Volumetric heat transfer coefficient [ $Wm^{-3}K$ ]	$PPC$	Particles per centimeter [ $cm^{-1}$ ]
$H$	Total enthalpy of the mixture [ $Jkg^{-1}$ ]	$Pr$	Prandtl number [-]
$h_i$	Enthalpy of $i^{th}$ species [ $Jkg^{-1}$ ]	$k$	Heat conduction coefficient [ $Wm^{-1}K^{-1}$ ]
$k_r$	Radiative conductivity [-]	$Le$	Lewis number [-]
$K$	Permeability of porous media [ $m^2$ ]	$\vec{u}$	Fluid velocity [ $ms^{-1}$ ]

$P$	Pressure [Pa]
$R_i$	Gas constant of $i^{\text{th}}$ species [ $\text{Jkg}^{-1}\text{K}^{-1}$ ]
$R_u$	Universal gas constant [ $\text{Jmol}^{-1}\text{K}^{-1}$ ]
$T$	Temperature [K]
$t$	Time [s]
$Y_i$	Mass fraction of $i^{\text{th}}$ species [-]
$Z$	Mixture fraction [-]
$\dot{\omega}_i$	Rate of production of $i^{\text{th}}$ species [ $\text{kgm}^{-3}\text{s}^{-1}$ ]

### Greek Symbols

$\beta$	Emmissivity [-]
$\epsilon$	Porosity of porous media [-]
$\chi$	Scalar dissipation rate [ $\text{s}^{-1}$ ]
$\xi$	Enthalpy defect [ $\text{Jkg}^{-1}$ ]
$\sigma$	Stephan-Boltzmann constant [-]

$\sigma_s$	Extinction coefficient [-]
$\rho$	Density [ $\text{kgm}^{-3}$ ]

### Subscripts

$g$	Gas phase
$s$	Solid phase
$v$	Volumetric
$p$	Particle
$F$	Fluid
$O$	Solid phase
$\infty$	Ambient

### Others

$\langle \rangle$	Volume averaging
-------------------	------------------

## INTRODUCTION

Combustion within a porous burner is a relatively new technology. The most important feature of this technology lies within the inherent feedback mechanism of the heat released from combustion towards unburnt gases via a solid matrix, which in turn yields several advantages such as; the enhancement of flame stability, effective mixing of the reactants, high power density, complete combustion, enabling ultra-lean combustion regimes and thus reduction of thermal nitric oxide emissions. The equivalent pore diameter of porous media should be chosen carefully since the stability of combustion in porous media depends on the modified Peclet number. Stable combustion occurs only when the modified Peclet number is over 65, otherwise flame cannot propagate in the porous media (Trimis et al., 2000).

To date, many numerical and experimental studies investigated pollutant emissions, operating limits and thermal efficiency of porous burners. Weinberg (1971) is one of the first researchers suggested that feedback of heat from burnt gases to unburnt gases can increase combustion efficiency and decrease the pollutant emission. Before the porous burner concept, the enhancement in heat feedback mechanism from burnt to unburnt gases was achieved by mixing a portion of burnt gases with unburnt gases. Takeno and Sato (1979b) introduced the idea of using porous media inside the combustion zone for the first time. Their mathematical model considers convection and conduction heat transfer while neglecting radiation and single-step global chemical reaction is used to account for combustion. In the same year, they conducted another study with experimental and numerical results where they included heat transfer with the environment in their mathematical model of the numerical solution (Takeno and Sato, 1979a). In porous burner technology, the idea of constructing the porous burner of two separate layers with different equivalent pore diameters was an important achievement (Hsu, Howell and Matthews, 1993).

There are one-dimensional studies investigating combustion inside porous media. Zhou and Pereira (1997) studied how burner power, excess air ratio, the conductivity of solid phase and radiation affects pollutant emissions and temperature profiles using a detailed methane-air reaction mechanism. Barra et al. (2003) investigated flame stabilization for two-layered porous burners. Their results showed that the operating limits are affected significantly by material properties such as thermal conductivity of solid phase, radiative extinction coefficient and heat transfer coefficient. Several one-dimensional studies were also conducted by Bouma and De Goey (1999), Barra and Ellzey (2004), and Coutinho and de Lemos (2012).

Smucker and Ellzey (2005) investigated a porous burner with two layers numerically and experimentally. Experiments identified the stable operating envelope of the burner for propane and methane fuels. In the computational part of this study, only propane was investigated with a complete chemical mechanism for a one-dimensional porous burner. Another two-layered porous burner was investigated experimentally by Khanna, Goel and Ellzey (1994). Pollutant emissions were measured at the exit plane of the burner for different equivalence ratios, and results showed that both NO<sub>x</sub> and CO levels decreased with decreasing equivalence ratio.

Mishra et al. (2006) solved two different energy equations for gas and solid phases while investigating methane-air combustion numerically in two dimensions. Vijaykant and Agrawal (2007) studied liquid kerosene combustion for a two-layered porous burner with several configurations of SiC foam of different pore sizes. The aim of their study was reducing pollutant emissions. Baytas (2003) studied a non-Darcy porous medium with the thermal non-equilibrium assumption for natural convection in a square enclosure porous medium that generates heat. In another study, Baytas and Pop (2002) investigated thermal non-equilibrium model for free convection flow in a square cavity filled with a porous medium and compared their results for the local heat transfer rates with previous studies.

In more recent studies, Keramiotis, Stelzner and Trimis (2012) performed a comprehensive experimental study to investigate thermal efficacy, pollutant emissions and stable operating range of a porous burner for methane and LPG. Shakiba et al. (2015) experimentally investigated the effects of foam properties on the porous burner performance. Experiments are conducted for different materials, pore densities and porosities. Their results showed that low emission values and high efficiencies were obtained when the burner is operated at low excess-air-ratios for foams with high pore densities and high excess air ratios for foams with lower pore densities.

Understanding the combustion process is an important issue to obtain higher thermal power and lower pollutant emissions. Large number of chemical species and the widely disparate range of time-scales make the investigation of combustion with realistic chemical kinetics computationally expensive in numerical calculations (Lu et al., 2009). In order to reduce this computational cost, methods that simplify the reaction kinetics based on partial-equilibrium and steady-state assumption, assuming that most chemical processes occur in much smaller time scales than the flow time scale have been developed.

Flamelet models are introduced for non-premixed combustion by Peters (1984). This approach decouples fluid dynamics and combustion chemistry via a tabulation approach. Flamelet tables are generated at a pre-processing step. Carbonell et al. (2009) studied both interactive and non-interactive flamelet models considering differential diffusion and non-differential diffusion conditions as well as adiabatic and non-adiabatic situations, and their square porous enclosure was studied using Darcy model and thermal non-equilibrium approach by Baytas (2003). Authors found that the thermal non-equilibrium model affects considerably the flow characteristics and heat transfer between solid and fluid phases in the porous matrix. The natural convection in a porous enclosure was examined using non-Darcian and the two-equation model (LNTE) by Khanna, Goel and Ellzey (1994). Authors studied the flow field by taking into account non-Darcian effects, Brinkman effect and Forchheimer quadratic inertial effect. The effects of viscous dissipation on free convection in a porous cavity under thermal non-equilibrium case were examined by Baytas and Pop (2002). Their results showed that the average Nusselt number of the fluid decreases and the average Nusselt number of the solid increases by increasing the modified conductivity ratio. This result is valid for all of the viscous dissipation parameters. Barra and Ellzey (2004) investigated the effect of local thermal non-equilibrium (LTNE) state on the phenomenon of thermosolutal convection in a square porous enclosure with the non-Darcy model. They showed that the effect of LTNE model was meaningful for temperature distribution and the heat transfer rate; however, negligible on the mass transfer rate. Compared their results with detailed numerical calculations, Van Oijen and De Goey (2000) presented a method referred as Flamelet-Generated

Manifold (FGM) that can be considered as a combination of flamelet and manifold approaches to simplify chemical kinetics. Pope (2000) described a computational technique based on the In-Situ-Adaptive-Tabulation (ISAT) of the accessed region of the combustion space that can decrease the computational cost of reacting flows with realistic chemical kinetics in numerical calculations.

The purpose of this study is to numerically investigate combustion inside a two-dimensional channel with three porous layers to obtain the effect of excess-air-ratios (EAR), thermal powers and different equivalent pore diameters for the third layer on CO and NOx emission. Combustion in porous media is modelled with the flamelet approach using the well-established GRI 3.0 mechanism (53 species, 325 reactions). Since temperature difference shall be recognizably high during combustion between solid and gas phases, non-thermal equilibrium model for energy equations in porous media are used. Thermophysical properties of both solid matrix and gas mixture are considered to be functions of temperature.

## MATHEMATICAL MODEL

A two-dimensional rectangular porous burner is depicted in Figure 1.

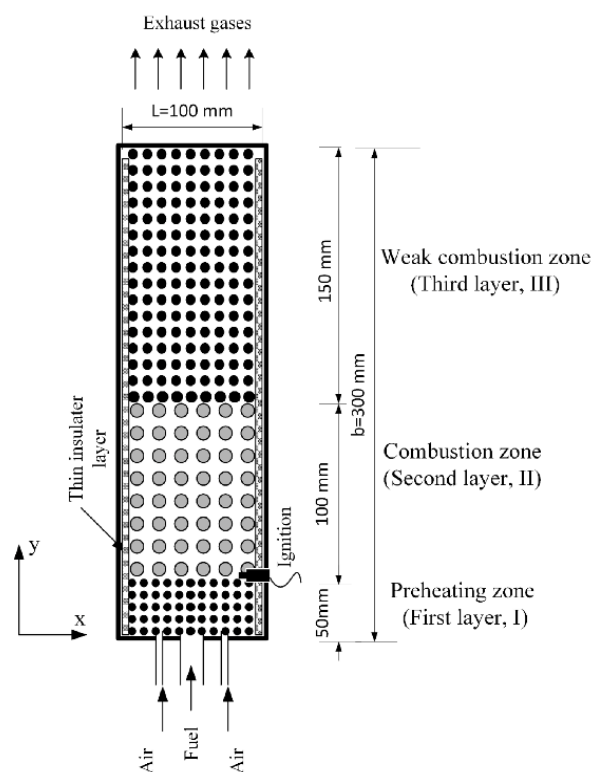


**Figure 1.** Schematic illustration of the porous burner.

The height and width of the porous channel are  $b=300$  mm and  $L=100$  mm respectively, and each inlet for air and fuel have the same width of 20 mm. Vertical walls of the porous channel are insulated. There are three entrances at the bottom of the channel. The entrance in

the middle belongs to fuel and the other two entrances belong to air. There is also ignition spark which is installed the interface of first and second porous layers. There are three layers in the channel of the porous burner with different porosities. The first layer is for preheating zone and its porosity is 20 PPI (Particle Per Inch). In this zone, combustion does not occur. The second layer is for the combustion zone and its porosity is 10 PPI. The third and last layer in the porous burner is for post-oxidation and its porosity range varies between 8-30 PPI. Porosity ( $\epsilon$ ) of each layer is considered to be 0.85. The fluid flow and combustion are considered to be unsteady and laminar. The Non-Darcian fluid flow model is used for a porous medium with local thermal non-equilibrium assumption.

The governing equations for fluid and porous layer can be presented as follows;

Continuity Equation;

$$\epsilon \frac{\partial \langle \rho \rangle}{\partial t} + \nabla \cdot \langle \rho \vec{u} \rangle = 0 \quad (1)$$

Where the angle brackets ( $\langle \rangle$ ) denotes the volume averaging for solid and fluid phases.

Momentum Balance Equation;

$$\begin{aligned} \frac{\rho_g}{\epsilon} \frac{\partial \langle \vec{u} \rangle}{\partial t} + \frac{\rho_g}{\epsilon^2} \langle \vec{u} \rangle \cdot \nabla \langle \vec{u} \rangle = -\nabla \langle p \rangle + \\ \frac{\mu_g}{\epsilon} \nabla^2 \langle \vec{u} \rangle + \rho_g \mathbf{g} - \nabla \langle p \rangle^g \end{aligned} \quad (2)$$

where  $\epsilon$  is porosity of porous medium,  $\mu_g$  is the dynamic viscosity of the gas phase. The pressure loss due to porous matrix is taken into account using Ergun equation (1952) modified by Macdonald et al. (1979) as

$$\nabla \langle p \rangle^g = 180 \frac{(1-\epsilon)^2}{\epsilon^3} \frac{\mu \langle \vec{u} \rangle}{d_p^2} + 1.8 \frac{1-\epsilon}{\epsilon^3} \frac{\rho \langle \vec{u} \rangle \langle \vec{u} \rangle}{d_p}. \quad (3)$$

Mixture fraction equation is;

$$\frac{\partial \epsilon \rho Z}{\partial t} + \nabla \cdot (\rho \vec{u} Z) = \nabla \cdot (\epsilon \rho D_z \nabla Z). \quad (4)$$

Lewis number of mixture fraction,  $Le_z \approx 1$ , is;

$$Le_z = \frac{k}{\rho D_z c_p}. \quad (5)$$

Scalar dissipation rate can be calculated with;

$$\chi = 2D_z (\nabla Z \cdot \nabla Z). \quad (6)$$

Thermal non-equilibrium energy equation for gas phase is;

$$\begin{aligned} \rho_g \left\{ \frac{\partial (\epsilon \langle H \rangle_g)}{\partial t} + \langle \vec{u} \rangle \cdot \nabla \langle H \rangle_g \right\} = \nabla \cdot \\ \left\{ \frac{k_g}{c_{p_g}} \nabla (\epsilon \langle H \rangle_g) \right\} + h_{gs} a_{gs} (T_s - T_g). \end{aligned} \quad (7)$$

Here  $H$  denotes enthalpy of the gas and  $k$  is the thermal conductivity. Enthalpy defect is calculated with the equation

$$\xi = H - [H_o + Z(H_f - H_o)]. \quad (8)$$

Here  $H_o$  and  $H_f$  represent air and fuel enthalpies, respectively. The thermal non-equilibrium energy equation for solid-phase is

$$\begin{aligned} (1 - \epsilon) \rho_s c_{p_s} \frac{\partial \langle T \rangle_s}{\partial t} = \nabla \cdot \{ k_s \nabla (1 - \epsilon) \langle T \rangle_s \} + \\ h_{gs} a_{gs} (T_g - T_s) - \nabla \cdot \mathbf{q}_r. \end{aligned} \quad (9)$$

Here  $h_{gs}$  and  $a_{gs}$  are the convective heat transfer coefficient and the specific surface area or surface per unit volume between gas and solid phases which can be defined as

$$a_{gs} = \frac{6(1 - \epsilon)}{d_p}. \quad (10)$$

Where  $d_p$  is the mean pore diameter. It is approximated by the following equation suggested by Fu and Gore (1998)

$$d_p = \frac{0.0254}{PPI} \sqrt{\frac{4\epsilon}{\pi}} \quad (m). \quad (11)$$

$\nabla \cdot \mathbf{q}_r$  is the radiation flux in solid region and it can be defined as

$$\mathbf{q}_r = 4 \frac{\sigma}{3 \sigma_s} \frac{\partial T_s^4}{\partial y} = \frac{16 \sigma T_s^3}{3 \sigma_s} \Delta T_s. \quad (12)$$

Where the bold terms show a vector quantities. The equation above is commonly known as Rosseland approximation or diffusion approximation since it is of the same type as Fourier's law of heat conduction (Modest, 1993).  $\sigma$  is the Stephan-Boltzmann constant and it can be rearranged as

$$\mathbf{q}_r = -k_r \nabla T_s. \quad (13)$$

$k_r$  is described as radiation conductivity, and defined as

$$k_r = -\frac{16 \sigma T_s^3}{3 \sigma_s}. \quad (14)$$

Radiation problem reduces to a simple conduction problem when conductivity is strongly temperature-dependent. In equation (14)  $\sigma_s$  is the radiation extinction

coefficient for the SiC foam it can be calculated with (Fu and Viskanta R. Gore, 1998)

$$\sigma_s = \frac{3}{d_p} (1 - \epsilon). \quad (15)$$

A correlation for Nu is proposed by Kuwahara, Shiota and Nakayama (2001) for laminar flow and ceramic foam as

$$Nu_{gs} = \left(1 + \frac{4(1 - \epsilon)}{\epsilon}\right) + \frac{1}{2}(1 - \epsilon)^{\frac{1}{2}} Re_{d_p} Pr^{\frac{1}{3}} \quad (16)$$

$$0.2 \leq \epsilon \leq 0.9.$$

Nu, Re and Pr are Nusselt, Reynolds and Prandtl numbers, respectively. Reynolds number is based on the mean pore diameter,  $d_p$ . The solid properties, conductivity and specific heat are considered as functions of temperature, and they are calculated from the results of an experimental study (Rashed, 2002). Gas properties, viscosity and conductivity are also calculated as functions of temperature. Single component viscosity is given by the standard kinetic theory expression in a study (Hirschfelder, Curtiss and Bird, (1955))

$$\mu_k = \frac{5}{16} \frac{\sqrt{\pi m_k k_B T}}{\pi \sigma_k^2 \Omega^{2.2}}. \quad (17)$$

Here  $\sigma_k$  is the Lennard-Jones collision diameter,  $m_k$  is the molecular mass,  $k_B$  is the Boltzmann constant and  $\Omega^{(2,2)}$  is the collision integral. After calculating viscosity for each species, gas mixture viscosity can be calculated using the equation

$$\mu = \frac{\sum_{i=1}^K X_i \mu_i}{\sum_{j=1}^K X_j \phi_{ij}}. \quad (18)$$

Where  $\phi_{ij}$  is defined as;

$$\phi_{ij} = \frac{1}{\sqrt{8}} \left(1 + \frac{W_i}{W_j}\right)^{-\frac{1}{2}} \left[1 + \left(\frac{\mu_i}{\mu_j}\right)^{\frac{1}{2}} \left(\frac{W_j}{W_i}\right)^{\frac{1}{4}}\right]^2 \quad (19)$$

where W is molecular weight. Thermal conductivity of each species can be calculated using viscosity as,

$$k_i = 0.25(9\gamma_i - 5)\mu_i C_{v,i} \quad (20)$$

Here  $\gamma$  is the heat capacity ratio. Gas mixture conductivity can be calculated using each species conductivity.

The initial and boundary conditions of the simulation are listed below.

$t = 0$  (Initial conditions for the solution for entire domain)

$$u_x = u_y = 0, \quad H = H_{air}, \quad T_s = 300 \text{ K}, \quad Z = 0$$

and  $t > 0$  (Boundary conditions)

At the left and right walls;

$$u_x = u_y = 0, \quad \frac{\partial H}{\partial x} = 0, \quad \frac{\partial T_s}{\partial x} = 0, \quad \frac{\partial Z}{\partial x} = 0$$

At the outlet;

$$u_x = 0, \quad \frac{\partial u_y}{\partial y} = 0, \quad \frac{\partial H}{\partial y} = 0, \\ -k_s \frac{\partial T_s}{\partial y} = \sigma \beta (T_s^4 - T_\infty^4), \quad \frac{\partial Z}{\partial y} = 0$$

At the bottom wall;

$$u_x = u_y = 0, \quad \frac{\partial H}{\partial y} = 0, \quad \frac{\partial T_s}{\partial y} = 0, \quad \frac{\partial Z}{\partial y} = 0$$

At the air inlet;

$$u_x = 0, \quad u_y = U_o, \quad H = H_o, \\ -k_s \frac{\partial T_s}{\partial y} = \sigma \beta (T_s^4 - T_\infty^4), \quad Z = 0$$

At the fuel inlet;

$$u_x = 0, \quad u_y = U_f, \quad H = H_f, \\ -k_s \frac{\partial T_s}{\partial y} = \sigma \beta (T_s^4 - T_\infty^4), \quad Z = 1$$

### Laminar Flamelet Combustion Model

The laminar flamelet model is one of the methods of modelling combustion for non-premixed flames (Peters, 1984). In this model, the flame is considered as the sum of thin, laminar and locally one-dimensional flamelets. Mengi et al. (2015) studied this combustion model with Sandia-D flame which is similar with considered problem in terms of flow time scales. Because flow time scales are much slower than combustion time scales, flow and chemistry decoupling with flamelers is justifiable. Flamelet solutions can be computed from the solution of counter-flow diffusion flames or solving the following set of flamelet equations.

Species mass fraction equation is

$$\frac{\partial Y_i}{\partial t} = \frac{1}{Le_Z} \frac{\chi}{2} \frac{\partial^2 Y_i}{\partial Z^2} + \dot{w}_i. \quad (21)$$

Here mixture fraction is an independent coordinate,  $Y_i$  and  $(\dot{w}_i)$  denotes the mass fraction and mass formation of the  $i^{\text{th}}$  species, respectively.  $\chi$  is scalar dissipation rate and  $Z$  is the mixture fraction.

Energy Equation is

$$\frac{\partial T}{\partial t} = \frac{\chi}{2} \frac{\partial^2 T}{\partial Z^2} - \frac{1}{\rho c_p} \sum_{i=1}^n h_i \dot{w}_i + \frac{Q}{c_p}. \quad (22)$$

Here Q represents energy transfer while  $h_i$  denotes the specific enthalpy of the  $i^{\text{th}}$  species. Before calculations, laminar flamelet tables are constructed by solving flamelet equations for non-adiabatic conditions as pre-process using OpenFoam with libOpenSmoke. Flamelet tables are generated for ten different enthalpy defect values in the range of -85 to 100 (kJ/kg) and each enthalpy defect, tables are constructed for eleven scalar dissipation rate from an equilibrium state to quenching for better interpolation.

Boundary conditions for flamelet look-up tables are given as follows; temperature is 294 K, the pressure is 1 atm. Also, the mole fraction of  $\text{CH}_4$  is 1 for fuel and air consists of 21 %  $\text{N}_2$  and 79 %  $\text{O}_2$ .

In the present study, the scalar dissipation rate will be near zero in a quasi-laminar situation. As a result, the flamelet equations reduce to the thermodynamic equilibrium limit for slow flows. Therefore, equilibrium tables can be used for calculations.

Figure 2 shows the flamelets generated between equilibrium and quenching for both adiabatic and non-adiabatic conditions. As seen from Figure 2 quenching strain rate is  $29 \text{ s}^{-1}$  for adiabatic conditions. In the super-adiabatic condition where enthalpy defect is 50 kJ/kg, quenching strain rate increases to  $34 \text{ s}^{-1}$  and it decreases to  $25 \text{ s}^{-1}$  for a negative enthalpy defect of -50 kJ/kg.

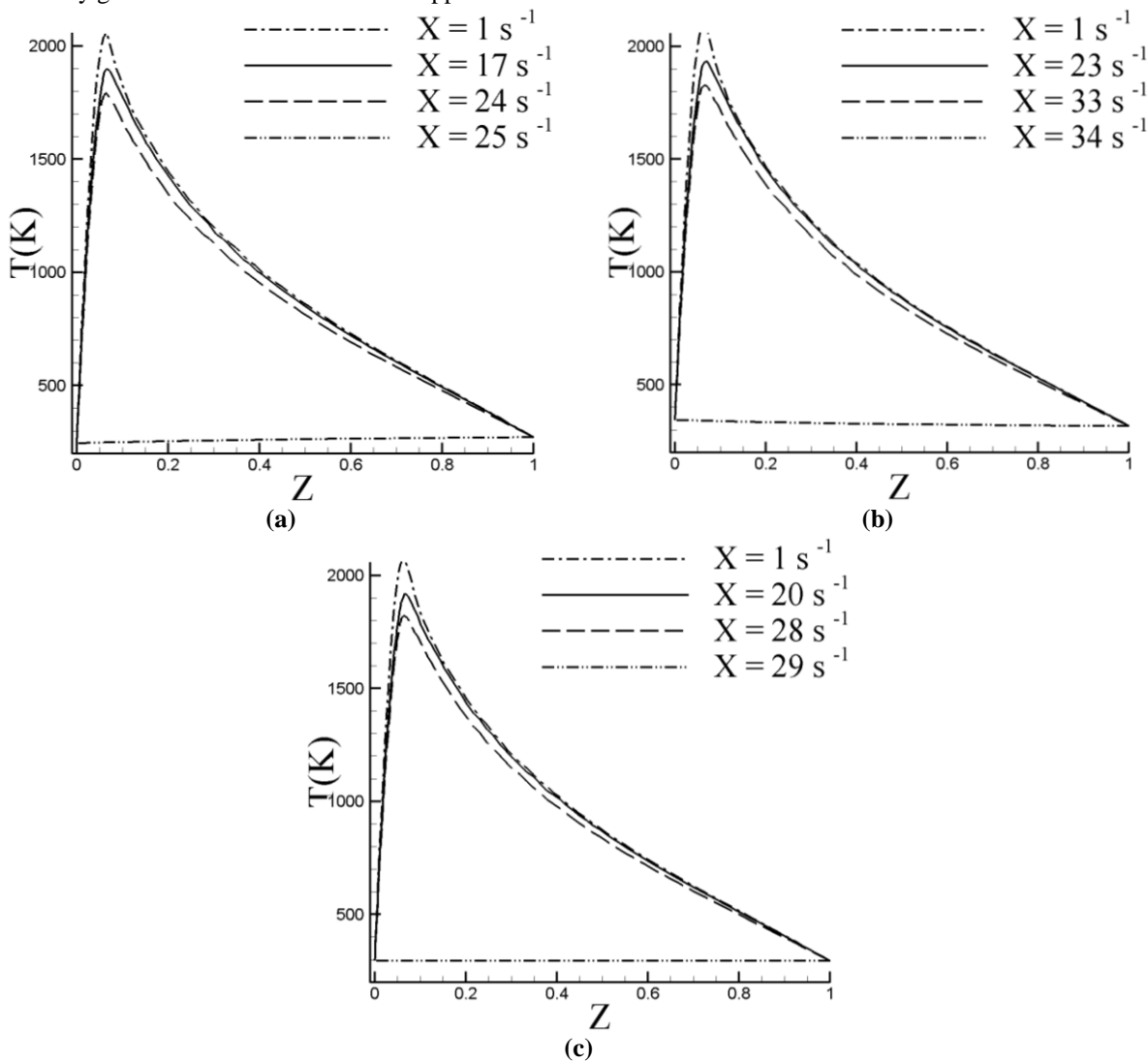
In the flamelet approach, the gas mixture temperature is determined by interpolation of mixture fraction, scalar dissipation rate and enthalpy defect values using previously generated flamelet tables. This approach does

not include combustion chemistry to flow field calculations; therefore, for complex combustion mechanisms, this is a great advantage in terms of computation time.

### Numerical Solution

For the spatial discretization of the governing equations, a finite volume method is employed. The solution domain is discretized with collocated, uniform, and structured quadrilateral elements. Velocity and pressure are coupled with the SIMPLE algorithm (Patankar, 1980), and simulations are run via in-house code.

The resulting system of algebraic equations is arranged with the ADI method and solved with the usage of the tri-diagonal matrix algorithm. To check the mesh independency of the results, centerline temperatures of solid and liquid phases that are obtained with three different mesh sizes compared.



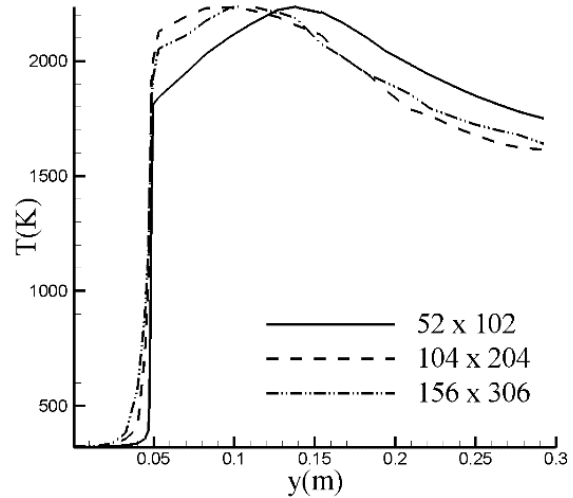
**Figure 2.** Flamelets for adiabatic and non-adiabatic conditions. (a)  $\xi = -50 \text{ kJ/kg}$  (b)  $\xi = 0 \text{ kJ/kg}$  (c)  $\xi = 50 \text{ kJ/kg}$

Figure 3 represents the results of an accuracy test conducted using three sets of grids for gas phase since solid phase graph has the same trend. As seen from the comparison of centerline temperature profiles, there is an insignificant difference between the results for 104x204 and 156x306 grid densities.

Figure 4 shows numerical results in comparison with other numerical and experimental data obtained by Farzaneh et al. (2012) and Durst, Trimis and Pickenacker (1996), respectively. For this study, maximum temperature is observed at the flame front since combustion occurs at stoichiometric conditions as a result of non-premixed combustion Turns (1996). Farzaneh et al.'s study includes a heat-exchanger which affects the entire flow domain since the governing equations of the system are elliptic in nature. Therefore, even though the heat-exchanger of their study is located at the end of their channel the effect of heat extraction can be observed within the all channel. As a result, the difference between present results and the others can be explained with the effects of heat-exchanger presence in the other studies.

Even though other studies have heat exchanger at the third layer which affects all domain; in the second layer, temperature profiles seem to have similar behavior after the peak temperature but then temperature decreases

drastically in the third layer because of the presence of a heat exchanger in Farzaneh's study.



**Figure 3.** Centerline temperature profiles of gas phase for different grid sizes.

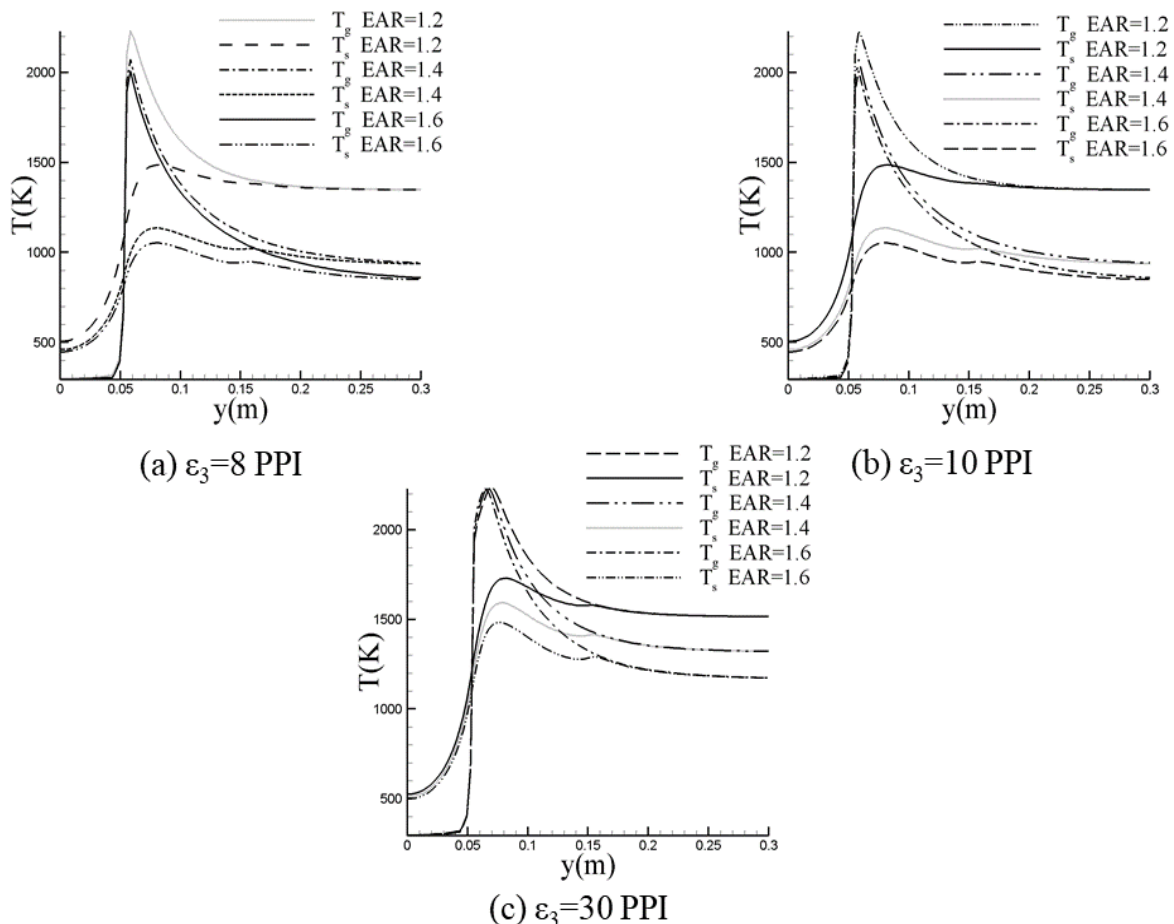


**Figure 5.** Temperature profile comparison for excess-air-ratio inside the 15 kW porous burner with three different porosities for the third layer (a)  $\epsilon_3 = 8$  PPI (b)  $\epsilon_3 = 10$  PPI (c)  $\epsilon_3 = 30$  PPI.

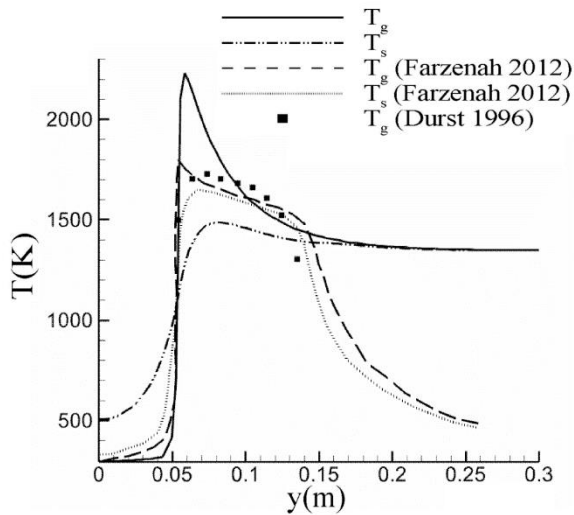


**Figure 4.** Comparison of calculated and experimental centerline temperature profiles for excess-air-ratio of 1.6.

## RESULTS AND DISCUSSION

In this study, non-premixed combustion in a porous burner is investigated with the laminar flamelet approach with non-equilibrium energy model of gas and solid phases. The investigated porous burner has three layers with different pore densities. Effect of thermal power, excess air ratio, and pore density at the third layer on CO and NOx emission is studied. To examine the effect of the third layer pore density; 3 different pore density is chosen which are 8 PPI, 10 PPI and 30 PPI. On the other hand, to examine the thermal power effect on emission, it is chosen in a range between 12.5 kW to 20 kW. Thermal power is adjusted by changing the mass flow rates of both fuel and air, and equivalence ratio (thus excess-air-ratio) is kept constant.

In Figure 5, temperature profiles are presented in the centerline of the channel for different excess-air-ratios. Increasing the excess-air-ratio resulted in exit gas temperature to decrease since the power of the burner kept constant while the total mass flow rate is increased. Another result of increasing excess-air-ratio is that the flame front moves backwards for higher excess-air-ratios.

Temperature distribution along the axial direction is presented for three different pore density values on the third layer of the burner in Figure 6. It shows that increasing the PPI of the third layer of the burner causes higher gas temperatures at the exit. Also, the flame front moves forward for higher PPI values of the third layer. Neither pore diameter nor excess-air-ratio affects the maximum temperature in the burner since combustion occurs at stoichiometric conditions at the flame front.

In Figure 7, temperature distribution in axial direction is compared for different thermal powers of the burner. As a result of increasing velocity, the flame front moves backwards, and the temperature of the gas mixture decreases at the exit of the burner. Again, the maximum temperature in the burner is not affected by velocity

change. Figure 7 also shows clearly that the heat transfer coefficient between the gas and the solid phase is increasing with pore density. There is a sudden change in solid temperature profile at the beginning of the third layer at  $y=150$  mm.

Mass fraction of major species in vertical direction centerline is presented in Figure 8. As mentioned before this figure shows that combustion occurs at stoichiometric conditions as oxygen and methane fraction goes zero at the flame front. occurs at stoichiometric conditions at the flame front as a result of non-premixed combustion.

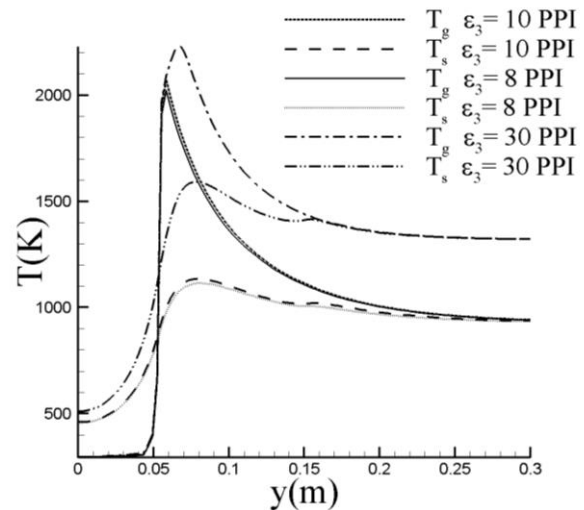


**Figure 6.** Temperature profiles comparison for the 15 kW porous burner with three different porosities for the third layer with excess air ratio 1.4.

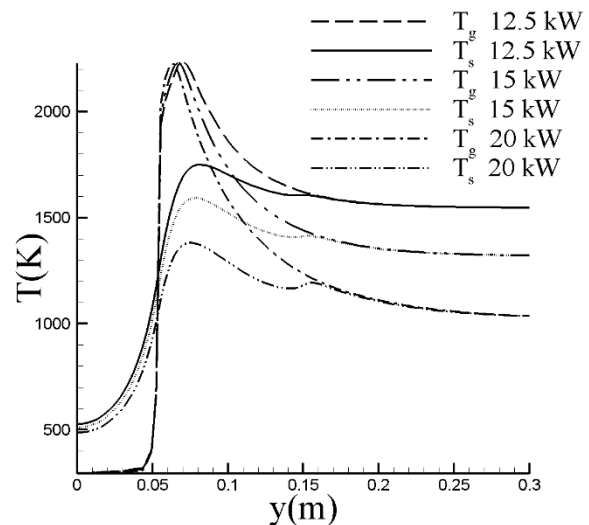


**Figure 7.** Temperature profiles comparison for different thermal power with excess air ratio 1.4 and third layer porosity 30 PPI.



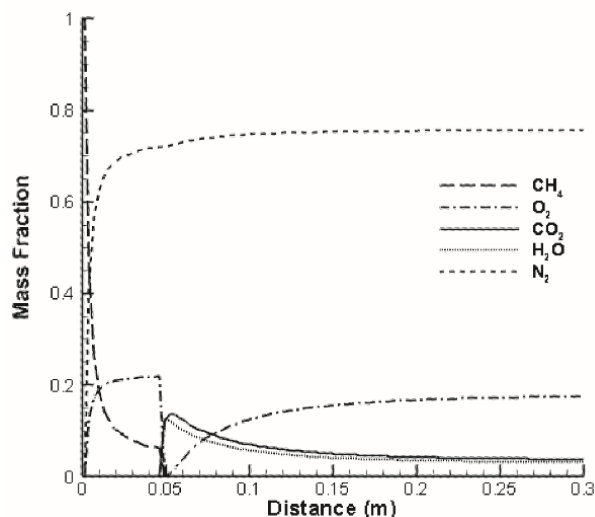


**Figure 8.** Mass fraction distribution of the major species at centerline of the burner.

Enthalpy defect distribution is shown in Figure 9. Since heat transfer between gas and solid phase is taken into account with the thermal non-equilibrium model, combustion does not occur adiabatically inside the porous burner. Positive values of enthalpy defect mean that combustion occurs in super-adiabatic conditions.

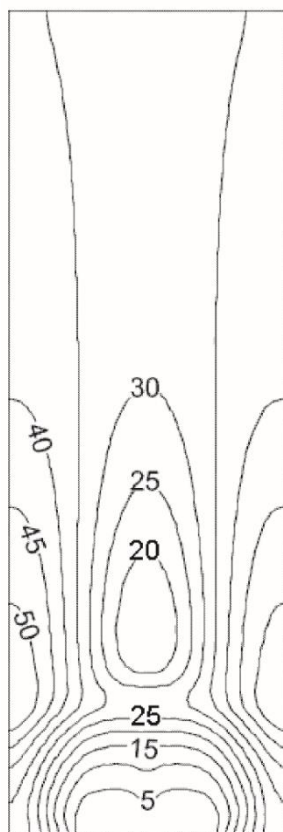


**Figure 9.** Enthalpy defect distribution inside the burner (kJ/kg).

Temperature isotherms inside the porous burner are shown for gas and solid phases in Figure 10. As expected, the combustion does not occur in the first layer because of the small equivalent pore diameter. The heat feedback mechanism works successfully as seen in Figure 10.

In Table 1, international gas emission standards are presented to compare with the results of this study. Comparison of these results with international gas standards shows that CO emissions of the porous burner are always within the limits of all standards for each pore density and excess air ratio. On the other hand, NOx emissions are not always in compliance with standards. When combustion occurs in low excess-air-ratios with high pore density at the third layer of the burner NOx emission exceeds the limits. However, if the EAR is increased or pore density of the third layer is decreased, the emission values of NOx and CO decreases dramatically below the limits of international gas emission standards.

In Table 2, gas emissions are compared for different pore densities at the third layer of the porous burner and results are given for various excess air ratios. It can be seen from the table that increasing pore density in the third layer of the burner leads to higher gas pollutant emissions. Even a small change in pore density such as from 8 PPI to 10 PPI cause higher emission values. This result is valid for both NO<sub>x</sub> and CO emissions for each excess air ratio.

In Table 3, gas emissions are compared for different thermal powers of the porous burner where combustion occurs at four different excess air ratios. The results of CO emission for each simulation seem to be below the limits of all compared international standards but NOx emissions exceed the standards for small values of EAR and thermal power. Operating the burner at higher thermal powers results in less pollutant emission.

## CONCLUSION

In this study, the non-adiabatic flamelet approach is applied to model combustion in the porous burner. Simulations are conducted for thermal powers from 12.5 kW to 20 kW with EAR ranges from 1.2 to 1.8. Based on the numerical results, the following conclusions can be drawn.

- Pore density at the third layer of the burner is an important parameter that can affect the temperature distribution and pollutant emissions dramatically. Increasing the pore density at the third layer helps to keep the heat inside the porous burner extracting more heat from the combustion products. This is an important observation in terms of design of practical porous media combustors.
- Effect of thermal power of the porous burner was also investigated in this study and results showed that operating the porous burner at higher thermal power leads to a decrease in pollutant emissions within the range of conducted simulations.
- Enthalpy defect distribution shows that combustion occur in super-adiabatic conditions which results to higher combustion temperature and therefore higher pollutant emissions.

- Flamelet model is used for modeling combustion inside a porous medium. With this approach, methane-air reaction is solved using GRI 3.0 mechanism but complexity of the chemical reactions was not involved in the computations since it was tabulated in the pre-processing process. Tabulated chemistry approach speeds up computations.

- Increasing the excess-air-ratio always decreased the exit temperature of the gas mixture and the pollutant levels.

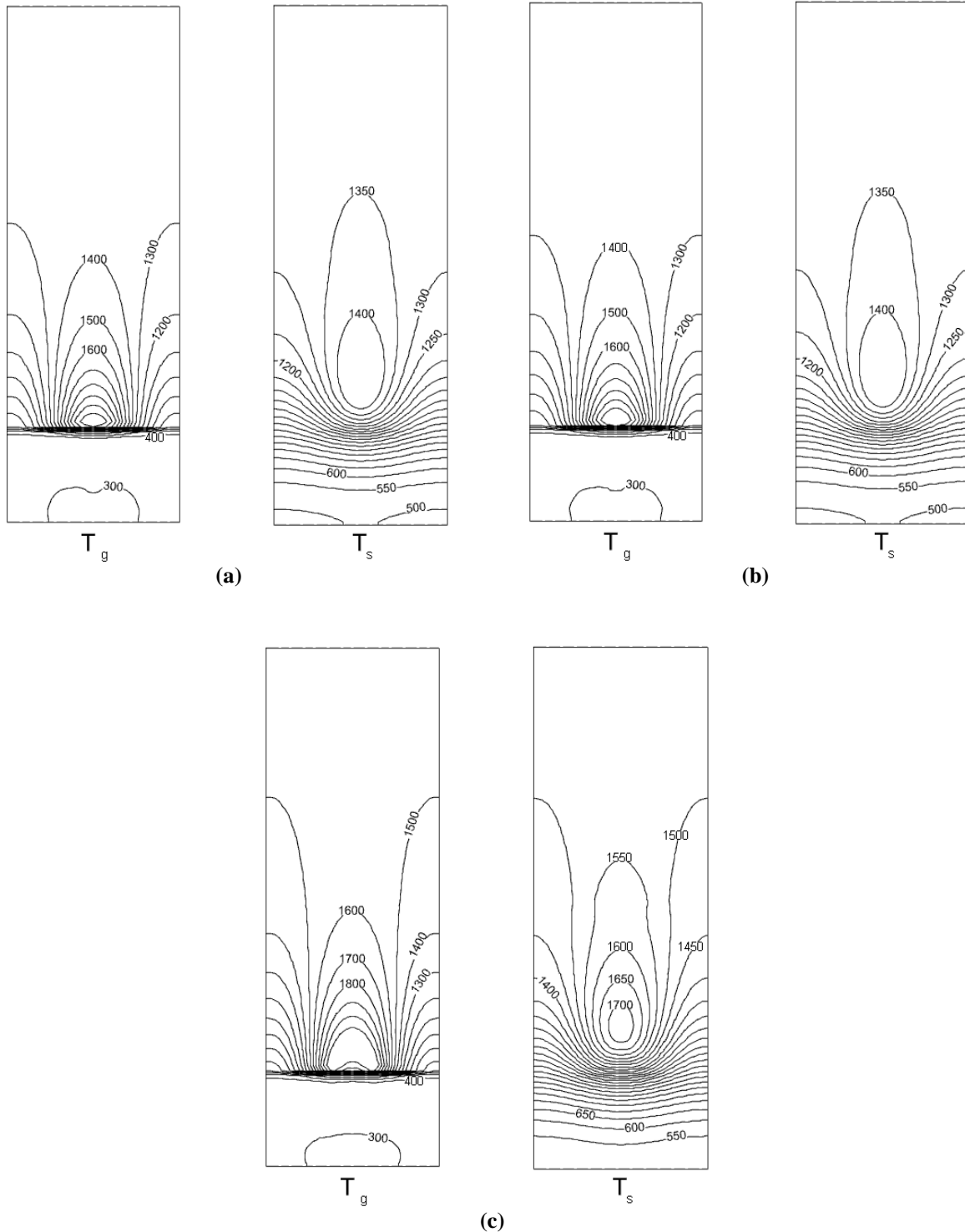


**Figure 10.** Isotherms of gas and solid phases temperatures for the 15 kW porous burner with three different porosities at the third layer (a)  $\epsilon_3 = 8$  PPI (b)  $\epsilon_3 = 10$  PPI (c)  $\epsilon_3 = 30$  PPI.

**Table 1.** International gas emission standards (Scheffler, Colombo and Wiley, 2005).

	DIN 4702	Swiss Standard	Blauer Engel	Hamburg Promoting
NO <sub>x</sub> (mg/kWh)	200	80	60	20
CO(mg/kWh)	100	60	50	10

**Table 2.** Gas emission comparison for 15 kW porous burners with different PPI at the third layer.

	EAR 1.2	EAR 1.4	EAR 1.6
<b>NO<sub>x</sub> Emission (mg/kWh)</b>			
8 PPI	201.24	16.43	6.12
10 PPI	210.32	16.49	6.22
30 PPI	409.02	216.35	103.67
<b>CO (mg/kWh)</b>			
8 PPI	0.03	0	0
10 PPI	0.03	0	0
30 PPI	0.04	0.03	0

**Table 3.** Gas emission comparison of the porous burner with 30 PPI third layer for different thermal powers

	EAR 1.2	EAR 1.4	EAR 1.6	EAR 1.8
<b>NO<sub>x</sub> Emission (mg/kWh)</b>				
12.5 kW	658.69	443.92	262.47	144.62
15 kW	409.02	216.35	103.67	50.64
20 kW	108.45	40.38	16.22	6.59
<b>CO (mg/kWh)</b>				
12.5 kW	9.62	8.81	5.65	4.16
15 kW	0.47	0.03	0	0
20 kW	0	0	0	0

## ACKNOWLEDGEMENTS

Authors gratefully acknowledge the support received from Turkish Scientific and Technical Research Council under contract no 114M672.

## REFERENCES

Barra, A. J. and Ellzey, J. L. (2004) 'Heat recirculation, heat transfer in porous burners', *Combust. Flame*, 137, pp. 230–241.

Barra, A. J. et al. (2003) 'Numerical study of the effects of material properties on flame stabilization in a porous burner', *Combust. Flame*, 134, pp. 369–379. doi: 10.1016/S0010-2180(03)00125-1.

Baytas, A. C. (2003) 'Thermal Non-Equilibrium natural convection in a square enclosure filled with a heat generating solid phase, non-Darcy porous medium', *International Journal of Energy Research*, 27, pp. 975–988. doi: 10.1002/er.929.

Baytas, A. C. and Pop, I. (2002) 'Free convection in a square porous cavity using a thermal nonequilibrium model', *International Journal of Thermal Sciences*, 41(9), pp. 861–870. doi: 10.1016/S1290-0729(02)01379-0.

Bouma, P. H. and De Goey, L. P. H. (1999) 'Premixed Combustion on Ceramic Foam Burners', *Combust. Flame*, 119, pp. 133–143. doi: 10.1016/S0010-2180(99)00050-4.

Carbonell, D. et al. (2009) 'Flamelet mathematical models for non-premixed laminar combustion', *Combustion and Flame*, 156(2), pp. 334–347. doi: 10.1016/j.combustflame.2008.07.011.

Coutinho, J. E. A. and de Lemos, M. J. S. (2012) 'Laminar flow with combustion in inert porous media', *Int. Communications in Heat and Mass Transfer*, 39, pp. 896–903. doi: 10.1016/j.icheatmasstransfer.2012.06.002.

Durst, F., Trimis, D. and Pickenacker, K. (1996) 'Compact porous medium burner and heat exchanger for household applications.', *European Union commission project report*, pp. 1–85.

Ergun, S. (1952) 'Fluid flow through packed columns', *Chemical Engineering and Progress*, 8(2), pp. 89–94.

Farzaneh, M. et al. (2012) 'Numerical investigation of premixed combustion in a porous burner with integrated heat exchanger', *Heat and Mass Transfer*. Springer-Verlag, 48(7), pp. 1273–1283. doi: 10.1007/s00231-012-0966-1.

Fu, X. and Viskanta R. Gore, J. P. (1998) 'Measurement and correlation of volumetric heat transfer coefficients of cellular ceramics.', *Experimental Thermal and Fluid Science*, 17, pp. 285–293.

- Hirschfelder, J. O., Curtiss, C. F. and Bird, R. B. (1955) 'Molecular theory of gases and liquids. Wiley, New York, 1954', *Journal of Polymer Science*, 17(83), p. 116. doi: 10.1002/pol.1955.120178311.
- Hsu, P. F., Howell, J. R. and Matthews, R. D. (1993) 'A numerical investigation of premixed combustion within porous inert media', *Journal of Heat Transfer*, 115(3), pp. 744–750. doi: 10.1115/1.2910746.
- Keramiotis, C., Stelzner, B. and Trimis D. Founti, M. (2012) 'Porous burners for low emission combustion: An experimental investigation', *Energy*, 45, pp. 213–219. doi: 10.1016/j.energy.2011.12.006.
- Khanna, V., Goel, R. and Ellzey, J. L. (1994) 'Measurements of Emissions and Radiation for Methane Combustion with in a Porous Medium Burner', *Combustion Science and Technology*, 99, pp. 133–142. doi: 10.1080/00102209408935429.
- Kuwahara, F., Shirota, M. and Nakayama, A. (2001) 'A numerical study of interfacial convective heat transfer coefficient in two-energy equation model for convection in porous media', *International Journal of Heat and Mass Transfer*. Pergamon, 44(6), pp. 1153–1159. doi: 10.1016/S0017-9310(00)00166-6.
- Lu, L. et al. (2009) 'Computationally efficient implementation of combustion chemistry in parallel PDF calculations', *Journal of Computational Physics*. Academic Press, 228(15), pp. 5490–5525. doi: 10.1016/j.jcp.2009.04.037.
- Macdonald, I. F. et al. (1979) 'Flow Through Porous Media: Ergün equation revisited', *Indust. Eng. Chem. Fundamentals*, 18, pp. 199–208. doi: 10.1021/i160071a001.
- Mengi, S., Tunçer, O., Baytaş, A.C., "Sandia-D Alevi Simülasyonunda Radyasyon Etkisinin Flamelet Modeli Kullanılarak İncelenmesi", 20. Ulusal Isı Bilimi ve Tekniği Kongresi, Balıkesir, Türkiye, Eylül 2015
- Mishra, S. C. et al. (2006) 'Heat transfer analysis of a two-dimensional rectangular porous radiant burner', *Int. Commun. Heat Mass Transfer*, 33, pp. 467–474. doi: 10.1016/j.icheatmasstransfer.2005.12.006.
- Modest, M. F. (1993) *Radiative Heat Transfer*. Mc Graw Hill International Editions. doi: 10.1017/CBO9781107415324.004.
- Patankar, S. (1980) *Numerical heat transfer and fluid flow*. CRC press.
- Peters, N. (1984) 'Laminar diffusion flamelet models in non-premixed turbulent combustion', *Progress in Energy and Combustion Science*. Pergamon, 10(3), pp. 319–339. doi: 10.1016/0360-1285(84)90114-X.
- Pope, S. B. (2000) 'Computationally efficient implementation of combustion chemistry using in situ adaptive tabulation', *Combustion Science and Technology*, 161, pp. 113–137.
- Rashed, A. H. (2002) 'Properties and characteristics of silicon Carbide'. Decatur, TX. doi: 10.5772/615.
- Scheffler, M., Colombo, P. and Wiley (2005) *Cellular ceramics: structure, manufacturing, properties and applications*. Wiley-VCH. Available at: [https://books.google.com.tr/books?hl=tr&lr=&id=LP6HpxX0A8MC&oi=fnd&pg=PR5&dq=scheffer+colombo+cellular+ceramics+structure+manufacturing&ots=Z7YtG8TTBe&sig=756Q5nXisaKWyg-jWxIzhAOFZyI&redir\\_esc=y#v=onepage&q=scheffer+colombo+cellular+ceramics+structure+manufacturing&f=false](https://books.google.com.tr/books?hl=tr&lr=&id=LP6HpxX0A8MC&oi=fnd&pg=PR5&dq=scheffer+colombo+cellular+ceramics+structure+manufacturing&ots=Z7YtG8TTBe&sig=756Q5nXisaKWyg-jWxIzhAOFZyI&redir_esc=y#v=onepage&q=scheffer+colombo+cellular+ceramics+structure+manufacturing&f=false) (Accessed: 27 September 2017).
- Shakiba, S. A. et al. (2015) 'Effects of foam structure and material on the performance of premixed porous ceramic burner', *Proceedings of the Institution of Mechanical Engineers, Part A: Journal of Power and Energy*, 229(2), pp. 176–191. doi: 10.1177/0957650914558166.
- Smucker, M. T. and Ellzey, J. L. (2005) 'Computational experimental study of two-section porous burner', *Combust. Sci. Technol.*, 176, pp. 1171–1189. doi: 10.1080/00102200490457385.
- Takeno, T. and Sato, K. (1979a) 'A theoretical and experimental study on an excess enthalpy flame', in *ICOGER*. doi: 10.1016/S0082-0784(81)80052-5.
- Takeno, T. and Sato, K. (1979b) 'An Excess Enthalpy Flame Theory', - *Combustion Science and Technology*, 20(1–2), pp. 73–84. doi: 10.1080/00102207908946898.
- Trimis, D. et al. (2000) *Porous Medium Combustor versus Combustion Systems with Free Flames*.
- Turns, Stephen R. 'Introduction to combustion'. Vol. 287. McGraw-Hill Companies, 1996.
- Van Oijen, J. A. and De Goey, L. P. H. (2000) 'Modelling of Premixed Laminar Flames using Flamelet-Generated Manifolds', *Combustion Science and Technology*, 161, pp. 113–137. doi: 10.1080/00102200008935814.
- Vijaykant, S. and Agrawal, A. K. (2007) 'Liquid fuel combustion within silicon-carbide coated carbon foam', *Exp. Therm. Fluid Sci.*, 32, pp. 117–125. doi: 10.1016/j.expthermflusci.2007.02.006.
- Weinberg, F. J. (1971) 'Combustion Temperatures: The Future?', *Nature*, 233(5317), pp. 239–241. doi: 10.1038/233239a0.
- Zhou, X. Y. and Pereira, J. C. F. (1997) 'Numerical study on combustion and pollutions formation in inert non homogenous porous media', *Combustion Sci. Technol.*, 130, pp. 335–364. doi: 10.1080/00102209708935748



**Tanju ERGEN** has received his bachelor and master degrees in Aeronautical Engineering from Istanbul Technical University in 2013 and 2016 respectively. He is currently a PhD student in the same university.



**Tamer ŞENER** has received his bachelor and master degrees in Aeronautical Engineering from Istanbul Technical University in 2016 and 2019 respectively. He is currently a PhD student in the same university.



**Prof. Dr. Onur TUNCER** has received his bachelor degree in Mechanical Engineering from Middle East Technical University and PhD from Louisiana State University in 2001 and 2006 respectively. He has been teaching Combustion, Fluid Mechanics, Engineering Mathematics and Heat Transfer courses at Istanbul Technical University, Faculty of Aeronautics and Astronautics since 2009.



**Prof. Dr. A. Cihat BAYTAŞ** has received his PhD degree from Istanbul Technical University Nuclear Energy Institute in 1988. He has been teaching Fluid Mechanics, Aircraft Icing, Convective Heat Transfer and Heat Transfer courses at Istanbul Technical University, Faculty of Aeronautics and Astronautics since 2002.



## SU<sup>2</sup> REAL GAS MODELS' PERFORMANCE PREDICTIONS ON A COLD GAS THRUSTER

Aysu ÖZDEN\*, Özgür Uğraş BARAN\*\*, Mehmet Halûk AKSEL\*\*\* ve Mehmet Ali AK\*\*\*\*

\*\*\*Orta Doğu Teknik Üniversitesi Makina Mühendisliği Bölümü, 06800, Ankara

\*aysu.ozden@metu.edu.tr, ORCID: 0000-0001-9257-1377

\*\*ubaran@metu.edu.tr, ORCID: 0000-0002-8437-7862

\*\*\*aksel@metu.edu.tr, ORCID: 0000-0003-0563-4216

\*\*\*\* ROKETSAN A.Ş. Elmadağ, 06780, Ankara

mehmetali.ak@roketan.com.tr ORCID: 0000-0001-8204-8961

(Geliş Tarihi: 22.07.2020, Kabul Tarihi: 25.01.2021)

**Abstract:** Cold gas propulsion systems are preferred, especially for the altitude and trajectory control for satellites, since the 1960s. Both depressurizing the propellant in the propellant tank throughout the mission and the expansion occurring in the divergent part of the thruster nozzle are the reasons for observing very low temperatures and pressure at the outlet section. We have decided to use an open-source compressible CFD tool, SU<sup>2</sup>, in order to predict the performance of the propulsion system in the early design phase. The scope of this study is the comparison of the results of the vacuum chamber performance tests and the outcomes of unsteady simulations with SU<sup>2</sup> using different gas models, including ideal gas, van-der Waals, and Peng-Robinson models. Then, the accuracy and performance of these models are evaluated for the extremely low temperature and pressure conditions. Thruster performance tests have been conducted in the thermal vacuum chamber test campaign at the specially built testing facilities. In order to simulate nominal and low-temperature operation conditions, a propellant tank is thermally conditioned to the predetermined values, and performance test parameters are used as the input for the CFD simulations. The obtained results showed that the van der Waals gas model is the most appropriate gas model for both cases and provides the most realistic results in terms of performance parameters.

**Keywords:** Cold gas thruster, Real gas models, Vacuum chamber test, SU<sup>2</sup>.

## SU<sup>2</sup> GERÇEK GAZ MODELLERİNİN SOĞUK GAZ İTİCİSİ PERFORMANS TAHMİNLERİ

**Özet:** Soğuk gaz itki sistemleri 1960'lı yıllardan bu yana özellikle uyduların yörünge kontrolünde tercih edilen sistemler olmuşlardır. Yakıt tankındaki yüksek basıncın görev süresince azalması nedeniyle, tank içindeki yakıtta oldukça düşük sıcaklıklar gözlenmektedir. Ayrıca itici lülesinin çıkışında da, vakuma yakın basınçlara genleşen yakıtın sıcaklığı oldukça düşmektedir. Bu koşullar altında, itki sisteminin performansının tasarım sürecinde gerçekçi olarak tahmin edilebilmesi için, açık kaynaklı, sıkıştırılabilir akışkanlar için uygun bir hesaplamalı akışkanlar dinamiği aracı olan SU<sup>2</sup>'nin kullanılması kararlaştırılmıştır. Bu çalışmada, itki sisteminin doğası gereği karşılaşılan düşük sıcaklık ve basınç etkilerinin doğru modellenebilmesi adına, SU<sup>2</sup>'nin ideal gaz, van-der Waals ve Peng-Robinson gaz modelleri kullanarak elde edilen performans tahminleri ile itici vakum odası performans test sonuçları karşılaştırılmıştır. İtici performans testleri için bu amaçla kurulan termal vakum odası test alt yapısı kullanılmıştır. İtici simülasyonları ve performans testleri, yakıt tankının nominal ve düşük sıcaklıkta koşulladığı durumlar için yürütülmüştür. Elde edilen veriler, SU<sup>2</sup> van der Waals gaz modelinin, her iki sıcaklık koşulunda da vakum odası performans testlerine en yakın sonuçları verdiğini göstermektedir.

**Anahtar Kelimeler:** Soğuk gaz iticisi, Gerçek gaz modelleri, Vakum odası testi, SU<sup>2</sup>.

### NOMENCLATURE

CFL Courant-Friedrichs-Lewy number

MFP mean free path

A area [m<sup>2</sup>]

a measure of intensity of the molecular attraction force

b co-volume

c speed of sound [m/s]

$c_p$  heat capacity at constant pressure [J/molK]

$c_v$  heat capacity at constant volume [J/K]

$d_m$  molecular diameter [Å]

$e$  total energy per unit mass [J/kg]

$F$  thrust [N]

$k_b$  Boltzmann constant [J/K]

Kn Knudsen number

$M$  Mach number

$\dot{m}$  mass flow rate [g/s]

$p$	pressure [Pa,bar]
$R$	gas constant [J/kgK]
$s$	total entropy per unit mass [J/kgK]
$T$	temperature [K]
$V$	velocity [m/s]
$\alpha$	measure of intermolecular attraction force
$\rho$	density [kg/m <sup>3</sup> ]
$\lambda$	distance traveled by a molecule between two consecutive collisions
$\lambda_n$	nozzle efficiency
$\gamma$	ratio of specific heats
$v$	specific volume [m <sup>3</sup> /kg]
$\omega$	acentric factor
subscripts	
$a$	ambient
$c$	chamber
$cr$	critical value
$e$	exit
$ref$	reference value
$t$	throat

## INTRODUCTION

Space exploration has always been at the center of human attention, and one of the most studied space objects has been the satellites since the 1960s. Aim to control satellite maneuverability and trajectory has emerged the need to have a compact and efficient propulsion system. From the beginning, the cold gas propulsion systems have been preferred considering their design simplicity, lower mass, cost-effectiveness and compatibility. Providing low thrust and specific impulse compared to chemical propulsion systems are the primary disadvantages of such systems. However, they are considered broadly in satellite propulsion since their simple construction provides reliability and robustness.

A simple sketch of a cold gas propulsion system is given in Fig. 1. As can be seen from the figure, usually, there is one propellant tank, a pipeline to deliver the propellant to the rest of the system, valves to control the propellant motion and thrusters. Thrusters are the combination of the nozzle and the thruster valve, which allow the propellant to the nozzle. The propellant tank usually contains a high-pressure gaseous propellant, yet the operational pressure level is considerably lower. A pressure regulator is located downstream of the propellant tank to decrease the high pressure in the tank to operational levels. Thrust is obtained by discharging the pressurized gas through the nozzle using only the available enthalpy of the propellant without any combustion, heat addition, or other mechanisms to add energy [2].

There are three different cold gas propulsion system configurations according to their operating principle. These are pressurized gas systems, heated gas systems and liquified gas systems, and their general schematics are provided in Fig. 2. Pressurized gas systems are the simplest among the three considering the operating principle, and the propulsion system examined in this study is the first one of these three.

The operation principle of a cold gas propulsion system is reasonably straightforward. The main propellant tank is filled with a highly pressurized (~ 30 MPa) gas propellant. The pressurized propellant is kept in the tank with the help of a latch valve. After initiating the operation of the propulsion system, a pressure regulator is used to decrease the high pressure to the operational levels (~1 MPa). The gas flow is controlled by the solenoid valves before the thruster. Once the solenoid valves are activated, high pressurized propellant gas is expanded and accelerated through the nozzle, and the desired thrust is obtained.

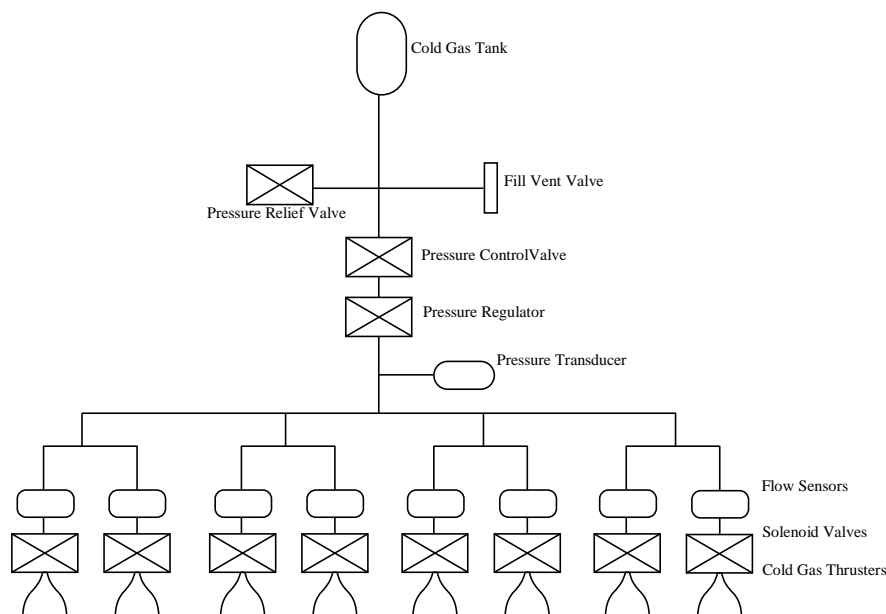


**Figure 1.** Schematic drawing of a cold gas propulsion system with main components. Recreated after Anis [Anis, 2012]

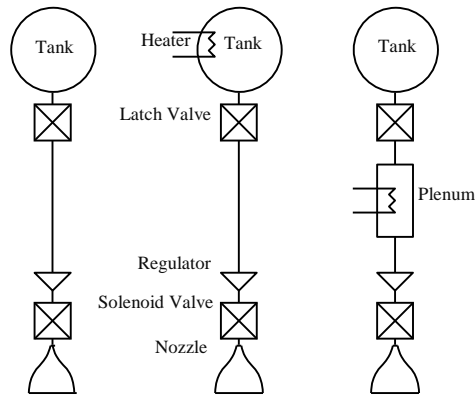


**Figure 2.** Cold gas propulsion systems from left to right; pressurized, heated and liquefied gas systems. Recreated after Lev. [Lev et al., 2014]

It is possible to find many successful cold gas propulsion systems in operation in the literature. Two Canadian-based cold gas propulsion system applications were studied and launched successfully in 2008 and 2014 in the nanoscale satellite experimental program CanX (Canadian Advanced Nanospace eXperiment). CanX-2 was using Nano Propulsion System (NANOPS) in April 2008 [Sarda et al., 2008] while CanX-5 was using the Canadian Nanosatellite Advanced Propulsion System (CNAPS) and sulfur hexafluoride had chosen as the propellant for both propulsion systems [Risi, 2014]. The propulsion system designed for Microelectromechanical System PICOSAT Inspector was using Xenon as the propellant [Hinkley, 2008]. Propulsion Operation Proof SATellite – High Performance 1 (POP AT-HIP1), which had Argon-based thrusters were fired successfully in 2014 [Manzoni et al., 2015].

Propellant selection is an essential step in the design of the propulsion system since it directly affects both the propellant tank and thruster design. Moreover, using a contamination-free propellant is crucial, considering that it may affect the sensing devices and mechanical actuators with their residues [Bzibziak, 2000]. Considering the propellant tank design parameters in terms of handling and storage, using a propellant, which has a moderately low boiling point, low melting temperature and mass-efficient, is generally preferred [Jerman et al., 2011]. There are many options for gaseous propellants, including hydrogen, helium, Nitrogen, Argon, Xenon. However, due to its storage density, performance, cost-effectiveness, and contamination-free nature, Nitrogen has been used in this study.

Thruster design is one of the most critical phases of the overall design process of the propulsion system since this component is responsible for delivering the desired performance. A thruster is typically the combination of the thrust chamber and the nozzle. Thrust chamber design is crucial since it determines the thrust delay following the actuation of the thruster valve. Nozzle design should also be performed carefully, since this is the part where the flow is accelerated and the desired thrust is obtained. Cold gas thrusters generally have converging or

converging-diverging (De Laval) nozzle configurations. The aim of obtaining higher performance led to the use of De Laval nozzles widely in thrusters. De Laval nozzle is designed such that flow through its throat reaches sonic velocity to maximize the allowable mass flow rate and hence to maximize the allowable thrust. There are two options for the divergent part of these nozzles, conical or bell-shaped. Since the physical dimensions of these thrusters are exceedingly small, conical nozzles are preferred for practical applications by taking into account the ease of manufacturing and design procedure. The nozzle used in the scope of this study is also designed to include a conical and divergent section. The main design parameter, half cone angle ( $\alpha$ ), has been chosen as  $15^\circ$  by comparing the performance of  $8^\circ$ ,  $15^\circ$ , and  $25^\circ$  half cone angles.

## CURRENT STUDIES IN THE LITERATURE

There are many studies in the literature to evaluate the performance of a cold gas thruster using both numerical and experimental approaches. Matticari et al. (2010) conducted experimental and numerical studies on a cold gas system in which Xenon was used as the propellant. CFD simulations were performed for the 2D axisymmetric flow domain with commercial software, including the viscous effects. Pressure and velocity contours are provided in their article.

Nozzle exit pressure and temperature are obtained as 21 Pa and 12.40 K [Matticari et al., 2010]. These cryogenic values give rise to a question of the possibility of phase change of the propellant at any location of the flow inside the nozzle. A related experimental study was performed in the vacuum chamber facility at the European Space Research and Technology Centre (ESTEC) Electronic Propulsion Laboratory. During the performance tests, mass flow rate, gas inlet temperature and pressure measurements were taken. In the case of a phase change, it was expected to observe a loss in thrust compared to the estimated value. However, experimental results did not show any reduction in nozzle performance. A similar result was obtained for a cold gas thruster, which uses compressed air as the propellant, by Ranjan et al. (2017). Numerical simulation showed that the nozzle exit temperature approximately 35 K for vacuum conditions. Corresponding experiments that were conducted in a vacuum chamber showed that the expected thrust and specific impulse values were reached.

Another important issue to be proved was the capability of SU2 to solve problems, including real gas models. A numerical comparison was performed to simulate the flow in a nozzle to show whether SU2 was capable of solving real gas equations for nozzle applications. Navier-Stokes equations were solved by using the second-order Roe scheme and implicit Euler algorithm based on CFL adaptation [Pini et al., 2017]. Comparison has been performed between the results of SU2 and ANSYS-CFX using the Span-Wagner equation of state. The authors provided both the Mach and pressure ratio contours. The results of both simulations were matching



reasonably well. These results show that SU2 is an appropriate solver for the cold gas thruster simulations.

Experimental test setups are also widely presented in the literature. One of the most related experimental procedures has been performed for the design and testing of Pakistan's first cold gas propulsion system (PRSS) prototype. The propellant of this system was chosen as Nitrogen, and it has eight 1 N thruster, which operates at a chamber pressure of 8 bar (0.8 MPa) [Anis, 2012]. Thrusters employed in this prototype were conical nozzles with a 16° half-angle and an area ratio of 50:1, and the nozzle efficiency was taken as 98% [Anis, 2008, 2012]. An experimental test campaign has been designed by using load cells for the force measurements. The specific impulse was measured as 73 s for continuous operation as a result of the tests, which was the expected value.

Another experimental study of a cold gas thruster was performed by Rickermers (2004). The vacuum chamber at the University of Bremen's Hochschule Hyperschall Kanal was used. The chamber has a volume of 1.5 m<sup>3</sup>, and the minimum achievable pressure level is 10 to 3 mbar (1000 to 300 Pa). Besides the Schlieren visualization technique, pressure and temperature sensors were used to track down the flow through the nozzle. The authors provided pressure and thrust test results.

Pressure readings show that the pressure inside the vacuum chamber increases following the thruster operation as expected. Another outcome is while the chamber pressure is constant, thrust decreases in continuous operation. It was concluded that the first reason might be maintaining larger ambient pressure at the nozzle exit than the theoretical calculations. Additionally, it was considered that the boundary layer at the throat might decrease the mass flow rate, which may result in having lower thrust values. Another reason behind this might be the decrease in specific impulse due to the decrease in the temperature following the continuous operation.

## METHODOLOGY

Flow field simulations are performed by employing an open-source solver considering their flexibility compared to commercial software. The Middle East Technical University Mechanical Engineering CFD group has a strong background in SU2. Hence SU2 is chosen as the platform for the flow simulations. SU2 is capable of solving multi-physics Partial Differential Equation (PDE) problems and PDE constrained optimization problems on unstructured meshes. The mesh generation flow diagram is provided in Fig. 3. The mesh generation has been performed in Salome, yet since its output is not compatible with the SU2 native mesh format, Gmsh and enGrid open source software are used.

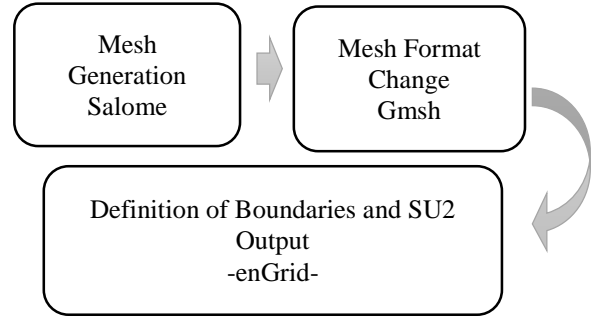


Figure 3. Tools used for SU<sup>2</sup> native mesh generation

## Compressible Gas Models

Developers of SU2 coupled a built-in thermodynamic library with the main solver considering the non-ideal gas applications. Ideal gas, van der Waals and Peng-Robinson gas models are the available thermodynamic models embedded in the code. In this section, the capabilities of these models are investigated.

**Ideal Gas Thermophysical Model:** This model describes the volumetric and caloric behaviour of the polytropic ideal gas.

$$\begin{cases} p(T, v) = \frac{RT}{v} \\ e(T, v) = e(T) = e_{\text{ref}} + c_v(T - T_{\text{ref}}) \\ s(T, v) = s_{\text{ref}} + c_v \ln \frac{T}{T_{\text{ref}}} + R \ln \frac{v}{v_{\text{ref}}} \\ c_v = \frac{1}{\gamma - 1} R \end{cases} \quad (1)$$

where  $p$  is the pressure,  $T$  is the temperature,  $R$  is the gas constant,  $v$  is the specific volume,  $e$  is the total energy per unit mass, and  $s$  is the total entropy per unit mass.  $\gamma$  is the ratio of specific heats and can be expressed as  $\gamma = c_p / c_v$  where  $c_p$  is the heat capacity at constant pressure and  $c_v$  is the heat capacity at constant volume. These sets of equations are calculated based on reference energy and entropy. Reference energy and entropy are defined as follows:

$$\begin{cases} e_{\text{ref}} = c_v T_{\text{ref}} \\ s_{\text{ref}} = -c_v \ln T_{\text{ref}} + R \ln v_{\text{ref}} \end{cases} \quad (2)$$

Reference temperature and specific volume are defined by the user according to the reference pressure. These values are used to non-dimensionalize the problem. The following form of the equations is obtained.

$$\begin{cases} e(T, v) = c_v T \\ s(T, v) = c_v \ln T + R \ln v \end{cases} \quad (3)$$

In order to be used in the numerical schemes, derivatives are given in Eqn. (4) to (7) should be calculated for the ideal gas thermodynamic equation of state.

$$\left(\frac{\partial p}{\partial e}\right)_\rho = (\gamma - 1)\rho \quad (4)$$

$$\left(\frac{\partial p}{\partial \rho}\right)_e = (\gamma - 1)e \quad (5)$$

$$\left(\frac{\partial T}{\partial e}\right)_\rho = \frac{(\gamma - 1)}{R} \quad (6)$$

$$\left(\frac{\partial T}{\partial \rho}\right)_e = 0 \quad (7)$$

where  $\rho$  is the density. The final step is the calculation of the speed of sound,  $c$  as

$$c^2 = \left(\frac{\partial p}{\partial \rho}\right)_e + \frac{p}{\rho^2} \left(\frac{\partial p}{\partial e}\right)_\rho \quad (8)$$

van-der Waals Gas Thermophysical Model: The set of equations for this thermophysical model is provided in Eq. (9).

$$\begin{cases} p(T, v) = \frac{RT}{v - b} - \frac{a}{v^2} \\ e(T, v) = c_v T - \frac{a}{v} \\ s(T, v) = c_v \ln T + R \ln(v - b) \end{cases} \quad (9)$$

Two new coefficients are introduced in this model. These coefficients are dependent on the chemical composition and gas properties. The coefficient  $a$  is the measure of the intensity of the intermolecular attraction force. The coefficient  $b$  is the co-volume, which represents the volume of the atoms or molecules in one mole of the gas. These coefficient are given as

$$\begin{cases} a = \frac{27 R^2 T_{cr}^2}{64 p_{cr}} \\ b = \frac{1 R T_{cr}}{8 p_{cr}} \end{cases} \quad (10)$$

Constants  $a$  and  $b$  are dependent on critical temperature and the pressure of the propellant. For the sake of consistency, energy and entropy equations are defined as in the ideal gas model. Here  $T_{cr}$  and  $p_{cr}$  are the critical pressure and temperature. The critical point is unique in the  $(p - T - v)$  phase diagram, where both  $(dp/dv)_T$  and  $(d^2p/dv^2)_T$  are zero. The critical point is related to the size of the atom. Around the critical point, the distance between gas atoms becomes small as the molecules almost touch each other. Then a strong short-range repulsive force between gas atoms becomes significant. This force is correlated to  $b$ , which is roughly equal to the volume of a gas molecule.

Thermodynamic derivatives are also calculated in terms of coefficients  $a$  and  $b$ , as shown in equations (11) to (14).

$$\left(\frac{\partial p}{\partial e}\right)_\rho = \frac{(\gamma - 1)\rho}{1 - \rho b} \quad (11)$$

$$\left(\frac{\partial p}{\partial \rho}\right)_e = \frac{(e + 2\rho a - \rho^2 ab)}{\rho(1 - \rho b)} \left(\frac{\partial p}{\partial e}\right)_\rho - 2\rho a \quad (12)$$

$$\left(\frac{\partial T}{\partial e}\right)_\rho = \frac{(\gamma - 1)}{R} \quad (13)$$

$$\left(\frac{\partial T}{\partial \rho}\right)_e = \frac{1}{a} \left(\frac{\partial T}{\partial e}\right)_\rho \quad (14)$$

In order to calculate the speed of sound, Eq.(8) is utilized.

Peng-Robinson Gas Thermophysical Model: The model modifies the Soave-Redlich-Kwong(SRK) equation of state. The model is developed to improve the predictions for liquid density, vapor pressure and equilibrium ratio. The set of equations is to be solved in this model is provided in Eqn. (15).

$$\begin{cases} p(T, v) = \frac{RT}{v - b} - \frac{a\alpha^2(T)}{v^2 + 2bv - b^2} \\ e(T, v) = c_v T - \frac{a\alpha(T)(k + 1)}{b\sqrt{2}} \tanh^{-1} \frac{b\sqrt{2}}{v + b} \\ s(T, v) = c_v \ln T + R \ln(v - b) - \frac{a\alpha(T)k}{b\sqrt{2}T T_{cr}} \tanh^{-1} \frac{b\sqrt{2}}{v + b} \end{cases} \quad (15)$$

For this model, parameters of  $\alpha(T)$ ,  $a$  and  $b$  have to be defined.  $\alpha(T)$  is the measure of the intermolecular attraction force, and it is temperature-dependent. As mentioned in the van-der Waals gas model, coefficients  $a$  and  $b$  depend on both the critical temperature and pressure.

$$\begin{cases} a = 0.45724 \frac{(RT_{cr})^2}{p_{cr}} \\ b = 0.0778 \frac{RT_{cr}}{p} \\ \alpha(T, \omega) = \left[ 1 + k \left( 1 - \sqrt{\frac{T}{T_{cr}}} \right) \right] \\ k = \begin{cases} 0.37464 + 1.54226\omega - 0.26992\omega^2 & \omega \leq 0.49 \\ 0.379642 + 0.48503\omega - 0.164423\omega^2 + 0.016666\omega^3 & \omega > 0.49 \end{cases} \end{cases} \quad (16)$$

As can be seen from the above equations,  $\alpha(T)$  depends both on temperature and the acentric factor, which is a function of the saturated vapor pressure and the critical pressure. This parameter also varies with the chemical composition of the gas. Entropy and energy equations are defined as the same as the ideal gas model to satisfy consistency.

The solution of thermodynamic derivatives is more challenging compared to the other gas models. First, the second derivatives are provided in Eqn. (17) to (20):

$$\left(\frac{\partial p}{\partial e}\right)_\rho = \frac{\left(\frac{\partial p}{\partial T}\right)_\rho}{\left(\frac{\partial e}{\partial T}\right)_\rho} \quad (17)$$

$$\left(\frac{\partial p}{\partial \rho}\right)_e = \left(\frac{\partial p}{\partial \rho}\right)_T - \left(\frac{\partial p}{\partial e}\right)_\rho \left(\frac{\partial e}{\partial \rho}\right)_T \quad (18)$$

$$\left(\frac{\partial T}{\partial e}\right)_\rho = \frac{1}{\left(\frac{\partial e}{\partial T}\right)_\rho} \quad (19)$$

$$\left(\frac{\partial T}{\partial \rho}\right)_e = \left(\frac{\partial T}{\partial \rho}\right)_p - \left(\frac{\partial T}{\partial p}\right)_\rho \left(\frac{\partial e}{\partial T}\right)_p \quad (20)$$

The complexity of the second derivatives is due to the fact that the coefficient  $\alpha$  depends both on the temperature and the acentric factor. Hence, partial derivatives are implemented as in Eqn. (21) and (22):

$$\left(\frac{\partial p}{\partial T}\right)_\rho = \frac{R}{(v-b)} - \frac{2a\alpha'}{[v(v+b) + b(v-b)]} \quad (21)$$

where

$$\alpha' = \frac{d\alpha}{dT} \quad (22)$$

According to the information provided above, partial derivatives are calculated as in Eqn. (23) to (30).

$$\left(\frac{\partial e}{\partial T}\right)_\rho = \frac{R}{(\gamma-1)} - \frac{a}{b\sqrt{2}} \left[ 2\alpha\alpha' + k\alpha' \sqrt{\frac{T}{T_{cr}}} + \frac{1}{2}k\alpha(TT_{cr})^{-0.5} \right] f(v) \quad (23)$$

$$\begin{aligned} \left(\frac{\partial p}{\partial \rho}\right)_T &= -\frac{1}{\rho^2} \left(\frac{\partial p}{\partial v}\right)_T \\ &= -\left( -\frac{RT}{(v-b)^2} + \frac{2a\alpha'(v+b)}{[v(v+b) + b(v-b)^2]} \right) v^2 \end{aligned} \quad (24)$$

$$\begin{aligned} \left(\frac{\partial e}{\partial \rho}\right)_T &= -\frac{a\alpha(T)}{b\sqrt{2}} \left[ \alpha(T) + k \sqrt{\frac{T}{T_{cr}}} \frac{b\sqrt{2}}{a + 2\rho b - \rho^2 b^2} \right] \end{aligned} \quad (25)$$

$$\left(\frac{\partial \rho}{\partial T}\right)_p = -\rho^2 \left(\frac{\partial v}{\partial T}\right)_p \quad (26)$$

$$\left(\frac{\partial T}{\partial \rho}\right)_p = \frac{1}{\left(\frac{\partial \rho}{\partial T}\right)_p} \quad (27)$$

$$\left(\frac{\partial v}{\partial T}\right)_p = -\left(\frac{\partial p}{\partial v}\right)_T^{-1} \left(\frac{\partial p}{\partial T}\right)_v \quad (28)$$

$$\left(\frac{\partial e}{\partial T}\right)_p = \left(\frac{\partial h}{\partial T}\right)_p - p \left(\frac{\partial v}{\partial T}\right)_p \quad (29)$$

$$\left(\frac{\partial h}{\partial T}\right)_p = \left(\frac{\partial e}{\partial T}\right)_v + T \left(\frac{\partial p}{\partial T}\right)_v \left(\frac{\partial v}{\partial T}\right)_p \quad (30)$$

Finally, the speed of sound is calculated again, according to Eq.(8).

### Experimental Test Setup

A series of performance tests for the cold gas propulsion system have been performed to observe the characteristics of the system. The challenging part of these experiments is the simulation of very low pressure to simulate space conditions. In order to satisfy operation conditions, a vacuum chamber test campaign is used. This facility is designed and manufactured by national resources and by Turkish sub-contractors. The test facility, which is shown in Fig. 4, has a vacuum chamber of 3.1 m<sup>3</sup>, and the desired low-pressure environment is maintained by using vacuum pumps. The vacuum chamber has the ability to depressurize down to 5 Pa. Real-time pressure and temperature sensors are located inside the chamber to observe the chamber conditions.

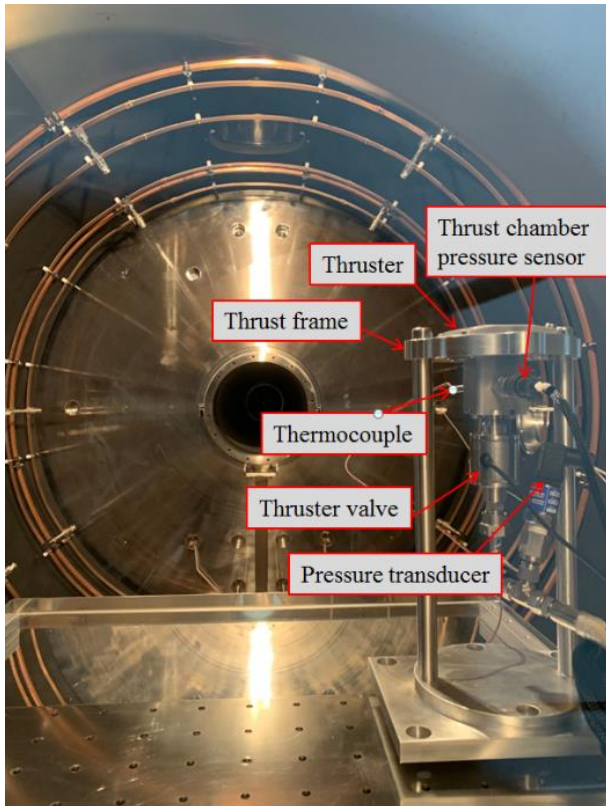


Figure 4. Thrust chamber test setup

The test setup contains a propellant tank, a commercial regulator, a fill-drain system, a manifold, a thruster valve and the thruster itself, which is fitted by the required pressure and temperature sensors. Schematic drawing, which can be seen in Fig. 5, shows the test setup clearly. Pressure measurements are taken from the propellant tank exit, regulator and manifold downstream, thruster

valve upstream and thrust chamber. The temperature readings are taken from both the tank exit and the thrust chamber. The propellant tank, which is made from 4130 steel and painted to prevent corrosion, is pressurized by using a compressor booster. A 44-1362 series TESCOM regulator is used to lower the propellant pressure to the operating level. A thruster valve is basically a solenoid valve that operates at 28 V DC and 1 A. Pressure measurements from the thrust chamber have been taken by using a Kulite HKM-375 series pressure sensor. TRAFQA EPI400.0A 8287 pressure transmitters are used for the rest of the pressure sensors. The precision load cell of Burster 9431 series is used. The load cell has the capability to measure forces up to 500 N. Experimental test setup inside the vacuum chamber is given in Fig. 6.

A thrust frame is designed to transfer the produced thrust to the load cell. Alignment of the thrust vector and the load cell is taken into account during the design process in order to prevent the measurement of the side loads. Connection through the vacuum chamber is accomplished by using a flexible hose in order not to affect the thrust measurements.



**Figure 5.** Thruster and thrust frame inside the vacuum chamber

## THRUSTER DESIGN

The thruster is the main component responsible for satisfying the performance requirements of the propulsion system. Thrusters that operate in space are designed to provide optimum expansion performance in vacuum conditions, which means infinite expansion. A realistic design procedure includes the decision of the

outlet pressure, which determines the produced thrust. Thrust chamber pressure is another critical parameter since it affects the propellant tank weight and also the pipeline weight. Since it is desired for systems to be as light and compact as possible, thruster design becomes more crucial. Thrust for an ideal gas and expansion to an ambient pressure  $p_a$  is calculated as follows [Dorado Et. Al. 2013]:

$$F = A_t p_c \gamma \left[ \left( \frac{2}{\gamma - 1} \right) \left( \frac{2}{\gamma + 1} \right)^{\frac{\gamma - 1}{\gamma + 1}} \left\{ 1 - \left( \frac{p_e}{p_c} \right)^{\frac{\gamma - 1}{\gamma}} \right\}^{\frac{1}{2}} + (p_e - p_a) A_e \right] \quad (31)$$

In this equation,  $F$  is the thrust,  $A_t$  is the throat area,  $p_c$  is the chamber pressure,  $A_e$  is the nozzle exit area,  $p_e$  is the nozzle exit pressure,  $p_a$  is the ambient pressure, and  $\gamma$  is the ratio of specific heats. Exit pressure for the nozzle might be chosen by considering the lowest altitude at which the thruster starts its operation. This is because lowering the exit pressure results in longer and heavier nozzles, which is not desired for the overall propulsion system. Determination of the chamber pressure is also important. It is clear that higher chamber pressure will result in higher performance, yet it requires a heavier thruster. Considering the weight and performance optimization of the nozzle, we have chosen 1.0 MPa (10 bar) and 300 Pa as the chamber pressure and nozzle exit pressure, respectively.

The pressure difference between nozzle exit and ambient pressure is small, as well as the nozzle exit area, the contribution of pressure to the thrust is negligible compared to momentum thrust. The thrust equation can be expressed in Eqn. (32) which shows the relation of mass flow rate, exit velocity, and specific impulse. Determining the mass flow rate will lead to geometrical parameters of the thruster.

$$F = \dot{m} V_e \quad (32)$$

$\dot{m}$  is the mass flow rate which is maximized when the Mach number at the throat reaches unity, and  $V_e$  is the nozzle exit velocity. The next step is the calculation of nozzle exit velocity to determine the mass flux rate since the desired thrust is already known as 10 N. Nozzle exit velocity can be found through the following relation.

$$V_e = \lambda_n \sqrt{\left( \frac{2\gamma}{\gamma - 1} \right) R T_c \left[ 1 - \left( \frac{p_e}{p_c} \right)^{\frac{\gamma - 1}{\gamma}} \right]} \quad (33)$$

For the current thruster design, chamber pressure and temperature are taken as 1 MPa and 293 K, respectively. The gas constant for the propellant, Nitrogen, is taken as 296.8 J/kg K, and the specific heat ratio is taken as 1.4. The nozzle efficiency,  $\lambda_n$ , includes losses in the nozzle and taken as 95%. At the end of the nozzle, the exit

velocity is calculated as 704 m/s. The mass flow rate is calculated as 14.2 g/s to satisfy the desired thrust level. The nozzle exit area can be obtained by using the design values through Eqn. (34).

$$\frac{\dot{m}}{A_e} = \sqrt{\frac{\gamma}{RT_c}} p_c \sqrt{\left(\frac{2\gamma}{\gamma-1}\right) \left[ \left(\frac{p_e}{p_c}\right)^{\frac{2}{\gamma}} - \left(\frac{p_e}{p_c}\right)^{\frac{\gamma+1}{\gamma}} \right]} \quad (34)$$

Nozzle exit diameter is obtained as 520 mm<sup>2</sup> and the corresponding nozzle exit diameter is found as 25.7 mm. To obtain the throat area, first, the nozzle exit Mach number has to be obtained. The exit Mach number is calculated as 6.76 using the chamber pressure and nozzle exit pressure. Finally, the expansion ratio is obtained as 84, which corresponds to the nozzle throat diameter of 2.8 mm from the following relation.

$$\frac{A_e}{A_t} = \frac{1}{M_e} \left\{ \left( \frac{2}{\gamma+1} \right) \left( 1 + \frac{\gamma-1}{2} M_e^2 \right) \right\}^{\frac{\gamma+1}{2(\gamma-1)}} \quad (35)$$

The thrust chamber diameter is determined considering the thruster valve exit cross-section in order not to suffer from pressure loss. The length of the thruster is decided to fit the overall propulsion system. Fig. 7 shows the final thruster geometry.

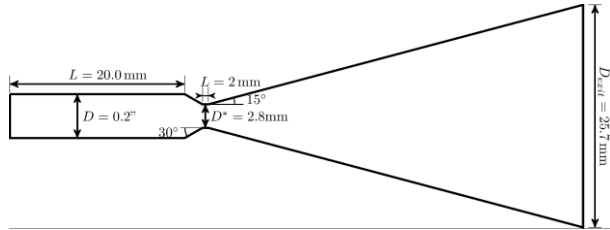


Figure 6. Thruster dimensions

## RESULTS

The operational environment of the cold gas thrusters is space that has extremely low pressure. In addition, the nature of the propulsion system results in having cryogenic temperature and pressure values, which give rise to the question of whether the continuum postulate is still valid or not. This is also necessary for the sake of the numerical simulations to check the validity of the applicability of Navier-Stokes equations.

### Continuum Postulate Validation

The non-dimensional Knudsen number, Kn, is used to decide whether the continuum postulate is valid or not. Knudsen Number is defined as the ratio of the molecular mean free path of fluid to the characteristic length of the flow field [Greer et al., 1967].

$$Kn = \frac{\text{Molecular mean free path}}{\text{Characteristic linear dimension of the flow field}} \quad (36)$$

Even though the Knudsen number is desired to be as close to zero as possible, in order for the continuum postulate to be valid, it should be less than approximately 0.01 [Aksel, 2011].

In order to calculate the Knudsen number, first, the molecular mean free path (MFP) of the fluid should be calculated. MFP,  $\lambda$ , is the distance traveled by a molecule between two consecutive collisions and can be calculated as follows:

$$\lambda = \frac{k_B T}{\sqrt{2} \pi p d_m^2} \quad (37)$$

In the above equation,  $k_B$  is the Boltzmann constant (1.38064910-23 J/K) and  $d_m$  is the molecular diameter of the gas. The outlet of the thruster is the section in which the lowest temperature and pressure values are expected. As a result, to calculate the MFP, the outlet pressure of 300 Pa and corresponding outlet temperature of 28.9 K are used. The molecular diameter of the Nitrogen is taken as 3.64 Å [Kentish et al., 2008]. Corresponding MFP is obtained as 2.2594x10<sup>-6</sup> m. Since the nozzle outlet is decided as the critical section, the nozzle diameter is taken as the characteristic length. Design procedure gives the nozzle outlet diameter as 25.7x10<sup>-3</sup>m and the corresponding Kn is calculated as 8.79x10<sup>-5</sup>. Since it is lower than the critical value of 0.01, it is clear that the continuum postulate is applicable to this problem.

### Thruster Nozzle Verification

The first step is the generation of the computational grid in order to capture the physics of the problem correctly. Grid sizing and distribution is important for the accuracy and stability of the solution. For the mesh generation, the unstructured NETGEN 1D-2D-3D grid generator in Salome is used. Mesh independency analysis has been conducted by applying the nominal operation conditions and solving Euler equations to the grid sizes of 13732, 49468, 114399, 506172, 1240249, and 5356379.

Table 1. Mesh verification study results

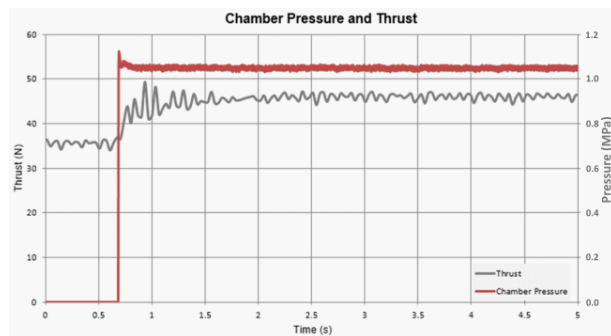
Mesh size	$\dot{m}$ per area [kg/m <sup>2</sup> s]	% Error in $\dot{m}$ per area
13732	2321.4	1.84
49468	2248.3	4.93
114399	2392.3	1.16
506172	2324.9	1.69
1240249	2319.9	1.90
5356379	2313.6	2.29

Table 1 compares the mass flow rate through the nozzle for different mesh densities. As a result of this comparison, the grid having 114,399 cells is decided to be used for the rest of the simulations.

Nominal Operational Conditions: The first set of comparisons has been performed for the nominal

operating condition of the thruster, which is 1MPa of chamber pressure and 293 K of the propellant temperature.

Vacuum chamber performance test results for thrust chamber pressure and the thrust are provided in Fig. 8. Following the thruster valve actuation, both the pressure inside the chamber and the thrust value increase. It is seen that the pressure inside the chamber reaches the steady-state value of 1.05 MPa in 3 ms. The difference of 50 kPa between the expected and experimental value is due to the imprecise adjustment of the mechanical pressure regulator. In idle condition, 35 N of thrust reading is observed. This non-zero force reading is due to the overall weight of the thruster, sensors and thrust frame. After the actuation of the thruster valve, a steady-state thrust value of 45 N is obtained. The difference between the idle and when the thruster on conditions reads 10 N, which is the expected value.



**Figure 7.** Nominal operating conditions vacuum chamber test results for chamber pressure (red line) and thrust (gray line)

Experimental measurements are applied as the initial and boundary conditions for the numerical simulations. Chamber pressure and gas temperature values of 1 MPa and 293 K are defined as the initial conditions at the inlet. The environmental pressure and temperature values of 200 Pa and 293 K, respectively, similar to the pressure-outlet boundary conditions, are defined as the initial conditions.

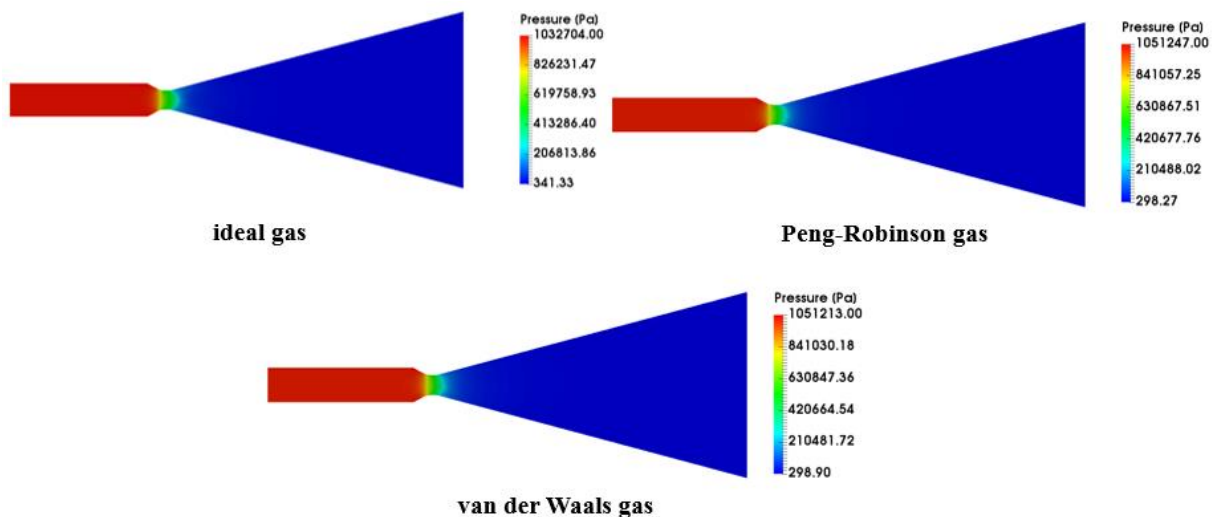


**Figure 8.** Nominal temperature operation condition results for different gas models

Euler equations are solved with the Roe flux splitting scheme. For real gas models, additional Riemann boundary conditions are defined in the SU2 configuration file. A CFL adaptation between 0.4 and 5 is used to obtain faster convergence.

Numerical simulation results are provided in Fig. 9 for the three gas models. In general, real gas models predicted higher chamber pressures compared to the ideal gas model. Again, the pressure at the outlet section obtained from real gas models is closer to the design value compared to the ideal gas result.

Another comparison is performed in terms of thrust. Thrust is calculated by the area integration at the nozzle outlet section by using the open-source visualization tool, ParaView. As shown in Table 2, the real gas models predicted closer thrust values compared to the design values.

**Table 2.** Thrust comparison between gas models

Gas Model	Thrust [N]	% Error in Thrust	Solution Time [min]
Ideal Gas	10.86	+8.6	600
van-der Waals	9.31	-6.9	170
Peng-Robinson	9.31	-6.9	159

In the preliminary design phase, it is crucial to obtain the fastest solution as well as the most accurate one. Therefore, the final comparison of the model performance has been carried out for the computational time. The ideal gas simulation takes approximately 600 minutes to converge, while Peng-Robinson takes approximately 170 minutes. The fastest convergence is obtained with the van-der Waals gas model within 159 minutes. It should be noted that the ideal gas model overpredicts the thrust, while real gas models underpredict it.

**Low-Temperature Operational Conditions:** Low-temperature operation conditions are for a chamber pressure of 1 MPa and a propellant temperature of 243 K. For low-temperature conditions, initially, the propellant inside the tank is thermally conditioned to 262 K by using a thermal chamber in. Then, to obtain 243 K in the chamber, additional depressurization is performed by discharging the propellant through extra flexible hoses attached to the manifold.

First, the results obtained from the performance test is provided in Fig. 10. Steady-state chamber pressure of 1 MPa is achieved at the beginning of the continuous operation. However, due to the sensitivity of the pressure regulator to low temperatures, the pressure inside the chamber is decreased during the operation. Prior to the thruster valve actuation, it can be seen that the load cell measures 34 N corresponding to the dead weight, as explained before. Steady-state measurement of the load cell reports 10 N of thrust for the low-temperature case.

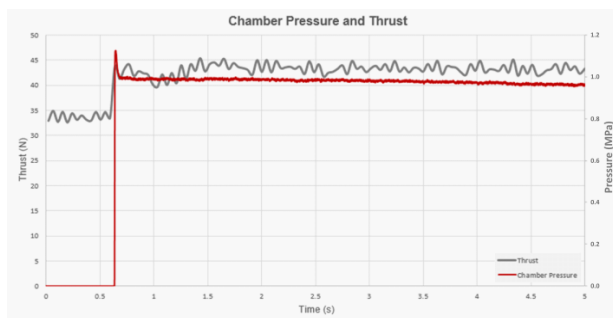


**Figure 9.** Low temperature operating conditions vacuum chamber test results for chamber pressure (red line) and thrust (gray line)

The same logic applies to the low-temperature numerical simulations as in nominal operating conditions. Chamber conditions of 1 MPa and 243 K are defined as the initial condition at the inlet, while vacuum chamber conditions of 200 Pa and 293 K are defined as for the nominal operating temperature case as the initial condition at the outlet section, respectively.

Simulations have been performed by using the same conditions as the nominal conditions. Euler equations with the Roe flux splitting scheme are used while additional Riemann boundary conditions are applied for the real gas models. CFL adaptation is also used in order to increase the convergence rate.

As seen from the results provided in Fig. 11, the real gas models predict closer values to the experiments when compared to the ideal gas model. When the temperature values are compared, it can be seen that the outlet temperatures obtained in this set of simulations are lower than the nominal temperatures. This is expected due to the lower temperature initialization at the inlet of the nozzle.

Thrust calculation is followed by temperature and pressure comparison. Results provided in Table 3 show that the ideal gas model predicts closer results to the experimental thrust value. However, considering that these simulations will be used in the preliminary design phase, prediction with an error of approximately 10% error can be considered as acceptable. Once again, the ideal gas model overpredicts the thrust, while real gas models underpredict it.

The reason for the thrust loss stems from the momentum thrust. Fig. 12 shows that the pressure change is not significant between the ideal gas and real gas models. Fig 13 shows the velocity variation through the nozzle. The momentum thrust reduces with the reduced exit velocity with real-gas models for the given inlet stagnation conditions and mass flow rate.

**Table 3.** Thrust comparison between gas models

Gas Model	Thrust [N]	% Error in Thrust	Solution Time [min]
Ideal Gas	10.44	+4.6	400
van-der Waals	9.01	-9.9	152
Peng-Robinson	9.01	-9.9	162

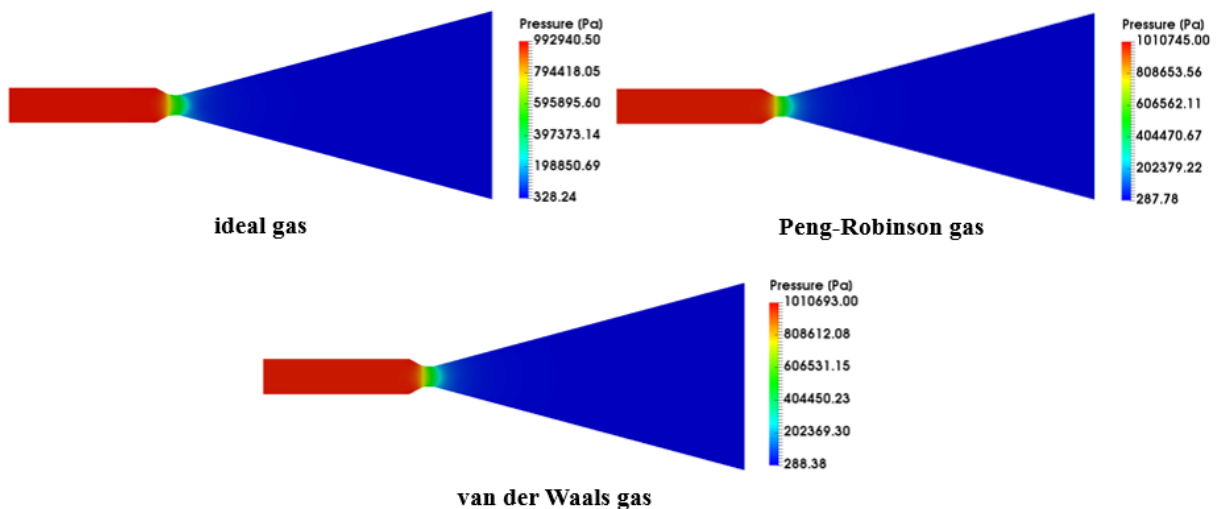


**Figure 10.** Low-temperature operation condition results for different gas models

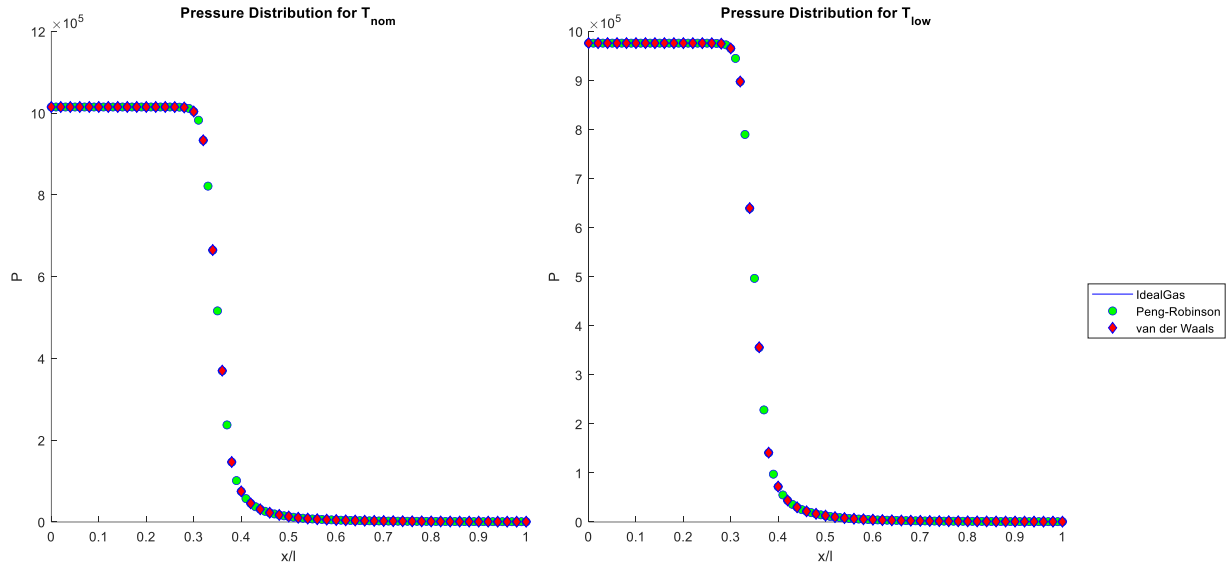


Figure 11. Center pressure solutions by different gas models

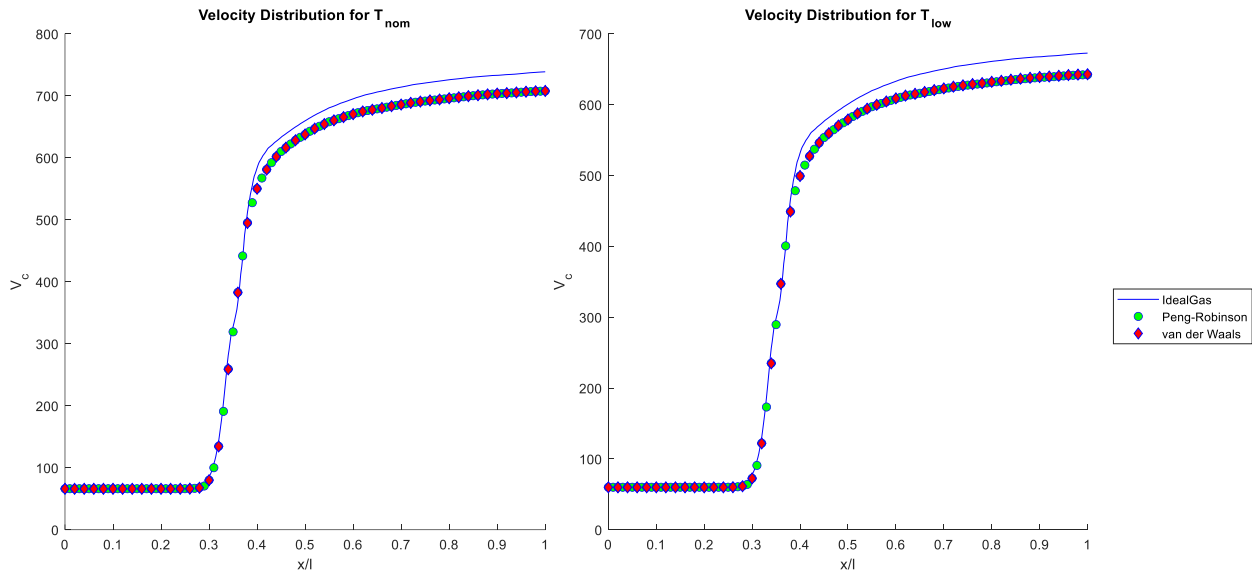


Figure 12. Center velocity solutions by different gas models

Last but not least, the computational time for each simulation is compared. Calculations are performed on a single core. The ideal gas simulation takes 400 minutes, while the Peng-Robinson gas model takes 162 minutes for convergence. For the van der Waals gas model, simulation time takes 152 minutes. It is seen that, for the van der Waals gas model, the percentage error observed in predicting the thrust is higher than the ideal gas model, yet the simulation time is much shorter. The main aim of the preliminary design phase is to obtain realistic performance predictions as fast as possible. Hence, the van der Waals gas model is preferred since it gives the performance predictions of the nozzle with an acceptable deficiency in the shortest time.

It is interesting to observe shorter solution times with real-gas models. The lower compressibility factor at lower temperatures makes the solution matrix less stiff. That allows larger pseudo-time steps and shorter convergence time. Also, during the expansion, the pressure and the

temperature drops, which results in less compressibility. This shows less expansion than a real gas. Less expansion simply results in less exit velocity, less exit pressure, and hence less thrust. Less expansion also means smaller flow gradients, hence improves the solution time.

## CONCLUDING REMARKS

Experimental and numerical performance predictions of a cold gas thruster have been performed. The vacuum chamber facility utilized in this study has been employed for the experiments, while the open-source platform SU2 has been used for the numerical simulations. The effects of the utilization of different gas models already available in SU2 are investigated, and its impact is evaluated considering the requirements for the preliminary design phase.

The comparison of experimental and numerical simulations shows that the van der Waals gas model is



accurate enough to predict the performance of a cold gas thruster for both nominal and low-temperature operational conditions. Even though the thrust calculated for low-temperature simulations is lower than the experimental values, it is concluded that the performance predictions of this model satisfy the requirements for the preliminary design phase. Moreover, it is crucial to calculate the results quickly in addition to have accurate predictions. The van der Waals gas model provides the solution 2.5-4 times faster compared to the ideal gas model depending on the initial temperature condition. Even though the simulation duration is almost the same for the Peng-Robinson and the van der Waals gas models, still the van der Waals model is faster. Hence, since it allows us to compare many design alternatives in a very short period of time, the van der Waals gas model is favorable for companies. Another point that should be considered while assessing the simulation results at the preliminary design phase is that the ideal gas model tends to overpredict the net thrust, while real gas models tend to underpredict.

As mentioned before, Euler equations are solved in the scope of this study. Therefore, the effect of viscosity is neglected. Furthermore, turbulence is not included in the simulations. This becomes apparent in the low thrust predictions with real-gas models. With the current implementation of  $SU^2$  we are not able to conduct unsteady, viscous real-gas simulations. For further studies, the effect of viscosity and turbulence can be investigated. Also, the real gas model implementations in  $SU^2$  can be modified to improve the thrust predictions.

## ACKNOWLEDGEMENTS

The experimental research in this project has been performed by the test facilities offered by ROKETSAN A.Ş. Authors like to show gratitude for the support.

## REFERENCES

- Aksel, M. H., 2011, Fluid Mechanics. Middle East Technical University.
- Anis, A., 2012, Cold Gas Propulsion System - An Ideal Choice for Remote Sensing Small Satellites. *Remote Sensing - Advanced Techniques and Platforms, IntechOpen*.
- Anis, A., 2008, Design & Development of Cold Gas Propulsion System for Pakistan Remote Sensing Satellite (PRSS). *2nd International Conference on Advances in Space Technologies*, pp. 49–53, IEEE.
- Bzibziak, R., 2000, Update of Cold Gas Propulsion at MOOG. *36th AIAA/ASME/SAE/ASEE Joint Propulsion Conference and Exhibit*.
- Dorado, V., Grunder, Z., Schaefer, B., Sung, M., & Pedersen, K., 2013, NASA Marshall Space Flight Center Tri-gas Thruster Performance Characterization. *AIAA/ASME/SAE/ASEE Joint Propulsion Conference*
- Greer, H., & Griep, D.J., 1967, Dynamic Performance of Low-Thrust, Cold-Gas Reaction Jets in a Vacuum. *Journal of Spacecraft and Rockets*, vol. 4, no. 8, pp. 983–990.
- Hinkley, D., 2008, A Novel Cold Gas Propulsion System for Nanosatellites and Picosatellites. *22nd AIAA/USU Conference on Small Satellites*, Logan, UT.
- Jerman, T., & Langus, J., 2011, Calculating Cold Gas Microthruster Velocity Flow Using Finite Volume Analysis. University of Ljubljana, Ljubljana.
- Kentish, S.E., Scholes, C.A., & Stevens, G.W., 2008, Carbon Dioxide Separation Through Polymeric Membrane Systems for Flue Gas Applications. *Recent Patents on Chemical Engineering*, vol. 1, no. 1, pp. 52–66.
- Lemmer, K., 2017, Propulsion for Cubesats. *Acta Astronautica*, vol. 134, pp. 231–245.
- Manzoni, G., & Brama, Y. L., 2015, Cubesat Micropropulsion Characterization in Low Earth Orbit. *29th Annual AIAA/USU Conference on Small Satellites*.
- Matticari, G., Noci, G., Siciliano, P., Miccolis, M. & Strada, S., 2010, Cold Gas Thruster Assembly for SGEO Platform: Review of Development Activities by Thales Alenia Space Italia. *Space Propulsion Conference*, San Sebastian, Spain.
- Lev, R., Herscovitz, J., & Zuckerman, Z., 2014, Cold Gas Propulsion System Conceptual Design for the SAMSON Nano-satellite. *50th AIAA/ASME/SAE/ASEE Joint Propulsion Conference*, p. 3759.
- Pini, M., Vitale, S., Colonna, P., Gori, G., Guardone, A., Economon, T., Alonso, J., & Palacios, F., 2017,  $SU^2$ : The Open-Source Software for Non-Ideal Compressible Flows. *Journal of Physics: Conference Series*, vol. 821, p. 012013, IOP Publishing.
- Ranjan, R., Chou, S., Riaz, F., & Karthikeyan, K., 2017, Cold Gas Micro Propulsion Development for Satellite Application. *Energy Procedia*, vol. 143, pp. 754–761.
- Rickmers, P., 2004, Performance Enhancement Through Flow Control in Cold Gas Thruster Nozzles. *55th International Astronautical Congress*.
- Risi, B. W., 2014, Propulsion System Development for the CanX-4 and CanX-5 Dual Nanosatellite Formation Flying Mission. University of Toronto.
- Sarda, K., Grant, C., Eagleson, S. Kekez, D., & Zee, R., 2008, Canadian Advanced Nanospace Experiment 2: n-orbit Experiences with a Three-kilogram Satellite. *22nd AIAA/USU Conference on Small Satellite*, Logan, UT.



## A NUMERICAL INVESTIGATION OF NANOFLUID FLOW IN RECTANGULAR FINNED MICROCHANNEL

Halime ÇELİK\* and Nezaket PARLAK\*\*

\*Sakarya Uygulamalı Bilimler Üniversitesi Teknoloji Fakültesi Makine Mühendisliği Bölümü,  
54050 Serdivan, Sakarya, halimeclik@sakarya.edu.tr, ORCID: 0000-0002-0279-046X

\*\*Sakarya Üniversitesi Mühendislik Fakültesi Makine Mühendisliği Bölümü,  
54050 Serdivan, Sakarya, naydemir@sakarya.edu.tr, ORCID: 0000-0002-8469-2192

(Geliş Tarihi: 15.06.2020, Kabul Tarihi: 29.01.2021)

**Abstract:** A numerical study and parameter optimization was carried out to find the effects of geometric parameters and nanofluid concentration on heat transfer and pressure drop characteristics of a finned microchannel. Six dual rectangular fins with different layouts were placed in a single microchannel having rectangular cross section. The hydraulic diameter of the microchannel was kept constant and the length, width and angle of fin between the horizontal axes were determined as parameters. The water was selected as base fluid and the effect of volumetric concentration of nanofluids ( $Al_2O_3$  (0% to 0.4%)) on fluid flow and heat transfer were investigated. Volumetric concentration of nanofluids and fin geometry was optimized with Response Surface Optimization method for the levels of different parameters and Computational Fluid Dynamics (CFD) analyses (ANSYS Fluent 18) was performed at different flow rates. CFD results calculated for the optimum finned microchannel were compared to those of the straight (finless) microchannel. As a result of the study, nanofluid concentration increment and fins improved the heat transfer and increased the pressure drop.

**Keywords:** Microchannel, Nanofluid, Fin, CFD Analysis, Optimization

## KANATÇIKLI DİKDÖRTGEN KESİTLİ MİKROKANALDA NANOAKIŞKAN AKIŞININ SAYISAL İNCELENMESİ

**Özet:** Kanatçıklı bir mikrokanalın ısı transferi ve basınç düşüşü özellikleri üzerindeki geometrik parametrelerin ve nanoakışkan konsantrasyonunun etkilerini bulmak için sayısal bir çalışma gerçekleştirilmiştir. Dikdörtgen kesite sahip tek bir mikrokanala farklı yerleşimlere sahip altı adet ikili dikdörtgen kanat yerleştirildi. Mikrokanalın hidrolik çapı sabit tutularak yatay eksenler arasındaki kanat uzunluğu, genişliği ve açısı parametre olarak belirlendi. Baz akışkan olarak su seçilmiş ve hacimsel nanoakışkan konsantrasyonunun ( $Al_2O_3$  (% 0 -% 0.4)) akış ve ısı transferi üzerindeki etkisi araştırılmıştır. Nanoakışkanların hacimsel konsantrasyonu ve kanatçık geometrisi, farklı parametrelerin seviyeleri için Yanıt Yüzey Optimizasyon (Response Surface Optimization) yöntemi ile optimize edilmiş ve farklı akış hızlarında Hesaplamalı Akışkanlar Dinamiği (CFD) analizleri (ANSYS Fluent 18) gerçekleştirilmiştir. Optimum kanatlı mikrokanal için hesaplanan CFD sonuçları, düz (kanatsız) mikrokanallinkilerle karşılaştırıldı. Çalışma sonucunda nanoakışkan konsantrasyon artışı ve kanatçıklar ısı transferini iyileştirmiş ve basınç düşüşünü artırmıştır.

**Anahtar kelimeler:** Mikrokanal, Nanoakışkan, kanatçık, CFD analizi, Optimizasyon

### NOMENCLATURE

$L$  Microchannel length (mm)  
 $W$  Microchannel Width (mm)  
 $H$  Microchannel Height (mm)  
 $A$  Surface area ( $m^2$ )  
 $c_p$  Specific heat capacity at constant pressure ( $Jkg^{-1} K^{-1}$ )  
 $D$  Hydraulic diameter (m)  
 $f$  Darcy friction factor  
 $h$  Heat transfer coefficient ( $W m^{-2} K^{-1}$ )  
 $k$  Thermal conductivity ( $W m^{-1} K^{-1}$ )  
 $L$  Microchannel length (m)  
 $\dot{m}$  Mass flow rate ( $kg s^{-1}$ )

$P$  Pressure (Pa)  
 $Nu$  Nusselt number  
 $Pr$  Prandtl number  
 $Re$  Reynolds number  
 $T$  Temperature (K)  
 $V$  Velocity ( $m s^{-1}$ )

### Greek symbols

$\phi$  Volume fraction (%)  
 $\mu$  Dynamic viscosity (Pa s)  
 $\rho$  Density ( $kg m^{-3}$ )  
 $\alpha$  Thermal diffusion ( $m^2 s^{-1}$ )

## Subscripts

*nf* nanofluids

*bf* basefluid

*p* particles

*f* fluid

## INTRODUCTION

Today, research on nanofluids to improve heat transfer is rapidly ongoing. Nanofluids are suspensions formed by adding nanometer-sized (<100 nm) solid particles of copper, aluminum, silver, gold, silicon dioxide to a base fluid such as water, ethylene and propylene glycol. The purpose of using nanofluids is to passively increase the heat transfer by obtaining fluids with better thermal properties than conventional fluids.

Another passive technique of heat transfer enhancement is to increase the heat transfer surface by means of fins, rods, protrusions. Expanded or extended surfaces are widely used in many areas such as spacecraft, airplanes, cooling, heating, air conditioning, chemical and petrochemical industries, electronics, and industrial furnaces, nuclear, solar and traditional power plants where heat transfer occurs. The enlarged surfaces can be cast in a variety of geometric shapes with the main surface in the form of fins and protrusions, or they may be attached to the main body separately by means of engagement, screwing, welding. In practice, it is seen that rectangular and circular (pipe) fins are mostly used (DeWitt and Incropera, 2002). The use of micro-scale systems in flow applications, creating a larger surface area in a small volume, and providing the opportunity to work in small areas have provided many advantages. These miniature devices with microchannels are known to be used in various fields such as environment, automotive, process control, metrology, defense, aviation, aerospace, pharmaceuticals, chemistry, medicine and biology. Triangular, square and circular fins are placed inside a duct to increase the heat transfer in a macro-scale duct. These fins both act as a vortex generator and increase the surface area, allowing the heat flux to dissipate faster. On the other hand, fins increase the drag coefficient in the channel and affect the pressure drop negatively.

In micro-scale channels, single-phase flow and heat transfer are of interest for cooling electronic and similar devices due to the small boundary layer thickness, but the high pressure drop constitutes an obstacle to its use as an efficient cooling method. For this reason, micro-scale studies have focused on finding the optimum geometry in a certain working pressure range. Within the scope of this study, the literature survey includes finned microchannels studies and studies in which nanofluids are used as fluids in microchannels. Considering the studies on finned microchannels, it is seen that there is a crucial lack of experimental data due to insufficient of precision manufacturing and measurement techniques. (Ma et al., 2010) have investigated the effect of fins (vortex generators) placed longitudinally in rectangular channels with hydraulic diameter of 5.58 mm on flow

and heat transfer. Water has been used as a working fluid. They have observed an increase of 11.4% in pressure drop and 101% in heat transfer under water laminar flow conditions ( $310 < Re < 4220$ ). (Liu et al., 2011) have experimentally studied the effect of fins placed in a rectangular channel with hydraulic diameter of 187.5 mm on the single phase water flow and heat transfer for the range of  $170 < Re < 1200$ . They have reported that heat transfer increased by 21% in the laminar flow conditions and 90% under turbulent flow conditions thanks to the fins placed in the channel. On the other hand, the pressure drop increased by 83% in laminar flow conditions and by 169% under turbulent flow conditions. The average uncertainties caused by experimental apparatuses in determining  $f$  and  $Nu$  for tests are found to be 5.86% and 19.6%, respectively. They also stated that the transition from laminar to turbulent flow occurs earlier in finned rectangular microchannels compared to the straight (finless) rectangular microchannel. (Chen et al., 2014) have conducted an experimental study using water as a fluid to investigate flow and heat transfer in finned rectangular microchannels. The experiments have been carried out under constant wall temperature boundary conditions for the Reynolds numbers ranging from 350 to 1500. The hydraulic diameters of the rectangular microchannels were reported to be 160  $\mu\text{m}$  and 188  $\mu\text{m}$  with an aspect ratio of 0.25 and 0.0667, respectively. The results have shown that the pressure losses increased by 40% and heat transfer performance increased by 12.3% in finned channels. The maximum uncertainties of friction factor and Nusselt number are 5.78 and 20.98% respectively. In addition, it has been reported that the critical Reynolds number decreases as the number of fins (vortex generators) placed inside the channel increases. Experiments have shown that the fins placed in the channel increase the heat transfer and pressure drop and decrease the critical Re number. (Ugurlubilek, 2014) has numerically investigated convective heat transfer and flow in a channel with two semi-circular obstacles under uniform wall temperature boundary conditions. The conservation equations have been solved by Ansys Fluent and Nusselt numbers and friction coefficients have been presented comparatively for the channel with and without obstacles. They have reported that an improvement of 47% in heat transfer. (Ebrahimi et al., 2015) have numerically investigated the single phase laminar flow and heat transfer in rectangular microchannels with vortex generators (fin). Numerical results have been compared with the available experimental data and comparison have showed to be in a good agreement. They have also stated that the Nusselt number increased by 25% in the Reynolds range of 100 to 1100, while the friction factor increased by about 30% in the finned channels. (Lelea, 2011) has investigated the effect of particle diameter on the flow and heat transfer of  $\text{Al}_2\text{O}_3$ /water nanofluid in a microchannel heat exchanger numerically. Nanofluids was encountered with  $\text{Al}_2\text{O}_3$  nanoparticles with diameters of 13, 28 and 47  $\mu\text{m}$  at different volumetric concentrations (from 1% to 9%). Results revealed that heat transfer augmentation decreases as the particle's diameter increases and for

higher pumping power and cooling case it remains constant as long as particle's diameter is  $dp > 28$  nm. In addition, as the volume concentration and Reynolds numbers are increased, heat transfer have increased. The improvement of heat transfer in a 3D microchannel cooler using nano fluids has been studied in a numerical study (Hung et al., 2012). Results have shown that the use of  $Al_2O_3$ /water nanofluids in the microchannel cooling system can improve heat transfer. The effectiveness of  $Al_2O_3$ /water nanofluids in improving the overall performance of the microchannel refrigerant has been numerically investigated using the SIMPLEC algorithm by (Wu et al., 2016). Results have shown that the effectiveness of nanofluid on improving the heat management capability of MCHS is related to the given pumping power of electronic device and a reduction of thermal resistance could be gained only when the given pumping power is high. (Ebrahimi et al., 2016) have performed three-dimensional simulations using a single-phase flow model. Their results show that nanofluids increase the pressure drop by 3.5 to 16% compared to pure water.

When studies on nanofluids are reviewed, it was seen that a lot of articles were published in the open literature. In general, experimental and numerical studies on nanofluids have showed that nanoparticle type (Lelea, 2011; Hung, et al., 2012; Karimzadehkhoei, 2017), nanoparticle size (Hu et al., 2011) and volumetric concentration (Lelea, 2011; Hung et al., 2012; Zarringhalam et al., 2016; Khaleduzzaman et al., 2017), mass flow rate (Lelea, 2011; Khaleduzzaman et al., 2017) have important effects on flow and heat transfer. (Sohel et al., 2014) have conducted an experimental study with  $Al_2O_3$ /water nanofluids in a minichannel heat sink for electronics cooling. In experiments,  $Al_2O_3$ /water nanofluids are made in four different concentration i.e. 0.10 Vol. %, 0.15 Vol. %, 0.20 Vol. % and 0.25 Vol. % and the Reynolds number ranged from 395 to 989. The mini channels in the cooler have a rectangular section with hydraulic diameter of 0.615 mm. Nusselts numbers were between 3.3 and 3.8. The results showed that the heat transfer coefficient increased by 18% and also 15.72% less thermal resistance at 0.25 vol.% compared to the distilled water. (Sivakumar et al., 2016) have conducted experimental studies with  $Al_2O_3$ /water nanofluids in a microchannel heat sink. Nu numbers for 0.3% volumetric concentration in experiments ranged from 0.57 to 3.01 for  $107 < Re < 622$ . (Ho et al., 2019) have conducted an experimental study on the convection heat transfer of  $Al_2O_3$ /water nanofluids with 2–8 wt% concentrations in a parallel minichannel heat sink. Findings showed that the maximum pressure drop ratio (nanofluid to pure water) of 1.41 is observed by flowing nanofluid with 8% nanoparticle concentration for  $Re = 258$  and the maximum heat transfer effectiveness is achieved 1.4 for  $Re = 1549$ . Two general numerical methods are used to simulate single-phase nanofluid flow and heat transfer in macro / micro channels: single-phase methods and two-phase methods. The former includes both homogeneous and dispersion models, while the second includes Eulerian-Eulerian (fluid volume, mixing

and Eulerian) and Eulerian-Lagrangian models and Discrete Phase Model (Liang and Mudawar, 2019).

In recent years, it has been observed that numerical studies are conducted using a single phase nanofluids models or a two phase models. (Arshi Banu et al., 2020) performed a numerical study on the hydrodynamic and thermal behavior of the micro-pin-fin heat exchanger using a single phase model to investigate the pressure drop variations and heat transfer rate using  $Al_2O_3$ /water and CuO-water nanofluids for different volume fraction. On the other hand, a numerical investigation is conducted by implementing a two-phase model based on the mixture theory with the aim of assessing the attributes associated with the thermohydraulic performance of the Cu/water nanofluid through a square channel (Bahraei et al., 2019). Moreover, using single and two phase models thermal and hydraulic performances of minichannel heat sink were studied by (Saeed and Kim, 2018), numerically. Comparison of single-phase model with the experimental results revealed that single phase model under-predicted the values of convective heat transfer coefficient. Maximum disagreement between single phase numerical model and experimental results was found to be 5.02% against volume concentration of 1.0%. On the other hand, two-phase model over-predicted the convective heat transfer coefficient values. Maximum disagreement found between numerical two-phase and experimental values are 5.01% respectively. (Ghasemi et al., 2017) have simulated laminar forced convection heat transfer in the rectangular and circular minichannel heat sinks with nanofluid for various volume fraction of CuO nanoparticles. Single phase and Two-phase methods were utilized for solving the incompressible, three dimensional and steady state problem with particle volume fraction range between 0.25% and 0.75%. Even if they stated that the double phase model results were more accurate than the single phase model results; maximum and minimum disagreement between experimental and single-phase numerical results for 1 % volume concentration was reported to be 1.3% and 3.5%, respectively. On the other hand, it has been reported that the maximum and minimum difference between the experimental and the numerical two-phase model results are 0.2% and 1.9%, respectively. The maximum deviation between the findings obtained in both studies (Saeed and Kim, 2018; Ghasemi et al., 2017) is around 5%. Moreover, (Turkyilmazoglu, 2019) concluded that two phase model is in compliant with the single phase in the special case of his problem.

Considering the methods of improving heat transfer, studies on nanofluids are noteworthy. It achieves a fluid with better thermal properties than conventional fluids and increases the heat transfer passively. Another passive heat transfer enhancement method is to increase the heat transfer surface by means of fins, rods, protrusions. When the literature is reviewed, single-phase laminar flow and heat transfer in rectangular microchannels have been investigated by (Ugurlubilek, 2014) and (Ebrahimi et al., 2015), (Lelea, 2011) and (Hung et al., 2012) have

examined the effect of  $\text{Al}_2\text{O}_3/\text{water}$  nanofluids on heat transfer in finned microchannels, numerically. As can be seen from the literature, parametric optimization studies have not been conducted, yet. In the literature, there are studies showing that the fins placed in the channel increase the heat transfer and increase the pressure drop. In addition, there is a need for geometric studies that provide optimum pressure drop and heat transfer. For this reason, it is very important to make a single phase flow and heat transfer characteristic by performing a geometric optimization study on micro scale. The current study has two main objectives. The first is to find the best/optimum finned microchannel geometry, which gives the highest heat transfer and the lowest pressure drop. The second is to perform CFD simulations of  $\text{Al}_2\text{O}_3/\text{water}$  nanofluids in the optimum finned microchannel for velocities in the range of 1 to 7 m/s. Thus, 6 pairs of rectangular fins were placed in a single microchannel of rectangular cross-section. By keeping the hydraulic diameter of the microchannel constant, the length, width, angle of the fins and volumetric concentration of nanofluids were determined as parameters. Using water as the base fluid, the flow and heat transfer properties of the volumetric concentration of  $\text{Al}_2\text{O}_3/\text{water}$  nanofluids (volume fractions between 0 and 0.4%) were investigated. Geometric parameters were optimized by Response Surface Optimization method and volumetric concentrations were determined with optimum geometry and analyzed at different flow rates. Computational Fluid Dynamics (CFD) analysis was performed with Ansys Fluent 18 commercial software. In a finned microchannel, the nanofluid flow was investigated by CFD analysis, which are under constant temperature thermal conditions.

## PARAMETRIC DESIGN AND OPTIMIZATION

ANSYS enables extensive design exploration and optimization in Workbench environment. Default (2nd order polynomial) Response Surface Optimization method has been selected for the optimization. Response surface methodology (RSM) focuses on input-output relationships and it an efficient way to get the variation of a given performance with respect to input parameters. Optimization studies are carried out by following the steps, shown in Fig. 1. First, the parameters affecting the nanofluids flow and heat transfer in the finned microchannel have been identified. Then, boundary conditions are set and CFD simulations are performed. The parameters that affect the optimization problem and their levels are defined and CFD-based optimization calculations are made.

### Microchannel Geometry and Parameters

An optimization study has been performed in order to find the finned microchannel geometry which gives the highest heat transfer rate and the lowest pressure drop. The height of the rectangular microchannel has been indicated by H, the width by W, and the length of the microchannel by L. The geometry details of the microchannel have been given in Table 1.

In the microchannel, width, length and the angle of the fins have been taken as parameters. In Fig. 2, the designed fins geometry. The parameters and their constraints (upper and lower bound) and the targets in the optimization are given in Table 2.

The fins which are in the shape of a rectangular prism and whose geometric parameters have been identical to each other have been positioned adjacent to the lower wall, mutually along the channel. There have been totally 12 fins in the microchannel. Here the optimization parameters of the angle [P2], width [P3] and length [P4] of the fins have been shown in Fig. 2b.

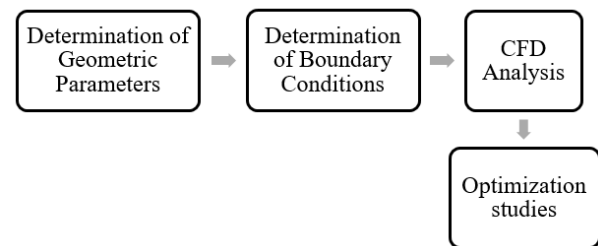


Figure 1. CFD optimization study scheme

Table 1. Microchannel Geometry

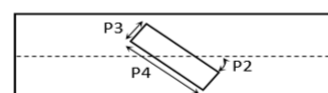
Microchannel Geometry	[mm]
Microchannel Width, W	0.35
Microchannel Height, H	0.1
Microchannel Length, L	10

Table 2. Parameters and constraints

Target	Constraints		
	Parameters	Lower bound	Upper bound
To maximize the heat transfer rate	P2 - Fin Angle (°)	30	60
To minimize the pressure drop	P3 - Fin Thickness [mm]	0.03	0.05
	P4 - Fin Length [mm]	0.05	0.15
	Volume flow rate [%]	0	0.4



(a)



(b)

Figure 2. a) Top view of finned microchannel b) Fin parameters

Values of geometric constraint parameters and nanofluids volume flow rates (lower and upper band) have been defined in the Fluent Parameter set section

given in the Table 2. Water has been taken as the base fluid and alumina have been preferred as nano particles. It is assumed that the  $Al_2O_3$  nanoparticles have a near-spherical shape, 99.8% purity, specific surface area between 85 and 115 ( $m^2/g$ ) and particle sizes of 13 nanometers. The properties of water and nanoparticles have been given in Table 3. The correlations for calculating the thermophysical properties of the nanofluid are given in the Table 4. The equations given in Table 4 are defined in the parameter set section, in order to calculate the thermophysical properties according to the volumetric flow rates.

**Table 3.** Properties of water ( $H_2O$ ) and nanoparticles

Fluid and/or nanoparticles	$\rho$ ( $kg/m^3$ )	$c_p$ ( $J/kgK$ )	$k$ ( $W/mK$ )	$\mu$ ( $Pa.s$ )
$H_2O$	998.2	4175.78	0.601	$8.8325 \times 10^{-4}$
$Al_2O_3$	3890	778	46	–

The highest heat transfer and lowest pressure drop have been determined as target in optimization process. When the optimization process is completed, the candidate values of parameters are suggested by DesignXplorer. The candidate values are presented with stars, crosses and dashes where three stars mean that the parameter meets all the specified objectives. In this study, candidate points with 3 stars achieving both targets have been considered as optimum values. Afterwards, CFD simulations have been performed at different flow rates using the optimum model. In the analysis, the flow was assumed to be single phase, laminar, incompressible and fluid was Newtonian. The fluid velocity was varied from 1 to 7 m / s.

## COMPUTATIONAL FLUID DYNAMICS (CFD) ANALYSIS

### CFD Analysis For Optimum Finned Microchannel With $Al_2O_3$ /Water Nanofluids

In this analysis,  $Al_2O_3$ /water was used as the fluid and only the bottom surface of the microchannel was assumed to be constant temperature at 358. The nanofluid entered the microchannel with temperature and velocity

of 298 K and 1 m/s. The outlet pressure was taken as 0 Pa and the inlet pressure was assumed as the pressure drop. The three dimensional modeling was created in the ANSYS Workbench interface; boundary conditions, conservation equations were solved in Fluent interface. A structured non-uniform mesh spacing distribution was used to solve the computational domain. Triangular elements were chosen forming mesh. Structured grid of finned microchannel was shown in Fig.3.

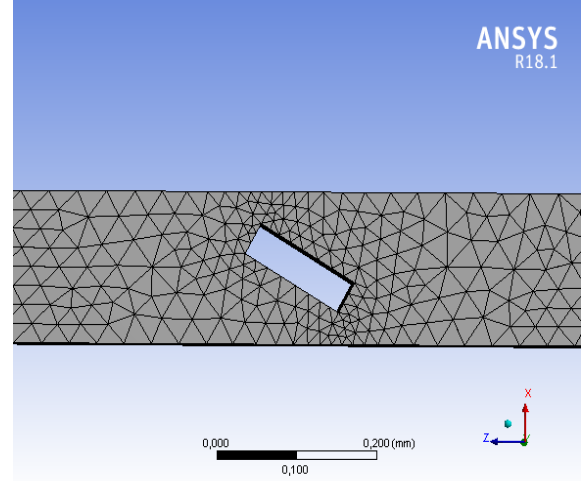


**Figure 3.** Grid structure of finned microchannel model

### Grid independence analysis

In the analysis, several different grid densities have been tested to provide that numerical results are grid independent. Table 5 shows numerical results obtained from grid independence analysis. Percentage deviation has been calculated by  $\left(\frac{f_2 - f_1}{f_1} \times 100\right)$ . The number of elements ranged from  $1.7E+6$  to  $3.4E+6$  and the percentage deviations between the results remained below 5%. The deviations for outlet temperature and pressure drop obtained in the analysis after 2 million elements were below 1%. 3.1 million elements were found acceptable with a deviation of 0.8%. In addition, the solution was considered to converge and the relative residuals of continuity, momentum and energy equations were less than 0.0001.

**Table 4.** The correlations of thermophysical properties of  $Al_2O_3$ /water nanofluids

Thermophysical properties	Correlations	Models [References]
$\rho$ ( $kg/m^3$ )	$\rho_{nf} = \rho_{np}\varphi + \rho_{bf}(1 - \varphi)$	(Cho and Pak, 1998)
$c_p$ ( $J/kgK$ )	$\rho_{nf}c_{nf} = \rho_{np}c_{np}\varphi + \rho_{bf}c_{bf}(1 - \varphi)$	(Roetzel and Xuan, 2000)
$k$ ( $W/mK$ )	$\frac{k_{eff}}{k_f} = \frac{k_p + 2k_f - 2\varphi(k_f - k_p)(1 + \eta)^3}{k_p + 2k_f - \varphi(k_f - k_p)(1 + \eta)^3}$	(Choi and Yu, 2003)
$\mu$ ( $Pa.s$ )	$\frac{\mu_{nf}}{\mu_{bf}} = (1 - \varphi)^{-2.5}$	(Brinkman, 1952)

**Table 5.** Grid independence test results

Cases	Grid numbers	Pressure drop [kPa]	Percentage Deviations [%]	Outlet temperature [K]	Percentage Deviations[%]
Case 1	$1.7E+6$	35242.63	-	329.36	-
Case 2	$2.2E+6$	33781.76	4.14	326.72	0.8
Case 3	$3.1E+6$	33509.82	0.80	326.68	0.01

## OPTIMIZATION RESULTS

### Optimization Results For Finned Microchannel Al<sub>2</sub>O<sub>3</sub>/Water

The optimum geometric parameters that provide the lowest pressure drop and the highest heat transfer were determined by CFD based parametric optimization. The optimum parameters obtained were given in Table 6.

**Table 6.** Finned Microchannel (FMC) Al<sub>2</sub>O<sub>3</sub>/Water Optimization Studies

P2 - Fin angle [°]	34.058
P3 - Fin thickness [μm]	36.5
P4 - Fin Length [μm]	50.6
Volumetric concentration [%]	0.392
Outlet temperature [K]	349.05
Pressure drop [kPa]	95.93
Heat transfer [W]	3.2592

The effects of parameters on the output temperature and pressure drop results were examined in detail. In order to show the effects of geometric parameters, additional simulations were performed three different levels of each geometric parameter by keeping the volumetric concentration constant. Effect of fin angle on results was shown in Fig. 4. The fin angle was changed from 30 to 60°. As a result of the optimization, the optimum fin angle was 34°. The increase of the fin angle increased the inlet pressure and outlet temperature and it led to a 60% increase in pressure drop, as shown in Fig 2. Since an increase in angle of fin will decrease the cross section through which the fluid passes, it affects the pressure drop significantly. On the other hand, it did not significantly affect the outlet temperature.

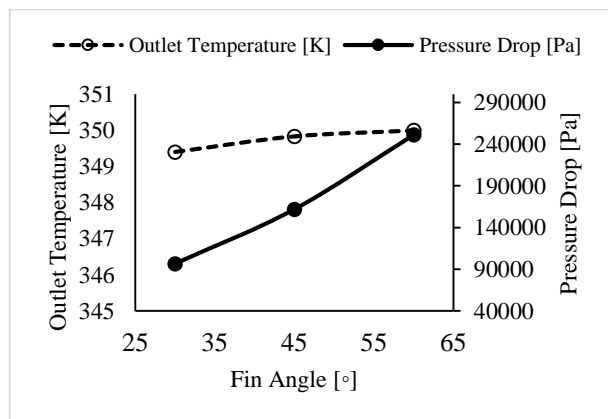


**Figure 4.** Effect of fin angle on results

In the calculations, the fin thickness was changed from 0.03 to 0.05 mm, shown in Fig. 5. The optimal fin thickness was calculated as 0.03649 mm. The increase of the fin thickness caused a change in the outlet temperature of less than 1%. The thickness of the fin was increased from 0.3 value to 0.05 while the inlet pressure increased. Similarly, the change in pressure drop remained below 1%.

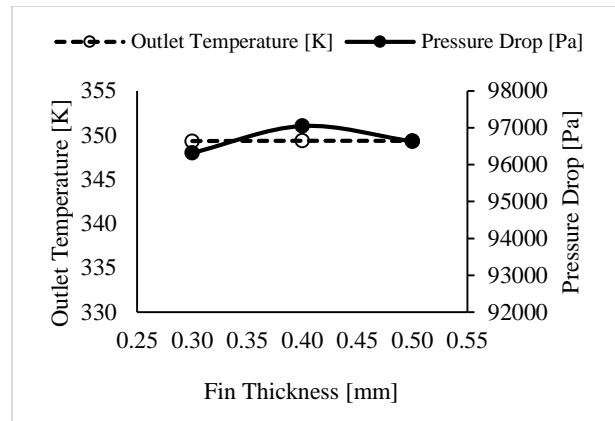


**Figure 5.** Effect of fin thickness on results

Effect of fin length on results was shown in Fig. 6. The fin length was changed to 0.05, 0.1 and 0.15 mm. Increased fin length increased inlet pressure and outlet temperature by 1%. The fin length was found to have no effect on the results for these 0.05 mm to 0.15 mm values.

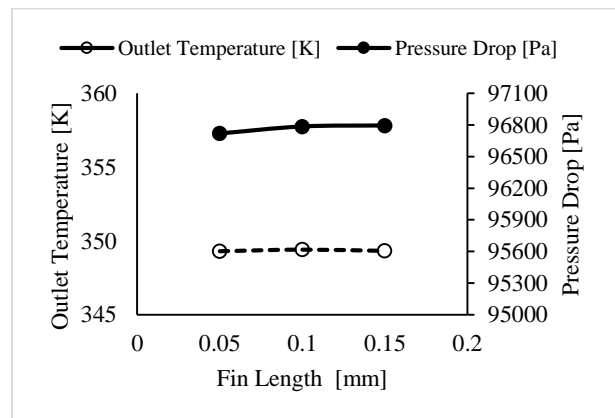


**Figure 6.** Effect of fin length on results

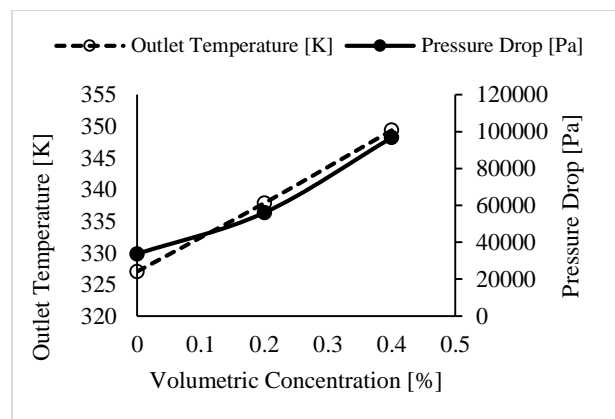


**Figure 7.** Effect of volumetric concentration on results

The volumetric concentrations of Al<sub>2</sub>O<sub>3</sub>/water nanofluids were varied from 0% to 0.4%. as shown in Fig. 7. Optimal volumetric concentration value was found to be 0.39. As expected, the increase in volumetric concentration led to an increase in pressure drop and outlet temperature. With increasing volumetric concentration, the outlet temperature increased from 327 K to 349 K. However, the increase in volumetric concentration also caused the pressure drop to increase

significantly. Similarly, there were studies showing that nanofluids provided better heat transfer from water with increasing volumetric concentration, however, an increase in pressure drop (Lelea, 2011; Ebrahimi et al., 2016).

## CFD RESULTS

### CFD Results of Optimum Channel

CFD simulations of the nanofluids flow of the optimum finned microchannel have been performed in the range of 1 to 7 m/s. Figs. 8 and 9. show velocity vectors and temperature changes around the fin in the microchannel. The flow characteristics of the nanofluid in the finned microchannel is shown in Fig. 8. In the laminar flow, fluid layers move in straight lines, and the flow continues without eddies and swirls. Then flow changes direction when it encounters fins. The fins appear to cause turbulence under laminar flow conditions, resulting in flow rates ranging from 1 to 3.73 m/s. Since fins narrow the flow cross-section, it has been found the maximum flow velocity increases up to 3.73 m/s.

At higher Reynolds numbers, when an obstacle is placed in front of the flow, the fluid mixes more vigorously, covering longer distances. In this study, it was observed that the fins placed in the microchannel narrowed the cross-sectional area and caused instantaneous velocity increases. It was found that behind the fins, the curl of the velocity fields were formed. No vortex formation in front of fins was observed. The low flow rate also has an effect here. Sequentially placed fins allow the liquid to mix in the microchannel while at the same time causing heat transfer from the hot bottom wall. In this way, the liquid contacts the fin, which is warmer than the liquid.

The bottom wall is cooled more effectively by the nanofluids flow. Fig. 9 shows the temperature distribution around the fin located close to the outlet. The fins also cause an increase in heat transfer surface area and thus an increase in convective heat transfer. In the analysis, the bottom wall was set at a constant temperature, 358 K.

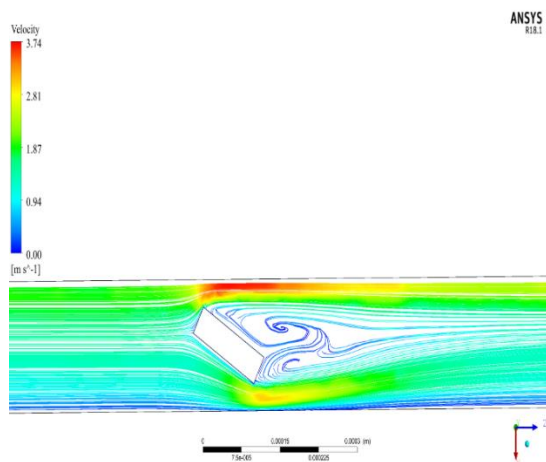


**Figure 8.** Finned Microchannel (FMC)  $\text{Al}_2\text{O}_3/\text{Water}$  CFD Analysis; Velocity zones

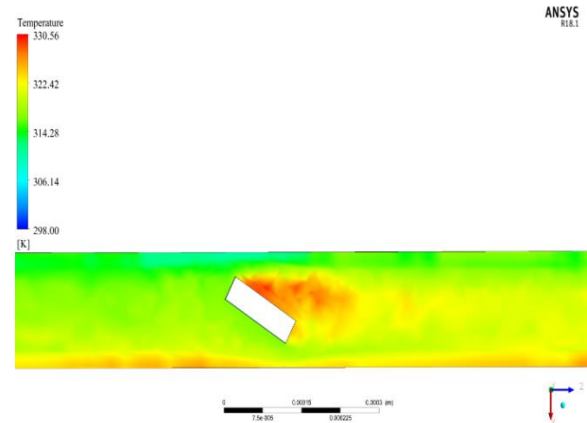


**Figure 9.** Finned Microchannel (FMC)  $\text{Al}_2\text{O}_3/\text{Water}$  CFD Analysis; Temperature zones around the fins

CFD simulations were repeated for different volumetric concentrations of nanofluids at a fluid velocity of 4 m/s in the optimum finned channel. Figure 10 shows the effect of volumetric concentration of nanofluids on heat transfer coefficient and thermal conductivity in the optimum finned channel. It has been observed that as the volumetric concentration increases, the heat transfer coefficient and heat transfer coefficient increase. When the volumetric concentration increased to 0.4, it was observed that the heat transfer coefficient increased by 48% compared to base fluid water. As mentioned before, the optimum volumetric concentration was found to be 0.392%. The following results are given for optimum volumetric concentration.

In order to show the effects of fin on heat transfer and pressure drop separately; the CFD analysis were also carried out at flow velocities of 1 m/s to 7 m/s for a straight (finless) microchannel (Straight MC) having same hydraulic diameter and length. CFD analysis for Straight MC with nanofluid were performed with grid density and convergence criterion similar to the main model.

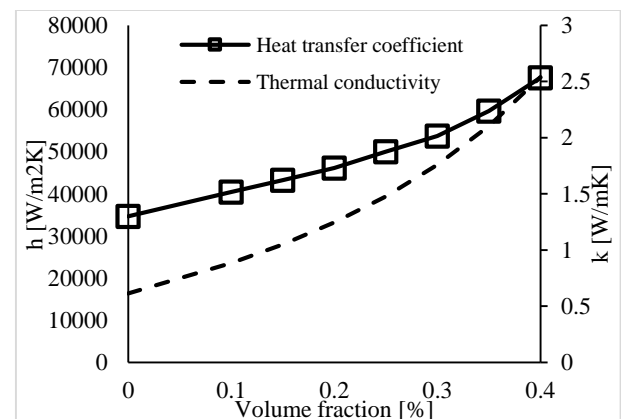


**Figure 10.** Effect of volume fraction of nanofluids on heat transfer coefficient

The results from the two analysis (for Finned MC and Straight MC) are presented comparatively. Heat transfer coefficients and pressure drop values calculated by CFD analysis are shown in Figs. 11 and 12. As expected, the



heat transfer coefficients of the Finned MC with nanofluid have been found higher than obtained for Straight MC. Although the analysis have been made under the same boundary conditions, the heat transfer in Finned MC has been better. Because there have been a total of 12 fins in the Finned MC. These fins not only mix the nanofluids flow, but also increase the surface area. Thus, fins have caused to better convective heat transfer. Pressure drop values obtained by analysis in the range of  $87 < Re < 998$  have been given in Fig. 12. Pressure drop data for Finned MC have exceeded  $\Delta P > 50000$  Pa after  $Re > 87$  and reached  $2E+6$  Pa. It is not possible to industrialize microchannel heat sinks with these pressure drops. Looking at the pressure drop graph, it has been concluded that a Finned MC can be used as a heat sink, only at low flow velocity ( $V < 1$  m/s).

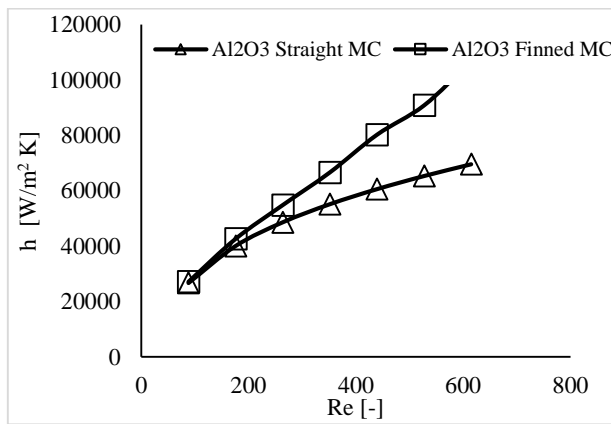


**Figure 11.** Effect of Reynolds number on heat transfer coefficient

Nusselt and friction factor results of nanofluids flow in Finned and Straight MC can be seen in Fig. 13. The Nusselts and friction factor values increased with the increase in Reynolds number for Finned and Straight MC. As seen in the graphic, Nusselts numbers in the case of Finned MC have been found higher than Straight MC. However, this increase was higher in high Reynolds numbers.

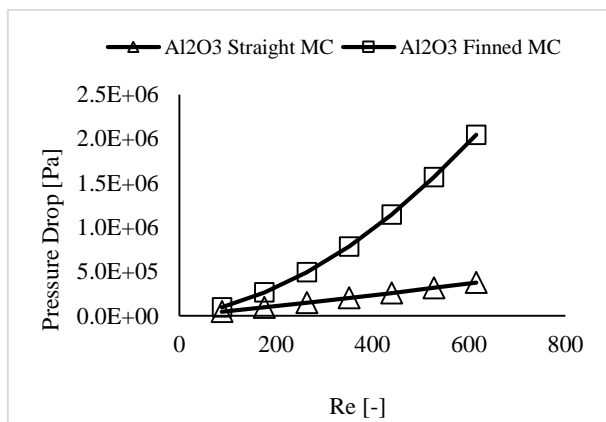


**Figure 12.** Effect of Reynolds number on pressure drop

The Reynolds number was 615, while the Nusselt number increased by about 40%. In addition, friction coefficient values  $[f]$  were lower in Straight MC, whereas Finned MC was five times higher.

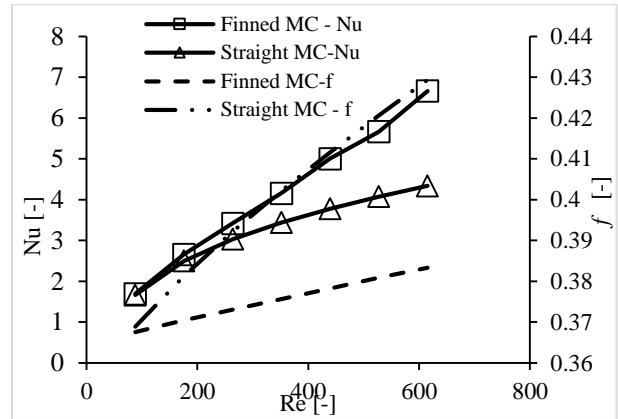


**Figure 13.** Comparison between the results of straight and finned microchannel

The CFD results also has been compared with existing correlations. Hausen equation (Eq.1) is used for inner fluid flow, at constant surface temperature, hydrodynamically developed and thermally developing flow. Hausen equation is defined as follows (Kaya et al., 2019);

$$Nu = 3,66 + \frac{0,0668 Re Pr \frac{D}{L}}{1 + 0,04 \left( (Re Pr \frac{D}{L})^{\frac{2}{3}} \right)} \quad (1)$$

Experimental and numerical studies on different types of nanofluids by (Ambren and Kim, 2018) were reviewed and  $Nu$  and  $f$  correlations published by various researchers in recent years are presented.  $Nu$  correlation of  $Al_2O_3$ /water nanofluids at constant wall temperature is presented below (Ambren and Kim, 2018; Maiga et al., 2005).

$$Nu_{nf} = 0.28 Re^{0.35} Pr^{0.36} \quad (2)$$

In the numerical study of (Kaya et al., 2019), the results of the nanofluids flow in the circular microchannel for different nanoparticle volume concentrations were compared with the results obtained from the Hausen equation. Investigation was done under constant laminar flow condition and with different Reynolds numbers ( $100 < Re < 1000$ ) at different nanoparticle volumetric concentrations. Their results showed that the numerical results were compatible with the data obtained from Hausen equation.  $Pr$  number in the equation (1) was determined by  $Pr = v_{nf} / \alpha_{nf}$  for optimal volumetric concentration. Other properties of nanofluids were calculated by correlations given in the Table 4. Calculated Nusselt numbers by Hausen eq. (1) changed from 3.66 to 3.68 and remained almost constant.  $Nu$  numbers calculated by Eq. 2 were found between 2.26 and 3.5 and these values were lower than the CFD results.

Nusselt numbers obtained via CFD changed from 1.66 to 6.66 with increasing Reynolds number. As can be seen in Fig. 14, Nusselt numbers were higher than the data obtained from Hausen equation for  $Re > 263$ . Nusselt numbers were found to be lower than those obtained from the Hausen equation for smaller  $Re$  numbers.

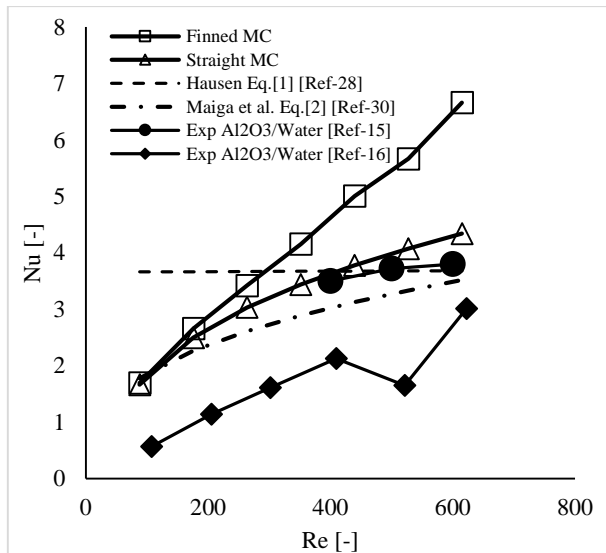


**Figure 14.** Comparison of Nusselt number between correlations and experimental data for Al<sub>2</sub>O<sub>3</sub>/water nanofluids.

The closest experimental data to our study in terms of hydraulic diameter and nanofluids type were reported by (Sivakumar et al., 2016) and (Sohel et al., 2014). Experimental results were found to increase with increasing Re numbers. The Nu numbers reported by (Sivakumar et al., 2016) were found to be lower than the CFD results. On the other hand, experimental data reported by (Sohel et al., 2014) were close to straight microchannel results. Consequently, the experimental data confirm the CFD results.

## CONCLUSION

In this study, 6 pairs of rectangular fins were placed in a single microchannel of rectangular cross-section. Geometry of finned microchannel and the volumetric concentration of nanofluid were optimized with Response Surface Optimization method for the levels of different parameters and CFD simulations for optimal finned microchannel were performed at different flow rates. The results were summarized as follows;

- As a result of the optimization, the optimum fin angle, thickness and length were found as 34°, 36.5  $\mu\text{m}$  and 50.6  $\mu\text{m}$ , respectively. Additionally, optimal volumetric concentration of Al<sub>2</sub>O<sub>3</sub>/water nanofluids was found to be 0.39 %.
- The fins caused an increase in the surface area in the microchannel and thus an increase was observed in heat transfer. At the same Reynolds number, pressure drop and heat transfer coefficients in finned microchannel were found higher than in straight microchannel.
- The results also confirmed that the heat transfer coefficient, thermal conductivity, pressure drop increased with an increase in the volume concentration of nanoparticles. It was observed that the pressure drop and heat transfer increased when the inlet flow velocity of nanofluids increased.

- The Nusselt numbers obtained from CFD changed from 1.66 to 6.66 for the range of Reynolds number, 87 < Re < 615. The Nusselt numbers for optimal finned microchannel have been found higher than data from traditional correlation and available experimental results.
- In further studies, it is recommended to investigate the effects of the height and distance of the fins on flow and heat transfer, both experimentally and numerically.

## REFERENCES

- DeWitt, D. P., and Incropera, F. P., 2002, *Fundamentals of Heat and Mass Transfer*, 5th Edition, John Wiley & Sons, Inc., New York.
- Huang, Y.P., Huang, J., Ma, J., Wang, Y.L., and Wang, Q.W., 2010, Experimental investigations on single-phase heat transfer enhancement with longitudinal vortices in narrow rectangular channel, *Nuclear Engineering and Design*, 240.
- Chao Liu, J.T., Chu, Y.L., Chiu, S., Dang, R., Greif, R., Huang, S., Jin, T., Pan, H.H., and Teng, J.C., 2011, Experimental investigations on liquid flow and heat transfer in rectangular microchannel with longitudinal vortex generators, *International Journal of Heat and Mass Transfer*, 54.
- Chen, C., Cheng, C.H., Greif, R., Huang, S., Jin, S., Lee, M.T., Liu, C., Pan, H.H., and Teng, J.T., 2014, A study on fluid flow and heat transfer in rectangular microchannels with various longitudinal vortex generators, *International Journal of Heat and Mass Transfer*, 69.
- Ugurlubilek, N., 2014, Numerical investigation of convective heat transfer and fluid flow in a channel with two semi-circular shaped obstacles, *Sileyman Demirel University, Journal of Engineering Sciences and Design* 2, 85-89.
- Ebrahimi, A., Kheradmand, S. E., and Roohi, 2015, Numerical study of liquid flow and heat transfer in rectangular microchannel with longitudinal vortex generators, *Applied Thermal Engineering*, 78.
- Lelea, D., 2011, The performance evaluation of Al<sub>2</sub>O<sub>3</sub>/water nanofluid flow and heat transfer in microchannel heat sink, *International Journal of Heat and Mass Transfer*, 54, 3891-3899.
- Chang, C.Y., Hung, T.C., Yan, W.M., and Wang, X.D., 2012, Heat transfer enhancement in microchannel heat sinks using nanofluids, *International Journal of Heat and Mass Transfer*, 55, 2559-2570.
- Lei, J., Liu, Bo., Zhao, J., and Wu, J., 2016, Effectiveness of nanofluid on improving the performance of microchannel heat sink, *Applied Thermal Engineering*, 101, 402-412.

- Ebrahimi, A., Rikhtegar, F., Roohi, E., and Sabaghan, A., 2016, Heat transfer and entropy generation in a microchannel with longitudinal vortex generators using nanofluids, *Energy*, 101, 190-201.
- Karimzadehkhoei, M., Kosar, A., Menguc, M. P., Sendur, K., and Shojaeian, M., 2017, The effect of nanoparticle type and nanoparticle mass fraction on heat transfer enhancement in pool boiling, *International Journal of Heat and Mass Transfer*, 109, 157–166.
- Ding, G., Hu, H., Jiang, W., and Peng, H., 2011, Effect of nanoparticle size on nucleate pool boiling heat transfer of refrigerant/oil mixture with nanoparticles, *International Journal of Heat and Mass Transfer*, 54, 9–10, 1839-1850.
- Karimipour, A., Toghraie, D., and Zarringhalam, M., 2016, Experimental study of the effect of solid volume fraction and Reynolds number on heat transfer coefficient and pressure drop of CuO/Water nanofluid, *Experimental Thermal and Fluid Science*, 76, 342–351.
- Khaleduzzaman, S.S., Mahbulul, I.M., Niza, M.E., Saidur, R., Selvaraj, J., Sohel, M.R., and Ward, T.A., 2017, Experimental analysis of energy and friction factor for titanium dioxide nanofluid in a water block heat sink, *International Journal of Heat and Mass Transfer*, 115, 77–85.
- Hepbasli, A., Khaleduzzaman, S.S., Mahbulul, I.M., Sabri, M. F. M., Saidur, R., and Sohel, M.R., 2014, An experimental investigation of heat transfer enhancement of a minichannel heat sink using Al<sub>2</sub>O<sub>3</sub>/H<sub>2</sub>O nanofluid, *International Journal of Heat and Mass Transfer*, 74, 164–172.
- Alagumurthi, N., Senthilvelan, T., and Sivakumar, A., 2016, Experimental investigation of forced convective heat transfer performance in nanofluids of Al<sub>2</sub>O<sub>3</sub>/water and CuO/water in a serpentine shaped micro channel heat sink, *Heat Mass Transfer*, 52, 1265–1274.
- Amanid, M., Ho, C.J., Liaoa, J.C., Lib, C.H., and Yan, W.M., 2019, Experimental study of cooling characteristics of water-based alumina nanofluid in a minichannel heat sink, *Case Studies in Thermal Engineering*, 14, 100418.
- Liang, G., and Mudawar, I., 2019, Review of single-phase and two-phase nanofluid heat transfer in macro-channels and micro-channels, *International Journal of Heat and Mass Transfer*, 136, 324–354.
- Arshi Banu, P.S., Krishnan, A., Sagaya Raj, A.G., and Shafee, S.M., 2020, Numerical investigation of micro-pin-fin heat exchanger using nanofluids, *Materials Today: Proceedings*, 22, 1020–1025.
- Bahiraie, M., Hosseini, Y., Mazaheri, N., and Moayedi, H., 2019, A two-phase simulation for analyzing thermohydraulic performance of Cu/water nanofluid within a square channel enhanced with 90° V-shaped ribs, *International Journal of Heat and Mass Transfer*, 145, 118612.
- Kim, M.H., and Saeed, M., 2018, Heat transfer enhancement using nanofluids (Al<sub>2</sub>O<sub>3</sub>/H<sub>2</sub>O) in mini-channel heatsinks, *International Journal of Heat and Mass Transfer*, 120, 671–682.
- Ghasemi, S. E., Hosseini, M.J., and Ranjbar, A.A., 2017, Forced convective heat transfer of nanofluid as a coolant flowing through a heat sink: Experimental and numerical study, *Journal of Molecular Liquids*, 248, 264–270.
- Turkyilmazoglu, M., 2019, Fully developed slip flow in a concentric annuli via single and dual phase nanofluids models, *Computer Methods and Programs in Biomedicine*, 179, 104997.
- Cho, Y. I., and Pak, B.C., 1998, Hydrodynamic and heat transfer study of dispersed fluids with submicron metallic oxide particles, *Experimental Heat Transfer An International Journal*, 11:2, 151-170.
- Roetzel, W., and Xuan, Y., 2000, Conceptions for heat transfer correlation of nanofluids, *International Journal of Heat and Mass Transfer*, 43, 3701±3707.
- Choi, S.U.S., and Yu, W., 2003, The role of interfacial layers in the enhanced thermal conductivity of nanofluids: A renovated Maxwell model, *Journal of Nanoparticle Research*, 5, 167–171.
- Brinkman, H.C., 1952, The Viscosity of Concentrated Suspensions and Solutions, *The Journal of Chemical Physics*, Volume 20, Number 4, Pg.571.
- Arslan, K., Ekiciler, R., and Kaya, H., 2019, CFD analysis of laminar forced convective heat transfer for TiO<sub>2</sub>/Water nanofluid in semi circular cross sectioned microchannel, *Journal of Thermal Engineering*, 5, 123-137.
- Ambreen, T., and Kim, M.H., 2018, Heat transfer and pressure drop correlations of nanofluids: A state of art review, *Renewable and Sustainable Energy Reviews*, 91, 564–583.
- Galanis, N., Maiga, S. E. B., Nguyen, C. T., Palm, S.J., and Roy, G., 2005, Heat transfer enhancement by using nanofluids in forced convection flows, *International Journal of Heat and Fluid Flow*, 26, 530–546.



**Nezaket Parlak** is an Associate Professor in Mechanical Engineering Department at Sakarya University (SAU), Turkey. She graduated from University of Trakya in 2000 with a BSME Degree. She received an MSc (2003) and a PhD (2010) in Mechanical Engineering from Sakarya University. Her PhD concerned experimental and theoretical analysis of laminar single-phase fluid flow and heat transfer in microchannels. Between 2005 and 2006, she worked as a visiting student on Stirling engines at Regensburg University of Applied Sciences, Germany. Her field of interest includes single and two phase fluid flow and heat transfer, nanofluids, heat transfer enhancement techniques, drying agricultural products and renewable energy applications.



**Halime Çelik**, received his B.Sc. and M.Sc. degree in Mechanical Engineering from Sakarya University in 2016 and 2019, respectively. In her master's thesis, she worked on CFD modeling of nanofluids passing through microchannel. Her field of interest includes micro-scale devices and manufacturing techniques, heat recovery methods, renewable energy sources.



## A COMPARATIVE STUDY OF DIFFUSION, THERMAL WAVE AND DUAL-PHASE-LAG HEAT CONDUCTION IN THIN LAYER

R. YUVARAJ\* and D. SENTHILKUMAR\*\*

\*Assistant Professor, Mechanical Engineering, Sona College of Technology, Salem - 636005, India  
yuvarajr@sonatech.ac.in, ORCID: 0000-0002-5322-6084

\*\*Professor and Head, Mechanical Engineering, Sona College of Technology, Salem - 636005, India  
senthilkumard@sonatech.ac.in, ORCID: 0000-0001-9538-100X

(Geliş Tarihi: 09.04.2020, Kabul Tarihi: 05.02.2021)

**Abstract:** In the present work, three different modes of heat conduction, diffusion, thermal wave, and dual-phase lag, across a thin layer subjected to a constant temperature and insulated boundary conditions are compared by using a finite element solution. The finite element model is developed by considering relaxation time to heat flux and relaxation time to temperature gradient for a single element. After assembling all the elements, the number of algebraic equations obtained is solved to predict the temperature distribution across the thin layer using Python. The solution predicted by the dual-phase lag is compared with that obtained by the single-phase Cattaneo–Vernotte’s model and diffusion Fourier model. The developed model is validated with analytical, numerical, and experimental solutions with good agreement. The temperature contours are plotted for all three conditions and the way it propagates differently through the thin layer is clearly shown. Further, the temperature variation at the center of the layer, at which collision occurred, is predicted and the speed of the thermal wave, infinite in the Fourier diffusion model and finite in both single and dual-phase lag, is examined under transient to steady-state condition.

**Keywords:** dual-phase lag, CV model, relaxation time, finite element model, python.

## İNCE TABAKADA DİFÜZYON, TERMAL DALGA VE ÇİFT FAZLI-LAG ISI İLETİMİNİN KARŞILAŞTIRMALI BİR ÇALIŞMASI

**Özet:** Bu çalışmada, sabit bir sıcaklığa ve yalıtılmış sınır koşullarına maruz kalan ince bir katman boyunca üç farklı ısı iletimi, difüzyon, termal dalga ve çift fazlı gecikme modu, sonlu bir eleman çözümü kullanılarak karşılaştırılmıştır. Sonlu eleman modeli, tek bir eleman için akıyı ısıtmak için gevşeme süresi ve sıcaklık gradyanı için gevşeme süresi dikkate alınarak geliştirilmiştir. Tüm elemanları birleştirdikten sonra, elde edilen cebirsel denklemlerin sayısı Python kullanılarak ince katman boyunca sıcaklık dağılımını tahmin etmek için çözülür. Çift fazlı gecikme ile tahmin edilen çözüm, tek fazlı Cattaneo – Vernotte modeli ve difüzyon Fourier modeli ile elde edilen çözüm ile karşılaştırılır. Geliştirilen model, analitik, sayısal ve deneysel çözümlerle iyi bir uyum içinde doğrulanmıştır. Her üç koşul için sıcaklık sınırları çizilmiştir ve ince katman boyunca farklı şekilde yayılma şekli açıkça gösterilmiştir. Ayrıca, çarpışmanın meydana geldiği katmanın merkezindeki sıcaklık değişimi tahmin edilir ve Fourier difüzyon modelinde sonsuz ve hem tek hem de çift fazlı gecikmede sonlu olan termal dalganın hızı, geçici olarak kararlı durum koşulu.

**Anahtar Kelimeler:** çift fazlı gecikme, CV modeli, gevşeme süresi, sonlu eleman modeli, python.

### NOMENCLATURE

#### Symbols

q	heat flux [W/m <sup>2</sup> ]
k	thermal conductivity [W/m·K]
T	temperature [K]
$\nabla T$	temperature gradient [K/m]
t	time [s]
L	thickness of the layer [m]
$c_p$	specific heat capacity [J/kg·K]
l	element length [m]
Z	dimensionless relaxation time
[M]	mass matrix
[C]	capacitance matrix
[K]	stiffness matrix

{F} force vector

#### Greek Symbols

$\tau$	relaxation time [s]
$\rho$	density [kg/m <sup>3</sup> ]
$\alpha$	thermal diffusivity [m <sup>2</sup> /s]
$\xi$	dimensionless distance
$\eta$	dimensionless time
$\theta$	dimensionless temperature
$\zeta$	dimensionless heat flux

#### Subscripts

q	heat flux
T	temperature gradient

## INTRODUCTION

The synthesis of thin coatings is of great interest to engineers and physicists in modern technology. The energy transfer takes place over extremely small dimensions and time scales like etching of printed circuits, thin-film superconductors, fins, reactor walls, the satellite in orbit, thermal barrier coatings used in gas turbines, heating and cooling of micro-electronic elements involving a duration time of nanosecond or even picosecond in which energy is absorbed within a distance of microns from the surface. It is always required a correct prediction of thermal behavior to avoid thermal damage in devices. A major factor that depicts the energy transfer of the above applications requires certain non-Fourier conduction effects that need to be taken into account for the accurate prediction of heat transfer across thin layers.

The Fourier diffusive mode of heat conduction, parabolic in nature,

$$q = -k \nabla T \quad (1)$$

is accurate and appropriate in most common engineering situations for solving heat conduction problems. The most important drawbacks of the Fourier heat conduction model for solids are the prediction of thermal wave propagation speed and the simultaneous development of heat flux and temperature gradient. The rise of electron temperature is much faster than that of the lattice because of the faster interaction between the photons and electrons when large energy fluxes are deposited onto a metallic substrate in the form of electromagnetic radiation and the distinct relaxation time activates the electrons ballistically (Qui and Tien, 1992). Moreover, finite relaxation time is required for local thermal equilibrium to be established between the electrons and photons. The infinite speed of thermal wave leads to inaccurate results in situations where short-time inertial effects are dominant. Thus, Cattaneo (1958) and Vernotee (1958) proposed the thermal wave (CV) model,

$$\tau \frac{\partial q}{\partial t} + q = -k \nabla T \quad (2)$$

to consider a finite speed of thermal propagation by considering relaxation time  $\tau$ . Tan and Yang (1997) investigated the propagation of the thermal wave in thin films subjected to sudden temperature changes on its surfaces. This investigation was extended to study the asymmetrical temperature changes on both sides (Tan and Yang, 1997). Li *et al.* (2005) developed an implicit difference scheme by considering the non-Fourier conduction effects in multilayer materials for rapid transient heat conduction under pulsed heating. Torii and Yang (2005) examined the heat transfer mechanism in a thin layer with symmetrical heat source impingement on its boundaries. Lewandowska and Malinowski (2006) presented an analytical solution of the hyperbolic heat conduction equation for the case of a thin slab

symmetrically heated on both sides. Mitra *et al.* (1995) presented experimental evidence of hyperbolic heat transfer in processed meat for different conditions and experimentally determined the relaxation time for processed meat. Lam and Fong (2011) considered the effect of thermal diffusion and wave propagation in solids subjected to a time-varying and spatially decaying laser irradiation and the temperature profiles. Further, this study examined the temperature across the thin film subjected to asymmetrical boundary conditions by solving the CV model with non-homogeneous boundary conditions with the superposition principle (Fong and Lam, 2014).

The relaxation time  $\tau$  in Eq. (2) is the phase lag between the heat flux and the temperature gradient. When  $\tau = 0$ , Eq. (2) reduces to the classical Fourier equation and  $\tau$  is small, Eq. (2) reduces to the exponential relaxation model. The CV model does not account for the finite thermal relaxation time for the electrons and lattice to reach local thermal equilibrium. A two-step model for phonon-electron interaction has been proposed to account for the microscale response of thin metallic films subjected to short-pulse laser heating (Fujimoto *et al.*, 1984; Elsayed-Ali, 1991; Hector *et al.*, 1992; Majumdar, 1993). Korner and Bergman (1998) found that the hyperbolic approach to the heat current density violates the fundamental law of energy conservation and the solution obtained by the CV model is physically impossible solutions with negative local heat content. Tzou (1995; 1996) proposed a dual-phase lag (DPL) model,

$$\tau_q \frac{\partial q}{\partial t} + q = -k \nabla T - k \tau_T \frac{\partial}{\partial t} (\nabla T) \quad (3)$$

where  $\tau_q$  and  $\tau_T$  are the phase lags for the heat flux and the spatial temperature gradient concerning the local temperature, which is capable of predicting both the observed microscale and macroscale effects in conduction and found that the wave model overestimates the peak value of transient temperatures and the DPL model accurately describes the entire transient response. In fact,  $\tau_q$  is related to the thermal wave speed and  $\tau_q$  represents the time constant for electron-phonon equilibrium. When  $\tau_q = 0$  and  $\tau_T = 0$  the Eq. (3) reduces to classical Fourier equation, and  $\tau_T = 0$  Eq. (3) reduces to CV model. Antaki (1998) used the DPL model to study the microscale transient heat conduction in a semi finite slab with surface flux. Tang and Araki (2000) solved the DPL model analytically to analyze the transient heat conduction in a finite medium subjected to pulse surface heating. Al-Nimr and Al-Hunaiti (2000) used the DPL model to explore the transient thermal stresses induced by rapid heating in a thin plate. Siva Prakash *et al.* (2000) identified the origin of the discrepancy in the available analytical results as the sensitivity of the predicted solution to the way of implementing the surface boundary condition. Also employed finite element method and fourth-order Runge–Kutta time marching procedure for the prediction

of spatial and temporal discretization, respectively. Liu and Cheng (2006) investigated heat conduction induced by a pulsed volumetric source in a two-layered film with the dual-phase-lag model. An analytical method and a numerical scheme are used to solve the DPL problem. Recently, Dhanaraj *et al.* (2019) resolved the DPL heat conduction using a three-time level finite difference scheme in a micro-scale gold film subjected to spontaneous temperature boundary conditions without knowing the heat flux. Tang *et al.* (2007) employed the dual-phase-lagging model (DPL), including the thermal wave situation, to simulate the temperature responses of the specimens and shown the absence of temperature jump caused by thermal wave propagation by comparing with the experimental results. Also found a wave-like shape predicted by the DPL model, which is almost the same as the numerical results from the Fourier model for heterogeneous medium.

Although there are, many articles available for solving the DPL model numerically and analytically, only very few finite element solutions are available for solving the DPL model due to the large discrepancy, identified by Al-Nimr and N. S. Al-Hunti (2000), exists between the analytical and finite element results. The reason for this discrepancy is due to the electron-phonon interaction term dominates and as a result, the overall temperature reached is higher than that predicted by the classical conduction equation. To overcome this in the finite element method, Siva Prakash *et al.* (2000) and Liu and Cheng (2006) used an analytical method to solve DPL when the value of  $\tau_T > \tau_q$ . Dhanaraj *et al.* (2019) used a three-time level finite difference scheme to resolve the dual-phase lag's heat conduction in a micro-scale gold film subjected to spontaneous temperature boundary conditions without knowing the heat flux. In the previous works, a complete finite element solution for the DPL problem is not given and the comparative temperature distribution of diffusive model, CV model, and DPL model at the same instant from transient to steady-state are not presented.

In the present work, one-dimensional dual-phase-lag heat conduction across a thin layer subjected to a constant temperature and insulated boundary conditions are predicted by using a complete finite element solution without using an analytical method for DPL when the value of  $\tau_T > \tau_q$ . The DPL model is solved to predict the temperature distribution across the thin layer using Python 3.6.3 after considering the relaxation time to heat flux  $\tau_q$  and to the temperature gradient  $\tau_T$ . The three different modes of heat conduction, diffusion (Fourier model), thermal wave (CV model), and dual-phase lag (DPL model), across the thin layer, are compared for the same instants against the initial and boundary conditions. The developed finite element DPL model is validated with the analytical solution given by Tzou (1995), numerical solutions given by Dhanaraj *et al.* (2019), and experimental work presented by Tang *et al.* (2007) with good agreement. Recently, Yuvaraj and Senthilkumar (2020) presented the length and time scale at which the

thermal wave propagation vanishes from the CV model to the Fourier model. Also, to distinguish the diffusion, thermal wave, and DPL model, temperature variation at the center of the layer is predicted and shown that the speed of the thermal wave, infinite in the Fourier diffusion model and finite in both single and dual-phase lag are examined under transient to steady-state. Further, temperature contours plotted are evident for the DPL mode of heat conduction in a thin layer is entirely different from diffusion mode and thermal wave mode of heat conduction across the thin layer.

## PROBLEM DESCRIPTION

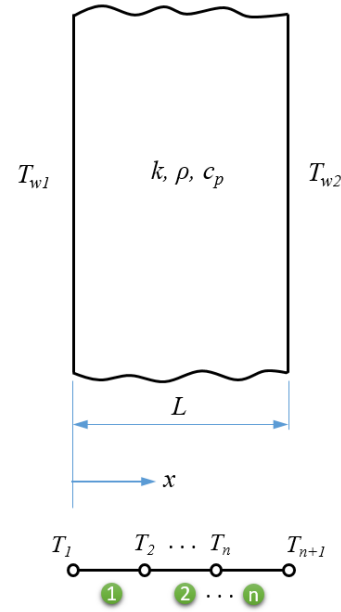


**Figure 1.** Thin layer subjected to symmetrical boundary conditions.

A thin layer of length  $L$  with thermal conductivity  $k$ , density  $\rho$ , and specific heat capacity  $c_p$  shown in Fig. 1 is subjected to two cases symmetrical and insulated boundary conditions respectively. In the first case, the left side and right side of the boundary are subjected to a constant temperature of  $T_{w1} = T_{w2}$  maintained to be constant and in the second case, the left side boundary is maintained at a constant temperature  $T_{w1}$  and the right side boundary is insulated. When the heat is transferred from  $x = 0$  to  $x = L$ ,  $L$  is in macro size, the infinite speed of the thermal wave is assumed and followed by Fourier's mode of heat conduction across the thin layer. When  $L$  is in micro/nano-size, the finite speed of thermal waves caused the wave-like mode and DPL mode of heat conduction across the thin layer. In diffusion mode, the heat transfer is decided by thermal diffusivity  $\alpha$  and in thermal wave mode of heat conduction, it is decided by thermal diffusivity and relaxation time  $\tau$ . Whereas in the DPL mode of heat conduction, the heat transfer decided by thermal diffusivity, relaxation time for heat flux  $\tau_q$  and relaxation time for temperature gradient  $\tau_T$ . Heat transfer through a thin layer is assumed as one-dimensional and thermophysical properties are constant.

## Governing equations

One dimensional heat conduction in a thin layer is governed by the Tzou (1995) DPL heat conduction equation and local energy balance equation.

The energy equation for anisotropic material can be written as

$$\nabla q = -\rho c_p \frac{\partial T}{\partial t} \quad (4)$$

where  $\rho$  is the density and  $c_p$  is the specific heat capacity. The given governing equations in the form of dimensional characters are converted into non-dimensional form by using the following dimensionless parameters,

$$\xi = \frac{x}{L}, \eta = \frac{t\alpha}{l^2}, \theta = \frac{T_w - T}{T_w - T_0}, z_q = \frac{\tau_q \alpha}{l^2}, \quad (5)$$

$$z_T = \frac{\tau_T \alpha}{l^2}, \zeta = \frac{q}{q_r}$$

where  $\xi$  is the dimensionless distance in  $x$  direction as shown in Fig. 1,  $\eta$  is the dimensionless time,  $\theta$  is the dimensionless temperature,  $z_q$  is the dimensionless heat flux relaxation time,  $z_T$  is the dimensionless temperature gradient relaxation time and  $\zeta$  is the dimensionless heat flux. Rearranging Eqn. (1-4), the general form of DPL heatwave equation can be written as,

$$\alpha \tau_T \frac{\partial^3 T}{\partial x^2 \partial t} + \alpha \frac{\partial^2 T}{\partial x^2} = \tau_q \frac{\partial^2 T}{\partial t^2} + \frac{\partial T}{\partial t} \quad (6)$$

where  $\alpha$  is thermal diffusivity ( $\alpha = k/\rho c_p$ ). If  $\tau_q = \tau_T = 0$ , Eqn. (6) reduces to the first-order diffusion equation,  $\tau_T = 0$  then Eqn. (6) becomes second-order thermal wave heat equation.

After substituting the non-dimensional terms from Eqn. (5) in to the Eqn. (6), the governing partial differential equation for one-dimensional DPL heat conduction equation can be given in the form of the dimensionless equation as

$$z_T \frac{\partial^3 \theta}{\partial \xi^2 \partial \eta} + \frac{\partial^2 \theta}{\partial \xi^2} = z_q \frac{\partial^2 \theta}{\partial \eta^2} + \frac{\partial \theta}{\partial \eta} \quad (7)$$

Initial conditions:

$$\theta(\xi, \eta) = 1 \quad \text{at } \eta = 0, \quad 0 < \xi < 1 \quad (8)$$

Boundary conditions:

*Case – 1: The prescribed temperature at both side of the thin layer*

$$\frac{\partial \theta}{\partial \eta}(\xi, \eta) = 0 \quad \text{at } \eta > 0, \xi = 0, \xi = 1 \quad (9)$$

$$\theta(\xi, \eta) = 1 \quad \text{at } \xi = 0, \quad \eta > 0 \quad (10)$$

$$\theta(\xi, \eta) = 1 \quad \text{at } \xi = 1, \quad \eta > 0 \quad (11)$$

*Case – 2: The prescribed temperature at the left side and insulated at the right side of the thin layer*

$$\theta(\xi, \eta) = 1 \quad \text{at } \xi = 0, \quad \eta > 0 \quad (12)$$

$$\zeta(\xi, \eta) = 0 \quad \text{at } \xi = 1, \quad \eta > 0 \quad (13)$$

The nodal temperatures  $T_2$  to  $T_n$  as shown in Fig. 1 can be predicted by applying the initial and boundary conditions given in Eqn. (8-13) using the finite element method. The dimensionless temperature of 1 is maintained at the left and right side of the thin layer and maintained constant for case-1 and insulated condition for case-2. Initially, the temperature of the thin layer in length  $L$  is maintained at a dimensionless temperature of  $\theta = 0$  at the dimensionless time is  $\eta = 0$  and suddenly changed to the boundary conditions. The nodal temperatures are predicted by executing the finite element model using Python 3.6.3 (2020). The  $n$  numbers of linear algebraic equations are solved and the nodal temperatures and temperature contours are predicted by using the *NumPy* and *matplotlib* modules available in Python.

## FINITE ELEMENT MODEL

In the finite element method, the given domain is discretized into several subdomains, called a finite element, the approximation functions of weighted-residual are constructed on each element for the solution of the problem. The step by step procedure followed in the present work to develop a finite element model is given by Reddy (2015).

The finite element model for the heat transfer problem, the one-dimensional steady-state without heat generation, can be developed by making a weak form of Eqn. (6)

$$z_T \frac{\partial^3 \theta}{\partial \xi^2 \partial \eta} + \frac{\partial^2 \theta}{\partial \xi^2} - z_q \frac{\partial^2 \theta}{\partial \eta^2} - \frac{\partial \theta}{\partial \eta} = 0 \quad (14)$$

The finite element formulation for the governing equation (14) is,

$$z_q [M] \{\dot{\theta}\} + ([C] + z_T [K]) \{\theta\} + [K] \{\theta\} = \{F\} \quad (15)$$

where,  $[K] = \frac{1}{l} \begin{bmatrix} 1 & -1 \\ -1 & 1 \end{bmatrix}$  is the stiffness matrix,  $[C] = \frac{l}{6} \begin{bmatrix} 2 & 1 \\ 1 & 2 \end{bmatrix}$  is the capacitance matrix,  $[M]$  is the mass matrix, and  $\{F\}$  is the force vector for a linear element. Eqn. (15) is the DPL mode of finite element model which contains a first-order time derivative  $\{\dot{\theta}\}$  and second-



order time derivative  $\{\dot{\theta}\}$ . The solution for the DPL heat equation in the form of a finite element model can be obtained using Newmark's scheme as follows

$$\dot{\theta}_{n+1} = \dot{\theta}_n + \Delta\eta((1 - \gamma)\ddot{\theta}_n + \gamma\ddot{\theta}_{n+1}) \quad (16)$$

$$\theta_{n+1} = \theta_n + \Delta\eta\dot{\theta}_n + \Delta\eta^2\left(\frac{1}{2} - \beta\right)\ddot{\theta}_n \quad (17)$$

$$z_q[M]\{\ddot{\theta}_{n+1}\} + ([C] + z_T[K])\{\dot{\theta}_{n+1}\} + [K]\{\theta_{n+1}\} = \{F_{n+1}\} \quad (18)$$

The value of  $\gamma$  and  $\beta$  are taken as  $\frac{1}{2}$  and  $\frac{1}{4}$  respectively. By applying initial and boundary conditions as given in Eqn. (8-13), first the value of  $\ddot{\theta}_n$  can be obtained by solving Eqn. (15). The finite-difference form of  $\ddot{\theta}_n$  can be written as

$$\{\ddot{\theta}_n\} = \frac{\dot{\theta}_{n+1} - \dot{\theta}_n}{\Delta\eta} \quad (19)$$

After finding  $\ddot{\theta}_n$ , substitute it in Eqn. (19) to find  $\dot{\theta}_{n+1}$  and from Eqn. (16) the value of  $\ddot{\theta}_{n+1}$  can be obtained. The value of  $\theta_{n+1}$  for the first time step can be obtained from Eqn. (17) and repeating this procedure for the consecutive time steps. Then Eqn. (18) is the element level DPL heat equation for  $n + 1^{th}$  time step.

## RESULTS AND DISCUSSION

### Mesh sensitivity test

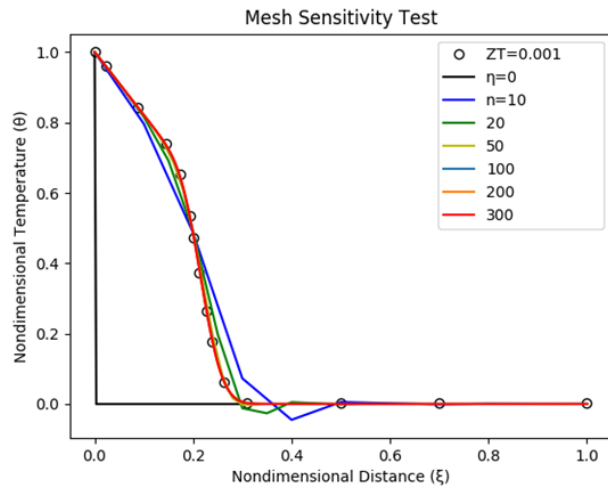


**Figure 2.** Mesh sensitivity test.

The mesh sensitivity study was conducted for the range of several elements from 10 to 300. Fig. 2 shows the propagation of the thermal wave, at  $Z_q = 0.05$ ,  $Z_T = 0.001$  and  $\eta = 0.045$ , for a different number of elements. The non-dimensional temperature variation is negligible for the mesh 200 and 300 elements. When the time scale increases the convergent solution for the present model requires more number of elements than 200. Hence, 300

elements and time step  $10^{-4}$  have been chosen for the execution of all the three models from transient to steady-state. The temperatures of each nodal point are predicted by solving Eqn. (15-19) for DPL heat transfer across a thin layer. The code is generated and the finite element model is solved by using Python 3.6.3 (2020), an open-source software.

### Validation of the present model with the Analytical and Numerical solutions

The present finite element model is validated with the analytical solution given by Tzou (1995) for different  $Z_T$  values as shown in Fig. 3 (a). Tzou considered the dimensionless heat flux relaxation time  $Z_q = 0.05$  and varied the dimensionless temperature gradient relaxation time  $Z_T$  and found that when  $Z_T > 0.05$  the heat conduction follows the dual-phase lag model. All three models,  $Z_T = 0.001$ ,  $Z_T = 0.05$  and  $Z_T = 0.5$  validated with the analytical solution with good agreement. The present model is also compared and validated with the numerical solution given by Dhanaraj *et al.* (2019) for different dimensionless times  $\eta = 0.02$ ,  $\eta = 0.05$ , and  $\eta = 0.16$ . The similar kind of boundary conditions used and obtained good results as shown in Fig. 3 (b).

Fig. 3 (c) shows the validation of present model with experimental work presented by Tang *et al.* (2007). They conducted an experiment for DPL heat conduction in meat specimens with three different thickness 2 mm, 3 mm and 4 mm by using 1 sec IR light pulse. The experimental result for 2 mm specimen is used to validate with the present work shows very good agreement than the Fourier and CV model. The table of errors for different mode of heat transfer Fourier model, CV model and DPL model of analytical data are compared with the present numerical data and obtained the positive errors of 2.2% for Fourier model, 0.67% for CV model, and negative errors 0.41% for DPL model.

### Case-1: Comparison of diffusion model, CV model, and DPL model

In case-1, the temperature of  $\theta = 1$  is maintained constantly on both side of the thin layer and the heat flux relaxation time  $Z_q$  is taken as 0.05 and the temperature gradient relaxation time  $Z_T$  is varied from 0 – 0.5 similar to the work carried numerically by Dhanaraj *et al.* (2019). Then Eqn. (14) can be reduced to the diffusion model when  $Z_q = Z_T = 0$  and CV model when  $Z_T = 0$ . The dual-phase lag model predicts the precised temperature variation across the thin layer when  $Z_T > 0$ . In the present work, the value of  $Z_T = 0$  is considered as CV model, the value of  $Z_T = 0.05$  is taken as the diffusion model and other non zero values of  $Z_T$  are taken as the DPL model.

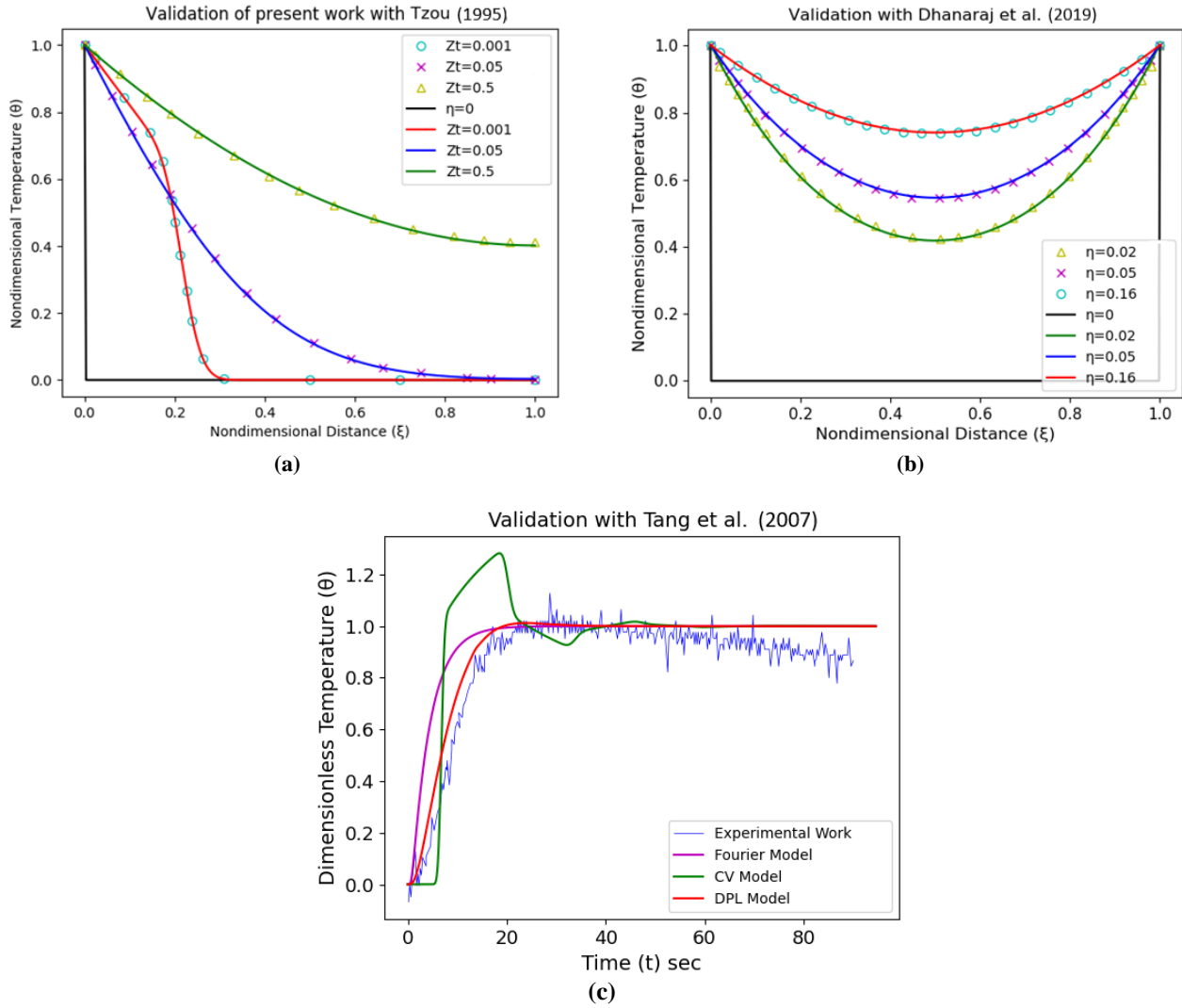


**Figure 3.** Validation of present model with (a) Analytical solution given by Tzou (1995), (b) Numerical solution presented by Dhanaraj et al. (2019) and (c) Experimental work presented by Tang et al. (2007).

**Table 1.** Present numerical work error table.

Fourier model			CV model			DPL model		
Analytical work	Present work	Error %	Analytical work	Present work	Error %	Analytical work	Present work	Error %
1.0000	1.0000	<b>0.0000</b>	1.0000	1.0000	<b>0.0000</b>	0.9976	0.9976	<b>0.0000</b>
0.9398	0.9373	<b>0.2564</b>	0.9639	0.9542	<b>1.0000</b>	0.9735	0.9735	<b>0.0000</b>
0.8482	0.8458	<b>0.2841</b>	0.8410	0.8434	<b>-0.2865</b>	0.9084	0.9108	<b>-0.2653</b>
0.7398	0.7373	<b>0.3257</b>	0.7373	0.7373	<b>0.0000</b>	0.8410	0.8458	<b>-0.5731</b>
0.6434	0.6337	<b>1.4981</b>	0.6530	0.6458	<b>1.1070</b>	0.7880	0.7928	<b>-0.6116</b>
0.5518	0.5494	<b>0.4367</b>	0.5349	0.5325	<b>0.4505</b>	0.7301	0.7349	<b>-0.6601</b>
0.4506	0.4482	<b>0.5348</b>	0.4699	0.4675	<b>0.5128</b>	0.6651	0.6699	<b>-0.7246</b>
0.3639	0.3590	<b>1.3245</b>	0.3711	0.3663	<b>1.2987</b>	0.6024	0.6120	<b>-1.6000</b>
0.2578	0.2530	<b>1.8692</b>	0.2651	0.2602	<b>1.8182</b>	0.5614	0.5663	<b>-0.8584</b>
0.1807	0.1759	<b>2.6667</b>	0.1735	0.1663	<b>4.1667</b>	0.5157	0.5229	<b>-1.4019</b>
0.1108	0.1060	<b>4.3478</b>	0.0602	0.0602	<b>0.0000</b>	0.4747	0.4795	<b>-1.0152</b>
0.0627	0.0602	<b>3.8462</b>	0.0024	0.0024	<b>0.0000</b>	0.4434	0.4458	<b>-0.5435</b>
0.0361	0.0361	<b>0.0000</b>	0.0000	0.0000	<b>0.0000</b>	0.4265	0.4217	<b>1.1299</b>
0.0217	0.0200	<b>7.8833</b>	0.0000	0.0000	<b>0.0000</b>	0.4120	0.4120	<b>0.0000</b>
0.0048	0.0042	<b>12.2500</b>	0.0000	0.0000	<b>0.0000</b>	0.4024	0.4024	<b>0.0000</b>
Average Fourier model error		<b>2.2 %</b>	Average CV model error		<b>0.67 %</b>	Average DPL model error		<b>0.41 %</b>

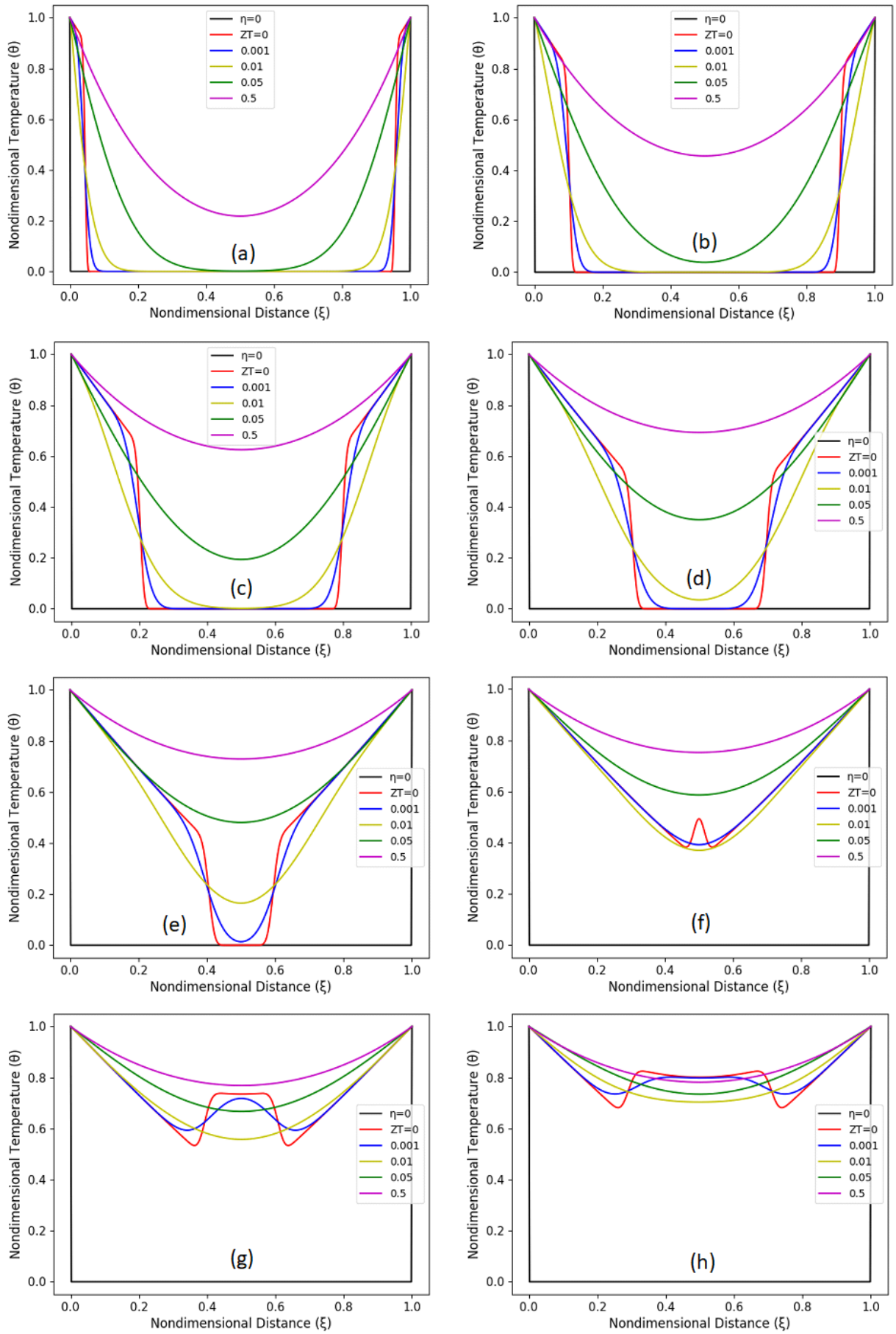


**Figure 4.** Case-1 Temperature variation for different  $ZT$ , (a)  $\eta = 0.01$ , (b)  $\eta = 0.02$ , (c)  $\eta = 0.045$ , (d)  $\eta = 0.068$ , (e)  $\eta = 0.091$ , (f)  $\eta = 0.114$ , (g)  $\eta = 0.136$ , and (h)  $\eta = 0.159$ .

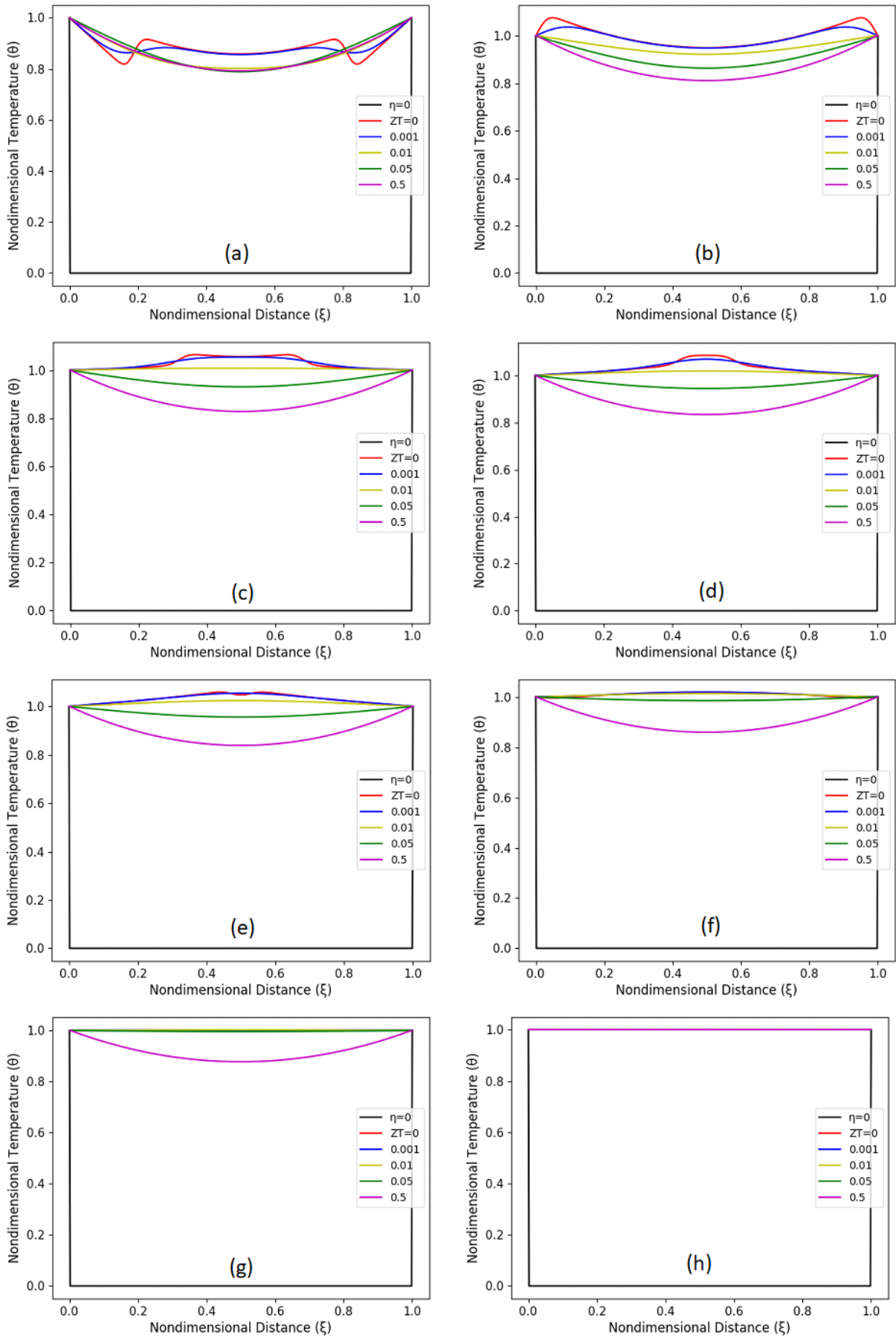


**Figure 5.** Case-1 Temperature variation for different  $Z_T$ , (a)  $\eta = 0.182$ , (b)  $\eta = 0.227$ , (c)  $\eta = 0.295$ , (d)  $\eta = 0.318$ , (e)  $\eta = 0.341$ , (f)  $\eta = 0.432$ , (g)  $\eta = 0.568$ , and (h)  $\eta = 2.468$ .

**Case-1: Temperature contours**

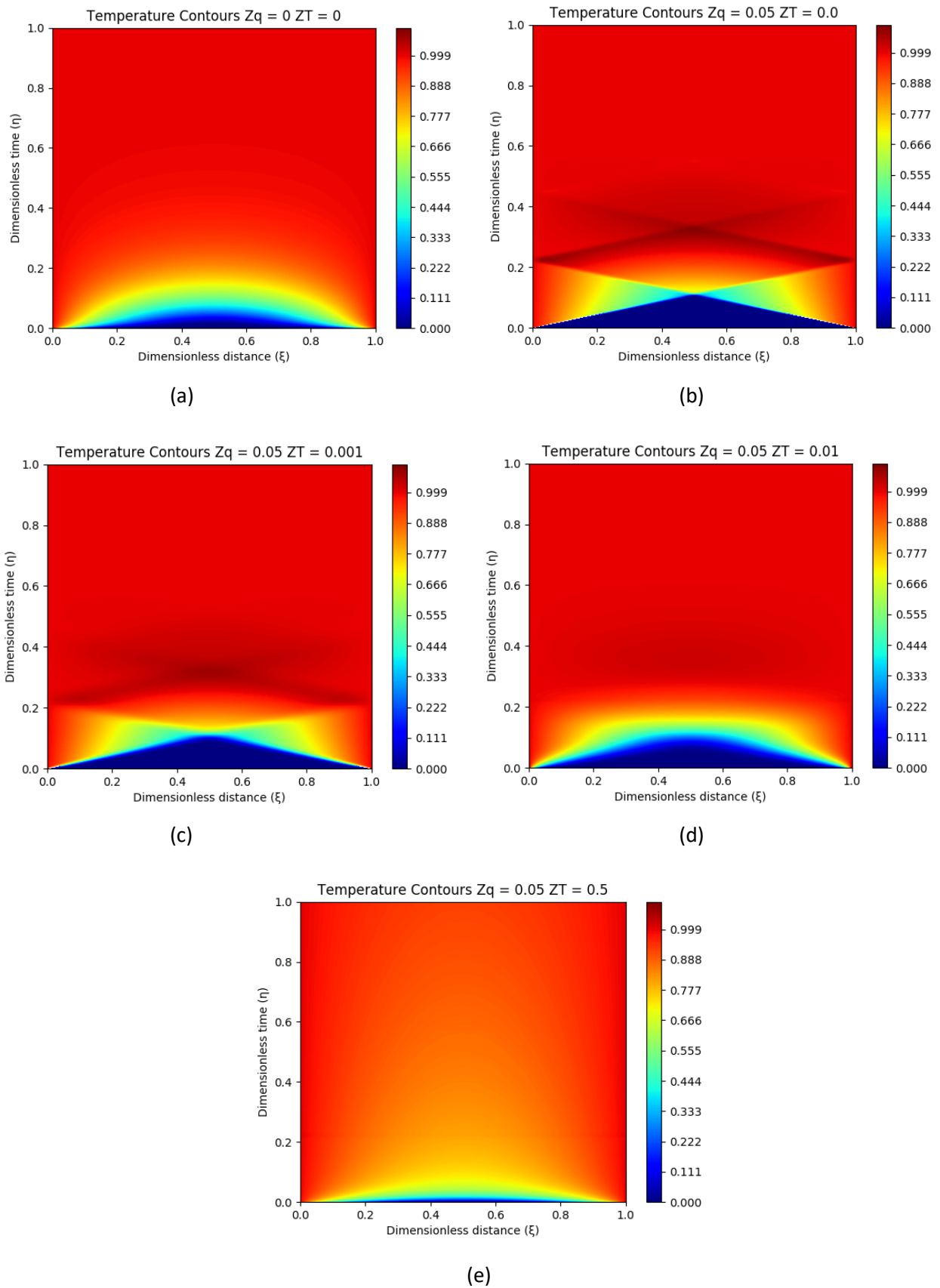


**Figure 6.** Case-1 Temperature contours, (a) Diffusion model  $Z_q = Z_T = 0$ , (b) CV model  $Z_T = 0$ , (c) DPL model  $Z_T = 0.001$ , (d) DPL model  $Z_T = 0.01$ , (e) DPL model  $Z_T = 0.5$ .

The variation of temperature for different  $Z_T$  values from 0 – 0.5 are shown in Fig. 4 (a-h) and Fig. 5(a-h) for different time  $\eta$ . Fig. 4(a) shows the temperature variation across the thin layer, at  $\eta = 0.01$ , due to heat conduction. Thermal wave-like temperature variation occurs, when  $Z_T = 0$ , due to only the heat flux relaxation time  $Z_q$  exist in a thin layer. The diffusion mode of heat conduction occurs at  $Z_q = Z_T = 0.05$  and the thermal wave propagates smoothly without any collision as shown in Fig. 4(b-e). The thermal wave speed is assumed as infinite in the diffusion mode of heat conduction and finite in the CV model and DPL model. Fig. 4 (f) shows the collision of thermal wave occurs at the center of the layer at  $\eta = 0.114$  and the temperature increases after the collision and propagates in reverse order towards either side of the boundary. The dual lag affects the propagation time and both diffusion and CV model catching the DPL model at  $\eta = 0.182$  and overtake afterward which is clearly shown in Fig. 5 (a). From Fig. 5 (b-e) it is noted that the DPL model propagates slower than the diffusion and CV model to reach a steady state. The diffusion model reaches a steady-state first at time  $\eta = 0.432$ , Fig. 5 (f), second CV model at  $\eta = 0.568$ , Fig. 5 (g), finally DPL model at  $\eta = 2.468$  as shown in Fig. 5 (h).

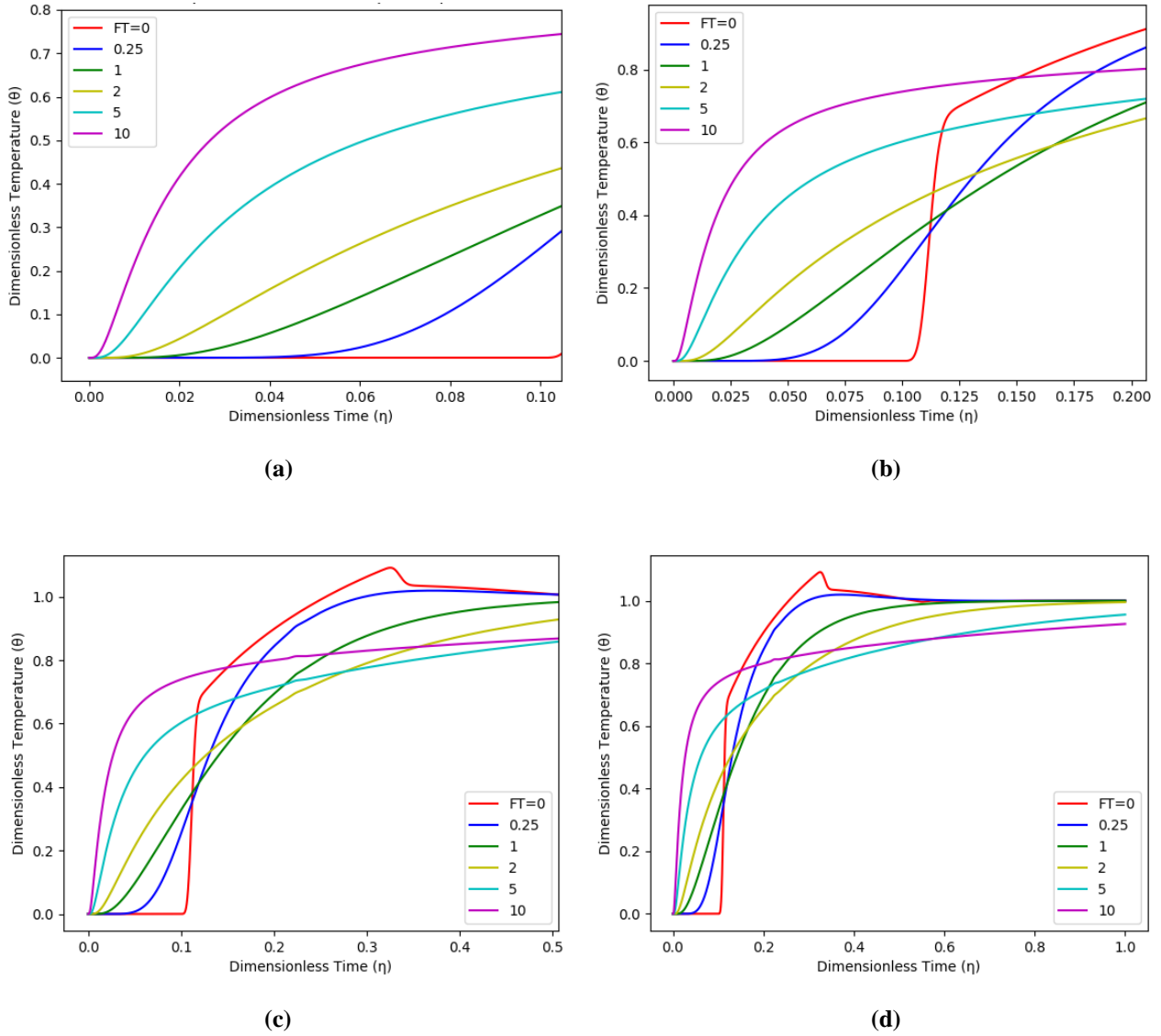
The temperature contours are plotted for different conditions, the diffusion model  $Z_q = Z_T = 0$ , the CV model  $Z_T = 0$ , DPL model  $Z_T = 0.001$ , DPL model  $Z_T = 0.01$  and DPL model  $Z_T = 0.5$  as shown in Fig. 6 (a-e) respectively. In the diffusion model, there is no lag,  $Z_q = Z_T = 0$ , in response between applied heat flux and the temperature gradient, causes no collision in the thin layer. The immediate response of temperature gradient against the applied heat flux causes smooth conduction of heat across the thin layer and the temperature contours from  $\eta = 0$  to  $\eta = 1$  is shown in Fig. 6 (a). Whereas in Fig. 6 (b), the evidence of collision is clearly shown as the triangular contours with sharp corners. The thermal wave propagates with relaxation time  $Z_q = 0.5$  and  $Z_T = 0$ . Each sharp corner represents the occurrence of collisions and five times the collision consecutively happens at the center of the layer and boundary of the layer. The first collision of thermal wave occurred at  $\xi = 0.5$  and  $\eta = 0.114$  with an increase in temperature and move towards either side of the boundary. The second collision occurs at the boundary of the layer and propagates back towards the center of the layer with a further increase in temperature. After the third collision at the center of the layer the temperature decreases and repeats alternatively and after fifth collision smooth propagation occurred. In DPL model, Fig. 6 (c-e), both relaxation time  $Z_T$  and  $Z_q$  are considered and the wave-like heat propagation disappears and propagates slower than the diffusion and CV model. In Fig. 6 (c), the sharp corners have vanished and the triangular shape of contours are smudged due to relaxation time  $Z_T = 0.001$ .

Fig. 6 (d) shows that the increase in relaxation time  $Z_T = 0.01$  the wave-like propagation are disappeared and transition from CV mode of heat conduction to DPL mode of heat conduction happened. The temperature contours for  $Z_T = 0.5$  is shown in Fig. 6 (e) is the complete evidence for the DPL mode of heat conduction in entirely different from diffusion and CV mode of heat conduction.

### Case-1: Temperature variation at the center of the layer $\xi = 0.5$

The heat conduction model number,  $F_T = \frac{\tau_T}{\tau_q}$  [26], is used to analyze the temperature variation at the center of the layer  $\xi = 0.5$ . The Fig. 7 (a-d) shows the temperature variation at the center of the layer for different values of  $F_T$  from time  $\eta = 0$  to  $\eta = 1$ . When  $\tau_T = 0$ , heat conduction model number  $F_T$  becomes zero and the heat propagates like a wave across the thin layer followed by the CV model with single relaxation time. When  $F_T = 1$ , both relaxation times are equal in magnitude and it follows the diffusion mode of heat conduction. When  $F_T < 1$ , it follows the DPL mode of heat conduction followed by the transition from the CV model to the diffusion model. Whereas  $F_T > 1$ , diffusion mode is changed to the DPL mode of heat conduction.

Fig. 7 (a) shows that the temperature variation at the center of the layer  $\xi = 0.5$  from  $\eta = 0$  to  $\eta = 0.1$ . The temperature remains in the initial state,  $\theta = 0$ , for CV model up to  $\eta = 0.1$  and  $F_T = 0$ . Whereas  $F_T > 0$ , in case of diffusion and DPL model, the temperature at the center of the layer varies earlier than the CV model. At  $\eta = 0.114$  and  $F_T = 0$ , the thermal wave from either side of the boundary reaches the center of the layer and causes the first collision to occur at  $\xi = 0.5$ . After the first collision, the temperature increases immensely from  $\theta = 0$  to  $\theta = 0.7$  as shown in Fig. 7 (b) and then it continuously increases the temperature and reaches maximum temperature  $\theta = 1.1$  which is greater than the applied boundary condition. This unrealistic phenomenon is the main cause for considering the DPL mode of heat conduction across the thin layer. At time  $\eta = 0.2$ , the temperature at the center of the layer is greater for the CV model  $F_T = 0$  and smaller for diffusion and DPL model  $F_T > 0$ . After time  $\eta = 0.3$ , the collision of the thermal wave,  $F_T = 0$  decreases the temperature at the center of the layer as shown in Fig. 7 (c) and it follows the diffusion model,  $F_T = 1$ . After time  $\eta = 0.6$  onwards, CV model and DPL model  $F_T = 0.25$  follows a similar way of diffusion model as clearly shown in Fig. 7 (d). The temperature at the center in the DPL model, when  $F_T > 1$ , are smaller than the diffusion and CV model at time  $\eta = 1$ .



**Figure 7.** Case-1 Temperature variation at  $\xi = 0.5$  for different  $F_T$ , (a) up to  $\eta = 0.1$ , (b) up to  $\eta = 0.2$ , (c) up to  $\eta = 0.5$  and (d) up to  $\eta = 1$

### Case-2: Comparison of diffusion model, CV model and DPL model

In case-2, the temperature of  $\theta = 1$  is maintained constant at left side boundary of the thin layer and insulated boundary condition is taken at right side of the boundary. The relaxation times  $Z_q$  and  $Z_T$  are varied similar to that of case-1. The initial and boundary conditions given in Eqn. (8-11) and the Eqn. (14-19) are applied to solve the DPL model for insulated boundary condition and the temperature variations from transient state to steady state are shown in Fig. 8 (a-h) and Fig. 9 (a-h).

Fig. 8 (a) shows the temperature variation at  $\eta = 0.023$  in which the DPL model with  $Z_T = 0.5$  reaches the right boundary earlier than the diffusion and CV model. The diffusion model with  $Z_T = 0.5$  marching towards the

right insulated boundary faster than the DPL model, with  $Z_T = 0.01$  and  $Z_T = 0.001$ , and CV model with  $Z_T = 0$  as shown in Fig. 8 (b). At time  $\eta = 0.068$ , Fig. 8 (c) shows the diffusion model reaches the right side boundary and still the DPL model, with  $Z_T = 0.01$  and  $Z_T = 0.001$ , and the CV model are well behind the diffusion model. After time  $\eta = 0.114$ , there is no collision occurs at the center of the layer  $\xi = 0.5$  due to there is no source of heat comes from the right side boundary and the thermal wave propagates towards the right side boundary as shown in Fig. 8 (d-e). The CV model finally reaches the right side boundary after time  $\eta = 0.205$ , Fig. 8 (f-h), and makes the first collision at the right side of the boundary with an increase in temperature. After the first collision, reverse propagation occurs towards the left side boundary of the thin layer as shown in Fig. 9 (a-b). The diffusion model, CV model and DPL model with  $Z_T = 0.001, Z_T = 0.01$  are chasing

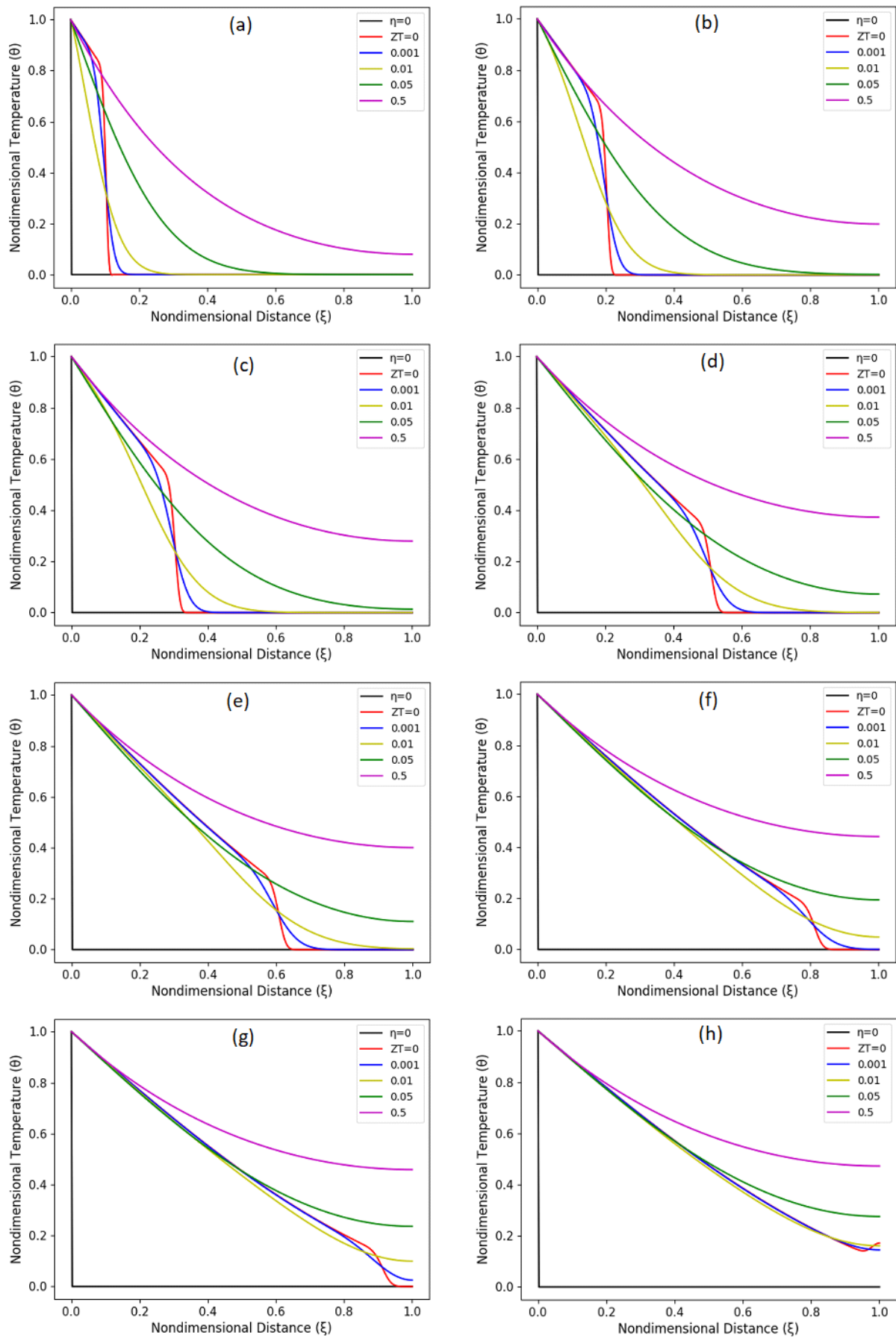


**Figure 8.** Case-2 Temperature variation for different  $Z_T$ , (a)  $\eta = 0.023$ , (b)  $\eta = 0.045$ , (c)  $\eta = 0.068$ , (d)  $\eta = 0.114$ , (e)  $\eta = 0.136$ , (f)  $\eta = 0.182$ , (g)  $\eta = 0.205$ , and (h)  $\eta = 0.227$ .



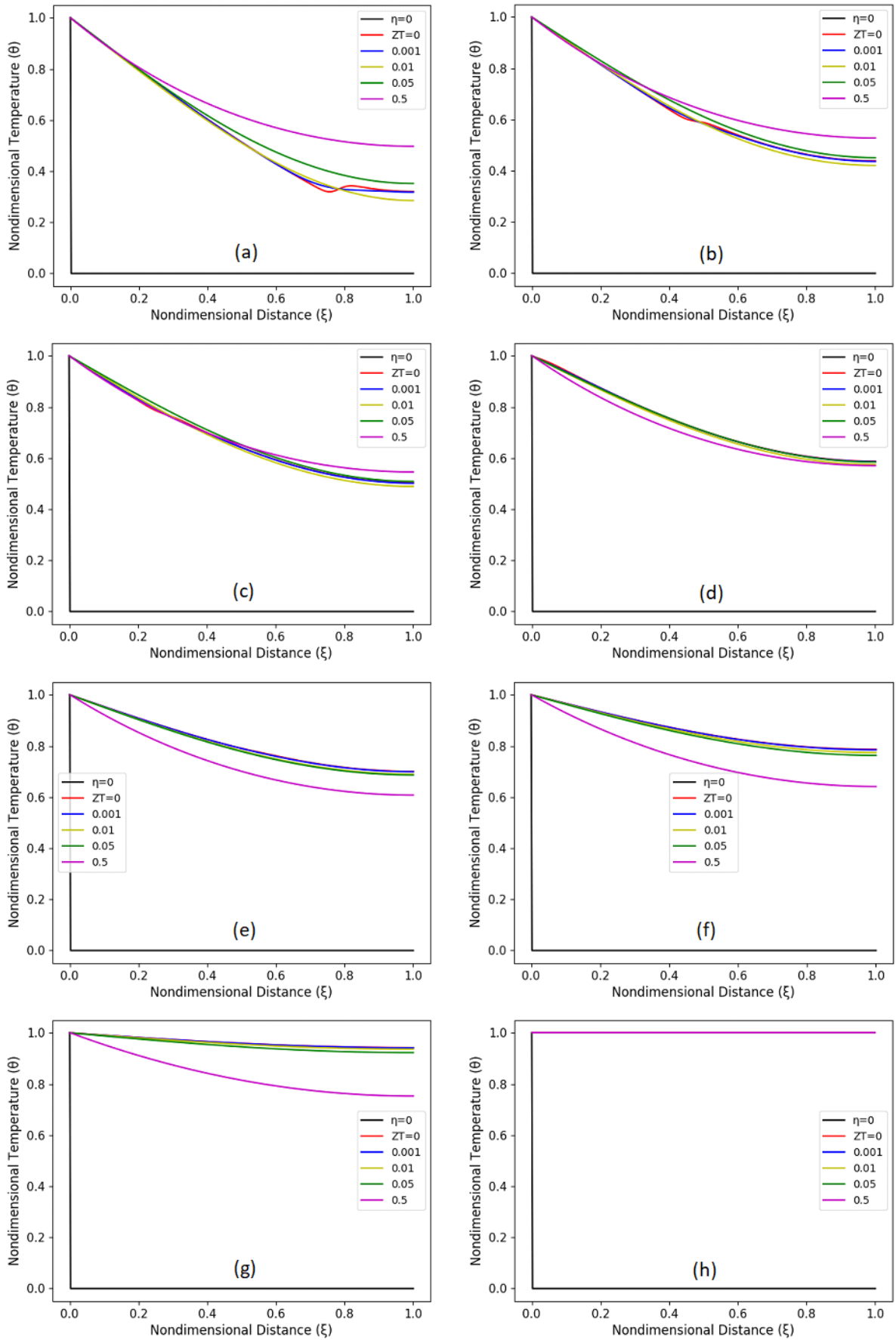


**Figure 9.** Case-2 Temperature variation for different  $Z_T$ , (a)  $\eta = 0.273$ , (b)  $\eta = 0.341$ , (c)  $\eta = 0.386$ , (d)  $\eta = 0.454$ , (e)  $\eta = 0.568$ , (f)  $\eta = 0.682$ , (g)  $\eta = 1.136$ , and (h)  $\eta = 4.122$ .

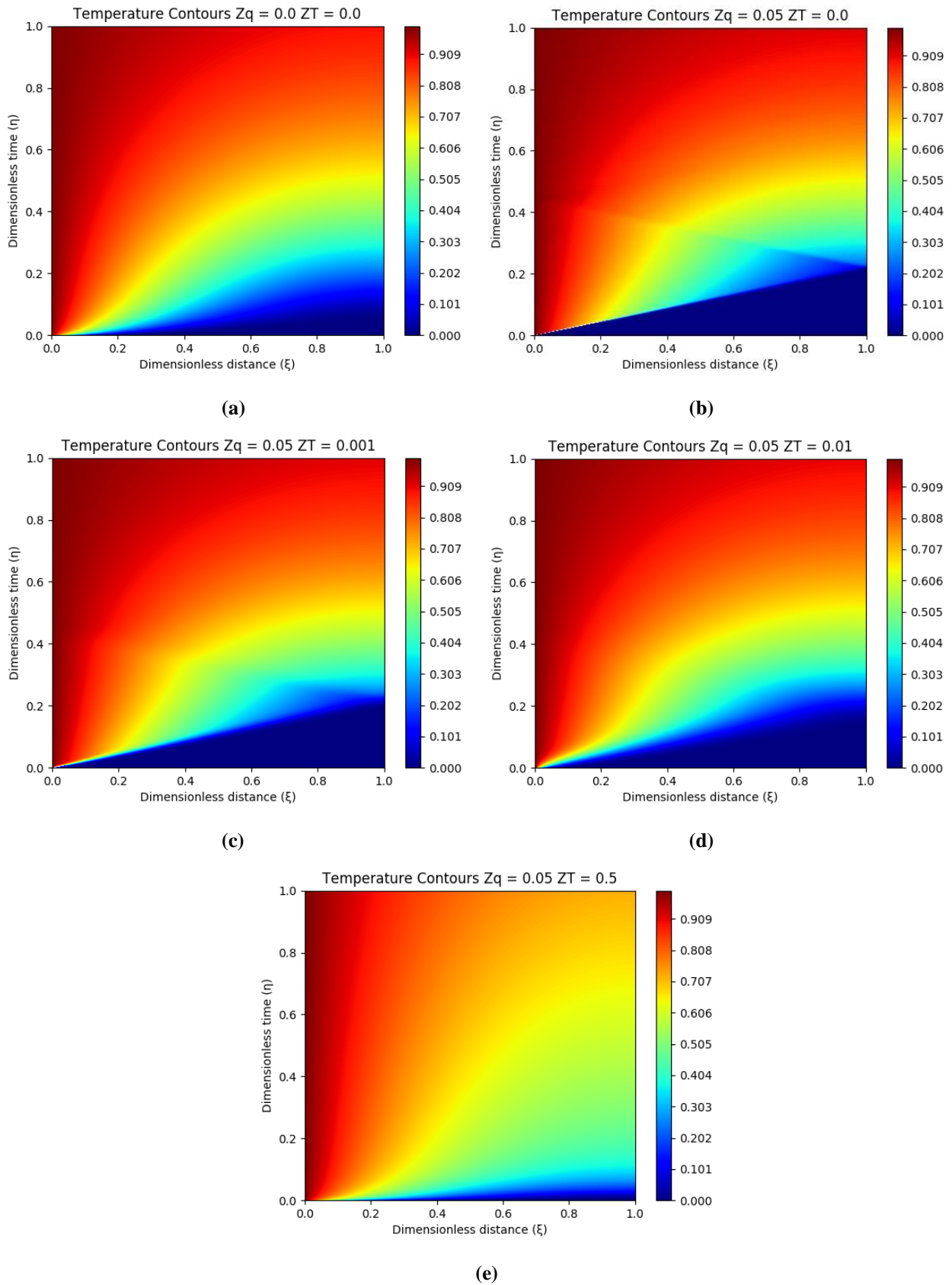


**Figure 10.** Case-2 Temperature contours, (a) Diffusion model  $Z_q = Z_T = 0$ , (b) CV model  $Z_T = 0$ , (c) DPL model  $Z_T = 0.001$ , (d) DPL model  $Z_T = 0.01$ , (e) DPL model  $Z_T = 0.5$ .

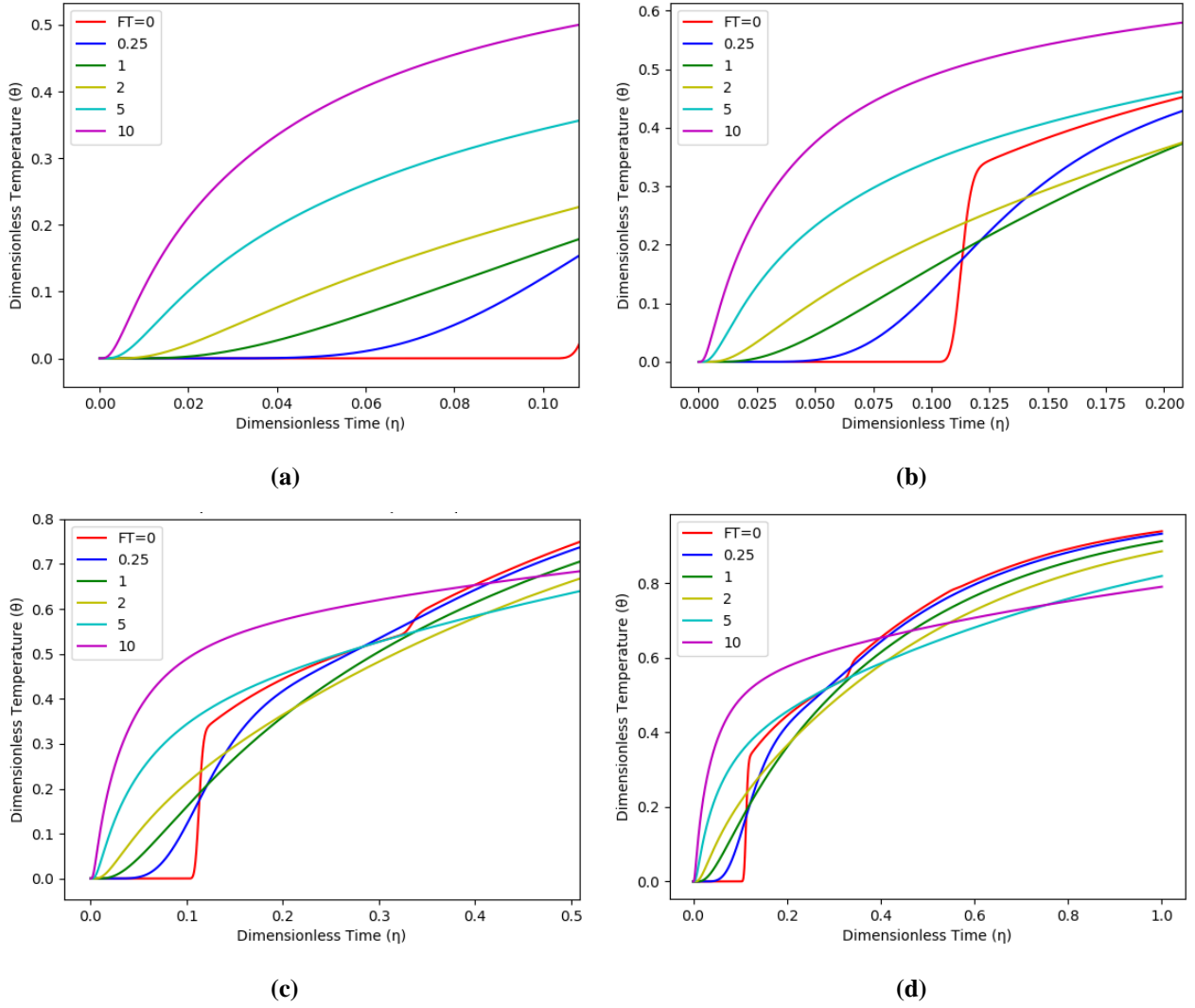


**Figure 11.** Case-2 Temperature variation at  $\xi = 0.5$  for different  $F_T$ , (a) up to  $\eta = 0.1$ , (b) up to  $\eta = 0.2$ , (c) up to  $\eta = 0.5$  and (d) up to  $\eta = 1$ .

the DPL model with  $Z_T = 0.5$ , Fig. 9 (c) and overtakes at  $\eta = 0.454$  as shown in Fig. 9 (d). This lag in heat propagation across the thin layer is caused by the large value of relaxation time  $Z_T = 0.5$  and the other model marching towards steady state are shown in Fig. 9 (e-g). The CV model first reaches a steady state at time  $\eta = 1.212$  then the diffusion model reaches a steady state at time  $\eta = 1.286$  and finally DPL model with  $Z_T = 0.5$  reaches a steady state at  $\eta = 4.122$  as shown in Fig. 9 (h).

### Case-2: Temperature contours

The temperature contours are plotted for different conditions, diffusion model  $Z_q = Z_T = 0$ , CV model  $Z_T = 0$ , DPL model  $Z_T = 0.001$ , DPL model  $Z_T = 0.01$  and DPL model  $Z_T = 0.5$  as shown in Fig. 10 (a-e) respectively. In diffusion model there is no lag in heat flux.  $Z_q = 0$ , and temperature gradient,  $Z_T = 0$ . The response between applied heat flux to the temperature gradient is instantly obtained and no collision occurs anywhere across the thin layer. The immediate response

of temperature gradient against the applied heat flux causes smooth conduction of heat across the thin layer for the diffusion model and the temperature contours from  $\eta = 0$  to  $\eta = 1$  is shown in Fig. 10 (a). Whereas in Fig. 10 (b), the evidence of collision is clearly shown as the triangular contours with sharp corners for the CV model with relaxation time  $Z_q = 0.5$  and  $Z_T = 0$ . The first collision of the thermal wave occurs at the right side boundary at  $\xi = 1$  and  $\eta = 0.214$  then it follows reverse propagation and reaches the left side boundary at  $\eta = 0.454$  with the second collision. After the second collision the temperature decreases and the CV model marching towards a steady-state without any further collision. Fig. 10 (c) and Fig. 10 (d) are the shreds of evidence of vanishing sharp corners and the thin layer follows DPL mode of heat conduction with  $Z_T = 0.001$  and  $Z_T = 0.01$  respectively.

It is noted that, from Fig. 10 (a-e), the DPL mode of heat conduction is entirely different from the diffusion model and CV model. The maximum temperature zone is nearer to the left boundary at  $\xi = 0$  in case of DPL model with

$Z_T = 0.5$  as shown in Fig. 10 (e). Whereas in the diffusion model, Fig. 10 (a), the maximum temperature zone uniformly distributed towards the right side of the boundary. This is due to the presence of both relaxation time  $Z_q$  and  $Z_T$ , decreases the response between given heat flux and temperature gradient. In the DPL model, the heat propagates slowly and reaches a steady-state after diffusion model and the CV model. For example, take gas turbine blade, the ceramic thin coating are used as thermal barriers with thermal diffusivity of  $\alpha = 1.16 \times 10^{-7} \text{ m}^2/\text{s}$ , coating thickness of  $x = 1 \text{ }\mu\text{m}$ , initial all the points the temperature is assumed as 303 K, one side of the blade is suddenly exposed to a temperature of 373 K. After time  $t \approx 9 \text{ }\mu\text{s}$ , at the center of the thin layer  $x = 0.5 \text{ }\mu\text{m}$ , the temperature becomes  $T \approx 317 \text{ K}$  for DPL mode of heat transfer. Whereas, for the same condition the temperature becomes  $T \approx 307 \text{ K}$  for CV model and  $T \approx 310 \text{ K}$  for Fourier model. The Fourier model and CV model reaches steady state faster than the DPL model due to the dual relaxation time responses.

### Case-2: Temperature variation at the center of the layer $\xi = 0.5$

The temperature variation at the center of the thin layer  $\xi = 0.5$  for different values of  $F_T$  from time  $\eta = 0$  to  $\eta = 1$  are shown in Fig. 11 (a-d). From Fig. 11 (a) it is noted that, the CV model  $F_T = 0$ , the temperature remains in the initial state,  $\theta = 0$ , up to  $\eta = 0.1$ . Whereas in the case of diffusion and DPL model,  $F_T > 0$ , the temperature at the center of the layer varies earlier than the CV model similar to case-1. At  $\eta = 0.114$  and  $F_T = 0$ , the thermal wave from the left side of the boundary meets the center of the layer and propagates without any collision at  $\xi = 0.5$ . The rise in temperature shown in Fig. 11 (b) for  $F_T = 0$  is the immediate response of temperature gradient with the absence of  $\tau_T$ . At  $\eta = 0.2$ , the temperature at the center of the layer for the CV model and DPL model are greater than the diffusion model. The second rise in temperature, at  $\eta = 0.342$  as shown in Fig. 11 (c), for the CV model, is happened due to the first collision occurs in the right side boundary and reverse propagation of thermal wave towards the left side boundary. At  $\eta = 0.5$ , the temperature at the center of the layer reduces for  $F_T > 1$  and increase for  $F_T < 1$  compared to the diffusion model  $F_T = 1$ . When the time moves on and becomes  $\eta = 1$ , the temperature variation is shown in Fig.11 (d) and DPL model with  $F_T = 10$  the temperature further decreases than the that of DPL model with  $F_T = 5$ . From Fig. 11 (d), it is noted that when the conduction number  $F_T$  increases the temperature decreases after time  $\eta = 1$  and when  $F_T$  decreases the temperature increases after time  $\eta = 1$ .

## CONCLUSION

The finite element model for dual phase-lag heat conduction across a thin layer is developed successfully to predict the temperature when it is subjected to two cases, case-1 constant temperature at both sides and case-2 left side constant temperature and right side insulated condition. The developed code is executed in Python 3.6 and the obtained results are validated with analytical, numerical, and experimental results with excellent agreement. Uniquely in this work, a comparative study of diffusion mode, CV mode, and DPL mode of heat conduction across the thin layer is examined numerically from transient to steady-state. The temperature contours are plotted for all three conditions and the way it propagates differently through the thin layer is clearly shown. Further, the temperature variation at the center of the layer, at which collision occurred, is predicted and the speed of the thermal wave, infinite in the Fourier diffusion model and finite in both single and dual-phase lag, is examined under transient to steady-state condition.

The temperature contours for different  $z_q$  and  $z_T$  are plotted and revealed the way of diffusion model with  $z_q = z_T = 0$ , the CV model with  $z_T = 0$ , and DPL model  $z_q > 0$  and  $z_T > 0$  follows a different way. Also, the temperature variation at the center of the layer is analyzed for both the cases. It is found that, the diffusion model with the conduction number  $F_T = 1$  reaches steady state first at time  $\eta = 0.432$ , CV model and DPL model with  $F_T < 1$  reaches steady state second at time  $\eta = 0.568$  and DPL mode with  $F_T > 1$  reaches steady-state finally at  $\eta = 2.468$ .

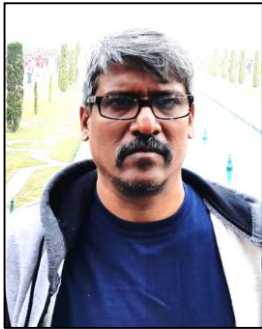
## REFERENCES

- Al-Nimr M. A., Naser S. Al-Huniti, 2000, Transient Thermal Stresses In A Thin Elastic Plate Due To A Rapid Dual-Phase-Lag Heating, *Journal of Thermal Stresses*, 23, 8, 731-746.
- Antaki P. J., 1998, Solution for non-Fourier dual phase lag heat conduction in a semiinfinite slab with surface heat flux, *International Journal of Heat and Mass Transfer*, 41, 14, 2253-2258.
- Cattaneo C., 1958, Sur une forme de l'equation de la chaleur eliminant la paradoxe d'une propagation instantanee, *Compt. Rendu*, 247, 431-433.
- Dhanaraj S. N., Karthikeya Sharma T., Amba Prasad Rao G., and Madhu Murthy K., 2019, Numerical Technique for Resolving the Dual Phase Lag Heat Conduction in Thin Film Metal, *Heat Transfer Engineering*, 41, 6-7, 665-675.

- Elsayed-Ali H. E., Juhasz T., Smith G. O., and Bron W. E., 1991, Femtosecond thermorefectivity and thermotransmissivity of polycrystalline and single-crystalline gold films, *Physical Review B*, 43, 5, 4488-4491.
- Fong E. and Lam T. T., 2014, Asymmetrical collision of thermal waves in thin films: An analytical solution, *International Journal of Thermal Sciences*, 77, 55-65.
- Fujimoto J. G., Liu J. M., Ippen, E. P. and Bloembergen, N., 1984, Femtosecond Laser Interaction with Metallic Tungsten and Nonequilibrium Electron and Lattice Temperatures, *Physical Review Letters*, 53, 19, 1837-1840.
- Hector L. G., Kim W. S. and Özisik M. N., 1992, Hyperbolic heat conduction due to a mode locked laser pulse train, *International Journal of Engineering Science*, 30, 12, 1731-1744.
- Körner C. and Bergmann H. W., 1998, The physical defects of the hyperbolic heat conduction equation, *Applied Physics A*, 67, 4, 397-401.
- Lam T. T. and Fong E., 2011, Heat diffusion vs. wave propagation in solids subjected to exponentially-decaying heat source: Analytical solution, *International Journal of Thermal Sciences*, 50, 11, 2104-2116.
- Lewandowska M. and Malinowski L., 2006, An analytical solution of the hyperbolic heat conduction equation for the case of a finite medium symmetrically heated on both sides, *International Communications in Heat and Mass Transfer*, 33, 1, 61-69.
- Li J., Cheng P., Peterson G. P. and Xu J. Z., 2005, Rapid Transient Heat Conduction In Multilayer Materials With Pulsed Heating Boundary, *Numerical Heat Transfer, Part A: Applications*, 47, 7, 633-652.
- Liu K. C., and Cheng P. J., 2006, Numerical Analysis for Dual-Phase-Lag Heat Conduction in Layered Films, *Numerical Heat Transfer, Part A: Applications*, 49, 6, 589-606.
- Majumdar A., 1993, Microscale Heat Conduction in Dielectric Thin Films, *Journal of Heat Transfer*, 115, 1, 7-16.
- Mitra K., Kumar S., Vedevarz A., and Moallemi M. K., 1995, Experimental Evidence of Hyperbolic Heat Conduction in Processed Meat, *Journal of Heat Transfer*, 117, 3, 568-573.
- Python 3.6.3, <https://www.python.org/>
- Qiu T. Q., and Tien C. L., 1992, Short-pulse laser heating on metals, *International Journal of Heat and Mass Transfer*, 35, 3, 719-726.
- Reddy J. N., 2015, *An Introduction to the Finite Element Method*, McGraw Hill Education (India) Private Limited, New Delhi.
- Siva Prakash G., Sreekanth Reddy S., Sarit K. Das, Sundararajan T., and Seetharamu K. N., 2000, Numerical Modelling Of Microscale Effects In Conduction For Different Thermal Boundary Conditions, *Numerical Heat Transfer, Part A: Applications*, 38, 5, 513-532.
- Tan Z. M., and Yang W. J., 1997, Heat transfer during asymmetrical collision of thermal waves in a thin film, *International Journal of Heat and Mass Transfer*, 40, 17, 3999-4006.
- Tan Z. M., and Yang, W. J., 1997, Non-Fourier Heat Conduction in a Thin Film Subjected to a Sudden Temperature Change on Two Sides, *Journal of Non-Equilibrium Thermodynamics*, 22, 1, 75.
- Tang D., Araki N., and Yamagishi N., 2007, Transient temperature responses in biological materials under pulsed IR irradiation, *Heat and Mass Transfer*, 43, 6, 579-585.
- Tang D. W., and Araki N., 2000, Non-fourier heat conduction behavior in finite mediums under pulse surface heating, *Materials Science and Engineering: A*, 292, 2, 173-178.
- Torii S., and Yang W. J., 2005, Heat transfer mechanisms in thin film with laser heat source, *International Journal of Heat and Mass Transfer*, 48, 3, 537-544.
- Tzou D. Y., 1995, Experimental support for the lagging behavior in heat propagation, *Journal of Thermophysics and Heat Transfer*, 9, 4, 686-693.
- Tzou D. Y., 1995, The generalized lagging response in small-scale and high-rate heating, *International Journal of Heat and Mass Transfer*, 38, 17, 3231-3240.
- Tzou D. Y., 1995, A Unified Field Approach for Heat Conduction From Macro- to Micro-Scales, *Journal of Heat Transfer*, 117, 1, 8-16.
- Tzou D. Y., 2014, *Macro- to Microscale Heat Transfer: The Lagging Behavior*, pp. 25-56, Wiley Online Library.
- Vernotte P., 1958, Les paradoxes de la theorie continue de l'equation de la chaleur, *Compt. Rendu*, 246, 3154-3155.
- Yuvaraj R., and Senthil Kumar D., 2020, Numerical simulation of thermal wave propagation and collision in thin film using finite element solution, *Journal of Thermal Analysis and Calorimetry*, 142, 6, 2351-2369.



**R. YUVARAJ** is an Assistant Professor, Department of Mechanical Engineering, Sona College of Technology, Salem, Tamilnadu, India. He received his B.E. Mechanical Engineering degree from Government College of Engineering Salem, Periyar University, Salem, Tamilnadu, India, in the year 2004. He obtained his M.E. Thermal Engineering degree from Government College of Engineering Salem, Anna University, Chennai, Tamilnadu, India, in the year 2012. He has submitted his Ph.D thesis to Anna University, Chennai, Tamilnadu, India. His research focuses on macro-, micro- and nano-scale heat transfer, dropwise condensation, thin film preparation for superhydrophobicity, defrosting on superhydrophobic surface, droplet condensation modeling and simulations. He currently teaches “Applied Thermodynamics, Python Programming and Problem Solving” courses in Sona College of Technology, Salem, Tamilnadu, India.



**Dr. D. SENTHILKUMAR** is a Professor and Head of Department of Mechanical Engineering, Sona College of Technology, Salem, Tamilnadu, India. He received his B.E. Mechanical Engineering degree from Annamalai University, Tamilnadu, India, in the year 1995. He obtained his M.E. Thermal Power Engineering degree from Annamalai University, Tamilnadu, India, in the year 1997. He obtained his Ph.D degree from Indian Institute of Technology Roorkee, Uttarakhand, India. His research focuses on heat transfer, dropwise condensation, thin film preparation for superhydrophobicity, defrosting on superhydrophobic surface, pool boiling heat transfer, vaporization bio-fuel droplet, flow visualization, alternative fuels, double diffusive mixed convection, and moisture transport. He received grants from AICTE India, MHRD-ISTE India, and filed a Patent “A method surface texture of copper for the enhancement of dropwise condensation”.



## ÇİFT KABUK CEPHE SİSTEMİNİN BİNA ISIL PERFORMANSINA ETKİSİNİN DENEYSSEL VE SAYISAL OLARAK İNCELENMESİ

**Selin HÜLAGÜ\***, **Türkan GÖKSAL ÖZBALTA\*\*** ve **Tahsin BAŞARAN\*\*\***

\*İstanbul Teknik Üniversitesi İnşaat Fakültesi İnşaat Mühendisliđi Bölümü  
34467 Sarıyer/İstanbul, hulaguselin@itu.edu.tr, ORCID: 0000-0002-2864-3062

\*\*Ege Üniversitesi Mühendislik Fakültesi İnşaat Mühendisliđi Bölümü  
35040 Bornova/İzmir, turkan.ozbalta@ege.edu.tr, ORCID: 0000-0001-5195-0741

\*\*\*İzmir Yüksek Teknoloji Enstitüsü, Mimarlık Fakültesi Mimarlık Bölümü  
35430 Urla/İzmir, tahsinbasaran@iyte.edu.tr, ORCID: 0000-0003-0988-9355

(Geliş Tarihi: 15.07.2020, Kabul Tarihi: 21.02.2021)

**Özet:** Bu çalışmada, çift kabuk ve geleneksel tek kabuk cephe sistemlerindeki ısı transferi zamana bađlı tek boyutlu yaklaşımla ele alınarak, deneysel ve sayısal olarak incelenmiş ve cephelerin bina enerji performansına özellikle de ısıtma enerjisine etkisi araştırılmıştır. Bu kapsamda tek kabuk ve kutu tipi tampon bölge kullanımındaki çift kabuk cephelerdeki ısı transferinin hesaplanması için bölgesel analiz yöntemi aracılığı ile kullanıcı davranışı ve alüminyum doğrama elemanı etkisi dikkate alınarak matematiksel model kurulmuş ve kurulan model deneysel olarak doğrulanmıştır. Deneysel çalışma Ege Üniversitesi İnşaat Mühendisliđi Bölümü binasının güney cephesinde yer alan, tek kabuk ve çift kabuk cephe kuruluşlarına sahip ofis mekanlarında 2017 Ocak ayı içerisinde ölçümler alınarak gerçekleştirilmiştir. Ardından, doğrulanan model, İzmir İli için, yıl içerisinde meydana gelen ısı transferini aylık ortalama günlük zaman dilimlerinde incelemek üzere kullanılmıştır. Akdeniz ikliminin hüküm sürdüğü İzmir İlinin 10 yıllık ortalama iklim verileri kullanılarak, tek kabuk ve çift kabuk cephe sistemlerinde ısı performansını deđiştiren yıl içerisinde iklime bađlı olarak araştırılmıştır. Çift kabuk cephelerin ısı yalıtımı işlevini görenek iç ortamda meydana gelebilecek çok yüksek ve çok düşük sıcaklık deđerlerini dengelediđi, dolayısıyla deđişen dış ortam koşullarına karşın iç ortamda konforun sağlanmasına katkıda bulunduğu görülmüştür.

**Anahtar Kelimeler:** Çift kabuk cephe, Tek kabuk cephe, Tampon bölge, Isı transferi, Enerji verimliliđi.

## EXPERIMENTAL AND ANALYTICAL EXAMINATION OF THE EFFECT OF DOUBLE SKIN FAÇADE SYSTEM ON BUILDING THERMAL PERFORMANCE

**Abstract:** In this study, heat transfer in conventional single skin façade and double skin façade system was studied experimentally and numerically by using one dimensional time dependent approach and the effects of the façade systems on building energy performance especially heating energy was investigated. In this context, a mathematical model considering user behavior and window aluminum frame element effect was build by zonal analysis method to calculate the heat transfer in single and box type closed cavity double skin façade systems, and build model was experimentally verified. Experimental study was conducted in office spaces having single and double skin façade systems in Ege University, Civil Engineering Building's south façade in January 2017. Next, verified model was used to study the heat transfer in the façade systems for İzmir's climatic condition by using monthly average daily data. The change in thermal performance of single and double skin façade systems due to the climatic condition during a year was investigated by using the 10 year average climate data of İzmir (Mediterranean climate). It was found that double skin façade system acts as an insulator preventing extreme indoor temperature values, thus contributing to the indoor comfort level against changing outdoor conditions.

**Keywords:** Double skin façade, Single skin façade, Closed cavity, Heat transfer, Energy efficiency.

### SEMBOLLER

$A_{al}$	Alüminyum yüzey alanı [ $m^2$ ]
$A_c$	Cam yüzey alanı [ $m^2$ ]
$c_p$	Sabit basınçta havanın özgül ısısı [ $J/kg^{\circ}C$ ]
ÇKC	Çift kabuk cephe
EPS	Polistiren köpük
$g$	Yerçekimi ivmesi [ $m/sn^2$ ]
$h_a$	Ara boşluk ısı taşınım katsayısı [ $W/m^2^{\circ}C$ ]
HAD	Hesaplamalı akışkanlar dinamiđi

### HOBO Veri toplayıcılar

$h_r$	Dış kabuk ile iç kabuk arasındaki ısı radyasyon katsayısı [ $W/m^2^{\circ}C$ ]
$I_g$	Yatay yüzeye gelen güneş ışınımı [ $W/m^2$ ]
$k_a$	Alüminyum ısı iletim katsayısı [ $W/mK$ ]
$k_c$	Cam ısı iletim katsayısı [ $W/mK$ ]
$k_h$	Hava ısı iletim katsayısı [ $W/mK$ ]
$L$	Ara boşluk genişliđi [ $m$ ]
$Nu$	Nusselt sayısı [ $=hL/k$ ]
$Q_{g,çk}$	Çift kabuk cephe güneş kaynaklı ısı kazanımı [ $W$ ]

$Q_{g,tk}$	Tek kabuk cephe güneş kaynaklı ısı kazanımı [W]
$Q_{isi,çk}$	Çift kabuk cephe iç yüzey ile dış ortam sıcaklık değerleri arasındaki sıcaklık farkı dolayısıyla meydana gelen ısı transfer hızı [W]
$Q_{isi,tk}$	Tek kabuk cephe iç yüzey ile dış ortam sıcaklık değerleri arasındaki sıcaklık farkı dolayısıyla meydana gelen ısı transfer hızı [W]
$Q_i$	Varlık kaynaklı iç ortam ısı kazanımları [W]
$Ra_L$	Rayleigh sayısı [= $(g\beta(T_2-T_1)L^3/(\nu\alpha))$ ]
$T_a$	Ara boşluk sıcaklığı [ $^{\circ}C$ ]
$T_{çk,al}$	Tek kabuk cephe kuruluşundaki alüminyum iç yüzey sıcaklığı [ $^{\circ}C$ ]
$T_{çk,c}$	Çift kabuk cephe kuruluşundaki cam iç yüzey sıcaklığı [ $^{\circ}C$ ]
$T_d$	Dış ortam sıcaklığı [ $^{\circ}C$ ]
$T_{dk}$	Dış kabuk iç yüzey sıcaklığı [ $^{\circ}C$ ]
$T_i$	İç ortam sıcaklığı [ $^{\circ}C$ ]
$T_{i,çk}$	Çift kabuk cepheye sahip mekan iç ortam sıcaklığı [ $^{\circ}C$ ]
$T_{i,tk}$	Tek kabuk cephe kuruluşu iç mekan sıcaklığı [ $^{\circ}C$ ]
$T_{ik}$	İç kabuk dış yüzey sıcaklığı [ $^{\circ}C$ ]
TKC	Tek kabuk cephe
$T_{tk,al}$	Tek kabuk cephe kuruluşundaki alüminyum iç yüzey sıcaklığı [ $^{\circ}C$ ]
$T_{tk,c}$	Tek kabuk cephe kuruluşundaki cam iç yüzey sıcaklığı [ $^{\circ}C$ ]
$U_{al}$	Alüminyum kesit ısıl geçirgenliği [ $W/m^2^{\circ}C$ ]
$U_c$	Cam kesit ısıl geçirgenliği [ $W/m^2^{\circ}C$ ]
$U_{dk}$	Dış kabuk modifiye edilmiş toplam ısı transferi katsayısı [ $W/m^2^{\circ}C$ ]
$U_{ik}$	İç kabuk modifiye edilmiş toplam ısı transferi katsayısı [ $W/m^2^{\circ}C$ ]
$w$	Cephe yüksekliği [m]
$W_i$	Aydınlatma elemanı/bilgisayar kullanımı kaynaklı iç ortam ısı kazanımları [W]
$\alpha$	Havanın ısıl yayılım katsayısı [ $m^2/sn$ ]
$\alpha_{al}$	Alüminyum yutuculuk değeri
$\alpha_{çc}$	Çift cam yutuculuk değeri
$\alpha_{tc}$	Tek cam yutuculuk değeri
$\beta$	Havanın ısıl genişleme katsayısı [ $1/K$ ]
$\nu$	Havanın kinematik viskozitesi [ $m^2/sn$ ]
$\rho$	Ara boşluk havasının yoğunluğu [ $kg/m^3$ ]
$\tau_{çc}$	Çift cam geçirgenlik değeri
$\tau_{tc}$	Tek cam geçirgenlik değeri

## GİRİŞ

Bina kabuğunun başlıca bileşeni olan cepheler iç ortam ile dış ortam arasında etkileşimin kontrolü ve iç ortam konfor koşullarının korunması işlevleri nedeniyle bina enerji tüketiminde önemli bir role sahiptir. Ancak geleneksel cephe kuruluşlarında havalandırma, aydınlatma ve sıcaklık gibi faktörler bakımından iç mekanda ısıl ve görsel konfor koşullarının sağlanabilmesi için yüksek enerji tüketimine gereksinim duyulmaktadır (Ghaffarianhoseini *vd.*, 2016, Shameri *vd.*, 2011). Bu kapsamda çözüm olarak geliştirilen çift kabuk cephe sistemleri, iç ortam ve dış ortam arasındaki etkileşimi kontrol ederek, doğal havalandırma ve doğal aydınlatmayı olanaklı kılanın yanı sıra bina ısıtma/soğutma enerji gereksinimini azaltmada etkili yöntemlerden biri olarak görülmektedir (Shameri *vd.*,

2011). Kullanım alanı giderek yaygınlaşan çift kabuk cepheler, yönlenme, bina geometrisi, havalandırma sistemi, güneş korunumu ve iklimsel koşullar gibi parametrelere bağlı olarak tasarlanmakta olup, binada ısı ve ses yalıtımının yanında özellikle doğal havalandırma ve aydınlatmayı olanaklı kılarak, bina performansına bütüncül olarak etki etmektedir.

Çift kabuk cephe sistemleri pek çok araştırmacı tarafından tanımlanmış ve incelenmiştir. Bu kapsamda, çift kabuk cephe sistemi, binanın mevcut cephesinin önüne genellikle saydam olan ikinci bir cephe yerleştirilmesi ile oluşan özel bir bina kabuğu tipi olarak tanımlanmaktadır (Safer *vd.*, 2005). Pomponi *vd.* (2016), çift kabuk cephe sistemini, iç kabuğu oluşturan bina ana cephesi ve dış cam kabuktan meydana gelen, ara hava boşluğu ile birbirinden ayrılmış bir hibrit sistem olarak tanımlamaktadır. Boake *vd.* (2003) ise çift kabuk cepheyi çeşitli hava koşullarına dinamik olarak karşılık veren ve bünyesinde gölgeleme, doğal havalandırma, ısı yalıtım elemanlarını bütünleştirebilen dış duvar tasarımı olarak tanımlamaktadır. Ara boşluğu tampon bölge işlevi gören kutu tipi çift kabuk cephe sistemindeki ısı transferinin hesaplanmasında, dikey boşluktaki (kavite) doğal taşınım probleminin incelenmesi de gerekir. Bu kapsamda Saury *vd.* (2011), ısıtılan ve soğutulan iki plaka arasındaki sıcaklık farkı ile plakaların emisivitesine bağlı olarak ara boşluktaki sıcaklık tabakalaşmasını, ara boşluktaki hava akışını ve Nusselt sayısının değişimini deneysel olarak incelemişlerdir. Sıcaklık tabakalaşmasında Rayleigh sayısının çok etkili olmadığını, ancak duvarın yatay ve dikey en/boy oranı ile emisivite değerlerinin etkili olduğunu belirtmişlerdir. Nastase *vd.* (2016), kutu tipi çift kabuk cephe sistemlerinde ısı transferi için önerdikleri tek boyutlu kararlı hal ısı transfer hesaplamasının kullanılabildiğini deneysel çalışma ile doğrularak ortaya koymuşlardır. İnan *vd.* (2016), kapalı bir kavitedeki doğal taşınımın gerçekleşen ısı transferi için, Rayleigh sayısının belirli bir aralığında geçerli olan, boyutsuz bir ısı transferi korelasyonunu, deneysel olarak doğruladıkları hesaplamalı akışkanlar dinamiği (HAD) yardımıyla geliştirmişlerdir. Bu çalışmalarda güneş ışınımı ihmal edilmiştir. Güneş ışınımı etkisinin göz önünde bulundurulduğu Yılmaz ve Çetintaş (2005)'in çalışmasında, kış dönemi için tek kabuk cephelerden olan ısı kaybının çift kabuk cepheye kıyasla %40 oranından daha fazla olduğu görülmüştür. Sanchez *vd.* (2016), güneş ışınımını da göz önünde bulundurarak, yaz ve kış dönemlerinde ara boşluktaki sıcaklık değişimlerini incelemiş ve çift kabuk ile tek kabuk cephelerdeki ısı transferlerini HAD analizi kullanarak kıyaslamışlardır. He *vd.* (2011), kış ve yaz koşullarında ara boşluğun havalandırılması veya tampon bölge olarak kullanılmasına bağlı olarak dış kabuktaki ısı kaybını, iç ortam ısı kazancını ve tek kabuk cepheye göre enerji tasarrufu oranlarını ortaya koymuştur. HAD yaklaşımının kullanıldığı bu çalışmalarda hız ve hafızaya dayalı bilgisayar gereksinimi ortaya çıkmaktadır. Bu kapsamda sayısal yöntemlerden "bölgesel yaklaşım", HAD modellerine kıyasla daha küçük ve daha kabuk çözülebilen denklemler oluşturulmasını olanaklı kılarak, daha az hesaplamayla daha hızlı sonuçlar elde edilmesini



sağlayan kullanışlı bir yöntem olarak karşımıza çıkmaktadır. HAD modelleri ve yığık modeller arasında kalan bölgesel yaklaşım, yığık modellere göre de daha doğru ve detaylı sonuçlar vermektedir (Jiru ve Haghghat, 2008). Jiru ve Haghghat (2008), çift kabuk cephelerin performansını analiz etmek için bölgesel yaklaşımda bulunarak ara boşluk yüksekliği, hava akım oranı, gölgeleme elemanı gibi faktörlerin dış ve iç sıcaklığa etkisi ile ilgili detaylı bilgi sunmuşlardır. Ayrıca Kuznik *vd.* (2011), Saelens (2002), Stec *vd.* (2005), Eicker *vd.* (2008), Lou *vd.* (2012) ile İnan ve Başaran (2019) gibi birçok araştırmacı da çift kabuk cephe sistemlerinin analizinde bölgesel yaklaşımı kullanarak uygunluğunu ortaya koymuşlardır. Bu bölgesel yaklaşımla çift kabuk cephelerdeki ısı transferinin analiz edilmesi daha hızlı ve kolay bir şekilde gerçekleştirilirken, elde edilen sayısal sonuçlar da deneysel sonuçlarla, kabul edilebilir sınırlar içerisinde, doğrulanabilmektedir. HAD yaklaşımında ise akış modellemesi ayrıntılı olarak gerçekleştirildiği için; akışa bağlı olan enerji denkleminin çözümü de, deneysel sonuçlarla doğrulandıktan sonra, daha hassas sonuçlar verebilmektedir. Buna karşılık, HAD yaklaşımı; zaman gerektiren, ayrıntılı modelleme ve bilgisayar kapasitesi ihtiyacı olan yoğun bir çalışmaya gereksinim göstermektedir. Çift kabuk cephe sistemlerinin ısı performanslarının bölgesel analiz yöntemiyle değerlendirildiği çalışmalar (Jiru *vd.* (2008), Kuznik *vd.* (2011), Saelens (2002), Stec *vd.* (2005), Eicker *vd.* (2008), Lou *vd.* (2012) ile İnan ve Başaran (2019)); birincil ve ikincil kabuktaki çerçeve elemanlarını sayısal analizlerine dahil etmemiş, cephelerin tamamen saydam elemanlardan oluştuğu varsayımıyla ilgili hesaplamaları gerçekleştirmişlerdir. Bununla birlikte, bölgesel analiz yönteminin uygulandığı söz konusu çalışmalar kapsamında kullanıcı davranışı etkisiyle meydana gelecek (örneğin; kullanıcı varlığı, aydınlatma elemanı kullanımı ve bilgisayar kullanımı) ısı kazanımları göz ardı edilmiştir. Bu çalışmada, çift kabuk cephelerin bina enerji performansına, özellikle de ısıtma enerjisine etkisinin araştırılması kapsamında literatürdeki sayısal analiz yöntemlerinden bölgesel analiz yöntemi tercih edilmiş, yapılan çalışmalardan farklı olarak bina cephelerinde seçilen malzeme özelinde ısı kayıplarını oldukça etkileyen çerçeve elemanları ve ayrıca öznel niteliğe sahip kullanıcı davranışı etkisi de göz önünde bulundurulmuştur. Geliştirilen matematiksel model, gerek literatürdeki analizler, gerekse çalışma kapsamındaki yaklaşım bağlamında, İzmir İli özelinde, yerinde alınan ölçüm sonuçları ile deneysel olarak doğrulanmıştır. Doğrulanmış model geliştirilerek çift

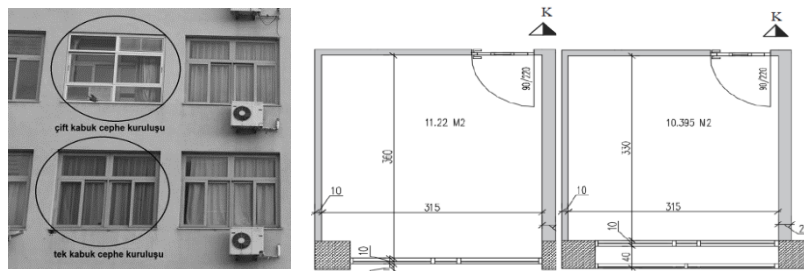
kabuk cephelerin ısı performansına etkisi hakkında çıkarımlarda bulunulmuş, bu kapsamda İzmir İli için çift kabuk cephe uygulamalarının ısıtma ve soğutma yüklerine olan etkisi yıl boyunca değerlendirilmiştir. Geliştirilen model, Erzurum iline uygulanarak çift kabuk cephelerin ısı transferine etkisi yıl boyunca değerlendirilmiş ve ayrıca bir başka çalışmada sunulmuştur (Hülagü *vd.*, 2018).

## DENEYSEL ÇALIŞMA

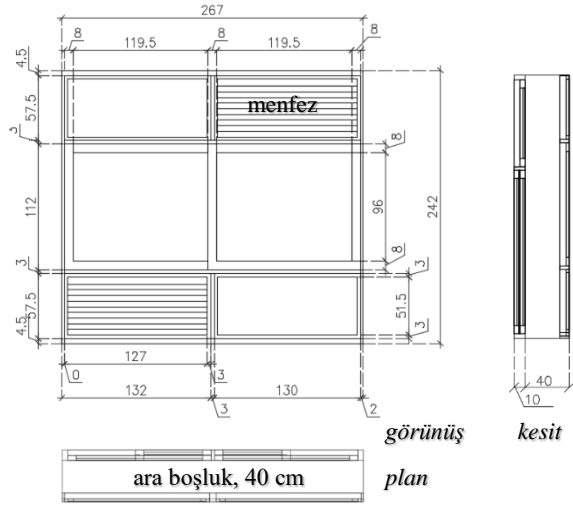
Kutu tipi tampon bölge kullanımında çift kabuk cephe kuruluşunun ısı performansı, İzmir İlinde deneysel çalışma ile incelenmiştir. Alan çalışması olarak belirlenen tek ve çift cephe kuruluşuna sahip mekanlarda ısı kayıp ve kazançları, deneysel olarak analiz edilmiş, matematiksel model sonuçları ile karşılaştırılarak değerlendirilmiştir.

### Deney Düzenegi

İzmir, Ege Üniversitesi İnşaat Mühendisliği Bölümü binasında yürütülen deneysel çalışma için, tek kabuk cephe (TKC) ve çift kabuk cephe (ÇKC) kurgusunun ayrı ayrı ele alınarak karşılaştırılacağı bir deneysel düzenleme yapılmıştır (Şekil 1a). Bu kapsamda binanın güney cephesinde bulunan tek ve çift kabuk cephe kuruluşuna sahip ofis mekanları (Şekil 1b ve c) cephelerin ısı performansını değerlendirmek üzere kullanılmıştır. Alan çalışmasının yapıldığı binada tüm cepheler tek kabuk kuruluşa sahiptir. Tek kabuk cepheye sahip ofis 11,22 m<sup>2</sup> kullanım alanı ve 44,88 m<sup>3</sup> hacmi olan, tek kullanıcıya sahip bir mekandır (Şekil 1b). Pencere elemanı alüminyum çerçeveli 12 mm hava dolgulu 2x4 mm çift düz camlı kuruluşa sahiptir. Cephede cam yüzey alanı 4,28 m<sup>2</sup> ve alüminyum çerçeve yüzey alanı ise toplam 1,31 m<sup>2</sup>'dir. Çift kabuk cephe kuruluşuna ve tek kullanıcıya sahip diğer ofis mekanı ise 2. katta, tek kabuklu cepheye sahip ofis mekanının üst katında bulunmaktadır. Mekan 10,39 m<sup>2</sup> kullanım alanına ve 41,58 m<sup>3</sup> hacme sahiptir (Şekil 1c). Çift kabuk cephe kuruluşu mevcut pencere kurgusunun 40 cm ara boşluk bırakacak şekilde içeri alınmasıyla oluşturulmuştur (Şekil 2). İkincil kabuk tek kabuk cepheyle özdeş, alüminyum çerçeveli 4+12+4 mm hava boşluklu çift camdır. Birincil cephe ise, alüminyum çerçeveli 4 mm tek cam ve doğal havalandırmaya katkı sağlayan çapraz konumlandırılmış alüminyum menfez pencere kurgusuna sahiptir. Birincil cephedeki cam yüzey alanı 3,57 m<sup>2</sup> ve alüminyum yüzey (menfez ve çerçeve eleman) 2,89 m<sup>2</sup>'dir.



Şekil 1. Deneysel çalışma mekanları a) Tek kabuk cephe ve çift kabuk cephe kuruluşuna sahip ofis mekanlarının dış görünüşü b) Tek kabuk kuruluşa sahip ofis mekan planı c) Çift kabuk kuruluşa sahip ofis mekan planı.



Şekil 2. Çift kabuk cephe pencere kurgusu, plan, kesit ve görünüş.

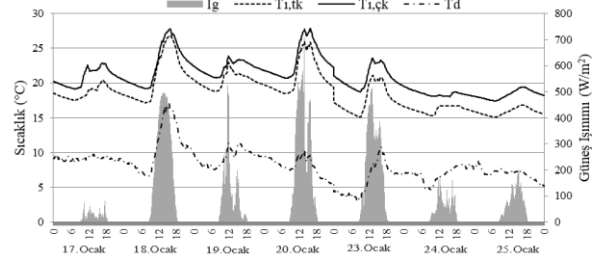
### Deneysel Ölçümler

Deneysel çalışmada, ofis mekanlarında 7 gün boyunca ölçümler alınmıştır. Hesaplamalarda kullanıcı etkisi de göz önünde bulundurulduğu için ölçümler 17.01-26.01.2017 tarihleri arasında hafta içi günlerinde yapılmıştır. Dış ortam sıcaklığı, yatay yüzeye gelen güneş ışınımı, rüzgar hızı ve yönü Davis Vantage Pro2 meteoroloji istasyonu ile ölçülmüş ve kayıt edilmiştir. Ofis ortam sıcaklığı birer HOBO sıcaklık ölçer ile ve çift kabuk cephe ara boşluğunda ise, farklı yüksekliklerdeki sıcaklık ölçümleri, 5 adet HOBO ile yapılmıştır. 10 dakika aralıklarla ölçüm verileri alınan cihazlara ilişkin bilgiler Tablo 1’de verilmiştir. Ayrıca ofis mekanlarında ısı kazancı bağlamında kullanıcı davranışları odaklı varlık, aydınlatma, ısıtıcı ve bilgisayar kullanımı da kayıt altına alınmıştır.

Tablo 1. Ölçüm aletlerinin özellikleri.

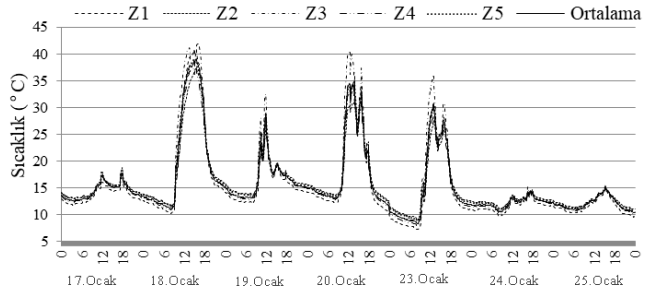
Ölçüm Aleti	Ölçüm Türü	Ölçüm Aralığı	Doğruluk
DAVIS Vantage PRO2	Dış sıcaklık	-40°- 65°	+/- 0,3°C
	Güneş ışınımı	0-1800 W/m <sup>2</sup>	+/- %5
	Rüzgar hızı	0-89 m/s	+/- 0,5m/s
	Rüzgar yönü	0°-360°	+/-3°
Onset HOBO	İç ortam ve ara boşluk sıcaklıkları	-20°- 70°	+/- 0,21°C

Şekil 3’de, dış ortam sıcaklığı ile birlikte güneş ışınım değerlerinin 7 gün için zamana bağlı ölçüm sonuçları yer almaktadır. Ayrıca, cephe özelliği ve iç ortam ısı kazanımlarına bağlı olarak değişiklik gösteren tek kabuk cepheye sahip mekan ( $T_{i,tk}$ ) ve çift kabuk cepheye sahip mekan ( $T_{i,çk}$ ) için iç ortam sıcaklık ölçümleri verilmiştir. Şekil 3’de görüldüğü üzere, özellikle gece saatlerinde mekanlar arası sıcaklık farkı artmakta, gündüz ise benzer sıcaklıklar izlenmektedir.



Şekil 3. Tek kabuk ( $T_{i,tk}$ ) ve çift kabuk ( $T_{i,çk}$ ) cephe kuruluşuna sahip mekan iç sıcaklıkları, dış ortam sıcaklığı ( $T_d$ ) ve yatay yüzeye gelen güneş ışınımı ( $I_g$ ) değerleri.

Çift kabuk cephe kuruluşu ara boşluk sıcaklık ölçümleri ikincil cepheye 10 cm uzaklıkta, üç farklı yükseklikteki 5 noktadan veri toplayıcılar (HOBO) ile gerçekleştirilmiştir. Birincil ve ikincil kabuktaki pencereler kapalı konumda tutulmuş, birincil cephedeki menfezler polistiren köpük (EPS) ile kapatılarak sızdırmaz hale getirilmiş, ara boşluğa hava giriş/çıkışı engellenmiştir. Ara boşlukta alınan ölçümler ve sonuçların ortalaması Şekil 4’de verilmiştir.



Şekil 4. Çift kabuk cephede ara boşluk ölçülen sıcaklık değerleri ve ortalama değeri.

Kullanıcıların ölçüm tarihleri süresince, gün içerisinde bilgisayar, aydınlatma ve ısıtıcı kullanma davranışlarını işaretledikleri çizelgelerde, sistemlerden en az biri kullanıldığında kullanıcı varlığı olduğu, hiçbir sistem kullanılmadığında ise kullanıcı varlığının olmadığı kabul edilmiştir (Hülagü, 2017).

### Ön Hesaplamalar

#### Cephe düzlemine etkiyen güneş ışınımın hesabı

Bir düzlem ile direkt güneş ışınımı arasındaki ilişki açılar aracılığıyla tanımlanabilir (Duffie ve Beckman, 2013). Dolayısı ile enlem, deklinasyon, eğim, yüzey azimut, güneş geliş ve zenit açıları elde edilmiştir. Aylık ortalama deklinasyon açısının hesaplanması için, güneş ışınımının Ocak ayı ortalama değerini veren 17 Ocak tarihi seçilmiştir (Klein, 1977). 17-26.01.2017 tarihleri arasında hafta içi 7 gün için yatay yüzeye gelen güneş ışınımından dik cepheye etkiyen ışınım hesaplanmıştır (Hülagü, 2017).

#### Dış ortam taşınım katsayısının hesaplanması

Çalışmada dış ortam dış yüzeydeki ısı taşınım katsayısı, Liu ve Harris (2007)’in rüzgâr yönü ve şiddetine bağlı olarak geliştirdiği formüller aracılığı ile hesaplanmıştır.

Çalışmada duvara etkiyen rüzgar hızına göre rüzgarüstü ve rüzgaraltı bölgeleri için ısı taşınım katsayısının elde edilmesine yardımcı iki denklem geliştirmişlerdir.  $V_r$  rüzgar hızı olmak üzere, Eş. 1 cephenin rüzgarüstü, Eş. 2 ise rüzgaraltı bölgeleri için ısı taşınım katsayısını vermektedir.

$$h_d = 6,31V_r + 3,32 \quad (1)$$

$$h_d = 5,03V_r + 3,19 \quad (2)$$

Belirlenen rüzgar etki açılarına göre, ölçüm süresince etkiyen rüzgarın; bina kesitinin rüzgarüstü ve rüzgaraltı bölgesinde olma durumu belirlenmiştir. Buna göre Eş. 1 ve 2 aracılığıyla, 10 dakikalık aralıklarla rüzgar yönü ve hızına bağlı olarak dış ortam yüzey ısı taşınım katsayıları hesaplanmıştır (Hülagü, 2017).

### Ara boşluk taşınım katsayısının hesaplanması

Çift kabuk ısı transfer analizinde, tampon bölge işlevi gören ara boşluk, doğal taşınımın meydana geldiği kapalı bir dörtgen hacim olarak değerlendirilmiştir. Ara boşluk ısı taşınım katsayısı hesabı ( $h_a$ ), Nusselt sayısı (Nu), havanın ısıl geçirgenliği ( $k_h$ ) ve ara boşluk genişliği (L) olmak üzere, 3 numaralı eşitlik yardımıyla hesaplanmıştır;

$$h_a = \frac{Nu k_h}{L} \quad (3)$$

Eş. 3'deki Nusselt sayısı, MacGregor ve Emery (1969)'nin geliştirdiği Eş. 4 aracılığıyla hesaplanmıştır:

$$Nu = 0,46 Ra_L^{1/3} \quad (4)$$

Eş. 4'deki Rayleigh ( $Ra_L$ ) sayısının hesaplanmasında; g yerçekimi ivmesi,  $\beta$  havanın ısıl genleşme katsayısı,  $T_{ik}$  iç kabuk dış yüzey sıcaklığı,  $T_{dk}$  dış kabuk iç yüzey sıcaklığı,  $\nu$  havanın kinematik viskozitesi ve  $\alpha$  havanın ısıl yayılım katsayısı olmak üzere, Eş. 5 kullanılmaktadır:

$$Ra_L = \frac{g \beta (T_{ik} - T_{dk}) L^3}{\nu \alpha} \quad (5)$$

Eş. 3 ve 5'deki havanın  $\beta$ ,  $\alpha$ ,  $\nu$  ve  $k$  değerleri belirlenirken ara boşluktaki 5 ölçüm noktasının ortalaması olan  $T_a$  ara boşluk sıcaklık değeri, Eş. 5'de dış kabuk ve iç kabuk ( $T_{ik}$  ve  $T_{dk}$ ) sıcaklık değerleri yerine ise iç ortam ve dış ortam ( $T_i$  ve  $T_d$ ) sıcaklık değerleri kullanılmıştır. Sonrasında iteratif yaklaşımla  $T_{ik}$  ve  $T_{dk}$  sıcaklıkları belirlenmiştir. Ara boşluk taşınım katsayısının zamana bağlı değişimi, (Hülagü, 2017) referansında verilmiştir.

### İç ısı kazanımlarının hesabı

Ofis mekanlarında, kullanıcı davranışı takibiyle iç ısı kazanımları da hesaplanmıştır. Kullanıcı varlığı, aydınlatma elemanı, bilgisayar ve ısıtma sistemi kullanımları, çizelgeler aracılığıyla kayıt altına alınmıştır. Ölçüm yapılan mekanlarda herhangi bir merkezi ısıtma-soğutma sistemi bulunmamakta sadece elektrikli ısıtıcılar

bulunmaktadır. Ölçüm süresince bu cihazlar kullanılmamıştır. Kullanıcıların varlık kaynaklı ( $Q_i$ ) ve aydınlatma elemanı/bilgisayar kullanımı kaynaklı ( $W_i$ ) iç ortam ısı kazanımları ise Tablo 2'de verilen değerler aracılığıyla hesaplanmıştır.

**Tablo 2.** Kullanıcı davranış türüne göre toplam ısı kazanımı (ASHRAE, 2009).

Davranış Türü	Enerji Transfer Hızı
Kullanıcı Varlığı	130 W
Aydınlatma Elemanı	12 W/m <sup>2</sup>
Bilgisayar	36 W

Tek kabuk cephe kuruluşuna sahip ofis kullanıcısı (1), ölçüm süresince 6 gün (17, 18, 19, 20, 23, 24.01.2017) ofisi aktif olarak kullanmış, 1 gün (25.01.2017) ise ofisi kullanmamıştır. Kullanıcı 1'in ofiste bulunduğu anlarda aydınlatma elemanı kullanımına çok ihtiyaç duymadığı, bilgisayarı aktif olarak kullandığı görülmektedir. Çift kabuk cephe kuruluşuna sahip ofis kullanıcısı (2), ölçüm süresince 3 gün (17, 18, 19.01.2017) ofisi kullanmış, ara boşluk ölçümleri pencere kapalı konumda alındığı ve odada güneş kırıcı (perde) olmadığı için, ofisin özellikle öğle/öğleden sonra çok sıcak olduğunu belirterek, 4 gün (20, 23, 24, 25.01.2017) ofisi kullanmayı tercih etmemiştir. Kullanıcı 2'nin ofiste bulunduğu anlarda, bilgisayarı aktif olarak kullanmadığı görülmektedir. Kullanıcının aydınlatma elemanı kullanımına bakıldığında ise 1. ve 3. gün kullanıldığı, güneş ışınım şiddetinin görece artmasına bağlı olarak (Şekil 3'de görüldüğü üzere) 2. gün kullanmadığı anlaşılmaktadır (Hülagü, 2017).

### TEORİK METOD

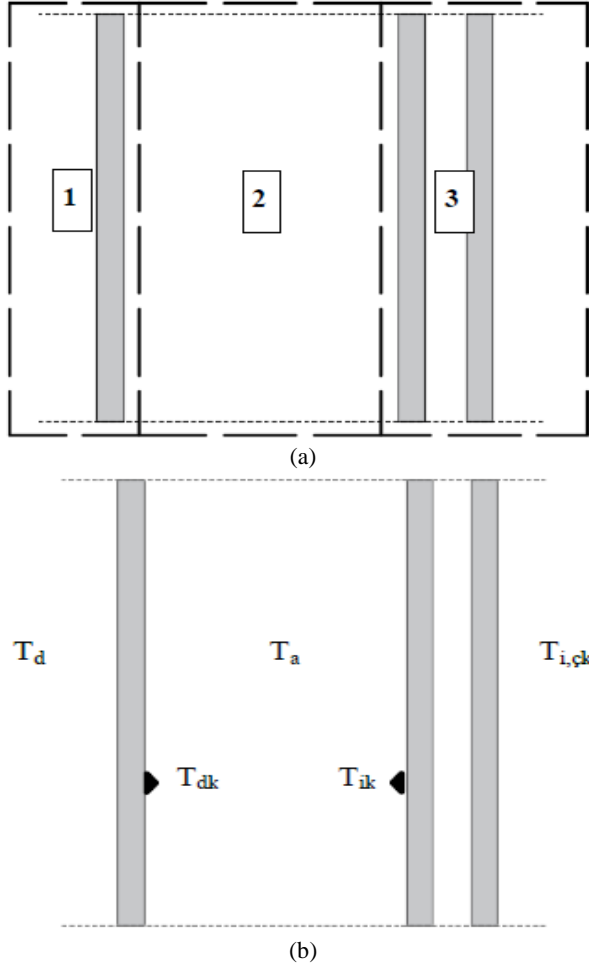
Tek ve çift kabuk cephe kuruluşlarındaki ısı transfer hızlarındaki değişimler karşılaştırılmış, önceki bölümde belirtilen ölçüm ve hesaplamalar da göz önünde bulundurularak tek ve çift kabuk cephe kuruluşundaki cam ve alüminyum iç yüzey sıcaklıkları ( $T_{tk,c}$ ,  $T_{tk,al}$  ve  $T_{çk,c}$ ,  $T_{çk,al}$ ) bulunmuştur. İç yüzey ile dış ortam sıcaklık değerleri arasındaki sıcaklık farkı dolayısıyla meydana gelen ısı transferi ( $Q_{tk,ısı}$ ,  $Q_{çk,ısı}$ ) ve güneş kaynaklı ısı kazanımı ( $Q_{tk,g}$ ,  $Q_{çk,g}$ ) hesaplanmıştır. Tablo 3'de malzemelerin yutuculuk, geçirgenlik ve ısı iletim katsayıları verilmiştir.

**Tablo 3.** Cephe malzemelerinin fiziksel özellikleri (Çengel, 2015).

Isı İletim Katsayısı (W/mK)	Alüminyum ( $k_a$ )	
	Cam ( $k_c$ )	0,92
	Hava ( $k_h$ )	0,025
Yutuculuk	Alüminyum ( $\alpha_{al}$ )	0,09
	Tek cam ( $\alpha_{tc}$ )	0,12
	Çift cam ( $\alpha_{çc}$ )	0,22
Geçirgenlik	Tek cam ( $\tau_{tc}$ )	0,83
	Çift cam ( $\tau_{çc}$ )	0,71

## Çift Kabuk Cephedeki Isı Transfer Hızının Belirlenmesi

Çift kabuk cephede ısı transferi hesaplanırken bölgesel analiz yapılmış ve cephe kurgusu; dış kabuk (1), ara boşluk (2) ve iç kabuk (3) olmak üzere 3 bölgeye ayrılmıştır (Şekil 5). Her bölge için ayrı enerji dengesi denklemleri yazılarak, meydana gelen ısı transferleri hesaplanmıştır.



Şekil 5. Çift kabuk cephe a) Çift kabuk cephe bölgelemesi b) Sıcaklık gösterimleri.

Şekil 5a'da belirtilen bölgelerdeki enerji dengeleri yazılarak; 3 bölge için sırasıyla Denklem 6, 8 ve 9'da verilen enerji dengeleri oluşturulmuştur. Denklemlerin ortak çözümüyle dış kabuk iç yüzey ( $T_{dk}$ ), iç kabuk dış yüzey ( $T_{ik}$ ) ve ara boşluk ( $T_a$ ) değerlerinin bulunması hedeflenmiştir (Şekil 5). Denklem çözümünde sadeleştirme yapmak ve yüzey türünden bağımsız bir  $T_a$  değeri elde etmek amacıyla, cam ve alüminyum yüzeyleri için tek boyutlu ısı transferi kabulü ile ortak çözüm yaparak; yüzeyler için  $T_{dk}$  ve  $T_{ik}$  değerlerinin olduğu kabul edilmiştir.

### Dış kabuktaki enerji dengesi

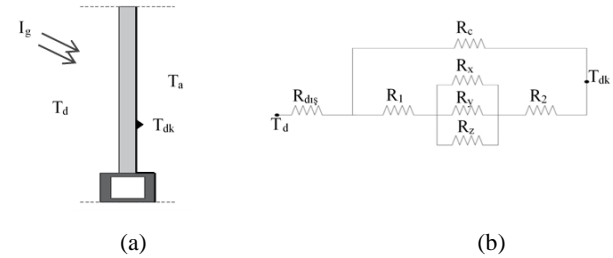
Dış kabuktaki enerji dengesi Eş. 6'da gösterilmiştir. Denklemden verilen  $\alpha_{tc}$  ve  $\alpha_{al}$  sırasıyla tek cam ve

alüminyum yutuculuk değerleri Tablo 3'den,  $A_{dk}$ ,  $A_{dk,c}$  ve  $A_{dk,c}$  sırasıyla dış kabuk toplam, dış kabuk cam ve dış kabuk alüminyum alanlarıdır ve yerinde ölçüm ile hesaplanmıştır (Hülügü, 2017).  $T_d$  dış ortam sıcaklığı deneysel olarak ölçülmüştür. Ara boşluk taşınım katsayısı ( $h_a$ ) yukarıda belirtildiği gibi hesaplanmış ve dış kabuk ile iç kabuk arasındaki ısı radyasyon taşınım katsayısı ( $h_r$ ) ise başlangıçta  $4 \text{ W/m}^2\text{°C}$  olarak kabul edilmiş; sonrasında ise belirlenen iç yüzey sıcaklık değerlerine göre değiştirilmiştir. Dış kabuk modifiye edilmiş toplam ısı transferi katsayısı  $U_{dk}$  ise Eş. 7 aracılığıyla hesaplanmıştır. Dış kabuk kesiti ve ısı diyagramı Şekil 6'da gösterilmiştir.

$$I_g \alpha_{tc} A_{dk,c} + I_g \alpha_{al} A_{dk,al} - U_{dk} A_{dk} (T_{dk} - T_d) - h_a A_{dk} (T_{dk} - T_a) - h_r A_{dk} (T_{dk} - T_{ik}) = 0 \quad (6)$$

$$U_{dk} = [R_{dış} + R_{dk}]^{-1} = \left[ \frac{1}{h_{dış}} + \left[ \frac{1}{R_{dk,al}} + \frac{1}{R_{dk,c}} \right]^{-1} \right]^{-1} \quad (7)$$

$$R_{dk,al} = R_1 + R_2 + R_3, \quad R_2 = \left[ \frac{1}{R_x} + \frac{1}{R_y} + \frac{1}{R_z} \right]^{-1}, \quad R_{dk,c} = \frac{L_c}{k_c} \quad (7a, b, c)$$



Şekil 6. 1. Bölge a) Dış kabuk kesiti b) Dış kabuk ısı direnç diyagramı.

### Ara boşluktaki enerji dengesi

Ara boşluktaki enerji dengesi,  $\rho$  ara boşluk havasının yoğunluğu,  $c_p$  sabit basınçta ara boşluk havasının özgül ısı,  $w$  cephe yüksekliği olmak üzere Eş. 8'de verilmiştir.

$$\rho w c_p \frac{dT_a}{dt} = h_a (T_{dk} - T_a) + h_a (T_{ik} - T_a) \quad (8)$$

### İç kabuktaki enerji dengesi

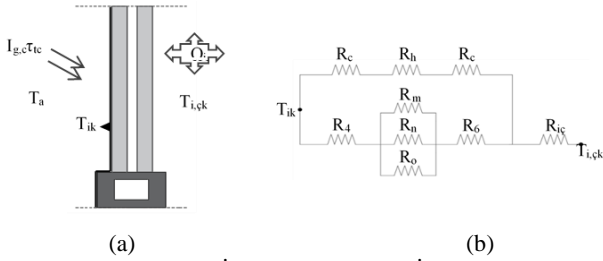
İç kabuktaki enerji dengesi Eş. 9'da gösterilmektedir.  $\tau_{tc}$  tek cam geçirgenlik değeri,  $\alpha_{cc}$  çift cam ve  $\alpha_{al}$  alüminyum yutuculuk değerleri Tablo 3'den alınmıştır.  $A_{ik}$ ,  $A_{ik,c}$ ,  $A_{ik,al}$ ; iç kabuk toplam, cam ve alüminyum alanları ölçülerek hesaplanmıştır. Çift kabuk cephe kuruluşu iç mekan sıcaklığı ( $T_{i,çk}$ ) deneysel olarak ölçülmüştür. Modifiye edilmiş toplam ısı transferi katsayısı ise Eş. 10 ile belirlenmiştir.  $Q_i$  ve  $W_i$  varlık ve elektrikli alet kullanımına bağlı iç ısı kazanımıdır. Dış kabuktan, dış kabuğun geçirgenlik değeri ( $\tau_{tc}$ ) oranında güneş ışınımı geçerek iç kabuğu etkileyecektir. Güneş ışınımı ( $I_{g,c}$ ) hesaplanırken, dış kabuk birim yüzeye gelen güneş ışınımı ( $I_g$ ), dış kabuktaki cam yüzdesine göre, alüminyum yüzey alanı da göz önünde bulundurularak hesaplanmıştır (Şekil 7).

$$I_{g,c} \tau_{tc} \alpha_{cc} A_{ik,c} + I_{g,c} \tau_{tc} \alpha_{al} A_{ik,al} - U_{ik} A_{ik} (T_{ik} - T_{i,\check{k}}) - h_a A_{ik} (T_{ik} - T_a) - h_r A_{ik} (T_{ik} - T_{dk}) + Q_i + W_i = 0 \quad (9)$$

$$U_{ik} = [R_{ik} + R_{i\check{k}}]^{-1} = \left[ \left[ \frac{1}{R_{ik,al}} + \frac{1}{R_{ik,c}} \right]^{-1} + \frac{1}{h_{i\check{k}}} \right]^{-1} \quad (10)$$

$$R_{ik,al} = R_4 + R_5 + R_6, \quad R_5 = \left[ \frac{1}{R_m} + \frac{1}{R_n} + \frac{1}{R_o} \right]^{-1},$$

$$R_{ik,c} = R_c + R_h + R_c = 2 \frac{L_c}{k_c} + \frac{L_h}{k_h} \quad (10a,b,c)$$



Şekil 7. 3. Bölge a) İç kabuk kesiti b) İç kabuk ısı direnç diyagramı.

Enerji dengesi eşitliklerinde (6, 8 ve 9); dış kabuk iç yüzey ( $T_{dk}$ ), ara boşluk ( $T_a$ ) ve iç kabuk dış yüzey ( $T_{ik}$ ) sıcaklıkları bilinmemektedir. 6, 8 ve 9 numaralı eşitliklerin ortak çözülmesiyle bu değerler bulunmuştur. Hesaplamalar, Eicker (2003)'in ayrıntılandığı yöntemin modifiye edilmesi ile gerçekleştirilmiş ve detaylı bir biçimde referans Hülagü (2017)'de verilmiştir. Buna göre 6 numaralı eşitlikten  $T_{dk}$  çekilirse;

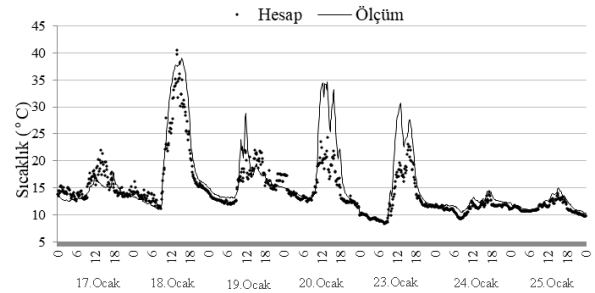
$$T_{dk} = \frac{I_g \alpha_{dk,c} A_{dk,c} + I_g \alpha_{dk,al} A_{dk,al} + U_{dk} A_{dk} T_d + h_a A_{dk} T_a + h_r A_{dk} T_{ik}}{U_{dk} A_{dk} + h_a A_{dk} + h_r A_{dk}} \quad (11)$$

bağıntısı elde edilir. Ara bölge sıcaklığı  $T_a$ , iç yüzeylerin ( $T_{dk}$  ile  $T_{ik}$ ) ortalama sıcaklığı olarak tanımlanmıştır.  $T_a$  değeri buna göre Eş. 11'de yerine konur. Böylece, sırasıyla, iç kabuk dış yüzey ( $T_{ik}$ ), buna bağlı olarak dış kabuk iç yüzey ( $T_{dk}$ ) ve bu değerlere bağlı olarak da ara boşluk ( $T_a$ ) sıcaklık değerleri hesaplanmıştır.  $T_{ik}$ ,  $T_a$  ve  $T_{dk}$  sıcaklık değerlerinin bulunmasıyla, bu değerlerin hesaplama başında bilinmemesinden ötürü yapılan kabuller gözden geçirilmiştir. Buna göre öncelikle ısı radyasyon taşınım katsayısı için,  $4 \text{ W/m}^2\text{°C}$  olarak alınan  $h_r$  değeri, sıcaklık değerlerinin belirlenmesiyle zamana bağlı olarak yeniden hesaplanmıştır (Hülagü, 2017). Bir diğer kabul ise ara boşluk ısı taşınım katsayısı ( $h_a$ ) hesaplanırken yapılmıştır. Eş. 3'e göre bulunan  $h_a$  değerinde Rayleigh ( $Ra_L$ ) sayısı hesaplanırken (Eş. 5), denklemdaki  $T_{ik}$  ve  $T_{dk}$  değerleri yerine sırasıyla  $T_i$  iç hava ve  $T_d$  dış hava sıcaklıkları kullanılmıştır.  $h_r$  değeri değiştirilerek hesaplanan  $T_{ik}$  ve  $T_{dk}$  sıcaklıklarıyla, ara boşluk ısı taşınım katsayısında ( $h_a$ ) iterasyonlar yapılmıştır. Yapılan ilk iterasyonda  $h_a$  ortalama %26 oranında bir azalma göstermiştir. İkinci iterasyonun yapılması ile  $h_a$  değerinde ortalama %4 oranında artış yaşanmıştır. Yapılan üçüncü iterasyon ile ikinci iterasyon arasında ortalama %0,08 oranında fark olduğu için, ikinci iterasyon sonuçları  $h_a$  değeri olarak kabul edilmiştir.

Yapılan kabullerin değiştirilmesiyle hesaplar tekrarlanmıştır. Şekil 8'de hesaplama yöntemiyle elde edilen ara boşluk sıcaklığı ( $T_a$ ) ve deneysel ölçüm ile 5 noktadan kayıt altına alınan ara boşluk sıcaklıklarının ortalama ( $\bar{T}_a$ ) değeri kıyaslanmıştır. Hesaplanan ve ölçülen ara boşluk sıcaklık değerleri benzer sonuçlar gösterse de, aralarında ortalama %11,2 fark oluşmuştur. Bu farkın yaşanmasındaki belli başlı sebepler aşağıdaki gibi sıralanabilir;

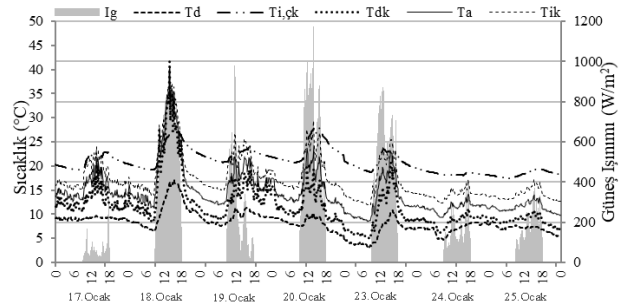
- Yapılan ısı transfer analizinin bir boyutlu yaklaşımla gerçekleştirilmesi,
- Cephe elemanlarının depoladığı enerji değişimleri göz ardı edilerek kararlı durum yaklaşımının kullanılması,
- Dış ve iç kabuk alüminyum çerçeve eleman U değerinin teorik bir kesit üzerinden hesaplanması,
- Dış kabuk menfezlerinin alüminyum çerçeve eleman olarak kabul edilişi,
- Cam ve alüminyum malzemelerin fiziksel ve termofiziksel özelliklerinin referans veriler ile tayin edilişi,
- İç kabuk ve dış kabuk arasında 40 cm ara boşluk olması dolayısıyla, dış kabuğa etkileyen güneş ışınımının bir kısmının iç kabuğa direkt etkilediği, bir kısmının ise ara boşluk zemininden yansıtılarak iç kabuk yüzeyine etkilediği göz ardı edilerek, dış kabuktan geçen güneş ışınımının iç kabuğa direkt etkilediğinin varsayılışı.

Şekil 8'de de görüleceği üzere yapılan hesaplamaların düşük hata oranına sahip olması nedeniyle, varsayımların kabul edilebilir olduğu sonucuna varılmış ve hesaplamalara devam edilmiştir.



Şekil 8. Hesaplanan ( $T_a$ ) ve ölçülen ortalama ( $\bar{T}_a$ ) ara boşluk sıcaklık değerleri.

Ara boşluk sıcaklığı ile hesaplanan  $T_{dk}$  ve  $T_{ik}$  değerlerinin ölçüm süresi boyunca güneş ışınımı ( $I_g$ ), dış ortam sıcaklığı ( $T_d$ ) ve iç ortam sıcaklık ( $T_{i,\check{k}}$ ) değerlerine göre değişimi Şekil 9'da gösterilmiştir.



Şekil 9. Sıcaklık değerleri ve cepheye etkileyen güneş ışınımı.

$T_{dk}$ ,  $T_a$ ,  $T_{ik}$  sıcaklık değerlerinin öğle saatlerinde  $T_{i,çk}$  değerinden fazla olduğu ancak hava sıcaklığının azaldığı ve güneş ışınımının olmadığı gece vaktinde ise, dış ortam ve iç ortam sıcaklık değerleri arasında kaldığı görülmektedir (Şekil 9).  $T_{ik}$  iç kabuk dış yüzey sıcaklığı kullanılarak çift kabuk cephedeki ısı transferi hesaplanmıştır. Isı transferi hesaplanırken iç kabuk cam ve alüminyum yüzeylerden meydana gelen ısı transferleri ayrı ayrı hesaplanmış ve iç ortam ısı kazanımları göz önünde bulundurulmuştur. Eş. 12’de iç kabuk cam yüzey ve iç ortam arasındaki enerji dengesi yazılmıştır.  $I_{g,c}$  güney cephe birim yüzeye gelen güneş ışınımının dış kabuk cam yüzey oranına göre payı olup,  $\tau_{tc}$ ,  $\alpha_{çc}$  değerleri Tablo 3’den,  $A_c$  iç kabuk cam yüzey alanı ise ölçümle belirlenmiştir. Denklemdaki  $Q_{çk,c}$  ve  $W_{çk,c}$  ise çift kabuk cephe kuruluşuna sahip ofisin, iç ısı kazanımlarının iç kabuk cam yüzdesine karşılık gelen payını,  $U_{cam}$  iç kabuk cam yüzey modifiye edilmiş toplam ısı transferi katsayısını (Eş. 13) ifade etmektedir.

$$\left[ I_{g,c} \tau_{tc} \alpha_{çc} - U_{cam} (T_{c,çk} - T_{ik}) - h_i (T_{c,çk} - T_{i,çk}) \right] A_c + Q_{çk,c} + W_{çk,c} = 0 \quad (12)$$

$$U_{cam} = [2R_c + R_{h,c}]^{-1} = \left[ 2 \frac{L_c}{k_c} + \frac{L_{h,c}}{k_{h,c}} \right]^{-1} \quad (13)$$

12 numaralı eşitlikten  $T_{c,çk}$  çekilerek iç kabuk cam bölgesinin ortalama iç yüzey sıcaklığı hesaplanır:

$$T_{c,çk} = \frac{(I_{g,c} \tau_{tc} \alpha_{çc} + U_{cam} T_{ik} + h_i T_{i,çk}) A_c + Q_{çk,c} + W_{çk,c}}{(U_{cam} + h_i) A_c} \quad (14)$$

$T_{c,çk}$  değerinin hesaplanmasıyla çift kabuk cephe cam yüzeyden sıcaklık farkı dolayısıyla meydana gelen ısı transferi ( $Q_{ısı,çk1}$ ) Eş. 15, güneş kaynaklı ısı kazanımı ( $Q_{g,çk}$ ) ise Eş. 16 ile hesaplanmıştır. Eş 16’da tek cam ( $\tau_{tc}$ ) ve çift cam ( $\tau_{çc}$ ) geçirgenlik değerleri Tablo 3’den alınmıştır.

$$Q_{ısı,çk1} = h_i A_c (T_{c,çk} - T_{i,çk}) \quad (15)$$

$$Q_{g,çk} = I_{g,c} \tau_{çc} A_c \quad (16)$$

İç kabuk alüminyum yüzey ile iç ortam arası enerji dengesi ise Eş. 17’de verilmiştir. Eşitlikteki alüminyum yutuculuk değeri ( $\alpha_{al}$ ) Tablo 3’den, alüminyum yüzey alanı  $A_{al}$  ise yerinde ölçüm ile belirlenmiştir. İç kabuk alüminyum alanının toplam alandaki yüzdesine göre iç kazanımlar alüminyum yüzeye paylaştırılarak denklemden  $Q_{çk,al}$  ve  $W_{çk,al}$  olarak ifade edilmişlerdir. Alüminyum kesit ısıl geçirgenliği Eş. 18’deki gibi hesaplanmıştır.

$$\left[ I_{g,c} \tau_{tc} \alpha_{al} - U_{al} (T_{al,çk} - T_{ik}) - h_i (T_{al,çk} - T_{i,çk}) \right] A_{al} + Q_{çk,al} + W_{çk,al} = 0 \quad (17)$$

$$U_{al} = \left[ 2R_{al,1} + \left[ 2 \frac{1}{R_{al,2}} + \frac{1}{R_{al,h}} \right]^{-1} \right]^{-1} = \left[ 2 \frac{L_{al,1}}{k_{al}} + \left[ 2 \frac{k_{al}}{L_{al,2}} + \frac{k_h}{L_{h,al}} \right]^{-1} \right]^{-1} \quad (18)$$

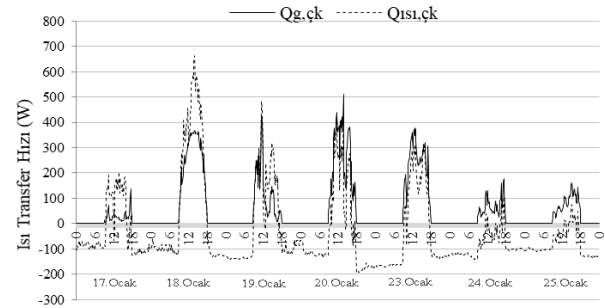
Alüminyum iç yüzey sıcaklığı ( $T_{al,çk}$ ), 17 numaralı eşitliğin düzenlenmesiyle bulunur:

$$T_{al,çk} = \frac{(I_{g,c} \tau_{tc} \alpha_{al} + U_{al} T_{ik} + h_i T_{i,çk}) A_{al} + Q_{çk,al} + W_{çk,al}}{(U_{al} + h_i) A_{al}} \quad (19)$$

Çift kabuk cephe iç kabuk alüminyum yüzeyden sıcaklık farkı dolayısıyla olan ısı transferi ( $Q_{ısı,çk2}$ ) Eş. 20 ile hesaplanmıştır.

$$Q_{ısı,çk2} = h_i A_{al} (T_{çk,al} - T_i) \quad (20)$$

Çift kabuk cephede meydana gelen toplam ısı transferi ( $Q_{ısı,çk}$ ), cam ( $Q_{ısı,çk1}$ ) ve alüminyum ( $Q_{ısı,çk2}$ ) yüzeylerde sıcaklık farkı dolayısıyla olan ısı transferlerinin toplamı olarak Eş. 15 ve 20 ile ve toplam güneş ışınımı kazanımı ( $Q_{g,çk}$ ) ise cam yüzeyden güneş ısı kazanımı olup Eş. 16 ile gösterilmiştir. Çift kabuk cephede, cam ve alüminyum iç yüzeyleri ile iç ortam sıcaklık değerleri arasındaki sıcaklık farkı dolayısıyla meydana gelen toplam ısı transferi ( $Q_{ısı,çk}$ ) ve cam yüzeyden toplam güneş ısı kazanımının ( $Q_{g,çk}$ ) gösterildiği Şekil 10’dan, güneş ısı kazanımının, sıcaklık farkı dolayısıyla ısı kazanımına yakın değerlerde olduğu görülmektedir.



**Şekil 10.** Çift kabuk cephe güneş kaynaklı ısı kazanımı ( $Q_{g,çk}$ ) ve sıcaklık farkı dolayısıyla cam ve alüminyum yüzeyden yaşanan toplam ısı transfer hızı ( $Q_{ısı,çk}$ ).

### Tek Kabuk Cephede Meydana Gelen Isı Transfer Hızının Belirlenmesi

Tek kabuk cephede ısı transferi, tek boyutlu zamana bağlı olarak ele alınmış, buna karşılık cephe elemanlarının zamana bağlı depoladığı ısıl enerji değişimleri göz önüne alınmayarak kararlı durum yaklaşımı kullanılmış ve hesaplamalar yapılırken de çift camdan olan ısı transferinin yanında, cephe kuruluşunun yaklaşık %34’ünü oluşturan çerçeve bileşeninden de yaşanacak ısı transferi ile birlikte kullanıcı kaynaklı iç ısı kazanımları göz önünde bulundurulmuştur. Tek kabuk cephe kuruluşunda; cam ve alüminyum yüzeylerde meydana gelen ısı transferi ayrı ayrı hesaplanmıştır. Tek kabuk cephe cam yüzeydeki enerji dengesi Eş. 21’de gösterildiği

gibidir.  $I_g$  cepheye etkiyen güneş ışınımı,  $T_{i,tk}$  ve  $T_d$  ise iç ve dış ortam sıcaklık değerleri olup, deneysel olarak ölçülmüştür.  $U_{c,tk}$  tek kabuk cephe çift cam modifiye edilmiş toplam ısı transfer katsayısı Eş. 22 ile hesaplanmıştır.  $A_c$  cam yüzey alanıdır.  $\alpha_{cc}$  çift cam yutuculuk değeri için Tablo 3'deki değerler, iç ortam yüzey ısı taşınım katsayısı,  $h_i$  için ise  $7,69 \text{ W/m}^2\text{°C}$  değeri kullanılmıştır (TS 825, 2009).  $Q_i$  ve  $W_i$  değerleri cephedeki cam ve alüminyum yüzey oranına göre dağıtılmış ve cam yüzeyin iç ısı kazanım payı, Eş. 21'de  $Q_{i,c}$  ve  $W_{i,c}$  olarak gösterilmiştir.

$$\left[ I_g \alpha_{cc} - U_{c,tk} (T_{c,tk} - T_d) - h_i (T_{c,tk} - T_{i,tk}) \right] A_c + Q_{i,c} + W_{i,c} = 0 \quad (21)$$

$$U_{c,tk} = \left[ R_{dış} + 2R_c + R_{h,c} \right]^{-1} = \left[ \frac{1}{h_{dış}} + 2 \frac{L_c}{k_c} + \frac{L_{h,c}}{k_{h,c}} \right]^{-1} \quad (22)$$

21 numaralı eşitliğin bilinmeyenini olan  $T_{c,tk}$  tek kabuk cephe cam iç yüzey sıcaklığıdır ve denklemden çekilerek hesaplanır. Tek kabuk cephe cam yüzeyden sıcaklık farkı dolayısıyla iç ortamda olan ısı transferi ( $Q_{i,tk}$ ), Eş. 23 ile, güneş kaynaklı ısı kazanımı ( $Q_{g,tk}$ ) ise Eş. 24 ile belirlenmiştir. Eş. 24'de bulunan  $\tau_{cc}$  çift cam geçirgenlik katsayısı için Tablo 3'de belirtilen değer kullanılmıştır.

$$Q_{i,tk} = h_i A_c (T_{c,tk} - T_{i,tk}) \quad (23)$$

$$Q_{g,tk} = I_g \tau_{cc} A_c \quad (24)$$

Tek kabuk cephe kuruluşundaki alüminyum yüzeydeki enerji dengesi Eş. 25'de verilmiştir. Eş. 25'deki  $\alpha_{al}$  alüminyum yutuculuk katsayısı Tablo 3'den alınmıştır.  $U_{al,tk}$  tek kabuk cephe alüminyum modifiye edilmiş toplam ısı transferi katsayısı Eş. 26 ile hesaplanmıştır. Toplam iç ortam ısı kazanımından yüzey alanlarına göre hesaplanan alüminyum iç ortam ısı kazanım payı ise Eş. 25'de  $Q_{i,al}$  ve  $W_{i,al}$  ifadeleriyle gösterilmiştir.

$$\left[ I_g \alpha_{al} - U_{al,tk} (T_{al,tk} - T_d) - h_i (T_{al,tk} - T_{i,tk}) \right] A_{al} + Q_{i,al} + W_{i,al} = 0 \quad (25)$$

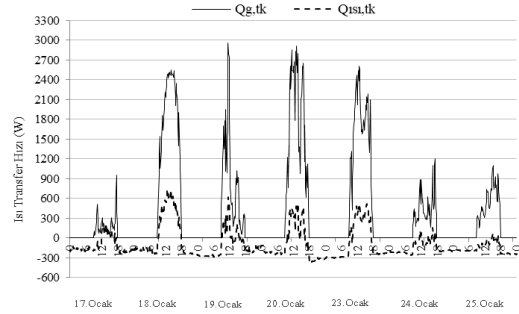
$$U_{al,tk} = \left[ R_{dış} + 2R_{al,1} + \left[ 2 \frac{1}{R_{al,2}} + \frac{1}{R_{al,h}} \right]^{-1} \right]^{-1} = \left[ \frac{1}{h_{dış}} + 2 \frac{L_{al,1}}{k_{al}} + \left[ 2 \frac{k_{al}}{L_{al,2}} + \frac{k_h}{L_{h,al}} \right]^{-1} \right]^{-1} \quad (26)$$

25 numaralı denklemin bilinmeyenini olan  $T_{al,tk}$ , tek kabuk cephe alüminyum iç yüzey sıcaklığı eşitliğinden çekilerek bulunur.  $T_{al,tk}$  sıcaklık değerinin bulunmasıyla, tek kabuk cephe alüminyum yüzeyinden sıcaklık farkı dolayısıyla oluşan ısı transferi ( $Q_{i,tk2}$ ), Eş. 27 kullanılarak hesaplanmıştır.

$$Q_{i,tk2} = h_i A_{al} (T_{al,tk} - T_{i,tk}) \quad (27)$$

Tek kabuk cephedeki toplam ısı transferi ( $Q_{i,tk}$ ), cam ve alüminyum yüzeylerde sıcaklık farkı dolayısıyla olan ısı transferlerinin toplamı olarak Eş. 23 ve 27 değerlerinin toplanmasıyla hesaplanır. Toplam güneş ısı kazanımı

( $Q_{g,tk}$ ) ise cam yüzeyden güneş ışınımı kazanımı olup Eş. 24'de verilmiştir. Denklemlerdeki yüzey alanları yerinde ölçümle belirlenmiş ve hesaplamalarda kullanılmıştır. Tek kabuk cephede cam ( $T_{c,tk}$ ) ve alüminyum ( $T_{al,tk}$ ) iç yüzey sıcaklıkları ile iç ortam sıcaklığı ( $T_{i,tk}$ ) arasındaki sıcaklık farkı dolayısıyla olan ısı transferi ( $Q_{i,tk}$ ) ile tek kabuk cepheye etkiyen güneş ışınımı dolayısıyla iç ortamda yaşanan ısı kazanımı ( $Q_{g,tk}$ ) Şekil 11'de gösterilmiştir.

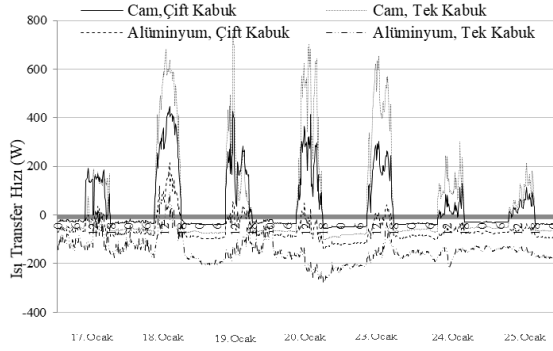


Şekil 11. Tek kabuk cephe güneş ısı kazanımı ( $Q_{g,tk}$ ) ve sıcaklık farkı dolayısıyla ısı transfer hızı ( $Q_{i,tk}$ ).

Eş. 24 kullanılarak hesaplanan  $Q_{g,tk}$ , cepheye etkiyen güneş ışınımı ve cephenin geçirgenliğine bağlıdır. Dolayısıyla, cephede kullanılan saydam malzemenin geçirgenlik değeri ile birlikte çerçeve eleman alanı da iç ortam güneş ısı kazanımı değerini etkilemekte, cepheye etkiyen güneş ışınımının gün ve hafta içerisinde değişim göstermesi ise Şekil 11'de görüldüğü üzere güneş ısı kazanımında artma veya azalmaya yol açmaktadır. Sıcaklık farkı dolayısıyla yaşanan toplam ısı transferinde se, gündüz vakti güneş ısı kazanımına oranla daha az olsa da ısı kazanımı olduğu, hava sıcaklığının azaldığı gece vaktinde ise cephede ısı kaybı yaşandığı görülmektedir.

### Tek ve Çift Kabuk Cephe Performans Karşılaştırması

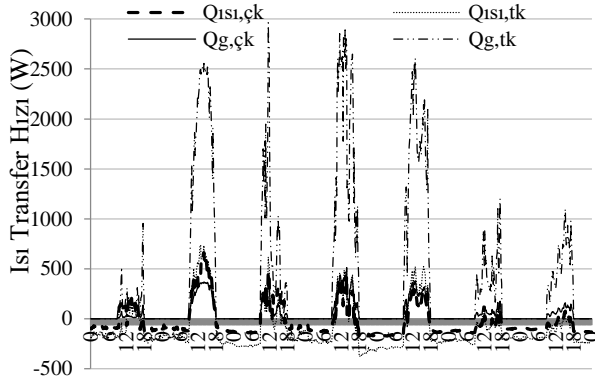
Tek kabuk ve çift kabuk cephe kuruluşların ısı performansları Şekil 12 ve 13'de kıyaslanmıştır. Tek kabuk cephe cam ve alüminyum iç yüzey sıcaklıklarının çift kabuğa göre gün içerisindeki sıcaklık değişiminin daha büyük salınım gösterdiği görülmektedir. Tek kabuk cephe kuruluşunda gün içerisinde cam iç yüzey sıcaklığı  $30\text{°C}$ , alüminyum iç yüzey sıcaklığı  $15\text{°C}$  değişim gösterebilirken, bu değer çift kabuk cephede cam yüzey için  $20\text{°C}$ , alüminyum yüzey için  $10\text{°C}$ 'dir. İç kabuk yüzey sıcaklıklarının gün içerisinde daha az değişim göstermesinden, çift kabuk cephelerin değişen dış ortam koşullarına karşın iç ortam konfor koşullarının sağlanmasına yardımcı olmaktadır. Sıcaklık farklılıkları ısı transfer hızlarına da etkimektedir. Tek kabuk ve çift kabuk cam ve alüminyum yüzeylerde sıcaklık farkı dolayısıyla meydana gelen ısı transfer hızlarını gösteren Şekil 12'de, çift kabuk cephelerin ısı yalıtım özelliği görülebilmektedir.



**Şekil 12.** Tek kabuk ve çift kabuk cephelerde sıcaklık farkı dolayısıyla ısı transfer hızlarının zamana bağlı değişimi.

Şekil 13'de tek kabuk ve çift kabuk cephe iç yüzey ve iç ortam sıcaklık farkıyla meydana gelen ısı transferi ( $Q_{isi,tk}$  ve  $Q_{isi,çk}$ ) ve güneş dolayısıyla ısı kazanımının ( $Q_{g,tk}$  ve  $Q_{g,çk}$ ) ölçüm süresince değişimi gösterilmiştir.

Çift kabuk cephe kuruluşunun sıcaklık farkı dolayısıyla yaşanan ısı kaybını azalttığı görülmektedir. Dış kabuğun düşük saydamlık oranına da bağlı olarak, çift kabuk cephe kuruluşu ile güneş ışınımının yüksek olduğu günlerde, güneş kaynaklı ısı kazanımında büyük azalış gösterdiği belirlenmiştir.



**Şekil 13.** Tek ve çift kabuk cephede güneş kaynaklı ısı kazanımları ( $Q_g$ ) ve sıcaklık farkı dolayısıyla ısı transfer hızlarının ( $Q_{isi}$ ) zamana bağlı değişimi.

## GELİŞTİRİLEN YÖNTEM İLE İZMİR İÇİN ISI TRANSFERİNİN BELİRLENMESİ

Tek kabuk ve çift kabuk cephe kuruluşlarında meydana gelen ısı transferi, İzmir İli için ay bazında incelenmiştir. Bu çalışmada geliştirilen yöntem kullanılarak, kutu tipi tampon bölge kullanımındaki çift kabuk cephe kuruluşlarının İzmir için ısıtma yüküne etkisi hesaplanmıştır. Hesaplama; dış sıcaklık ve rüzgar hızı Meteoroloji Genel Müdürlüğü (2017)'nden, güneş ışınım şiddeti; PVPS (2002) programından alınmış, iç ortam sıcaklığı sabit 22°C kabul edilmiş ve iç ortam ısı kazanımları ihmal edilmiştir. Önceki bölümde, yalıtımsız alüminyum çerçevenin cephe kuruluşunda büyük miktarda ısı kaybına yol açtığı ortaya konmuştur. Yalıtımsız alüminyum çerçeve kullanımının uygulanabilir olmayışı ve ısı geçirgenlik değeri düşük bir

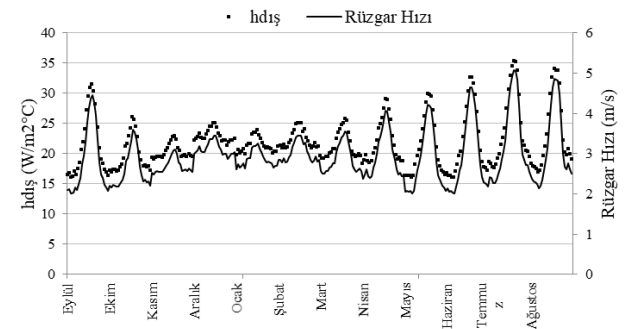
çerçeve kurgusunun kullanılmasının kaçınılmaz olduğu göz önünde bulundurulduğunda, çerçeve elemanları ihmal edilerek, cephe tümüyle cam kabul edilmiştir. Tablo 4'de tek ve çift kabuk cephe kurgusunun ayrıntıları verilmiştir.

**Tablo 4.** Cephe kurgusu ayrıntıları.

Cephe yönelimi	Güney	
Cephe alanı	6,461 m <sup>2</sup>	
Tek kabuk cephe kuruluş	4+12+4 mm çift cam	
Çift kabuk cephe kuruluş	Dış kabuk	4 mm tek cam
	İç kabuk	4+12+4 mm çift cam
Ara boşluk genişliği	40 cm	

## Toplanan Veriler ve Ön Hesaplamalar

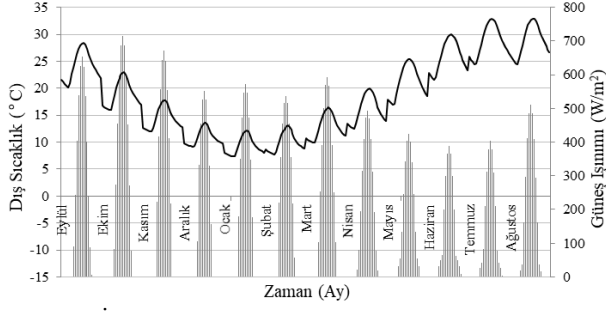
38°43'N, 27°17'E'de yer alan İzmir İli, Binalarda Isı Yalıtım Kuralları, TS 825 (2009)'e göre birinci bölgede yer almakta; Isıtma Gün Dereceleri (Heating Degree Days - HDD) ve Soğutma Gün Dereceleri (Cooling Degree Days - CDD) 985 ve 660 olarak tanımlanmaktadır. Orta Enlem kuşağında yer alan İzmir'de Akdeniz iklimi karakteri hakimdir. Buna göre, yazlar sıcak ve kurak, kışlar ılık ve bol yağışlı, bahar ayları ise geçiş özelliği göstermektedir (Meteoroloji Genel Müdürlüğü, 2017). İzmir İlinin 2005-2014 yılları arasındaki aylık ortalama günlük dış sıcaklık ve rüzgar hızı değerleri saat bazında Meteoroloji Genel Müdürlüğü'nden elde edilmiştir. Aylık ortama rüzgar hızı verileriyle İzmir'deki dış yüzey ısı taşınım katsayısı 1 ve 2 numaralı eşitliklerden, hakim rüzgar yönleri (Güney/Güneydoğu) dikkate alınarak hesaplanmıştır (Meteoroloji Genel Müdürlüğü, 2017). Güneye yönelmiş cepheler rüzgarüstü bölgede kalacaktır. İzmir'de güney cephe için aylık ortalama günlük dış ortam yüzey ısı taşınım katsayıları Şekil 14'de verilmiştir.



**Şekil 14.** İzmir İli aylık ortalama günlük dış ortam yüzey ısı taşınım katsayısı ( $h_{dış}$ ) değeri ve rüzgar hızı.

İzmir için güney cephe aylık ortalama günlük güneş ışınımı değerleri PVPS programıyla (2002) hesaplanmıştır. Şekil 15'de aylık ortalama günlük dış sıcaklık ile güney yüzeyine gelen güneş ışınımı verilmiştir.



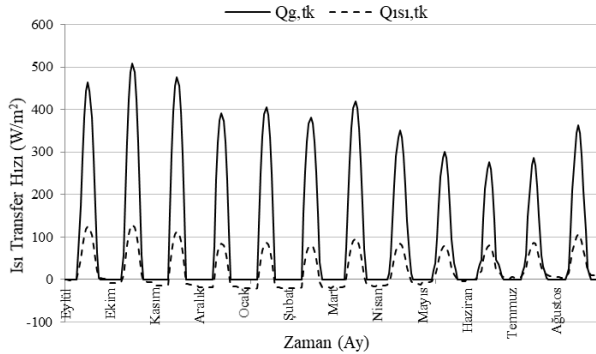


Şekil 15. İzmir ili aylık ortalama günlük dış sıcaklık ve güneş ışınımı değerleri.

## Isı Transfer Sonuçları

### Tek kabuk cephede ısı transfer hızının değişimi

İzmir'de güney yönelime sahip tek kabuk cephe kuruluşundaki ısı transferi hesaplanırken deneysel çalışma bölümünde ayrıntılı olarak anlatılan hesaplama yöntemi kullanılmış ancak varlık, aydınlatma ve elektrikli alet kullanımına bağlı iç ısı kazancı ihmal edilmiş ve cephe %100 saydam kabul edilmiştir.  $T_i$ , iç ortam sıcaklığı sabit 22°C kabul edilmiş, çift cam yutuculuk değeri ( $\alpha_{c,c}$ ) Tablo 3'den, cephe alanı (A) Tablo 4'den ve iç yüzey ısı taşınım katsayısı 7,69 W/m<sup>2</sup>°C (TS 825, 2009) alınmıştır. Hesaplamalar sonucunda; dış ortam, cam ve iç ortam sıcaklık değişimlerine bağlı olarak cephede birim yüzey alanında meydana gelen ısı transfer hızı ve güneş kaynaklı ısı kazanımı, Şekil 16'da gösterilmektedir. Sıcaklık farkı dolayısıyla yaşanan ısı kaybının yalnızca kış dönemi gece vakitlerinde olduğu ortaya konmaktadır. Burada saydam yüzeylerdeki güneş ısı kazanımı dikkat çekmektedir.

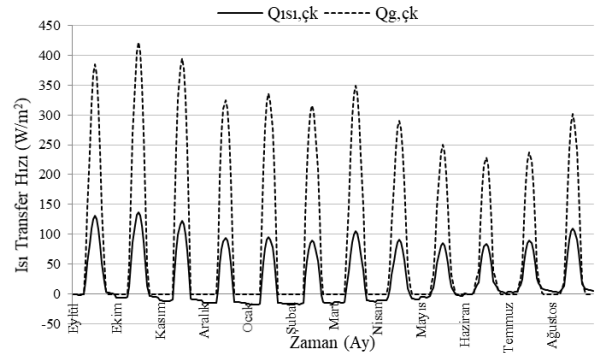


Şekil 16. İzmir için tek kabuk cephedeki güneş kaynaklı ısı kazanımı ( $Q_{g,tk}$ ) ve sıcaklık farkı ısı transfer hızının ( $Q_{ısı,tk}$ ) değişimi.

### Çift kabuk cephede ısı transfer hızının değişimi

İzmir için güney cephede uygulanacak kutu tipi çift kabuk cepheden yıl içerisinde meydana gelecek aylık ortalama günlük ısı transferi hesaplanırken bu çalışmada önerilen bölgeleme yöntemi kullanılmıştır. Buna göre çift kabuk cephe kuruluşu dış kabuk (1), ara boşluk (2) ve iç kabuk (3) olmak üzere 3 bölgeye ayrılmış ve bu bölgelerin enerji dengeleri ayrı ayrı yazılmıştır. Bu çalışmada ayrıntılandırılan hesaplama yöntemi, çift kabuk cephede sadece cam kullanımına göre modifiye edilerekten, 3 bölge için çıkarılan enerji denklemleri çözülerek,

bilinmeyen sıcaklık değerleri olarak; dış kabuk iç yüzey ( $T_{dk}$ ), ara boşluk ( $T_a$ ) ve iç kabuk dış yüzey ( $T_{ik}$ ) sıcaklıklarının zamana göre değişimleri hesaplanmıştır. Buradan hareketle de güneşe yönelmiş, Tablo 4'de tanımlanmış özelliklere sahip bir çift kabuklu cephe için, ısı transfer hız değerlerinin zamana bağlı değişimlerine ulaşılmıştır. Ayrıntılı çözüm yöntemi (Hülagü, 2017) numaralı tez çalışma referansında paylaşılmıştır. Elde edilen sonuçların verildiği Şekil 17 incelendiğinde, ikincil cephenin entegre edilmesiyle, yıl içerisinde değişkenlik gösteren güneş ışınımı değerlerine karşın (Şekil 15) güneş ısı kazanımının yıl boyunca daha dengeli bir dağılım sergilediği görülmektedir. Söz konusu etki birincil ve ikincil cephenin geçirgenlik değerlerine göre farklılık gösterecek olmakla birlikte, çift kabuk cepheler ile bina kabuğunda saydamlık oranının değişimine bağlı olarak meydana gelecek güneş ısı kazanımı dengelenebilecektir.

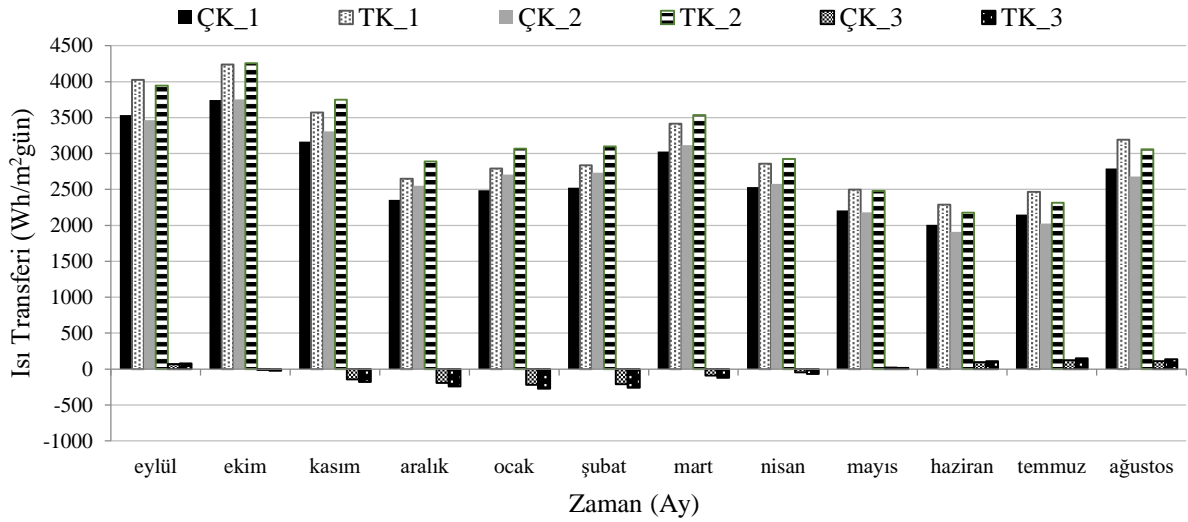


Şekil 17. İzmir için çift kabuk cephedeki güneş kaynaklı ısı kazanımı ( $Q_{g,çk}$ ) ve sıcaklık farkı ısı transfer hızının ( $Q_{ısı,çk}$ ) değişimi.

### Tek ve çift kabuk cephelerin ısı performans karşılaştırması

İzmir için tek kabuk ve çift kabuk cephe ısı transfer hızlarının karşılaştırılmasında, çift kabuk cephe sistemlerinin Eylül ayından Mayıs ayına kadar sıcaklık farkından dolayı olan ısı kazanımını arttırmada etkili olmakla birlikte; soğutma döneminde (Haziran-Ağustos) görece yüksek ısı kazancına yol açmadığını, dolayısıyla aşırı sıcaklık değerlerinin yaşanmasının önüne geçtiğini ortaya koymaktadır. Çift kabuk cephe sistemlerinde, güneş ışınlarının iki geçirgen yüzeyden geçmesinden; güneş kaynaklı ısı kazanımının azalması kaçınılmazdır. Tek camın geçirgenliğinin 0,83, çift camın ise 0,71 kabul edildiği hesaplamalara göre çift kabuk cephe kuruluşu ile iç ortam güneş ısı kazanımı yaklaşık %17 oranında azalmaktadır.

Tek kabuk cephe ve çift kabuk cephe kuruluşlarının İzmir için güney cephesi uygulamalarında yaşanacak aylık ortalama günlük ısı transferleri incelenerek kıyaslanmıştır. Sıcaklık farkı dolayısıyla meydana gelen ısı transferinin yanında, güneş kaynaklı ısı kazanımı da, Türkiye'nin görece yüksek güneş ışınımı etkisinde olduğu göz önünde bulundurulduğunda, cephenin ısı performansını önemli ölçüde etkilemektedir. Toplam ısı transferi, İzmir için gün bazında (1 / 24 saat), ofis kullanım süresinde (2 / 08:00 - 18:00) ve ofis kullanım



**Şekil 18.** İzmir için gün bazında (1), 08:00-18:00 (2) ve 18:00-08:00 (3) arasındaki toplam ısı transferinin aylık ortalama değişimi.

süresi dışında (3 / 18:00 - 08:00) incelenmiş ve kıyaslanmıştır (Şekil 18). Buna göre gün bazında ve ofis kullanım süresinde tek kabuk ve çift kabuk cephe kullanımıyla yıl boyunca ısı kazanımı meydana geldiği ve toplam ısı kazanımının çift kabuk cephe kullanımıyla azaldığı görülmektedir. Bu yaz dönemi için bir kazanım olsa da kış dönemi için olumsuzluk yaratmaktadır. Toplam ısı transferinde gün bazında ve ofis kullanım süresinde yaşanan bu değişimin, güneş ışınımı etkisinin çok baskın olmasından kaynaklandığı söylenebilir. Ofis kullanım süresi dışında meydana gelen toplam ısı transferi incelendiğinde ise, çift kabuk cephenin ısı kaybını azalttığı görülmektedir.

## SONUÇ VE TARTIŞMA

Bu çalışmada çift kabuk cephelerin bina enerji ihtiyacına etkisi araştırılmıştır. Bu kapsamda tek kabuk ve çift kabuk cephe kuruluşlarında meydana gelen ısı transferi için bölgesel analiz yöntemiyle bir matematiksel model kurulmuş ve deneysel olarak doğrulanmıştır. Deneysel çalışma Ege Üniversitesi İnşaat Mühendisliği binasına kurulan çift kabuk ve tek kabuk cephe sistemlerinde Ocak 2017 tarihinde gerçekleştirilmiştir. Dış ortam iklim koşulları (sıcaklık, rüzgar hızı, güneş ışınımı), iç ortam koşulları (sıcaklık), kullanıcı davranışı (ısıtıcı, bilgisayar, aydınlatma) ve pencere alüminyum çerçeve eleman etkileri göz önünde bulundurulmuştur. Geliştirilen hesap yönteminin deneysel olarak doğrulanmasının ardından, çift kabuk cephelerde yıl içerisinde meydana gelen ısı transferi aylık ortalama günlük zaman dilimlerinde İzmir için incelenmiştir. Çalışmada kullanıcı davranışı ve çerçeve eleman etkileri modele dahil edilmemiş, iç ortam iklim koşulları da sabit tutularak değişen dış ortam iklim koşullarına karşın, saydam eleman ısı transferleri tek kabuk ve çift kabuk cepheler için incelenmiştir. Buna göre:

- Çalışma kapsamında önerilen matematiksel model deneysel bağlamda doğrulanmış olup, ileriki çalışmalarda uygulanabilir bir modeldir,

- Çift kabuk ile cepheden yaşanacak ısı kaybı tek kabuk cephe kuruluşuna kıyasla azalmaktadır,
- Çift kabuk cephenin ısı kaybını azaltmakla birlikte, güneş ısı kazanımını da azaltması dolayısıyla, yüksek sıcaklık farkının ve düşük güneş ışınımının olduğu bölgelerde daha iyi ısı performans gösterecektir,
- Güneş kaynaklı ısı kazanımı çift kabuk cephe kullanımıyla yaklaşık %17 oranında azaltılmıştır,
- Çerçeve eleman ile saydam eleman yüzey sıcaklıkları arasındaki farkın %50 oranına çıkabildiği, dolayısıyla çerçeve elemanların saydam elemanlardan farklı ele alınarak ısı performans sayısal analizine dahil edilmesinin önemi vurgulanmıştır,
- İzmir İlinde tampon bölge çift kabuk cephe kullanımıyla sıcaklık farkı dolayısıyla yaşanan ısı kazançları ısıtma döneminde (Aralık-Şubat) %64, geçiş döneminde (Mart-Mayıs ve Eylül-Kasım) %16, soğutma döneminde (Haziran-Ağustos) ise %0,09 oranında artmaktadır. Çift kabuk yalıtıcı işlev gören sıcaklıktaki dalgalanmaları önleyerek iç ortam konfor koşullarının sağlanmasına katkıda bulunduğunu göstermektedir.

Çalışma kapsamında geliştirilen zamana bağlı tek boyutlu ısı transfer analiz modeli; çerçeve elemanları ve saydam elemanları ayrı ayrı ele alarak, kullanıcı davranışını da göz önünde bulundurmaktadır. Deneysel çalışma ile doğrulanan söz konusu model kapsamında çerçeve ve saydam elemanların ısı özellikleri ile ilgili kabuller yapılmış, kullanıcı davranışına bağlı olarak meydana gelecek ısı kazanımı da kullanıcı varlığı, ısıtıcı kullanımı ve bilgisayar kullanımı ile sınırlandırılmıştır. Önerilen modelin geliştirilerek yıl bazlı ısı performans analizi yapılırken, çerçeve eleman etkisi ile kullanıcı davranışının etkisi göz ardı edilerek, yalnızca ikincil saydam bir cephenin bina kabuğuna entegre edilmesinin yıl içerisindeki ısı transferine etkileri tek kabuk cepheler ile kıyaslamalı olarak tartışılmıştır. Deneysel çalışmada kullanıcı davranışı ve çerçeve elemanın ısı performans etkisi vurgulanırken, İzmir ili için yapılan yıllık

hesaplamalarda daha genel ve geçerli (örneğin kullanıcı davranışına ve/veya seçilen çerçeve eleman özelliklerine bağlı olmadan) bir ısı performans analizi yapılmasına odaklanılmıştır. Elde edilen yıllık sonuçlar çeşitli kullanıcı davranışı ve çerçeve eleman malzemesine göre farklılık gösterecektir.

Gelecek çalışmaların, çift kabuk cephelerin havalandırma modlarına göre bina soğutma enerjisi ihtiyacına etkisinin incelenmesine, özellikle çerçeve eleman etkisiyle cephe yüzeyindeki sıcaklık dağılımının değişimi göz önünde bulundurularak iki boyutlu ısı transfer modelinin kurulmasına, kararsız durum yaklaşımıyla cephe elemanlarının zamana bağlı ısı enerji değişimlerinin hesaba katılmasına ve güney cepheye ek olarak diğer yönelimlerin de etkisine odaklanmayla, bu çalışmanın ortaya koyduğu sonuçlar geliştirilebilir.

## KAYNAKLAR

ASHRAE Fundamentals, *Non residential cooling and heating load calculations*, 2009.

Boake T.M., Harrison K., Collins D., Chatham A., Lee R., 2003, Understanding the Principles of the Double Façade System, School of Architecture, University of Waterloo.

Çengel Y., 2015, *Heat and Mass Transfer, Fundamentals & Applications*, Fifth Edition, McGraw-Hill Education, New York.

Duffie J.A., Beckman W.A., 2013, *Solar Engineering of Thermal Processes*, Fourth Edition, Wiley, NY.

Eicker U., 2003, *Solar Technologies for Buildings*, John Wiley and Sons, West Sussex.

Eicker U., Fux V., Bauer U., Mei D., Infield D., 2008, Façade and summer performance of buildings. *Energy and Building*, 40, 600-611.

Ghaffarianhoseini A., Ghaffarianhoseini A., Berardi U., Tookey J., Li D.H.W., Kariminia S., 2016, Exploring the advantages and challenges of double-skin façades (DSFs), *Renewable and Sustainable Energy Reviews*, 60, 1052-1065.

He G., Shu L., Zhang S., 2011, Double skin facades in the hot summer and cold winter zone in China: Cavity open or closed?, *Building Thermal Lighting and Acoustic Modeling*, 4, 283-291.

Hülagü S., Özbaltalı T.G., Başaran T., 2018, Çift Kabuk Kutu Tipi Cephe Kuruluşunun Bina Isıl Performansına Katkısı, *IV. Uluslararası Katılımlı Anadolu Enerji Sempozyumu*, Trakya Üniversitesi, Edirne.

Hülagü S., 2017, *Çift kabuk cephe sisteminin bina ısı performansına etkisinin deneysel ve sayısal olarak incelenmesi*, Yüksek Lisans Tezi, Ege Üniversitesi İnşaat Mühendisliği.

İnan T., Başaran T., Ezan M.A., 2016, Experimental and numerical investigation of natural convection in a double skin facade, *Applied Thermal Engineering*, 106, 1225-1235.

İnan T., Başaran T., 2019, Experimental and numerical investigation of forced convection in a double skin façade by using nodal network approach for Istanbul, *Solar Energy*, 183, 441-452.

İnternet, 2017, Meteoroloji Genel Müdürlüğü, Türkiye, *İzmir İlinin İklim Durumu* [http://www.izmir.mgm.gov.tr/files/iklim/izmir\\_iklim.pdf](http://www.izmir.mgm.gov.tr/files/iklim/izmir_iklim.pdf)

Jiru T.E., Haghghat F. 2008, Modeling ventilated double skin façade—A zonal approach, *Energy and Buildings*, 40, 1567-1576.

Klein, S.A., 1977, Calculation of monthly average insolation on tilted surfaces, *Solar Energy*, 19, 325-329.

Kuznik F., Catalina T., Gauzere L., Woloszyn M., Roux J.J., 2011, Numerical modelling of combined heat transfers in a double skin façade- Full scale laboratory experiment, *Applied Thermal Engineering*, 31, 3043-3054.

Liu Y., Harris, D.J., 2007, Full-scale measurement of convective coefficient on external surface of a low-rise building in sheltered conditions, *Building and Environment*, 42, 2718-2736.

Lou W., Huang M., Zhang M., Lin N., 2012, Experimental and zonal modeling for wind pressures on double-skin facades of a tall building, *Energy and Buildings*, 54, 179-191.

Macgregor R.K., Emery A.P., 1969, Free Convection Through Vertical Plane Layers: Moderate and High Prandtl Number Fluids, *Journal of Heat Transfer*, 91, 391-401.

Nastase G., Şerban A., Dragomir G., Bolocan S., Brezeanu A. I., 2016, Box window double skin façade. Steady heat transfer model proposal for energetic audits, *Energy and Buildings*, 112, 12-20.

Pomponi F., Piroozfar P.A.E., Southall R., Ashton P., Farr E.R.P., 2016, Energy performance of Double-Skin Façades in temperate climates: A systematic review and meta-analysis, *Renewable and Sustainable Energy Reviews*, 54, 1525-1536.

PVPS, IEA, 2002, *Evaluation of Islanding Detection Methods for Photovoltaic Utility Interactive Power Systems*, Report IEA PVPS T5-09.

Saelens D., 2002, *Energy performance assessment of single storey multiple-skin facades*, Ph.D. Thesis, Katholieke Universiteit Leuven, Belgium.

Safer N., Woloszyn M., Roux J.J., Rusaouen G., Kuznik F., 2005, Modeling Of The Double-Skin Facades For Building Energy Simulations: Radiative And Convective Heat Transfer, Building Simulation, *Ninth International IBPSA Conference*, Montreal, Canada.

Sanchez E., Rolando A., Sant R., Ayuso, L., 2016, Influence of natural ventilation due to buoyancy and heat transfer in the energy efficiency of a double skin facade building, *Energy for Sustainable Development*, 33, 139-148.

Saury D., Rouger N., Djanna F., Penot F., 2011, Natural convection in an air-filled cavity: Experimental results at large Rayleigh numbers, *International Communications in Heat and Mass Transfer*, 38, 679-687.

Shameri M., Alghoul A., Sopian K., Fauzi M., Zain M., Elayeb O., 2011, Perspectives of double skin façade systems in buildings and energy saving, *Renewable and Sustainable Energy Reviews*, 15, 1468-1475.

Stec W. J., van Passen A. H. C., Maziarz A., 2005, Modelling the double skin façade with plants, *Energy and Buildings*, 37, 419-427.

TSE Türk Standardı, 2009, *Binalarda Isı Yalıtım Kuralları*, TS 825.

Yılmaz Z., Çetintaş F., 2005, Double skin facade's effects on heat losses of office buildings in Istanbul, *Energy and Buildings*, 37, 691-697.



**Selin Hülagü** İnşaat Mühendisliği lisans ve yüksek lisans derecelerini 2015 ve 2017 yıllarında Ege Üniversitesinde almıştır. İstanbul Teknik Üniversitesinde Ulaştırma Mühendisliği yüksek lisansını 2020 yılında tamamlamasının ardından, doktora çalışmalarına devam etmektedir.



**Prof. Dr. Türkan Göksal Özbalta**, Mimarlık lisans eğitimini Hamburg FH, yüksek lisans derecesini Mimar Sinan Üniversitesi, doktora derecesini Dortmund Üniversitesinden almıştır. 1985-2007 yıllarında Anadolu Üniversitesi MMF Mimarlık Bölümünde, 2007 yılından bu yana Ege Üniversitesi Mühendislik Fakültesi İnşaat Mühendisliği Bölümünde akademisyen olarak görevini sürdürmektedir. Binalarda Enerji Verimliliği, Enerji Etkin Tasarım alanında çalışmaktadır; Avrupa Birliği FP7 ve Horizon 2020 kapsamında Binalarda Enerji Etkin İyileştirme ve Yaklaşık Sıfır Enerjili Binalar konulu projelerde araştırmacı ve yürütücü olarak görev almıştır. 2018 yılı itibarıyla Balıkesir Üniversitesi Mimarlık Fakültesi Dekanlığı görevini yürütmektedir.



**Prof. Dr. Tahsin Başaran**, araştırma görevlisi ve yardımcı doçent olarak çalıştığı Dokuz Eylül Üniversitesi Makina Mühendisliği Bölümünden, lisans, yüksek lisans ve doktora derecelerini almıştır. 2010 yılı itibarıyla, İzmir Yüksek Teknoloji Enstitüsü, Mimarlık Bölümünde çalışmalarına, 2017 itibarıyla profesör olarak, devam etmektedir. Bina enerji performansı üzerine çalışmaları bulunmaktadır.



## EFFECTIVE FLOW CONTROL AROUND A CIRCULAR CYLINDER BY USING BOTH A SPLITTER PLATE AND PLASMA ACTUATORS AS PASSIVE AND ACTIVE CONTROL METHODS

Hürrem AKBIYIK\* and Yahya Erkan AKANSU\*\*

\*Çukurova University, Mechanical Engineering Department 01330, Adana,  
hakbiyik@cu.edu.tr, ORCID: 0000-0002-1880-052X

\*\* Niğde Ömer Halisdemir University, Mechanical Engineering Department 51240, Niğde,  
akansu@ohu.edu.tr, ORCID: 0000-0003-0691-3225

(Geliş Tarihi: 26.08.2020, Kabul Tarihi: 02.03.2021)

**Abstract:** In this study, passive and active flow control methods were used together to manipulate the flow around a circular cylinder. The experiments were conducted in a wind tunnel for the Reynolds number range of 4000 and 10000 based on the diameter of the circular cylinder ( $D$ ). A splitter plate was used as passive flow control device and its length was chosen to be about  $3.75D$ . Plasma actuators were placed on the circular cylinder at a position of  $\pm 90^\circ$  as an active flow control device. Combining the active and passive flow control methods, a greater reduction of the drag coefficient was achieved compared to that of the cases when using these methods separately. For Reynolds numbers of 5000 and 10000, the hybrid method gives a reduction in drag of 48% and 45%, respectively. The velocity measurements were carried out by using the hot-wire anemometry and velocity profiles were obtained in the wake region. The flow was visualized by using a smoke wire method. The results revealed that the wake region of the circular cylinder with plasma actuator and splitter plate has a narrower width than the plain cylinder and with splitter plate. Also, it can be seen from spectral analysis that the vortex shedding frequency was suppressed significantly by usage of the hybrid flow control method was used.

**Keywords:** Circular cylinder, Plasma actuator, Splitter plate, Hybrid flow control, Vortex shedding frequency.

## PASİF VE AKTİF KONTROL YÖNTEMLERİ OLARAK HEM BİR AYIRICI PLAKA HEMDE PLAZMA AKTÜATÖRLER KULLANILMASIYLA DAİRESEL BİR SİLİNDİR ETRAFINDA ETKİLİ AKIŞ KONTROLÜNÜN SAĞLANMASI

**Özet:** Bu çalışmada, pasif ve aktif akış kontrol metotları birlikte kullanılarak bir dairesel silindir etrafındaki akış manipüle edilmiştir. Deneysel dairesel silindirin çapına bağlı ( $D$ ) Reynolds sayısının 4000 ve 10000 olduğu değerlerde rüzgâr tüneline gerçekleştirilmiştir. Pasif akış kontrol metodu olarak  $3.75D$  uzunluğa sahip ayırıcı plaka seçilmiştir. Aktif akış kontrol metodu elemanı olarak ise plazma aktüatörler seçilmiştir ve dairesel silindirin  $\pm 90^\circ$  konumuna yerleştirilmiştir. Aktif ve pasif akış kontrol yöntemleri birlikte kullanılarak, bu yöntemleri ayrı ayrı kullanılmasına göre daha büyük bir azalma elde edilmiştir. Reynolds sayısının 5000 ve 10000 olduğu değerler için hibrit yöntem, sürüklenme katsayısında sırasıyla %48 ve %45 azalma sağlamıştır. Hız ölçümleri kızgın tel anemometresi kullanılarak yapılmıştır ve iz bölgesindeki hız profilleri elde edilmiştir. Akış, duman-tel yöntemi kullanılarak görselleştirilmiştir. Plazma aktüatörlü ve ayırıcı plakalı dairesel silindirin iz bölgesinin sade silindire ve ayırıcı plaka kullanılan silindirin iz bölgesine kıyasla daha dar bir genişliğe sahip olduğu sonuçlarla ortaya koyulmuştur. Ayrıca, spektral analizden, hibrit akış kontrol yöntemi kullanılarak girdap kopma frekansının önemli ölçüde baskılandığı gözlemlenmiştir.

**Anahtar Kelimeler:** Dairesel silindir, Plazma aktüatör, Ayırıcı plaka, Hibrit akış kontrol, Girdap kopma frekansı.

### NOMENCLATURE

$AC$	Alternative current
$C_D$	Drag coefficient
$DBD$	Dielectric barrier discharge
$DC$	Direct current
$D$	Diameter of the circular cylinder [mm]
$L$	length of the splitter plate [mm]
$Re$	Reynolds number [ $=U_o \rho D/\mu$ ]
$St$	Strouhal number [ $=fD/U_o$ ]
$U_o$	Free stream velocity [m/s]

$V_{pp}$	Peak to peak voltage [kV <sub>pp</sub> ]
$f$	Excitation frequency [kHz]
$V$	Applied voltage [kV]

### INTRODUCTION

Flow around bluff bodies receives a great deal of attention in different engineering applications. The circular cylinder is one of those bluff bodies under consideration. The separated shear layer generates vortices in the near wake region of the circular cylinder

and vortex shedding leads to vibrations due to unsteady forces which affects the stability of the bluff bodies. In engineering applications, some flow control methods are used in order to suppress the vortex shedding and vibration, and also to reduce drag force that acts on the bluff bodies. These methods are mainly classified as active and passive control methods. The active control methods use energy in order to manipulate the flow. In recent years, the plasma actuators gathered interest as an active flow control method (Akbiyik et al., 2017; Messanelli and Belan, 2017). The plasma actuators consist of two electrodes which are separated by a dielectric material and are placed on the surface of the bluff bodies. One of the electrodes is grounded and the other one is supplied with a high voltage. The plasma actuators are easy to integrate into the model because of its simple structure which does not contain any moving parts. In the study of Sung et al. (2006), the effects of the plasma actuators on the circular cylinder to change flow separation point and flow field in the wake were investigated. Six electrode pairs were placed on the circular cylinder oppositely and directly to the flow direction. These electrode pairs were placed at  $\pm 90^\circ$ ,  $\pm 120^\circ$  and  $\pm 150^\circ$  (angles) and the experiments were conducted at the range of Reynolds between  $10^4$  and  $4 \times 10^4$ . Wake width of the cylinder was reduced when the exposed electrodes were placed in streamwise direction. But, the wake width was increased remarkably when the exposed electrode pairs were placed in reverse direction configuration. Jukes and Choi (2009) studied about the near-wake structure of a circular cylinder with plasma actuators at  $Re = 15000$ . They reported a reduction of lift/drag fluctuations of 70% and 32%, respectively at  $f_p^+ = 2.0$  (nondimensional frequency) and increase in lift/drag fluctuations of 87% and 7.5%, respectively at  $f_p^+ = 0.2$ . They also emphasized that the flow separation was delayed periodically when pulsed plasma actuators were placed near the natural separation point. Tabatabaeian et al. (2012) also modified the flow around the circular cylinder by using plasma actuators. They markedly decreased pressure coefficient of a circular cylinder and this reduction led to enhancement in pressure drag coefficient by using plasma actuators. The experiments of the Thomas et al. (2008) were conducted at  $Re = 3.3 \times 10^4$  in order to eliminate Kármán shedding and to reduce noise. The plasma actuators were placed on the circular cylinder at  $\pm 90$  and  $\pm 135$  degrees and the plasma actuators were activated as steady and unsteady.

In contrary to active control, passive control methods which are based on the principle of geometrical modifications or adding additional bodies, do not need energy input to control the flow (Güler et al., 2018). Some illustrative examples of passive control techniques are perforated fairing (Durhasan et al., 2016), a splitter plate (Akansu et al., 2004; Sarioglu, 2016; Sarioglu et al., 2016), a control rod (Akansu et al., 2011; Gim et al., 2011), helical wires (Ekmekci, 2014). Among the passive flow control methods, the splitter plate is one of the most commonly used methods. Roshko (1961) reported that the splitter plate affects the flow and it decreases drag

coefficient of the circular cylinder at  $Re = 3.5 \times 10^6$ . Akansu et al. (2004) studied the effect of the splitter plate placed on the rear of the circular cylinder at a Reynolds number range of  $8 \times 10^3$  to  $6 \times 10^4$ . It was shown that usage of the splitter plate on the back of the circular cylinder at different angles change the Strouhal numbers, pressure distributions and lift coefficients of the circular cylinder. Also, the circular cylinder with the splitter plate has smaller drag coefficient than the circular cylinder alone. The splitter plate, attached on a circular cylinder appears to dramatically decrease the drag coefficient (Apelt et al., 1973, Apelt and West, 1975). In the study of Apelt and West (1975), different splitter plate lengths were used ( $L/D \leq 2D$ ). Apelt et al. (1973) changed the  $L/D$  ratio from 2 to 7 at Reynolds numbers between  $10^4$  and  $5 \times 10^5$ . The increasing  $L/D$  ratio from  $2D$  to  $5D$  is reported to have affected the drag and vortex shedding. However, when the ratio of  $L/D > 5$ , there was no change in the vortex shedding and drag coefficient. In the study of Cimbalá and Leon (1996), both the circular cylinder with rigidly fixed splitter plate at 0 degree and circular cylinder with rotatable splitter plate were tried at  $2 \times 10^4 < Re < 8 \times 10^4$  in order to obtain drag forces. The splitter plates with different lengths (between 0 and  $5D$ ) were attached behind the circular cylinder. Both rotatable splitter plates and fixed ones at an angle of 0 degrees provided the same drag reduction. Nakamura (1996) examined five different bluff body models with splitter plate with lengths varying from 0 to  $15D$  for the Reynolds number between 300 and 5000. Also, Strouhal number and pressure coefficient change against  $L/D$  ratio were investigated at Reynolds number of 1600 and 5300.

In this study, a hybrid flow control method is presented aiming to achieve better flow control such as drag reduction and flow structure manipulation. The hybrid flow control methods could be considered as the combinations of passive-passive, passive-active (Reza-zadeh, 2013), and active-active methods. In this study, combination of passive and active methods was chosen. For this purpose, the splitter plate is used for passive flow control and the dielectric barrier discharge (DBD) plasma actuators are used for active control. It is shown that combining the flow control methods reduced the drag coefficient of the circular cylinder far more effectively. Furthermore, the flow structure was changed and the wake region was narrowed far more effectively.

## EXPERIMENTAL SETUP

The experiments were conducted in an open-suction type wind tunnel. The wind tunnel has a 570 mm x 570 mm x 1000 mm test section and a 6.25:1 contraction ratio. The plexi-glass test model consists of four parts. First one is a smooth circular cylinder with 40mm diameter ( $D$ ) and 4mm (wall) thickness. The second one is a two circular end plates with 280mm diameter and with a spanwise distance of 400mm between them. The circular cylinder is placed at 100mm offset from the end plate circle centers. The third one is a 10mm diameter chrome rod strut which is used to connect the test model to a load cell.

The last part is the plexi-glass splitter plate with 3mm thickness. The visualization of the test model is given in Fig. 1.

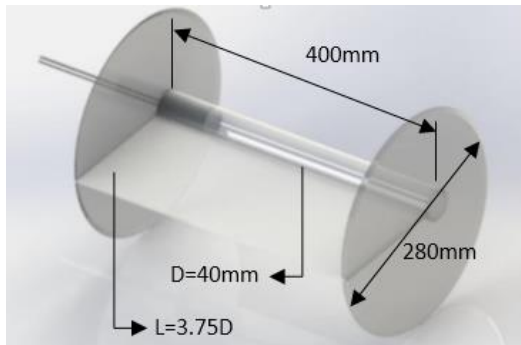


**Figure 1.** Schematic view of the test model

It is reported that the increase in splitter plate length leads to reduction in the drag of the circular cylinder (Cimbala and Leon, 1996). Thus, the splitter plate length in our study was chosen to be 3.75D to achieve streamlined body. The splitter plate was placed on the center axis of the rear side of the circular cylinder. The plasma actuators were used as active flow control component. In order to produce plasma, the embedded electrode was grounded and the exposed one was connected to high voltage. The plasma actuators were placed along the test model and had a thickness of 0.06mm. Kapton tape dielectric material was placed between these two electrodes. The symmetrical actuator pair was placed on the cylinder with  $\theta = \pm 90^\circ$  angle (with respect to the splitter plate, where positive values correspond to a counter clockwise direction). Since forcing with plasma actuators is most effective just before the separation point. Significant effects were observed when the plasma actuators located very close to the laminar separation point (Jukes and Choi, 2009). Fig. 2 shows the schematic of the test model and electrodes.

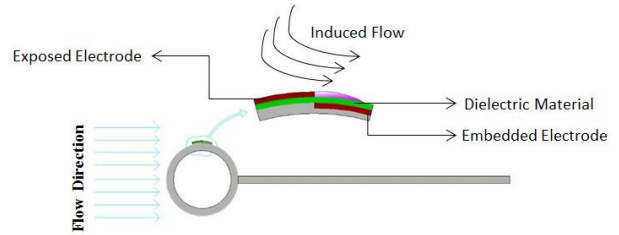


**Figure 2.** Schematic of the model and flow control components.

The actuators were driven with the sinusoidal signal TREK 20/20C-HS model high voltage power amplifier. In order to produce plasma, applied voltage and frequency were varied from 4.8 to 10 kV<sub>pp</sub> and from 3.5 kHz to 4.5 kHz, respectively. The solid blockage ratio was 5% in the open circuit suction type wind tunnel. There is no correction if blockage ratio was smaller than 6% at  $10^4 < Re < 5 \times 10^4$  (Apelt et al., 1973).

The velocity profile and vortex shedding frequency measurements were made by using Dantec Multichannel CTA 54N81 model hot-wire anemometer. During the experiments, 2 hot-wire probes were used as shown in Fig. 3. One of them was moveable probe (55P11), and the other one was fixed probe (55P16) used for measuring the free stream velocity. The moveable probe was positioned at 9D distances behind the circular cylinder. The velocities were normalized by dividing to the velocity values taken from the fixed probe. When the plasma was on, the velocity measurements were conducted at 2 kHz sampling frequency and 10000 velocity values were taken from each point. For the case without plasma, 16384 velocity values were taken from each point with the same sampling frequency.

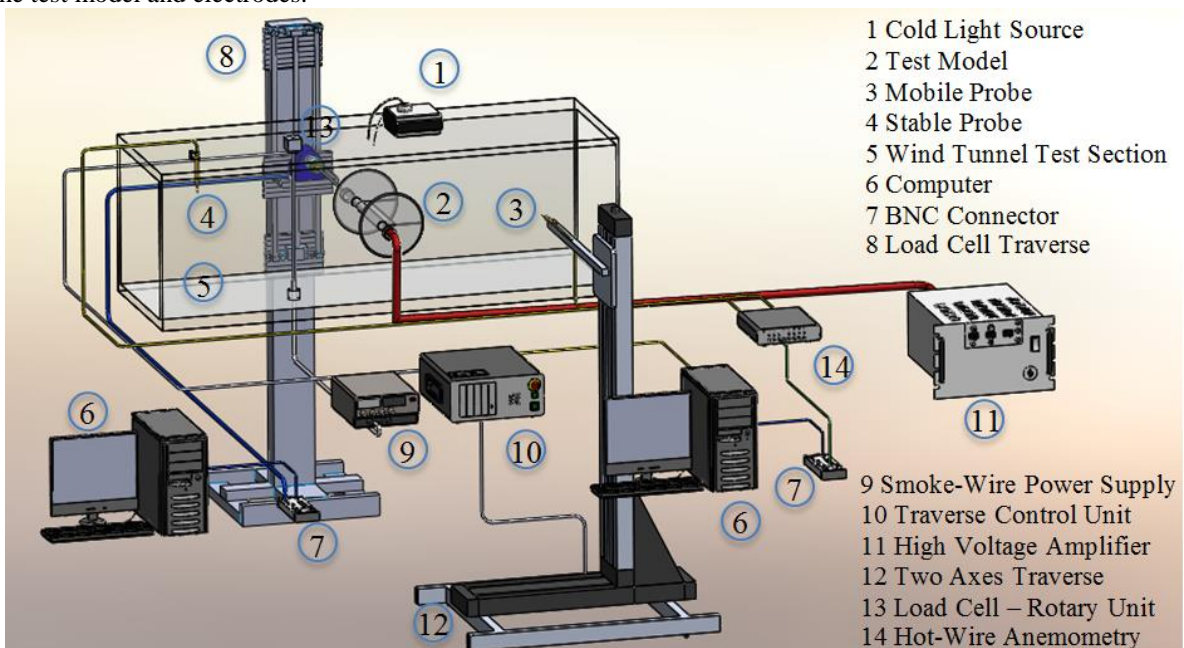


**Figure 3.** The schematic diagram of experimental setup.

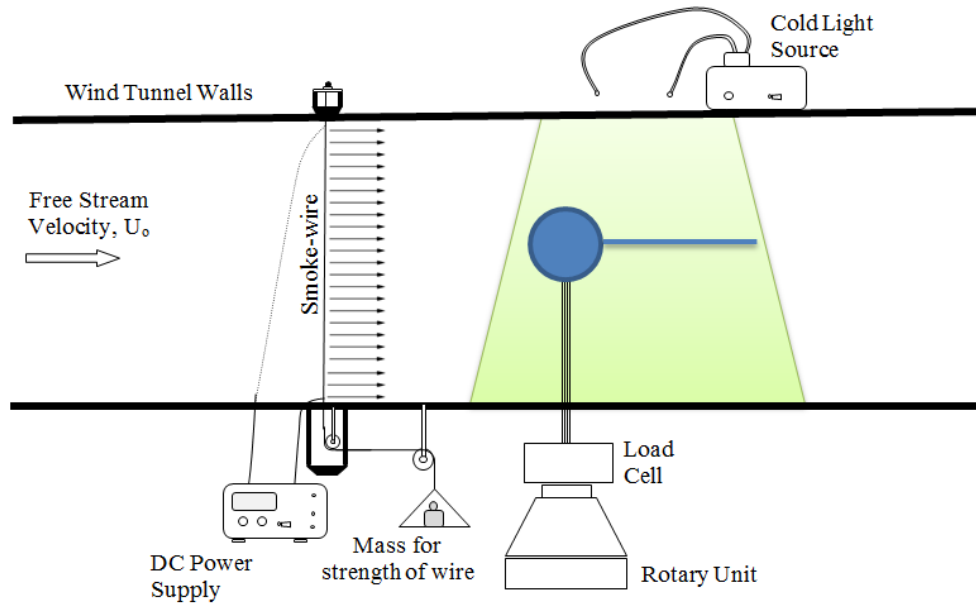


Figure 4. Schematic of smoke-wire method.

The test section of the wind tunnel consists of plexiglass and has a divergence angle of 0.3 degrees to keep the static pressure constant between the test section inlet and outlet. Free-stream turbulence intensity is about 0.5 % in the working Reynolds number range.

In order to measure the drag forces, ATI model six-axis load cell was used. This device was integrated on a computer controlled rotary unit. The measurements were taken at 100 Hz frequency and 50 values were averaged. For each measurement, 80 values were acquired in 40 seconds and each measurement was repeated 3 times for all parameters tested. Therefore, repeatability of the experiment was tested and reduction in error margin was aimed. The drag forces acting on the other components of the model, end-plates and the rod strut were extracted from the total drag force. As a result, the net drag force acting on the circular cylinder was calculated.

The uncertainty in the force measurement system was estimated to be less than  $\pm 5\%$ . The uncertainties of the load cell and data acquisition card were calculated in order to determine the uncertainty of the force measurements. The uncertainty in velocity measurement by the hot-wire anemometer was calculated to be less than  $\pm 5.2\%$ . To observe the flow around the circular cylinder, a smoke-wire method was used. Fig. 4 shows the schematic of the smoke-wire flow visualization method. A DC power supply was used to produce smoke from liquid paraffin.

## RESULTS AND DISCUSSION

The flow separation from the circular cylinder surface was manipulated by using plasma actuators. Flow visualization images of the experiments are given in Fig. 5 and Fig. 6 for Reynolds number of 4200. The voltage and frequency were  $6.5 \text{ kV}_{pp}$  and 3.5 kHz, respectively. As seen in Fig. 5, the plasma actuator without splitter

plate caused a smaller vortex formation region and the plasma actuator delayed the flow separation point to the rear side of the circular cylinder. In the case of splitter plate without plasma actuators (Fig.6), the vortex shedding region was extended towards the backside. By combining both flow control methods (plasma actuators and splitter plate), the width of the wake behind the circular cylinder was reduced (even further).

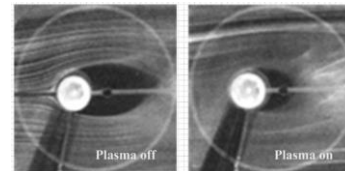


Figure 5. The effect of the plasma actuator on the flow visualization around the circular cylinder without splitter plate

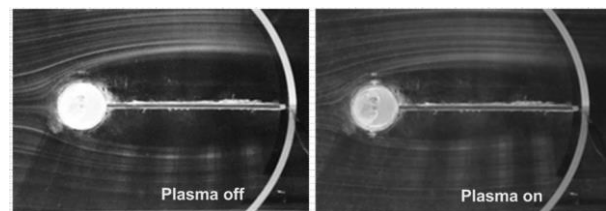
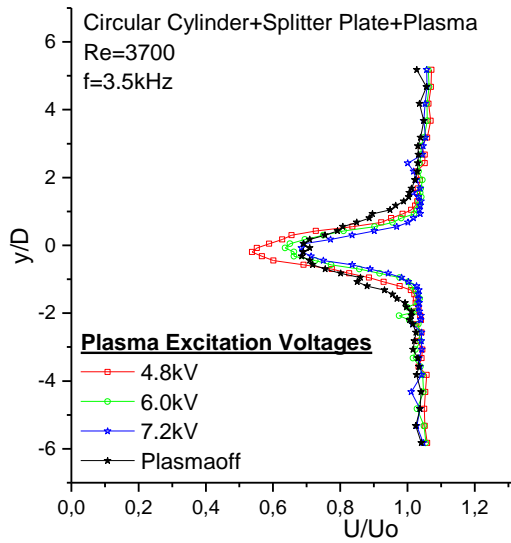


Figure 6. The effect of the plasma actuator and splitter plate on the flow visualization around the circular cylinder

The applied voltage is one of the most important parameters of the plasma generation. In this study, the effect of the applied voltage was investigated at  $Re = 4200$ . The applied signal frequency was a constant 3.5 kHz, the applied plasma voltage had 3 values, 4.8 kV, 6.0 kV, and 7.2 kV. Fig. 7 shows graphically the effect of the applied voltage on the ability of the plasma actuators to manipulate the wake region of the circular cylinder. For the lowest applied voltage value (4.8 kV), the ability of the plasma to control the flow around the circular cylinder was observed to be weak. But, an increase in the applied voltage gave rise to narrower wake



region. It is known that a narrow wake region cause reduction in the drag force by changing the base pressure. The narrowest wake region was obtained at 7.2 kV and wake region width ( $y/D$ ) was reduced from  $\pm 2$  to  $\pm 1$ .

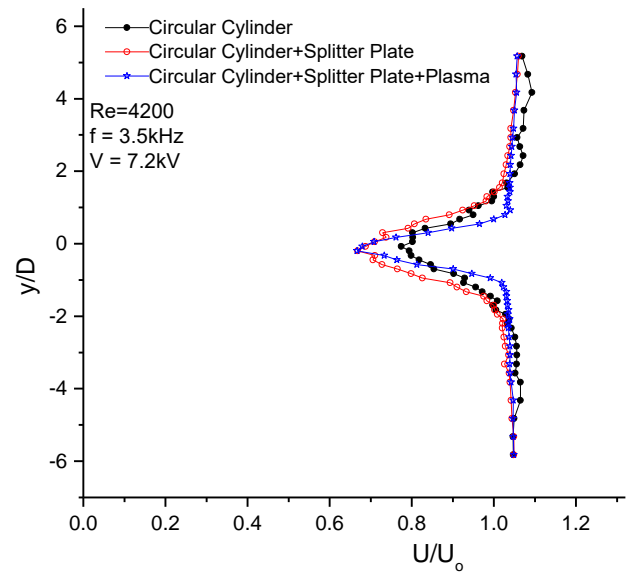


**Figure 7.** In case of the hybrid flow control method, the wake region analysis of the circular cylinder for the applied voltages (4.8kV, 6.0kV, 7.2kV) at  $Re = 4200$ .

Fig. 8 shows the wake region profiles for bare circular cylinder, circular cylinder with splitter plate, and circular cylinder with plasma actuator and splitter plate at  $Re = 4200$ . In this case, the applied voltage and signal frequency are kept constant at 7.2 kV<sub>pp</sub> and 3.5 kHz, respectively. The flow separation started earlier for the bare cylinder and the vortex shedding was observed at a shorter distance. The width of the wake was dramatically reduced when the hybrid control method was used. The splitter plate augmented the vortex formation length (distance between the center of the circular cylinder to the end of the splitter plate). The location of the flow separation delayed on a rear position. In addition to this, thinner wake region of the circular cylinder is observed. This can be seen easily from the flow visualization in Fig. 6. A spectral analysis was made to obtain the vortex characteristics for the bare circular cylinder the cylinder with splitter plate, and the hybrid flow control model. Fig. 9 shows the velocity time-histories and their power spectrums which were recorded at  $Re = 4200$  by using the moveable probe placed at  $x/D = 9$  and  $y/D = 0.9$ . In Fig. 9a, the vortex shedding is regular and the time-history of the bare circular cylinder has periodic fluctuations due to regular vortex shedding. On the other hand, the vortex shedding frequency decreases and bigger vortex formation length occurs for the circular cylinder with splitter plate.

The vortex shedding was almost prevented and random weak vortices occurred when the plasma actuators were activated. According to the instantaneous velocity distribution and the power spectrum analysis in Fig 9, the amplitude range of the velocity fluctuating values for the circular cylinder with splitter plate and the base circular cylinder (varied between 0.5 and 2.5) were

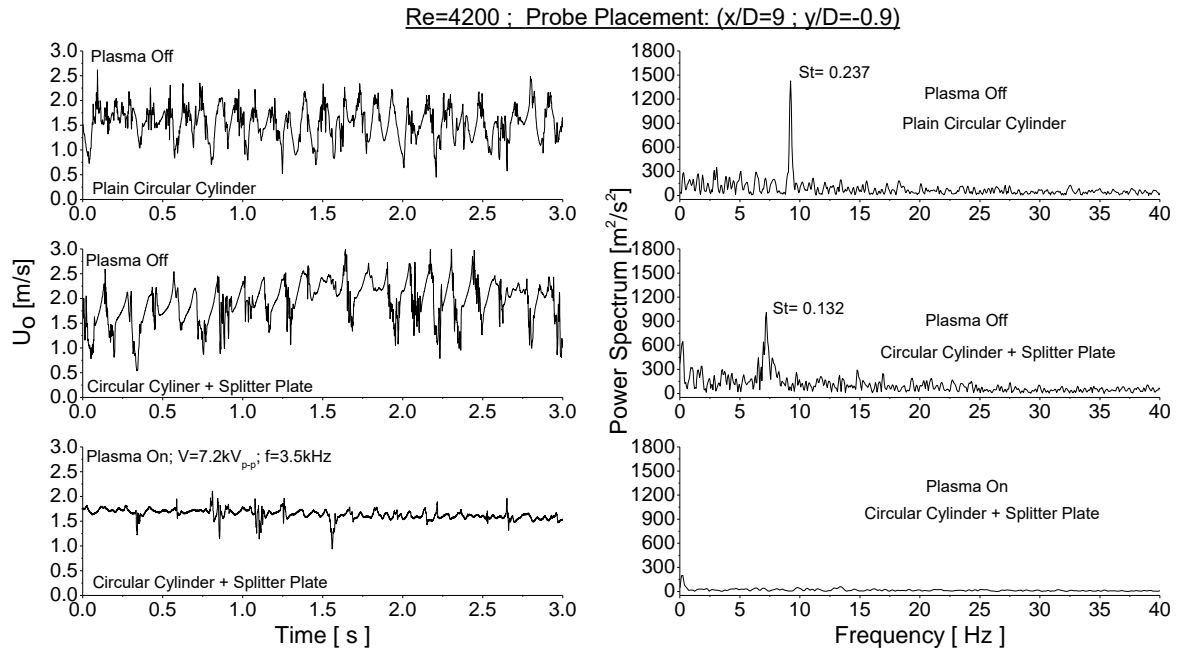
suppressed by the using plasma actuators. In the case of the circular cylinder with the plasma actuator and the splitter plate, the velocity amplitude range was attenuated between 1 and 2. Moreover, this disappearance of fluctuations in the velocity time history indicates that regular and strong vorticities are inhibited. Therefore, no pick values are observed in the frequency domain of the power spectrum analysis. When the plasma was activated, the vortex shedding was suppressed. Moreover, no peak value was observed for the vortex shedding frequency because of the random vortex shedding. In the study of Jukes and Choi, (2009), the vortex shedding was also suppressed when the surface plasma was placed on the separation point.



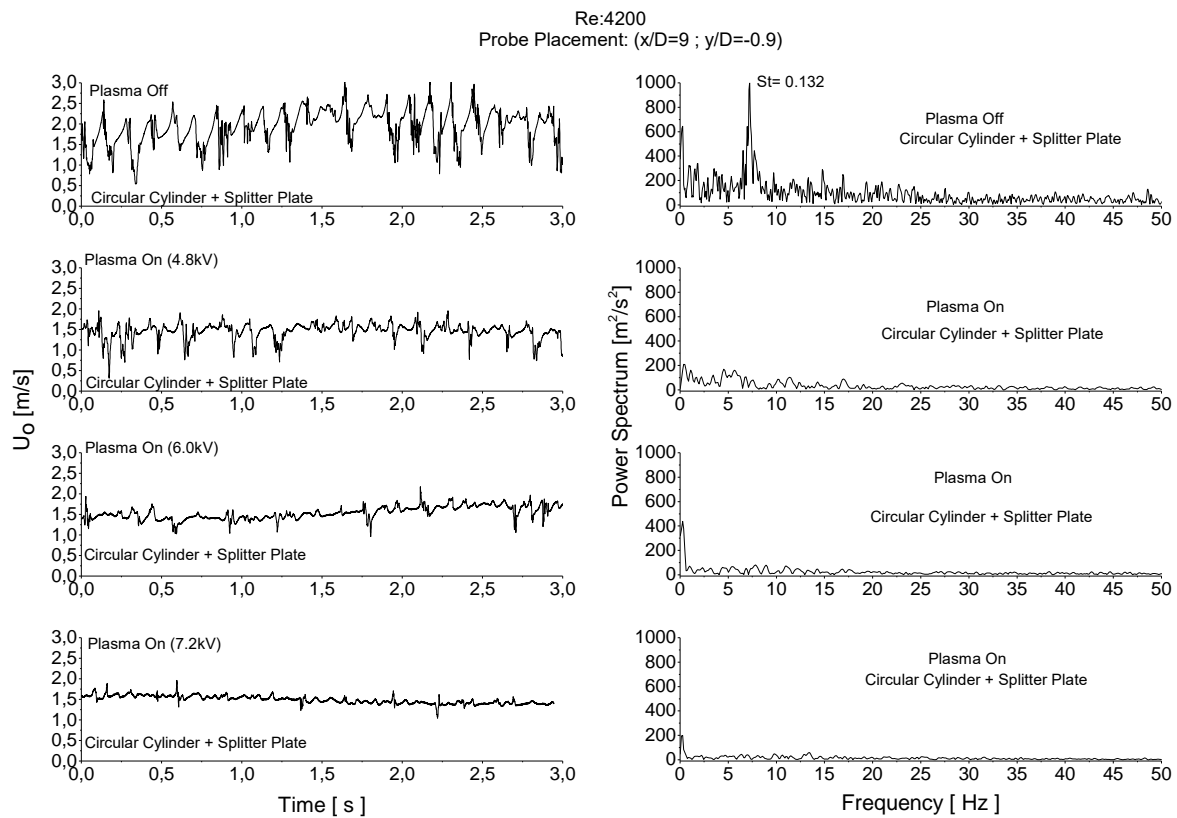
**Figure 8.** The wake region analysis for different flow control method.

Fig. 10 shows the effect of the applied voltage for the hybrid flow control method at  $Re = 4200$ . When the plasma was off, the vortex shedding behind the circular cylinder with the splitter plate occurred periodically. The vortex shedding started to become disordered when the plasma was on. The regular vortex shedding frequency was prevented when the applied plasma voltage was 4.8kV. Increasing the voltage value to 6 kV, random and small size vortices did not cause a dominant peak at the spectral area. Moreover, the irregular vortices were suppressed further when the voltage was increased gradually.

The drag coefficients of the four different cases of the test models were calculated based on the force measurement results. Table 1 shows the drag coefficients at  $Re = 5000$  and  $10000$ . In the active flow control method, the drag reduction was increased when the applied voltage was increased. But, the effect of the active flow control method was decreased with an increasing Reynolds number. The hybrid flow control method reduced the drag coefficient of the circular cylinder more than the case of passive or active control methods alone.



**Figure 9.** The time history and power spectrum analysis for the hybrid, active and passive flow control method at  $x/D = 9$  and  $y/D = 0.9$  probe positions.







**Figure 10.** The time history and power spectrum analysis for the hybrid and passive flow control method at  $x/D = 9$  and  $y/D = 0.9$  probe positions

In the case without a splitter plate, it is observed that the drag coefficient of the circular cylinder with the plasma actuator at an applied voltage of 10kV was less than the drag coefficient of the bare circular cylinder for all Reynolds numbers. The active flow control method was

more effective than passive flow control at  $Re = 5000$  when the applied voltage increased. The drag coefficient of the circular cylinder decreases from 1.24 to 0.73 when using active control with an applied volt of 10kV. However, when the Reynolds number increased to

10000, the splitter plate behind circular cylinder gave better results than the plasma actuator. The splitter plate decreases the drag coefficient to 0.90 while the plasma actuator decreases it from 1.35 to 0.98. In case of the hybrid flow control at Reynolds numbers of 5000 and 10000, the reduction in drag coefficient was calculated to be about 48% and 45%, respectively. For a Reynolds number of 5000, the passive flow control method reduced the drag coefficient from 1.24 to 0.84. By adding the effect of the active control, its value dropped down to 0.65.

**Table 1.** Variation of the coefficient of the test models depending on Reynolds numbers and the applied voltage.

Model type	Supply voltage [kV]	Reynolds Number		Drag Coefficient, $C_b$
		5000	10000	
	Plasma Off	1.24	1.35	
	6	1.13	1.35	
	8	0.76	1.13	
	10	0.73	0.98	
	Plasma Off	0.84	0.90	
	6	0.74	0.84	
	8	0.70	0.76	
	10	0.65	0.74	

## CONCLUSIONS

The presented study proposes a novel flow control approach based on the splitter plate and DBD plasma actuator used simultaneously. The proposed hybrid flow control method has been shown to have greater effect in order to control of the flow around the circular cylinder. A splitter plate was chosen as passive flow control device and its length was chosen to be 3.75D. Plasma actuators were placed on the circular cylinder at a position of  $\pm 90^\circ$  as active flow control device.

With the effect of the splitter plate, the vortex forming region was elongated to a point far from the rear side of the circular cylinder and separation shear layers from the surface of the cylinder gave rise to the narrow wake region. When the plasma was activated, the vortex shedding was suppressed. The use of plasma actuators prevents the natural vortex shedding from the bluff body due to the reattachment of the separated flow. In addition, when the plasma actuators are activated, the induced flow generates a cycle in which air are ionized. With the help of induced flow, the shear layer which tends to separate from the surface has been continued to flow on the surface of the cylinder. Thus, flow separation occurs at a more rear position of the cylinder which generates smaller, weaker and random vorticities. Moreover, no peak value was observed for the vortex shedding frequency because of the random and smaller vortex shedding. The usage of the plasma actuators delays the separation point. Furthermore, the wake width of the circular cylinder became narrower when the plasma voltage was increased. At the highest plasma voltage, the wake region width was decreased approximately 50% by suppressing the separated shear layer from the circular cylinder. However, no effect was

observed when the plasma excitation frequency was changed within our experimental range.

The drag force was also reduced significantly by means of the narrowing wake width when the plasma voltage increased (Table 1). It is observed that the hybrid flow control method is far more effective than just using either the passive or active method alone in an attempt to reduce drag coefficient. The reduction in drag of the circular cylinder with plasma actuator was not much effective compared to the bare circular cylinder when the Reynolds number increased. Therefore, the applied plasma voltage should be increased for higher Reynolds numbers. In this study, the reduction in the drag force was approximately 48% for the studied ranges of the voltages.

## ACKNOWLEDGEMENTS

The authors would like to acknowledge the financial support of this work by the Scientific and Technological Research Council of Turkey (TUBITAK) under the Contract Number of 110M056. The authors also thank the rest of the project team and Prof. Dr. Hakan YAVUZ for their assistance in the performing of the study.

## REFERENCES

- Akansu Y. E., Bayindirli C. and Seyhan M., 2016, The Improvement of Drag Force on a Truck Trailer Vehicle By Passive Flow Control Methods, *Isı Bilim. Tek. Derg./Journal Of Thermal Science And Technology*, 36(1), 133–141.
- Akansu Y. E., Ozmert M., and Firat E., 2011, The effect of attack angle to vortex shedding phenomenon of flow around a square prism with a flow control rod, *Isı Bilim. Tek. Derg./Journal of Thermal Science And Technology*, 31(1), 109–120.
- Akansu Y. E., Sarioglu M., and Yavuz T., 2004, Flow around a rotatable circular cylinder-plate body at subcritical Reynolds numbers, *AIAA J.*, 42(6), 1073–1080.
- Akbıyık H., Akansu Y. E., and Yavuz H., 2017, Active control of flow around a circular cylinder by using intermittent DBD plasma actuators, *Flow Meas. Instrum.*, 53, 215–220.
- Apelt C. J. and West G. S., 1975, The effects of wake splitter plates on bluff-body flow in the range  $10^4 < R < 5 \times 10^5$ , Part 2, *J. Fluid Mech.*, 71(1), 145–160.
- Apelt C. J., West G. S., and Szweczyk A. A., 1973, The effects of wake splitter plates on the flow past a circular cylinder in the range  $10^4 < R < 5 \times 10^4$ , *J. Fluid Mech.*, 61(1), 187–198.
- Cimbala J. M., and Leon J., 1996, Drag of freely rotatable cylinder/splitter-plate body at subcritical Reynolds number, *AIAA J.*, 34(11), 2446–2448.

Durhasan T., Aksoy M. M., Pinar E., Ozkan G. M., Akilli H., and Sahin B., 2016, Vortex street suppression of a circular cylinder using perforated semi-circular fairing in shallow water, *Exp. Therm. Fluid Sci.*, 79, 101–110.

Ekmekci A., 2014, Circular cylinders fitted with small-scale straight and helical wires: A comparative study on the wire-induced critical effects. *Exp. Therm. Fluid Sci.*, 53, 179–189.

Gim O. S., Kim S. H., and Lee G. W., 2011, Flow control behind a circular cylinder by control rods in uniform stream. *Ocean Eng.*, 38(17–18), 2171–2184.

Güler A. A., Seyhan M., and Akansu Y. E., 2018, Effect of signal modulation of dbd plasma actuator on flow control around NACA 0015. *Isi Bilim. Tek. Derg./Journal of Thermal Science and Technology*, 38(1), 95–105.

Jukes T. N. and Choi K.S., 2009, Active control of a cylinder wake using surface plasma, In *IUTAM Symposium on Unsteady Separated Flows and their Control*, (pp. 539–550), Springer.

Jukes T. N. and Choi K.S., 2009, Flow control around a circular cylinder using pulsed dielectric barrier discharge surface plasma. *Phys. Fluids*, 21(8), 84103.

Messanelli F., and Belan M., 2017, A comparison between corona and DBD plasma actuators for separation control on an airfoil, In *55<sup>th</sup> AIAA Aerospace Sciences Meeting*.

Nakamura Y., 1996, Vortex shedding from bluff bodies with splitter plates, *J. Fluids Struct.*, 10(2), 147–158.

Reza-zadeh S., 2013, Investigation of fluid flow around a cylinder with EHD actuation on inclined plates behind the cylinder, In *Proceedings of the 2013 International Conference on Applied Mathematics and Computational Methods in Engineering*.

Roshko A., 1961, Experiments on the flow past a circular cylinder at very high Reynolds number, *J. Fluid Mech.*, 10(03), 345–356.

Sarioglu M., 2016, Control of flow around a square cylinder at incidence by using a splitter plate, *Flow Meas. Instrum.*, 90(462), 1–21.

Sarioğlu M., Seyhan M., and Akansu Y. E., 2016, Aerodynamic forces acting on a circular cylinder with splitter plate at incidence, *KSÜ. Müh. Bil. Derg./Kahramanmaraş Sutcu Imam University Journal of Engineering Sciences*, 19(3), 1–6.

Sung Y., Kim W., Mungal M.G., and Cappelli M.A., 2006, Aerodynamic modification of flow over bluff objects by plasma actuation, *Exp. Fluids*, 41(3), 479–486.

Tabatabaeian S., Mirzaei M., Sadighzadeh A., Damideh V., and Shadaram A., 2012, Experimental investigation of the effects of various plasma actuator configurations on lift and drag coefficients of a circular cylinder including the effects of electrodes, *Chinese J. Aeronaut.*, 25(3), 311–324.

Thomas F. O., Kozlov A., and Corke T. C., 2008, Plasma Actuators for Cylinder Flow Control and Noise Reduction, *AIAA J.*, 46(8), 1921–1931.



**Hürrem AKBIYIK**, received his B.Sc. degree and M.Sc. degree in Mechanical Engineering from Niğde University in 2012 and 2014, respectively. He is currently a PhD student at Çukurova University, where he also works as research assistant. His research interests include plasma actuators for flow control and flow control applications.



**Yahya Erkan AKANSU**, received his B.Sc. degree in Mechanical Engineering from Erciyes University in 1993, M.Sc. degree and Ph.D. degree from Karadeniz Technical University in 1998 and 2004, respectively. He currently works as Professor in Mechanical Engineering Department of Niğde Ömer Halisdemir University. His research interests include active and passive aerodynamic flow control applications.



## NODAL THERMODYNAMIC AND DYNAMIC ANALYSIS OF A FREE DISPLACER STIRLING ENGINE

Can CINAR\*, A. Onur OZDEMIR\*\*, Halit KARABULUT\*\*\* and Mesut DUZGUN\*\*\*\*

Department of Automotive Engineering, Faculty of Technology, Gazi University, 06560, Ankara, Turkey

\*cancinar@gazi.edu.tr; ORCID: 0000-0001-6944-8864

\*\*onurozdemir@gazi.edu.tr; ORCID: 0000-0002-6475-1976

\*\*\*halitk@gazi.edu.tr; ORCID: 0000-0001-6211-5258

\*\*\*\*mduzgun@gazi.edu.tr; ORCID: 0000-0003-0582-4183

(Geliş Tarihi: 20.07.2020, Kabul Tarihi: 03.03.2021)

**Abstract:** In this study, the dynamic and thermodynamic features of free displacer Stirling engines were investigated by preparing a simulation program. The dynamic component of the simulation program involves the movement equations of power piston, crankshaft and displacer. The thermodynamic component is a nodal analysis based on 24 nodal volumes. The study indicates that starting these engines requires an initial speed is required as the displacer system natural frequency. While the engine is running, the displacer exhibits some secondary vibrations (named as beatings) and causes irregularities in its work and power generation however, it can be minimized by changing some working parameters such as displacer mass, working fluid mass, external loading, spring constant etc. For each value of the working fluid charging pressure, a different spring is needed. While the spring constant is the same, the displacer mass can vary in a limited range. The thermal performance of the engine increases as the displacer mass is decreasing. For an engine working between 1000 K heater temperature, 356 K cooler temperature and 18 bar charging pressure, the effective thermal efficiency ranges between 21 and 26 %. An engine with a 3.5 liter total inner volume is capable of generating about 3.9 kW effective power and 4.7 kW indicated power. A strong relation is observed between engine performance and phase angle.

**Keywords:** Dynamic and thermodynamic simulation, Free displacer Stirling engine, Performance prediction, Optimization of displacer mass, Optimization of spring constant.

## SERBEST DİSPLAYSIRLI BİR STİRLİNG MOTORUNUN NODAL TERMODİNAMİK VE DİNAMİK ANALİZİ

**Özet:** Bu çalışmada, serbest displaysırlı Stirling motorlarının dinamik ve termodinamik özellikleri bir simülasyon programı hazırlanarak incelenmiştir. Simülasyon programının dinamik kısmı, güç pistonu, krank mili ve displaysırın hareket denklemlerini içermektedir. Termodinamik kısmında da 24 nodal hacme dayanan bir nodal analiz yapılmıştır. Çalışmada, bu motorları ilk harekete geçirmek için, displaysırın doğal frekansı olarak bir başlangıç hızı gerektiği görülmektedir. Motor çalışırken displaysır vuru olarak adlandırılan bazı ikincil titreşimler sergilemekte, bu durum iş ve güç üretiminde düzensizliklere sebep olmaktadır. Bu durum, displaysır kütlesi, çalışma maddesi kütlesi, harici yük ve yay sabiti gibi bazı çalışma parametreleri değiştirilerek en aza indirilebilir. Çalışma maddesi şarj basıncının her bir değeri için farklı bir yaya ihtiyaç duyulmaktadır. Aynı yay sabiti değeri için, displaysır kütlesi sınırlı bir aralıkta değiştirilebilmektedir. Displaysır kütlesi azalırken motorun termal performansı artmaktadır. 1000 K sıcak uç sıcaklığı ve 356 K soğuk uç sıcaklığı arasında ve 18 bar şarj basıncında çalışan bir motor için efektif termik verim %21-26 arasındadır. 3,5 litre toplam iç hacme sahip bir motor, 3,9 kW efektif güç ve 4,7 kW indike güç üretebilmektedir. Motor performansı ile faz açısı arasında güçlü bir ilişki olduğu görülmektedir.

**Anahtar Kelimeler:** Serbest displaysır, Stirling motoru, Dinamik ve termodinamik simülasyon, Performans tahmini, Displaysır kütlesinin optimizasyonu, Yay sabitinin optimizasyonu.

### NOMENCLATURE

$A_v$	Heat transfer area of nodal volumes [ $m^2$ ]	$C_q$	Torsional damping constant of dynamometer [ $Nms/rad$ ]
$A_R$	Regenerator heat transfer area [ $m^2$ ]	$C_v$	Specific heat at constant volume [ $J/kg.K$ ]
$c$	Damping coefficient of displacer [ $Ns/m$ ]	$F_b$	The force applied by connecting rod to the piston, Fig. 3, [ $N$ ]
$C_{km}$	Hydrodynamic friction coefficient of crank pin bearing [ $Nm.s$ ]	$F_{bc}$	The force applied by piston rod to the crank pin [ $N$ ]
$C_{mj}$	Hydrodynamic friction coefficient of main journal bearing [ $Nm.s$ ]	$F_{bx}$	Horizontal component of $F_b$ [ $N$ ]

$F_{ch}$	The force generated by crankcase pressure, Fig. 3, [N]
$F_w$	The force generated by working volume pressure [N]
$F_\infty$	Coulomb friction generated by piston ring [N]
$H$	Length of piston rod [m]
$H_i$	Enthalpy flowing into the nodal volumes [J]
$H_o$	Enthalpy flowing out of the nodal volumes [J]
$h$	Heat transfer coefficient, Fig. 4, [W/m <sup>2</sup> K]
$h_i$	Specific enthalpy flowing into the nodal volumes [J]
$h_o$	Specific enthalpy flowing out of the nodal volumes [J]
$h_p$	Dimension of piston above the pin, Fig. 3, [m]
$I$	Mass moment of inertia of the crankshaft [kg.m <sup>2</sup> ]
$k$	Stiffness of spring [N/m]
$m$	Mass [kg]
$M_c$	The moment generated by $F_{bc}$ [Nm]
$m_d$	Displacer mass, Fig. 5, [kg]
$m_g$	Mass of working fluid [kg]
$m_i$	Mass flow into the nodal volumes [kg/s]
$m_o$	Mass flow out of the nodal volumes [kg/s]
$m_p$	The mass of power piston [kg]
$M_q$	External load [Nm]
$\bar{M}_q$	The cyclic average of external load [Nm]
$M_s$	Starter motor moment [Nm]
$P_e$	Effective power [W]
$P_i$	Indicated power [W]
$p_w$	Working space pressure [bar]
$p_{ch}$	Crankcase pressure [bar]
$R$	Crack radius [m]
$\mathfrak{R}$	Gas constant [J/kg.K]
$Q_c$	Cold source heat [J]
$Q_h$	Hot source heat [J]
$s$	Stroke of displacer [m]
$T_c$	Cooler temperature, Fig. 4, [K]
$T_h$	Heater temperature, Fig. 4, [K]
$T$	Working fluid temperature [K]
$T_w$	Wall temperature [K]
$V$	Volume [m <sup>3</sup> ]
$W_i$	Indicated work, Fig. 8, $W_i = \int_0^{2\pi} P dV$ , [J]
$W_Q$	Indicated work from heats, $W_Q = Q_h - Q_c$ , [J]
$x, y$	Coordinate elements, Fig. 1, [m]
$z$	Displacer position, Fig. 1, [m]
$\delta T$	Temperature difference between regenerator cells, Fig. 4, [K]
$\Delta m$	Mass variation in nodal volumes within time steps [kg]
$\Delta Q$	Heat exchange in nodal volumes within time steps [J]
$\Delta T$	Temperature variation in nodal volumes within time steps [K]
$\Delta t$	Time step [s]

$\Delta U$	Internal energy variation in nodal volumes during time steps [J]
$\Delta V$	Volume variation within time steps [m <sup>3</sup> ]
$\Delta W$	Work generation in nodal volumes within time steps [J]
$\alpha$	Convection heat transfer coefficient [J/m <sup>2</sup> K]
$\phi$	Phase angle [deg]
$\Omega$	A dummy parameter
$\psi$	The angle between the cylinder axis and connecting rod [rad]
$\sigma$	Coolant friction coefficient
$\eta_e$	Effective thermal efficiency [%]
$\eta_i$	Indicated thermal efficiency [%]
$\omega$	Nominal angular speed of crank shaft or engine [rad/s]
$\theta$	Crank shaft angle, Fig. 1, [rad]

## INTRODUCTION

Stirling engine is a technology that can be used to convert alternative energies into mechanical energy. Stirling engine is also eligible to improve the performance of the current energy conversion systems by hybridizing them with the Stirling engine. However, the current level of the Stirling technology is not sufficient to use them in industrial energy conversion systems. For the current situation at least 40 research teams are working on Stirling engines. Some of the recent research is presented in the following review of the literature.

Zhou et al. (Zhou *et al*, 2018) designed a miniature integrated nuclear reactor with reactor core and energy transfer system of the Stirling engine and a linear electric motor to convert fission energy into electric power. The authors analyzed the physical and thermodynamic properties and the safety performance of the nuclear reactor. It was concluded that the reactor could be used for space flight propulsion, Mars and the Moon base power supply and the deep sea applications. Kwankaomeng and coworkers (Kwankaomeng *et al*, 2014) conducted a thermodynamic and dynamic analysis of a free piston Stirling engine. The authors also manufactured and tested the free piston Stirling engine to evaluate the engine characteristic and performance. The engine provided 0.68 W maximum power at 6.4 Hz frequency with 10 W electrical heat supply. De la Bat et al. (De la Bat *et al*, 2020) described the thermodynamic and electrodynamic behavior of a free piston Stirling engine generator. To validate the numerical model, the linear generator and the free piston Stirling engine were tested and a good agreement was obtained with the numerical model. Zare and coworkers (Zare *et al*, 2020) investigated the performance of a free piston Stirling engine by describing the function technique and genetic algorithm. The authors predicted the amplitudes of the piston and displacer, operating frequency, phase angle, work and the output power. The simulation results were verified with the experimental data of SUTech-SR-1 prototype Stirling engine and a good agreement was obtained. Park et al. (Park *et al*, 2020) designed and tested a free piston Stirling engine equipped with a linear alternator. In the engine

two identical power pistons were used to ensure balancing.

The engine was tested with helium at 525 °C heater temperature and 20 °C cooler temperature using natural gas as fuel. The linear alternator produced 961 W at a frequency of 60 Hz and 23 % overall efficiency was obtained. Chi and coworkers (Chi *et al.*, 2020) developed a two-dimensional CFD model of a 100 W free piston Stirling engine using ANSYS Fluent. In the analysis, the variations of temperature and velocity field in the expansion chamber and compression chamber were investigated. The results of the simulation were compared with the experimental data using helium at 5 MPa. Tavakolpour-Saleh *et al.* (Tavakolpour-Saleh *et al.*, 2017) conducted a comprehensive mathematical modeling on a novel free piston Stirling engine. The authors concluded that the output power and efficiency were obtained as 7.8 W and 19.2 % at the operating frequency of 9.25 Hz. An active Stirling convertor namely SUTech-SR-2, was used to verify the numerical results and generated about 3.1 W output power. Karabulut (Karabulut, 2011) investigated the dynamic model of a free piston Stirling engine. In the engine, the piston and displacer were connected to the engine casing with springs. The engine having 50 mm piston diameter produced 200 W power at 700 K heater temperature and 15 bar charging pressure. Zare and Tavakolpour-Saleh (Zare and Tavakolpour-Saleh, 2020) studied the self-starting conditions of a free piston Stirling engine using analytical solution and Lyapunov function. Two prototype oscillators, named SUTech-SR-1 and B10-B were used to verify the numerical simulation result. By comparing the simulation and experimental results, the authors concluded that this method precisely predicts the onset condition of free piston Stirling engines. Cheng and coworkers (Cheng *et al.*, 2013) conducted the dynamic analysis of a thermal-lag Stirling engine. The authors optimized the brake thermal efficiency and engine power for different working parameters, such as bore, stroke and volume of the working spaces. The authors pointed out that, compared to other Stirling engine types relatively lower thermal efficiency was obtained with thermal-lag engines because the working fluid might not be swept effectively between the hot and cold compartments by the displacer. Masoumi and Tavakolpour-Saleh (Masoumi and Tavakolpour-Saleh, 2020) calculated the heat transfer and damping coefficients of an active free piston Stirling engine using a genetic algorithm. The authors also conducted two experimental tests for the identification of the heat transfer and damping coefficients. The identified parameters showed a good match with the experimental results. Majidniya *et al.* (Majidniya *et al.*, 2020) carried out a study on a free-piston Stirling engine coupled with a permanent magnet linear synchronous generator. The authors modeled the free piston Stirling engine and validated the model with experimental results. They also modeled the permanent magnet linear synchronous machine and then combined the dynamic equations of these systems to obtain the best performance. Ye and coworkers (Ye *et al.*, 2018) optimized the performance of a free piston Stirling engine using a regression model.

The authors obtained the output power, thermal and exergy efficiencies from the model. Operating and structural parameters such as hot and cooler temperatures, charging pressure, frequency, phase angle, lengths of heater and cooler were optimized to achieve maximum output power, thermal and exergy efficiencies. The error between the predicted and experimental results was found to be less than 5 %. Mou and Hong (Mou and Hong, 2017) analyzed a free piston Stirling engine using the experimental data. In the thermodynamic model, the non-isothermal effects, the regenerator effectiveness and the heat losses were taken into account. The authors calculated the output work, efficiency, pressure-volume variations and gas temperatures. Maximum output work and thermal efficiency were calculated as 120 W and 18 %, respectively with 90  $\mu\text{m}$  piston gap and 80° phase angle. Formosa (Formosa, 2011) conducted a coupled thermodynamic and dynamic analysis of a free piston Stirling engine. Thermal variables were defined using thermodynamic analysis, and the authors validated the model using experimental data from NASA RE-1000 free piston Stirling engine and a good agreement was obtained. Lin *et al.* (Lin *et al.*, 2020) developed a free piston Stirling generator and high temperature potassium heat pipes. Sage software was used for the thermodynamic modeling. The novel free piston Stirling generator was manufactured to weigh only 4.2 kg and was coupled with the potassium heat pipe. The authors obtained 142.4 W output power and 17.4 % thermal to electric conversion efficiency at a heater temperature of 574 °C. Mehdizadeh and Stouffs (Mehdizadeh and Stouffs, 2000) conducted the dynamic and thermodynamic analysis of a free piston Stirling engine with Martini configuration. In the engine the displacer was driven by an electric motor and two symmetrical free pistons were used. Helium was used as the working substance and the piston and the displacer diameters were 36 mm and 60 mm. The authors concluded that the phase angle between the piston and displacer could be controlled by variable electrical resistance without any modification in engine geometry. Begot and coworkers (Begot *et al.*, 2013) conducted the stability analysis of a free piston Stirling engine. In the analysis, the effects of operational and construction parameters such as mean pressure, hot source temperature, piston and displacer mass, pressure losses and dead volumes on the performance and stability were investigated. The numerical model was compared with the experimental results of the NASA RE1000 engine. It was obtained that regular mechanical parameters were obtained with large piston masses; however, more power was obtained with a light displacer. Wood and Lane (Wood and Lane, 2003) designed a free piston Stirling engine having linear alternator for space applications. The specific power of the engine was 100 W/kg and thermal to electric conversion efficiency was more than 50 % of Carnot. The authors compared the analysis results and test data of the Sunpower EG 1000 engine and small power level free piston Stirling engines. Abbas and coworkers (Abbas *et al.*, 2011) investigated a 100 MW solar power plant based on dish/Stirling technology for electricity production. The SAM software was used to evaluate monthly energy production, annual energy

output and cost of energy. The authors concluded that Tamanrasset in Algeria is a suitable site for solar electricity production. Zhu et al. (Zhu *et al.*, 2019) manufactured and tested a free piston Stirling engine combined with a parabolic trough collector. The optical and thermal losses of the Stirling engine/concentrated solar power system were analyzed. Test results showed that 2008 W maximum electric power with 15 % thermal to electric efficiency were obtained at a heater temperature of 300°C.

In free displacer Stirling engines the absence of mechanical linkage between the displacer and crankshaft provides some advantages such as more compact design, manufacturing simplicity, lower friction losses, longer life time and lighter weight etc. However, there is an uncertainty about the thermodynamic and dynamic behaviors of the engine. In a recent theoretical study, its dynamic behaviors were examined by Karabulut et al. (Karabulut *et al.*, 2020) via a dynamic simulation where the gas force was calculated with an isothermal nodal model. In the isothermal nodal model, the gas temperatures in the compartments are assumed to be equal to the solid surface temperatures. This assumption results in a zero entropy generation at internal heat transfer processes, and the thermodynamic cycle becomes internally reversible. Therefore, the isothermal nodal model does not provide data about the thermal efficiency of the engine.

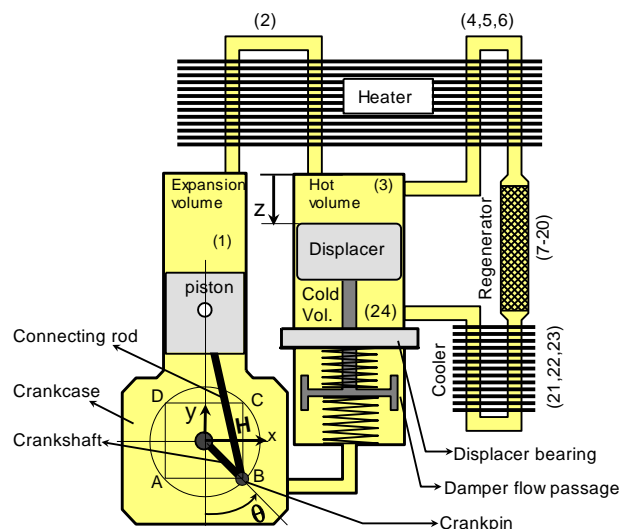


**Figure 1.** Schematic view of the free displacer engine (Karabulut *et al.*, 2020).

In this study, a combined thermodynamic and dynamic analysis of free displacer Stirling engines has been conducted. The main difference of this study from the paper of Karabulut et al. (Karabulut *et al.*, 2020) is that the gas force applied on the power piston and displacer is calculated via a polytropic nodal analysis where the gas temperature in nodal volumes is calculated with the first law of the thermodynamic differently from isothermal nodal analysis. In isothermal nodal analysis, as explained above, the gas temperatures in nodal volumes are assumed to be equal to the solid temperatures surrounding the nodal volumes. The combined thermodynamic and dynamic analysis conducted in this

study enables the prediction of heat transfer areas in the heater, cooler and regenerator as well as providing data about the thermal performance parameters of the engine. The analysis presented in this study provides also more realistic data about the dynamic behavior of the engine such as oscillation amplitude of the displacer and stable working conditions of the engine.

## ELEMENTS OF THE MECHANISM AND WORKING PROCEDURE

Figure 1 illustrates schematic view of the free displacer engine (Karabulut *et al.*, 2020). The engine consists of two principal sections as work generation and heat transfer modules. The work generation unit involves a crankshaft, a crankcase, a cylinder, a piston and its connecting rod. The heat transfer module involves a displacer and its cylinder, an axial rod bearing for displacer rod, a heater, a cooler, a regenerator, a spring, a damper and a room for displacer spring. The spring room is a cylindrical cavity. The pressure in the spring room is equated to the crankcase pressure by connecting the spring room to the crankcase with a pipe. The regenerator is a tub filled with porous material. The heater and cooler are flow passages filled with porous material as well. The damper may be built by mounting a perforated disc or a piston to the end of displacer rod. While the perforated disc or the piston is performing reciprocal motion in spring room, the gas in the spring room performs reciprocating flow through narrow flow channels and generates a damping force acting to displacer. The flow resistance appearing in the heater regenerator and cooler may also generate adequate damping force to stabilize the motion of the displacer.

The working procedure of the engine could be described by means of the crankshaft rotation diagram shown in Fig. 1 where, 360° rotation of the crankshaft is divided into 4 sections. As crankpin is moving from B to C, the displacer stays at upper end of the displacer cylinder. The piston moves upwards and sweeps the working substance from the expansion cylinder to the cold compartment of the displacer cylinder through the heater, regenerator and cooler. When this process is ended, the bulk of working fluid becomes compressed in the cold compartment of the displacer cylinder. While the crankpin is moving from C to D, the piston stays at the top dead center. The displacer moves down and sweeps the compressed working substance from the cold compartment to the hot compartment through the cooler, regenerator and heater. When this process ended, the temperature of the compressed gas becomes increased. The pressure of the gas is at the highest level of the thermodynamic cycle. While the crankpin is moving from D to A, the displacer stays at the lower end of the cylinder. The piston moves from up to down and the hot gas in the hot compartment of the displacer cylinder expands into the expansion cylinder and generates work. As the crankpin is moving B, the piston stays almost at the bottom dead center of its stroke. The volume of the expansion cylinder remains unchanged. The volume of the expansion cylinder remains unchanged. The displacer moves up and sweeps the gas from hot compartment to the cold compartment. When this process ended, the bulk temperature of the gas in the



working space of the engine becomes relatively lower. As a result of lower bulk temperature, the gas pressure in the working space decreases to its lowest value and becomes ready for a new cycle. According to this working procedure of the free displacer Stirling engine, the down motion of the displacer occurs  $90^\circ$  before the down motion of the piston in terms of crankshaft angle. This difference is named as phase angle.

## MATHEMATICAL MODEL

The mathematical model used in this study is a combination of a thermodynamic model and a dynamic model (Karabulut *et al*, 2020). The thermodynamic model consists of the first law of the thermodynamic, the perfect gas relation, the pressure formulae of Schmidt and kinematic formulations describing hot volume, cold volume and expansion cylinder volume. The thermodynamic model used in this study provides an opportunity to increase the number of nodal volumes in the heater, cooler and regenerator as desired. The dynamic model used in this study possesses two degrees of freedom such as freedom for the crankshaft mechanism and freedom for the displacer. The dynamic model consists of the movement equation of the displacer, the movement equation of the crankshaft and the movement equation of the power piston. The movement equation of the connecting rod was excluded from the analysis by increasing the piston mass about 30 % of the connecting rod mass. The independent variable of the analysis is time ( $t$ ). The principal dependent variables are displacer location ( $z$ ) and crankshaft angle ( $\theta$ ). The location of the piston ( $y$ ) is kinematically related to  $\theta$  and it is not a principal dependent variable.

The displacer performs an oscillatory motion under the influence of forces illustrated in Figure 2, which are; the gas force  $A_R(p_w - p_{ch})$ , spring force  $k(z - z_0)$  and damping force  $c\dot{z}$ . The damping forces are caused by the displacer damper as well as the viscous friction around the displacer rod and the flow resistances appearing in regenerator and connecting pipes. The damping coefficient  $c$  involves the contributions of all of these factors. The movement equation of the displacer is derived according to the local coordinate axis illustrated in Figure 2. The movement equation of the displacer is

$$m\ddot{z} + c\dot{z} + k(z - z_0) = A_R(p_w - p_{ch}) \quad (1)$$

where  $\dot{z}$  and  $\ddot{z}$  indicate the instantaneous velocity and acceleration of the displacer.

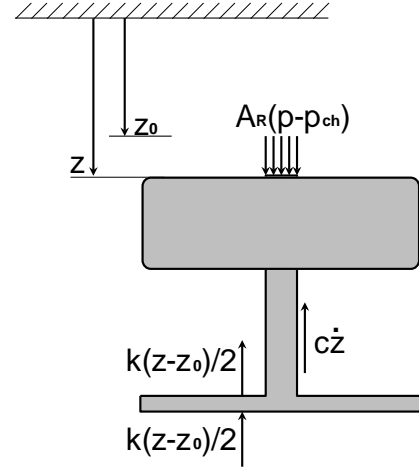


Figure 2. Forces acting on the displacer.

The forces considered in the establishment of movement equation of the piston are the gas force acting on the piston top ( $F_w$ ), the gas force acting to the down surface of the piston ( $F_{ch}$ ), the connecting rod force ( $F_b$ ), the frictional force generated by the piston rings ( $F_\infty$ ), the force generated by the solid contact friction at the piston side surface ( $\sigma F_{bx}$ ) and the force generated by the hydrodynamic friction at side surface of the piston ( $C_p \dot{y}$ ). The piston ring force ( $F_\infty$ ) and the solid contact friction force ( $\sigma F_{bx}$ ) are Coulomb type force. The forces acting on the piston and the local coordinate system used in the derivation of the movement equation of the piston are illustrated in Figure 3.

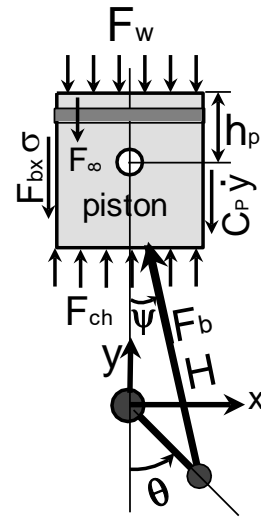


Figure 3. Forces acting on the piston.

The movement equation of the piston is

$$m_p \ddot{y} + C_p \dot{y} = F_b \cos \psi + F_{ch} - F_w - F_\infty \operatorname{sgn}(\dot{y}) - |\sigma F_{bx}| \operatorname{sgn}(\dot{y}) \quad (2)$$

In the last equation  $\psi$ ,  $\dot{y}$  and  $\ddot{y}$  indicate respectively the angle between the connecting rod and  $y$  axis, the velocity of the piston and the acceleration of the piston.

From the Equation (2), the force of connecting rod is defined as

$$F_b = \frac{m_p \ddot{y} + F_w - F_{ch} + C_p \dot{y}}{\cos \psi} + \frac{F_\infty \operatorname{sgn}(\dot{y}) + |\sigma F_{bx}| \operatorname{sgn}(\dot{y})}{\cos \psi} \quad (3)$$

In the last equation the numerator is equal to the vertical component of the force vector exerted by the connecting rod to the crankpin. According to the  $x, y$  coordinate system indicated in Figure 1, the force vector applied by the connecting rod to the crankpin is defined as

$$\vec{F}_{bc} = (F_b \sin \psi) i - \left[ \begin{array}{l} m_p \ddot{y} + F_w - F_{ch} + C_p \dot{y} + \\ F_\infty \operatorname{sgn}(\dot{y}) + |\sigma F_{bx}| \operatorname{sgn}(\dot{y}) \end{array} \right] j \quad (4)$$

The moment rotating the crankshaft is generated by the force vector defined by the last equation. The crank radius ( $R$ ) is the moment arm of this force vector. Considering the coordinate system indicated in Figure 1, the vector form of the moment arm is defined as

$$\vec{R} = R \sin \theta i - R \cos \theta j \quad (5)$$

By performing the vector product of the vectors given by the last two equations, the moment rotating the crankshaft is determined as

$$M_c = (-\sin \theta + \cos \theta \operatorname{tg} \psi) R \left[ \begin{array}{l} m_p \ddot{y} + F_w - F_{ch} + C_p \dot{y} + \\ (F_\infty + |\sigma F_{bx}|) \operatorname{sgn} \dot{y} \end{array} \right] \quad (6)$$

In the derivation of the movement equation of the crankshaft, the moment defined with Equation (6), the moment of the main journal viscous friction ( $C_{mj} \dot{\theta}$ ), the moment of the crankpin viscous friction ( $C_{km} \dot{\theta}$ ), the moment of the starter motor ( $M_s$ ) and the external load applied to the engine ( $M_q$ ) are considered. The movement equation of the crankshaft may be written as

$$\ddot{\theta} = \frac{M_c}{I} + \frac{M_s}{I} - \frac{M_q}{I} - \frac{C_{mj}}{I} \dot{\theta} - \frac{C_{km}}{I} (\dot{\theta} - \dot{\psi}) \quad (7)$$

The external load ( $M_q$ ) may be considered to be generated by an electrical or hydrodynamic torque generator and defined as

$$M_q = C_q \dot{\theta} \quad (8)$$

The velocity and acceleration of the piston, taking part in above equations, vary with the position angle of the

crankshaft ( $\theta$ ) and obtained from the kinematic relation defining the position of the piston top in terms of  $\theta$ . According to the coordinate system seen in Figure 3, the position of the piston top is defined as

$$y = -R \cos \theta + H \cos \psi + h_p \quad (9)$$

where  $H$  and  $h_p$  were shown in Figure 3. The velocity and acceleration of the piston are

$$\dot{y} = R \sin \theta \dot{\theta} - H \sin \psi \dot{\psi} \quad (10)$$

$$\ddot{y} = R \cos \theta \dot{\theta}^2 + R \sin \theta \ddot{\theta} - H \cos \psi \dot{\psi}^2 - H \sin \psi \ddot{\psi} \quad (11)$$

The angular speed ( $\dot{\psi}$ ) and acceleration ( $\ddot{\psi}$ ) of the connecting rod are obtained from

$$\psi = \arcsin \left( \frac{R}{H} \sin \theta \right) \quad (12)$$

which are not presented here for the brevity of the paper.

The Schmidt formula was used to calculate the engine inner pressure. In this analysis the pressure difference between the nodal volumes due to flow friction is disregarded. The inner volume of the mechanism was divided into 24 nodal volumes. The first of the nodal volumes is the expansion volume seen in Figure 1. The second of the nodal volumes is the volume of a pipe connecting the expansion volume to the displacer cylinder. The third of nodal volumes is the hot end volume of the displacer cylinder which is a periodically varying volume. Nodal volumes 4, 5 and 6 take part in heater. Nodal volumes 7-20 take part in regenerator. Nodal volumes 21, 22 and 23 take part in cooler. The nodal volume 24 is the cold end volume of the displacer cylinder which is a varying volume as well. For a nodal analysis with 24 volumes Schmidt formula is written as

$$p_w = \frac{m \mathfrak{R}}{\sum_{n=1}^{n=24} \frac{V_n}{T_n}} \quad (13)$$

Within a time step, the variation of gas temperature in a nodal volume ( $\Delta T$ ) may be calculated with the first law of thermodynamics.

By canceling the kinetic energy, potential energy and heat generation terms, the first law is written as

$$\Delta Q - \Delta W = (m_o h_o) - (m_i h_i) + (\Delta U) \quad (14)$$

In this equation  $\Delta Q$ ,  $\Delta W$ ,  $\Delta U$ ,  $(m_o h_o)$  and  $(m_i h_i)$  indicate nodal values of the heat exchange, work generation, internal energy variation, outflow of enthalpy

and inflow of enthalpy. By using the definitions  $\Delta Q = \alpha A_v (T_w - T) \Delta t$ ,  $\Delta W = p \Delta V$ ,  $\Delta U = m C_v \Delta T + C_v T \Delta m$ ,  $m_o h_o = H_o$  and  $m_i h_i = H_i$ , Equation (14) is transformed to

$$\alpha A_v (T_w - T) \Delta t - p_w \Delta V = H_o - H_i + m C_v \Delta T + C_v T \Delta m \quad (15)$$

By adding  $\Omega \Delta T$  to both sides of the last equation and then solving for  $\Delta T$  results in

$$\Delta T = \left[ \frac{\alpha A_v (T_w - T) \Delta t - p_w \Delta V + (H_i - H_o)}{C_v T \Delta m + \Omega \Delta T} \right] / (m C_v + \Omega) \quad (16)$$

The temperature variation in nodal volumes during time steps is calculated with the above form of the first law. In this equation, the difference between inflowing and outflowing enthalpies is calculated with

$$(H_i - H_o) = -C_p \frac{T_{n-1} + T_n}{2} \left[ \begin{aligned} &(m_1 - m_1^F) + \\ &(m_2 - m_2^F) + \\ &\dots + (m_{n-1} - m_{n-1}^F) \end{aligned} \right] - C_p \frac{T_n + T_{n+1}}{2} \left[ \begin{aligned} &(m_{n+1} - m_{n+1}^F) + \\ &(m_{n+2} - m_{n+2}^F) + \\ &\dots + (m_{24} - m_{24}^F) \end{aligned} \right] \quad (17)$$

In the last equations, the superscript  $F$  indicates the time-step before the current one. For the current time step, gas temperatures in cells are calculated as

$$T = T^F + \Delta T \quad (18)$$

The gas masses in cells are calculated with the state equation of the perfect gasses, which is

$$m = \frac{p_w V}{\mathfrak{R} T} \quad (19)$$

The instantaneous values of the expansion volume (1), hot volume (3) and cold volume (24) are simply formulated by using kinematic relations which are not given here to sake the brevity of the analysis.

The solution of the equations (1) and (7) in time domain requires two boundary conditions for each. The appropriate boundary conditions are  $t=0$ ,  $z=0$ ,  $\dot{z}=0$ ,  $\theta=0$ ,  $\dot{\theta}=0$ . To initiate the solution process, the initial pressure in the refrigerator, the initial gas temperatures in cells and initial gas masses in cells are needed. For initial gas temperatures in cells, values equal to the wall temperatures of cells may be

introduced. So, the initial pressure in the engine is able to be calculated with equation (13). The initial values of nodal masses can be calculated with Equation (19). After the determination of all initial values, the calculation of unknowns at subsequent time steps are conducted. For numerical procedure, readers may refer to the reference (Karabulut *et al.*, 2020; Altin *et al.*, 2018; Karabulut *et al.*, 2019).

## Inputs Used In the Analysis

In this study, the solid surface temperatures of the heater, cooler, expansion cylinder and displacer cylinder are assumed to be pre-known values. The distribution of matrix temperature in the regenerator is also assumed to be a pre-known. Figure 4 indicates the temperature of solid surfaces and regenerator matrix.

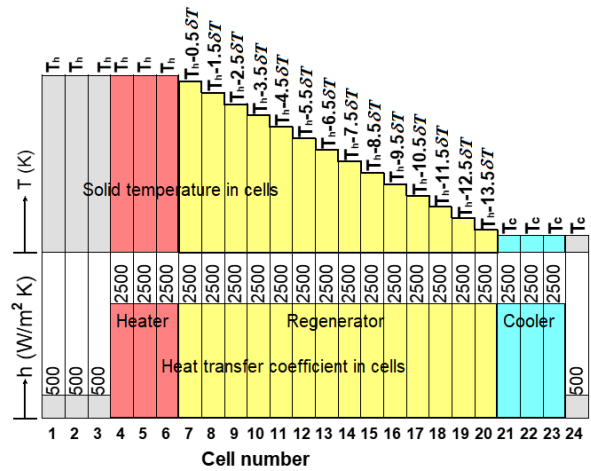


Figure 4. Solid surface temperature and heat transfer coefficient in cells of the engine.

Figure 4 also indicates the distribution of the heat transfer coefficient in cells of the engine. The heat transfer coefficient in the regenerator has been used from Tanaka and coworkers (Tanaka *et al.*, 1990). The heat transfer coefficients in cooler and heater were taken to be equal to that in the regenerator matrix because the cooler and heater were assumed to be flow passages filled with porous material. The heat transfer coefficient of expansion and displacer cylinders were predicted via theoretical approximations. Specific values and inputs used in the analysis are presented in Table 1. Specific values were determined by aiming an engine able to provide 3 kW or more power.

## RESULT AND DISCUSSION

The robustness of the results depends on the magnitude of time steps and rotation number of the engine from starting instant. The time step has influences on the precision of numerical results as well as the robustness of work calculation with numerical integration. The magnitude of time steps was determined to be 0.00001 s by trial and error. The rotation number of the engine is related to obtaining steady running conditions of the engine. Unless the rotation number of the engine reaches to a certain value, the calculated parameters involves the

influence of initial condition. If the engine rotates about 300 revolutions, steady state conditions are reached.

**Table 1.** Specific values and inputs used in the analysis.

Specific values and inputs	Numerical value
Torsional damping constant of crankshaft main bearings ( $Nsm/rad$ )	0.00019
Torsional damping constant of crankshaft connecting rod bearing ( $Nsm/rad$ )	0.00012
Damping constant of piston ( $Ns/m$ )	2.0
Coulomb friction coefficient of piston	0.04
Crosscut area of displacer cylinder ( $m^2$ )	100/10000
Piston mass ( $kg$ )	1.5
Crosscut area of expansion cylinder ( $m^2$ )	100/10000
Working substance	Helium
Crank radius ( $m$ )	0.04
Piston connecting rod length ( $m$ )	0.16
Total stroke length of the displacer cylinder ( $m$ )	0.09
Regenerator heat transfer area ( $m^2$ )	5
Regenerator porosity	0.7
Regenerator total volume ( $m^3$ )	1.04166/1000
Dead volume in regenerator ( $m^3$ )	7.29166/10000
Heater heat transfer area ( $m^2$ )	1.5
Heater temperature, $T_h$ , ( $K$ )	1000
Dead volume in heater ( $m^3$ )	2.1875/10000
Cooler heat transfer area ( $m^2$ )	1.5
Cooler temperature, $T_c$ , ( $K$ )	356
Dead volume in cooler ( $m^3$ )	2.1875/10000
Average heat transfer area in expansion cylinder ( $m^2$ )	400/10000
Average heat transfer area in hot compartment of displacer cylinder ( $m^2$ )	300/10000
Average heat transfer area in cold compartment of displacer cylinder ( $m^2$ )	300/10000

## Dynamic Behaviors of the Engine

In the Stirling engine examined here, the vibration of the displacer is governed by several parameters such as, engine pressure variation, the crosscut area of the displacer rod, the spring constant, the mass of displacer itself and the damping force exerting on displacer etc. To run a free displacer Stirling engine, the power piston should make a reciprocational motion at a frequency equal to the displacer system natural frequency. When the engine is rotated via a starter motor, the working gas pressure in the engine performs periodic variations. Because of periodically varying pressure, the displacer tends to make vibrational motions. If the frequency of the pressure variation increases to the displacer system natural frequency, the amplitude of the vibrational motion of the displacer increases to an adequate magnitude and causes the working gas to displace between the hot and cold compartments. While the piston and displacer are performing up and down periodic motions, the inertia of the displacer generates a phase angle and enables heating, expansion, cooling and compression processes.

Unless the piston frequency increases to the displacer system natural frequency, the engine does not run. Therefore, a high speed starter motor is needed, to start free displacer Stirling engines.

Another dynamic problem of the free displacer Stirling engine is running irregularities named beating. Beating is some periodic increases and decreases in the stroke length of the displacer. Due to beating, the work generation of the engine exhibits some increases and decreases. Beating may be minimized but not eliminated completely. If there is a certain equilibrium between the spring constant, mass of oscillating object and damping constant of the system; beating becomes small enough. In oscillating linear systems, the equilibrium between the spring constant, damping constant and mass of the oscillating system may be treated analytically, but the free displacer Stirling engine is not a linear system. In free displacer Stirling engines, the minimization of beating requires an interactive process via a simulation program.

Table 2 indicates an optimized set of interactive parameters corresponding to 160000 N/m spring stiffness. Figure 5 indicates the variation of displacer position with crankshaft angle for a non-optimized set of working parameters. Data used in Figure 5 were obtained by using the optimized set of working parameters given in Table 2 except the mass of the displacer. The mass of the displacer was taken to be 1.75 kg. As shown in Figure 5, the amplitude of the displacer motion exhibits some increases and decreases. This variation of the displacer amplitude repeats itself periodically over a certain number of engine cycles or, in a certain interval of crankshaft angle. Figure 6 indicates some sequential PV diagrams of the engine which were obtained also with 1.75 kg displacer mass and interactive parameters given in Table 2. As seen from Figure 6, the PV diagrams are varying from cycle to cycle.

**Table 2.** An optimized set of interactive parameters determined for 160000 N/m spring stiffness.

Interactive parameters	Numerical value
Spring constant ( $N/m$ )	160000
Torsional damping constant of the dynamometer ( $Nsm/rad$ )	0.03
Damping constant of displacer rod ( $Ns/m$ )	15.0
Crosscut area of displacer rod ( $m^2$ )	6/10000
Working gas mass ( $kg$ )	0.0065
Displacer mass ( $kg$ )	1.722
Static position of displacer top, $x_0$ , ( $m$ )	0.05
Mass moment of inertia of the crankshaft ( $m^2kg$ )	0.1

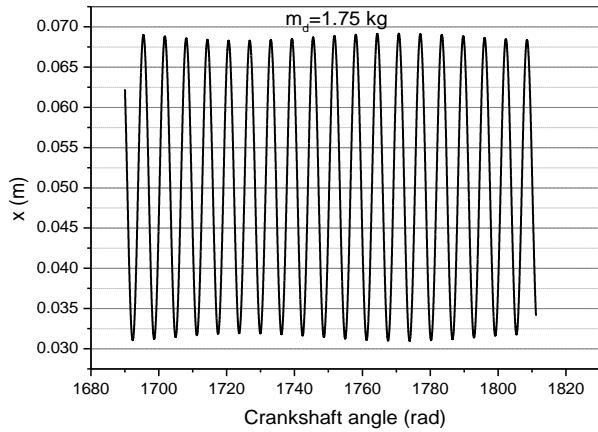


**Figure 5.** Variation of displacer position with time for optimized inputs.

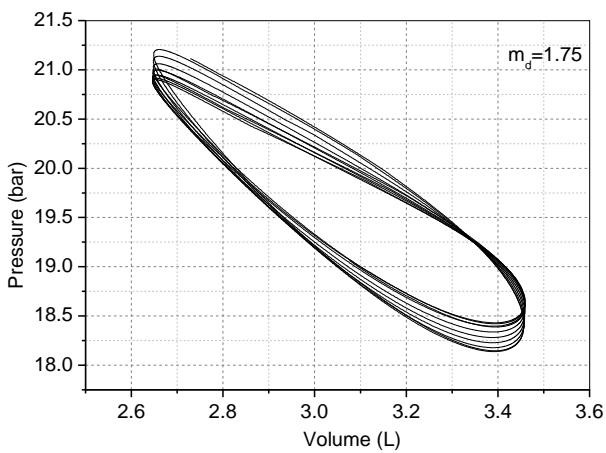


**Figure 6.** Sequential PV diagram obtained for optimized inputs excluding displacer mass.

In simulation program, in case of setting 1.722 kg displacer mass, which is given in Table 2, beating becomes insignificant and variations of the work and other thermodynamic values from cycle to cycle are avoided. Figure 7 indicates variation of the displacer position with crankshaft angle while Figure 8 is indicating a number of sequential PV diagrams. As seen in Figure 7, the displacer motion exhibits no visible beating. According to Figure 8, the overlap of PV diagrams is quite good.

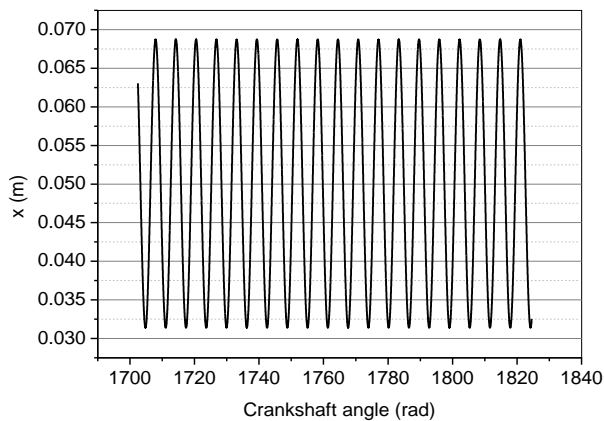


**Figure 7.** Variation of the displacer position with time.

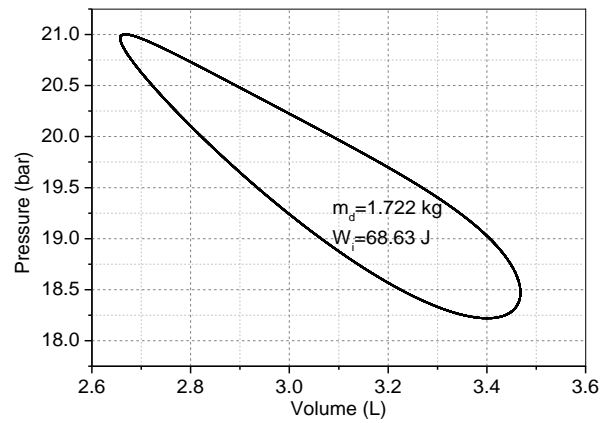


**Figure 8.** PV diagram obtained for inputs in Table 1 and 2.

### Examination of the Engine Performance with Respect to Displacer Mass

In free displacer Stirling engines, one of the principal parameters having influence on the working performance of the engine is the displacer mass. In this examination, by using the inputs given in Table 2 and by introducing different values for the displacer mass, results presented in Table 3, in Figure 9 and in Figure 10 were obtained. At 1.353 kg, 1.47 kg, 1.589 kg, 1.722 kg and 1.87 kg values of the displacer mass, very robust results were obtained. Just under 1.353 kg, and just over 1.87 kg, the engine keeps working, but overlapping of the sequential PV diagrams becomes imperfect. If the displacer mass is further decreased after giving an initial motion to the engine via the starter motor, it does not continue to run and gradually goes to stop. In case the displacer mass increases further, it performs steadily increasing strokes and goes out of stable working. The most perfect overlapping of the sequential PV diagrams occurs at some certain values of the displacer mass, which are given in the Table 3. Between these values of the displacer mass, the overlapping of the sequential PV diagrams is poor. In Table 3, Figure 9 and Figure 10, it is seen that as the displacer mass is decreasing, the performance parameters of the engine (torque, speed, thermal efficiency and power) become profoundly better although the heat exchanges between the working fluid and heat sources are almost the same. Therefore, the increase in engine performance is not relevant to the heat exchange rates between working fluid and heat sources. As seen in Table 3, while the displacer mass is decreasing from 1.87 kg to 1.353 kg, the phase angle between the piston and displacer varies from 120° to 103°. In most of the kinematic engine, the highest performance appears at about 90° phase angle. This situation implies that the increase of the engine performance is mainly raised due to the phase angle variation.

In Table 3, it is seen that the indicated thermal efficiency of the engine varies between 23.7 % and 27.7 %. For the working temperature limits of the current engine, the Carnot efficiency is about 64 %. The big difference between these thermal efficiencies is caused by insufficient circulation of the working fluid between the hot and cold compartments of the displacer cylinder. In

this engine, as seen in Table 3, the stroke of the displacer varies between 36.7 mm and 37.89 mm although that the displacer cylinder length is 90 mm. This indicates that more than half of the working fluid contained by the displacer cylinder is left out of circulation. As a result of this disadvantage, the thermal efficiency of the free displacer engines becomes too lower than the Carnot efficiency.

While the displacer mass is decreasing, the natural frequency of the displacer system increases consistently with the nature of the vibrating systems. As a result of this phenomenon, the speed of the engine performs an accelerating increase as shown in Figure 10. As the displacer mass is decreasing, the torque of the engine

increases as well. The increase of the torque is likely to be related to the variation of the phase angle. As a result of the increase in engine speed and torque, the indicated power and effective power exhibit better increase as shown in Figure 10. The mechanical efficiency of the engine ( $P_e / P_i$ ) varies between 83.7 % and 80.6 %. The highest values of the indicated power and effective power are 4394 and 3588 W respectively. The density of indicated power of the engine is about 1275 W/L. At 1.353 kg displacer mass, and the engine provides the highest performance parameters. A displacer mass of 1.353 g is found to be appropriate for manufacturing as well.

**Table 3.** Variation of performance parameters with respect to the displacer mass.

$m_d$ (kg)	$\omega$ (rad/s)	$\bar{M}_q$ (Nm)	$W_i$ (J)	$W_Q$ (J)	$Q_h$ (J)	$Q_c$ (J)	$\eta_e$ (%)	$\eta_i$ (%)	$P_e$ (W)	$P_i$ (W)	$\phi$ (deg)	$s$ (mm)
1.353	345.81	10.375	79.84	80.80	288.6	207.8	0.2258	0.2766	3587.6	4394.1	103	36.70
1.47	329.72	9.892	74.20	72.79	292.1	219.3	0.2128	0.2540	3261.5	3893.5	109	36.90
1.589	316.03	9.482	71.26	69.57	292.2	222.7	0.2038	0.2438	2996.5	3584.0	113	37.08
1.722	303.60	9.108	68.63	67.45	291.0	223.5	0.1967	0.2359	2765.1	3316.2	117	37.28
1.87	295.45	8.863	69.11	68.40	291.8	223.1	0.1908	0.2368	2618.6	3249.7	120	37.89

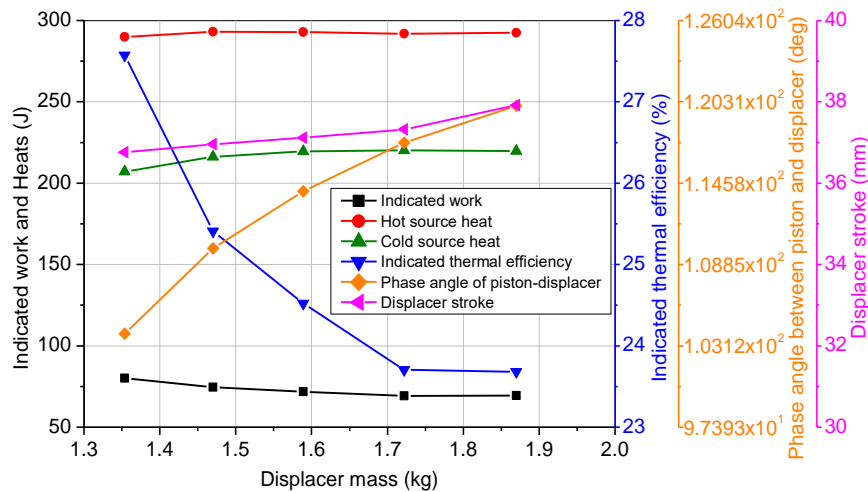


**Figure 9.** Variations of indicated work, heats, thermal efficiency, phase angle and stroke.

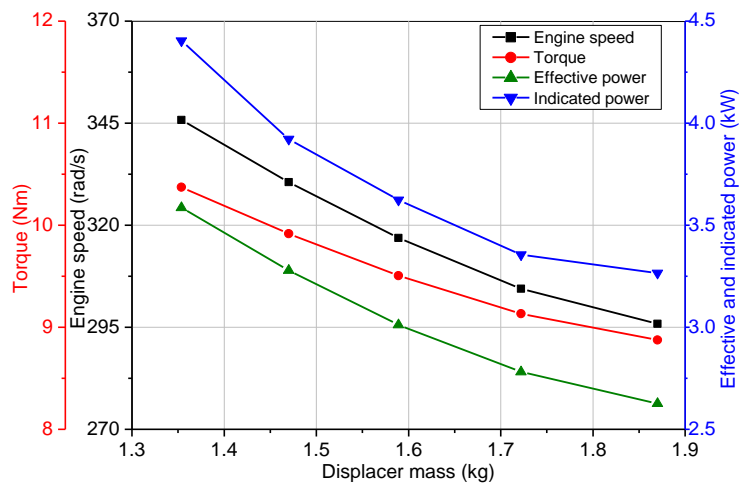


**Figure 10.** Variations of speed, torque and power with displacer mass.

### Examination of the Engine Performance with Respect to Working Gas Mass

In Stirling engines, the only way to increase specific power is to increase the mass of the working fluid. The appropriate amount of the working fluid to be charged is determined by optimizing the performance parameters of the engine with respect to the working fluid mass. In this examination, excluding the working fluid mass and spring stiffness, all of the inputs were kept constant. The working fluid mass was varied between 6.5 g and 4.75 g. Therefore, in the above examination the highest performances were obtained at 1.353 kg displacer mass, and the mass of displacer was taken to be 1.353 kg. As the working fluid mass was varying, at some values of the spring stiffness, the sequential PV diagrams become overlapped and robust performance data are obtained. Appropriate values of the spring stiffness that meet the overlapping condition of PV diagrams are presented in Table 4, as well as the performance parameters of the engine. Figure 11 and Figure 12 illustrate the variations of the performance parameters with respect to working fluid mass. As seen in Figure 11 and Table 4, while the gas mass is varying from 4.75 g to 6.5 g, the speed displays a decelerating increase from 295 rad/s to 338 rad/s. In essence, the relation between the working fluid mass and speed is an indirect relation as the speed is dependent on the displacer system natural frequency. Therefore, the real cause of the speed variation is the variation of the spring stiffness. As shown in Figure 11, the variation of the torque with the working fluid mass is also a decelerating increase. While the mass of working fluid is varying from 4.75 g to 6.5 g, the torque varies from 8.832 Nm to 10.15 Nm. The variation of the torque profile is related to the temperature limits of the thermodynamic cycle as well as frictional losses. While the mass of the working fluid increases, inherently its heat storage capacity increases as well. Due to the larger heat storage capacity of the working fluid, the difference between the upper and lower limits of the temperature of the cycle becomes narrow. The increasing speed of the engine has also some effects on narrowing the temperature difference of the thermodynamic cycle thereby reducing the heat exchange time. As a result of narrowing temperature difference, the torque becomes lower inherently. It is also inherent that the higher working fluid mass is higher working fluid pressure and higher frictional losses. As seen in Figure 11, the effective and indicated powers display decelerating increases in working fluid mass as well. The reason for this deceleration is again the narrowing temperature difference of the cycle. In Figure 11 and Table 4, it is seen

that the effective thermal efficiency of the engine performs an accelerating decrease with working fluid mass. This is caused by weakening heat exchanges due to decreasing heat exchange time and narrowing temperature difference of the cycle as well.

As the gas mass is increasing from 4.75 g to 6.5 g, the indicated work exhibits a decelerating increase as shown with the black line in Figure 12. About 6.5 g working fluid mass, the increase in indicated work seems to be terminating. This is related to the temperature limits of the thermodynamic cycle as well as the minimal variation of the phase angle. Within the examined range of the mass of working fluid, as the gas mass is increasing, the hot source heat and cold source heat increase respectively from 221 J to 290 J and from 158 J to 213 J. Both the hot source and the cold source heats are varying almost linear. In Stirling engines, the heat transfer in the heater is not always from solid to fluid. The heat transfer in the cooler is also not always from fluid to solid. The heat exchange in the regenerator has also a complicated mechanism. Therefore, the work calculated with  $W_Q = Q_h - Q_c$  may not be very robust. In this analysis the work calculated with  $dW = PdV$  is assumed as the correct value of the indicated work. Within the examined limits of the working fluid mass, the variation of the phase angle and displacer stroke are 1 degree and 0.6 mm respectively. As the working fluid mass is increasing, the indicated thermal efficiency exhibits an increasing and decreasing trend. The maximum value of the indicated thermal efficiency appears at about 5 g working fluid mass as 29.35 %. Above 5 g mass, the indicated thermal efficiency presents an accelerating decrease. The cause of this accelerating decrease is the narrowing temperature difference of the thermodynamic cycle. 5 g working fluid mass is advantageous in terms of thermal efficiency. The second column of Table 4 indicates the variation of the spring stiffness with the working fluid mass. At above 5 g mass of working fluid, the stiffness of the spring increases linearly with working fluid mass however, at below 5 g working fluid mass its decrease becomes sharper. As mentioned above, overlapping of PV diagrams is accomplished via using the interaction between PV diagrams and stiffness of the spring. Below 4.75 g and above 6.5 g working fluid mass, this interaction becomes inadequate. There is a need for another parameter to use for this purpose such as displacer rod diameters, damping constant, displacer mass etc. That means, these engines are able to work within limited change-ranges of design parameters.

**Table 4.** Variation of performance parameters with respect to working fluid mass.

$m_g$ (g)	$k$ (kN/m)	$\omega$ (rad/s)	$\bar{M}_q$ (Nm)	$W_i$ (J)	$W_Q$ (J)	$Q_h$ (J)	$Q_c$ (J)	$\eta_e$ (%)	$\eta_i$ (%)	$P_e$ (W)	$P_i$ (W)	$\phi$ (deg)	$s$ (mm)
4.75	116.6	294.81	8.832	64.72	63.21	220.83	157.63	25.13	29.30	2603.8	3036.5	106.2	37.1
5.0	126.6	304.17	9.125	67.52	66.72	230.05	163.33	24.92	29.35	2775.5	3268.6	105.5	36.91
5.5	136.9	318.11	9.54	72.5	72.4	250.06	177.66	23.98	28.99	3035.7	3670.6	105	36.80
6.0	147.6	329.74	9.892	76.52	77.15	270.86	193.71	22.95	28.25	3261.8	4015.8	105	36.66
6.5	158.7	338.38	10.15	77.80	76.92	290.18	213.26	21.98	26.81	3435.1	4190.3	105	36.54

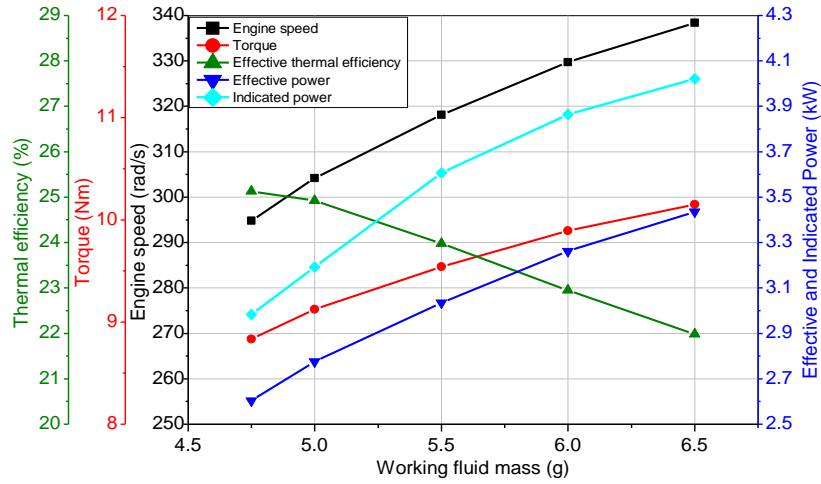


Figure 11. Variations of speed, torque, thermal efficiency, effective power and indicated power with working fluid mass.

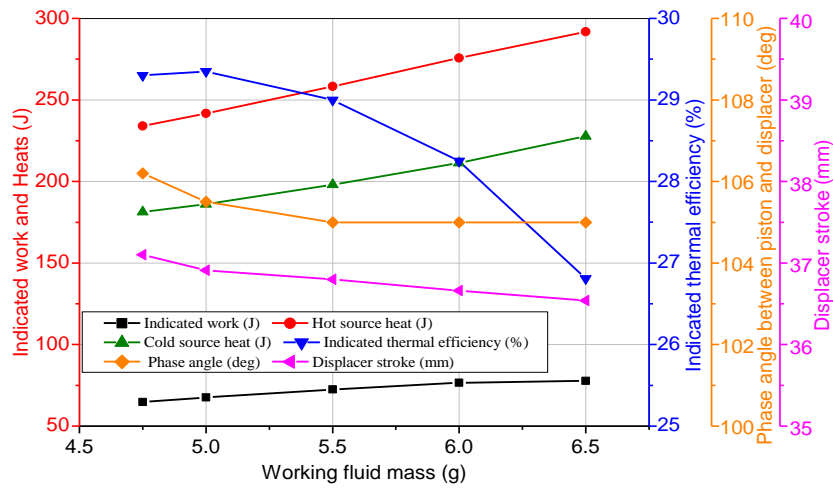


Figure 12. Variations of indicated work, hot source heat, cold source heat, indicated thermal efficiency, phase angle and displacer stroke with working fluid mass.

### Examination of Engine Performance with Respect to External Loading

In this analysis, the external loading of the engine is considered to be accomplished with a fluid dynamometer. In such a case, the cyclic average of the external torque applied to the engine may be calculated as  $\bar{M}_q = C_q \omega$  where  $\omega$  and  $C_q$  are the nominal speed of the engine and the torsional damping constant of the dynamometer. In this examination,  $C_q$  varied between 0.028 and 0.034 Nsm/rad. All other parameters were kept constant. Overlapping of PV diagrams is ignore however, while the variation interval of  $C_q$  was limited in  $0.028 \leq C_q \leq 0.034$ , the diversity of PV diagrams was able to be disregarded. The mass of displacer and working fluid and spring constant were taken to be 1.353 kg, 6.5 g and 158700 N/m respectively. Other inputs are given in Table 2 and 3. The results of this examination were presented in Figure 13 and Figure 14 as well as Table 5.

As  $C_q$  is varying from 0.028 to 0.034 Nsm/rad, the engine speed ( $\omega$ ) remains almost constant. As long as the speed of the engine is controlled by the natural

frequency of the displacer, the expected result is that the engine speed is constant. Since  $\omega$  is constant and the relation between  $C_q$  and torque is linear, the variation of torque with  $C_q$  is expected to be linear. The values of the torque given in Table 5 verifies this expectation. It is shown in Figure 13 that the indicated work variation with  $C_q$  is a decelerating increase. The increase of work is related to the phase angle variation. As seen from Table 5 and Figure 13, while  $C_q$  increases, the phase angle approaches to  $90^\circ$ . As a result of these, heating and cooling occurs at more isochoric conditions and the efficiency of the thermodynamic cycle increases at a certain rate. As seen in Figure 13, the hot source heat is almost constant. This is a specific property of free displacer Stirling engines and its explanation is difficult. The variation of cold source heat is relatively higher. In Table 5, the effective and indicated thermal efficiencies are seen to be varying between 21.54-25.92 % and 25.67-31.56 % respectively. As seen in Figure 14, variations of effective and indicated thermal efficiencies are not very similar to each other. While the effective thermal efficiency varied linearly, the indicated thermal efficiency deviates slightly from linearity. This may be caused by the irregularity of the work generation due to



beating which is disregarded in this examination. Within the examined range of  $C_q$ , the effective power varies from 3256 W to 3870 W, and the indicated power varies from 3880 W to 4713 W. These variation ranges of effective and indicated powers are fair enough for practical implementations. On the other hand, the variations of powers are not limited in these ranges. Beyond these ranges, the engine will continue to run and generate higher power but beating may be higher. As shown in Figure 14, the effective and indicated power curves are not very similar to each other as well which is also caused by beatings.

## CONCLUSION

The thermodynamic and dynamic analysis of a free displacer Stirling engine has been conducted, and its practical problems and performance characteristics were investigated corresponding to displacer mass, working fluid mass and external load. It was determined that the starting speed of the engine was equal to the displacer natural frequency. At non-optimized working conditions, the work generation of the engine was found to be not uniform due to beating. At low values of the displacer mass, the engine provides higher performance. The circulation ratio of the working fluid between the hot and

**Table 5.** Variation of performance parameters with respect to external loading.

$C_q$ (Nms/rad)	$\omega$ (rad/s)	$\bar{M}_q$ (Nm)	$W_i$ (J)	$W_Q$ (J)	$Q_h$ (J)	$Q_c$ (J)	$\eta_e$ (%)	$\eta_i$ (%)	$P_e$ (W)	$P_i$ (W)	$\phi$ (deg)	$s$ (mm)
0.028	341.0	9.548	71.49	70.07	278.5	208.42	21.54	25.67	3256	3880	104.6	36.03
0.029	337.76	9.795	73.07	72.46	278.94	206.47	22.06	26.19	3308	3928	103.5	36.18
0.030	337.68	10.13	77.30	79.01	280.37	201.35	22.70	27.57	3421	4154	102.8	36.45
0.031	337.58	10.465	80.699	81.65	280.51	198.85	23.44	28.77	3533	4336	101.2	36.62
0.032	337.53	10.801	84.14	84.94	279.05	194.11	24.32	30.15	3646	4520	97.6	36.92
0.033	337.44	11.136	86.646	84.97	278.5	193.53	25.12	31.11	3758	4653	95.6	37.13
0.034	337.39	11.471	87.77	88.33	278.03	189.7	25.92	31.56	3870	4713	93.3	37.44

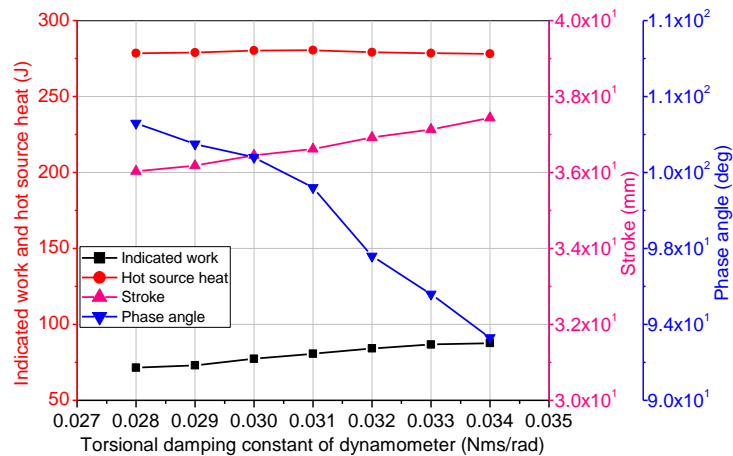


**Figure 13.** Variations of indicated work, hot source heat, stroke and phase angle with  $C_q$ .

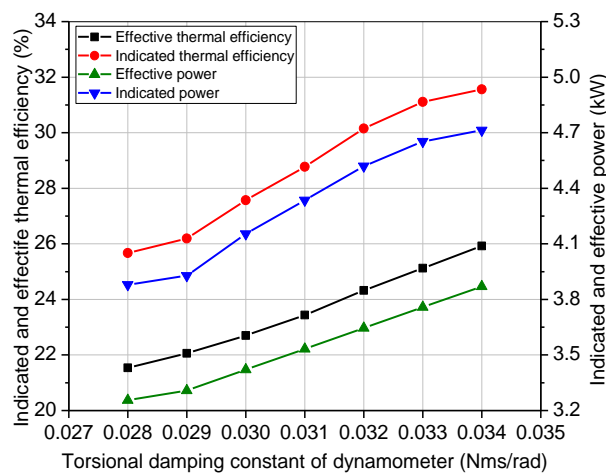


**Figure 14.** Variations of effective and indicated efficiencies and powers with  $C_q$ .

cold compartments of the displacer cylinder was found to be comparatively lower than the other types of Stirling engines, and as a result of this, the thermal efficiency and other performance values of the engine were found to be a bit lower. While the working fluid mass is increasing, the thermal efficiency of the engine becomes lower, but speed, power and torque increase by slowing down. The displacer stroke of the engine exhibits a little variation, but its influence on the engine performance is insignificant. As the external load increases within a certain range, the thermal performance of the engine increases while speed remained almost constant. An engine with 3.5-liter inner volume provides 3.9 kW effective power and 26 % effective thermal efficiency at 1000 K heater temperature, 356 K cooler temperature and 18 bar working fluid charge pressure.

## REFERENCES

- Abbas M, Boumeddane B, Said N, Chikouche A. Dish Stirling technology: A 100 MW solar power plant using hydrogen for Algeria. *International Journal of Hydrogen Energy*, 2011;36:4305-4314. doi.org/10.1016/j.ijhydene.2010.12.114.
- Altin M, Okur M, Ipci D, Halis S, Karabulut H. Thermodynamic and dynamic analysis of an alpha type Stirling engine with Scotch Yoke mechanism. *Energy*, 2018;148:855-865. doi:10.1016/j.energy.2018.01.183
- Begot S, Layes G, Lanzetta F, Nika P. Stability analysis of a free piston Stirling engines. *The European Physical Journal Applied Physics*, 2013;61:30901. doi:10.1051/epjap/2013120217.
- Cheng CH, Yang HS, Jhou BY, Chen YC, Wang YJ. Dynamic simulation of thermal-lag Stirling engines. *Applied Energy*, 2013;108:466-476. doi:10.1016/j.apenergy.2013.03.062.
- Chi C, Moua J, Lina M, Honga G. CFD simulation and investigation on the operating mechanism of a beta-type free piston Stirling engine. *Applied Thermal Engineering*, 2020;166:114751. doi:10.1016/j.applthermaleng.2019.114751.
- De la Bat BJG, Dobson RT, Harms TM, Bell AJ. Simulation, manufacture and experimental validation of a novel single acting free-piston Stirling engine electric generator. *Applied Energy*, 2020;263:114585. doi:10.1016/j.apenergy.2020.114585.
- Formosa F. Coupled thermodynamic-dynamic semi-analytical model of free piston Stirling engines. *Energy Conversion and Management*, 2011;52:2098-2109. doi:10.1016/j.enconman.2010.12.014.
- Karabulut H. Dynamic analysis of a free piston Stirling engine working with closed and open thermodynamic cycles. *Renewable Energy*, 2011;36:1704-1709. doi:10.1016/j.renene.2010.12.006.
- Karabulut H, Cinar C, Okur M. Dynamic simulation and performance prediction of free displacer Stirling engines. *International Journal of Green Energy*, 2020;17(7):427-439. doi:10.1080/15435075.2020.1761814.
- Karabulut H, Okur M, Ozdemir AO. Performance prediction of a Martini type of Stirling engine. *Energy Conversion and Management*, 2019;179:1-12. doi:10.1016/j.enconman.2018.10.059.
- Kwankaomeng S, Silpsakoolsook B, Savangvong P. Investigation on stability and performance of a free-piston Stirling engine. *Energy Procedia*, 2014;52:598-609. doi:10.1016/j.egypro.2014.07.115.
- Lin M, Mou J, Chi C, Hong G, Ge P, Hu G. A space power system of free piston Stirling generator based on potassium heat pipe. *Frontiers in Energy*, 2020;14(1):1-10. doi:10.1007/s11708-019-0655-6.
- Majidniya M, Boileau T, Remy B, Zandi M. Nonlinear modeling of a free piston Stirling engine combined with a permanent magnet linear synchronous machine. *Applied Thermal Engineering*, 2020;165:114544. doi:10.1016/j.applthermaleng.2019.114544.
- Masoumi AP, Tavakolpour-Saleh AR. Experimental assessment of damping and heat transfer coefficients in an active free piston Stirling engine using genetic algorithm. *Energy*, 2020;195:117064. doi:10.1016/j.energy.2020.117064.
- Mehdizadeh NS, Stouffs P. Simulation of a Martini displacer free piston Stirling engine for electric power generation. *International Journal of Applied Thermodynamics*, 2000;3(1):27-34. doi:10.5541/ijot.30.
- Mou J, Hong GA. A numerical model on thermodynamic analysis of free piston Stirling engines. *IOP Conference Series: Materials Science and Engineering*, 2017;171:012090. doi:10.1088/1757-899X/171/1/012090.
- Park J, Ko J, Kim H, Hong Y, Yeom H, Park S, In S. The design and testing of a kW-class free-piston Stirling engine for micro-combined heat and power applications. *Applied Thermal Engineering*, 2020;164:114504. doi:10.1016/j.applthermaleng.2019.114504.
- Tanaka M, Yamashita I, Chisaka F. Flow and heat transfer characteristics of the Stirling engine regenerator in an oscillating flow. *JSME International Journal*, 1990;33(2):283-289. doi:10.1299/jsmeb1988.33.2\_283.
- Tavakolpour-Saleh AR, Zare SH, Bahreman H. A novel active free piston Stirling engine: modeling, development, and experiment. *Applied Energy*, 2017;199:400-415. doi:10.1016/j.apenergy.2017.05.059.
- Wood JG, Lane N. Advanced 35 W free-piston Stirling engine for space power applications. *AIP Conference Proceedings* 2003;654:662-667. doi:10.1063/1.1541353.

Ye W, Yang P, Liu Y. Multi-objective thermodynamic optimization of a free piston Stirling engine using response surface methodology. *Energy Conversion and Management*, 2018;176:147-163. doi:10.1016/j.enconman.2018.09.011.

Zare S, Tavakolpour-Saleh AR. Predicting onset conditions of free piston Stirling engine. *Applied Energy* 2020;262:114488. doi:10.1016/j.apenergy.2019.114488.

Zare S, Tavakolpour-Saleh AR, Sangdani MH. Investigating limit cycle in a free piston Stirling engine using describing function technique and genetic algorithm. *Energy Conversion and Management*, 2020;210:112706. doi:10.1016/j.enconman.2020.112706.

Zhou Q, Xia Y, Liu G, Ouyang X. A miniature integrated nuclear reactor design with gravity independent autonomous circulation. *Nuclear Engineering and Design*, 2018;340:9-16. doi:10.1016/j.nucengdes.2018.09.013.

Zhu S, Yu G, Ma Y, Cheng Y, Wang Y, Yu S, Wu Z, Dai W, Luo E. A free-piston Stirling generator integrated with a parabolic trough collector for thermal-to-electric conversion of solar energy. *Applied Energy*, 2019;242:1248-1258. doi:10.1016/j.apenergy.2019.03.169.



**Can ÇINAR** was born in Eskişehir in 1975. In 1996, he graduated from Automotive Education Program at Technical Education Faculty of Gazi University. He completed his MSc and PhD degrees in the Department of Mechanical Education in Graduate School of Natural and Applied Sciences at Gazi University, in 1998 and 2001. He worked as a Research Assistant between 1996- 2002, as an Instructor Doctor between 2002-2003, and as an Assistant Professor between 2003-2008 at the Faculty of Technical Education of Gazi University. He became Associate Professor in 2008. He has been working as a Professor at the Department of Automotive Engineering at the Faculty of Technology in Gazi University since 2013.



**Abdullah Onur ÖZDEMİR** graduated from Automotive Education and Mechanical Engineering bachelor programs. He completed his MSc degree in Mechanical Education. He received his PhD degree in the field of Automotive Engineering. Ozdemir is working as a Research Assistant in the Department of Automotive Engineering at Gazi University, Turkey. His researches focus on engine thermodynamic cycle analysis and thermoplastic composites.



**Halit KARABULUT** was born in 1959 in Antalya. He graduated from the Higher Technical Teachers Academy in 1980. In 1987, he completed his MSc degree at the Mechanical Education Department, Institute of Science, Gazi University. He completed his PhD at Heriot-Watt University in 1991. In 1992, he was appointed as Assistant Professor at Technical Education Faculty, Gazi University. In 1997, he became an Associate Professor at the Technical Education Faculty of Gazi University. In 2000, he was assigned as an Associate Professor at Akdeniz University. In 2003, he became a Professor at the Technical Education Faculty, Gazi University. He has been working as a Professor at Automotive Engineering Department of Technology Faculty at Gazi University, since 2011.



**Mesut DÜZGÜN** is currently a lecture of Automotive Engineering Department at the Gazi University, which he joined in 2002. He received his first B.E. in Automotive Education Department in 2000, from Gazi University in Turkey. He graduated from the Gazi University with Graduate School of Natural and Applied Sciences an M.Sc. in 2002 and received his Ph.D. degree; in 2008 at Gazi University. After working for 2 years in the Republic of Turkey Ministry of National Education, he joined the Gazi University as a Research Assistant Automotive Department in 2002. He became an Assistant Professor in the same department in 2009 and he became an Associate Professor in 2017. His current research areas are Vehicle Dynamics, Vehicle Technology and Engine Technologies. He is specialized in the field of brake systems and applications. He has worked on some projects in vehicle technology area and as researcher in numerous international projects in Turkey.



## BUHAR SIKIŞTIRMALI SOĞUTMA TEST ÜNİTESİNE İLERİ EKSERJİ METODUNUN UYGULANMASI

Betül SARAÇ

Karadeniz Teknik Üniversitesi Sürmene Deniz Bilimleri Fakültesi Gemi İnşaatı ve Gemi Makineleri Mühendisliği Bölümü 61530, Trabzon  
bsarac@ktu.edu.tr, ORCID: 0000-0003-3876-7314

(Geliş Tarihi: 09.01.2020, Kabul Tarihi: 09.03.2021)

**Özet:** Termodinamiğin Birinci Kanunu ile yapılan hesaplamalarda her bir üniteye oluşan sıcaklık farkından ve basınç kayıpları nedeniyle oluşan tersinmezliklerin sistem performansı üzerindeki etkileri belirlenmemektedir. Bu nedenle Termodinamiğin ikinci kanunu ve ileri ekserji analizi metodu kullanılarak, seçilen termal sistemde her bir üniteye oluşan ekserji tahribatının büyüklükleri ve ekserji tahribatı tipleri hesaplanmalıdır. Bu çalışmada, buhar sıkıştırma soğutma sistemi ile çalışan bir test ünitesinin performansı ekserji ve ileri ekserji analiz metodu ile incelenmiştir. İleri ekserji analizi sonucunda buhar sıkıştırma soğutma test ünitesindeki her bir bileşenin günümüzde ulaşılabilen en son teknolojiyi içeren ürünlerin kullanıldığını göstermektedir. Yapılan çalışmada evaporatörün diğer bileşenler arasında en yüksek termal performans ile çalıştığı bulunmuştur.

**Anahtar kelimeler:** Ekserji, İleri ekserji, Ekserji tahribatı tipleri, Buhar sıkıştırma soğutma çevrimi

## APPLICATION OF ADVANCED EXERGY METHOD TO THE VAPOUR COMPRESSION COOLING TEST UNIT

**Abstract:** In the calculations made using the first law analysis method of Thermodynamics, the effects of irreversibility caused by temperature difference, pressure losses and heat transfer in each unit can not be determined on thermal system performance. Therefore, by using the second law of thermodynamics and advanced exergy analysis method, the magnitude of the exergy destructions and the types of exergy destructions occurring in each unit in the selected thermal system can be used in the performance evaluation stage of the system. In this study, the performance of the test unit which is operated by a vapor compression cooling system was investigated by means of the exergy and advanced exergy analysis methods. Advanced exergy analysis is showed that each component of vapour compression refrigeration test uses the latest technology available today. In the study, it was found that the evaporator operates with the highest thermal performance among the other components.

**Keywords:** Exergy, Advanced exergy, Exergy destruction types, Vapor compression refrigeration cycle

### SEMBOLLER VE KISALTMALAR

AV	Önlenbilir
Bil.	Bileşen
CD	Kondensör
CM	Kompresör
ç	Çıkış
D	Tahribat
e	Özgül ekserji [j/kg]
E	Ekserji [W]
EN	Endojen
EX	Eksojen
EV	Evaporatör
F	Yakıt
g	Giriş
h	Entalpi [j/kgk]
k	bileşen
K	Kayıp
M	Mekanik ekserji
mekso	Meksojen
$\dot{m}$	Kütleli debi [kg/s]
P	Basınç [kPa]
p	Ürün
R	Gerçek

s	Entropi [j/kgK]
T	Sıcaklık [K], Teorik
TOP	Toplam
TV	Genleşme valf
UN	Kaçınılmaz
$\epsilon$	Ekserji verimi [%]
y	Ekserji tahribatı oranı
0	Ölü durum

### GİRİŞ

Günümüzde iklimlendirme cihazlarındaki enerji tasarrufu üzerine yapılan çalışmalar, çevre kirliliği ve enerjinin verimli kullanılması açısından önem arz etmektedir. Özellikle iklimlendirme cihazlarında kullanılan her bir ünitenin verimliliği doğrudan soğutma sisteminin soğutma tesir katsayısını etkilemektedir. Günümüzde hava şartlandırılması için kullanılan iklimlendirme cihazları buhar sıkıştırma soğutma sistemi esasına dayanmaktadır. Bu konu günümüzün en önemli araştırma konuları olarak literatürde yerini almaktadır.

Soğutucu sistemlerin ileri ekserji uygulamaları (Kelly vd, 2009) tarafından ele alınmıştır. Bu araştırmacılar, soğutucu sistemin performansının ulaşabileceği en yüksek potansiyeli hesaplamışlardır. Sonuç olarak sistemde evaporatörde oluşan tersinmezliklerin giderilmesiyle sistem performansının iyileşebileceğini belirtmişlerdir. İleri ekserji metodunda ekserji tahribatı farklı kayıpları temsil eden tahribat parçalarına ayrılmıştır. Bu tahribat parçalarından ilk grubu oluşturan *kaçınılmaz ekserji tahribatı parçası*, üniteye bir bileşenin, üniteye kullanıldığı müddetçe, bu bileşene en yüksek teknolojiler uygulanması halinde bileşende yok edilemeyen ekserji tahribatını temsil ederken, *önlenilebilir ekserji tahribatı parçası* ise sistemdeki bileşenin iyileştirme potansiyelini temsil eder. Tahribat parçalarında ikinci grubu oluşturan *endojen (içsel) ekserji tahribatı parçası* sadece üniteye bir bileşenin kendi tersinmezliğini gösteren ekserji tahribatının parçası olarak tanımlanmaktadır, *eksojen (dışsal) ekserji tahribatı parçası* da gerçek ekserji tahribatı ile endojen ekserji tahribatı parçasının farkı olarak tanımlanmaktadır (Wang vd, 2019). Ekserji tahribat parçalarının belirlenmesi amaçlı yapılan diğer bir çalışma, bir gaz türbini motoruna ileri ekserji metodunun uygulanmasıyla (Şöhret vd, 2015) tarafından tanıtılmıştır. Bu çalışmada yanma odasının iyileştirilmesi gerekliliği tespit edilmiştir. Sistemde %93.55 büyüklüğünde kaçınılmaz ekserji tahribatı olduğu hesaplanmış ve bundan dolayı sistemin iyileştirilme potansiyelinin düşük olduğu belirlenmiştir. Endojen ekserji tahribatı ise %81.33 olarak bulunmuş ve bu değere göre bileşenler arasındaki etkileşimin zayıf olduğu belirlenmiştir.

Bir askeri turbojet motoruna ileri ekserji metodu uygulanarak sistemde oluşan ekserji tahribat tiplerini belirleme ile (Balli, 2017) iyileştirmenin yapılacağı elemanların alçak basınç kompresörü, yanma odası, ve tepki lülesi olduğu bulunmuştur. Doğal gaz sıvılaştırma ve üretim tesisinde ileri ekserji ve sistemde oluşan ekserji tahribatlarının parasal olarak değerlendirilmesi (Ghorbani ve Roshani, 2018) tarafından ele alınmıştır. Bu çalışmada oluşan ekserji tahribatının çoğunun eksojen, diğer ünitelerde oluşan ekserji tahribatının endojen türde oldukları belirlenmiştir. Araştırmacılar, bu çalışmada ekserjetik ekonomiklik analiz sonuçlarına göre endojen ekserji tahribatının en yüksek maliyete sebep olduğunu belirtmişlerdir. (Bai vd, 2016) ve (Gullo vd, 2019) süper market soğutucularında R744 ile yapılan soğutmalardaki performans analizi için ileri ekserji metodunu uygulamışlardır. (Bai vd, 2016) sistemde kullanılan R744 ejektör bloğunun toplam ekserji kaybındaki %43.44 oranındaki azalmayı buhar sıkıştırma soğutma ünitesi ile karşılaştırarak belirlemişlerdir. (Chen, 2014) ejektörlü soğutma sistemi ile buhar sıkıştırma soğutma sistemini ileri ekserji metodunu kullanarak karşılaştırmasını yapmıştır. Birleşik güç ünitesinde ileri ekserji ve ekserji ekonomiklik metodunun uygulandığı tipik bir örnek (Azizi ve Boyarchihih, 2014) tarafından ele alınmıştır. Ekserji ekonomiklik metodu, sistemde oluşan ekserji tahribatlarının parasal olarak değerlendirilmesidir. Araştırmacılar, çalışmalarında sistemin performansında %14 iyileştirme olabileceğini ve maliyette %15 maliyet

düşüsü elde edilebileceğini belirtilmiştir. Süt işleme fabrikasının performans analizi için enerji, ekserji ve ileri ekserji analiz metodları (Fabrian vd, 2016) tarafından ele alınmıştır. Her bir üniteye oluşan ekserji tahribatının tipleri hesaplanarak işletim parametrelerinin limitleri belirlenmiştir. İleri ekserji metodunda ekserji tahribatının matematiksel olarak belirlenmesinde detay çalışma (Tsatsaronis ve Morosuk 2012)' de bulunabilir. Bu çalışmada, bir buhar sıkıştırma soğutma sistemi ve basit gaz türbini sistemi örneklenerek matematiksel ileri ekserji analiz metodu açıklanmıştır. İleri ekserji metodunun uygulandığı tipik bir örnek hava sıkıştırma bir enerji depolama sistemi (Liu vd, 2016) tarafından yapılmıştır. Bu sistemde bir sıkıştırılmış hava deposu, çok kademeli kompresörler ve ara soğutucularının yanında bir gaz türbini ünitesi bulunmaktadır. Sistemde bulunan bileşenlerin etkileşiminden doğan kaçınılabılır ekserji tahribatının yarısından çoğunun eksojen tipte olduğu değerlendirilmiştir. HFC-134a'ya alternatif bir soğutucu akışkan olan HFO-1234yf kullanan buhar sıkıştırma soğutma çevriminde termodinamiğin birinci ve ikinci yasasının analiz çalışmaları gerçekleştirilmiştir (Özgür vd, 2014). Araştırmacılar, her iki soğutucu akışkan için de çevrim verimleri arasında önemli farklılıklar gözlemlemişlerdir. Ancak HFO-1234yf ile elde edilen kompresörün ekserji tahribatı oranı, R-134a akışkanına göre hesaplanandan daha düşüktür. Elde edilen ekserji ve enerji analiz sonuçlarına göre HFO-1234yf, R-134a'ya iyi bir alternatif olarak değerlendirmişlerdir. Gerçek bir endüstriyel tesisinde ekserji, ileri ekserji analizi ve ekserji ekonomiklik metodu değerlendirmesi (Vuckovic vd, 2012) tarafından yapılmıştır. Tesis bileşenlerinde ekserji tahribatının kaçınılmaz ve teknolojik, fiziksel ve ekonomik sınırlamalarla sınırlandırıldığı belirlenmiştir. Sistemde kazanım çalışma şartlarının iyileştirilmesiyle sistemin performansının artırılabilmesi sonucuna varılmıştır. Belli bir soğutma kapasitesine sahip paralel sıkıştırma süper market tipi buzdolabının performansının optimizasyonuna dayalı bir araştırmayı (Gullo vd, 2016) ileri ekserji analizi metodu kullanarak gerçekleştirmişlerdir. Uyguladıkları ileri ekserji metodu sonucunda kondensörün, yüksek basınç kompresörünün ve alçak basınç kompresörlerinin en yüksek geliştirme potansiyeline sahip olduklarını belirtmişlerdir.

Bu çalışmanın literatürdeki yeri, ele alınan mevcut evaporatör test ünitesindeki soğutucu ve havalandırma sisteminde oluşan olumsuzlukların, deney düzeneğindeki ölçümlere etkisinin azaltılması yönünde test ünitesine ait performanslarının değerlendirilmesidir. Diğer bir deyişle test ünitesinin termodinamik kalibrasyonunun incelenmesidir.

Ekserji analizi, enerji dönüştürüm sistemleri için rasyonel bir verim tanımlamak amacıyla termodinamiğin birinci ve ikinci kanunlarından geliştirilmiş metottur. Bu çalışmada konvansiyonel ekserji analizi metoduna ek olarak *ileri ekserji analiz* metodu tanıtılmış ve bir buhar sıkıştırma soğutma test ünitesine uygulanarak sistemde oluşan tersinmezliklerin yeni üretilmiş evaporatörün performansına olan etkileri içsel ve dışsal tersinmezlik

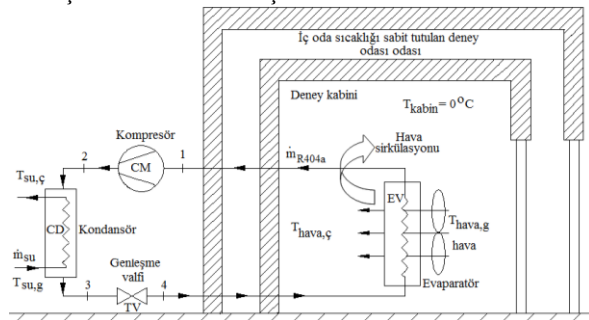
miktarları göz önüne alınarak araştırılmıştır. Meksojen ekserji tahribatının hesabı ile düşünülen amaca ulaşılmıştır. Çalışmanın özgünlüğü buhar sıkıştırma test ünitesinin bütün bileşenlerinde oluşan tersinmezliklerin test edilen evaporatör performansına etkilerinin belirlenmesi ile deney setinin termodinamik kalibrasyonunun yapılmış olmasıdır. (Ballı, 2017) yaptıkları çalışmada ileri ekserji metodunu askeri turbojet motoruna uygulanarak sistemde oluşan ekserji tahribat tiplerini belirlemişlerdir. Çalışmalarında alçak basınç kompresörü, yanma odası, ve tepki lülesinde iyileştirme yapılması gerektiğini meksojen ekserji tahribatının sonucuna bağlı olarak açıklamışlardır. Sunulan bu çalışmada da kondensörün iyileştirilmesi veya işletme şartlarının iyileştirilmesinin gerektiği tespit edilmiştir.

İleri ekserji metodunun enerji sistemlerinde çok kullanışlı bir yöntem olduğu literatürdeki çalışmalarda belirtilmiş ve ekserji tahribat parçalarının belirlenmesi sistemin iyileştirme potansiyelinin hangi elemanlara uygulanabileceğini açıklamaktadır. Bu bağlamda sunulan çalışmanın amacı buhar sıkıştırma soğutma çevrimine göre çalışan evaporatör test ünitesinin ileri ekserji analizi metodu ile test ünitesinde oluşan tersinmezlik bölgeleri ve değerleri, ekserji tahribatı tipleri miktarları ve ünite içindeki elemanların ekserji tahribatı oluşumundaki etkileşimlerin belirlenmesidir.

## MATERYAL VE METOD

Frierm firmasında bulunan buhar sıkıştırma soğutma sistemi içeren evaporatör test ünitesinin verileri bu çalışmada referans olarak alınmıştır.

Firmada bulunan test ünitesi üzerinde kompresör, yoğurturucu, evaporatör, genişleme valfi, basınç, sıcaklık ölçerler, akışkan debisi ölçerler, termostatlar, valfler, otomatik kontrol ünitesi ve baypas akış devreleri gibi elemanlar bulunmaktadır. Ancak bu çalışmada buharlaştırıcı performans ölçümleri yapılacağından, yalnızca ilgili soğutucu akışkan devresinin çevrimi el alınmıştır. Buharlaştırıcı test ünitesinde kullanılan buhar sıkıştırma soğutma ünitesi ile deney kabini şematik resmi Şekil 1.' de verilmiştir.



Şekil 1. Evaporatör test ünitesinin ve test odasının şematik resmi

Soğutma sisteminin bulunan evaporatörün soğutma kapasitesi  $\dot{Q}_{EV} = 9,887 \text{ kW}$ , soğutucu akışkanın R404a kütleli debisi  $\dot{m}_{R404a} = 0,08 \text{ kg/s}$  ve deney kabini

sıcaklığı  $T_{kabin} = 0^\circ\text{C}$  olarak firma tarafından beyan edilmiştir.

Kabuller:

Termodinamik modellerin oluşturulmasında aşağıdaki kabuller göz önüne alınmıştır.

1. Sistemdeki bütün bileşenler kararlı rejimde (zamandan bağımsız) bir boyutlu olarak ele alınmıştır.
2. Bileşenlerdeki ve boru bağlantılarındaki basınç kayıpları ihmal edilmemiştir.
3. Kompresörün adyabatik ve tersinmez çalıştığı kabul edilerek izantropik verimi 0.75 alınmıştır.
4. Ekserji analizinde ölü noktasının termodinamik şartları için sıcaklık  $T_o = 15^\circ\text{C}$  ve basınç  $P_o = 100 \text{ kPa}$  değerlerinde alınmıştır.

## Ekserji Analizi

Ekserji analizi termal sistemdeki tersinmezlikleri içeren üniteleri ve tersinmezliğin büyüklüğünü araştıran genel bir metottur. Her bir ünite içindeki ekserji tahribatı oluşumunun ve büyüklüğünün belirlenmesinde ekserji eşitliği sistemdeki her bir üniteye ayrı ayrı uygulanarak bulunur. Göz önüne alınan termodinamik modeli oluşturan sistem elemanlarına ekserji eşitliği uygulanarak her bir elemana akışkan giriş ve çıkış ekserjileri aşağıdaki bağıntıyla hesaplanmıştır.

$$e = h - h_0 - T_0(s - s_0) \quad (1)$$

Göz önüne alınan akışkan akımlarındaki, toplam akışkan ekserjisi Eş. (2) ve her bir elemanda oluşan ekserji tahribatı da ekserji eşitliğinden Eş. (3) ile hesaplanmıştır.

$$\dot{E} = \dot{m} e \quad (2)$$

$$\dot{E}_D = \sum_k \left(1 - \frac{T_0}{T_k}\right) \dot{Q}_k - \dot{W} + \sum_k \dot{E}_{k,in} - \sum_k \dot{E}_{k,out} \quad (3)$$

Termal genişleme valfinde kısımla sürecindeki akışkanın termal ve mekanik ekserji tanımları Eş. (4) ve Eş. (5), (Kotas, 16).

Termal ekserji

$$e^{\Delta T} = [h_{(T,P)} - h_{(T_o,P)} - T_o(s_{(T,P)} - s_{(T_o,P)})]_{P=sabit} \quad (4)$$

Mekanik ekserji

$$e^{\Delta P} = [h_{(T,P)} - h_{(T_o,P)} - T_o(s_{(T,P)} - s_{(T_o,P)})]_{T=sabit} \quad (5)$$

Termal genişleme valfinde denklem 4' de verilen termal ekserji bağıntısında sabit basınç değeri olarak; valfin giriş ve çıkış noktalarındaki basınç değerleri alınmıştır. Eş. (5) de verilen mekanik ekserji bağıntısındaki sabit sıcaklık değeri için ise ölü haldeki sıcaklık değeri alınmıştır. Termal genişleme valfinin ekserji verim ifadesi, ekserji ürününün ekserji yakıtı oranı tanımına göre Eş. (6) ile hesaplanmıştır (Kotas, 16).

$$\varepsilon_{TV} = \frac{(\dot{E}_4 - \dot{E}_3)_{Termal}}{(\dot{E}_3 - \dot{E}_4)_{Mekanik}} \quad (6)$$

**Tablo 1.** Enerji, ekserji eşitlikleri ve ekserjetik verim ifadeleri.

Bil.	Enerji eşitliği	Ekserji eşitliği
CM	$\dot{W}_{CM} = \dot{m}_1(h_2 - h_1) + \dot{Q}_{K,CM}$	$\dot{E}_{D,CM} = \dot{W}_{CM} - (\dot{E}_2 - \dot{E}_1) + \dot{E}_{K,CM}$
EV	$\dot{m}_{hava}(h_{hava,g} - h_{hava,\zeta}) = \dot{m}_1(h_4 - h_1)$	$\dot{E}_{D,EV} = (\dot{E}_4 - \dot{E}_1) - (\dot{E}_{hava,g} - \dot{E}_{hava,\zeta})$
CD	$\dot{m}_w(h_{su,g} - h_{su,\zeta}) = \dot{m}_2(h_2 - h_3) - \dot{Q}_{K,CD}$	$\dot{E}_{D,CD} = (\dot{E}_2 - \dot{E}_3) - (\dot{E}_{su,\zeta} - \dot{E}_{su,g}) - \dot{E}_{K,CD}$
TV	$\dot{m}_3 h_3 = \dot{m}_3 h_4$	$\dot{E}_{D,TV} = \dot{E}_3 - \dot{E}_4$

**Tablo 2.** Ekserji yakıtı ve ekserji ürünü tanımlarına dayalı ekserji tahribatı ve ekserji verimi.

Bil.	$\dot{E}_F$	$\dot{E}_P$	$\dot{E}_D$	Ekserji verimi
CM	$\dot{W}_{CM}$	$\dot{E}_2 - \dot{E}_1$	$\dot{W}_{CM} - (\dot{E}_2 - \dot{E}_1) + \dot{E}_{K,CM}$	$\varepsilon_{CM} = \frac{\dot{E}_2 - \dot{E}_1}{\dot{W}_{CM}}$
EV	$\dot{E}_4 - \dot{E}_1$	$\dot{E}_{hava,\zeta} - \dot{E}_{hava,g}$	$(\dot{E}_4 - \dot{E}_1) - (\dot{E}_{hava,g} - \dot{E}_{hava,\zeta})$	$\varepsilon_{EV} = \frac{\dot{E}_{hava,g} - \dot{E}_{hava,\zeta}}{\dot{E}_4 - \dot{E}_1}$
CD	$\dot{E}_2 - \dot{E}_3$	$\dot{E}_{su,\zeta} - \dot{E}_{su,g}$	$(\dot{E}_2 - \dot{E}_3) - (\dot{E}_{su,\zeta} - \dot{E}_{su,g}) - \dot{E}_{K,CD}$	$\varepsilon_{CD} = \frac{\dot{E}_{su,g} - \dot{E}_{su,\zeta}}{\dot{E}_2 - \dot{E}_3}$
TV	$(\dot{E}_3 - \dot{E}_4)_M$	$(\dot{E}_4 - \dot{E}_3)_T$	$(\dot{E}_3 - \dot{E}_4)_M - (\dot{E}_4 - \dot{E}_3)_T$	$\varepsilon_{TV} = \frac{(\dot{E}_4 - \dot{E}_3)_T}{(\dot{E}_3 - \dot{E}_4)_M}$
Top	$\dot{W}_{CM}$	$\dot{E}_{hava,\zeta} - \dot{E}_{hava,g}$	$\dot{E}_{D,CM} + \dot{E}_{D,CD} + \dot{E}_{D,TV} + \dot{E}_{D,EV}$	$\varepsilon_{Top,Sistem} = \frac{\dot{E}_{hava,\zeta} - \dot{E}_{hava,g}}{\dot{W}_{CM}}$

Ele alınan gerçek ve teorik modellerde sistem elemanlarına uygulanan enerji ve ekserji eşitlikleri Tablo 1.' de özetlenmiştir. Kompresördeki sıkıştırma süreci iç ve dış tersinmezlikleri içerdiğinden, kompresörden çevreye atılan ısı hesaplara dahil edilmiştir.

Ekserji yakıtı ve ekserji ürünü tanımları kullanılarak ileri ekserji metodunda kullanılan ekserji tahribatı ve ekserji verimi ifadeleri Tablo 2.' de sunulmuştur.

### İleri Ekserji Analizi

Termodinamik açık sistem tanımında, sistem sınırında giren enerji türleri literatürde “ ekserji yakıtı”, sistem sınırından çıkan enerji türleri ise “ekserji ürünü” olarak tanımlanmıştır (Kelly vd, 2009), (Wang vd, 2019), (Chen, 2014), (Aziziz ve Boyarhchihi, 2014), (Fabrianvd, 2016). Yakıt-ürün ekserji analizi, bir termik sistemin ve bu sistemin bileşenlerinin performanslarına etki eden tersinmezliklerin belirlenmesini ve performansı en düşük olan bileşenin belirlenmesine imkan sağlar (Wang vd, 2019) (Balli, 2017), (Bai vd.), (Chen, 2014). Sistem bileşenlerine ait ekserji yakıtı  $\dot{E}_{F,k}$ , ekserji ürünü  $\dot{E}_{P,k}$  ile gösterilir. Termodinamik süreçte çevreye atılan veya tekrar kullanılmayan ekserji ise “kayıp ekserji” olarak tanımlanır ve  $\dot{E}_K$  sembolü ile gösterilir. Çevrime ait toplam yakıt-ürün ekserjisi, toplam ürün ekserjisi, toplam ekserji tahribatı  $\sum_{n=1}^n E_{D,k_n}$  ve toplam kayıp ekserji, ekserji denkliği gözönüne alınarak aşağıda olduğu gibi matematiksel olarak yazılabilir.

$$\dot{E}_{F,tot} = \dot{E}_{P,tot} + \sum_{n=1}^n E_{D,k} + \dot{E}_{K,tot} \quad (7)$$

Ekserji analizi açısından, bileşenlerin ve sistemin incelenmesinde iki gösterge kullanılmaktadır. Bunlardan birincisi, sistemi oluşturan bileşenlerin ekserji verimleri, “ $\varepsilon$ ” ile gösterilir ve ürün ekserjisinin yakıt ekserjisine oranı olarak tanımlanır. İkinci gösterge ise, her bir bileşende oluşan ekserji tahribatının toplam sistem ekserji tahribatına oranı olarak tanımlanır ve “ $y$ ” sembolüyle gösterilir. İki göstergede kullanılan tanımlardan ekserji verim  $\varepsilon$ , ve ekserji tahribatı oranı  $y$ ,

sistemdeki her bir eleman için yazılabildikleri gibi, sistemin tümü içinde yazılabilirler. Bu göstergeler aşağı eşitliklerde yazılmıştır.

$$\varepsilon_k = \frac{\dot{E}_{P,k}}{\dot{E}_{F,k}} \text{ “k” nıncı eleman için} \quad (8)$$

$$\varepsilon_{top} = \frac{\dot{E}_{P,top}}{\dot{E}_{F,top}} \text{ çevrim için (ve tüm sistem için)} \quad (9)$$

$$y_k = \frac{\dot{E}_{D,k}}{\dot{E}_{F,k}} \text{ “k” nıncı eleman için} \quad (10)$$

$$y_{top} = \frac{\dot{E}_{D,top}}{\dot{E}_{F,top}} \text{ çevrim için (ve tüm sistem için)} \quad (11)$$

### Ekserji tahribatı tipleri

İleri ekserji analizi, ekserji tahribatını bölünmüş parçalara ayırarak, bileşenlerdeki tersinmezliklerin daha iyi araştırılmasına imkan verir. Gerçek ekserji tahribatı iki ana sınıfa ayrılır. Birinci bölünmüş parçası endojen ( $\dot{E}_{D,k}^{EN}$ ) ve eksojen ( $\dot{E}_{D,k}^{EX}$ ) olarak, ikinci bölünmüş parçası ise önlenebilir ekserji tahribatı ( $\dot{E}_{D,k}^{AV}$ ) ve kaçınılmaz ekserji tahribatı ( $\dot{E}_{D,k}^{UN}$ ) olarak tanımlanırlar.

$$\dot{E}_{D,k} = \dot{E}_{D,k}^{EN} + \dot{E}_{D,k}^{EX} \quad (12)$$

$$\dot{E}_{D,k} = \dot{E}_{D,k}^{AV} + \dot{E}_{D,k}^{UN} \quad (13)$$

Bu iki ana sınıf ekserji tahribatı alt parçalara ayrılarak daha hassas analiz yapma imkanı vermektedir. Parçalanmış ekserji tahribat tipleri aşağıda açıklanmıştır.

### Endojen ekserji tahribatı; $\dot{E}_{D,k}^{EN}$

$\dot{E}_{D,k}^{EN}$  Endojen ekserji parçası sistemdeki “k”nıncı bileşenin kendi içinde oluşan tersinmezliğini gösterir ve

çevrimdeki diğer bileşenlerin tersinmezlikleri ile alakası yoktur.

#### Eksojen ekserji tahribatı; $\dot{E}_{D,k}^{EX}$

$\dot{E}_{D,k}^{EX}$  Eksojen ekserji tahribatı parçası, gerçek ekserji tahribatı ile  $\dot{E}_{D,k}^{EN}$  endojen ekserji tahribatı parçasının farkıdır ( $\dot{E}_{D,k}^{EX} = \dot{E}_{D,k} - \dot{E}_{D,k}^{EN}$ ). Sistemin “k”ncü bileşeni dışındaki diğer bileşenlerin oluşturduğu tersinmezliklerin “k”ncü bileşen üzerine uyguladığı ekserji tahribatıdır.

#### Kaçınılmaz ekserji tahribatı; $\dot{E}_{D,k}^{UN}$

$\dot{E}_{D,k}^{UN}$  Kaçınılmaz ekserji tahribatı parçası sistemdeki “k”ncü bileşen çalıştırıldığı müddetçe, bu bileşende en yüksek teknolojiler uygulanması halinde, bileşende yok edilemeyen ekserji tahribatıdır. Bileşendeki tersinmezlikler teknik sınırlamalardan kaynaklanmaktadır.

#### Önlenebilir ekserji tahribatı; $\dot{E}_{D,k}^{AV}$

$\dot{E}_{D,k}^{AV}$  Önlenebilir ekserji tahribatı parçası, sistemdeki “k”ncü bileşendeki gerçek ekserji tahribatı ile kaçınılmaz ekserji tahribatı arasındaki fark ( $\dot{E}_{D,k}^{AV} = \dot{E}_{D,k} - \dot{E}_{D,k}^{UN}$ ) olarak tanımlanır ve bu fark giderilebilir özelliğe sahiptir. Ekserji tahribatının bu bölünmüş parçası sistemdeki bu bileşenin iyileştirme potansiyelini temsil eder. Dolayısıyla önlenebilir ekserji tahribatı parçasına daha fazla dikkat edilmelidir. Önlenebilir ekserji tahribat parçasının değerinin büyük olması “k”ncü bileşenin bir yenilenme potansiyelinin olduğunu gösterir.

Yukarıda iki sınıfa ayrılan ekserji tahribat parçalarında daha çok yararlanabilmek için ekserji tahribat parçalarının birleşik etkileşimleri mantıksal olarak göz önüne alınır ve aşağıda sunulan kombinasyonları elde edilir (Chen, 2014).

- **Kaçınılmaz endojen ekserji tahribatı:**  $\dot{E}_{D,k}^{UN,EN}$
- “k”ncü bileşen teknik sınırlamalar nedeniyle giderilemez.
- **Kaçınılmaz eksojen ekserji tahribatı:**  $\dot{E}_{D,k}^{UN,EX}$
- “k”ncü bileşenin dışındaki diğer bileşenler teknik sınırlamalar nedeniyle iyileştirilemez.
- **Önlenebilir endojen ekserji tahribatı:**  $\dot{E}_{D,k}^{AV,EN}$
- “k”ncü bileşenin veriminin artırılmasıyla (iyileştirilmesiyle) giderilebilir. Bu ekserji tahribatının değeri büyükse, bileşenin iyileştirilmesiyle azaltılması yönüne gidilir.
- **Önlenebilir eksojen ekserji tahribatı:**  $\dot{E}_{D,k}^{AV,EX}$
- “k”ncü bileşenin dışında kalan diğer bileşenlerin yapısal iyileştirilmesi ve verimlerinin artırılmasıyla “k”ncü bileşenin  $\dot{E}_{D,k}^{AV,EX}$  azaltılamaz.

“k”ncü bileşendeki toplam ekserji tahribatı, alternatif olarak birleştirilmiş kombinasyonlu ekserji tahribat parçalarını içeren şekliyle aşağıdaki gibi yazılır.

$$\dot{E}_{D,k} = \dot{E}_{D,k}^{UN,EN} + \dot{E}_{D,k}^{UN,EX} + \dot{E}_{D,k}^{AV,EN} + \dot{E}_{D,k}^{AV,EX} \quad (14)$$

Bu eşitlikteki ifadeler aşağıdaki gibi hesaplanmıştır (Balli, 2017), (Chen, 2014), (Gullo *vd*, 2016).

$$\dot{E}_{D,k}^{UN,EN} = \frac{\dot{E}_D^{UN} \dot{E}_D^{EN}}{\dot{E}_{D,gerçek}} \quad (15)$$

$$\dot{E}_{D,k}^{AV,EN} = \frac{\dot{E}_D^{AV} \dot{E}_D^{EN}}{\dot{E}_{D,gerçek}} \quad (16)$$

$$\dot{E}_{D,k}^{UN,EX} = \frac{\dot{E}_D^{UN} \dot{E}_D^{EX}}{\dot{E}_{D,gerçek}} \quad (17)$$

$$\dot{E}_{D,k}^{AV,EX} = \frac{\dot{E}_D^{AV} \dot{E}_D^{EX}}{\dot{E}_{D,gerçek}} \quad (18)$$

Literatürde, ileri ekserji analizinde sistemin her bir bileşeninin performanslarının iyileştirilmesinde  $\dot{E}_{D,k}^{AV,EN}$  ile  $\dot{E}_{D,k}^{AV,EX}$  bölünmüş parçalarına önem verilmesinin gerekliliği vurgulanmaktadır. İleri ekserji analizinde sistemi oluşturan bileşenler arasındaki ekserji tahribat etkileşimlerini daha iyi analiz edebilmek için, birleştirilmiş meksojen ekserji tahribatı tanımlanmıştır (Wang *vd*, 2019), (Balli, 2017), (Chen, 2014), (Liu *vd*, 2016), (Gullo *vd*, 2016).

#### Meksojen-ekserji-tahribatı $\dot{E}_{D,k}^{Mekso}$

$\dot{E}_{D,k}^{Mekso}$  Meksojen ekserji tahribatı, bileşenin eksojen ekserji tahribatı ile sistem içindeki diğer bileşenlerinden oluşan toplam eksojen ekserji tahribatının “k”ncü bileşene olan etkisi olarak tanımlanır.

$$\dot{E}_{D,k}^{Mekso} = \dot{E}_{D,k}^{EX} - \sum_{n \neq k}^n \dot{E}_{D,k}^{EX,n} \quad (19)$$

## HESAPLAMALAR

Termodinamiğin birinci ve ikinci kanunları ile literatürde tanımlanan ileri ekserji metodu sistem bileşenlerine ayrı ayrı yazılarak her bir bileşende oluşan enerji tahribatı miktarları nitel ve nicel olarak hesaplanmıştır. Ele alınan soğutma ünitesinin Termodinamik çevrimi T-s ve P-h diyagramlarında gerçek işletim parametrelerine göre ve tasarlanan termodinamik verilerine göre çizilerek Şekil 2.’de gösterilmiştir. Buhar sıkıştırırmalı soğutma ünitesinin üç ayrı termodinamik çevrimi:

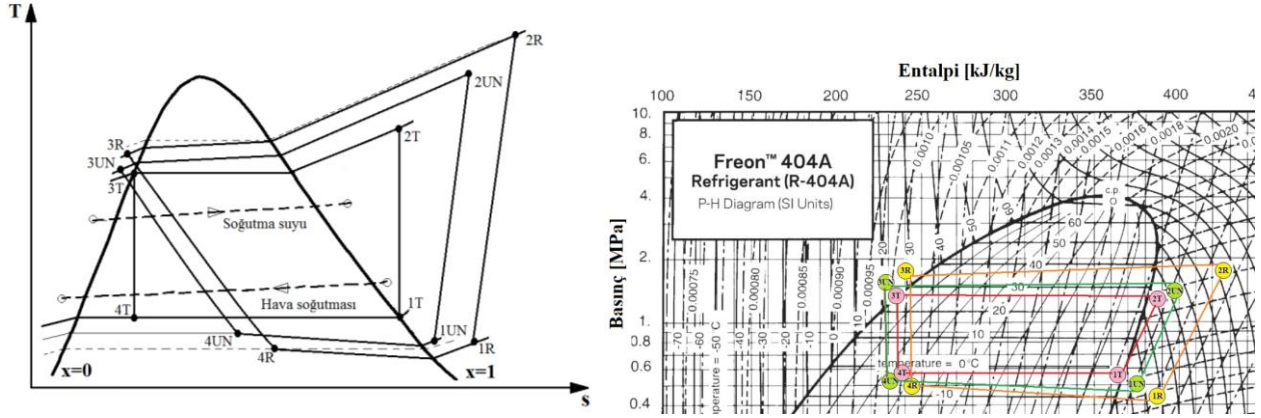
- 1- Gerçek verilere göre çizilen çevrim
- 2-Teknolojinin ulaşabileceği sınırları göz önüne alan termodinamik çevrim (kaçınılmaz çevrim)
- 3-Teorik (Tersinir) çevrim olarak ele alınmıştır.

İleri ekserji metodunda işletim parametreleri olarak kondensördeki ve evaporatördeki akışkan akımlarının minimum sıcaklık farkına göre termodinamik modeller geliştirilmiştir. Ele alınan gerçek ölçümler ve termodinamik model verileri Tablo 3.’de verilmiştir.



İleri ekserji analizinde çevrimin her bir bileşeninde oluşan  $\dot{E}_{D,k}^{EN}$  endojen ekserji tahribatının belirlenmesinde kullanılan dört ayrı çevrim Şekil 3.' de gösterilmiştir. Gerçek ve teorik modellerdeki çevrim noktalarına ait soğutucu akışkan R404a'nın, soğutma suyunun ve

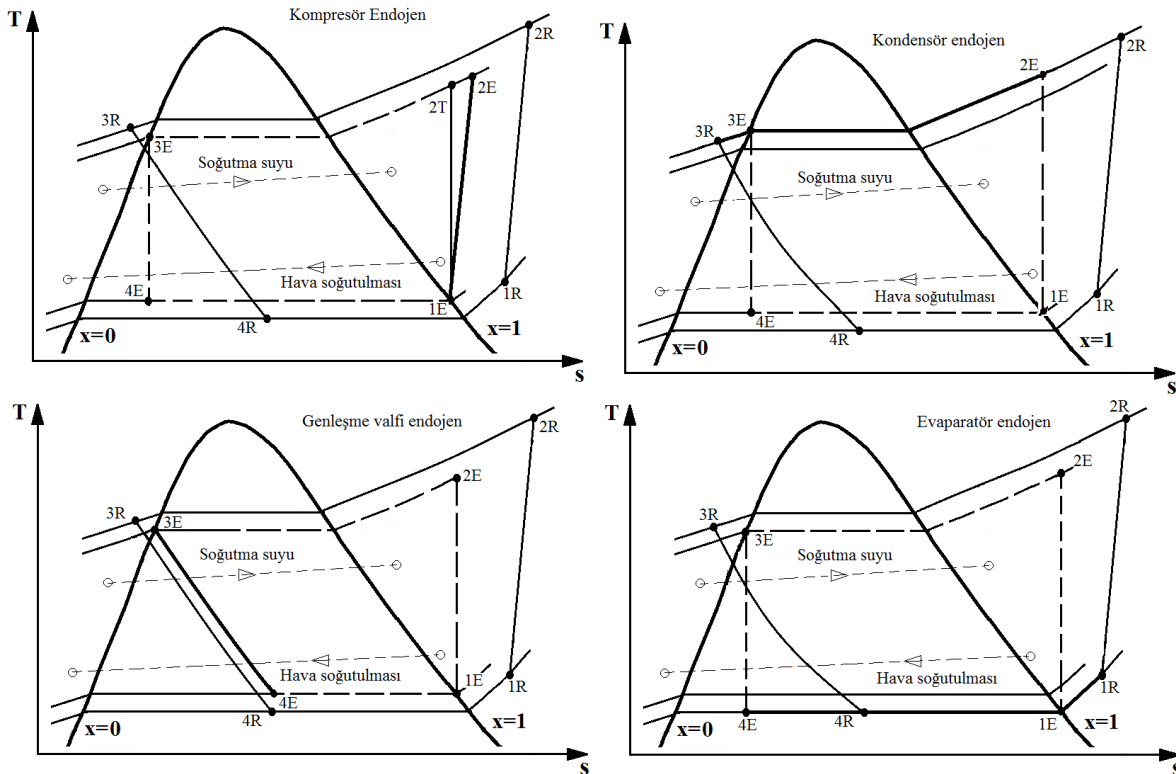
soğutma havasının termodinamik büyüklükleri hesaplanarak Tablo 4., Tablo 5. ve Tablo 6.' da verilmiştir.



Şekil 2. Çevrimlerin T-s ve P-h diyagramları (gerçek çevrim 1R-2R-3R-4R, kaçınılmaz çevrim, 1UN-2UN-3UN-4UN, teorik çevrim 1T-2T-3T-4T).

Tablo 3. Gerçek ve teorik çevrimler için çalışma şartları.

Parametreler	Gerçek çevrim şartları	Kaçınılmaz (UN) çevrim şartları	Teorik çevrim şartları
Basınç düşüleri $\Delta P$ [%]	1	1	0
Kondenser çıkışındaki minimum Sıcaklık farkı, $\Delta T$ [°]	13	0.5	0
Evaporatör çıkışındaki minimum Sıcaklık farkı, $\Delta T$ [°]	4	0.5	0
Kompresörün izantropik verimi, $\eta_{Kompresör}$ %	85	95	100
Kondensördeki R404a' nın yoğuşma sıcaklığı [°C]	39	26.5	26
Evaporatördeki R404a' nın yoğuşma sıcaklığı [°C]	-8.18	-4.68	-4.18
Kısımla süreci 3-4	Tersinmez	Tersinmez	Tersinir



Şekil 3. Soğutma ünitesinde her bir elemenda oluşan endojen ekserji tahribatı için kullanılan termodinamik çevrimler [8].

**Tablo 4.** Gerçek çevrimin termodinamik özellikleri.

Çevrim noktası	Akışkan	Termodinamik analiz					
		$\dot{m}$ [kg/s]	T [°C]	P [kPa]	h [kJ/kg]	s [kJ/kgK]	e [kJ/kg]
1	R404a	0.080	10.32	381.6	380.7	1.696	32.93
2	R404a	0.080	77	1790	426.2	1.73	68.75
3	R404a	0.080	30	1611	246.2	1.157	53.75
4 $x_4=0.328$	R404a	0.080	-8.18	424	246.2	1.176	48.51
$T_{su,g}$	Su	0.080	15	351	225.9	0.7549	0
$T_{su,ç}$	Su	0.080	26	101	272	0.8932	6.169
$T_{hava,g}$	Hava	2.161	0.06	101.3	3.76	-	0.764
$T_{hava,ç}$	Hava	2.161	-4.18	101.3	-0.818	-	1.058

**Tablo 5.** Kaçınılmaz çevrimin termodinamik özellikleri.

Çevrim noktası	Akışkan	Termodinamik analiz					
		$\dot{m}$ [kg/s]	T [°C]	P [kPa]	h [kJ/kg]	s [kJ/kgK]	e [kJ/kg]
1	R404a	0.0751	-3.68	468.5	366.5	1.632	37.26
2	R404a	0.0751	31.7	1160	387.1	1.62	61.35
3	R404a	0.0751	22	1160	233	1.114	52.94
4 $x_4=0.23$	R404a	0.0751	-4.68	520.5	233	1.13	50.27
$T_{su,g}$	Su	0.0751	15	351	225.9	0.7549	0
$T_{su,ç}$	Su	0.0751	26	101	272	0.8932	6.169
$T_{hava,g}$	Hava	2.16	0.06	101.3	3.76	-	0.764
$T_{hava,ç}$	Hava	2.16	-4.18	101.3	-0.818	-	1.058

**Tablo 6.** Teorik çevrimin termodinamik özellikleri.

Çevrim noktası	Akışkan	Termodinamik analiz					
		$\dot{m}$ [kg/s]	T [°C]	P [kPa]	h [kJ/kg]	s [kJ/kgK]	e [kJ/kg]
1	R404a	0.0768	-4.18	537.7	366.1	1.618	40.89
2	R404a	0.0768	29.7	1288	382	1.618	56.79
3	R404a	0.0768	26	1288	239.5	1.136	53.3
4 $x_4=0.24$	R404a	0.0768	-4.18	537.7	236.4	1.136	50.22
$T_{su,g}$	Su	0.0768	15	351	225.9	0.7549	0
$T_{su,ç}$	Su	0.0768	26	101	272	0.8932	6.169
$T_{hava,g}$	Hava	2.16	0.06	101.3	3.76	-	0.764
$T_{hava,ç}$	Hava	2.16	-4.18	101.3	-0.818	-	1.058

## BULGULAR VE TARTIŞMA

Literatürde sunulan yorumlar bu çalışmada yönlendirici olmuştur (Wang vd, 2019), (Chen 2014), (Fabrian vd, 2016), (Liu vd, 2016). Ekserji ve ileri ekserji metoduna göre göz önüne alınan soğutma sisteminde elde edilen gerçek çevrim verilerine göre yapılan çalışmadan elde edilen sonuçlar Tablo 7.' de verilmiştir. Tablo 7' de sunulan değerlere göre tüm sistemin ekserji verimi %18.12 olarak hesaplanmıştır.

Sistemin düşük performansla çalıştığı görülmektedir. Her bir bileşen kendi içinde değerlendirildiğinde kompresörün iyi çalıştığı buna karşılık en kötü performans kondensörde gözlemlenmiştir. Bunun nedeni olarak kondensörde soğutma suyu devresindeki basınç kayıplarının fazla olması gösterilebilir.

**Tablo 7.** Gerçek çevrime ait ekserji ve ekserji tahribatları.

Bil.	$\dot{E}_{Ex,yakıt}$ [kW]	$\dot{E}_{Ex,ürün}$ [kW]	$\dot{E}_{D,k}$ [kW]	$\epsilon$ [%]
CM	3.500	2.633	0.937	73.74
CD	1.103	0.3945	0.708	35.76
TV	1.001	0.616	0.385	61.54
EV	1.145	0.634	0.510	55.40
Top	4.964	0.634	2.969	18.12

Bu çalışmada soğutma sistemine uygulanan ekserji ve ileri ekserji metodundan elde edilen sonuçlar Tablo 8.' de verilmiştir. Bu tablo, her bir bileşende oluşan ekserji tahribatının, bölünmüş ekserji tahribatı parçalarının değerlerini içermektedir.

**Tablo 8.** İleri ekserji analizi-İki parçaya ayırıştırılan yaklaşım.

Bil.	$\dot{E}_{D, Gerçek}$ [kW]	$\dot{E}_{D, Teorik}$ [kW]	$\dot{E}_{D, k}^{UN}$ [kW]	$\dot{E}_{D, k}^{AV}$ [kW]	$\dot{E}_{D, k}^{EN}$ [kW]	$\dot{E}_{D, k}^{EX}$ [kW]
CM	0.937	0	0.319	0.617	0.353	0.584
CD	2.109	0.272	0.280	1.828	0.971	1.138
TV	0.385	0.235	0.280	0.104	0.258	0.127
EV	0.479	0.076	0.088	0.390	0.333	0.146
Top	2.969	0.583	0.969	1.999	1.915	1.054
%	100	19.66	32.64	67.35	64.49	35.50

Toplam sistem için ekserji tahribatı yüzdeleri karşılaştırıldığında,  $\dot{E}_{D, Gerçek}$  gerçek ekserji tahribatının % 100 değeri baz alındığında  $\dot{E}_{D, Teorik}$  teorik ekserji tahribat değerinin % 19.66 ve  $\dot{E}_{D, k}^{UN}$  önlenebilir ekserji tahribat değerinin ise % 32.64 olduğu Tablo 8.' de görülmektedir. Böylelikle gerçek çevrimi ile ele alınan termodinamik modellerle uzaklığı belirlenmiştir.  $\dot{E}_{D, k}^{AV}$  önlenebilir ekserji tahribat parçasının değerinin büyük olması, bileşenin performansının iyi olmadığını ve iyileştirme potansiyelinin gerekliliğini göstermektedir. Buna göre Tablo 8. incelendiğinde kompresörün, kondensörün  $\dot{E}_{D, k}^{AV}$  değerleri büyük olduğundan bu bileşenlerin iyileştirilme potansiyelinin olduğu bulunmuştur.  $\dot{E}_{D, k}^{UN}$  değerinin büyük olması teknolojik olarak bir geliştirme gerekliliğini gösterdiğinden; kompresörün ve kondensörün, genişleme valfinin  $\dot{E}_{D, k}^{UN}$  değerleri sırasıyla 0.319, 0.280 ve 0.280 kW olarak bulunduğundan, kompresör, kondensör ve genişleme valfinin teknolojik geliştirilmesi veya işletim şartlarının düzenlenmesi gerektiği bulunmuştur.  $\dot{E}_{D, k}^{EX}$  parçası incelendiğinde, bileşenler içinde en küçük değer evaporatör ve genişleme valfinde sırasıyla 0.127 kW ve 0.146 kW olarak görülmektedir. Bu verilere göre, diğer bileşenlerin evaporatöre tersinmezlik uygulamadığı sonucu çıkmaktadır. Böylelikle evaporatör testlerinden elde edilen sonuçların güvenilirliği elde edilmiştir.  $\dot{E}_{D, k}^{EN}$  Endojen ekserji parçası sistemdeki "k"nıncı bileşenin kendi içinde oluşan tersinmezliğini ifade ettiği için 0.971 kW değeri ile kondenserin teknolojik olarak iyileştirilmesi gerektiği sonucu çıkmaktadır.

Bu tablodan genel olarak, sistemin her bir bileşeninde oluşan  $\dot{E}_{D, k}^{EN}$  parçası, gerçek çevrimdeki her bir bileşende oluşan  $\dot{E}_{D, Gerçek}$  ekserji tahribatından küçük değerler aldığı görülmektedir. Kondensördeki ve evaporatördeki sıcak ve soğuk akışkan akımlarındaki minimum sıcaklık farklarının  $\dot{E}_{D, k}^{UN}$ ,  $\dot{E}_{D, Teorik}$  ile  $\dot{E}_{D, Gerçek}$  ekserji tahribatları karşılaştırıldığında  $\dot{E}_{D, Gerçek}$  gerçek ekserji tahribatının etkilerinin büyük kaldığı Tablo 7.' den görülmektedir. Bunun nedeni gerçek çevrimdeki tersinmezliklerin varlığından kaynaklanmaktadır.

Alt bölümlerine ayrılan ekserji tahribatı parçalarının, birleştirilmesi ile tanımlanan diğer ekserji tahribat parçaları ( $\dot{E}_{D, k}^{UN, EN}$ ,  $\dot{E}_{D, k}^{UN, EX}$ ,  $\dot{E}_{D, k}^{AV, EN}$ ,  $\dot{E}_{D, k}^{AV, EX}$ ) Tablo 9.' da değerleriyle birlikte sunulmuştur.

**Tablo 9.** İleri ekserji analizi metodunda birleştirilmiş yaklaşımı.

Bil.	$\dot{E}_{D, k}^{UN, EN}$ [kW]	$\dot{E}_{D, k}^{UN, EX}$ [kW]	$\dot{E}_{D, k}^{AV, EN}$ [kW]	$\dot{E}_{D, k}^{AV, EX}$ [kW]
CM	0.251	0.067	0.101	0.516
CD	0.649	-0.369	0.321	1.507
TV	0.286	-0.005	-0.028	0.132
EV	0.185	-0.096	0.147	0.242

Tablo 9. incelendiğinde,  $\dot{E}_{D, k}^{AV, EX}$  parçası kendi içerisinde karşılaştırıldığında kondensörün 1.507 kW değeri ile en büyük değeri aldığı görülmektedir. Kondensörün ve kompresörün dışında kalan diğer bileşenlerin yapısal iyileştirilmesi ve verimlerinin artırılmasıyla kondensörün ve kompresörün  $\dot{E}_{D, k}^{AV, EX}$  azaltılamaz. Yani kondensörün ve kompresörün iyileştirilmesi veya işletim performansının düzenlenmesi gerekmektedir. Bu sonuç yukarıdaki analiz sonuçları ile örtüşmektedir.

Tablo 9.'dan  $\dot{E}_{D, k}^{AV, EN}$  parçaları arasında kondensörün 0.321 kW olduğu sonucu çıkmıştır. Bu sonuç ile de kondensörün iyileştirilmesi gerektiği doğrulanmaktadır. Üniteden ele alınan bir bileşenin, ünitenin diğer bileşenlerinin etkilerinin oluşturduğu  $\dot{E}_{D, k}^{mekso}$  meksojen ekserji tahribatı paylaşım değerleri Tablo 10.' da verilmiştir.

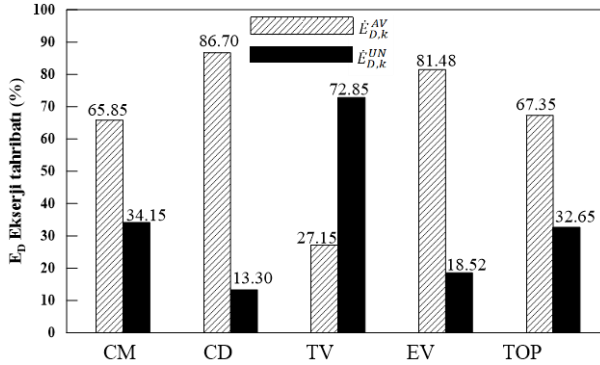
**Tablo 10.** Her bir bileşen için  $\dot{E}_{D, k}^{mekso}$  değerleri.

Bil.	$\dot{E}_{D, k}^{EX}$ [kW]	Etkili bileşen elemanı	$\dot{E}_{D, k}^{EX, r}$ [kW]
CM	0.937	CD	1.802
		EV	1.006
		TV	0.828
		<b>Mekso</b>	<b>-2.700</b>
CD	2.109	CM	-0.070
		EV	-0.590
		TV	-0.767
		<b>Mekso</b>	<b>3.541</b>
TV	0.385	CM	0.674
		EV	0.160
		CD	0.956
		<b>Mekso</b>	<b>-0.213</b>
EV	0.479	CM	0.758
		TV	0.066
		CD	0.104
		<b>Mekso</b>	<b>-1.384</b>

Tablo 10. incelendiğinde, en yüksek  $\dot{E}_{D, k}^{mekso}$  meksojen ekserji tahribatı 3.541 kW olarak kondensörde bulunmuştur.  $\dot{E}_{D, k}^{mekso}$  parçası tanımına göre yapılan bu analizde kondensörün sistem içerisinde iyileştirilmesi gereken bileşen olduğu tespit edilmiştir. Bu sonuç yukarıdaki ileri ekserji analiz sonuçlarıyla da desteklenmektedir.

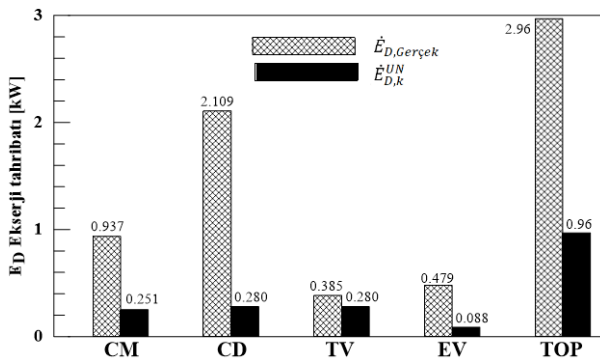
Şekil 4.' de ünitadaki her bir bileşende oluşan  $\dot{E}_{D, k}^{AV}$  parçası ve  $\dot{E}_{D, k}^{UN}$  parçasının toplam ekserji tahribatına oranı verilmiştir. Sistem bileşenlerinde oluşan  $\dot{E}_{D, k}^{AV}$  parçasının en küçük kısmı genişleme valfinde gerçekleştiği görülmektedir. Bu çalışmada kompresörün verimi %85 alınmıştır. Teknolojik verimliliği yüksek

olan kompresör kullanılması gerektiği ortaya çıkmaktadır. Benzer trend kondensör ve evaporatörde görülmektedir. Buna göre kondensörün yanında test yapılan evaporatöründe iyileştirme potansiyelinin var olacağı görülmektedir.



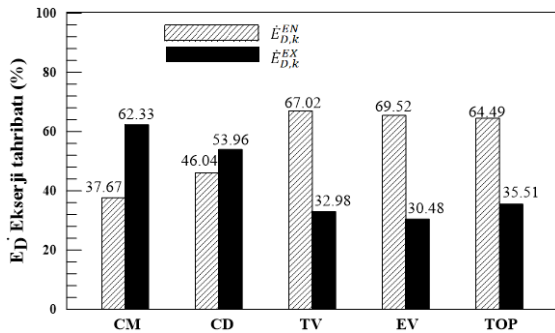
Şekil 4. Her bir ünite de oluşan  $\dot{E}_{D,k}^{AV}$  ve  $\dot{E}_{D,k}^{UN}$  parçasının toplam ekserji tahribatına oranı.

$\dot{E}_{D, Gerçek}$  ve  $\dot{E}_{D,k}^{UN}$  çevrimlerdeki bileşenlerde oluşan ekserji tahribatının karşılaştırılması Şekil 5.' de verilmiştir. Gerçek çevrim ile teknolojik limitleri kullanan çevrim arasındaki ayrıcalık Şekil 5.' de görülmektedir. Bu şekle göre  $\dot{E}_{D,k}^{UN}$  kondensördeki bugünün teknoloji şartlarına göre kalıcı ekserji tahribatı 0.192 kW değeri bulunmuştur.



Şekil 5.  $\dot{E}_{D, Gerçek}$  ve  $\dot{E}_{D,k}^{UN}$  parçalarının her bir bileşen için karşılaştırılması.

Şekil 6. da her bir ünite de oluşan  $\dot{E}_{D,k}^{EN}$  ve  $\dot{E}_{D,k}^{EX}$  parçalarının toplam ekserji tahribatına oranı verilmiştir. Şekil 6 incelendiğinde evaporatörün sistemde önemli bir tersinmezlik kaynağı oluşturmadığı görülmektedir.



Şekil 6. Her bir ünite de oluşan  $\dot{E}_{D,k}^{EN}$  ve  $\dot{E}_{D,k}^{EX}$  parçalarının toplam ekserji tahribatına oranı.

## SONUÇLAR

Sistem bileşenlerinin ileri ekserji analizinden elde edilen sonuçlar aşağıda belirtilmiştir.

- Eşitlik 14. verilen  $\dot{E}_{D,k}^{Mekso}$  tanımına göre kondensörde hesaplanan  $\dot{E}_{D,k}^{EX}$  parçası, diğer bileşenlerde oluşan toplam  $\sum_{n=1, n \neq k}^n \dot{E}_{D,k}^{EX,n}$  parçası büyük olduğundan kondensörün teknolojik yenilenmesi veya işletim şartlarının yenilenmesi gerekmektedir.
- Evaporatörün  $\dot{E}_{D,k}^{AV,EN}$  ve  $\dot{E}_{D,k}^{EN}$  değerlerinin küçük olması performansının iyi olduğunun göstergesidir. Diğer bir deyişle test ünitesinin termodinamik limitlere göre iyi çalıştığı ve evaporatör test sonuçlarına sistemdeki diğer bileşenlerin tersinmezlikler uygulamadığı görülmüştür.

## TEŞEKKÜR

DeneySEL verileri paylaşan Friterm firmasına, Dr. Hüseyin ONBAŞIOĞLU'nun bu çalışmaya yaptıkları değerli katkı ve önerilerine ayrıca, bu çalışmaya olanak sağlayan Prof. Dr. Seyhan UYGUR ONBAŞIOĞLU'na katkılarından dolayı teşekkürlerimi sunarım.

## KAYNAKLAR

Azizi T., Boyarhchihi F.A., 2014, Assessment of a Real Combined Cycle Power Plant with Supplementary Firing Based on Advanced Exergy/Exergoeconomic Methods. *Iranian Journal of Mechanical Engineering*, Vol. 15, No. 2.

Bai T., Yu J., Yan G., 2016, Advanced exergy analysis of an ejector expansion transcritical CO<sub>2</sub> refrigeration system, *Energy Conversion and Management*, 126, 850-861.

Balli O., 2017, Advanced exergy analysis to evaluate the performance of a military aircraft turbojet engine (TJE) with afterburner system: Splitting exergy destruction into unavoidable/avoidable and endogenous/exogenous, *Applied Thermal Engineering*, 111, 152-169.

Chen J., 2014, *Investigation of vapour ejectors in heat driven ejectors refrigeration system*. Ph.D. Thesis, Division of applied thermodynamics and refrigeration department of energy technology, Royal Enstitute of technology, KTH, SE-100 44 Stockholm, Sweden.

Fabrian B., Toung-Wang N., Kjean J.J., and Brian E., 2016, Energy, exergy and advanced exergy analysis of a milk processing factory, *Proceedings of ECOS, The 29th International conference on efficiency, cost, optimization, simulation and environmental impact of energy system*, 1-13.

Ghorbani B., Roshani H., 2018, Advanced exergy and exergoeconomic analysis of the integrated structure of simultaneous production of NGL recovery and liquefaction. *Trans Phenom Nano Micro Scales*, 6(Specials):8-14. Doi: 0 22111/tpnms.

- Gullo P., Hafner A., and Banasiak K., 2019, Thermodynamic Performance Investigation of Commercial R744 Booster Refrigeration Plants Based on Advanced Analysis, *Energies*, 354; doi:10.3390/en12030354.
- Gullo P., Elmegaard B., Cortell G., 2016, Advanced exergy analysis of a R744 booster refrigeration system with paralel compression, *Energy*, Doi:10.1016/j.energy.2016.04.043
- Kelly S., Tsatsaronis G., Morosuk T., 2009, Advanced exergetic analysis: Approaches for splitting the exergy destruction into endogenous and exogenous parts, *Energy*, 34 (2009) 384–391.
- Kotas T.J., 1985, *The exergy method of thermal plant analysis*. Anchor Brendon Ltd.
- Liu H., He Q., Saeed S.B., 2016, Thermodynamic analysis of a compressed air energy storage system through advanced exergetic analysis, *Journal of Renewable and Sustainable Energy*, 8, 1-17, 034101.
- Özgür A.E., Kabul A., Kizikan Ö., 2014, Exergy analysis of refrigeration systems using an alternative refrigerant (hfo-1234yf) to R-134a, *International Journal of Low-Carbon Technologies*, 9, 56–62.
- Şöhret Y., Açikkalp E., Hepbaşlı A., Karakoç TH., 2015, Advanced exergy analysis of an aircraft gas turbine engine: Splitting exergy destructions into parts. *Energy*, 90, 1219-1228.
- Tsatsaronis G., Morosuk T., 2012, Advanced thermodynamic (exergetic) analysis, *6<sup>th</sup> European Thermal Science Conferance (Eurotherm 2012) Journal of Physics Conferance Series* 395, 012160. doi:10.1088/1742-6596/395/1/012160.
- Vuckovic G.D., Vukic M.V., Stojiljkovic M.M., Vuckovic. D.D., 2012, Avoidable and Unavoidable Exergy Destruction and Exergoeconomic Evaluation of the Thermal Processes in a RealIndustrial Plant, *Thermal science*, Vol. 16, Suppl. 2, pp. S493-S506.
- Wang L., Yang Z., Sharama S., Mian A., Lin T E., Tsatsaronis T., Marechal F. And Yang Y., 2019, A Review of Evaluation, Optimization and Synthesis of Energy Systems: Methodology and Application to Thermal Power Plants., *Energies*, 12, 73; doi:10.3390/en12010073.

# ISI BİLİMİ VE TEKNİĞİ DERGİSİ İÇİN MAKALE HAZIRLAMA ESASLARI

Isı Bilimi ve Tekniği Dergisi'nde, ısı bilimi alanındaki özgün teorik ve deneysel çalışmaların sonuçlarının sunulduğu makaleler ve yeterli sayıda makaleyi tarayarak hazırlanmış olan literatür özeti makaleler yayınlanmaktadır. Makaleler, Türkçe veya İngilizce olarak kabul edilmektedir. Makaleler ilk sunumda serbest formatta hazırlanabilir. Ancak yayın için kabul edilmiş olan makaleler dergimizin basım formatına tam uygun olarak yazarlar tarafından hazırlanmalıdır. Aşağıda, ilk sunuş ve basıma hazır formatta makale hazırlamak için uyulması gereken esaslar detaylı olarak açıklanmıştır.

## İLK SUNUŞ FORMATI

İlk sunuşta, makale A4 boyutundaki kağıda tek sütun düzeninde, 1.5 satır aralıklı ve sayfa kenarlarından 25'er mm boşluk bırakılarak yazılmalıdır. Yazı boyutu 11 punto olmalı ve **Times New Roman** karakter kullanılmalıdır. Şekiller, tablolar ve fotoğraflar makale içinde **olmaları gereken yerlere** yerleştirilmelidir. Makale, elektronik olarak editörün e-posta adresine gönderilmelidir.

## BASIMA HAZIR MAKALE FORMATI

Hakem değerlendirmelerinden sonra, yayın için kabul edilmiş olan makaleler, dergimizin basım formatına tam uygun olarak yazarlar tarafından hazırlanmalıdır. Makaleler yazarların hazırladığı haliyle basıldığı için, yazarların makalelerini basım için hazır formatta hazırlarken burada belirtilen esasları titizlikle takip etmeleri çok önemlidir. Aşağıda, basıma hazır formatta makale hazırlamak için uyulması gereken esaslar detaylı olarak açıklanmıştır.

### Genel Esaslar

Makaleler genel olarak şu başlıklar altında düzenlenmelidir: Makale başlığı (title), yazar(lar)ın ad(lar)ı, yazar(lar)ın adres(ler)i, özet (abstract), anahtar kelimeler (keywords), semboller, giriş, materyal ve metod, araştırma sonuçları, tartışma ve sonuçlar, teşekkür, kaynaklar, yazarların fotoğrafları ve kısa özgeçmişleri ve ekler. Yazılar bilgisayarda tek satır aralıklı olarak, 10 punto Times New Roman karakteri kullanılarak Microsoft Office Word ile iki sütun düzeninde yazılmalıdır. Sayfalar, üst kenardan 25 mm, sol kenardan 23 mm, sağ ve alt kenarlardan 20 mm boşluk bırakılarak düzenlenmelidir. İki sütun arasındaki boşluk 7 mm olmalıdır. Paragraf başları, sütunun sol kenarına yaslanmalı ve paragraflar arasında bir satır boşluk olmalıdır.

Birinci seviye başlıklar büyük harflerle kalın olarak, ikinci seviye başlıklar bold ve kelimelerin ilk harfleri büyük harf olarak ve üçüncü seviye başlıklar sadece ilk harfi büyük olarak yazılır. Bütün başlıklar sütunun sol kenarı ile aynı hizadan başlamalıdır ve takip eden paragrafla başlık arasında bir satır boşluk olmalıdır. Şekiller, tablolar, fotoğraflar v.b. metin içinde ilk atıf

yapılan yerden hemen sonra uygun şekilde yerleştirilmelidir. İlk ana bölüm başlığı, Özetten (Abstract'tan) sonra iki satır boşluk bırakılarak birinci sütuna yazılır.

### Başlık, Yazarların Adresi, Özet, Abstract ve Anahtar Kelimeler

Yazılar Türkçe veya İngilizce olarak hazırlanabilir. Her iki durumda da makale özeti, başlığı ve anahtar kelimeler her iki dilde de yazılmalıdır. Eğer makale Türkçe olarak kaleme alınmışsa, Türkçe başlık ve özet önce, İngilizce başlık ve Özet (Abstract) sonra yazılır. Eğer makale İngilizce olarak kaleme alınmışsa önce İngilizce başlık ve özet (abstract) sonra Türkçe başlık ve özet yazılır. Başlık, sayfanın üst kenarından 50 mm aşağıdan başlar ve kalın olarak 12 punto büyüklüğünde, büyük harflerle bütün sayfayı ortalayacak şekilde yazılır. Yazar(lar)ın adı, adresi ve elektronik posta adresi başlıktan sonra bir satır boşluk bırakılarak yazılmalıdır. Yazarların adı küçük, soyadı büyük harflerle yazılmalı ve bold olmalıdır. Yazarların adresinden sonra üç satır boşluk bırakılarak, Özet ve Abstract 10 punto büyüklüğünde bütün sayfa genişliğinde yazılır. Özet ve Abstracttan sonra anahtar kelimeler (Keywords) yazılır.

### Birimler

Yazılarda SI birim sistemi kullanılmalıdır.

### Denklemler

Denklemler, 10 punto karakter boyutu ile bir sütuna (8 cm) sığacak şekilde düzenlenmelidir. Veriliş sırasına göre yazı alanının sağ kenarına yaslanacak şekilde parantez içinde numaralanmalıdır. Metin içinde, denklemlere '**Eş. (numara)**' şeklinde atıfta bulunulmalıdır.

### Şekiller

Şekiller 8 cm (bir sütun) veya 16 cm (iki sütun) genişliğinde olmalıdır ve makale içerisinde olmaları gereken yerlere bilgisayar ortamında sütunu (veya bütün sayfa genişliğini) ortalayacak şekilde yerleştirilmelidir. Şekil numaraları (sıra ile) ve isimleri şekil **altına, 9 punto büyüklüğünde** yazılmalıdır.

## Tablolar

Tablolar 8 cm (bir sütun) veya 16 cm (iki sütun) genişliğinde olmalıdır. Makale içerisinde olmaları gereken yerlere bilgisayar ortamında sütunu (veya bütün sayfa genişliğini) ortalayacak şekilde yerleştirilmelidir. Tablo numaraları (sıra ile) ve isimleri tablo **üstüne, 9 punto büyüklüğünde** yazılmalıdır.

## Fotograflar

Fotograflar, siyah/beyaz ve 8 cm (bir sütun) veya 16 cm (iki sütun) genişliğinde olmalıdır. Fotograflar digitize edilerek, makale içinde bulunmaları gereken yerlere bilgisayar ortamında sütunu (veya bütün sayfa genişliğini) ortalayacak şekilde yerleştirilmelidir ve şekil gibi numaralandırılmalı ve adlandırılmalıdır.

## Yazar(lar)ın Fotoğraf ve Kısa Özgeçmişleri

Yazarların fotoğrafları digitize edilerek, makalenin en sonuna özgeçmişleri ile birlikte uygun bir şekilde yerleştirilmelidir.

## SEMBOLLER

Makale içinde kullanılan bütün semboller alfabetik sırada Özetten sonra liste halinde tek sütun düzeninde yazılmalıdır. Boyutlu büyüklükler birimleri ile birlikte ve boyutsuz sayılar (Re, Nu, vb.) tanımları ile birlikte verilmelidir.

## KAYNAKLAR

Kaynaklar metin sonunda, ilk yazarın soyadına göre alfabetik sırada listelenmelidir. Kaynaklara, yazı içinde, yazar(lar)ın soyad(lar)ı ve yayın yılı belirtilerek atıfta

bulunulmalıdır. Bir ve iki yazarlı kaynaklara, her iki yazarın soyadları ve yayın yılı belirtilerek (Bejan, 1988; Türkoğlu ve Farouk, 1993), ikiden çok yazarlı kaynaklara ise birinci yazarın soyadı ve "vd." eki ve yayın yılı ile atıfta bulunulmalıdır (Ataer vd, 1995). Aşağıda makale, kitap ve bildirilerin kaynaklar listesine yazım formatı için örnekler verilmiştir.

Ataer Ö. E., Ileri A. and Göğüş, Y. A., 1995, Transient Behaviour of Finned-Tube Cross-Flow Heat Exchangers, *Int. J. Refrigeration*, 18, 153-160.

Bejan A., 1998, *Advanced Engineering Thermodynamics* (First Ed.), Wiley, New York.

Türkoğlu H. and Farouk B., 1993, Modeling of Interfacial Transport Processes in a Direct-Contact Condenser for Metal Recovery, *Proc. of 73<sup>rd</sup> Steel Making Conference*, Detroit, 571-578.

Türkoğlu H., 1990, *Transport Processes in Gas-Injected Liquid Baths*, Ph.D. Thesis, Drexel University, Philadelphia, PA, USA.

İnternet, 2004, Türkiye İstatistik Kurumu, *Atıksu İstatistikleri*, <http://www.tuik.gov.tr/HaberBulteni>.

## DIĞER HUSUSLAR

Hakem değerlendirmesinden sonra kabul edilen makaleler, yukarıda açıklandığı şekilde dizilerek basıma hazırlandıktan sonra, bir elektronik kopyası editöre gönderilmelidir. Makalenin basıma hazır kopyası ile birlikte, "Telif Hakkı Devri Formu" da doldurularak gönderilmelidir. Telif Hakkı Devri Formu'na ve bu yazım klavuzuna [www.tibt.org.tr](http://www.tibt.org.tr) adresinden ulaşılabilir.



**TÜRK ISI BİLİMİ VE TEKNİĞİ DERNEĞİ**  
**ÜYELİK BAŞVURU FORMU**

FOTOĞRAFINIZ

A. Adınız Soyadınız :  
Ünvanınız :  
Doğum yeri : : Doğum tarihi: / / 19 T.C. Kimlik No:  
İş Adresiniz :  
Ev adresiniz :  
Telefonunuz : İş Ev Cep  
E-posta :

B. \*Derneğe Asil üye Fahri üye olmak istiyorum.

1. Sizi tanıyan dernek üyesi (Üyelik için) :

2. Mezun olduğunuz  
Yüksek Okullar Yıl Branşınız Ünvanınız

3. İlgilendiğiniz konular :

2015 yılı aidatı olarak toplam 25 YTL (Yirmibeş Milyon TL) derneğin

İş Bankası Maltepe Şubesi Hesap No: 42120867567  
IBAN: TR08 0006 4000 0014 2120 8675 67

hesabına yatırılmıştır.

Tarih :

İmza :

\* Asil üye olmak için beş yıllık deneyim gereklidir.  
Fahri üyelik için yüksekokul mezunu olma şartı yoktur.



Türk Isı Bilimi ve Tekniđi Derneđi  
Gazi Üniversitesi  
Mühendislik Fakültesi  
Makina Mühendisliđi Bölümü  
06570 Maltepe/ ANKARA

<b>Releasing Hydrogen from NABH<sub>4</sub> via Hydrogel Based CoF<sub>2</sub> Catalyst</b>	<b>1</b>
<i>Hidrojel Esaslı CoF<sub>2</sub> Katalizör İle NABH<sub>4</sub>'den Hidrojen Salınımı</i>	
Tuğba AKKAŞ BOYNUEĞRİ and Metin GÜRÜ	
<b>Performance and Emission Characteristics of Pyridine and Isobutanol Added Gasoline-Ethanol-Water Blends in A Single Cylinder SI Gasoline Engine</b>	<b>11</b>
<i>Piridin ve İzobütanol Katkılı Benzin-Etanol-Su Karışımlarının Tek Silindirli Benzin Motorundaki Performans ve Emisyonlarının İncelenmesi</i>	
Amirkhan GARAYEV, Silver GÜNEŞ and Çiğdem GÜLDÜR	
<b>Design and Optimization of PCM-Air Cold Energy Storage Device to Be Used For Peak Electricity Shaving</b>	<b>23</b>
<i>Elektrikte PİK Talebi Törpüleme İçin Kullanılacak FDM-Hava Soğuk Enerji Depolama Cihazı Tasarımı ve Optimizasyonu</i>	
Göker TÜRKAKAR	
<b>Computational Analysis of Pulverized Coal Co-Firing with Biomass in 150MWe Unit Of Tuncbilek Thermal Power Plant</b>	<b>37</b>
<i>Tunçbilek Termik Santralinin 150MWe Ünitesinde Pülverize Kömürün Biyokütle İle Eş Yanmasının Hesaplamalı Analizi</i>	
Cansu DENİZ CANAL, Yakup Erhan BOKE, Ozer AYDIN and Ali Cemal BENİM	
<b>Analytical and Numerical Analyses of the Heat Conduction of Carbon Nanotubes Under Applied Voltages</b>	<b>51</b>
<i>Karbon Nanotüplerin Isı İletiminin Uygulanan Voltajlar Altında Analitik ve Sayısal Analizi</i>	
Yahya ÖZ	
<b>Numerical Investigation of Non-Premixed Combustion Inside a Three Layered Porous Burner with Flamelet Model</b>	<b>63</b>
<i>Üç Katmanlı Gözenekli Yakıcıda Ön Karışimsız Yanmanın Flamelet Modeli İle Sayısal İncelenmesi</i>	
Tanju ERGEN, Tamer ŞENER, Onur TUNCER and A. Cihat BAYTAŞ	
<b>SU<sup>2</sup> Real Gas Models' Performance Predictions on a Cold Gas Thruster</b>	<b>77</b>
<i>SU<sup>2</sup> Gerçek Gaz Modellerinin Soğuk Gaz İtici Performans Tahminleri</i>	
Aysu ÖZDEN, Özgür Uğraş BARAN, Mehmet Halük AKSEL ve Mehmet Ali AK	
<b>A Numerical Investigation of Nanofluid Flow in Rectangular Finned Microchannel</b>	<b>89</b>
<i>Kanatçıklı Dikdörtgen Kesitli Mikrokanalda Nanoakışkan Akışının Sayısal İncelenmesi</i>	
Halime ÇELİK* and Nezaket PARLAK	
<b>A Comparative Study of Diffusion, Thermal Wave and Dual-Phase-Lag Heat Conduction in Thin Layer</b>	<b>101</b>
<i>İnce Tabakada Difüzyon, Termal Dalga ve Çift Fazlı-Lag Isı İletiminin Karşılaştırmalı Bir Çalışması</i>	
R. YUVARAJ and D. SENTHILKUMAR	
<b>Çift Kabuk Cephe Sisteminin Bina Isıl Performansına Etkisinin Deneysel ve Sayısal Olarak İncelenmesi</b>	<b>119</b>
<i>Experimental and Analytical Examination of the Effect of Double Skin Facade System on Building Thermal Performance</i>	
Selin HÜLAGÜ, Türkan GÖKSAL ÖZBALTA ve Tahsin BAŞARAN	
<b>Effective Flow Control Around a Circular Cylinder by Using Both a Splitter Plate and Plasma Actuators as Passive and Active Control Methods</b>	<b>133</b>
<i>Pasif ve Aktif Kontrol Yöntemleri Olarak Hem Bir Ayırıcı Plaka Hem de Plazma Aktüatörler Kullanılmasıyla Dairesel Bir Silindir Etrafında Etkili Akış Kontrolünün Sağlanması</i>	
Hürrem AKBIYIK and Yahya Erkan AKANSU	
<b>Nodal Thermodynamic and Dynamic Analysis of a Free Displacer Stirling Engine</b>	<b>141</b>
<i>Serbest Displeysızlı Bir Stirling Motorunun Nodal Termodinamik ve Dinamik Analizi</i>	
Can CINAR, A. Onur OZDEMİR, Halit KARABULUT and Mesut DUZGUN	
<b>Buhar Sıkıştırma Soğutma Test Ünitesine İleri Ekserji Metodunun Uygulanması</b>	<b>157</b>
<i>Application of Advanced Exergy Method to the Vapor Compression Cooling Test Unit</i>	
Betül SARAÇ	